# Determination of the spatial and temporal variability of size-resolved $PM_{2.5}$ composition and mixing state in multiple regions in California

Final Report to California Air Resources Board
Contract No. 04-336
Prepared for the California Air Resources Board

December 1, 2009

*Principal Investigator*
Kimberly Prather

*Contributors*
Andrew P. Ault
Stephen M. Toner
Laura G. Shields
Xueying Qin
Kerri A. Pratt
Jessie M. Creamean
Margaret Yandell
Cassandra J. Gaston
Meagan J.K. Moore

Department of Chemistry & Biochemistry
University of California San Diego
9500 Gilman Drive MC 0314
La Jolla, CA 92093-0314

# DISCLAIMER

The statements and conclusions in this Report are those of the contractor and not necessarily those of the California Air Resources Board. The mention of commercial products, their source, or their use in connection with material reported herein is not to be construed as actual or implied endorsement of such products.

# ACKNOWLEDGEMENTS

We thank the following people for their contributions to the research described in this report:

Ms. Melanie Zauscher
Dr. Matt Spencer
Dr. Ryan Moffet
Dr. Ryan Sullivan
Dr. Robert Moison
Dr. Hiroshi Furutani
Dr. Thomas Rebotier

and thank Drs. Eileen McCauley and William Vance (CARB) for their assistance and advice during this contract.

This Report was submitted in fulfillment of Contract No. 04-336, “Determination of the spatial and temporal variability of size-resolved PM2.5 composition and mixing state in multiple regions in California” under the sponsorship of the California Air Resources Board. Work was completed as of October 13, 2009.

# TABLE OF CONTENTS

DISCLAIMER ..... ii
ACKNOWLEDGEMENTS ..... iii
TABLE OF CONTENTS ..... iv
LIST OF FIGURES ..... ix
LIST OF TABLES ..... xviii
ABSTRACT ..... xix
EXECUTIVE SUMMARY ..... xx
Background ..... xx
Methods ..... xx
Results and Conclusions ..... xxi
Body of Report ..... 1
I. Introduction ..... 1
1. Research Objectives and Studies Conducted ..... 1
2. Instrumentation ..... 2
3. Data Analysis Methods ..... 4
4. Summary of Chapters ..... 5
*i. Introduction ..... 5*
*ii. Time and Size Resolved Chemical Composition Measurements Detailing Short Term Changes in Composition ..... 5*
*iii. Spatial Variability of Particulate Matter and Sources ..... 6*
*iv. Seasonal and Interannual Variability in Particulate Matter Size and Composition ..... 7*
*v. Mass Comparisons and Investigations into the Volatile and Semivolatile Fraction of Particles ..... 9*
*vi. Changes in the Size-Resolved Particle Composition Linked with Meteorological Measurements and Air Mass Back Trajectories to Increase Understanding of Sources and Secondary Contributions to Particulate Matter ..... 10*
*vii. Development of Source Apportionment Algorithms ..... 11*
II. Objectives and Results ..... 13
Time and Size Resolved Chemical Composition Detailing Short Term Changes in Composition ..... 13
*1. Detection of ambient ultrafine aerosols by single particle techniques during the SOAR 2005 campaign ..... 13*
i. Introduction ..... 13
ii. Experimental ..... 14
iii. Results and discussion ..... 16
a. Ambient measurements ..... 16
b. Afternoon photochemical events ..... 23
c. Seasonal differences ..... 25
d. Comparison of ultrafine particle measurements ..... 27
iv. Acknowledgements ..... 28
*2. Characterization of the Single Particle Mixing State of Individual Ship Plume Events measured at the Port of Los Angeles ..... 29*
i. Introduction ..... 29
ii. Experimental ..... 29
a. Sampling Information ..... 29
b. Gas and Particle Peripheral Instrumentation ..... 30
c. Aerosol Time-of-Flight Mass Spectrometry (ATOFMS) ..... 30
d. Single Particle Analysis ..... 30
iii. Results and Discussion ..... 30
a. Ship Identification ..... 30
b. Plume Characterization ..... 32
c. In Plume Gas Phase Chemistry and Concentrations ..... 33
d. Unique Plume Chemistry ..... 34
e. Details on the OC-V-sulfate and Fresh Soot Particle Types ..... 36

f. Description of the Ca-ECOC Particle Type ....38
g. Background Particle Types During Plumes....39
h. Temporal Trends ....41
i. Size-resolved Chemistry....42
j. Correlation between sulfate and vanadium particle....43
iv. Acknowledgements....45
Spatial Variability of Particulate Matter and Sources....46
*3. Mobile Laboratory Observations of Temporal and Spatial Variability within the Coastal Urban Aerosol....46*
i. Introduction....46
ii. Experimental....47
a. Mobile ATOFMS Laboratory....47
b. 2009 San Diego Bay Measurements....47
c. Instrumentation....49
d. Aerosol Time-of-Flight Mass Spectrometry....50
e. Single Particle Data Analysis ....50
f. Scaling Single Particle Measurements to Mass Concentrations....50
iii. Results and Discussion ....51
a. Temporal Patterns of Meteorological and Gas Phase Concentrations ....51
b. Variability of Particle Mass and Number Concentrations ....53
c. Variation in Aerosol Size Distributions....55
d. Differing Aerosol Sources Determined by Particle Chemistry....57
e. Differences in Particle Aging and Mixing State ....59
f. Variations in Chemistry and Implications for Models and Regulations....61
iv. Acknowledgements....62
Season and Interannual Variability in Particulate Matter Size and Composition ....63
*4. Single Particle Characterization in Riverside, CA during the SOAR 2005 Campaign: Seasonal Comparisons....63*
i. Introduction....63
ii. Experimental....64
a. SOAR Campaign ....64
c. ATOFMS Data Analysis....65
iii. Results and Discussion ....66
a. $PM_{2.5}$ Concentrations ....67
b. Chemical Composition of ART-2a Clusters....68
c. SOAR-I Diurnal Variation....72
d. SOAR-II Episodic Variations....76
e. SOAR-I and SOAR-II Comparison ....80
iv. Acknowledgements....83
*5. Seasonal Volatility Dependence of Ambient Particle Phase Amines ....85*
i. Introduction....85
ii. Experimental....86
a. Ambient Measurements ....86
b. Amine Mass Calibration....88
iii. Results and Discussion ....94
iv. Acknowledgements....103
*6. Inter-annual Comparison of Ambient, Single-Particle Chemical Mixing State in Riverside, CA..104*
i. Introduction....104
ii. Experimental....105
iii. Results and Discussion ....106
a. Impact of meteorology on particulate mass concentrations....106
b. Overall submicron aerosol chemical composition....110
c. Assessment of single-particle mixing state and particle aging ....110
d. Relating particle chemistry to meteorology and $PM_{2.5}$ mass concentrations....113
iv. Conclusions....117
v. Acknowledgements....118

Mass Comparisons and Investigations into the Volatile and Semivolatile Fraction of Particles .....120
*7. Comparison of Two Methods for Obtaining Quantitative Mass Concentrations from Aerosol Time-of-Flight Mass Spectrometry Measurements*.....*120*
i. Introduction.....120
ii. Experimental.....121
a. ATOFMS Data Acquisition.....121
b. MOUDI Measurements.....122
c. APS Measurements.....122
iii. Results and Discussion.....122
a. Scaling with MOUDI.....122
b. Scaling with the APS.....128
c. $PM_{2.5}$ Measurement Intercomparison.....134
iv. Conclusions.....136
v. Acknowledgements.....137
*8. The Effect of APS Scaling Functions on the Quantification of Aerosol Time-of-Flight Mass Spectrometry Measurements*.....*138*
i. Introduction.....138
ii. Experimental.....139
a. CRPAQS ATOFMS Measurements and Data Analysis.....139
b. Reference Studies with APS Scaling Functions.....140
c. The Calculation of the Scaling Functions in Reference Studies.....141
iii. Results and Discussion.....141
a. Scaling Curves and Scaling Functions.....141
b. Major Particle Types in CRPAQS.....142
c. Scaled ATOFMS Mass Concentrations.....144
d. APS Scaled Particle Mass Fraction.....146
iv. Conclusions.....148
v. Acknowledgements.....149
Changes in Size-Resolved Particle Composition Linked with Meteorology Measurements and Air Mass Back Trajectories to Increase Understanding of Sources and Secondary Contributions to Particulate Matter.....150
*9. Characterization of trace metals in single urban particles during the SOAR 2005 campaign*.....*150*
i. Introduction.....150
ii. Experimental.....151
a. Sampling Location.....151
b. Instrumentation.....151
c. Data analysis.....151
iii. Results and Discussion.....152
iv. Acknowledgements.....165
*10. Impact of Emissions from the Los Angeles Port Region on San Diego Air Quality During Regional Transport Events*.....*166*
i. Introduction.....166
ii. Experimental.....166
a. Scripps Institution of Oceanography of Pier 2006 Study.....166
b. Real-Time Single Particle Mass Spectrometry.....167
c. Data Analysis.....167
d. Scaling ATOFMS to Mass Concentrations.....167
iii. Results and Discussion.....168
a. Mass Concentrations Across San Diego County.....170
b. Identification of Regional Events.....171
c. Air Mass History during Regional Events.....171
d. Particle Chemistry during Regional Transport Events.....173
e. General submicron particle types.....175
f. Sulfate Formation and Aging Processes During Transport.....176
g. Temporal Variations by Particle Type.....177
h. Correlation between Major Particle Types.....178

i. Size-Resolved Chemistry of Regional Events....179
i. Correlation between Ships at Sea and Selected Particle Types....179
j. Impact of Regional Events....180
iv. Acknowledgements....181
*11. Single Particle Composition, Hygroscopicity, and CCN Activity during the 2007 San Diego Wildfires*....*182*
i. Introduction....182
ii. Experimental....183
a. Sampling locations and instrumentation....183
b. ATOFMS data analysis....184
c. Single hygroscopicity parameter....184
iii. Results and Discussion....185
a. Temporal trends of UCSD CCN_0.3, UCSD CN....187
b. Composition, size and CCN....187
c. Air Mass and hygroscopicity....190
iv. Conclusions....191
v. Acknowledgements....192
Development of Source Apportionment Algorithms....193
*12. Using mass spectral source signatures to apportion exhaust particles from gasoline and diesel powered vehicles in a freeway study using UF-ATOFMS*....*193*
i. Introduction....193
ii. Experimental....194
iii. Results and Discussion....195
a. Creation and Comparison of Particle Seeds From Source Studies....195
b. Particles Detected that Match to HDDV/LDV Source Seeds....199
c. Temporal Trends and Correlations with UF-ATOFMS Data....202
iv. Acknowledgements....210
*13. Source apportionment of freeway-side PM2.5 using ATOFMS*....*211*
i. Introduction....211
ii. Experimental....211
iii. Results and Discussion....213
a. Quality Assurance of ATOFMS Data....213
b. Comparison with standard particle counts....214
c. Comparison of particle phase and gas phase data....216
d. Comparison of temporal trends from peripheral instruments....217
e. Upwind/Downwind Sampling....219
f. Data Analysis Used for Apportionment....228
g. Source Apportionment Using ART-2a....229
h. Size Resolved Source Apportionment Temporal Series....231
iv. Acknowledgements....234
*14. Aging effects on source apportionment from the single particle perspective*....*235*
i. Introduction....235
ii. Experimental....236
a. Sampling location and instrumentation....236
b. Data analysis....236
iii. Results and Discussion....237
a. Source signature library matching....237
b. Aging effects....245
c. Secondary species as aging markers....254
iv. Acknowledgements....258
III. Summary and Conclusions....259
IV. References....261
V. Appendices....295
Publications and Presentations....295
*1. Publications*....*295*
*2. Presentations*....*296*

# LIST OF FIGURES

Figure 1: Instrument schematic diagrams of the (a) ATOFMS and (b) UF-ATOFMS. ..... 3
Figure 2: Hourly UF-ATOFMS counts of single particles for which chemical information was obtained as a function of aerodynamic diameter during the summer (top) and fall (bottom). ..... 18
Figure 3 Representative mass spectra for the general chemical classes of ultrafine particles as determined by the UF-ATOFMS. "CT" in the negative spectra represents crosstalk due to the interference of extremely intense peaks in the positive polarity. ..... 19
Figure 4 Relative size distribution (10 nm bins) of ultrafine particle types during the summer (a) and fall (b). The black trace represents the total number of ultrafine particles chemically analyzed by the UF-ATOFMS in each 10 nm size bin. ..... 20
Figure 5 Hourly relative fractions of ultrafine particle types during the summer (top) and fall (bottom). The black trace represents the hourly total of ultrafine particles (50-100 nm) chemically analyzed by the UF-ATOFMS ..... 21
Figure 6: Temporal trends of gas- and particle-phase measurements, as well as meteorological variables, for one week (Sunday through Saturday) during the summer season. ..... 22
Figure 7: Temporal trends of gas- and particle-phase measurements, as well as meteorological variables, for one week (Sunday through Saturday) during the fall season. ..... 26
Figure 8: Map showing the Port of LA. The green diamond represents the sampling location and the red markers and line represent the one minute resolution positions and course of a container ship as it departed from the Port of LA at 03:30 on November 19, 2007. The blue line represents the average wind direction during transport of the plume to the sampling location ..... 32
Figure 9: Identification of the plume of Container1b. Gas phase measurements included $SO_2$ (orange), $NO_x$ (green), and $O_3$ (blue). Particle phase measurements were of black carbon (black), particle number concentration (white), and size-resolved number concentrations over time (color matrix). ..... 33
Figure 10: Average negative and positive ion mass spectra for the OC-V-sulfate (a) and fresh soot (b) particle types. ..... 35
Figure 11: A digital color stack for the OC-V-sulfate particle type showing the fraction of particles containing a specific peak on the y-axis versus mass-to-charge on the x-axis. The color represents the fraction containing a specific range of peak areas, with 500 being the lower peak area cutoff. The top portion of the figure represents the positive mass spectrum and the bottom portion represents the negative mass spectrum. ..... 37
Figure 12: A digital color stack for the fresh soot particle type showing the fraction of particles containing a specific peak on the y-axis versus mass-to-charge on the x-axis. The color represents the fraction containing a specific range of peak areas, with 500 being the lower peak area cutoff. The top portion of the figure represents the positive mass spectrum and the bottom portion represents the negative mass spectrum. ..... 38

Figure 13: Average mass spectrum of the Ca-ECOC particle type from a fresh soot plume..... 39
Figure 14: Average mass spectra of background particle types before and after the plume from Container1a. ..... 40
Figure 15: Average mass spectra of background particle types from before and after the plume from Container4. CT represents crosstalk on the detector..... 41
Figure 16: Time series of the differential counting rate (number of ATOFMS counts per 2 minutes) for the OC-V-sulfate and fresh soot particle types. Peaks that could be correlated with ships are labeled; plumes with asterisks were only tentatively identified. ..... 42
Figure 17: Size-resolved number fractions of the different particle types for the background before and after a) OC-V-sulfate (Container4) and b) fresh soot (Container1a) plumes. (c,d) Size-resolved chemical fractions of these plumes..... 43
Figure 18: Average sulfate (red circles) and sulfuric acid (blue circles) absolute peak areas for major particle types during the plume of the vessel Container4; errors are shown by 95% confidence intervals. Number fractions of particles containing sulfate (red diamond) and sulfuric acid (blue diamond) are shown. The inset shows a zoomed-in version of particle types with lower peak areas than the OC-V-sulfate type..... 44
Figure 19: Map of the San Diego metropolitan area around San Diego Bay with trailer sampling sites and air pollution control district (APCD) sites, as well as 200 meter HYSPLIT air mass back trajectories for (a) February 12, 2009 and (b) March 13, 2009..... 49
Figure 20: Comparison of meteorology conditions (temperature-red, relative humidity-light blue, wind speed-grey, wind direction-black markers) and gas phase concentrations ($O_3$-blue, $NO_x$-green, $SO_2$-gold) on February 12$^{th}$ and March 13$^{th}$.. 52
Figure 21: (a) $PM_{2.5}$ mass concentration data at each site for the: Scaled ATOFMS mass (blue bars), trailer BAM (red bars), and DT-APCD BAM (green bars). (b) Number concentration by site from summed SMPS scans (gold bars)..... 54
Figure 22: Size distribution measurements (SMPS and APS) for February 12$^{th}$ and March 13$^{th}$ as measured at the trailer sampling sites. The red traces correspond to Silver Strand, green traces to Cesar Chavez Park, yellow to Coronado, blue to Chula Vista, and purple to Pepper Park..... 56
Figure 23: Chemically-resolved relative mass fractions of particle types for (a) submicron (0.523 – 1 μm) and (b) supermicron (1-2.5 μm) particles at each site. The black diamonds represent the ATOFMS mass concentration by site..... 59
Figure 24: Peak areas related to aging for (a) Sea salt particles, (b) Biomass particles, and (c) ECOC particles. For sea salt particles, chloride (blue – $^{35}Cl^-$) and nitrate (green – $^{62}NO_3^-$) are plotted. For biomass and ECOC particles, nitrate and sulfate (purple – m/z $^{97}HSO_4^-$) are plotted. The ratio of the peak areas for nitrate and sulfate (d) are given for biomass and ECOC particle types..... 61
Figure 25: Map of SOAR sampling site on UCR campus..... 65
Figure 26: Temporal variations of ambient wind speed, wind direction, temperature, relative humidity, and ozone concentration during SOAR-I (a) and SOAR-II (b)... 67
Figure 27: Hourly temporal variations of BAM $PM_{2.5}$ mass concentration and size-resolved hourly APS $PM_{2.5}$ particle number concentration during SOAR-I (top) and

SOAR-II (bottom). Contour plots represent APS number concentration in log scale, and the red lines correspond to BAM data. ..... 68
Figure 28: Hourly temporal variations of $O_3$ concentration and hourly average peak area of m/z 43. ..... 69
Figure 29: ART-2a weight matrices of representative particle types during SOAR-I and SOAR-II. ..... 71
Figure 30: Temporal variations of the number fractions of major particle types for the top 50 clusters superimposed with PM2.5 mass concentrations (red line) and size distributions of total ATOFMS particle counts. ..... 73
Figure 31: Hourly size-resolved number fractions of SOAR-I top 50 clusters from ART-2a results averaged for 3:00, 9:00, 15:00 and 21:00 over all sampling days. Size resolution is 0.05 μm for the submicron range and 0.10 μm for the supermicron range. ..... 74
Figure 32: Size-resolved number fractions of SOAR-II top 50 clusters from ART-2a results averaged over each episode along with corresponding PM2.5 levels and representative 48-hour HYSPLIT back trajectories. ..... 78
Figure 33: Ternary plots of SOAR-I and SOAR-II submicron aged OC1 particles. In each plot, a particle mostly containing nitrate would appear at the lower left vertex, a particle mostly containing sulfate would appear at the lower right vertex, a particle mostly containing ammonium would appear at the top vertex. ..... 81
Figure 34: Temporal variation of the mass concentration of major ATOFMS particle types. Mass concentrations are obtained by scaling ATOFMS measurements with APS measurements. ..... 83
Figure 35: Size-resolved chemical composition of unheated particles during (a) SOAR-1 (summer) and (b) SOAR-2 (fall). Size resolution is 10 nm and 50 nm for the ranges of 100-350 nm and 350-1000 nm, respectively. The majority of the particles greater than ~150 nm show evidence of internally mixed organic carbon, ammonium, nitrate, and sulfate. ..... 88
Figure 36: Amine mass calibration experimental set-up (MFC = mass flow controller; TEA = triethylamine; DMA = differential mobility analyzer; CPC = condensation particle counter; ATOFMS = aerosol time-of-flight mass spectrometer). ..... 89
Figure 37: Size distributions of uncoated (solid) and TEA-coated (dashed) 270 nm PSLs. SMPS distributions of mobility diameter are shown in red; ATOFMS distributions of vacuum aerodynamic diameter are in black. The arrows indicate the shifts of the respective distributions. ..... 91
Figure 38: Average mass spectra of (a) PSLs coated with TEA and (b) uncoated 270 nm PSLs. The inset shows a comparison of the *m/z* 86 peak intensities. ..... 92
Figure 39: Absolute area of *m/z* 86 vs vacuum aerodynamic diameter for the TEA-coated PSLs. ..... 92
Figure 40: Absolute area of *m/z* 86 vs derived TEA mass for the TEA-coated PSLs. ..... 94
Figure 41: Average positive and negative mass spectra of the unheated aged OC (nitrate-sulfate) particles during (a) summer and (b) fall. Peak areas are reported in arbitrary units (A.U.). ..... 95
Figure 42: Positive and negative mass spectra of a single particle exhibiting *m/z* 130 measured during TEA-nitric acid chamber experiments. ..... 96

Figure 43: Summer (a,b) and fall (c,d) ternary plots show the relative distributions of peak areas of ammonium (*m/z* 18 ($NH_4^+$)), amines (*m/z* 86 ($(C_2H_5)_2NCH_2^+$)), nitrate (*m/z* -62 ($NO_3^-$)), and sulfate (*m/z* -97 ($HSO_4^-$)) for the unheated and heated (54-230°C) aged OC (nitrate-sulfate) particles. Random samples of ~2,000 single particles are plotted for each temperature. ..... 97
Figure 44: For aged OC (nitrate-sulfate) particles, the (a) fraction of *m/z* 86 peak area remaining over the range of thermodenuder temperatures from 54-230 °C is shown relative to the unheated particles (ambient temperature averages of 22.9 °C and 15.6 °C in the summer and fall, respectively). In addition, the (b) amine mass/particle and (c) amine mass percent/particle are shown for each temperature. ..... 98
Figure 45: Relative fractions of nitrate (*m/z* -62 ($NO_3^-$)) remaining on the aged OC (nitrate-sulfate) particles at each TD temperature during SOAR-1 and SOAR-2. ... 99
Figure 46: Relative acidity ratios for summer and fall for each thermodenuder period (unheated, 54°C, 83°C, 113°C, 142°C, 171°C, 201°C, 230°C) for the aged OC (nitrate-sulfate) particles. The ratios are defined as the sum of the absolute average peak areas of nitrate (*m/z* -62 ($NO_3^-$)) and sulfate (*m/z* -97 ($HSO_4^-$)) divided by ammonium (*m/z* 18 ($NH_4^+$)) or the sum of ammonium and amines (*m/z* 86 ($(C_2H_5)_2NCH_2^+$)). ..... 102
Figure 47: Illustrates the temporal profiles of gas-phase $O_3$ (ppb, green line), relative humidity (%, blue line), temperature (ºC, orange line), $PM_{2.5}$ mass concentrations (μg/m$^3$, black line), and wind speed (m/s, grey line) from the three summer studies in Riverside, CA. Plot a) has data from July 29 – August 15, 2005, b) August 10 – 21, 2006, and c) August 29 – September 7, 2007. Trends of these measurements are discussed in the main manuscript. ..... 108
Figure 48: Representative 48-hour HYSPLIT air mass back trajectories in Riverside for a) 2005, b) 2006, and c) 2007. Trajectories are labeled by source wind direction and terrain. The sampling site is represented by the star in each map..... 109
Figure 49: Mixing states of secondary species in major particle types from a) 2005, b) 2006, and c) 2007. The abscissa contains major ATOFMS particle types and the y-axis contains secondary species markers $C_2H_3O^+$ (*m/z* 43), $(C_2H_5)_2NCH_2^+$ (*m/z* 86), $NH_4^+$ (*m/z* 18), $HSO_4^-$ (*m/z* -97), $NO_2^-$ (*m/z* -46), and $NO_3^-$ (*m/z* -62). The color scale represents the number fraction of particles within a single particle type that contained each specific marker (secondary species). ..... 111
Figure 50: shows the ratio of the sum of peak areas m/z 43 to m/z 37 plotted as a function of $O_3$ concentration (ppm) from a) 2005, b) 2006, and c) 2007 with maroon being the lowest concentration and blue being the highest. Also pictured is the temporal profile of $PM_{2.5}$ mass concentrations (μg/m$^3$). ..... 113
Figure 51: Temporally-resolved submicron particle chemistry from a) 2005, b) 2006, and c) 2007. Hourly $PM_{2.5}$ mass concentrations are also plotted for each year (black line). ..... 115
Figure 52: Temporally-resolved relative number fraction of ECOC particle types (red diamonds) from a) 2005, b) 2006, and c) 2007. The black shaded regions are the $PM_{2.5}$ mass concentrations for each year. ..... 116
Figure 53: Size resolved submicron particle chemistry in Riverside, CA. ..... 117
Figure 54: (a) Linear interpolation over the Fresno high-miss period to obtain estimated hit counts and estimated missed counts for the period of January 28th, 3:35 – 11:15;

(b) estimated missed particle recording time vs. missed particle detection rate for all five high-miss periods with a time resolution of 6 minutes for Fresno dataset. ..... 124
Figure 55: Comparison of scaled ATOFMS mass concentrations and MOUDI measurements in Fresno. ..... 127
Figure 56: Temporal variation of hourly BAM and scaled ATOFMS PM2.5 mass concentrations in Fresno. The scaling function for the ATOFMS was obtained by comparison with MOUDI measurements. ..... 128
Figure 57: APS scaling curve for Angiola measurements. (a) hourly scaling curve for February 03, except for 13:00; (b) exponential regression of left half of scaling curve at 22:00; (c) polynomial regression of right half of scaling curve at 22:00..... 130
Figure 58: Correlations between BAM and APS scaled ATOFMS mass concentrations. (a) ATOFMS mass concentrations are obtained with single density ($\rho$) values for all particles ($\rho$ = 1.8 g·cm$^{-3}$, $\rho$ = 1.9 g·cm$^{-3}$, or $\rho$ = 2.0 g·cm$^{-3}$); (b) ATOFMS mass concentrations are obtained with different density pairs for submicron and supermicron particles: 1.2 and 2.7 g·cm$^{-3}$, 1.7 and 2.2 g·cm$^{-3}$, 1.7 and 2.7 g·cm$^{-3}$, 1.7 and 3.2 g·cm$^{-3}$, and 2.2 and 2.7 g·cm$^{-3}$. ..... 132
Figure 59: Temporal variation of Angiola particulate mass concentrations obtained with BAM and APS scaled ATOFMS ($\rho$ = 1.9 g·cm$^{-3}$). ..... 133
Figure 60: APS scaling curves for all studies, including TexAQS, NC-CCS-I, NC-CCS-II, CIFEX, Freeway, APMEX, and Angiola studies. ..... 142
Figure 61: Size-resolved un-scaled particle type mass concentrations and mass fractions for Fresno and Angiola. (a) un-scaled particle type mass concentrations in Fresno (b) un-scaled particle type mass fractions in Fresno (c) un-scaled particle type mass concentrations in Angiola (d) un-scaled particle type mass fractions in Angiola. 143
Figure 62: Fresno and Angiola size-resolved particle type mass concentrations scaled with TexAQS and APMEX scaling functions. (a) Fresno particle type mass concentrations with TexAQS APS scaling function (b) Fresno particle type mass concentrations with APMEX APS scaling function (c) Angiola particle type mass concentrations with TexAQS APS scaling function (d) Angiola particle type mass concentrations with APMEX APS scaling function. ..... 145
Figure 63: Fresno and Angiola individual particle type mass fractions for submicron, supermicron and PM2.5 range obtained with APS scaling functions from TexAQS, Freeway, CIFEX, NC-CCS, APMEX, and Angiola studies. ..... 147
Figure 64: Trends of the three main vanadium particle types: representative mass spectra (a-c); half-hourly temporal variations in summer (d) and fall (e); size-resolved total particle fractions in summer (f) and fall (g); and half-hourly wind direction profiles based on particle counts (h-j). ..... 154
Figure 65: Half-hourly wind direction and wind speed (color scale) distribution for all $PM_{2.5}$ particle types in summer (a) and fall (b). ..... 155
Figure 66: Half-hourly wind direction based on time of day for summer (a) and fall (b). Note that for the summer season, the meteorological data ended at 12:00 on August 14$^{th}$. ..... 156
Figure 67: Reported annual atmospheric emissions of the specified metal and metal compounds in Riverside, Los Angeles, Orange, and San Bernardino counties in 2005 based on the data from the Environmental Protection Agency (EPA) Toxics Release Inventory (TRI). ..... 157

Figure 68: Trends of the three main iron particle types: representative mass spectra (a-c); half-hourly temporal variations in summer (d) and fall (e); size-resolved total particle fractions in summer (f) and fall (g); and half-hourly wind direction profiles based on particle counts (h-j). ..... 158
Figure 69: Trends of the three main zinc particle types: representative mass spectra (a-c); half-hourly temporal variations in summer (d) and fall (e); size-resolved total particle fractions in summer (f) and fall (g); and half-hourly wind direction profiles based on particle counts (h-j). ..... 160
Figure 70: Trends of the three main barium particle types: representative mass spectra (a-c); half-hourly temporal variations in summer (d) and fall (e); size-resolved total particle fractions in summer (f) and fall (g); and half-hourly wind direction profiles based on particle counts (h-j). ..... 161
Figure 71: Trends of the three main lead particle types: representative mass spectra (a-c); half-hourly temporal variations in summer (d) and fall (e); size-resolved total particle fractions in summer (f) and fall (g); and half-hourly wind direction profiles based on particle counts (h-j). ..... 162
Figure 72: A) The lower portion of the graph shows time series of scaled $PM_{2.5}$ mass concentrations at the SIO Pier (red line) and $PM_{2.5}$ data from downtown San Diego (black line). B) Hourly size distributions measured by an aerodynamic particle sizer (APS) from 0.5-1 μm from August 17, 2006 – October 2, 2006. The overlaid blue line is the sum of ATOFMS counts in the 0.5-1 μm size range per hour. C) Scaled $PM_1$ (green line) and $PM_{2.5}$ (red line) mass concentrations are shown over the sampling period. The gray dashed line represents the average $PM_1$ mass concentration during the study, and the black dashed line represents the $PM_1$ threshold set for regional events. ..... 169
Figure 73: Fraction of scaled $PM_{2.5}$ corresponding to $PM_1$ hourly. ..... 170
Figure 74: HYSPLIT (24 hour) back trajectory analysis at 500 meters for the peak hour of each regional event. Large diamonds represent 24 hours back from the source and small diamonds present 12 hours. A) Trajectories in red pass near the LA Port while trajectories in blue pass over the SD Port. B) Trajectories in purple are representative of non-transport time periods. C) The table included displays the frequency of different air mass types and source regions, as well as the number of regional events observed during each back trajectory type. ..... 173
Figure 75: Average negative and positive ion mass spectra for a) ECOC(sulfate-nitrate) and b) V-Ni-Fe(sulfate-nitrate) particles. c) Time series of hourly ECOC(sulfate-nitrate) and V-Ni-Fe(sulfate-nitrate) particle type counts. ..... 174
Figure 76: Average negative and positive ion mass spectra for the top six particle types (excluding ECOC and V-Ni-Fe which are discussed in the main paper): a) Elemental carbon, b) Organic carbon, c) Biomass Burning, d) Sea salt, e) Sea salt with soot. 176
Figure 77: a) Time series of the relative fractions of submicrometer particles types b) Time series of counts of submicron particle types. The black line on both plots is the scaled $PM_1$ mass concentration ($\mu g/m^3$). ..... 178
Figure 78: Comparison of the average size-resolved mass distributions of major particle types during regional events and non-events. ..... 179
Figure 79: Time series of hourly counts of the ECOC and V-Fe-Ni particle types during 6 day period with ship positions recorded per hour. ..... 180

Figure 80: HYSPLIT back trajectories during wildfire sampling period. Each line is a representative 48 hour backtrajectory during that period at 500m. Corresponding periods for comparison to sampling data are in parenthesis. ..... 187
Figure 81: Overview of Urey Hall CCN (UCSD CCN_0.3) and SIO CCN (SIO CCN_0.1) concentrations (s=0.29, 0.13 respectively), fCCN_0.3, fCCN_0.1, Dact_0.3, meteorological data and Urey Hall SMPS ..... 187
Figure 82: Particle classification temporal. Shown is the classification of particles detected between 50 and 300 nm by the ATOFMS during the study. Biomass is shown in red and is the dominant type during most of the period. Gray is elemental carbon (EC) and grows in as biomass decreases. ..... 188
Figure 83: Comparison of CCN_0.3 and CCN_0.1 for entire study. ..... 189
Figure 84: Single parameter hygroscopicity (Kappa) values of the particles during different air mass periods for CCN_0.3. The top of the boxes are the 3$^{rd}$ quartile of kappa values for that period, the bottoms are the 1$^{st}$ quartile values for that period. Whiskers show the minimum and maximum values for each period. Median values are the middle lines dividing the top and bottom of the boxes. Black diamonds are average CCN concentrations for those periods with standard deviation as error bars. ..... 189
Figure 85: Single parameter hygroscopicity (Kappa) values of the particles during different air mass periods for CCN_0.1. The top of the boxes are the 3$^{rd}$ quartile of kappa values for that period, the bottoms are the 1$^{st}$ quartile values for that period. Whiskers show the minimum and maximum values for each period. Median values are the middle lines dividing the top and bottom of the boxes. Black diamonds are average CCN concentrations for those periods with standard deviation as error bars. ..... 190
Figure 86: Dot product comparisons of the representative area matrices between the general classes from the HDDV and LDV dynamometer experiments using UF-ATOFMS. Classes are labeled in the same manner as in the manuscripts from Sodeman *et al.* 2005 and Toner *et al.* 2006. ..... 197
Figure 87: ART-2a matching error analysis using non-exclusive matching of HDDV and LDV dynamometer particles. For each, the fraction of HDDV and LDV particles that matched to the HDDV, LDV, or both HDDV and LDV clusters from the HDDV/LDV reference library are shown for ultrafine (50–100nm) and accumulation (100–300nm) mode particles. ..... 198
Figure 88: ART-2a matching error analysis using exclusive matching of HDDV and LDV dynamometer particles. For each, the fraction of HDDV and LDV particles that matched to the HDDV or LDV clusters from the HDDV/LDV reference library are shown for ultrafine (50–100nm) and accumulation (100–300nm) mode particles. 199
Figure 89: Weight matrices of the top particle types detected during freeway study that match to vehicle study signatures. ..... 201
Figure 90: Temporal plots of A) NOx gas data vs. aethalometer data; and B) HDDV video counts vs. aethalometer data. Both NOx and aethalometer data show a good correlation with each other ($R^2$ = 0.7). The HDDV video counts also track the aethalometer data. ..... 203
Figure 91: Top: Wind data (blowing from: N = 0$^o$/360$^o$, E = 90$^o$, S = 180$^o$, W = 270$^o$) along with LDV & HDDV traffic counts (from video). HDDV counts are multiplied

by 20 to keep them on the same scale as LDV traffic counts. Middle: HDDV/LDV/Other ART-2a matching result unscaled counts from UF-ATOFMS data. Bottom: HDDV/LDV/Other ART-2a matching fraction results from UF-ATOFMS data. Data shown are accumulation mode particles ($D_a$ = 100–300nm) for July 24 to Aug 03, 2004. ..... 205
Figure 92: Top: SMPS data along with LDV & HDDV traffic counts (from video). HDDV counts are multiplied by 20 to keep them on the same scale as LDV traffic counts. Middle: HDDV/LDV/Other ART-2a matching result unscaled counts from UF-ATOFMS data. Bottom: HDDV/LDV/Other ART-2a matching fraction results from UF-ATOFMS data. Data shown are ultrafine mode particles ($D_a$ = 50–100nm) for July 24 to Aug 03, 2004. ..... 207
Figure 93: Time series of aethalometer data with HDDV/LDV apportioned particles. The $R^2$ values for aethalometer to HDDV is 0.77, and 0.56 for the aethalometer to LDV. ..... 209
Figure 94: A) QA plot of UF-ATOFMS particle scatters vs. particles scattered that produced a mass spectrum to determine if there are any chemical biases or particle types being missed. B) Comparison of the two standard inlet ATOFMS instruments particle detections when running side-by-side at the freeway site. Plots are in one hour resolution. ..... 214
Figure 95: A) Comparison of sub-100 nm particle counts with the SMPS to sub-100 nm particles detected (that produced mass spectra) with the UF-ATOFMS at the freeway site. B) Comparison of fine mode particles (500 – 1000 nm) with the APS to fine mode particles (200 – 1000 nm) detected (that produced mass spectra) with the standard inlet ATOFMS at the freeway site. Plots are in one hour resolution. 215
Figure 96: A) Comparison of sub-100 nm UF-ATOFMS particles detected that produced mass spectra with CO measurements. B) Comparison of sub-100 nm UF-ATOFMS particles detected that produced mass spectra with $NO_x$ measurements. C) Comparison of CO and $NO_x$ measurements at the freeway site. Plots are in one hour resolution..... 217
Figure 97: A) Comparison of aethalometer and $NO_x$ measurements at the freeway site. B) Comparison of aethalometer and nephelometer measurements at the freeway site. Plots are in one hour resolution. ..... 219
Figure 98: A) SMPS and APS particle number concentrations at the freeway site from. B) SMPS and APS particle number concentrations at the upwind sampling site. Both plots are shown from Jul. 24 to Aug. 3, 2004 in order to directly compare the two sites. The data is shown in log scale. ..... 221
Figure 99: Particle size distribution data of: A) Standard inlet ATOFMS at the upwind sampling site. B) Standard inlet ATOFMS at the freeway sampling site. C) UF-ATOFMS at the freeway site. The particle size data shown is only for particles that were detected that produced a mass spectrum with the particular ATOFMS instrument. The data shown is from Jul. 24 to Aug. 3, 2004 in order to compare the two sites and to the APS and SMPS data shown in Figure 98..... 223
Figure 100: Positive and negative ion mass spectra for the regional background (A) vanadium and (B) EC particle types. (C) The temporal trends of the vanadium particle type detected with all three ATOFMS instruments compared to wind data.

(D) Temporal trends (and correlation) of total background vanadium particles versus the total background EC particles for the three ATOFMS instruments..... 225
Figure 101: Hourly HYSPLIT model 24-hour back trajectories at 500 m for each day at the freeway study site..... 227
Figure 102: Size resolved source apportionment of the particles detected at the upwind (top) and freeway (bottom) sampling sites. Both plots are averages for ATOFMS data acquired from July 24 to Aug 3, 2004. In the bottom plot for the freeway site, the sizing region of overlap between the UF-ATOFMS and standard inlet ATOFMS is 200 – 300 nm..... 230
Figure 103: Time series of the size segregated source apportionment fractions for the freeway site ultrafine and accumulation mode particles detected with the UF-ATOFMS and ATOFMS. ..... 233
Figure 104: Hourly temporal series of the size segregated source apportionment fractions (VF = 0.85) for the summer SOAR ultrafine (UF), small accumulative mode (SAM), large accumulation mode (LAM), submicron (SUB), and supermicron (SUPER) particles detected with the UF-ATOFMS and ATOFMS. ..... 240
Figure 105: Hourly temporal series of the size segregated source apportionment fractions (VF = 0.85) for the fall SOAR ultrafine (UF), small accumulative mode (SAM), large accumulation mode (LAM), submicron (SUB), and supermicron (SUPER) particles detected with the UF-ATOFMS and ATOFMS. ..... 241
Figure 106: Number of summer particles matched to each source seed for a) UF (50-100 nm), b) SAM (100-140 nm), c) LAM (140-400 nm), d) SUB (140-1000 nm), and e) SUPER (1000-3000 nm) particles. ..... 242
Figure 107: Number of fall particles matched to each source seed for a) UF (50-100 nm), b) SAM (100-140 nm), c) LAM (140-400 nm), d) SUB (140-1000 nm), and e) SUPER (1000-3000 nm) particles. ..... 243
Figure 108: Average source contribution particles matched to the source library at different VF per size bin. ..... 247
Figure 109: Average mass spectra obtained by lowering the matching factor for summer SOAR LAM (140-400 nm) particles apportioned to LDV. ..... 248
Figure 110: Hourly temporal series of the size segregated source apportionment fractions (VF = 0.85) for the summer SOAR ultrafine (UF), small accumulative mode (SAM), large accumulation mode (LAM), submicron (SUB), and supermicron (SUPER) particles using the updated source signature library. ..... 249
Figure 111: Hourly temporal series of the size segregated source apportionment fractions (VF = 0.85) for the fall SOAR ultrafine (UF), small accumulative mode (SAM), large accumulation mode (LAM), submicron (SUB), and supermicron (SUPER) particles using the updated source signature library. ..... 250
Figure 112: Representative 48 hour HYSPLIT back trajectories at a height of 100 m for six defined regions. (LA = Los Angeles, SD = San Diego)..... 253
Figure 113: Relative class abundance based on air mass origin and size range. (LA = Los Angeles, SD = San Diego, SS = Salton Sea, SJV = San Joaquin Valley, NE = Northeastern)..... 254
Figure 114: Size-resolved average area of secondary markers for particles matched to specific sources during the summer (left column) and fall (right column)..... 256

# LIST OF TABLES

Table 1: The studies conducted as a part of this project. ..... 2
Table 2: Instrumentation. ..... 15
Table 3: Characteristics of ship plumes sampled including: Ship plume, plume peak time, plume duration, plume age, peak number concentration, identifying ATOFMS particle type, number of ATOFMS particles, number fraction of OC-V-sulfate particles, and number fraction of fresh soot particles. ..... 31
Table 4: Gas phase concentrations (max, baseline, and peak) of $SO_2$, $NO_x$, and Ozone during different plume events are shown along with the $NO_x/SO_2$ ratio. ..... 34
Table 5: Sampling times and locations at sites around San Diego Bay are described..... 48
Table 6: Averages and standard deviations of ozone, ambient meteorological conditions, $PM_{2.5}$ mass concentrations (measured at the California Air Resources Board Rubidoux site), and $PM_{1.0}$ agedOC-nitrate-sulfate particle type mass concentrations for July 30 – August 15, 2005 compared to August 12, 2005 (189)..... 87
Table 7: Measurements of $PM_{2.5}$ ($\mu g/m^3$), relative humidity (RH, %), temperature (T, °C), wind speed (WS, m/s), and gas-phase $O_3$ concentrations (ppb) for the sampling periods during 2005-2007. Standard deviations ($\sigma$) and measurement ranges are also listed. 'Avg. Daily Maxima' refers to the average time of the daily maximum of each particular factor..... 107
Table 8: Descriptions of the major ATOFMS particle types from 2005-2007. ..... 110
Table 9: Correlation coefficients of $PM_{2.5}$ measurements. (a) Fresno site. (b) Angiola site. ..... 135
Table 10: APS scaling parameters for all studies. ..... 142
Table 11: Metal association percentages (%) ..... 164
Table 12: Properties of different regional events are listed including: peak $PM_1$ and $PM_{2.5}$ mass concentrations, fraction of $PM_1$ contributing to $PM_{2.5}$ mass, and the mass percentage of V-Ni-Fe and ECOC particles contributing to the $PM_1$ mass..... 170
Table 13: Overview of different Urey Hall CCN periods based on CCN activity, size distributions, particle chemistry and hysplit back trajectories (see dividing lines in figure 2). SMPS data is the average mode for that period with the min/max mode of $dN/dlogD_p$ in parenthesis. ..... 185
Table 14: Overview of SIO Pier CCN, fCCN, CN and Dact during Urey Hall CCN periods (from table 1a). ..... 186
Table 15: List of instrumentation. ..... 194
Table 16: List of Instrumentation used at the freeway and upwind sampling sites. ..... 212
Table 17: Number of library seeds for each source per size range ..... 238
Table 18: Percent difference between particles matched to the original source library and particles matches to the updated source library. ..... 251

# ABSTRACT

In the past, the majority of research aimed at understanding the composition and sources contributing to $PM_{2.5}$ concentrations in California has been focused on major field campaigns that have been concentrated over relatively short periods of time (weeks to months). While these studies have contributed a great deal to our understanding of aerosol particles, they have focused primarily on one region during one season. This report will detail the significant progress that has been made towards understanding how aerosol sources and chemistry vary temporally and spatially within California, information that is critical to assessing the health impacts of air pollution on individuals living in various regions of the state. The development of a trailer housing many air pollution instruments as a mobile platform for sampling has been a key enabling step in this research that has allowed for rapid deployment and the ability to sample in multiple locations over short periods of time. This increased flexibility has allowed us to obtain detailed information regarding the variations of aerosol properties both seasonally and spatially. The variations in particle concentrations and chemistry over very short time periods have allowed us to investigate changes in plumes from both roadways and ship traffic. In addition to changes in particles over different intervals of time, studies were conducted to investigate the changes in aerosol particle properties within a city scale range over the period of one air mass (3 days) and one day. Observations were also made of particle transport within California both locally (city-scale) and regionally (city-to-city). The second focus of this project has been to provide more detailed mass concentrations from aerosol time-of-flight mass spectrometry (ATOFMS) data, which has been achieved through scaling with respect to standard mass based measurements such as the MOUDI and TEOM. Advances have also been made in our ability to apportion individual particles to different sources building on a library of source signatures that has been developed through work with CARB over the last decade. Specifically, measuring changes in particle properties as they age and take up secondary material and the impact on the original source signatures has been investigated through the use of a thermodenuder, which has led to improved source apportionment capabilities of aerosols in highly aged environments.

# EXECUTIVE SUMMARY

## *Background*

Many studies have detailed the human health and environmental impacts of atmospheric aerosols since the middle of the 20th century. The majority of studies that have investigated particulate matter in the California atmosphere have been over relatively short time periods with a strong regional focus. These studies have provided a much greater understanding of aerosol particle physical properties and composition; however the majority of these studies have focused on bulk measurements that limit their ability to perform source apportionment. Bulk measurements are also challenged by positive and negative sampling artifacts and poor time resolution. In order to complement traditional sampling methods while overcoming some of the issues associated with off-line sampling, a number of techniques are being developed and used for real-time PM composition analysis. Single Particle Mass Spectrometry (SPMS) offers complementary information to bulk sampling by determining the actual chemical associations or mixing state of individual particles. SPMS techniques measure the size and chemical composition of individual particles and offer an alternative approach for performing source apportionment of ambient PM. Aerosol time-of-flight mass spectrometry or ATOFMS is the specific SPMS instrument used throughout this project. The strength of ATOFMS lies in its ability to provide information on the number fractions of particles with a specific chemical signature and how these vary with aerodynamic size. Unique associations within individual particles can be measured between organic carbon, elemental carbon, amines, nitrate, sulfate, ammonium, and metals. A major goal of ambient studies performed using ATOFMS involves linking specific single particle chemical signatures with specific emission sources, as well as developing a more quantitative picture of the fraction of secondary species associated with aerosols in polluted air under a variety of conditions and locations. In an effort to understand the relative contributions from different sources in California, we have begun using ATOFMS to perform extensive source characterization studies, characterizing the emissions from heavy duty diesel trucks and gasoline passenger cars, wildfires, wood smoke from fireplaces, meat cooking, and ships in an effort to determine differences in single particle mass spectral fingerprints from these sources. The ultimate goal is to develop single particle mass spectral signature libraries for major PM sources that can be compared to ambient particle spectra to assign sources and assess the rate and degree of aging that occurs on ambient PM over time and space.

## *Methods*

A wide range of gas and particle phase instruments were used in this study. Measurements of particle size distributions, PM2.5 mass concentration, gas phase, black carbon concentrations, and single particle mass spectrometry were used in this project. The key unique instrument used for these studies was an aerosol time-of-flight mass spectrometer (ATOFMS), which analyzes individual particle size and composition in real time. Data from the ATOFMS was analyzed and incorporated into a mass spectral source library developed as a part of this project. The other gas and particle phase

instrumentation operated in the mobile trailer system included $SO_2$, $NO_x$, $O_3$, CO, scanning mobility particle sizer (SMPS), aerodynamic particle sizer (APS), condensation particle counter (CPC), cloud condensation nuclei counter (CCN), aethalometer, and TEOM. A trailer was modified and combined with low particle emission generators to provide flexibility with respect to sampling location and duration with the suite of instrumentation listed above.

## *Results and Conclusions*

This project was highly productive and accomplished a wide range of objectives including: high time resolution sampling, high spatial resolution sampling, seasonal and interannual comparisons, scaling and mass comparisons, changes in size-resolved particle composition linked with meteorological measurements and air mass back trajectories, and the development of source apportionment algorithms. High time resolution sampling led to the observation of ambient ultrafine aerosols by single particle techniques from both vehicle exhaust and photochemical events. It also allowed for the observation of individual ship plumes (~ 10-15 min in duration) and dramatic shifts in chemistry within them. Measurements looking at the spatial variability of aerosols were conducted in Riverside by comparing ATOFMS measurements at a stationary site with those made in the mobile laboratory during a Santa Ana period. Spatial analysis was also performed during a series of measurements made around San Diego Bay on days with different meteorological and aerosol characteristics. Seasonal variations were observed between SOAR I and SOAR II and led to analysis of diurnal variations (SOAR I) and episodic variations (SOAR II). Seasonal variations were also analyzed with respect to particle phase amines, as well as the ultrafine aerosols mentioned above. Interannual comparisons were also made for measurements made in Riverside during 2005, 2006, and 2007. Mass comparisons were made with TEOM, MOUDI, and BAM measurements allowing for the scaling of ATOFMS by APS data to quantitative mass concentrations. In depth analysis of the variation in APS scaling functions over numerous studies was investigated to refine the method. The link between meteorology measurements and air mass back trajectories were shown within the LA Basin with respect to trace metals. This link was also demonstrated regionally by showing the impact of the LA Port Region on San Diego air quality and its potential to significant contribute to particle mass concentrations. Lastly, with respect to the development of source apportionment algorithms, mass spectral source signatures were used to apportion exhaust particles from gasoline and diesel powered vehicles in a freeway study. Source apportionment of $PM_{2.5}$ was also performed at that site for all particles, including non-vehicle sources. The source library that was developed was then used to characterize $PM_{2.5}$ in Athens, Greece and Mexico City, showing the broad applicability of the source library method. The library was also updated to include aging effects on source apportionment and to evaluate the aged Riverside environment.

# Body of Report

## I. Introduction

### 1. Research Objectives and Studies Conducted

This project focused on using gas and particle phase instrumentation to analyze temporal and spatial variations as well as perform source apportionment of ambient aerosols in multiple regions of California. The project was divided into two phases and the major goals of Phase I were developing a mobile laboratory, acquiring and testing generators, conducting one field study in summer 2005, and performing source apportionment on previous ATOFMS source testing. The goals of Phase 2 (year 1) included combining the generators and mobile laboratory to allow for autonomous camping, sampling during multiple seasons in multiple regions, and analyzing the data. Phase 2 (year 2) included additional sampling periods, analyzing all collected data, expanding data analysis techniques, and preparing a final report.

The sampling periods that were conducted as a part of this study are shown in table 1. The major studies were the Study of Organic Aerosols in Riverside (SOAR) I, SOAR II, SOAR III, SD Mobile Study, Pier Study, Los Angeles Basin Mobile Study (LABMS) I, LABMS II. The goals of the SOARs were to characterize the size and chemical composition of individual particles, provide quantitative information on different chemical compositions, study how aging processes affect fresh emission signatures determine the fraction of aged aerosol versus fresh aerosol, compare with other organic aerosol techniques including the AMS (Jimenez), thermal desorption MS (Ziemann), EC/OC measurements (Schauer), and SVOC measurements (Eatough), and identify the sources of Riverside aerosols and determine the fraction of fresh versus aged aerosols. The SD Mobile Study was the initial testing of the mobile laboratory powered by the generators, with the main goal being to determine and refine the mobile laboratory's capabilities. The Pier Study at Scripps Pier in La Jolla was partially funded as a collaboration with Prof. Mark Thiemens (1$^{st}$ 2 weeks), but was continued as part of this project to provide longer term sampling (last 5 weeks). The LABMS studies consisted of sampling in Long Beach and Riverside, with mobile sampling (1-2 sites per day) during LABMS II in the eastern half of the LA basin.

| Year | Study Name | Location | Months | Season |
|---|---|---|---|---|
| 2005 | SOAR I | Riverside | July-August | Summer |
| 2005 | SOAR II | Riverside | November | Fall |
| 2006 | SOAR III | Riverside | August | Summer |
| 2006 | Pier Study | San Diego | August-September | Fall (early) |
| 2006 | SD Mobile Study | San Diego | December | Winter |
| 2007 | LABMS I | Long Beach, Riverside | August-September | Summer |
| 2007 | SD Fires | San Diego | October-November | Fall |
| 2007 | LABMS II | Riverside, Long Beach | November | Fall |

**Table 1:** A list of the studies conducted as a part of this project.

## 2. Instrumentation

The principal sampling technique for ambient particles used throughout this report is aerosol time-of-flight mass spectrometry (ATOFMS). ATOFMS simultaneously acquires positive and negative ion spectra, as well as size information, for single particles in real-time. A detailed description of operation and performance of the transportable version of this instrument has been provided previously (1), though a brief explanation is included here. A schematic diagram of the standard inlet ATOFMS is given in **Figure 1**. The inlet region consists of a converging nozzle, followed by two skimmers. Similar to the APS, the particles undergo supersonic expansion upon introduction into vacuum and are accelerated to velocities dependent on their aerodynamic sizes. The different regions separated by skimmers fulfill two primary functions: to permit differential pumping from atmospheric pressures to the pressures necessary to operate the mass spectrometer and to collimate the particle beam by removing those particles which do not follow a straight trajectory. The particle beam next enters the light-scattering region, which includes two continuous-wave 532 nm diode pumped Nd:YAG lasers. These lasers are positioned orthogonally to the particle beam, so that when a particle passes through the laser beam, its scattered light is focused onto PMTs by means of ellipsoidal mirrors. The PMTs send pulses to an electronic timing circuit that measures the time the particle takes to travel the known distance (6 cm) between the two laser beams. The velocity of the particle is calculated with the particle time of flight and the distance and is converted to a physical aerodynamic diameter via an external size calibration with particles of known size. With the determined particle velocity, the timing circuit counts down to when the tracked particle will reach the center of the ion source region of the mass spectrometer and sends a signal to a pulsed Nd:YAG laser (frequency quadrupled to 266 nm) to fire. Through direct laser desorption/ionization (LDI), the laser pulse produces ions, which are then mass analyzed in a dual-ion reflectron time-of-flight mass spectrometer. The dual polarity permits simultaneous acquisition of positive and negative ion spectra for an individual particle, which is unique as most SPMS techniques can only obtain spectra of single polarity at a given time. The standard ATOFMS instrument can analyze single particles with aerodynamic diameters over a broad size range from approximately 200 to 3000 nm.

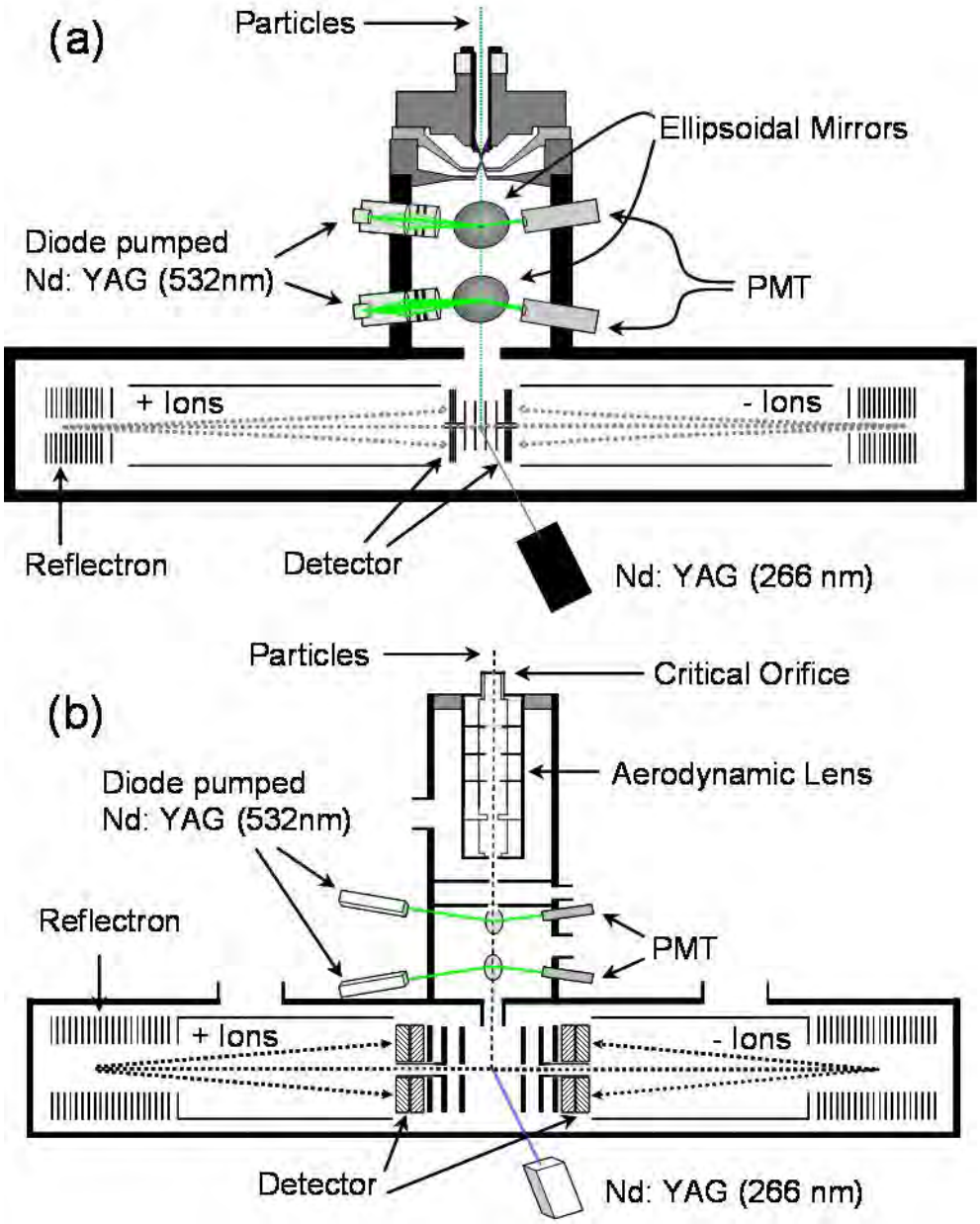


Figure 1: Instrument schematic diagrams of the (a) ATOFMS and (b) UF-ATOFMS.

Ultrafine aerosol time-of-flight mass spectrometry (UF-ATOFMS) has improved detection efficiency for small particles (< 300 nm) over the standard ATOFMS by replacing the converging nozzle inlet with an aerodynamic lens inlet (2). **Figure 1b** shows the schematic diagram of the UF-ATOFMS instrument. The lens system tightly collimates the particle beam, so that smaller ultrafine particles will be more efficiently transmitted in the instrument (3,4). Upon exiting the aerodynamic lens, the gas molecules undergo supersonic expansion, accelerating the particles to terminal velocities based on their aerodynamic diameter – just as with standard inlet ATOFMS. UF-ATOFMS also has enhanced light-scattering detection by incorporating a focusing lens to tighten the continuous laser beams, increasing the laser beam power density, and by employing a fast amplifier to improve the signal-to-noise ratio. All of these

enhancements, in addition to the aerodynamic lens systems, are necessary to improve the minimum optical detection size of ~100 nm down to 50 nm. Together, standard ATOFMS and UF-ATOFMS cover an aerodynamic size range of ~50 to 3000 nm when sampling side-by-side.

## 3. Data Analysis Methods

ATOFMS generates large quantities of data; the instrumentation is capable of collecting size and chemical information on greater than 500 individual particles per minute, depending upon the atmospheric concentrations. While simple laboratory experiments may run for only a few hours, ambient monitoring studies with ATOFMS may operate for weeks. Therefore, continuous sampling during a single ambient study can yield tens of millions of individual spectra – far too many to analyze by hand. For efficient analysis of such a volume of data, an ideal data analysis technique must perform automatic sorting and classification of individual particles. There are a number of available mathematical algorithms that have been adapted to cluster mass spectral data, such as fuzzy *c*-means clustering, *k*-means clustering, hierarchical clustering, and artificial neural networks (5-9). The two main data analysis methods used in this report are described in the next sections. Any adjustments to these methods or alternative approaches will be discussed in subsequent chapters. The adaptive resonance theory-based neural network algorithm, ART-2a, has been used to analyze ATOFMS data for several years. In a benchmark test against other clustering methods, ART-2a has been shown to yield comparable results (8). A modification of ART-2a analysis involves matching to predefined seeds, such as a source signature library described below.

Though more detailed descriptions of the ART-2a algorithm have been provided elsewhere (10-12), a brief description is included here. Using the mass spectral ion patterns and peak intensities, ART-2a separates particles into distinct classes (clusters) of chemically similar particles within large ATOFMS data sets and generates new clusters whenever a data point (mass spectrum) falls outside the proximity to all existing classes. Thereby, ART-2a provides the advantage of determining the contributions from previously detected particle classes while also introducing information on new particle types. For each particle, ART-2a combines all of the ion peak patterns and intensities in the positive and negative spectra to form an n-dimensional weight vector (normally 350 *m/z* units for each polarity, making 700 units total), in which the ion intensity at each *m/z* ratio is normalized with respect to the maximum peak intensity present in the vector. In the classification process, particles are selected randomly and their spectral information is compared to each particle cluster (weight vector) by calculating the dot product of the particle vector and cluster weight vector. The dot product value ranges from 0 to 1, where 1 represents identical vectors. If the dot product value between the particle vector and any of the existing weight vectors is above the user-defined threshold (vigilance factor - VF), that particle is added to the cluster with the highest dot product value. If a learning rate is defined, that cluster will slightly weight its vector toward the newly added particle. If the dot product value is below the VF, the particle defines a new cluster. Once all of the particles have been assigned, ART-2a then compares each particle against the entire set of created clusters to ensure proper placement. This final step is repeated for a number of set iterations (usually 20).

Upon completion of the ART-2a analysis, there may be hundreds to thousands of resulting clusters based on the complexity of the data and the VF used. For example, a low VF ($\leq 0.5$) will yield a low number of clusters with limited homogeneity, whereas a high VF ($\geq 0.7$) will yield a large number of clusters with high homogeneity. The user then visually inspects the ART-2a clusters to manually classify and label them based on their spectral characteristics. Some clusters may be combined by hand if they have similar spectral characteristics or key class features, in order to reduce the total number of clusters to a more manageable size.

One of the features of ART-2a is that it can compare the ambient particle vectors to a set of predefined weight vectors, known as seeds. In direct analogy to the procedure described in the previous section, the dot product of each particle vector is crossed with each seed weight vector. The particle is placed into the seed cluster that produces the highest dot product, assuming it is above the user-defined VF. The main difference between this matching method and the normal ART-2a procedure is that if no dot product value exceeds the VF, the particle is placed into an "unmatched" category, rather than initiating a new particle class. In addition, this method has no learning rate parameter, so the vectors of the seeds remain constant as particles are matched to them.

The matching function is ideal for apportioning individual ambient particles to specific sources using a source signature library. The recently developed source signature library is described in detail elsewhere (13), but a brief description is given here. The size-segregated library combines the carefully identified mass spectral source signatures from a series of source (such as vehicle dynamometer studies) and ambient characterization studies to serve as the predefined cluster seeds. Designed to expand as the ATOFMS signatures for particles from new sources are obtained, the library presently contains source fingerprints for heavy duty diesel vehicle (HDDV) and light duty gasoline vehicle (LDV) exhaust emissions, dust, sea salt, biomass, and meat cooking. It also has non-source specific signatures acquired in ambient studies, including aged elemental carbon (EC), aged organic carbon (OC), amine-containing particles, ammonium-rich particles, vanadium-rich particles, EC, and polycyclic aromatic hydrocarbon (PAH)-containing particles. The major advantages of using this data analysis technique are the elimination of user bias in labeling and the speed in which it can apportion particles.

## 4. Summary of Chapters

### i. Introduction

Chapter 0 introduces the goals of the project and motivation behind them, as well as the objectives and deliverables provided within the report. The aerosol time-of-flight mass spectrometer is then introduced as well as the trailer that was developed to transport it during this project. Previously developed as well as novel data analysis techniques are then described. Lastly, a brief summary of each chapter of the report is included.

### ii. Time and Size Resolved Chemical Composition Measurements Detailing Short Term Changes in Composition

Chapter 1 discusses the significant and largely unregulated presence of ultrafine particles in the atmosphere. Understanding the formation and sources of ambient

ultrafine particles represents a major goal, but analyzing such small particles is a considerable analytical challenge. This study demonstrates how real-time measurements of particle size and chemistry, coupled with gas-phase measurements, can provide unique insight into the daily and seasonal variations of the sources and chemistry of ultrafine particles. Measurements of ambient ultrafine particles are compared from three different single particle techniques which provide high temporal resolution during the 2005 summer (August) and fall (November) seasons in Riverside, CA in conjunction with the Study of Organic Aerosols at Riverside (SOAR) field campaign. During both seasons, vehicle exhaust emissions strongly contributed to the ultrafine particle concentrations during the weekday morning rush hour periods. SMPS measurements during the summer season showed high ultrafine particle concentrations during the afternoons most likely formed by photochemical events. In this study, different sources (and hence chemistry) contributed to the particles during periods of high ultrafine particle concentrations. Therefore, it is important to obtain simultaneous information on ultrafine particle sources as well as concentrations and advance beyond relying just on ultrafine particle concentrations as a proxy in future studies on health effects.

Chapter 2 investigates ship emissions, as they contribute significantly to gaseous and particulate pollution worldwide. To understand the impacts of ship emissions on human health and climate, the chemistry of the emitted particles must be well characterized. Therefore, the size-resolved chemistry distributions of individual particles in ship emissions were measured at the Port of Los Angeles using real-time, single-particle mass spectrometry. Ship plumes were identified through a combination of ship position information and measurements of gases and aerosol particles at a site 500 meters from the center of the main shipping channel of the Port of Los Angeles. Particles containing organic carbon, vanadium, and sulfate (OC-V-sulfate) resulted from residual fuel combustion (i.e. bunker fuel), whereas high quantities of fresh soot particles (when OC-V-sulfate particles were not present) represented distinct markers of plumes from distillate fuel combustion (i.e. diesel fuel) from ships as well as trucks in the port area. OC-V-sulfate particles from residual fuel combustion had significantly higher levels of sulfate and sulfuric acid than plume particles containing no vanadium. We hypothesize that these associations are due to the vanadium (or other metals such as iron or manganese) in the fuel catalyzing the oxidation of $SO_2$ to produce sulfate and sulfuric acid on these particles. This has been show previously in laboratory studies to occur at ambient temperatures (> 25 °C) in the presence of $H_2O$ and $NO_2$ (both present in ship plumes), but these results using single particle mixing state mark the first direct observation of this process under freshly emitted ambient conditions. Enhanced sulfate production on V-containing ship emission particles may lead to the measured levels of sulfate in California, which are currently higher than expected based on emissions inventories. Understanding the overall impact of ships emissions is critical for controlling regional air quality in coastal regions of the world.

### iii. Spatial Variability of Particulate Matter and Sources

Chapter 3 describes how understanding the spatial and temporal variability of particle concentrations and chemistry within the urban aerosol is critical to determining exposure levels and the impact on human health. However, it is difficult to accurately determine this variation by measurements or modeling over small distances with high

time resolution, such as a neighborhood scale of a few kilometers over a few hours. This challenge often leads to simplifications in how models treat the urban aerosol that are not always indicative of ambient conditions. To gain a better understanding of how particle size and chemistry changes on a neighborhood scale within the urban aerosol, the mobile aerosol time-of-flight mass spectrometry (ATOFMS) laboratory was deployed to 3-5 sites over a roughly 10 $km^2$ area on two days (3 sites on February 12, 2009 and 5 sites on March 13, 2009). ATOFMS measurements of size-resolved single-particle chemical composition (0.2 – 3.0 μm) in conjunction with aerosol mass concentration below 2.5 micrometers ($PM_{2.5}$) and size-resolved number concentration measurements provided a detailed characterization of the urban aerosol with high time resolution. Particle concentrations and chemistry were found to differ significantly on these two days, which were characterized by similar meteorological conditions and gas phase concentrations ($SO_2$, $NO_x$, and $O_3$). Clean conditions following rain, observed on the first day of sampling were characterized by low mass and number concentrations with similar chemistry observed across all sites, suggesting decreased influence of local sources. However, during sampling on the second day under more polluted conditions, substantial variation in particle mass, number, and chemistry particularly in the accumulation mode (0.2-1.0 μm), were observed at the various sites around the bay. For the high $PM_{2.5}$ concentration day, decreases in the mass fraction of organic carbon particles and decreases in nitrate on background particle types during the day followed a diurnal pattern. Thus, while minor particle variations were observed spatially on this second day, temporal trends played a greater role in controlling variation in particle concentration and chemistry. These results indicate that strengthening the link between particles and human health requires a more detailed understanding of temporal variations of single particle mixing state within the urban aerosol that $PM_{2.5}$ mass concentrations alone cannot provide.

### iv. Seasonal and Interannual Variability in Particulate Matter Size and Composition

Chapter 4 details aerosol time-of-flight mass spectrometry (ATOFMS) measurements that were conducted during the Study of Organic Aerosols in Riverside, California (SOAR) field campaign in the summer and fall of 2005. Time and size-resolved number fractions of the major particle types are presented for the size range of 0.2–2.5 μm. In general, carbonaceous particles which were mixed with nitrate, sulfate and ammonium dominated (>75%) the aerosols below 1.0 μm, and aged sea salt, dust and aged carbonaceous particles were the major particle types above 1.0 μm, except during the fall Santa Ana periods when dust and biomass particles were prevalent over the whole size range. Most of the major particle types during the summer displayed strong diurnal variations, with high carbonaceous number fractions appearing from night until the morning and aged sea salt, dust, biomass, and OC-vanadium particles peaking in the afternoon. In contrast, fall measurements showed distinct episodic events dominated by different particle types. The majority of the ambient particles contained secondary nitrate and sulfate with higher amounts of particle phase sulfate in the summer and nitrate in the fall. In both seasons, the beta attenuation monitor measurements displayed similar temporal trends when compared to the ATOFMS total carbonaceous fractions, indicating

that carbonaceous particles mixed with sulfate, nitrate, and ammonium were the major component of the $PM_{2.5}$ mass concentrations.

Chapter 5 describes how, during the summer and fall of 2005 in Riverside, California, the seasonal volatility behavior of submicrometer aerosol particles was investigated by coupling an automated thermodenuder system to an online single-particle mass spectrometer. A strong seasonal dependence was observed for the gas/particle partitioning of alkylamines within individual ambient submicrometer aged organic carbon particles internally mixed with ammonium, nitrate, and sulfate. In the summer, the amines were strongly correlated with nitrate and sulfate, suggesting the presence of aminium nitrate and sulfate salts which were nonvolatile and comprised ~6-9% of the average particle mass at 230 °C. In the fall, 86 ± 1% of the amines volatilized below 113 °C with aminium nitrate and sulfate salts representing less than 1% of the particle mass at 230 °C. In the summer, a more acidic particle core led to protonation of the amines and subsequent formation of aminium sulfate and nitrate salts; whereas, in the fall, the particles contained more ammonium and thus were less acidic, causing fewer aminium salts to form. Therefore, the acidity of individual particles can greatly affect gas/particle partitioning of organic species in the atmosphere, and the concentrations of amines, as strong bases, should be included in estimations of aerosol pH.

Chapter 6 discussses how to date most single-particle mixing state studies have focused on individual intensive field studies to draw conclusions about health-related impacts of aerosols. Health and pollution models develop parameters based on these studies and do not incorporate how particle characteristics can change on a yearly basis. Inter-annual variability of ambient particle characteristics was observed using single-particle mass spectrometry during three consecutive summer studies in Riverside, CA. Single-particle mixing states with secondary species and $PM_{2.5}$ mass concentrations were found to vary with meteorology. These inter-annual variations can be used to optimize parameters in health models such that input parameters representing different meteorological conditions each year could improve the predicted particle chemistry and concentrations and improve pollution regulations. For instance, 2005 represented a consistently diurnal year with an aged organic atmosphere, 2006 was a cool, moist year correlating with an amine-rich environment, and 2007 was a Santa Ana year correlating to the presence of dust and salts. Although the particle chemistry was different each year, particles containing elemental carbon internally mixed with organic carbon had similar temporal trends to $PM_{2.5}$ mass concentrations, comprising 13-31% of the total number of particles. This suggests a large influence of aged anthropogenic particles on particle mass; however, this pattern was not constantly observed because of the large presence of other types mentioned above. In the future, these results could be used as a first approximation as to what the detailed chemical composition of $PM_{2.5}$ may be given a set of meteorological conditions, which is what many health standards are based on. Since continuous intensive particle measurements are difficult long-term, the chemistry indicated by meteorological conditions can be used in models to predict how $PM_{2.5}$ changes impact human health.

## v. Mass Comparisons and Investigations into the Volatile and Semivolatile Fraction of Particles

Chapter 7 shows a comparison of two approaches for converting unscaled ATOFMS measurements into quantitative particle mass concentrations using (1) reference mass concentrations from a co-located micro-orifice uniform deposit impactor (MOUDI) with an accurate estimate of instrument busy time, and (2) reference number concentrations from a co-located aerodynamic particle sizer (APS). Aerodynamic-diameter-dependent scaling factors are used for both methods to account for particle transmission efficiencies through the ATOFMS inlet. Scaling with APS data retains the high-resolution characteristics of the ambient aerosol because the scaling functions are specific for each hourly time period and account for a maximum in the ATOFMS transmission efficiency curve for larger sized particles. Scaled mass concentrations obtained from both methods are compared with co-located $PM_{2.5}$ measurements for evaluation purposes. When compared against mass concentrations from a beta attenuation monitor (BAM), the MOUDI scaled ATOFMS mass concentrations show correlations of 0.79 at Fresno, and 0.91 for the APS scaled results at Angiola. Applying composition dependent density corrections leads to a slope of nearly one with zero intercept between the APS scaled absolute mass concentration values and BAM mass measurements. This paper provides details on the methodologies used to convert ATOFMS data into continuous, quantitative, and size resolved mass concentrations that will ultimately be used to provide a quantitative estimate of the number and mass concentrations of particles from different sources.

Chapter 8 provide greater detail on the challenges of scaling ATOFMS data with the aerodynamic particle sizer (APS). Quantitative mass concentrations of different particle types can be obtained by scaling the ATOFMS data with aerodynamic particle sizer (APS) number concentration measurements. A question arises as to the stability of this procedure in multiple field locations. In this study, the effect of correcting ATOFMS measurements of two studies in Fresno and Angiola with APS scaling functions from different reference field studies conducted in other locations was investigated. Notably, the particle type mass fractions obtained within the submicron ($0.2 \leq D_a < 1.0$ μm) size range were almost identical, regardless of the reference APS scaling function used. More differences (0.089% - 15%) were obtained in the supermicron ($1.0 \leq D_a \leq 2.5$ μm) mass fractions, mainly due to the shift in the minima of scaling curves at higher sizes. Higher mass fractions (~5% more) of aged sea salt particles and lower fractions of carbonaceous particles were obtained when scaling supermicron particles of object studies with the APS scaling functions from APMEX and NC-CCS-II studies. No substantial differences were observed when scaling the specific studies with either the co-located or reference scaling functions. Therefore, this study demonstrates that an estimate of the submicron particle type mass fractions within 10 % and of supermicron particle type mass fractions within 19% can be obtained by scaling ATOFMS measurements with APS scaling functions from other studies if no co-located APS measurements are available.

## vi. Changes in the Size-Resolved Particle Composition Linked with Meteorological Measurements and Air Mass Back Trajectories to Increase Understanding of Sources and Secondary Contributions to Particulate Matter

Chapter 9 discusses that trace metal-containing particulate matter (PM) has been associated with health effects and environmental contamination despite representing only a small mass fraction of ambient PM. Using aerosol time-of-flight mass spectrometry (ATOFMS), individual particles with sizes ranging from 100-2550 nm were examined during the 2005 summer and fall seasons in Riverside, California for the following trace metals: V, Fe, Ni, Cu, Zn, Sr, Mo, Sn, Sb, Ba, W, and Pb. The chemical speciation, temporal trends, seasonal differences, size distributions, and wind direction dependencies are reported for the five trace metals (V, Fe, Zn, Ba, and Pb) that exhibited the highest number concentrations. By combining this information, the potential sources of the trace metal-containing particles can be identified, whether they are local or from long-range transport. The metal-containing particles demonstrated different temporal and spatial trends in the summer versus the fall; both Ba and Pb particles were found to be more abundant during the fall due to their source locations and the wind direction. Many of the particle classes are identified as originating from anthropogenic sources (industrial and transport sector) in the Los Angeles Basin.

Chapter 10 shows that ship and other emissions near the Los Angeles and Long Beach Port region strongly influence air pollution levels in the San Diego area. During time periods with regional transport, atmospheric aerosol measurements in La Jolla, California show an increase in 0.5-1 μm sized single particles with unique signatures including soot, metals (i.e. vanadium, iron, and nickel), sulfate, and nitrate. These particles are attributed to primary emissions from residual oil sources such as ships and refineries, as well as traffic in the port region, and secondary processing during transport. During regional transport events, particulate matter concentrations were 2-4 times higher than typical average concentrations from local sources, indicating the health, environmental, and climate impacts from these emission sources must be taken into consideration in the San Diego region. Unless significant regulations are imposed on shipping-related activities, these emission sources will become even more important to California air quality as cars and truck emissions undergo further regulations and residual oil sources such as shipping continue to expand.

Chapter 11 discusses that during the 2007 wildfires in San Diego County over 2,000 homes and 300,000 acres of land were burned. For the duration of these fires, from October 21$^{st}$ through November 1$^{st}$, 2007, individual particle size and composition along with total particle and cloud condensation nuclei (CCN) concentrations were measured in real-time at the University of California San Diego (UCSD) main campus and Scripps Institution of Oceanography Pier. Aerosol hygroscopicity was estimated from the CCN measurements and compared to the simultaneous aerosol chemistry and size distribution measurements. Near the beginning of the wildfires CCN concentrations were between 2,000 -14,000 cm$^{-3}$ and biomass burning aerosol (BBA) made up more than 80% of the total particles <300nm. The BBA produced by the wildfires made a dominant contribution to the CCN populations observed. The lower hygroscopicity parameter ($\kappa$) range observed in this study for the UCSD campus ($\kappa$ =0.004-0.3) indicates that there were non-hygroscopic or insoluble compounds present in the BBA. The biomass emissions measured during these wildfires were somewhat below, and on the lower end

of, the range of previously determined BBA hygroscopicities from both controlled burns and ambient measurements. The BBA during the beginning of the fires were relatively fresh and consisted primarily of KCl and water soluble organic compounds (WSOC) including formic and acetic acids and levoglucosan, measured using aerosol time-of-flight mass spectrometry (ATOFMS). As the BBA aged they contained increased amounts of $KHSO_4$ compounds, and more oxidized organic compounds including oxalic acid. This was likely caused by a transition from flaming fires to predominantly smoldering fires, as well as increased atmospheric aging. Concurrent with these changes in particle chemistry, both the CCN concentration and particle hygroscopicity decreased. This indicates an important role of the inorganic component of the BBA in influencing the CCN population and particle hygroscopicity. A correlation between particle-phase ammonium and hygroscopicity during a particular event was also observed. The ammonium may have shifted the acid-base neutrality of the aerosols, possibly allowing additional weaker acids to partition to the aerosol phase.

## vii. Development of Source Apportionment Algorithms

Chapter 12 details how single particle mass spectrometry techniques such as aerosol time-of-flight mass spectrometry (ATOFMS) offer a unique approach for on-line source apportionment of ambient aerosols. Source signatures, or mass spectral "fingerprints", have been obtained using ATOFMS from a variety of sources with an emphasis placed on distinguishing between emissions from different types of vehicles. In this study, the signatures from previous source tests of diesel powered heavy duty vehicles (HDDV) and gasoline powered light duty vehicles (LDV) are matched to particle spectra acquired during a freeway-side study performed over a month in southern California to source apportion the particles. Using a relatively high matching (vigilance) factor of 0.85, particle mass spectral signatures from the vehicle source studies matched 83% of the freshly emitted particles detected alongside the freeway. The particle contributions alongside the freeway in the ultrafine and accumulation size range (aerodynamic diameter = 50–300nm) were apportioned to 32% LDV, 51% HDDV, and 17% from other sources. This paper discusses the apportionment process used and the methods used for validation with peripheral instrumentation.

Chapter 13 describes how several approaches for ambient aerosol source apportionment have been developed over the years. A number of these techniques involve determining organic and inorganic source markers from offline bulk filter analysis using a variety of analytical tools (such as mass spectrometry, chromatography, and microscopy). Some other methods have inferred that certain sources can be determined from correlations between particle size data and gas phase measurements. The technique presented here involves using a mass spectral source signature library to apportion single particles detected with an aerosol time-of-flight mass spectrometer (ATOFMS). The source signature library has been developed through a series of source and ambient characterization studies and currently contains signatures for heavy duty diesel vehicles (HDDV), light duty gasoline vehicles (LDV), dust, sea salt, biomass, and meat cooking. There are also additional non-source specific signatures, determined from the data acquired for several ambient ATOFMS studies, for aged organic carbon, aged elemental carbon, amine containing particles, PAH’s, ammonia rich particles, vanadium particles, and elemental carbon particles. Using the ART-2a algorithm to match

individual ambient particle mass spectra to the source signature library, it was found that 97% of ambient particles (50 – 3000 nm) detected with two ATOFMS instruments near a freeway matched the library signatures. The use of the ART-2a source signature matching method shows that particles from gasoline powered vehicles can be readily distinguished from heavy duty diesel powered vehicles in roadside ambient measurements. Additionally, it was discovered that regional background particles matching with specific elemental carbon and vanadium signatures from ship emissions dominate and overwhelm the local emissions; however, the library matching method is able to identify their presence and distinguish them from local emissions.

Chapter 14 describes a new source apportionment method using a library composed of unique source mass spectral signatures obtained by aerosol time-of-flight mass spectrometry (ATOFMS) has been developed. The goal of this chapter is to apply this source signature library to an ambient dataset collected in a highly aged environment to evaluate the performance of the source apportionment method in a more aged environment and to determine the relative contributions of the major primary and secondary sources to the atmospheric aerosol. Ambient particles ranging in aerodynamic diameter from 50 to 3000 nm were analyzed in Riverside, California in conjunction with the Study of Organic Aerosols at Riverside (SOAR) campaign in the summer and fall seasons of 2005. The apportionment results showed that the majority of small (50-140 nm) ambient particles came from local vehicle exhaust emissions. The larger (140+ nm) particles demonstrated strong seasonal differences. Based on differences in meteorological conditions, the time series for the summer particles followed diurnal patterns, whereas the fall particles displayed episodic behavior. It was determined that the original source signature library did not apportion a significant number of particles; therefore, multiple approaches were explored and tested to improve the total number of particles detected in this challenging environment that were matched. It was found that introducing new seeds made from aged ambient particles to the library yielded better results than by lowering the "matching" or data analysis factor. By adding additional aged seeds to the source signature library, the unclassified category was reduced (as much as 14%) and the contribution of the aged particle types increased, thus improving the source apportionment method so it can now be used on ambient datasets collected in aged environments. In addition, the extent of aging of particles from primary sources was investigated focusing on secondary species including nitrates, sulfates, and amines. It was revealed that although nitrate has different seasonal sources, it is the dominant secondary species on aged particles from primary sources in Riverside.

Chapter 16 includes a summary and concluding remarks regarding the major findings presented in this report.

# II. Objectives and Results

## Time and Size Resolved Chemical Composition Detailing Short Term Changes in Composition

### 1. Detection of ambient ultrafine aerosols by single particle techniques during the SOAR 2005 campaign

#### i. Introduction

High concentrations of atmospheric ultrafine particles (aerosols with diameters less than 100 nm) have been observed worldwide, from arctic areas and remote regions to coastal marine locations and urban environments (14). Growing evidence suggests that the inhalation of ultrafine particles may have more adverse health effects than larger particles has raised interest in the sources and atmospheric processing of these particles (15). Ambient particles can be divided into two basic categories based on their production mechanism: primary, which are directly emitted from sources such as vehicles and industrial processes, and secondary, which are formed via gas-to-particle conversions (16). The formation and growth of secondary ultrafine particles during nucleation events have been the focus of intensive research recently, leading to the proposal of several different formation mechanisms (14,17,18). From a regulation perspective, it is important to be able to distinguish the origin of the ultrafine particles, as primary and secondary particles require different means of control (direct emissions versus gaseous precursors).

The small size of ultrafine particles makes them much more challenging to detect than larger particles. Despite accounting for greater than 80% of the number of particles in $PM_{2.5}$ (particulate matter with diameters less than 2.5 μm), estimates suggest that ultrafine particles collectively represent very little mass (< 20%) (16,19,20). Therefore, $PM_{2.5}$ regulations based on mass concentrations do not provide a good control for the concentrations of ultrafine particles (21). The poor correlation between $PM_{2.5}$ and ultrafine particles suggests that number-based measurements may be better suited for studying ultrafine particles than a bulk $PM_{2.5}$ mass approach. Size-fractionated mass measurements by a NanoMOUDI (Nano-micro orifice uniform deposit impactor) have been obtained (22), but the continuous sampling time required to collect sufficient material for mass and chemical analysis can be as long as two weeks (23). With such long sampling periods, it is difficult to extract details about specific short-lived ultrafine particle episodes (19,21,24), which can be captured by high temporally-resolved continuous measurements. Techniques that rely on optical detection are problematic, because as the particle diameter becomes increasingly smaller than the wavelength of light, the intensity of the scattering signal quickly plummets; the minimum practical observable particle size using optical techniques commonly is ~100 nm (25,26). Therefore, in order to efficiently detect ultrafine particles optically, it is necessary to enhance previously developed instrumentation. Several approaches have been tried

successfully, such as growing small particles into detectable sizes for counting via the condensation particle counter (CPC) (27) or by using specific critical orifices to create an upstream pressure that focuses particles of a given size range such as with the single particle mass spectrometer known as RSMS (28-30).

The main goals of this study involve comparing the seasonal variability of ultrafine particle concentrations in Riverside, CA from three different techniques with high temporal resolution and to use the combined data in conjunction with other peripheral instrumentation for deriving a better understanding of ultrafine particle chemistry. Riverside is located east of the Los Angeles (LA) Basin and, due to generally consistent meteorological patterns, is regularly downwind of the pollutants emitted in the LA area. The instruments used in this study include a scanning mobility particle sizer (SMPS), an ultrafine condensation particle counter (UF-CPC), and an ultrafine aerosol time-of-flight mass spectrometer (UF-ATOFMS). Supporting data from co-located gas- and particle-phase instruments, as well as meteorological measurements, are used to provide additional insight into the origin of the ultrafine particles.

**ii. Experimental**

Sampling on the campus of the University of California, Riverside (33°58′18″N, 117°19′22″W) during the summer (July-August) and fall (October-November) of 2005 occurred in conjunction with the Study of Organic Aerosols at Riverside (SOAR) field campaign. Details on the sampling location and inlets of the mobile laboratory can be found elsewhere (31). **Table 2** provides the acronym, model, measurement, and sampling interval for each instrument used in this manuscript. All instrumentation, except for the CPCs and summer CO analyzer, were housed in a mobile laboratory; the other instruments were located in nearby trailers with similar sampling inlets ($PM_{2.5}$ inlet cutoffs and reflective insulation wrap on the sampling lines). Ambient temperature, relative humidity (RH), and photosynthetically active radiation (PAR) measurements were provided by the Goldstein group of the University of California, Berkeley. The work presented here focuses on one week of data collected in the summer (Sunday, August 7$^{th}$ through Saturday, August 13$^{th}$) and fall (Sunday, November 6$^{th}$ through Saturday, November 12$^{th}$) seasons. Though Santa Ana events, characterized by dry easterly winds, tend to occur during fall and winter months, they do

**Table 2: Instrumentation.**

| Instrument | Make & Model | Measurement | Averaging Interval |
|---|---|---|---|
| Scanning Mobility Particle Sizer (SMPS) | TSI Model 3936L 10 | particle number concentration (15-866 nm) | 5 min |
| Ultrafine Condensation Particle Counter (UF-CPC) | TSI Model 3025A | particle number concentration (> 3 nm) | 1 min |
| Ultrafine Aerosol Time-of-Flight Mass Spectrometer (UF-ATOFMS) | | chemical composition (50-400 nm) | real-time |
| Aethalometer | Magee Scientific AE-3 Series | optical absorption cross-section per unit mass | 5 min |
| CO Analyzer (summer) | TEI Model 48CTL | CO concentration levels | 30 min |
| CO Analyzer (fall) | Ecotech EC 9830 | CO concentration levels | 1 min |
| Chemiluminescence NO-$NO_2$-$NO_x$ Analyzer | TEI Model 42C | NO & $NO_x$ concentration levels | 1 min |
| UV Photometric $O_3$ Analyzer | TEI Model 49C | $O_3$ concentration levels | 1 min |

TEI: Thermo Environmental Instruments

not represent the average fall conditions. Therefore, the representative fall week for this study does not contain any Santa Ana events (31). Results are presented in Pacific Standard Time (PST), which is one hour behind local time during the summer.

It is important to briefly review the main operating principles of each instrument in order to understand how the measurements are made and upon which aerosol properties they depend. In this study, ultrafine particles are defined as having diameters less than 100 nm; although, each of the techniques in this study use different size metrics. CPCs provide continuous real-time ambient number concentration measurements by optically counting particles upon which a vapor has condensed. The CPC effectively lowers the minimum size detection cutoff by enlarging the particle diameter by the use of a condensable vapor such as an alcohol (27). The butanol-based TSI 3025A UF-CPC has a minimum diameter cutoff of 3 nm. An SMPS measures the number-based particle size distributions based on their electrical mobility diameter through the combination of a differential mobility analyzer (DMA) connected to a CPC. By scanning through the set voltage range, a range of mobility diameters can be selected and counted. In this study, the SMPS used a TSI 3010 CPC with a TSI 3080 electrostatic classifier (DMA) and was set to have a lower mobility diameter limit of 15 nm. The UF-ATOFMS simultaneously acquires positive and negative ion mass spectra, as well as aerodynamic diameter information, for single particles in real-time. It has improved detection efficiency for small particles (<300 nm) over the standard transportable ATOFMS (1) by replacing the converging nozzle inlet with an aerodynamic lens inlet (2). The lens system tightly collimates the particle beam, so that smaller ultrafine particles will be more efficiently transmitted in the instrument (3,4). The UF-ATOFMS also has enhanced light-scattering detection by the use of focusing lens to tighten the continuous laser beams, increasing the laser beam power density, and by employing a fast amplifier to improve the signal-to-noise ratio (2). All these enhancements, in addition to the aerodynamic lens systems, are necessary to improve the minimum optical detection size of ~100 nm down to 50 nm. In this study, chemical information was obtained for approximately 20.5% and 28.6% of the ultrafine particles that were sized by the UF-ATOFMS during the summer and fall, respectively. Just like ambient particles of larger sizes, less than 100% of the particles that are sized produce mass spectra due to factors such as the interaction between the particle beam and the 266 nm laser beam, chemical composition, and desorption/ionization capability of the particle (2,32). The percentages of the ultrafine particles that were chemically analyzed fit well within the overall range (15-35%) of all

ambient particles chemically analyzed by the UF-ATOFMS throughout both studies. Most of the observed variability in the percentage of particles that were chemically analyzed could be explained by busy time issues, as previously discussed in Sodeman et al. [*Sodeman et al.*, 2005]. During periods with very high particle concentrations (all sizes), the older data acquisition system used for this study was unable to save the spectra as quickly as they were produced, lowering the overall percentage of chemically analyzed particles.

The instruments detect particles based on their optical, electrical mobility, or aerodynamic diameters. The electrical mobility diameter of a particle is the diameter of a sphere with an identical migration velocity in a constant electric field (33), and the aerodynamic diameter of a particle is the diameter of a sphere of unit density with the same terminal velocity (26). DeCarlo and coworkers present a detailed theoretical review of the relationship between the electrical mobility and aerodynamic diameters of a particle (34). Briefly, both diameters are dependent upon the shape of the particle. With increasing irregularity, the mobility diameter increases, whereas the aerodynamic diameter decreases. As opposed to the electrical mobility diameter, the aerodynamic diameter also is governed by the density of the particle, increasing with higher particle densities. The particle density is mainly dictated by the chemical composition and shape of the particle. Spherical particles of unit density will have the same electrical mobility and aerodynamic diameters.

Among these instruments, only the UF-ATOFMS obtains chemical information in addition to the size of the single particles. The UF-ATOFMS chemically analyzed 16,321 ultrafine particles during the summer week-long period and 20,320 ultrafine particles during the fall period. In order to group the ultrafine particle (aerodynamic diameter 50-100 nm) mass spectra measured by the UF-ATOFMS into chemical classes, an adaptive resonance theory neural network algorithm (ART-2a) was employed. ART-2a sorts and categorizes individual particles into clusters based on similar mass spectral characteristics (35). The main user-defined parameters for ART-2a are the learning rate, number of iterations, and vigilance factor, which were set to 0.05, 20, and 0.80, respectively, for this work. The resulting most populated 50 clusters, which represent ~97% of the total sampled particles, were further combined by hand (based on chemical similarities) to yield the general classes presented herein.

**iii. Results and discussion**

## *a. Ambient measurements*

The UF-ATOFMS measured the chemistry of individual ultrafine particles detected during the SOAR campaigns. **Figure 2** displays the hourly number of particles for which the UF-ATOFMS obtained both size and chemical information as a function of aerodynamic diameter between 50-400 nm. Upstream of the UF-ATOFMS, a modified micro-orifice uniform deposit impactor (MOUDI) decreased the transmission of larger particles so that the UF-ATOFMS had more opportunity to analyze the smaller particles, which are harder to detect due to their lower transmission efficiencies. The figure shows that the UF-ATOFMS primarily detected particles with aerodynamic diameters between 150 and 300 nm, which was due to a combination of the high ambient concentrations and instrument detection abilities. The top plot clearly shows that the number of detected ultrafine particles (50-100 nm) spiked each morning during weekday rush hour periods.

While the UF-ATOFMS measurements do not represent true counting statistics due to transmission efficiency issues (2), it does provide chemical information about the single particles it detects and the relative percentages of each type. The top mass spectra representing each of the general chemical classes are shown in **Figure 3**. **Figure 4** provides the relative size distributions of the particle types during both the summer and fall seasons and also shows the size dependence of the particles that are chemically analyzed by the UF-ATOFMS. The 50-60 nm bin has the least number of chemically analyzed particles (55 and 78 particles for summer and fall, respectively), because they are the smallest and, therefore, most difficult to detect. The top five particle types have carbon cluster peaks ($C_1$, $C_2$, $C_3$, etc.) indicative of elemental carbon (EC) and

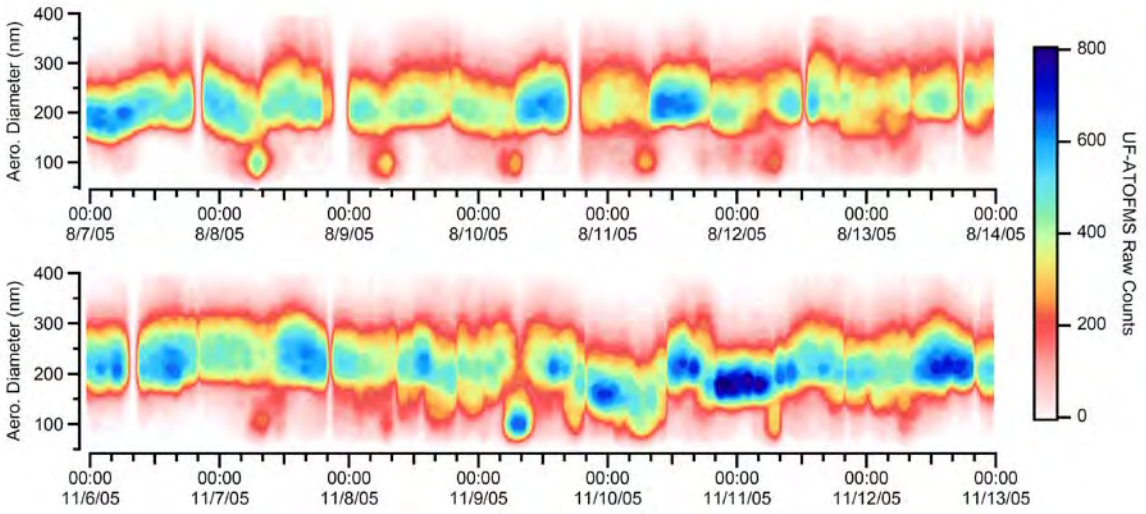


Figure 2: Hourly UF-ATOFMS counts of single particles for which chemical information was obtained as a function of aerodynamic diameter during the summer (top) and fall (bottom).

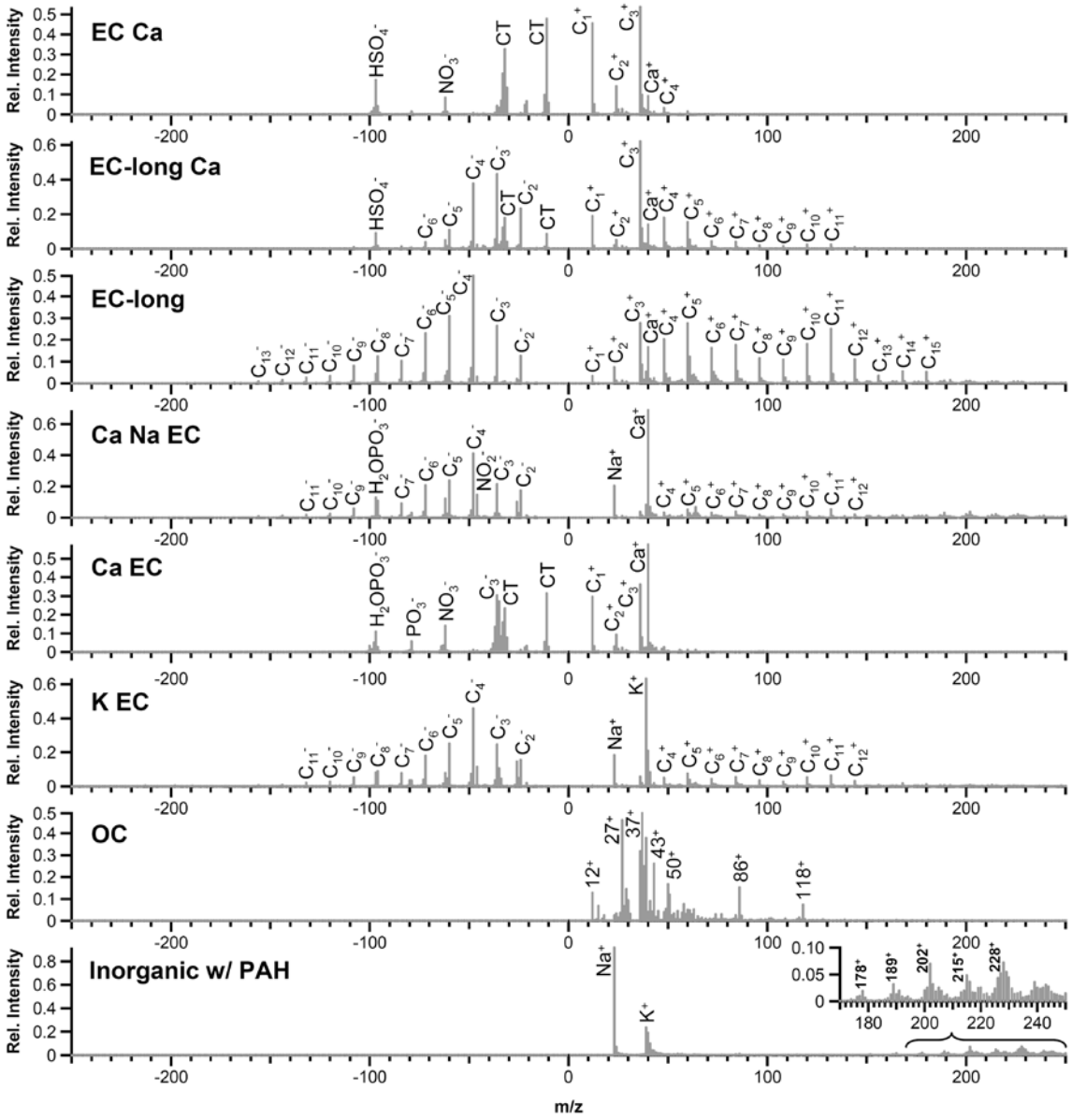


Figure 3 Representative mass spectra for the general chemical classes of ultrafine particles as determined by the UF-ATOFMS. "CT" in the negative spectra represents crosstalk due to the interference of extremely intense peaks in the positive polarity.

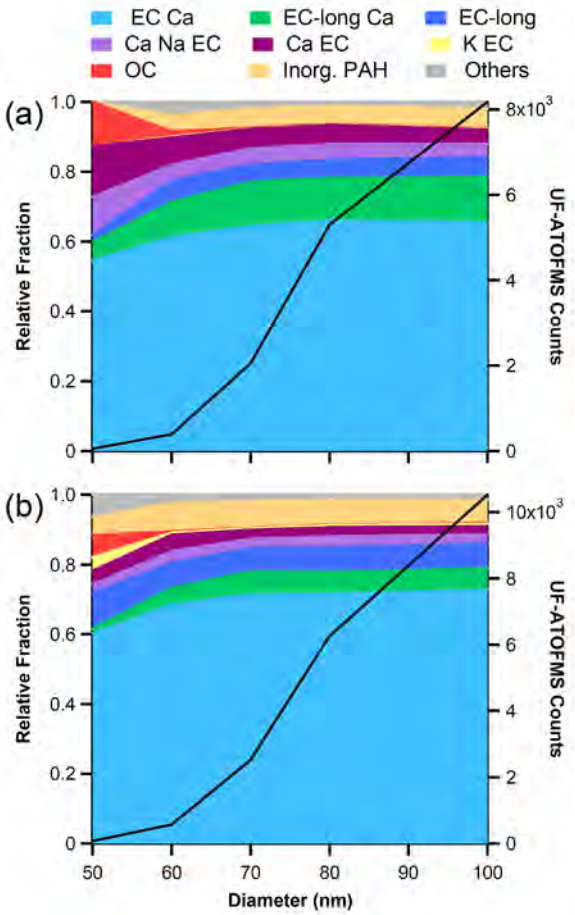


Figure 4 Relative size distribution (10 nm bins) of ultrafine particle types during the summer (a) and fall (b). The black trace represents the total number of ultrafine particles chemically analyzed by the UF-ATOFMS in each 10 nm size bin.

a peak of calcium at *m/z* 40 $[Ca]^+$ with the dominating class (EC Ca) representing over 60% of the ultrafine particles. These spectra very closely resemble the variations in the mass spectral signatures detected in previous source characterization studies of vehicle exhaust, showing Ca due to lubricating oil as well as EC (36-38). These particle types vary in their intensities of EC, calcium, sodium (23 $[Na]^+$), phosphate (79 $[PO_3]^-$ and 97 $[H_2O{\cdot}PO_3]^-$), sulfate (97 $[HSO_4]^-$), and nitrate (46 $[NO_2]^-$ and 62 $[NO_3]^-$) peaks. The K EC class, marked by intense potassium (39 $[K]^+$) and EC peaks, represents a very small percentage (< 1%) of the ultrafine particles in Riverside. It is not surprising that most of the particles detected by UF-ATOFMS belonged to these EC classes, because EC particles are fractal and thus optically larger. Laboratory tests with the commonly used standard of polystyrene latex spheres (PSLs) have indicated that the UF-ATOFMS does not detect spherical particles with diameters below 90 nm as well. Therefore, this observation indicates that the UF-ATOFMS is very sensitive and uniquely suited to measuring the impact of ultrafine particles from vehicle emissions. The organic carbon (OC) particle type contains hydrocarbon envelopes with peaks at *m/z* 27 $[C_2H_3]^+/[NCH]^+$ and 43 $[C_2H_3O]^+/[CHNO]^+$. It also contains peaks at *m/z* 86 and 118, which are markers for amines (39). The OC type is likely the only spherical particle type detected in the ultrafine mode, and it represents less than 1% of the ultrafine particles detected by the

UF-ATOFMS. The final class shown in **Figure 3** (Inorganic w/ PAH) is dominated by the inorganic species of sodium and potassium but also contains polycyclic aromatic hydrocarbons (PAH) at high *m/z*. This class describes ~6% of the ultrafine particles analyzed by the UF-ATOFMS. It is likely that this inorganic ash particle type adsorbs semivolatile PAH as they partition from the gas to particle phase during the cooling of emissions. It is worth noting that a high percentage (~70%) of the particles in the two non-EC containing classes (OC and Inorganic w/ PAH) did not produce appreciable negative ion signals, and thus these two classes are represented in **Figure 3** without negative ion peaks.

**Figure 5** provides the hourly relative fractions for the general chemical classes of the ultrafine particles (50-100 nm) observed by the UF-ATOFMS during the summer (top) and fall (bottom) seasons. The black trace represents the hourly total number of ultrafine particles sized and chemically analyzed by UF-ATOFMS to highlight the periods of higher detection. The missing periods (in white) occur during times when quality control procedures or effective density measurements were being conducted or some other factor led to low particle statistics (< 10 ultrafine particles in that hour). The figure clearly illustrates that the chemical classes associated with vehicle exhaust emissions dominate the ultrafine size mode. Regardless of the time of day, the relative fractions of the ultrafine particle types remain comparatively constant and show no diurnal trend. This agreement is further confirmed by the source apportionment of the SOAR campaigns in Chapter 5 (40). Although vehicle exhaust emissions are a major contributor of primary ultrafine particles and the local vehicle emissions can influence the sampling site at all times, it is expected that the largest contribution will occur during the weekday rush hour periods, which agrees with peaks in the *number* of ultrafine particles detected by the UF-ATOFMS. Despite the lack of large differences in the relative fractions of the chemical classes over time, the number of ultrafine particles detected by the UF-ATOFMS does change significantly. Therefore,

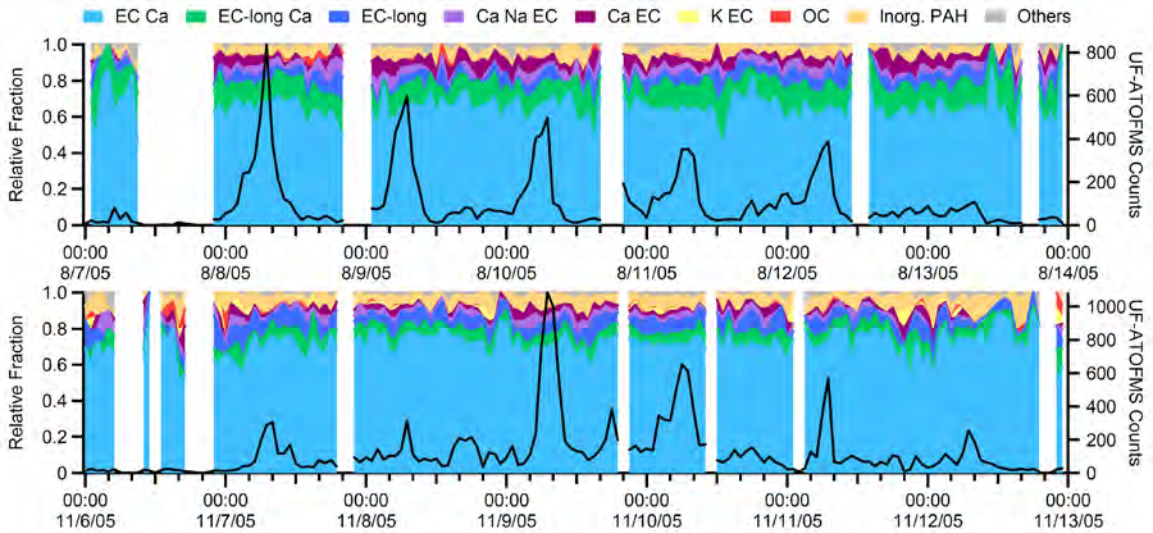


Figure 5 Hourly relative fractions of ultrafine particle types during the summer (top) and fall (bottom). The black trace represents the hourly total of ultrafine particles (50-100 nm) chemically analyzed by the UF-ATOFMS

the UF-ATOFMS unscaled counts represent a good tracer of periods of intense vehicle activity at this location. This observation makes sense, because vehicle exhaust emissions were the only significant source of primary ultrafine particles in close proximity to the sampling site. Any other potential source of ultrafine particles was too far away and the particles would have either coagulated or grown outside of the ultrafine size range before reaching the sampling site. It is also likely that any sources of spherical ultrafine particles would not be detected efficiently by the UF-ATOFMS, as described above.

Multiple gas- and particle-phase instruments, in addition to the UF-ATOFMS, were sampling in Riverside, CA in 2005. These supporting ambient measurements can provide complementary information to the observations made with the UF-ATOFMS. **Figure 6** displays the temporal trends of these other measurements observed for one week (Sunday through Saturday) during the summer. The top panel shows the overall $PM_{2.5}$ number concentration (particles $cm^{-3}$) as measured by the UF-CPC, as well as the meteorological parameters (PAR, RH, and temperature). The middle panel presents the black carbon (BC) concentrations determined using the 880 nm wavelength of the aethalometer, in addition to the gas-phase measurements of CO, $NO_x$, and $O_3$. The bottom contour plot illustrates the particle number concentration detected by the SMPS as a function of electrical mobility diameter (15- 200 nm).

The SMPS measurements showed increased ultrafine particle number concentrations during the weekday morning rush hour period from approximately 5:00 to 10:00 PST, as shown in **Figure 6**. The morning rush hours also were the main time window during which the smallest particles observed by the SMPS (< 30 nm) showed the

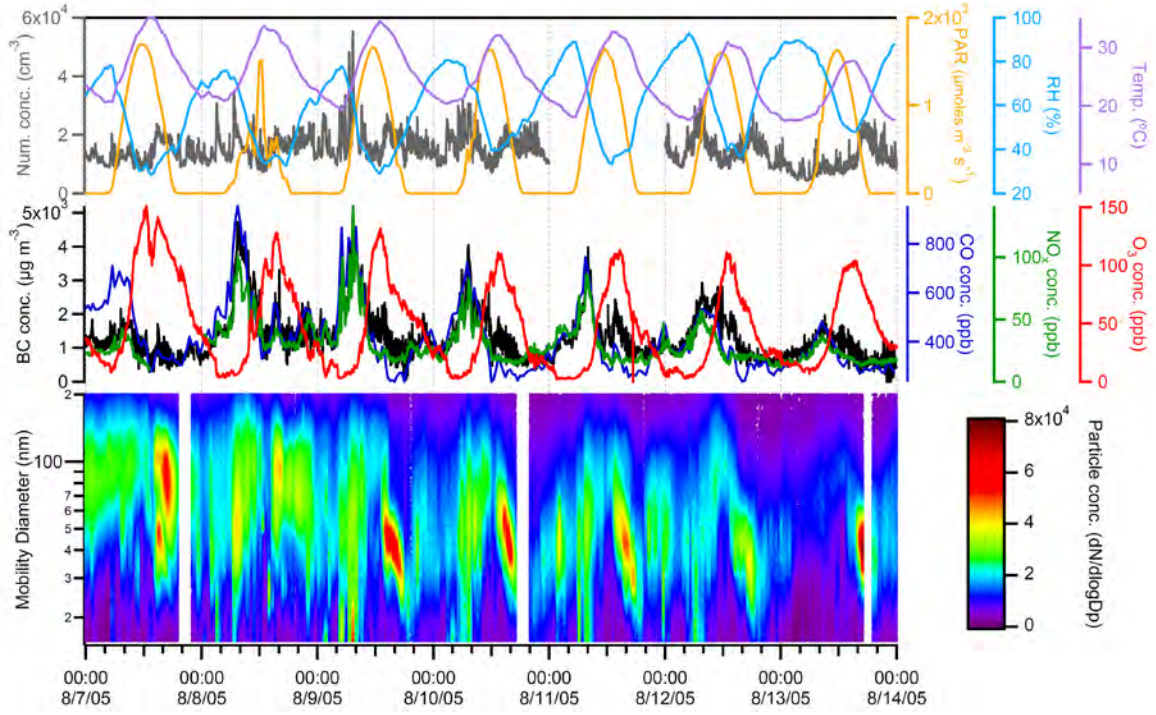


**Figure 6: Temporal trends of gas- and particle-phase measurements, as well as meteorological variables, for one week (Sunday through Saturday) during the summer season.**

highest concentrations. In addition, the BC, CO, and $NO_x$ measurements, which all tracked each other well (lowest $R^2$ value of 0.71), peaked during this same period (specifically between 8:00 and 9:00 PST). All three measurements correlated with the ultrafine counts from the UF-ATOFMS. For example, the $R^2$ value between $NO_x$ concentrations and UF-ATOFMS ultrafine counts was 0.68. Previous studies have reported high correlations between ultrafine number concentrations with both CO and $NO/NO_x$ measurements at traffic-orientated sampling sites (41-43). Even mass-based BC concentrations have shown significant correlations with ultrafine particle number concentrations (13,20), as also illustrated here. Based on these results, it appears the ultrafine particle number concentration can serve as a good proxy for traffic activity; however, the highest number concentrations (red regions between 30 and 60 nm) measured by the SMPS occurred during the afternoons and not during the traffic-dominated morning rush hour period. Therefore, at least during the summer, the ultrafine particle number concentrations measured by the SMPS are not a unique indicator of traffic activity. The next section explores the SMPS afternoon ultrafine particle peaks in more depth.

### *b. Afternoon photochemical events*

Previous studies of the diurnal trends of ultrafine particles in the source and receptor sites of the LA Basin have determined that an additional source or sources, other than direct emissions by vehicles, make significant contributions to the number of ultrafine particle in the afternoons of warm months in Riverside. Using the chemical composition data from MOUDI measurements, these studies identified photochemically generated secondary species as the source (44,45). This same photochemical source explains the high concentrations of particles with electrical mobility diameters between 30 and 60 nm in the afternoon hours (13:00–18:00 PST) in **Figure 6**. The daily ultrafine particle event started at the temperature peak which occurs just after the maximum levels of solar radiation and $O_3$ have been reached on both weekdays and weekends, when traffic activity is reduced. Moreover, the gas-phase tracer concentrations of fresh traffic emissions (CO and $NO_x$) were at their minimum values. A detailed study of the aethalometer measurements made during the SOAR campaign also indicated a change in the afternoon mixing state consistent with the condensation of secondary species on account of the diurnal weekday pattern in the absorption cross section, signifying that traffic is not the dominant source of ultrafine particles in the afternoons (46). Additionally, the chemistry of the afternoon particles is expected to be different, because the cloud condensation nuclei (CCN) activity was observed to peak in the afternoon during the summer SOAR campaign (47). As shown in **Figure 2**, few ultrafine (sub-100 nm) particles were chemically analyzed by the UF-ATOFMS during the afternoon photochemical events in the summer. Rather, the UF-ATOFMS detected mostly large (> 100 nm) and aged vehicle particle types and only a few fresh (ultrafine) vehicle particle types during the afternoons. As mentioned, the SMPS measurements indicate that the majority of the ultrafine particles during these events were between 30 and 60 nm, which is below the minimum detection size (50 nm) of the UF-ATOFMS. **Figure 4** shows that the smallest number of ultrafine particles that were chemically analyzed by the UF-ATOFMS was in the 50-60 nm size bin. The fact that the UF-ATOFMS detected few

ultrafine particles during the afternoon serves as further indication that these afternoon particles are not from vehicle exhaust emissions. If the SMPS had been the only instrument sampling at this location, it would have been difficult to rule out the possibility that the high concentrations of ultrafine particles in the afternoon were from vehicles. This study demonstrates how a combination of several different instruments can be used to uniquely identify the source or formation pathway of ultrafine particles.

It is noteworthy that while the SMPS measurements differ based on the time of day, the relative fractions of the particle types detected by the UF-ATOFMS stay relatively constant. Soot-like particles, formed from fossil fuel combustion in vehicles, have irregular shapes and effective densities less than unity. Based on these properties, such particles will have aerodynamic diameters smaller than and electrical mobility diameters larger than their physical diameters (34,48). In other words, the ultrafine particles characterized by the UF-ATOFMS based on their aerodynamic diameters would not be considered ultrafine particles based on their electrical mobility diameters. The effect of this size distinction was observed directly in experiments coupling a DMA with the UF-ATOFMS during the same field campaign; for example, elemental carbon particles with electrical mobility diameters of 400 nm had aerodynamic diameters of 100 nm (48). Under these circumstances, correcting the aerodynamic-based size distribution of the UF-ATOFMS by scaling directly (size for size) to the electrical mobility distribution measured by the SMPS without adjustments for the particle density and shape factor can lead to erroneous results. This discrepancy must always be taken into consideration, especially for the smallest particles ($\leq$200 nm ) which are the most fractal and have the greatest difference between their aerodynamic and electrical mobility diameters. This information had not been available at the time of analysis for the results presented in Chapter 2. Although the particles detected by the UF-ATOFMS indeed are considered ultrafine particles according to their aerodynamic diameters, the ultrafine particles observed by the SMPS, especially those during the summer afternoon photochemical events, are too small to be optically detected in the UF-ATOFMS. This fact explains why the UF-ATOFMS did not detect a change in the relative number fraction of particle types during the summer afternoon periods.

The lack of the diurnal trend in particles detected by the UF-ATOFMS could arise from the following reasons: only large fractal (non-spherical) vehicle particles with ultrafine aerodynamic diameters are able to optically trigger the timing circuit of the instrument and spherical ultrafine particles from non-vehicular ultrafine particles sources produce particles that are too small to be detected optically with the current configuration. The UF-ATOFMS detection efficiency decreases rapidly with the decreasing diameter of spherical particles; for example, the detection efficiency for the common standard of polystyrene latex spheres (PSLs) is only ~0.3% for 95 nm PSL particles, as opposed to ~44.5% for 290 nm PSL particles (Su et al. 2004). Additional improvements will be needed to directly obtain the chemical information of the ultrafine particles during the afternoon photochemical events by UF-ATOFMS, as they clearly originate from a different source than direct vehicle exhaust emissions and are currently below the UF-ATOFMS detection limit. One possibility is to grow the ultrafine particles by water condensation up to an optically detectable size; however, this condensation process can change the chemistry of the individual particles by gas-to-particle partitioning of water-soluble organic compounds (49-52). Laboratory experiments since

the SOAR campaigns have indicated that placing a neutralizer upstream of the UF-ATOFMS significantly improves the transmission of ultrafine particles to the ionization region of the mass spectrometer. Without the neutralizer, charged particles can deviate from the source region due to the voltages on the source plates of the mass spectrometer with smaller particles deviating more.

Closer examination of the particles analyzed by UF-ATOFMS that were considered to be ultrafine particles based on their size during the summer revealed little difference in the chemistry of the ultrafine particles during the morning rush hour and the afternoon periods. This result suggests that some of the fresh ultrafine vehicle exhaust particles are transported to the site without undergoing significant aging transformations, which would cause their growth into larger sizes. On the other hand, larger particles (>100 nm), which are not shown here, do illustrate chemical differences between the mornings and afternoons (31). Many of these larger afternoon particles are morning ultrafine particles that have grown and transformed by aging processes, becoming CCN active (40,47). Once spherical ultrafine particles from non-vehicle sources have aged and grown into larger sizes, they can then be optically detected with the UF-ATOFMS.

The afternoon photochemical events in Riverside have different properties from the different types of nanoparticle and ultrafine particle events observed elsewhere, because they show a reduction in particle size rather than growth behavior (21). The loss of chemical species from the particles via evaporation is most likely not the cause of the reduction in particle size during the afternoon events in Riverside, because the temperature is cooling down and the RH is increasing at the start of the event. Moore et al. reported similar behavior with their summer 2006 campaign near downtown LA; however, their photochemical event begins immediately following the morning commute and before the peak in $O_3$ (53). In Riverside, there are at least a few hours between the end of the morning traffic periods and the beginning of the afternoon photochemical events. Because Riverside is downwind of the LA Basin, this time difference suggests that, unlike in downtown LA, the necessary precursors responsible for the afternoon photochemical events are not immediately available in Riverside and must be transported to the site. Therefore, these results suggest that different sources and processes control the formation and most likely the chemistry of ultrafine particles throughout the day in Riverside; primary sources are dominant during the morning hours, and secondary sources control the afternoon hours.

### *c. Seasonal differences*

The temporal trends of the gas- and particle-phase measurements for one week (Sunday through Saturday) during the fall season are shown in **Figure 7**. As described in Qin et al., the summer weekdays in Riverside exhibited consistent diurnal trends, whereas $PM_{2.5}$ during the fall season was better characterized as being episodic; the week shown features a high mass period (November 6 15:00 – November 7 18:00) of stagnant meteorological conditions and a $PM_{2.5}$ mass concentration of 106 μm $m^{-3}$, as well as a scavenging period (November 8 22:00 – November 11 13:00) with light precipitation events and low mass concentrations (31). Likewise, the fall trends of ultrafine particle number concentrations show less diurnal trends than in

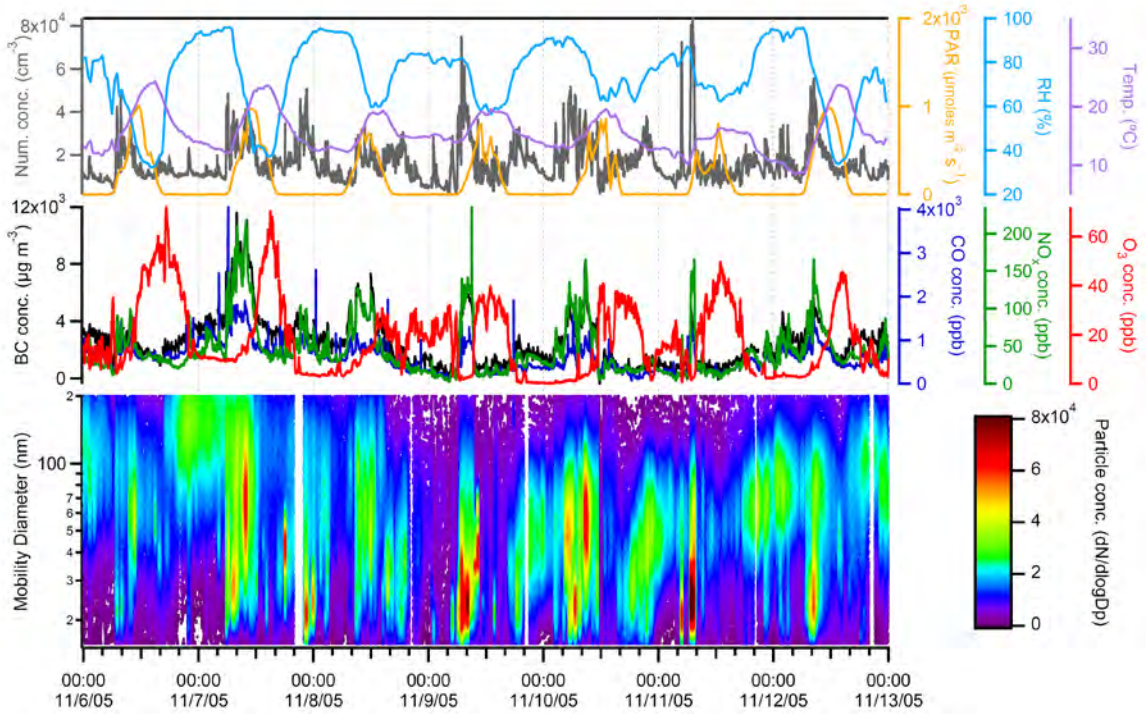


**Figure 7: Temporal trends of gas- and particle-phase measurements, as well as meteorological variables, for one week (Sunday through Saturday) during the fall season.**

the summer with the exception of the morning rush hour period, as shown in **Figure 7**. During the high mass period (November 6 15:00 – November 7 18:00), few ultrafine particles existed, most likely due to the presence of high numbers of larger particles (and therefore large surface areas available) with which the ultrafine particles could quickly coagulate. The precipitation events during the scavenging period reduced the concentrations of particles in all size ranges; however, after the rain ended, the ultrafine particles from local sources were the first to appear again at high concentrations. The highest number concentrations (based on the UF-CPC and SMPS measurements) correlated with the peaks in BC, CO, and $NO_x$ concentrations, agreeing with previous reports that vehicular emissions are the major contributor to particle number concentrations during the fall season in Riverside (23). The photochemical activity (and therefore afternoon photochemical ultrafine events) is seasonal (54), as the November PAR values are nearly 50% of those during August. Consistent with this lower PAR, very low afternoon ultrafine particle number concentration peaks were detected. The lack of afternoon ultrafine events during the fall season helps explain why the average ultrafine (15-100 nm) number concentration based on SMPS measurements during the fall ($6.7 \times 10^5$ particles $cm^{-3}$) was ~70,000 particles $cm^{-3}$ lower than that during the summer ($7.4 \times 10^5$ particles $cm^{-3}$).

Although the fall UF-ATOFMS raw ultrafine counts (shown at the bottom of **Figure 5**) tend to track the UF-CPC, BC, $NO_x$, and CO measurements, the morning rush hour spikes are not exactly consistent with those during the summer season. The Monday and Tuesday morning peaks during the fall are not as intense as the morning increases observed during the summer. The nearest major freeway was located ~600 m to the west of the sampling site. The local winds during the summer season came from a westerly

direction nearly all of the time, whereas the fall winds were split between the westerly (daylight hours) and easterly (nighttime hours) directions (31). In addition, the summer wind speeds were much stronger than the fall wind speeds, carrying the freshly emitted vehicle exhaust particles more rapidly to the sampling site. Therefore, both the meteorological conditions and episodic behavior resulted in less ultrafine vehicle particles being detected by the UF-ATOFMS during the fall.

### *d. Comparison of ultrafine particle measurements*

Because each of the ultrafine instruments used in this study make measurements based on different particle properties, it is interesting to compare their results. Differences in ultrafine particle detection between the SMPS and UF-ATOFMS were already discussed above. As shown in **Figure 6**, there is discrepancy between the summer SMPS measurements and the overall particle number concentrations determined by the UF-CPC. The UF-CPC shows increased concentrations during the morning rush hour periods (and likewise during the fall as seen in **Figure 7**), but it responds little to the afternoon photochemical ultrafine events, which displayed the highest concentrations observed by the SMPS during the summer. Because the fall season did not have significant afternoon photochemical events, the instruments agreed well with each other during the fall (**Figure 7**). Previous studies have shown significant differences in SMPS and CPC performance when there are high number counts for small sized particles (55,56). However, the numbers provided by the UF-CPC in the current study do not exceed its upper limit of $10^5$ particles $cm^{-3}$ nor are the particles (30-60 nm) of this event pushing the lower detection limit of the instrument (3 nm) (27).

This disagreement was not unique to this specific instrument, because its measurements compared well to those of other CPCs at the same location, including ones that use an alternative vapor (water) for particle growth (57). All CPC instruments followed the same temporal trend despite the use of different condensable vapors, and none appeared to detect the ultrafine particles during the photochemical events. Particles made of pure organic materials can be detected at 30 nm, so it is unlikely that the minimum detection cut point is higher than the diameters of these particles (58). It is possible to grow these particles through condensation, as they were optically counted by the CPC in the SMPS system. However, the particles introduced to the CPC after passing through the DMA were generally of uniform size,and there was a lower overall concentration of particles at a given time compared to the other CPCs. It may be possible that when all particles of a broad size range are sampled at the same time by the CPC, particles composed mainly of secondary materials recondense on larger sized particles rather than grow themselves. In addition, a laboratory comparison of a SMPS and CPC using monodisperse NaCl aerosols determined that more efficient neutralization of the charged particles upstream of the instruments improves their agreement, because the neutralizer that is part of the SMPS system left more multiply charged particles than predicted, which falsely gave the SMPS higher measurements (55). It is not yet known if this approach will work for the secondary aerosols produced in photochemical events. Most likely, the disagreement is caused by a combination of over-counting in the SMPS measurements due to inefficient neutralization and under-counting in the UF-CPC measurements due to high particle number concentrations, though it is important that future studies address this discrepancy occurring during the summer afternoon periods.

In summary, the UF-ATOFMS measurements provided single particle chemical information on the ultrafine particles based on their aerodynamic diameters. The major ultrafine particle types observed in Riverside resembled the mass spectral signatures observed in lubricant oil combustion from vehicular exhaust emissions. With this information on the chemical classes in combination with the measurements by supporting gas- and particle-phase instruments, it was determined that vehicle exhaust emissions are the major local source contributing to primary ultrafine particles during weekday morning rush hour periods. During the summer season only, an additional source of secondary ultrafine particles was detected during afternoon photochemical events that occurred after LA pollutants were transported to the site.

Real-time measurements of particle size and chemistry coupled with gas-phase measurements have provided unique insight into the daily and seasonal variations of ultrafine particles. In this study, it is demonstrated how ultrafine particle sources (and hence chemistry) can rapidly change over the course of the day, as well as show a strong seasonal dependence. High ultrafine particle concentrations were observed during different periods and seasons, yet the chemistry of the particles was often different. Thus, future studies of health effects aimed at understanding the impacts of ultrafine particles must take into account their sources, degree of aging, and overall chemistry rather than solely relying on their number concentration as a proxy.

**iv. Acknowledgements**

The authors express their gratitude to the entire Prather group for their help in the preparation and overall support of these studies. We thank Megan McKay and the Goldstein research group at the University of California, Berkeley for the summer CO measurements and the meteorology data. We also acknowledge Professor Paul Ziemann (University of California, Riverside) for hosting the SOAR field campaigns, as well as Professor Jose Jimenez (Colorado University, Boulder) and Dr. Ken Docherty (Colorado University, Boulder) for setting up the logistics. Finally, we thank Dr. Susanne Hering (Aerosol Dynamics) for the use of her CPC data and helpful suggestions. Funding for this project was supplied by the California Air Resources Board (Contract 04-336).

## 2. Characterization of the Single Particle Mixing State of Individual Ship Plume Events measured at the Port of Los Angeles

### i. Introduction

Ship emissions are among the least regulated forms of anthropogenic pollution given the challenges involved in establishing international policies. Ship emissions impact climate by initiating cloud formation and altering earth's radiation budget (59,60). Ships emit high concentrations of soot and heavy metals (i.e. vanadium and nickel) (61,62), in addition to an estimated 2.4 tons of $SO_2$ globally, producing up to 10% of sulfate mass globally through atmospheric reactions (63). Over the next century, $SO_2$ levels are predicted to rise significantly as global commerce expands (63). Ship emissions have been shown to have negative effects on human health through exposure studies and epidemiological models (64-66). For example, inhaled vanadium particles are toxic and synergistic effects with nickel and sulfate have been shown to enhance toxicity (65). To determine effective strategies for reducing the impact of shipping on climate and health, recent studies have focused on improving ship emission inventories which are used to estimate future scenarios for gas phase concentrations (67). Efforts to regulate shipping emissions have been difficult due to fuel and upgrade costs and international dependence on foreign trade (68,69).

Particulate emissions from ships have been characterized by multiple analytical methods including energy dispersive x-ray fluorescence measurements of particulate matter on filters (62), ion chromatography (IC) of particulate matter extracted from filters (61), real-time mass-based measurements (70,71), particle counters (72), cloud condensation nuclei measurements (70), and size distribution measurements (62). These measurements have led to updated emission inventories and emission factors for aerosol mass and particle number for ship emissions (70,71). Real-time, single-particle mass spectrometry has also been used to identify ship emissions at locations away from the source regions (73,74). Herein, we report in-situ measurements of the chemical mixing state of particles in fresh ship plumes measured at the Port of Los Angeles.

### ii. Experimental

#### *a. Sampling Information*

Ambient air sampling was conducted from November 16–26, 2007 at the Port of Los Angeles (LA) on Terminal Island in San Pedro, California. Particles were sampled through a four meter sampling mast, seven meters above the ground at a sampling site 500 meters east of the center of the main channel. Wind direction and speed were measured using a R.M. Young wind monitor. Winds exhibited a consistent diurnal pattern with southerly sea breezes during the day and light nocturnal land breezes from the north. Radio transmissions of the location, speed, and heading of ships entering and exiting the port were recorded in real-time with an automated identification system (AIS) antenna in La Jolla, CA (75). These transmission signals are required to be sent every minute for ships at sea over 299 gross tons by the International Maritime Organization.

### *b. Gas and Particle Peripheral Instrumentation*

Gas phase measurements were made of $NO_x$ (Thermo Environmental Instruments (TEI) Model 42C), $O_3$ (TEI Model 49), and $SO_2$ (TEI Model 43). Particle size distributions were measured with a scanning mobility particle sizer (SMPS, TSI Model 3936L) operating from 10 – 600 nm at a time resolution of 5 minutes; black carbon (BC) concentrations ($ng/m^3$) were measured using an aethalometer (Magee Scientific AE31).

### *c. Aerosol Time-of-Flight Mass Spectrometry (ATOFMS)*

The design and details of the ultrafine (UF)-ATOFMS used in this study are described in detail elsewhere (2). This instrument measures the size and chemical composition of individual particles between 100-1000 nm during this study. Briefly, particles are introduced into the UF-ATOFMS through an aerodynamic lens into a differentially pumped vacuum chamber where the particles are accelerated to a size-dependent velocity. Particles pass through two 532 nm continuous wave lasers located 6 cm apart. Particle speed is used to determine vacuum aerodynamic diameter by calibration with polystyrene latex spheres of known size. Sized particles are individually desorbed and ionized in the mass spectrometer source region by a 266 nm Q-switched Nd:YAG laser (1.2-1.4 mJ). Positive and negative ions produced from individual particles are detected using a dual-reflectron time-of-flight mass spectrometer.

### *d. Single Particle Analysis*

During sampling at the Port of LA, the aerodynamic size and chemical composition of 1,245,041 particles were analyzed using an UF-ATOFMS. Size and mass spectral information were imported into MatLab 6.5.1 (The Mathworks Inc.) and analyzed utilizing YAADA 1.2 (www.yaada.org). Individual particles were analyzed via two methods: 1) mass spectral ion intensities, aerodynamic size, and temporal information and 2) clustering via an adaptive resonance theory based neural network algorithm (ART-2a) at a vigilance factor of 0.8 (35). ART-2a classifies individual particles into separate clusters based on the presence and intensity of ion peaks in individual single-particle mass spectra. Peak identifications within this paper correspond to the most probable ions for a given mass/charge (m/z) ratio. General particle types are defined by the characteristic chemical species in an attempt to simplify the naming scheme; these labels do not reflect all of the species present within a specific particle class.

## iii. Results and Discussion

### *a. Ship Identification*

Characteristics of each positively identified ship plume over a 10 day period are listed in **Table 3** which includes: the peak time of the observed plume, length of time the plume was observed, calculated transport time from the point of emission to the peak of the plume at the sampling location using wind speed, peak particle number concentration, characteristic particle type, number of particles chemically characterized by the UF-ATOFMS, number fractions of OC-V-sulfate and fresh soot particles present during the plume detection period. The times when different ships passed the sampling location

were determined through a combination of arrival and departure logs (76), AIS ship position recordings, and pictorial documentation. As an example, **Figure 8** shows the arrival of the vessel Container1b on November 19, 2007 at 03:30 (PST). Red markers (1 minute resolution) represent the ship's position as recorded by the AIS, and the green diamond represents the sampling location. The blue line shows the path of the plume (550 meters) to the sampling location based on measured wind direction (292°) and speed (0.6 m/s). Ships that could be positively identified by time, position, and wind speed/direction are analyzed in detail; however, numerous ships and plumes passed the site during the sampling period that could not be confidently assigned using the criteria listed above. Due to changing wind direction and wind speed, calculated plume travel times to the sampling location varied from 5-20 minutes.

| Ship Plume | Plume Peak Time (PST) | Duration (min) | Age (min) | Peak Num Conc (#/cm$^3$) | Identifying ATOFMS Type | ATOFMS Particles | Number Fract OC-V-Sulfate | Number Fract Fresh Soot |
|---|---|---|---|---|---|---|---|---|
| Container1a | 11/17 5:00 | 15 | 15 | 9217 | Fresh Soot | 517 | 0.6 | 30.0 |
| Container2 | 11/17 6:05 | 20 | 15 | 8757 | OC-V-Sulfate | 752 | 18.8 | 3.2 |
| Container3 | 11/18 15:25 | 10 | 10 | 9884 | OC-V-Sulfate | 324 | 9.9 | 1.9 |
| Container1b | 11/19 3:30 | 10 | 15 | 11310 | OC-V-Sulfate | 1056 | 17.0 | 2.1 |
| Tanker1a | 11/19 18:05 | 20 | 20 | 44697 | OC-V-Sulfate | 747 | 24.0 | 4.8 |
| Container4 | 11/20 17:20 | 25 | 10 | 21177 | OC-V-Sulfate | 734 | 26.3 | 2.6 |
| Tanker1b | 11/20 18:20 | 15 | 10 | 12792 | Both | 345 | 34.2 | 9.3 |
| Container5 | 11/20 19:15 | 10 | 10 | 11806 | Fresh Soot | 1220 | 1.5 | 25.3 |
| Tanker2 | 11/21 5:35 | 25 | 45 | 8927 | Both | 756 | 6.5 | 7.3 |
| Container6 | 11/24 12:25 | 10 | 10 | 12984 | Both | 2077 | 10.8 | 25.6 |
| CruiseShip1 | 11/24 16:25 | 15 | 5 | 30231 | Fresh Soot | 2733 | 3.6 | 12.6 |
| Container7 | 11/25 18:10 | 20 | 30 | 9593 | Fresh Soot | 1370 | 3.6 | 9.5 |

**Table 3: Characteristics of ship plumes sampled including: Ship plume, plume peak time, plume duration, plume age, peak number concentration, identifying ATOFMS particle type, number of ATOFMS particles, number fraction of OC-V-sulfate particles, and number fraction of fresh soot particles.**

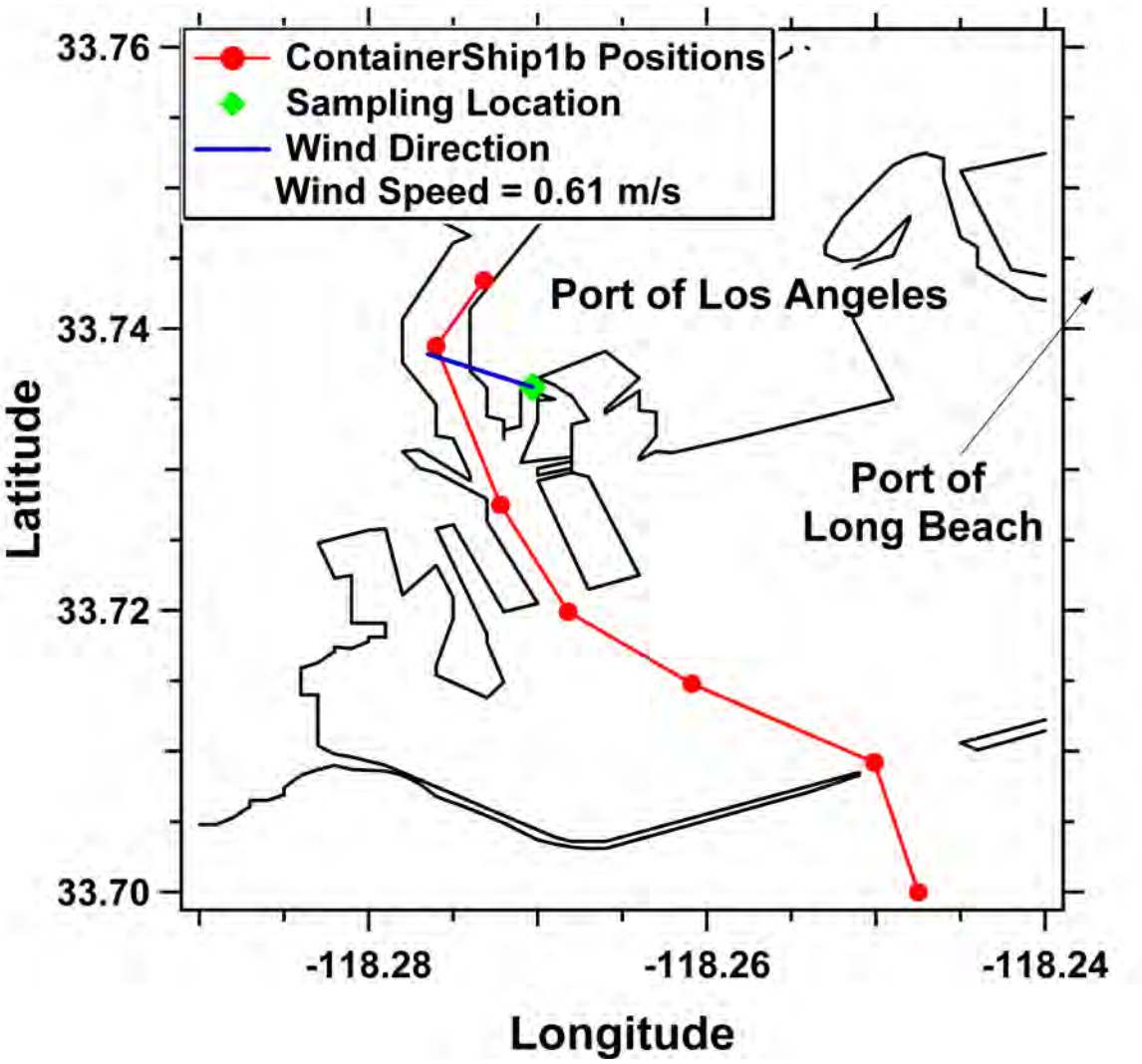


**Figure 8:** Map showing the Port of LA. The green diamond represents the sampling location and the red markers and line represent the one minute resolution positions and course of a container ship as it departed from the Port of LA at 03:30 on November 19, 2007. The blue line represents the average wind direction during transport of the plume to the sampling location.

### *b. Plume Characterization*

Characteristics of a representative plume observed on November 19, 2007 at 03:30 from the vessel Container1b are shown in **Figure 9**. The top portion shows $SO_2$, $NO_x$, and BC concentrations increasing sharply from background conditions at the onset of the plume and $O_3$ decreasing due to reaction with NO (62,72). Gas phase data were used to qualitatively identify the presence of ship plumes. The duration of this plume at the sampling site was ~15 minutes, which is similar to previously observed timescales (62) (13.6 min.). Similar trends for gas phase species were observed in most plumes; Table 4 lists $SO_2$ and $NO_x$ concentrations during different plume events and provides a detailed discussion. The bottom portion of **Figure 9** shows the temporal evolution of the

size-resolved particle number concentrations with 5 minute resolution during the plume sampling period. A rapid increase in the total number concentrations of 10-600 nm particles (white line) occurred as the plume passed the sampling location, representing an increase over background levels from 5000/cm$^3$ to 11,000/cm$^3$. The mode and shape of the size distribution did not shift significantly while sampling this plume.

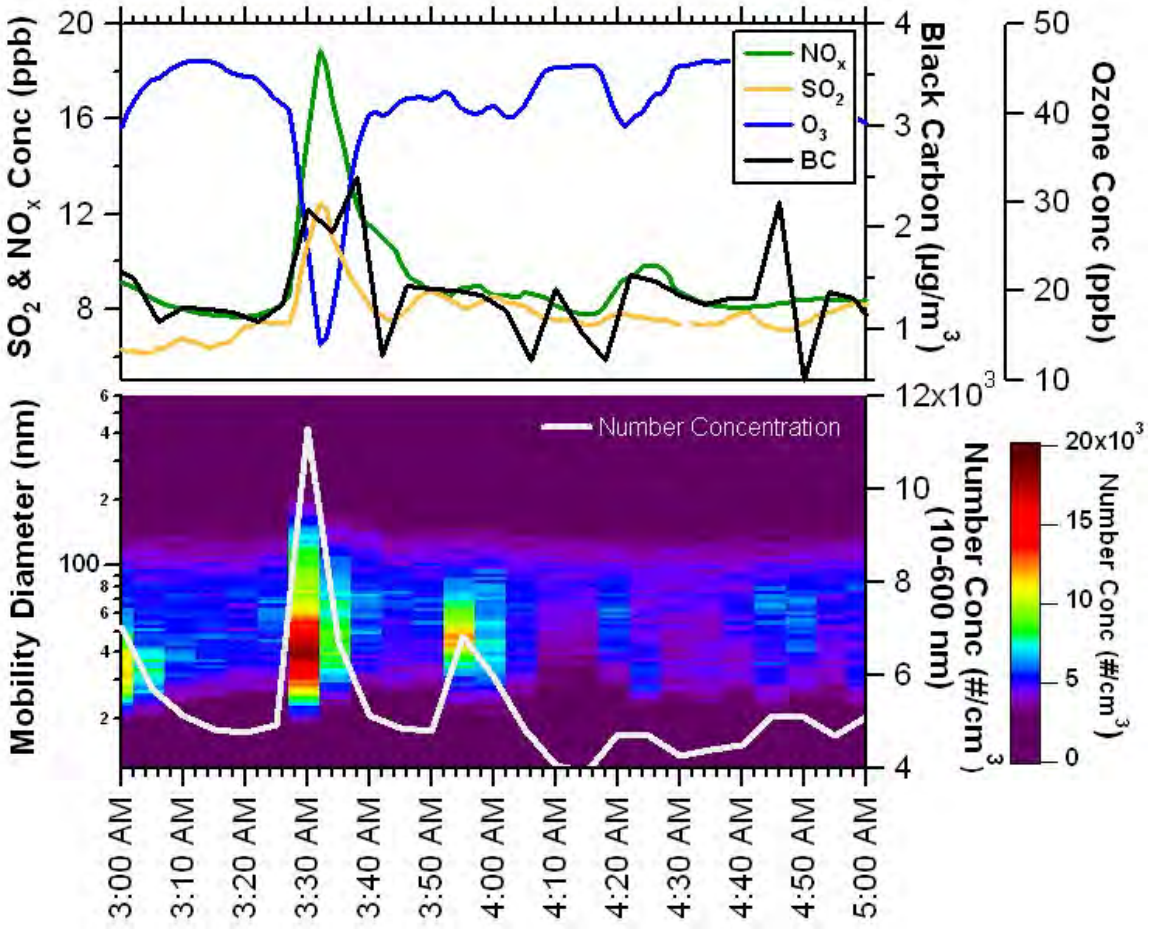


**Figure 9:** Identification of the plume of Container1b. Gas phase measurements included $SO_2$ (orange), $NO_x$ (green), and $O_3$ (blue). Particle phase measurements were of black carbon (black), particle number concentration (white), and size-resolved number concentrations over time (color matrix).

### *c. In Plume Gas Phase Chemistry and Concentrations*

The expected loss of $O_3$ shown in **Figure 9** should have a 1:1 ratio to the gain in $NO_x$ (assuming $NO_x$ is primarily NO in a fresh plume), but this was not observed. A number of factors may have contributed to this including: additional species reacting with NO and $O_3$ and the presence of aqueous particles and droplets that could have scavenged gas phase species. The peak concentration in $SO_2$, $NO_x$, and $O_3$ during the different ship plumes is given in Table 4, along with background concentrations and the net concentration increase. The ratio of $NO_x/SO_2$ is also given which can be an indicator of fuel type. Residual fuels have higher concentrations of sulfur and thus produce higher

concentrations of $SO_2$, while distillate fuels have less sulfur and produce less $SO_2$ (77). Changes in the gas phase data to lower $NO_x/SO_2$ (ppbv/ppbv) ratios presented here correspond to changes in particle chemistry in the plumes with higher levels of OC-V-sulfate particle levels. In contrast, fresh soot plumes have higher $NOx/SO_2$ ratios.

| | **$SO_2$ (ppbv)** | | | **$NO_x$ (ppbv)** | | | **$O_3$ (ppbv)** | | | **$NO_x/SO_2$** |
|---|---|---|---|---|---|---|---|---|---|---|
| | Max | Baseline | **Peak** | Max | Baseline | **Peak** | Min | Baseline | **Peak** | **Ratio** |
| Container1a | 7.2 | 3.5 | **3.7** | 26.2 | 7.3 | **18.9** | 30.0 | 55.1 | **25.1** | **5.1** |
| Container2 | 7.7 | 3.4 | **4.3** | 16.7 | 7.9 | **8.8** | 19.7 | 54.9 | **35.2** | **2.0** |
| Container3 | 11.2 | 5.0 | **6.2** | 19.1 | 10.7 | **8.4** | 45.0 | 68.0 | **23.0** | **1.4** |
| Container1b | 12.5 | 7.4 | **5.1** | 18.9 | 7.7 | **11.2** | 14.0 | 45.8 | **31.8** | **2.2** |
| Tanker1a* | 47.7 | 18.5 | **29.2** | 160.0 | 58.0 | **102.0** | No Min | No Min | **N/A** | **3.5** |
| Container4 | 10.7 | 4.1 | **6.6** | 39.5 | 14.9 | **24.6** | 27.8 | 57.1 | **29.3** | **3.7** |
| Tanker1b | 6.3 | 3.2 | **3.1** | No Peak | No Peak | **N/A** | No Min | No Min | **N/A** | **N/A** |
| Container5 | 4.1 | 3.1 | **1.0** | 38.0 | 7.1 | **30.9** | 37.4 | 45.4 | **8.0** | **30.9** |
| Tanker2 | 12.0 | 6.7 | **5.3** | 32.4 | 10.1 | **22.3** | 8.7 | 38.6 | **29.9** | **4.2** |
| Container6 | 12.0 | 8.6 | **3.4** | 41.6 | 15.8 | **25.8** | 23.7 | 44.8 | **21.1** | **7.6** |
| CruiseShip1 | 10.8 | 6.6 | **4.2** | 52.3 | 11.7 | **40.6** | 26.0 | 46.4 | **20.4** | **9.7** |
| Container7 | 9.0 | 4.7 | **4.3** | 13.2 | 10.5 | **2.7** | 23.0 | 35.1 | **12.1** | **0.6** |

* night-time chemistry altered by land breeze in Long Beach leading to high $NO_x$ & $SO_2$ levels, but low $O_3$

Table 4: Gas phase concentrations (max, baseline, and peak) of $SO_2$, $NO_x$, and Ozone during different plume events are shown along with the $NO_x/SO_2$ ratio.

### *d. Unique Plume Chemistry*

Two types of ship plumes were observed in this study: one with a large number fraction of internally mixed organic carbon, vanadium, and sulfate (OC-V-sulfate) particles and a second with a large number fraction of freshly emitted soot particles. The average mass spectrum of the OC-V-sulfate particle type is shown in **Figure 10**, showing intense vanadium peaks at $^{51}V^+$ and $^{67}VO^+$ and organic carbon markers including $^{27}C_2H_3^+$, $^{29}C_2H_5^+$, $^{37}C_3H^+$, and $^{43}C_2H_3O^+$, as well as a strong bisulfate ion signal ($^{97}HSO_4^-$). A sulfuric acid cluster peak ($^{195}H_2SO_4{\bullet}HSO_4^-$) was observed for ~80% of these OC-V-sulfate particles. Residual fuels used in shipping contain much higher concentrations of heavy metals than distillate fuels (77) with previous ATOFMS source studies of cars and trucks showing <1% of particles mixed with vanadium (36). Further, previous studies have noted the correlation of vanadium and sulfur in ambient single particles and attributed these particles to fuel oil combustion (78).

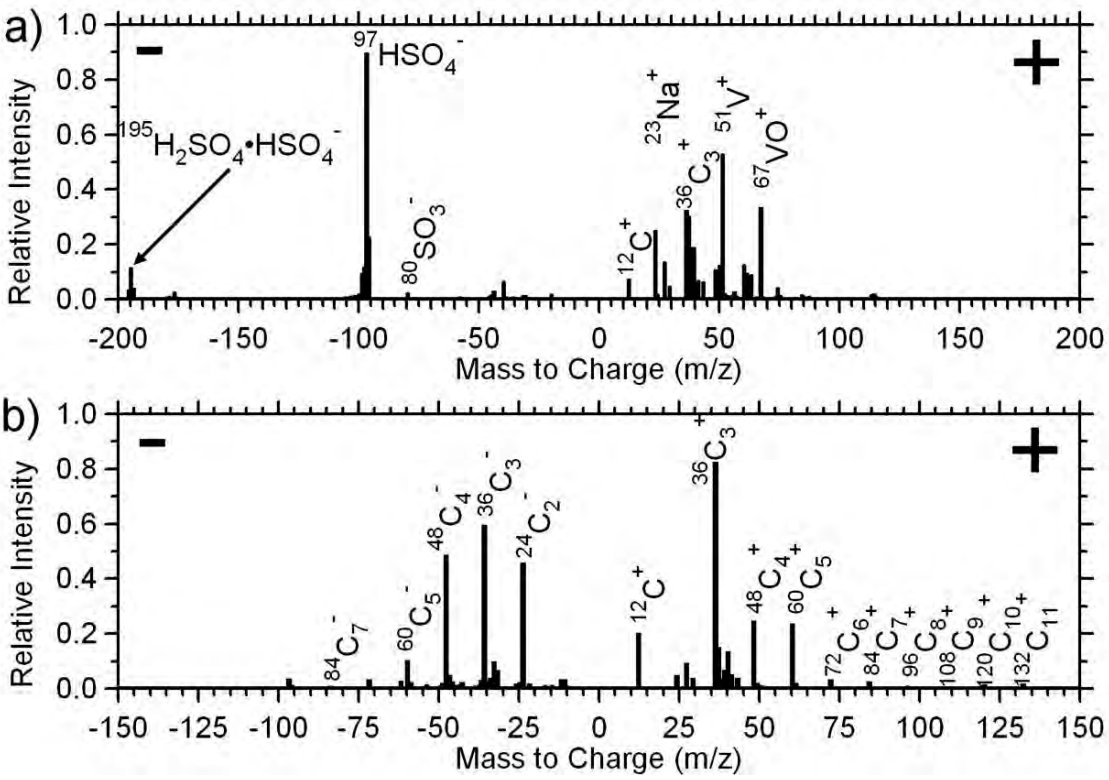


**Figure 10:** Average negative and positive ion mass spectra for the OC-V-sulfate (a) and fresh soot (b) particle types.

The average mass spectrum of the soot (or elemental carbon) particle type is shown in **Figure 10**, characterized by both positive and negative carbon cluster ions (e.g., $^{12}C_1^+$, $^{24}C_2^+$,…, $C_n^+$). These freshly emitted soot particles did not contain significant sulfate or nitrate ion markers, likely due to limited time for atmospheric aging between the point of emission and sampling. This contrasts most background particle types observed at the Port of LA which contained significant amounts of nitrate and/or sulfate, including other elemental carbon particle types, as discussed below. Particle types similar to these fresh soot particles have been observed during source testing of both cars burning gasoline and trucks burning distillate (i.e. diesel) fuel (36,37). Detailed information on mass spectral variability within the OC-V-sulfate and fresh soot types is included in the Supplemental Information. While other particle types were present within these plumes, the OC-V-sulfate and fresh soot particle types were observed as characteristic source markers for the two different plume types. Plumes were labeled as OC-V-sulfate and/or fresh soot when each particle type represented greater than 5% of particles sampled during the plume.

For the residual fuel combustion ship plumes described herein, the OC-V-sulfate type represented 10-34% of particles sampled in the 100-500 nm size range. The distinct OC-V-sulfate and fresh soot plumes likely result from the combustion of different fuels, with residual fuel oil producing the OC-V-sulfate plumes and distillate fuel forming the fresh soot plumes. The soot plumes also had elevated levels of Ca-ECOC particles. The presence of Ca-ECOC particles agrees with filter measurements in a marine distillate

exhaust study, which found calcium to be ~25% of the relative weighted emission factor for trace elements compared to <5% in residual fuel combustion exhaust (79). The Ca-ECOC particle type has been linked to distillate (i.e. diesel) fuel in previous ATOFMS source characterization studies (37); the mass spectrum is included in the Supplemental Information. While the average ratio of $NO_x$ to $SO_2$ (ppbv/ppbv) during the study was 3.7, it was lower in the OC-V-sulfate plumes (average 2.6, range: 1.4-4.2) and higher in the soot plumes (average 11.6, range: 0.6-30.9). This suggests a relative enrichment of $SO_2$ in the V-plumes as would be expected when burning residual fuels with high sulfur content (max 3.5 % (m/m)) (77). A study comparing an auxiliary engine burning distillate fuel and a main engine burning residual fuel found significantly higher vanadium levels associated with the residual fuel combustion and higher levels of calcium with the distillate fuel combustion, which agrees with diesel source testing by the UF-ATOFMS (37,79). This is also consistent with our findings of OC-V-sulfate particles in the residual fuel combustion plume and Ca-ECOC particles in the distillate fuel combustion plume. In addition, the amount of sulfate from IC of particulate matter in filter extracts does not shift significantly with ship engine load for residual or distillate fuels, suggesting that the presence of OC-V-sulfate particles under normal operating conditions further indicates a residual fuel combustion plume and a lack of OC-V-sulfate indicates a distillate fuel combustion plume (61).

### *e. Details on the OC-V-sulfate and Fresh Soot Particle Types*

The digital color stack (DCS) for the OC-V-sulfate particle type is shown in **Figure 11**. The x-axis is mass-to-charge and the y-axis shows the fraction of particles within this type containing a specific peak. The color represents the fraction of particles with different peak areas; a peak area > 500 (arbitrary units) was used to exclude noise in the spectra. The ion peaks with the largest fraction and highest intensity in the positive spectrum are the mass to charges corresponding to vanadium ($^{51}V^+$ and $^{67}VO^+$) and organic carbon ($^{27}C_2H_3^+$, $^{36}C_3^+$, $^{37}C_3H^+$, $^{41}C_3H_5^+$, $^{43}C_3H_3O^+$, etc.). These peaks are on nearly 100% of the particles in this type. In the negative spectrum the most intense peak is sulfate ($^{97}HSO_4^-$) and over 95% of these particles have a peak area above 20,000. These particles also have sulfuric acid ($^{195}H_2SO_4HSO_4^-$) on ~80% of the particles, which is even more striking when the transmission efficiency of ~49% at m/z 200 for the co-axial ATOFMS is considered (80). It should be noted that the intensity of the sulfate peak led to considerable ringing, which is seen by the continuum of lower intensity peaks between m/z -98 to -110.

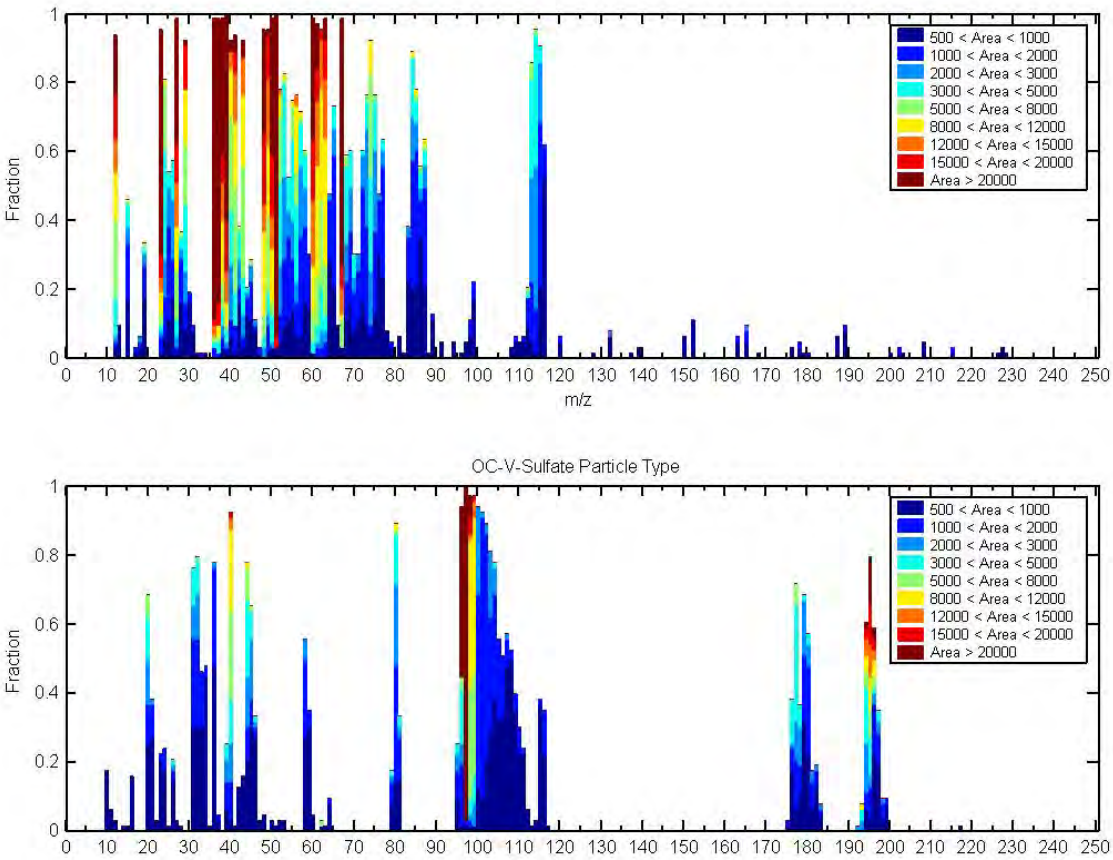


**Figure 11:** A digital color stack for the OC-V-sulfate particle type showing the fraction of particles containing a specific peak on the y-axis versus mass-to-charge on the x-axis. The color represents the fraction containing a specific range of peak areas, with 500 being the lower peak area cutoff. The top portion of the figure represents the positive mass spectrum and the bottom portion represents the negative mass spectrum.

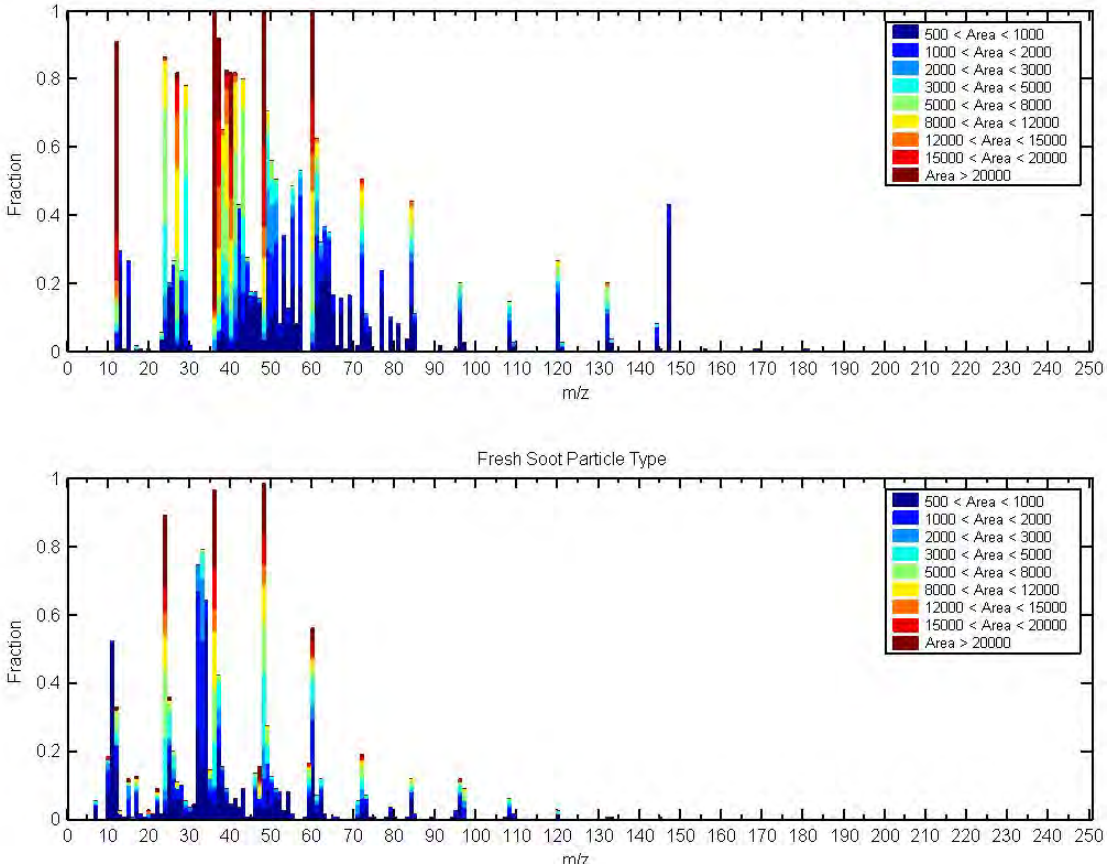


**Figure 12:** A digital color stack for the fresh soot particle type showing the fraction of particles containing a specific peak on the y-axis versus mass-to-charge on the x-axis. The color represents the fraction containing a specific range of peak areas, with 500 being the lower peak area cutoff. The top portion of the figure represents the positive mass spectrum and the bottom portion represents the negative mass spectrum.

The digital color stack for the fresh soot particle type is shown in **Figure 11**, with the same thresholds and range used in **Figure 11**. For Figure S2, intense peaks are observed at mass-to-charges corresponding to carbon clusters ($^{12}C^+$, $^{36}C_3^+$, $^{48}C_4^+$, …, $^{144}C_{12}^+$) in the positive plot (top). The negative (bottom) plot also shows a similar pattern with respect to the carbon clusters ($^{24}C_2^-$, $^{36}C_3^-$, $^{48}C_4^-$, …, $^{120}C_{10}^-$). What is notable about the fresh soot type is that < 10% of the particles have a sulfate peak and 0% have a sulfuric acid peak, demonstrating the difference between the two particle types produced in different plumes.

## *f. Description of the Ca-ECOC Particle Type*

**Figure 13** shows the average mass spectrum of the Ca-ECOC particle type, which is characterized by an intense calcium ion peak ($^{40}Ca^+$) and elemental carbon clusters in both the positive ($^{12}C_1^+$, $^{24}C_2^+$,…, $C_n^+$) and negative spectra ($^{12}C_1^-$, $^{24}C_2^-$,…, $C_n^-$). The significance of this particle type is that it is enhanced by number along with the fresh soot particle type in distillate fuel plumes. Previous studies have shown higher calcium mass

fractions in filter measurements from the stacks of ships burning distillate fuel compared to residual fuel (61,79).

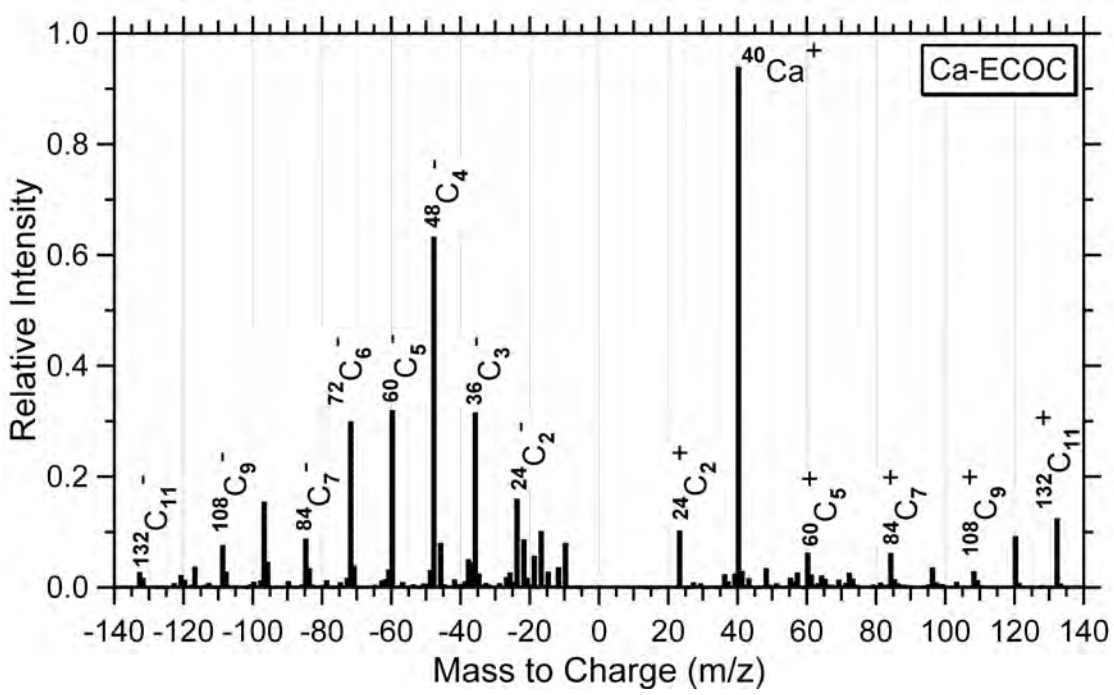


Figure 13: Average mass spectrum of the Ca-ECOC particle type from a fresh soot plume.

### *g. Background Particle Types During Plumes*

**Figure 14** and **Figure 15** show average mass spectra for the background particle types measured in the plumes from Container1b and Container4. The mass spectra of aged soot particles (**Figure 14a** and **Figure 15b**) were characterized by elemental carbon cluster ions ($^{12}C_1^+$, $^{24}C_2^+$,…, $C_n^+$) with less intense organic carbon markers ($^{27}C_2H_3^+$, $^{29}C_2H_5^+$, $^{37}C_3H^+$, and $^{43}C_2H_3O^+$) (81) and secondary markers for sulfate ($^{97}HSO_4^-$) and nitrate ($^{62}NO_3^-$). The biomass burning particle type is shown in **Figure 14b** and **Figure 15** and is characterized by a dominant potassium ion peak ($^{39}K^+$) with less intense elemental carbon markers ($^{12}C_1^+$, $^{24}C_2^+$,…, $C_n^+$) and organic carbon markers $^{27}C_2H_3^+$, $^{29}C_2H_5^+$, $^{37}C_3H^+$, and $^{43}C_2H_3O^+$ (81). The mass spectra of the V-background particle type (**Figure 14c** and **Figure 15c**) are characterized by intense peaks at $^{51}V^+$ and $^{67}VO^+$ with less intense iron ($^{56}Fe^+$) and nickel ($^{58,60}Ni^+$) ion peaks. Note the lack of peaks (other than detector crosstalk) in the negative spectrum which is commonly observed after particles undergo aging and take up significant amounts of water, leading to negative ion suppression (82). These particles have been shown in other marine environments and are likely highly aged (74). Although they share a strong vanadium signal, the temporal trend of the V-background particles did not correlate with those of the freshly emitted OC-V-sulfate particles.

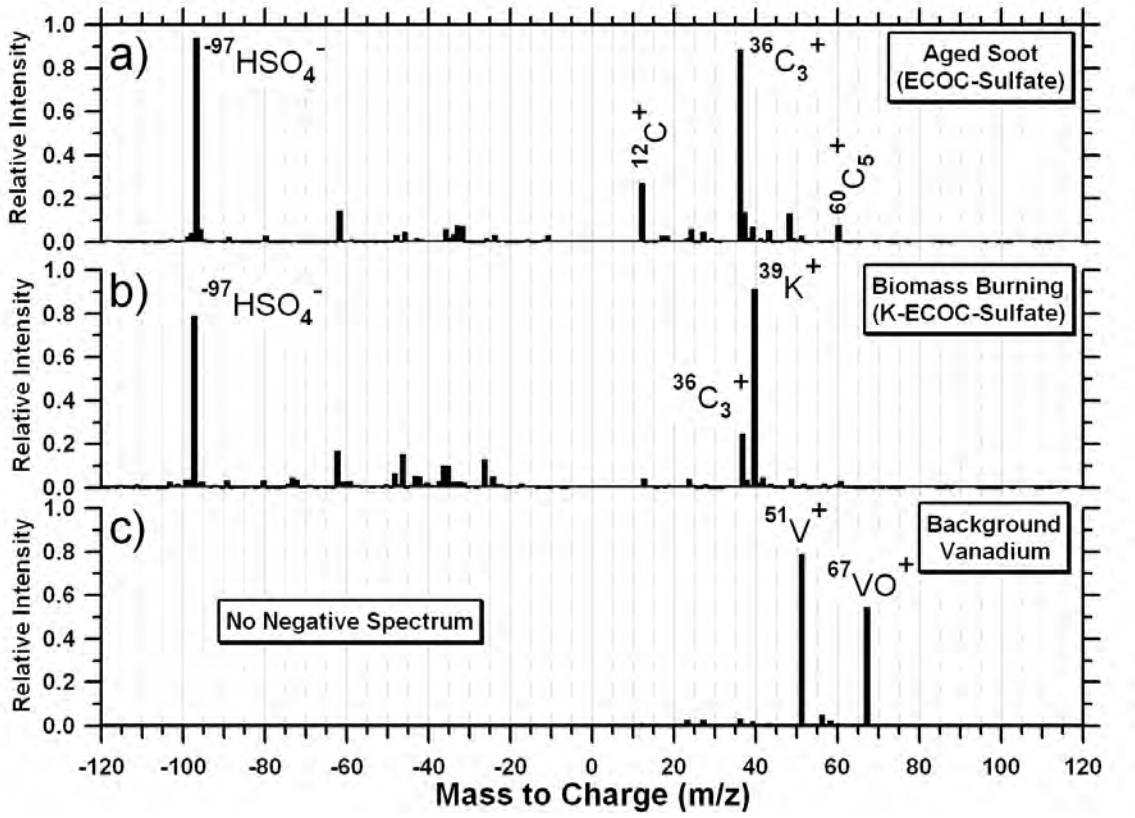


Figure 14: Average mass spectra of background particle types before and after the plume from Container1a.

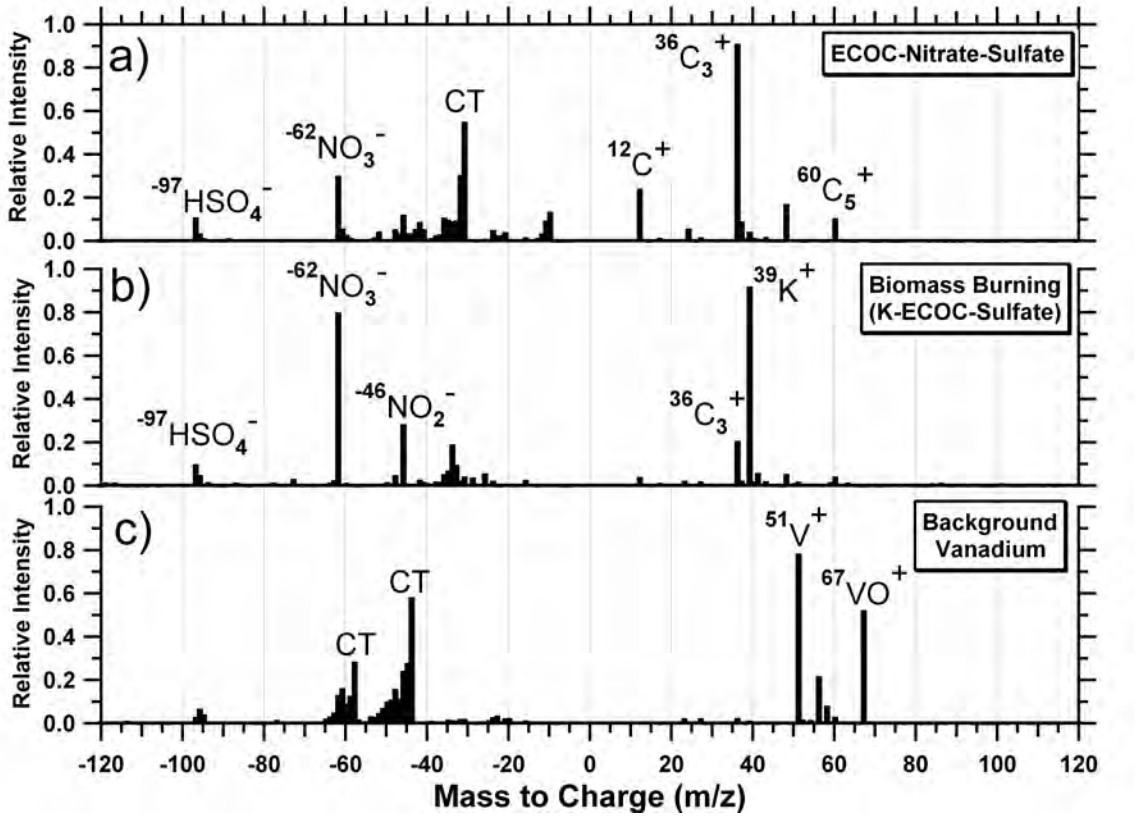


Figure 15: Average mass spectra of background particle types from before and after the plume from Container4. CT represents crosstalk on the detector.

### *h. Temporal Trends*

**Figure 16** shows the time series of the number of OC-V-sulfate (**Figure 16a**) and fresh soot particles (**Figure 16b**) analyzed by the UF-ATOFMS for the first 5 days of the study. After this period, Santa Ana winds disrupted normal wind patterns. Both time series are characterized by spikes lasting 5-20 minutes. However, as shown in **Figure 16**, OC-V-sulfate and fresh soot spikes frequently spike at different times. Over 65% of the spikes in OC-V-sulfate particles could be correlated to specific ships. Only 15% of the fresh soot spikes corresponded to specific ships, which is understandable as fresh soot is a more ubiquitous particle type associated with many distillate fuel combustion sources including trucks and tug boats (83). Some OC-V-sulfate plumes contained significant fresh soot, while others did not, suggesting that the varying amount of fresh soot in residual fuel combustion plumes may be due to different plume dynamics, engine type and condition, operating conditions, as well as background levels and other emission sources.

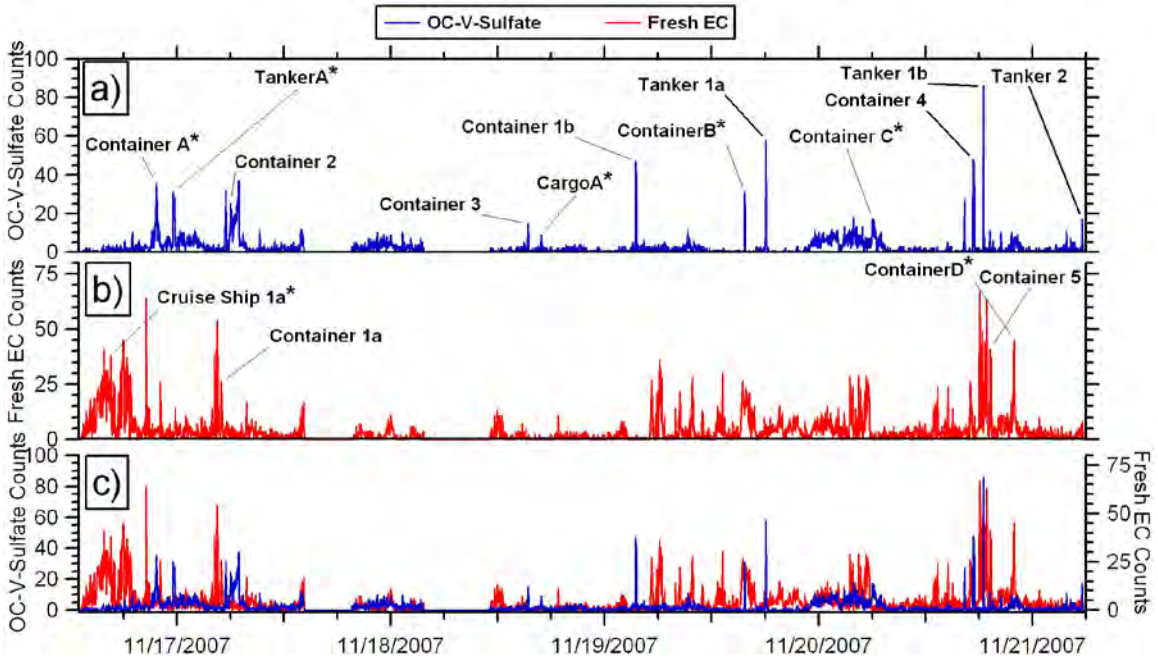


Figure 16: Time series of the differential counting rate (number of ATOFMS counts per 2 minutes) for the OC-V-sulfate and fresh soot particle types. Peaks that could be correlated with ships are labeled; plumes with asterisks were only tentatively identified.

### *i. Size-resolved Chemistry*

The chemical composition with respect to aerodynamic diameter for the urban background before and after both ship plume types is shown in **Figure 17a** (residual fuel combustion plume) and **Figure 17b** (distillate combustion plume). This background is defined as 10 minutes before the plume was detected until 10 minutes after the plume disappeared with the plume itself subtracted out. The particle types associated with the background urban aerosol, in addition to the OC-V-sulfate and fresh soot types, were aged soot, biomass burning, and a background vanadium type. These background particle types did not exhibit a temporal pattern similar to the OC-V-sulfate or fresh soot types, suggesting that they were not associated with the freshly emitted ship plumes.

**Figure 17c** and **Figure 17d** show the particle size-resolved chemical composition for specific ship plumes corresponding to an OC-V-sulfate plume (Container4) and a fresh soot plume (Container1a), respectively. The OC-V-sulfate particles in the residual fuel combustion plume increased 10-25 times in less than 2 minutes from a nearly negligible background level when the plume arrived (**Figure 17a**) to accounting for 28% of 150-500 nm particles (**Figure 17c**). While the UF-ATOFMS was unable to chemically characterize <100 nm particles, measurements of residual fuel combustion exhaust particles using transmission electron microscopy with energy dispersive x-ray spectroscopy have detected distinct peaks of sulfur and vanadium within particles between 30-100 nm in diameter (70). Thus, it is likely that the OC-V-sulfate particle type also represents a significant fraction of even smaller particles emitted in residual fuel combustion exhaust.

For the soot plume (Container1a) a unique mode was observed between 100 – 200 nm composed of fresh soot and Ca-ECOC particles. This differs from the majority of the study when the particle size with the highest detection efficiency was ~ 270 nm due to the combination of inlet transmission efficiencies and ambient concentrations (80), also shown in **Figure 17a**, **Figure 17b**, and **Figure 17c**. However, during the fresh soot plume this was not the case as particles with large geometric diameters (increasing their scattering signal), but small vacuum aerodynamic diameters (100 – 200 nm), were observed. Previous ATOFMS studies measuring particle optical properties have shown that these particles were non-spherical, fractal agglomerates, typical of fresh soot (84). This is supported by previous tandem measurements using a differential mobility analyzer in line with an ATOFMS, showing fresh soot particles having small aerodynamic diameters relative to their geometric diameters indicative of low effective density, fractal particles. (48).

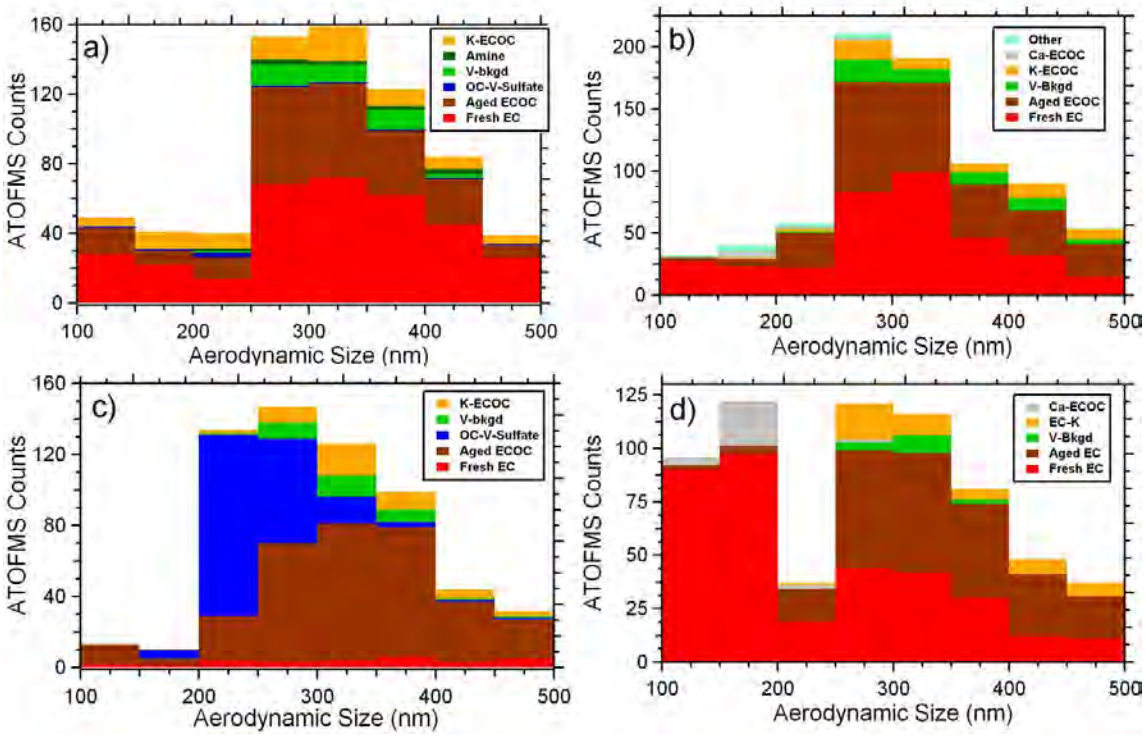


Figure 17: Size-resolved number fractions of the different particle types for the background before and after a) OC-V-sulfate (Container4) and b) fresh soot (Container1a) plumes. (c,d) Size-resolved chemical fractions of these plumes.

### *j. Correlation between sulfate and vanadium particle*

Rising sulfate levels are a major concern globally (60) and have been shown to influence ship tracks (59). In a representative OC-V-sulfate plume, high fractions of OC-V-sulfate particles contained sulfate (100%) and sulfuric acid (56%), with average absolute peak areas of ~57,000 and 7,000 for sulfate and sulfuric acid, respectively (**Figure 18**). For other particle types only 14-40% of the particles contained sulfate, while almost none (0-1%) contained sulfuric acid. Average absolute peak areas on the other

particle types ranged from only 75-3400 and 0-344 for sulfate and sulfuric acid, respectively. Since ATOFMS absolute peak areas are proportional to mass on a single-particle basis (85,86), differences in the sulfate and sulfuric acid peak areas of ~1-2 orders of magnitude clearly show that the OC-V-sulfate particles contained more sulfate and sulfuric acid compared to non vanadium-containing particles. The measured sulfate and sulfuric acid peak areas are substantially larger than previously measured in ATOFMS source combustion studies, including cars burning gasoline (36), trucks burning diesel (37), and biomass burning (87).

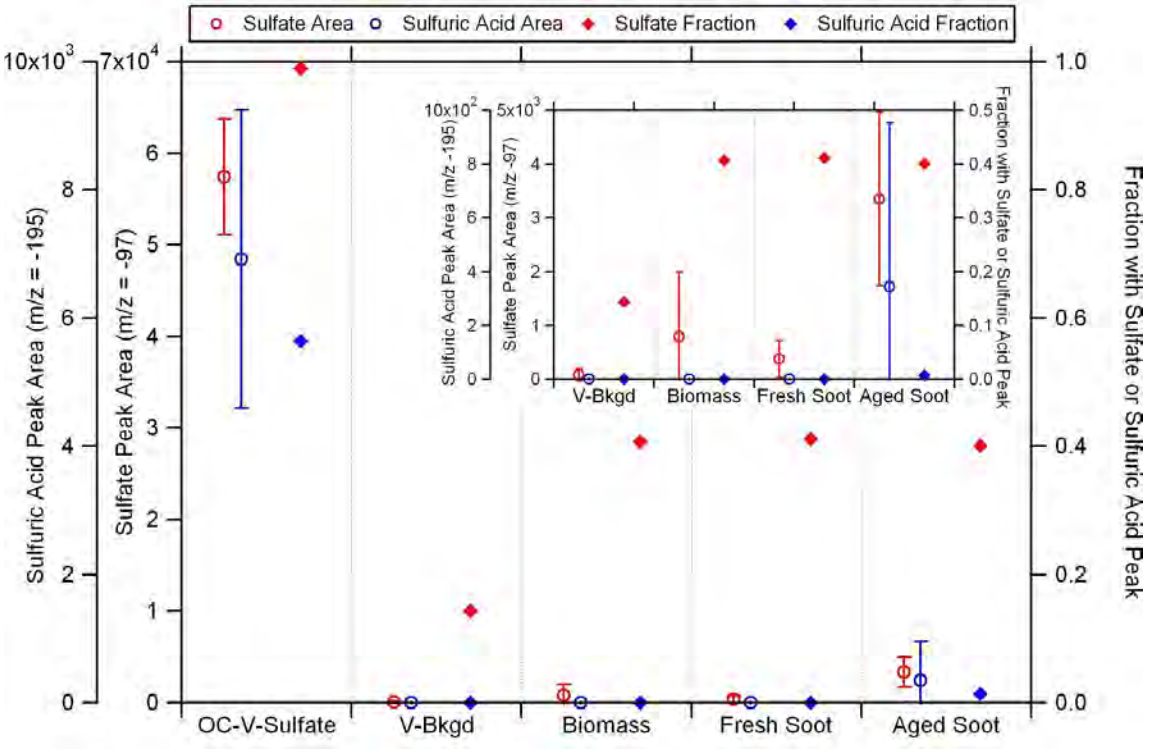


Figure 18: Average sulfate (red circles) and sulfuric acid (blue circles) absolute peak areas for major particle types during the plume of the vessel Container4; errors are shown by 95% confidence intervals. Number fractions of particles containing sulfate (red diamond) and sulfuric acid (blue diamond) are shown. The inset shows a zoomed-in version of particle types with lower peak areas than the OC-V-sulfate type.

There are several mechanisms that could lead to the high measured levels of sulfate in the particle phase of the plume: 1) homogeneous formation of sulfuric acid in the gas phase followed by condensation onto particles, 2) heterogeneous production of sulfate and sulfuric acid on the surface of particles, and 3) aqueous phase production within particles. The gas phase process is too slow to explain our observations of large amounts of sulfate and sulfuric acid forming within minutes of emission (88). This is supported by a study showing that at high relative humidity, aqueous processing is the main oxidation pathway (89). Also, if sulfuric acid was produced in the gas phase, it would condense on all particle surfaces present and lead to sulfate and sulfuric acid on all particle types, not selectively on one type (OC-V-sulfate) as we observe in this study. Thus, the heterogeneous and aqueous phase oxidation of $SO_2$ to sulfate and sulfuric acid

are the most likely routes. The stronger association of sulfate and sulfuric acid on V-containing particles further suggests the metal(s) are catalyzing this process. Vanadium could be catalyzing the oxidation process (90) or serving as a proxy for other metals present in residual fuel (i.e. Fe and Mn), which the UF-ATOFMS is not as sensitive to as vanadium, that are catalyzing the oxidation process (88). $V_2O_5$ was originally considered to be ineffective as an atmospheric catalyst below 150 °C (91), but subsequent work has shown that in the presence of $NO_2$ and adsorbed $H_2O$, catalysis of $SO_2$ by $V_2O_5$ can occur down to ambient temperatures (25°C) (90). Combine the fact that plumes quickly cool to ambient temperatures (92), that there was high relative humidity in the marine sampling location, and the presence of $NO_2$ (from the fast reaction between $O_3$ and NO) in the plumes, these atmospheric measurements show that catalytic sulfate production could indeed be an important atmospheric process. Recent work involving oxidation of other sulfur species by vanadium in the laboratory at temperatures between 80-280°C and in the atmosphere show the importance of the catalytic pathway for sulfate production (93,94).

Particulate emissions from ships must be considered as ship emissions are expected to increase ~5% globally by 2030. The production of large amounts of sulfate will impact climate through both cloud and radiative transfer processes (63). Increasing ship emissions will increase concentrations of submicron vanadium-containing particles (61), posing serious consequences for human health (64,65). Herein, direct single-particle measurements of ship plume particle mixing-states provide key insight into the chemistry of freshly emitted ship plumes. The ability to use vanadium as a tracer for ship plumes through single-particle mass spectrometry in the polluted environment of the Port of LA will strengthen efforts to accurately apportion particulate matter to source in other California environments. In addition, current emissions inventories do not account for fuel type and subsequent processing of sulfur species by vanadium and/or other metals (i.e. Fe and Mn) present in the plumes, which could be leading to incorrect estimates of atmospheric sulfate concentrations. Incorporating fuel type could help explain the enhanced sulfate levels being measured in places such as California that current emissions inventories cannot explain (95). Thus, the enrichment of sulfate and sulfuric acid on OC-V-sulfate particles due to catalytic aqueous phase reactions occurring on particle surfaces enriched with vanadium has important implications for regulating anthropogenic sulfate levels in coastal environments. The vanadium and sulfur content of fuels and subsequent impacts on sulfate production should be considered in future inventories and atmospheric models.

**iv. Acknowledgements**

The authors acknowledge Dr. Robert Moision and Melanie Zauscher for assistance during the study. Prof. V. Ramanathan and Dr. Craig Corrigan are acknowledged for providing an aethalometer. The Southern California Marine Institute, specifically Dr. Richard Peiper and Carrie Wolfe, hosted the sampling. Funding was provided by the California Air Resources Board (#04-336).

# Spatial Variability of Particulate Matter and Sources

## 3. Mobile Laboratory Observations of Temporal and Spatial Variability within the Coastal Urban Aerosol

### i. Introduction

Particulate matter (PM) has been shown to negatively impact human health over short and long term periods of exposure (96-98). Short term effects from elevated levels of particulate matter have also been observed, including increased hospital admissions for asthma, cardiovascular disease, and chronic obstruction pulmonary disease on days where PM less than 10 micrometers ($PM_{10}$) increased by 10 $\mu g/m^3$ (97). For example, at a series of hospitals in Utah, a recent study showed that a 10 $\mu g/m^3$ increase in $PM_{2.5}$ increased the risk of ischemic heart disease events (e.g. heart attacks) by 4.5% in patients (99). Long term studies have shown connections between particulate matter and lung cancer, cardiopulmonary mortality, and cardiovascular disease (97,98). Orru et al. found that the impact of particulate matter on human health had high spatial variability based on varying exposure levels to $PM_{2.5}$ in different neighborhoods throughout an urban environment (100). In addition to the mass concentration of PM present, negative health effects have also been linked to both particle size and chemical composition (97,98,101). Particle size plays a key role in determining where and to what extent inhaled particles deposit in the tracheobronchial and pulmonary systems (102-104). Where particles deposit in the body is also impacted by the degree to which particles grow when exposed to high relative humidity after inhalation, which is determined by particle size and chemical composition (102). In addition, single particle mixing state of particles plays a role in the negative health effects from particles. Synergistic effects have been shown when specific species are present together such as oxidative stress and NFκB activation (iron and soot), as well as cardiovascular and thermoregulatory effects (vanadium and nickel) (65,105). Thus, the health effects of PM are dependent on particle concentrations, size, and chemical composition.

As size, chemical composition, temporal variability, and spatial variability all contribute to the negative health effects of particulate matter, detailed measurements assessing these variables are necessary to understand and address this unique problem. However, understanding the urban aerosol has long been a challenge for aerosol researchers due to the complexity and the rapidly evolving nature of urban environments. For example, even determining the optimal metric for relating atmospheric measurements and human health has been challenging as basic parameters, such as particle number concentration and mass, do not always track each other (106). The merits of particle size distributions based on number concentration (107,108), surface area (109), and mass (110) have all been discussed as possibilities for linking particulate matter and health, but much is still unknown as to the causal link in ambient conditions. Increasing the understanding of urban aerosols is one portion of decreasing the uncertainty of the particle-health link and many studies have looked at both the long and short term trends in particle properties in an urban environment (111-116).

One of the more challenging aspects of decreasing uncertainty between exposure and health is determining the spatial variability of aerosols in an urban area. Three main

approaches have been utilized to measure aerosol spatial variability: multiple sampling sites operating simultaneously, models incorporating data from one or more sites, and mobile/portable laboratories. For instance, Mejia et al. compared measurements at 8 sites in Brisbane, Australia and found considerable variability in number concentrations and size distributions (depending on which whether the vehicle fleet was primarily cars or trucks) (117). Krudysz et al. monitored 13 sites around the Ports of Los Angeles and Long Beach and also found spatial variability in particle concentrations and size distributions, especially among ultrafine particles (111,117). When operating multiple sites continuously particle chemistry is often measured with only low resolution filter techniques. Models also have been used to expand the reach of studies with one or more sampling sites through meteorological or chemical mass balance models (118,119). Recently, many portable and/or mobile laboratories have been developed which can monitor and move quickly between sampling locations or sample while moving, which gives both high temporal and spatial resolution (120,121). Many of these laboratories have focused on fresh vehicle emissions (122-125) or spatial patterns of specific species (i.e. hexavalent chromium) (126). Herein, this paper will discuss measurements involving the development and deployment of the mobile aerosol time-of-flight mass spectrometry (ATOFMS) laboratory. These measurements of spatial and temporal variability with real-time particle size and chemistry mark the first single particle mass spectrometry measurements at multiple sites in a single day, providing particle concentrations, sizes, and chemistry that can be incorporated into future health studies.

## ii. Experimental

### *a. Mobile ATOFMS Laboratory*

A Pace American Class IV trailer (length 5.5 m; width 3.5 m; height 3 m; maximum gross trailer weight 4,500 kg) was modified to house an array of gas phase and aerosol instrumentation. The mobile ATOFMS laboratory was transported between sites by a Chevrolet Silverado 3500 pickup truck equipped with two Honda EB11000 gasoline generators (9.5 kVA) supported by a steel frame anchored to the truck bed. The generator exhaust passed through an exhaust manifold and 20 m of 6 cm diameter steel tubing to transport the emissions downwind of the sampling inlet. One generator was capable of powering the trailer at full load for 3-4 hours under normal operating conditions on a single tank of gas. This study focused on stationary sampling and at each site a 2.5 meter sampling line was attached to a sampling manifold on the mobile ATOFMS laboratory roof (5.5 meters above the ground). The manifold provided laminar sampling flow for 5-6 instruments in parallel with similar residence times.

### *b. 2009 San Diego Bay Measurements*

The mobile ATOFMS laboratory sampled the urban aerosol at multiple locations around San Diego Bay on both February 12 and March 13, 2009. Sampling times and locations are provided in **Table 5** and **Figure 19**. On February 12$^{th}$, sampling was conducted at three locations: Silver Strand State Beach (SS), Cesar Chavez Park (CC) in downtown San Diego, and Coronado Tidelands Park (Cor). These same three sites were sampled on March 13$^{th}$, as well as Chula Vista Bayfront Park (CV) and Pepper Park (Pep) in National City. Throughout this paper SS1, CC1, and Cor1 refer to the

measurements at the three sites on February 12th and SS2, Cor2, CC2, CV2, and Pep2 reference the measurements made on March 13th.

| Site | Abbreviation | Latitude (°N) | Longitude (°W) | Sampling Start | Sampling Stop |
|---|---|---|---|---|---|
| **Silver Strand** | SS1 | 32° 37' 58" | 117° 08' 29' | 2/12/2009 9:48 | 2/12/2009 12:18 |
| **Cesar Chavez Park** | CC1 | 32° 41' 46" | 117° 09' 01" | 2/12/2009 14:21 | 2/12/2009 16:10 |
| **Coronado** | Cor1 | 32° 41' 28" | 117° 09' 58" | 2/12/2009 17:26 | 2/12/2009 19:09 |
| **Silver Strand** | SS2 | 32° 37' 58" | 117° 08' 29" | 3/13/2009 8:29 | 3/13/2009 10:20 |
| **Coronado** | Cor2 | 32° 41' 28" | 117° 09' 58" | 3/13/2009 11:41 | 3/13/2009 13:03 |
| **Cesar Chavez Park** | CC2 | 32° 41' 46" | 117° 09' 01" | 3/13/2009 13:57 | 3/13/2009 15:02 |
| **Chula Vista Park** | CV2 | 32° 37' 11" | 117° 06' 11" | 3/13/2009 16:10 | 3/13/2009 17:03 |
| **Pepper Park** | Pep2 | 32° 39' 02" | 117° 06' 38" | 3/13/2009 18:35 | 3/13/2009 20:02 |

Table 5: Sampling times and locations at sites around San Diego Bay are described.

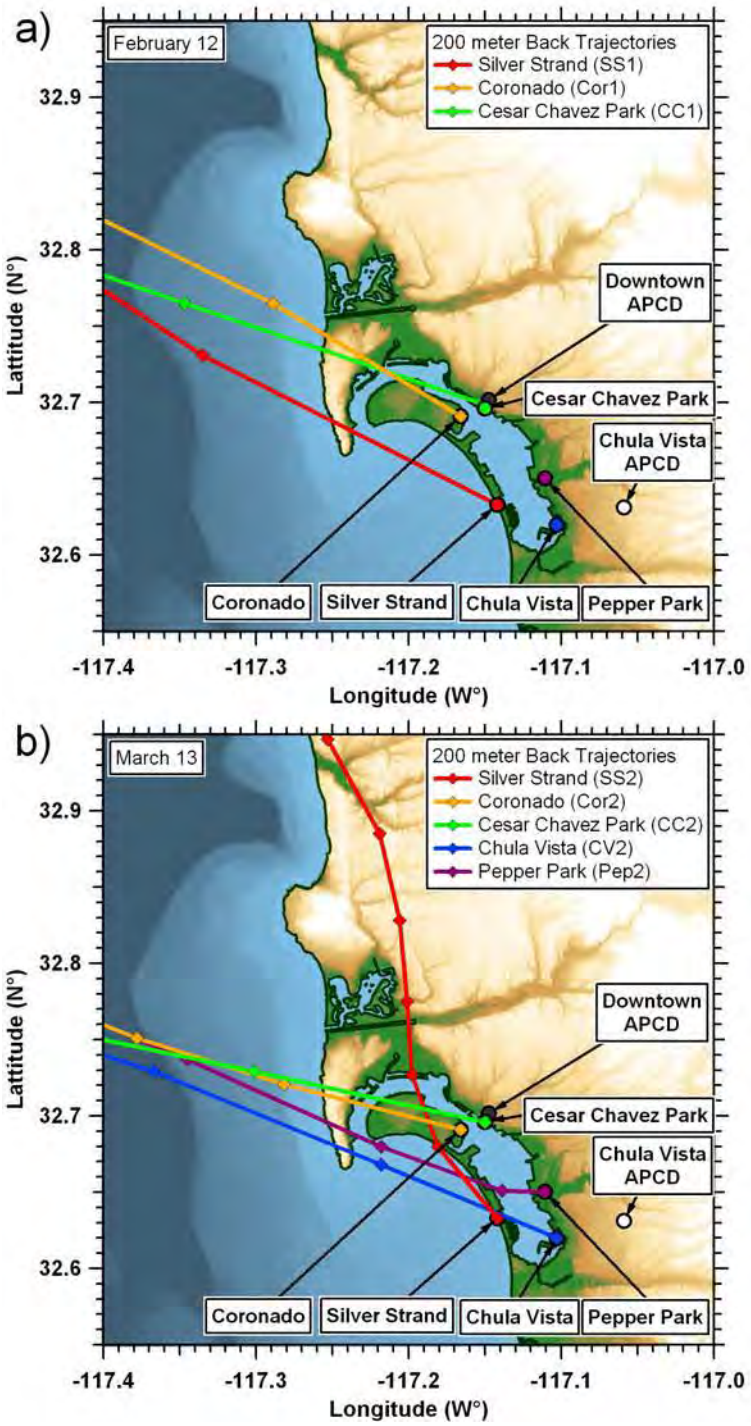


Figure 19: Map of the San Diego metropolitan area around San Diego Bay with trailer sampling sites and air pollution control district (APCD) sites, as well as 200 meter HYSPLIT air mass back trajectories for (a) February 12, 2009 and (b) March 13, 2009.

### *c. Instrumentation*

Standard aerosol instrumentation in the mobile ATOFMS laboratory included $PM_{2.5}$ mass concentrations from a beta attenuation monitor (BAM) (MetOne Model

BAM-1020) and black carbon mass concentrations from a seven wavelength aethalometer (Model AE31, Magee Scientific). Aerosol size distributions were collected between 0.011 - 0.604 μm by a scanning mobility particle sizer (SMPS) (Model 3936L, TSI Inc.) and 0.523 -10 μm by an aerodynamic particle sizer (APS) (Model 3321, TSI Inc.). Measurements of meteorology, gas phase concentrations, and mass concentrations ($PM_{2.5}$) were also incorporated from San Diego Air Pollution Control District (SD-APCD) sites in downtown San Diego (DT-APCD), Chula Vista (CV-APCD), and at the San Diego International Airport (SDAP).

### *d. Aerosol Time-of-Flight Mass Spectrometry*

An ATOFMS was operated inside the mobile laboratory measuring the size and chemical composition of individual particles between 0.2-3.0 μm in real-time at each site. The design and details of the ATOFMS have been described in detail previously (127). Briefly, particles are introduced into the ATOFMS through a converging nozzle into a differentially pumped vacuum chamber where the particles are accelerated to a size dependent velocity. The particles pass through two continuous wave lasers (diode pumped Nd:YAG lasers operating at 532 nm) located 6 cm apart. Particle speed is used to determine vacuum aerodynamic diameter by calibration with polystyrene latex spheres of known size. The sized particles are desorbed and ionized in the mass spectrometer source region by a 266 nm Q-switched Nd:YAG laser (1.2-1.4 mJ). Positive and negative ions from the same single particle are detected using a dual-reflectron time-of-flight mass spectrometer.

### *e. Single Particle Data Analysis*

Single particle size and mass spectral information were analyzed with YAADA 1.2 (www.yaada.org), a data analysis toolkit for MATLAB 6.5.1 (The MathWorks, Inc.). Particles were analyzed via two approaches: 1) searching mass spectral, aerodynamic size, and temporal features and 2) clustering mass spectra using an Adaptive Resonance Theory based neural network algorithm (ART-2a) at a vigilance factor of 0.8 (35). ART-2a combines particles into clusters based on the intensity of ion peaks in individual mass spectra. General particle types are defined by the characteristic chemical species or possible source to simplify the naming scheme; these labels do not reflect all of the species present within a specific particle type, but reflect the most intense ion peaks. Peak identifications within this paper correspond to the most probable ions for a given m/z ratio.

### *f. Scaling Single Particle Measurements to Mass Concentrations*

Number and mass concentrations were calculated for different particle types using APS size-resolved number concentrations, which has been shown previously to yield quantitative mass concentrations (128). Briefly, ATOFMS counts are divided into APS size bins (0.523 – 2.5 μm) and scaling factors were calculated for each site to account for ATOFMS transmission biases. Bins with less than 10 particles at a site were excluded due to low statistics, which might lead to slight undercounting of $PM_1$ and $PM_{2.5}$. After scaling to number concentration, mass was calculated using a representative density for particles in an urban atmosphere that have taken up water and secondary species, 1.5 $g/cm^3$ (129). Scaled ATOFMS mass concentrations have been shown previously to

correlate well with standard mass measurements and comparisons to the BAM $PM_{2.5}$ mass concentrations are included below (128). Previous ATOFMS measurements in San Diego used scaled mass concentrations to determine the impact of transported particles from the Los Angeles port region, demonstrating the utility of the method locally (74).

**iii. Results and Discussion**

### *a. Temporal Patterns of Meteorological and Gas Phase Concentrations*

To characterize the ambient conditions on February 12$^{th}$ and March 13$^{th}$ the meteorological and gas phase concentrations of each day are compared (**Figure 20**). The meteorological conditions recorded at the DT-APCD on both February 12$^{th}$ and March 13$^{th}$ had normal diurnal trends in temperature (red line – peaking late morning) and relative humidity (RH) (light blue line – minima midday). RH was monitored at the San Diego airport (6 km northwest). The wind direction (WD) (black markers) and wind speed (WS) (grey line) on February 12$^{th}$ was also diurnal, shifting from a light easterly land breeze (~ 1 m/s) before sunrise to a stronger westerly sea breeze (~ 3 m/s) during the day and shifting back to a light easterly land breeze after sunset. The wind data on March 13$^{th}$ were similar, with a difference being the absence of a shift back to easterly winds in the evening. Meteorological data from downtown San Diego (APCD) and Chula Vista (APCD) were compared on both days and agreed during the periods of sampling.

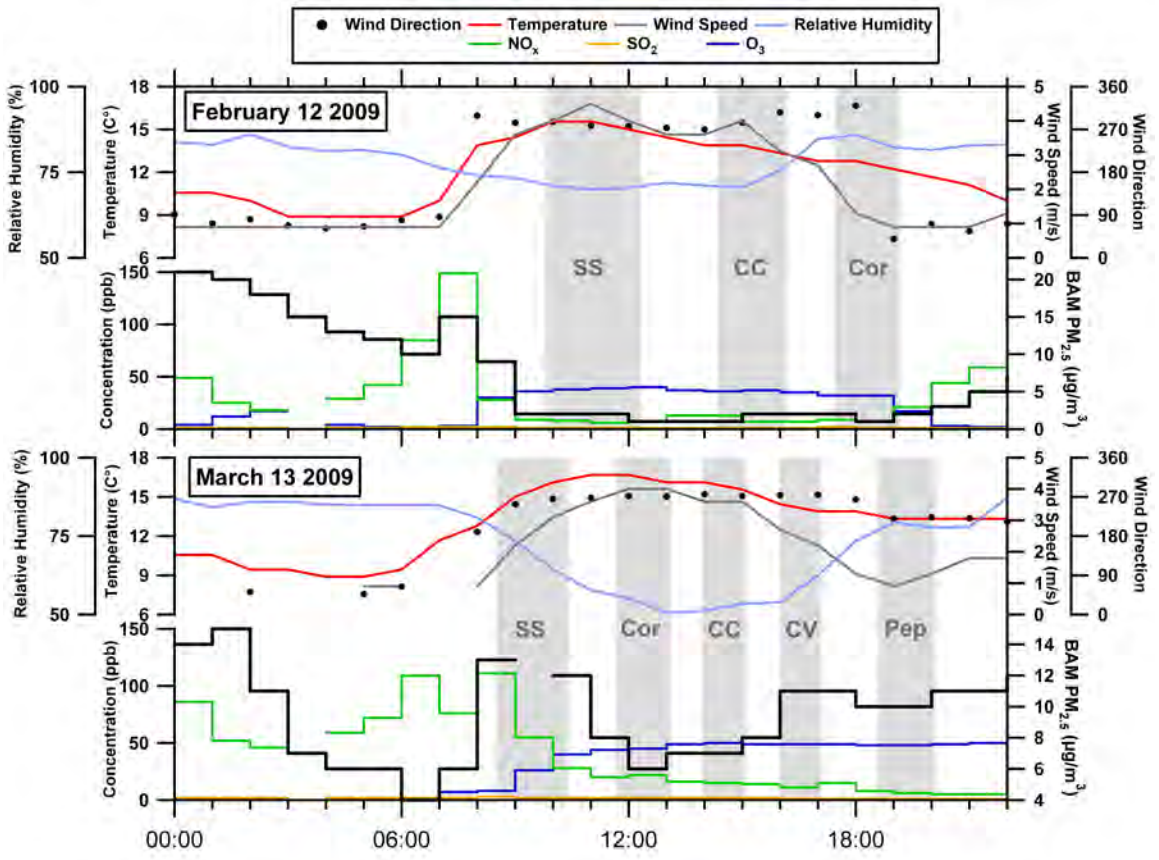


Figure 20: Comparison of meteorology conditions (temperature-red, relative humidity-light blue, wind speed-grey, wind direction-black markers) and gas phase concentrations ($O_3$-blue, $NO_x$-green, $SO_2$-gold) on February 12$^{th}$ and March 13$^{th}$.

The gas phase concentrations observed on February 12$^{th}$ and March 13$^{th}$ were also similar (**Figure 20**). An increase in $NO_x$ concentrations (green line) was observed before dawn, followed by a decrease after sunrise as $O_3$ concentrations (dark blue line) increased. On February 12$^{th}$, the $O_3$ decreased after sunset and the wind shifted to a land breeze with $NO_x$ increasing. The lack of a shift in wind direction on March 13$^{th}$ was accompanied by high $O_3$ concentrations well after dark and sustained low $NO_x$ concentrations. On both days, $SO_2$ concentrations were low, and no significant patterns were observed. The similar trends in the meteorological and gas phase data suggest that differences in particle mass, number concentration, and chemistry around San Diego Bay on these two days will provide insight into sources and aging, spatially and temporally.

Air mass back trajectories were calculated using HYSPLIT 4.9 for each site during the sampling periods (130). **Figure 19a** shows the 200 meter air mass backward trajectory for the three sites sampled on February 12$^{th}$ (SS1, CC1, and Cor1). All three back trajectories show a strong oceanic influence with each air mass overland for less than an hour, which corresponds with the wind direction in **Figure 20a**. The air mass back trajectories calculated for March 13$^{th}$ are not as homogeneous, with the initial sampling site for that day (SS2) showing an air mass that was over the San Diego area for ~ 6 hours. This slow moving air mass over a region with many sources indicates that the air mass is likely polluted, while the strong sea breeze that lasted through sampling at

(Cor2, CC2, CV2, and Pep2) is indicative of cleaner conditions. The two sampling days provide an informative contrast with a relatively clean day on February 12th versus March 13th, which transitioned from polluted conditions to cleaner marine conditions. This comparison can provide information about how quickly the aerosol changes in terms of particle types present and associated secondary species (i.e. nitrate and sulfate) during clean marine wind patterns.

Particulate mass concentration is the most commonly used metric to evaluate aerosol pollution levels by state and federal regulatory agencies and has led to the development of standardized methods for determining $PM_{10}$ and $PM_{2.5}$ mass concentrations, such as the BAM. BAM measurements at the DT-ACPD site on both days are shown in **Figure 20** (black line) and exhibit different patterns over the course of the day. On February 12th, a diurnal trend was observed with high nighttime mass concentrations (> 20 $\mu g/m^3$) that decreased in the pre-dawn hours and fell sharply after sunrise to low levels during the day (1-3 $\mu g/m^3$) with a slight increase in the late evening hours (3-5 $\mu g/m^3$). This pattern was also observed on February 10th and 11th, which were the first two non-precipitating days after five days and 43 mm of rain (February 5-9) (131). Overnight sampling at a site 21 km north of the DT site observed a similar overnight build-up in $PM_{2.5}$ with size distribution data (SMPS and APS). This increase in $PM_{2.5}$ is likely local as back trajectory analysis shows an oceanic origin, indicating that elevated $PM_{2.5}$ levels were likely not transported. On March 13th a peak in mass concentration between 08:00-10:00 PST related to morning rush hour was observed, but there was not a clear diurnal trend as $PM_{2.5}$ concentrations did not drop sharply to minimal levels during the day. $PM_{2.5}$ concentrations were >5 $\mu g/m^3$ throughout the day with levels of ~10 $\mu g/m^3$ from late afternoon through the evening (16:00-23:00 PST). The distinctly different temporal trends (high to very low on February 12th and higher, but less diurnal on March 13th) of $PM_{2.5}$ mass concentration on days with similar meteorological and gas-phase temporal patterns indicate differences in particle properties and dynamics, epitomizing the difficulty in understanding the urban aerosol.

### *b. Variability of Particle Mass and Number Concentrations*

To determine whether the mass concentrations observed at the downtown site were representative of particle mass at different points around the San Diego Bay, the ATOFMS $PM_{2.5}$ mass concentration (blue bars), and BAM $PM_{2.5}$ mass concentrations at the mobile ATOFMS laboratory sites (red bars) were compared with BAM measurements at the downtown site (green bars) (**Figure 21a**). On February 12th, the $PM_{2.5}$ concentrations for the downtown BAM and the trailer BAM match at 1 $\mu g/m^3$ (SS1, CC1, and Cor1). The ATOFMS mass concentrations are quite different from the trailer BAM and DT-APCD BAM concentrations at SS1, which we believe to be related to counting issues with the APS related to freshly generated sea salt particles from the ocean, which was 50 meters west of the sampling site. However, the measurements agree at the CC1 and Cor1 sites, where there was less of an influence from sea spray. During this period number concentrations (**Figure 21b** – orange bars) were also low (1865-4169 $\#/cm^3$). We believe this agreement is due to clean conditions resulting from the 5 days and 43 mm of rain in the week before sampling (February 5-9) mentioned above, which decreased concentrations of larger particles (i.e. > 0.5 $\mu m$) and led to similar conditions among larger particles around the bay.

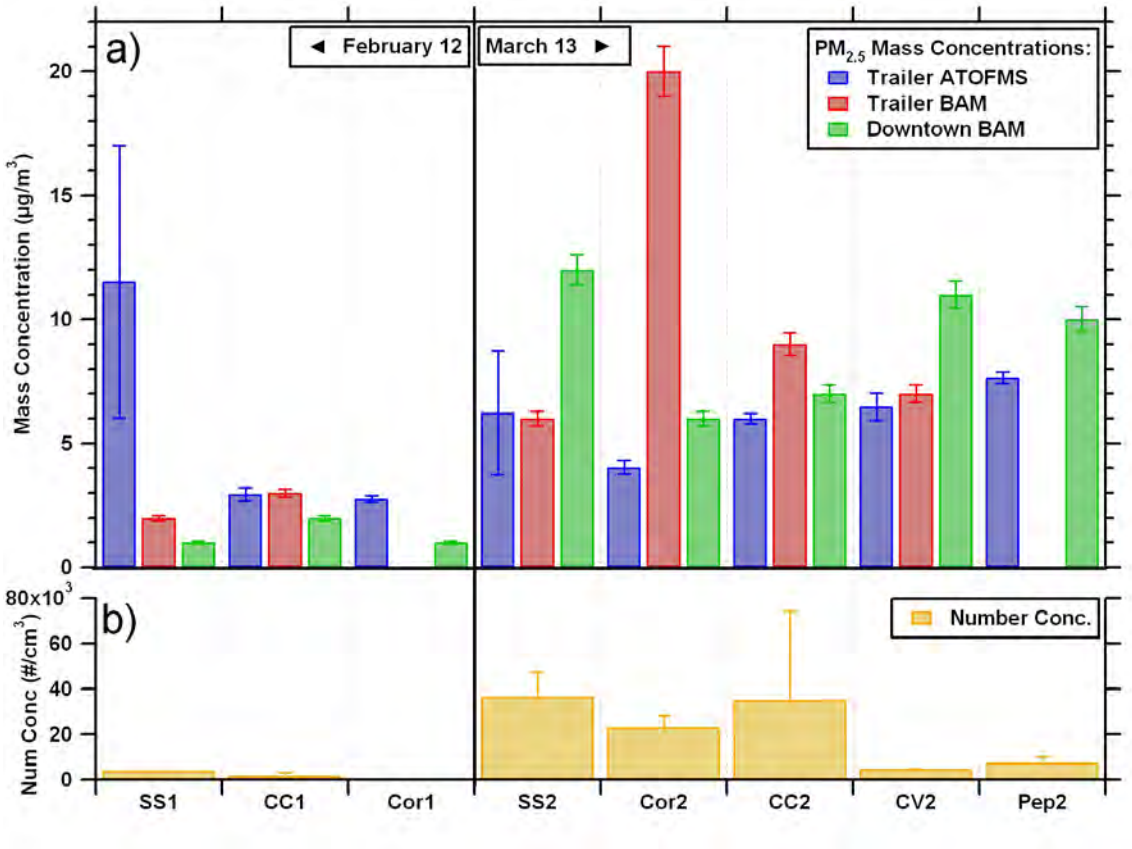


Figure 21: (a) $PM_{2.5}$ mass concentration data at each site for the: Scaled ATOFMS mass (blue bars), trailer BAM (red bars), and DT-APCD BAM (green bars). (b) Number concentration by site from summed SMPS scans (gold bars).

On March 13th the relationships between the mass measurements are more complex. At SS2, the trailer mass concentrations (ATOFMS and BAM) match within error, while the concentrations downtown are much higher. The Cor2 site had an anomalous BAM reading, but the Cor2 APS and DT mass measurements are similar for these sites that are ~1.5 km apart. The CC1 site has similar agreement between all three $PM_{2.5}$ measurements (distance between CC and DT ~0.6 km). The trailer measurements agree well at the CV2 site, but are quite different than the downtown site (distance ~ 4 km). Lastly, the ATOFMS mass is somewhat lower at the Pep2 site than the DT site (distance ~ 4 km), but more similar than at the CV2 site (the trailer BAM had a flow error at Pep2). Overall, at sites closer to downtown, there is better agreement between the trailer $PM_{2.5}$ and DT-ACPD $PM_{2.5}$, but the trailer $PM_{2.5}$ is smaller than DT mass when the distance between mobile and DT-APCD site were greater in the morning and late afternoon. Despite variations around the bay, these mass measurements indicate a background level of particulate matter mass, which is likely related to there being essentially no rain (only 1 day and <0.04 inches) between February 12th and March 13th. The similarity in mass concentrations throughout the day on March 13th does not match with the variability in particle number concentration and chemical composition observed with the SMPS, APS, and ATOFMS.

The number concentrations on March 13th have spatial and temporal variability. Temporally the SS2 or CV2 sites would be expected to have the highest number

concentrations as they were sampled during morning and evening rush hour, as well as SS2 having a back trajectory that spent significantly more time over the city than the other four. This initial hypothesis is correct with SS2, but far off with CV2. Spatially, the CC2 site is located closest to the source region of downtown San Diego and the San Diego Port. The number concentration observed at this site is higher than would be expected temporally, as concentrations should decrease during the day as winds shift to coming from the ocean, thus the increased concentration at CC2 shows spatial variation around the bay. CC2 also has the highest standard deviation of number concentrations indicating that the downtown aerosol is dynamic even over 1 hour of sampling. Thus, a gradient from north to south along the bay with higher concentrations downtown and lower concentrations to the south is hypothesized to exist during strong sea breezes and oceanic air mass back trajectories, while land based air masses such as SS2 are not necessarily expected to follow this trend. This is consistent with the many particle sources densely packed in the downtown area, while sources are less concentrated geographically as you travel out from downtown to the other sampling sites.

### *c. Variation in Aerosol Size Distributions*

Size distributions were analyzed for both February 12$^{th}$ and March 13$^{th}$ (**Figure 22**). **Figure 22a** shows SMPS and APS size distributions measured on February 12$^{th}$ (SMPS measurements are not available for Coronado on this date), while **Figure 22b** shows similar measurements from March 13$^{th}$. The aerosol number concentrations shown in **Figure 22a** are lower than those in **Figure 22b**. The concentrations are somewhat intuitive: SS1 is a coastal site that had a strong sea breeze during sampling leading to a higher concentration of larger particles (i.e. sea salt), while CC1 is an urban site in close proximity to major freeways and other sources leading to more small particles (0.010-0.030 μm) and fewer large particles (>0.030 μm). The APS traces for CC1 and Cor1 are also nearly identical as would be expected for two sites ~1.5 km apart on a day with somewhat homogeneous conditions for larger particles (> 0.5 μm) due to wash out of large particles by rain the previous days.

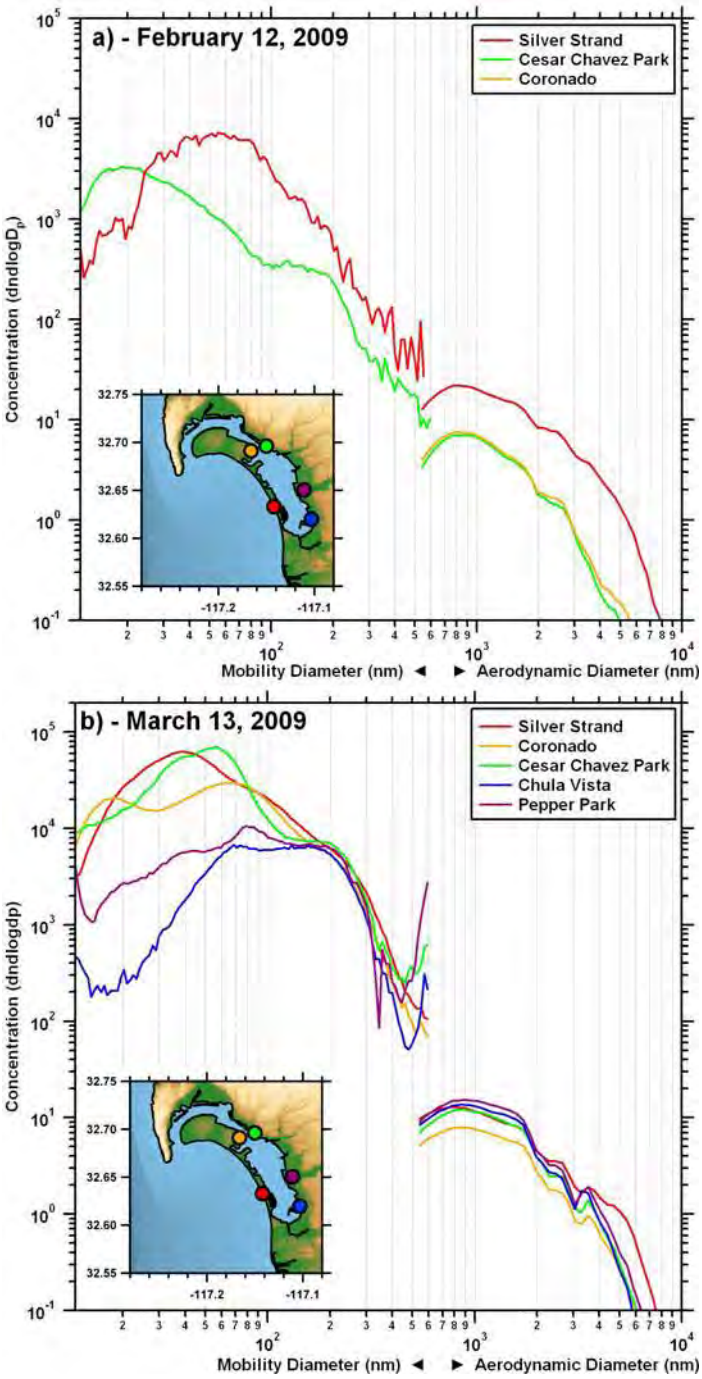


Figure 22: Size distribution measurements (SMPS and APS) for February 12th and March 13th as measured at the trailer sampling sites. The red traces correspond to Silver Strand, green traces to Cesar Chavez Park, yellow to Coronado, blue to Chula Vista, and purple to Pepper Park

A distinctive feature of **Figure 22b** is that the SMPS size distributions observed on March 13th show a great deal of variability. The small mode and relatively high number concentrations observed at Cor2 (18.8 nm and 23,103 #/cm$^3$) are likely the result of close proximity to a major highway (< 50 m south) and the larger modes and lower number concentrations at CV2 (68 nm and 4,745 #/cm$^3$) and Pep2 (79 nm and 7,609 #/cm$^3$) are the result of more distant sources and an older aerosol. The high number

concentration at SS2 (36,613 #/cm$^3$) is related to the air mass back trajectory as described above. Lastly, the high number concentration (34,928 #/cm$^3$) and standard deviation of number concentration (39,005 #/cm$^3$) (shown as error on **Figure 21b**) at CC2 indicate the dynamic nature of the sources.

An important aspect of **Figure 22** is that the size distributions on February 12$^{th}$ in the overlap region between the SMPS and APS (0.523-0.604 μm) are within instrumental error at those sizes, but there is a large disconnect in the overlap region between the SMPS and APS measurements on March 13$^{th}$ that is beyond error. This is due to the fact that the SMPS measures electrical mobility diameter ($d_m$) and the APS measures aerodynamic diameter ($d_a$). These two parameter are related to one another by the following equation (132) where $\rho_0$ is the unit density (1 g/cm$^3$), $\rho_p$ is the particle density, and $\chi$ is the shape factor:

$$\frac{d_a}{d_m} = \sqrt{\frac{\rho_p}{\chi \rho_0}} \tag{0.1}$$

As can be seen from the equation, as shape factor approaches 1 (spherical) and density approaches the unit density, aerodynamic and electrical mobility diameter converge. This indicates that particles in the overlap region on February 12$^{th}$ were both spherical and had taken up large amounts of water, as shown previously by Spencer et al. when atmospheric liquid water content increased, effective density approached unity (48). By comparison, on March 13$^{th}$ there is a multiple order of magnitude difference in number concentration in the overlap region indicating an aerosol that likely has non-unity density and shape factor, as mobility and aerodynamic diameter give different distributions. These differences show that particles are either denser, less spherical, or both when compared to the February 12$^{th}$ aerosol, indicating that the aerosol on March 13$^{th}$ is neither well-mixed nor homogeneous. This is a key point as high aerosol concentrations in urban environments are frequently assumed to be homogeneous due to atmospheric processing, but these results indicate that this is not a safe assumption.

### *d. Differing Aerosol Sources Determined by Particle Chemistry*

The main particle types observed at the different sampling sites included: sea salt, dust, elemental carbon mixed with organic carbon, organic carbon, and biomass particles. These particle types have been described for the San Diego area previously (74,133). Briefly, sea salt particles were identified by $^{23}Na^+$, $^{62}Na_2O^+$, $^{63}Na_2OH^+$, and $^{81,83}Na_2Cl^+$; dust particles were identified by peaks corresponding to $^{23}Na^+$, $^{27}Al^+$, $^{39}K^+$, $^{56}Fe^+$, $^{-76}SiO_3^-$, and $^{-77}HSiO_3^-$; elemental carbon particles mixed organic carbon (ECOC) were characterized by peaks at ($^{12}C_1^+$, $^{24}C_2^+$,…, $C_n^+$) with less intense organic carbon markers ($^{27}C_2H_3^+$, $^{29}C_2H_5^+$, $^{37}C_3H^+$, and $^{43}C_2H_3O^+$); organic carbon (OC) particles had high intensity peaks at $^{27}C_2H_3^+$, $^{29}C_2H_5^+$, $^{37}C_3H^+$, and $^{43}C_2H_3O^+$, as well as many other carbon fragments; and biomass particles identified by a strong potassium peak ($^{39}K^+$) and minor organic carbon ion markers. Mixing state of different particle types with markers for clean (chloride) and aged (nitrate and sulfate) particles will be discussed below.

The relative mass fractions for submicron and supermicron particle types are shown **Figure 23a** and **Figure 23b** respectively, with the black markers representing the total ATOFMS mass concentration at each site for that size range. In **Figure 23a** the very low concentrations of non-sea salt particle types (less than 10% at each site) on February

12th (SS1, CC1, Cor1) indicate very clean conditions, as discussed above. On March 13th between 25-50% of the particle mass under 1 μm are not sea salt particles, but rather carbonaceous particles (OC, ECOC, and biomass) indicating significant anthropogenic particle concentrations. This is significant as each site was within 200 meters of the salt water bay and heavily impacted by sea salt particles. On March 13th there is a decrease in mass for the OC particle type during the day, while ECOC and biomass are present throughout the day. The higher mass fraction of the OC particle type at SS2 was related to the different air mass history discussed above. As the sea breeze strengthens during the day, the OC particle type decreases to negligible levels by the time sampling is conducted at CV2 and Pep2, indicating the importance of temporal variation. The combined fraction of mass from ECOC and biomass particles is substantial throughout the day (14-32%), indicating particle types that are part of the urban background. The supermicron mass concentrations and mass fractions (**Figure 23b**) are remarkably consistent during the 8 time periods over 2 different days. This indicates that a large fraction of the spatial and temporal variability in particle number concentration and chemical composition is caused by the submicron particles.

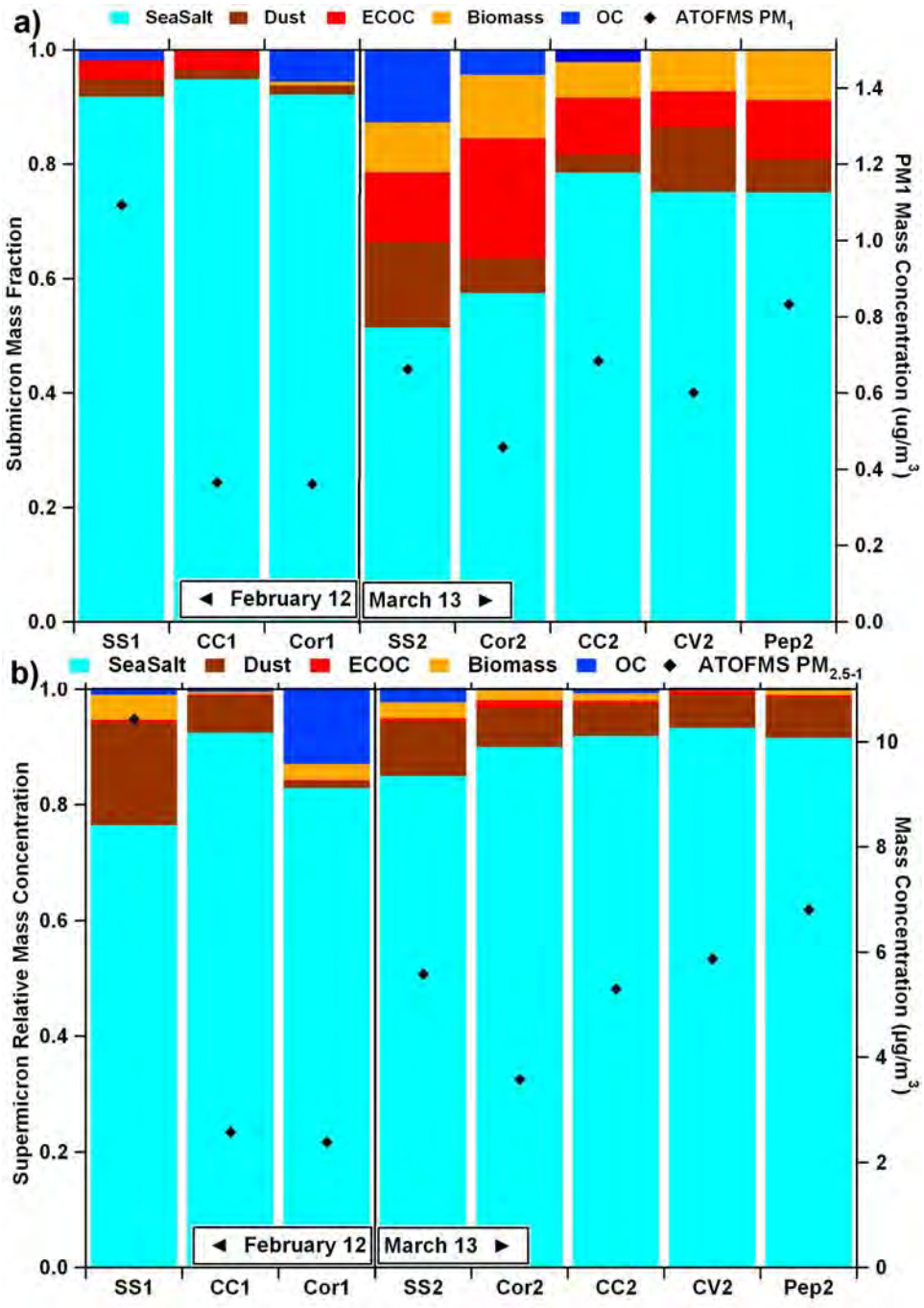


Figure 23: Chemically-resolved relative mass fractions of particle types for (a) submicron (0.523 – 1 µm) and (b) supermicron (1-2.5 µm) particles at each site. The black diamonds represent the ATOFMS mass concentration by site.

### *e. Differences in Particle Aging and Mixing State*

With respect to aging, mass spectral markers for chloride ($^{-35}Cl^-$), nitrate ($^{62}NO_3^-$), and sulfate ($^{97}HSO_4^-$ ) can provide information as to the degree and form of particle aging, as nitrate and sulfate can be markers of secondary processing. Chloride has been shown as a good marker for unreacted sea salt particles, while nitrate has been shown as a

marker for aging on many particle types (134,135). Sulfate is identified by the $^{97}HSO_4^-$ peak (136), except for sea salt particles where there is interference from the $^{23}Na^{37}Cl_2^-$ at m/z -97. Amongst different particle types, the aging and secondary species change temporally and spatially. **Figure 24a** shows the average nitrate and chloride peak areas at each site for sea salt particles, while **Figure 24b** and **Figure 24c** show nitrate and sulfate for biomass and ECOC particles, respectively. The February 12$^{th}$ sampling show higher chloride peak area for sea salt at all 3 sites, while on March 13$^{th}$ the nitrate peak area starts larger and decreases to roughly even with chloride during the day, suggesting fresh unreacted particles (**Figure 24a**). While there were not enough biomass and ECOC particles with negative mass spectra to analyze peak areas on February 12$^{th}$, on March 13$^{th}$ nitrate is seen to decrease during the day similar to sea salt, indicating that the particles are either less aged or have had nitrate volatilize (**Figure 24b** and **Figure 24c**). For biomass, sulfate peak area becomes larger throughout the day on March 13$^{th}$. This may be related in part to the strong ocean breeze observed for Cor2, CC2, CV2, and Pep2, which has had less time to react heterogeneously and take up nitrate. **Figure 24d** shows the ratio of the sulfate peak area and nitrate peak area at each site during the day. The ratio increases throughout the day for both particle types. The lower nitrate concentrations suggest that nitrate may not have been present on the particles sampled at CC2, CV2, or Pep2 due to cleaner conditions later in the day. Another possibility is that due to its semi-volatile nature, nitrate may have partitioned back to the gas phase in the late afternoon due to higher temperatures (137).

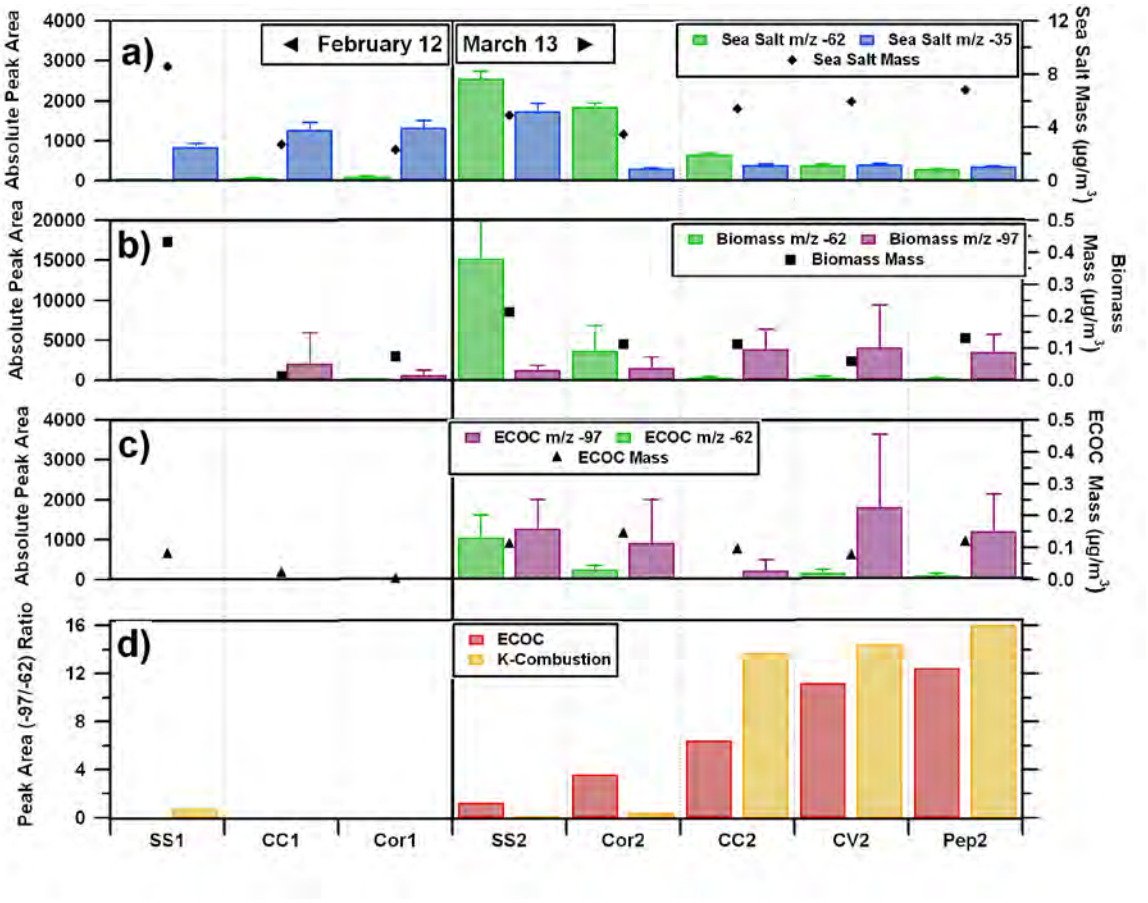


Figure 24: Peak areas related to aging for (a) Sea salt particles, (b) Biomass particles, and (c) ECOC particles. For sea salt particles, chloride (blue – $^{35}Cl^-$) and nitrate (green –$^{62}NO_3^-$) are plotted. For biomass and ECOC particles, nitrate and sulfate (purple – m/z $^{97}HSO_4^-$) are plotted. The ratio of the peak areas for nitrate and sulfate (d) are given for biomass and ECOC particle types.

### *f. Variations in Chemistry and Implications for Models and Regulations*

The measurements described above show that even on days with relatively similar meteorological conditions there can be considerable differences in particle mass and number concentrations and chemical mixing state within a marine-influenced urban atmosphere. During clean conditions similar mass concentrations, number concentrations, and particle chemistry were observed. During polluted time periods a strong diurnal pattern was observed with respect to particle types (decreasing organic carbon) and secondary species (nitrate) associated with the background particle types changed. Spatially, the downtown area represented a source region after the wind shift, as indicated by the size distributions and number concentrations, which fed into a general background level of particulate matter that appears to have built up over a month long period without rain. However, temporal patterns are shown to have a greater impact on particle properties than spatial patterns on this city-wide scale.

Submicron particles are more likely than supermicron particles to be inhaled and deposited into the tracheobronchial and pulmonary regions of the body than the naso-oro-pharyngo-laryngeal regions (138), which suggests that understanding the sources and

processing contributing to the urban aerosol is critical to determining the degree to which it impacts human health. The initial deployment of the mobile ATOFMS laboratory and single particle measurements from this platform demonstrate the importance of understanding these fluctuations in particle chemistry as they relate to sources and aging processes. The difference between a very clean day (February 12$^{th}$) and a day with higher mass concentrations (March 13$^{th}$) is shown by a less homogeneous aerosol that varies diurnal, more than spatially. The relative importance of temporal over spatial variation is only expected to increase as mass concentrations increase, except in close proximity to strong particle sources. Describing the urban aerosol from a single particle mixing state perspective will be a key to improving future models that will analyze the links between aerosol concentration and composition and their impact on human health. When crafting future regulations the vast variation possible within similar $PM_{2.5}$ mass concentrations needs to be considered and methods with higher time resolution chemical information are necessary as attempts are made at bridging the causal gap between air pollution and health.

**iv. Acknowledgements**

Andrew Ault acknowledges the Unified Port of San Diego Environmental Services Department for funding sampling with a graduate research grant. Joseph Mayer is thanked for his efforts with adapting the trailer and installing the generators. Additional funding was provided by the California Air Resources Board under contract 04-336. The authors gratefully acknowledge the NOAA Air Resources Laboratory for the provision of the HYSPLIT transport model and READY website used in this publication.

# Season and Interannual Variability in Particulate Matter Size and Composition

## 4. Single Particle Characterization in Riverside, CA during the SOAR 2005 Campaign: Seasonal Comparisons

### i. Introduction

The city of Riverside, California covers ~200 $km^2$ of area in the eastern Los Angeles (LA) basin and encounters some of the worst air pollution problems in the United States. In 2000, Riverside-San Bernardino was one of the six US metropolitan areas out of 296 that exceeded National Ambient Air Quality Standard levels due to high concentrations of $O_3$, $SO_2$ and particulate matter; furthermore, out of the nation's 94 largest metropolitan areas, Riverside-San Bernardino was one of three areas with unhealthy air quality levels for sensitive groups on more than 120 days each year between 1999 and 2002 (139). Great attention and effective policies are needed to alleviate the air pollution problem.

In addition to affecting climate and reducing visibility (140-142), ambient particles with aerodynamic diameters ($D_a$) less than or equal to 2.5 μm ($PM_{2.5}$) can cause serious adverse health effects (110,143). For example, a strong association was found between $PM_{2.5}$ concentration and mortality rate, particularly cardiopulmonary mortality (110); further, exposure to $PM_{2.5}$ and elemental carbon (EC) can lead to significant deficits in children's lung function growth and increase incidents of asthma (144). The distribution and deposition of inhaled particles strongly depend on particle size with smaller particles penetrating further into the respiratory system and even entering the blood stream (145-147). Therefore, in addition to aiding in source apportionment of aerosols in the LA basin and areas with similar emissions inventories and geographical and meteorological conditions, size-resolved ambient aerosol composition and chemical association will also provide valuable information for health effects studies.

Riverside is located along a typical air parcel pathway crossing the LA basin and is the receptor area of LA air pollutants, which transport east and transform along the way. In previous studies, the major components of $PM_{2.5}$ in Riverside were found to be nitrate, ammonium, EC and organic carbon (OC) by mass (148). Vehicle exhaust is the primary source of carbonaceous particles (EC and OC) (149), and the high ammonium concentrations are mostly influenced by emissions from nearby upwind Chino dairy farms, which is the largest single source of ammonia in the greater LA area (150). In summer, $PM_{2.5}$ concentrations reach maxima during the day due to elevated photochemical reactions as well as increased aerosol transport from the LA area in the west; whereas wintertime $PM_{2.5}$ concentrations peak at night due to the decrease in the altitude of inversion layers (44,45,151). Thus, the aerosol chemical composition and formation mechanisms vary considerably by season.

Numerous studies have been conducted in Riverside and other cities in the LA basin during the last three decades to study urban photochemical smog formation, aerosol transport and evolution across the basin, and size-resolved chemical composition of ambient particles (44,45,148,149,151-155). Recent developments in on-line techniques

for aerosol analysis have enabled high temporal resolution for particle number and size measurements. Studies investigating seasonal variability of particle number concentrations, size distributions, and chemical composition were also conducted in Riverside recently (151,155); however no detailed seasonal comparison is available on temporal variations of individual chemical classes and aerosol mixing state.

Aerosol time-of-flight mass spectrometry (ATOFMS) is an on-line mass spectrometry technique which allows the measurement of size and chemical composition of individual particles in real-time (156). ATOFMS can examine complicated aerosol mixtures on a single particle level and provide quantitative high temporal resolution chemical composition, size distribution, and chemical association information (157), which is useful for source apportionment. Previous continuous ambient ATOFMS measurements in Riverside were conducted in 1996 and 1997 (153,154,158); however, single polarity spectra without wide dynamic range (WDR) were collected, and seasonal differences were not the focus (157). Recent ATOFMS developments have allowed for simultaneous dual polarity collection with WDR, improving our ability to classify particles and identify aerosol associations especially with secondary signatures of nitrate and sulfate.

This paper presents summer and fall seasonal differences in aerosol size distribution, composition, and chemical association in Riverside from continuous ATOFMS single particle measurements. Particles with sizes between 0.2 and 2.5 μm are discussed, along with the meteorological conditions which play an important role in aerosol composition and formation mechanisms. Significant differences are observed between summer and fall temporal variations and percentages of individual chemical species. This work is the first attempt to study the seasonal variability of ambient aerosols using ATOFMS single particle measurements, illustrating the changes in the relative concentrations of the major particle types both by time and by size.

## ii. Experimental

### *a. SOAR Campaign*

The Study of Organic Aerosols in Riverside (SOAR) field campaign was conducted in the summer and fall of 2005 on the campus of the University of California, Riverside (UCR) for ambient aerosol characterization and source apportionment (159). The sampling site was located in the southeast of the UCR campus (33°58′18″N, 117°19′22″W), and a map is included in **Figure 25**. Immediately to the east and west of the sampling site are the satellite chiller plant and greenhouses, respectively, and a parking lot with a capacity of 129 parking spaces lies directly to the south. A major freeway (I-60/215) with heavy traffic neighbors the campus to the west and southwest and is ~600 meters away from the sampling site. Due to freeway construction, heavy traffic was observed as early as 3:00 and as late as 22:00. All data are presented in Pacific Standard Time (PST).

### *b. Ambient Sampling*

A standard ATOFMS was housed inside a mobile laboratory from July 30 to August 15 (SOAR-I) and from October 31 to November 21 (SOAR-II) with ~1 hour of downtime daily for maintenance mostly between 20:00 and 21:00. A co-located aerodynamic particle sizer (APS, TSI 3321) and UV photometric $O_3$ analyzer (TEI 49C)

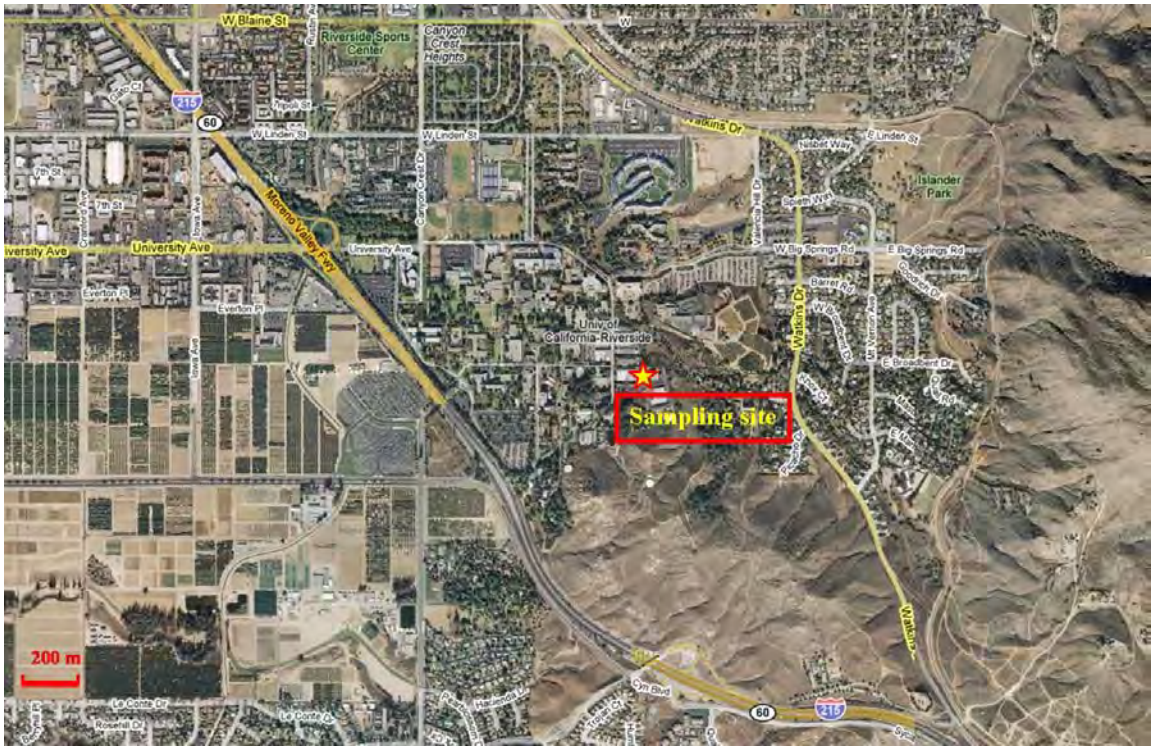


Figure 25: Map of SOAR sampling site on UCR campus.

measurements were also available. Both the ATOFMS and APS sampled off the same cylindrical stainless steel manifold which connected to the ambient atmosphere on one side with a single port and to several instruments on the other side through multiple ports. To prevent alteration of ambient aerosol composition, the sampling lines outside the mobile laboratory were covered with reflective insulation wrap to minimize the loss of semivolatile species during the daytime; the sampling lines inside the mobile laboratory were covered with insulated foam, placed inside of a large diameter plastic tubing and surrounded by constant flow of ambient air to prevent condensation of semivolatile species and water due to the temperature difference between ambient and mobile laboratory air.

The California Air Resources Board ambient air quality monitoring site at Rubidoux, CA is located ~10 km northwest of SOAR sampling site (149). Due to the absence of beta attenuation monitor (BAM) data at SOAR sampling site, ambient $PM_{2.5}$ mass concentrations are represented by Rubidoux BAM measurements, which are good estimates of the sampling site $PM_{2.5}$ levels during most of the study periods. Wind data, ambient temperature and relative humidity (RH), taken at the SOAR sampling site, were provided by the Goldstein group at University of California, Berkeley.

### *c. ATOFMS Data Analysis*

The chemical composition and $D_a$ of 1,076,812 and 1,061,506 ambient particles were collected using ATOFMS during SOAR-I and SOAR-II, respectively. The detailed

design and operating principles of ATOFMS are discussed in detail by Gard and co-workers (127). The desorption/ionization laser power used in the SOAR studies was 1.5 mJ, which has been shown to be able to fully ionize particles smaller than 1.0 μm (85). A custom software package was used to calibrate the mass spectra, and ion peaks were extracted into a peak list which were imported into Matlab using a single particle mass spectrometry data analysis tool, YAADA, for further analysis (160). The area and relative area of marker peaks in ATOFMS mass spectra can be related to the amount of specific species on each particle (85,161). To obtain major particle types over the study, an adaptive resonance theory-based clustering method (ART-2a) was used to classify ATOFMS measurements (35). By comparing the existence and intensity of ion peaks in single particle mass spectra, ART-2a classifies particles into separate clusters based on their mass spectral fingerprints. The "quintessential" mass spectra which represent the overall mass spectral characteristics of each cluster are referred to as its weight matrix. Submicron ($0.2\ \mu m \leq D_a < 1.0\ \mu m$) and supermicron ($1.0\ \mu m \leq D_a \leq 2.5\ \mu m$) particles during SOAR-I and SOAR-II were classified with ART-2a separately. A vigilance factor of 0.80 was used in this work, and particles in the most populated 50 (top 50) clusters account for ~90% of total ART-2a classified particles in both size ranges for SOAR-I and SOAR-II. Therefore, the top 50 clusters are representative of the overall aerosol composition and are the focus of this paper. The purpose of this paper is to present general pictures of major aerosol compositions over the course of the study during each season; thus information on unique species (such as metals) and distinct events will be the focus of future papers.

**iii. Results and Discussion**

General meteorological conditions exhibited diurnal variations for both seasons and are summarized in **Figure 26**. In summer, westerly winds dominated during the daytime between 6:00 and 18:00 reaching their maximum speeds at approximately 14:00. At night, the wind direction came from the east, associated with a decrease in wind speed. Temperature and $O_3$ concentrations showed similar diurnal trends as wind speed, while RH showed the opposite trend. Maximum temperature and $O_3$ concentrations and minimum RH were observed at approximately 14:00; minimum temperature and $O_3$ concentration and maximum RH occurred around 5:00. Overall, ambient meteorological conditions exhibited strong diurnal pattern without substantial day-to-day variation during SOAR-I.

Similar diurnal trends of wind speed, temperature, RH, and $O_3$ concentrations were still present during SOAR-II but the trend was weaker. Distinct differences were observed during certain periods including daytime wind directions. Easterly wind was observed at night throughout most sampling duration, which switched to westerly winds between 9:00 and 16:00 from November 2 to November 14. October 31 to November 1 and November 15 to November 21 were Santa Ana periods, during which warm, dry, and gusty offshore winds blows from the east-northeast to Southern California. Maximum wind speeds in SOAR-II (~1.6 m/s) were generally lower than those in SOAR-I (~2.5 m/s) except during the Santa Ana periods when wind speed can reach above 2.5 m/s. Moreover, wind speed spiked frequently in early mornings during SOAR-II besides the

daytime peak. Compared to SOAR-I, SOAR-II $O_3$ concentration displayed a similar diurnal variation with more irregularity during Santa Ana periods. However, the highest

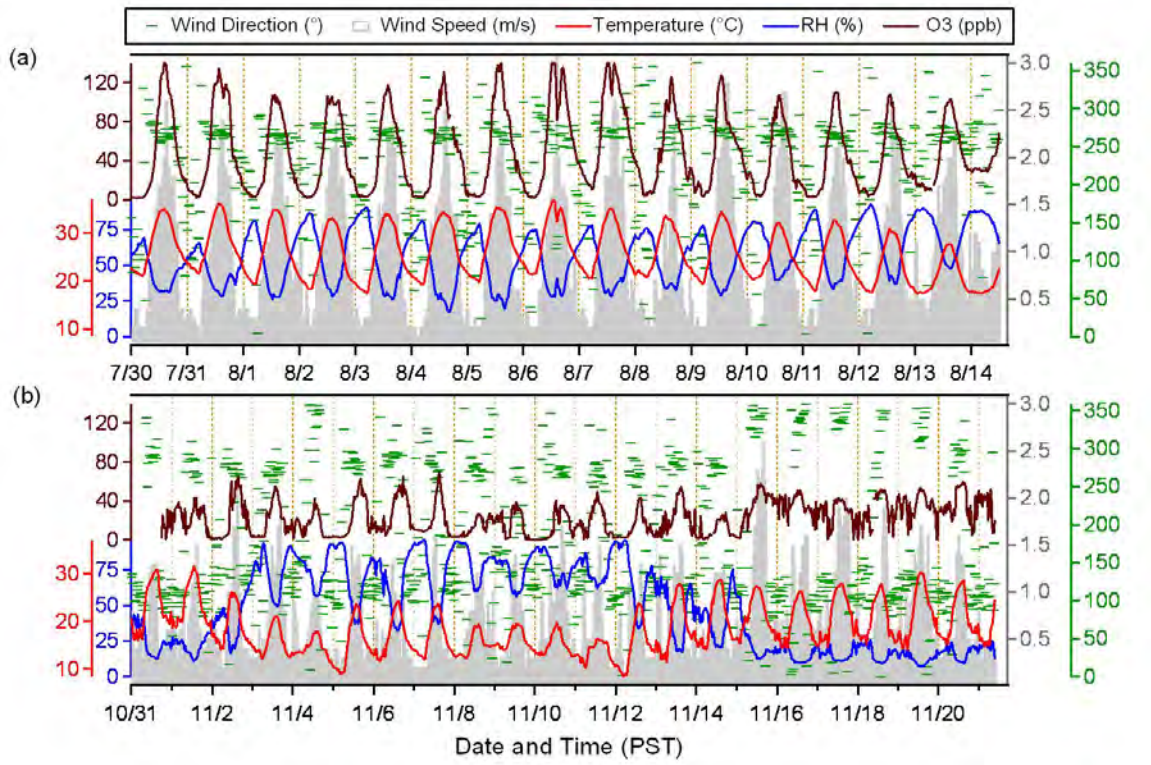


Figure 26: Temporal variations of ambient wind speed, wind direction, temperature, relative humidity, and ozone concentration during SOAR-I (a) and SOAR-II (b).

$O_3$ concentration throughout SOAR-II was only 70 ppb, whereas in SOAR-I, the daily $O_3$ concentration maximum frequently exceeded 100 ppb. SOAR-II will be segregated into more detailed episodes in the forthcoming sections.

### *a. $PM_{2.5}$ Concentrations*

BAM mass concentrations and APS size-resolved number concentrations for ambient $PM_{2.5}$ are compared in **Figure 27** for both SOAR-I and SOAR-II. The contour plots represent hourly temporal and size-resolved APS number concentrations in log scale with red being the highest concentrations and purple being the lowest. Hourly BAM measurements (brown line) are superimposed on APS measurements for more clear comparison. In SOAR-I, $PM_{2.5}$ mass concentrations displayed diurnal variations peaking mostly around noon with 79 $\mu g/m^3$ being the highest concentration observed. This daytime peak was likely due to a combination of transport of LA morning traffic pollution and secondary aerosol formation from photochemical reactions, which was dissipated by the increase in wind speed in early afternoon hours (from ~1.5 m/s to 2.5 m/s). No consistent diurnal trend was observed in SOAR-II ambient $PM_{2.5}$ concentrations, but there were episodes of extremely low mass concentrations during Santa Ana periods, as well as a gradual buildup between November 2 and November 7 with the highest concentration of 106 $\mu g/m^3$ in the Fall.

APS number concentration measurements showed results consistent with BAM measurements. The highest number concentrations during SOAR-I typically occurred around noon in the size range of 0.5 – 1.0 μm, during which the BAM also displayed daily peaks. The particles between 0.5 – 1.0 μm account for majority of particle mass and have a larger size distribution due to aging compared to freshly emitted particles.

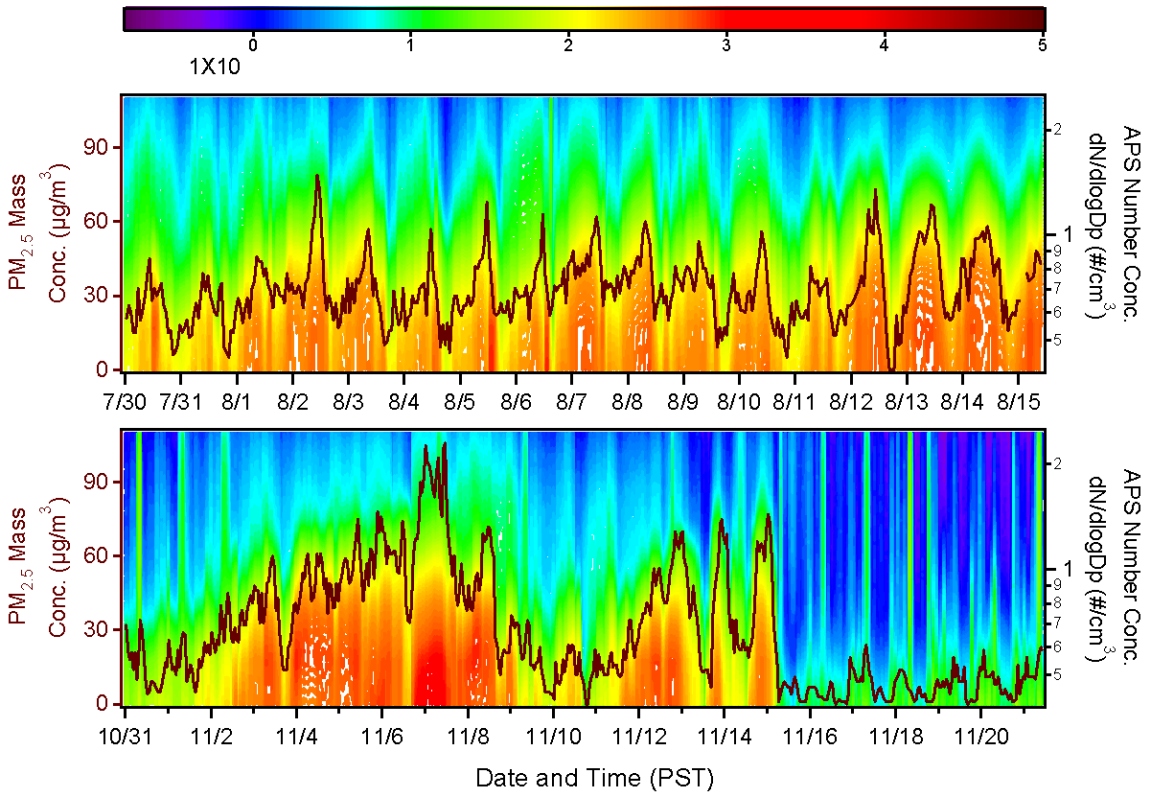


**Figure 27:** Hourly temporal variations of BAM $PM_{2.5}$ mass concentration and size-resolved hourly APS $PM_{2.5}$ particle number concentration during SOAR-I (top) and SOAR-II (bottom). Contour plots represent APS number concentration in log scale, and the red lines correspond to BAM data.

Late afternoons were generally characterized by the lowest particle number concentrations, which also agreed well with the trends shown by the BAM. SOAR-II episodes were also easily discerned with APS measurements. Similar to the agreement in SOAR-I, APS and BAM measurements displayed similar patterns in SOAR-II. Santa Ana periods featured extremely low number concentrations even in the smallest size ranges; a gradual buildup period between November 2 and November 7 was characterized by increased APS concentrations, with a maximum of >500 particles/$cm^3$ observed in the early morning of November 7. ATOFMS raw particle counts typically tracked well in both seasons with APS measurements having an $R^2$ of 0.59 in SOAR-I and 0.84 in SOAR-II.

### *b. Chemical Composition of ART-2a Clusters*

The ART-2a weight matrices of major Riverside particle types have been presented previously by Pastor et al. (154). Most particle types in Pastor's work were observed in the current studies although a few clusters were categorized differently based on more experience with ATOFMS measurements. Similar particle classes dominated both SOAR-I and SOAR-II; however, their relative fractions were different. The association of clusters with secondary species provides important information on aerosol aging. As observed previously in Riverside, the most common secondary marker peaks in this study are m/z 18 ($NH_4^+$), 30 ($NO^+$), 86 ($C_5H_{12}N^+$), -46 ($NO_2^-$), -62 ($NO_3^-$), -80 ($SO_3^-$), -97 ($HSO_4^-/H_2PO_4^-$), and -125 ($HNO_3NO_3^-$). The peak at m/z 43 ($CH_3CO^+/CHNO^+$) is also a secondary marker photo-oxidation reaction. **Figure 29** showed SOAR-I temporal variation of $O_3$ concentrations and the hourly average peak area of m/z 43. They track each other very closely indicating that m/z 43

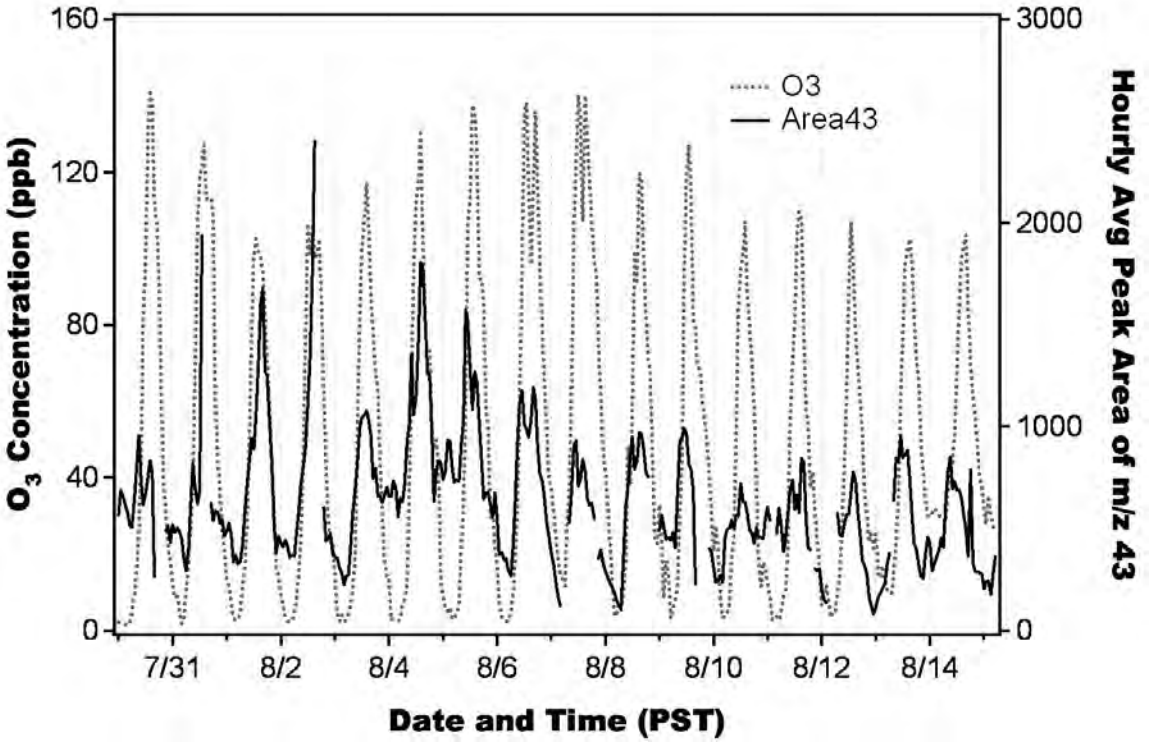


Figure 28: Hourly temporal variations of $O_3$ concentration and hourly average peak area of m/z 43.

($CH_3CO^+$/$CHNO^+$) is a secondary marker indicative of photo-oxidation reaction. No similar correlation was observed during SOAR-II, possibly due to the decrease in $O_3$ concentrations. Overall, secondary organic aerosol concentrations are lower in the Fall (48,54).

Representative ART-2a weight matrices of the SOAR major particle types are included in **Figure 29**. Aged OC1 represent typical OC particles showing the most intense fragment peaks at m/z 27 ($C_2H_3^+$/$CHN^+$), 37 ($C_3H^+$), and 43; their mass spectra also contain low intensity peaks representing secondary species including 18, 30, 86, and 118 ($(C_2H_5)_3NOH^+$). No negative ions were detected for this particle type. Aged OC-$SO_4$ have similar positive mass spectral features as aged OC1; additionally, they have intense negative spectra showing associations with nitrate (m/z -46, -62 and -125) and sulfate (m/z -80 and -97). The positive spectra of ECOC contain both EC and OC signatures. These particles contain similar OC mass spectral patterns as aged OC1 and have no negative spectra, but the most intense positive peaks are from characteristic EC fragments at m/z 12 ($C^+$) and 36 ($C_3^+$) along with other low intensity EC peaks. ECOC-$SO_4$ particles have similar positive spectra compared to ECOC and similar negative spectra to aged OC-$SO_4$; these particles contain a mixture of OC, EC, nitrate, and sulfate. Vanadium-rich particles contain mostly OC in the positive spectra, with the dominant peaks being m/z 51 ($V^+$) and 67 ($VO^+$). Aged sea salt and biomass are both associated with nitrate and sulfate as shown in their negative spectra. The most intense positive peak of aged sea salt particles is the peak at m/z 23 ($Na^+$), followed by lower intensity m/z 81 ($Na_2Cl^+$), 108 ($Na_2NO_3^+$), 39 ($K^+$) and carbonaceous peaks. Hughes and co-

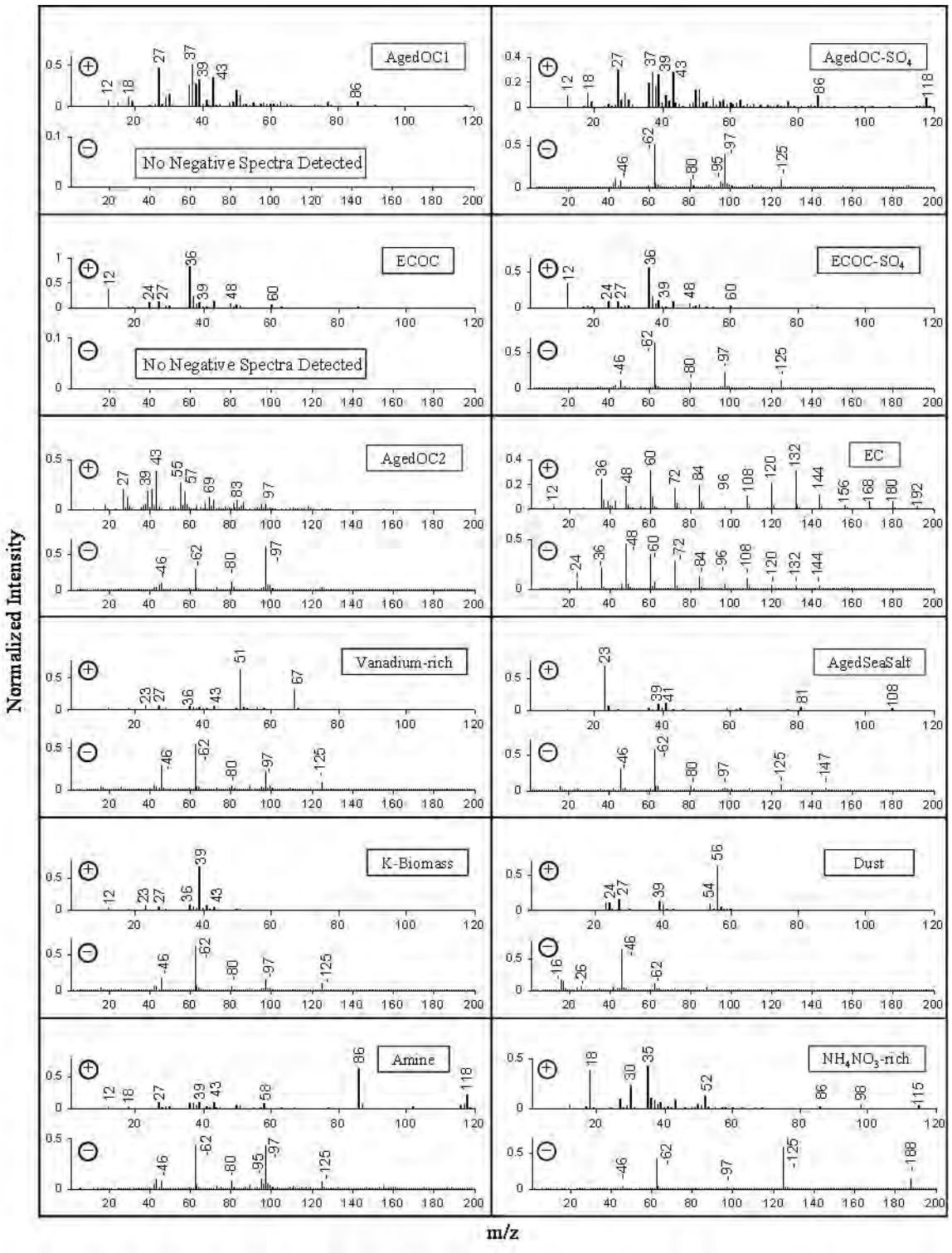


Figure 29: ART-2a weight matrices of representative particle types during SOAR-I and SOAR-II.

workers showed that sea salt is the only significant sodium source in Riverside (158). The most intense positive peak in biomass particles is m/z 39 ($K^+$) accompanied by low intensity OC peaks; many studies have shown that potassium is the marker for biomass emissions (162-164). Dust particles are mostly distributed in supermicron range and contain one or more inorganic species including sodium, magnesium, aluminum, silicon, potassium, calcium, iron, and manganese; the weight matrix of iron-rich particles is presented here as an example. The positive weight matrices of all the above particle types are consistent with the major ones presented previously in Pastor et al. (154). Having only single positive spectra limited the ability of Pastor et al. in differentiating between aged and fresh particle types (i.e. aged OC1 and aged OC-$SO_4$ and ECOC and ECOC-$SO_4$). These types are shown to have very different temporal variations in the following sections.

Four additional Riverside particle types were identified in the SOAR studies that were not shown in Pastor et al. EC is an elemental carbon dominant type showing very distinct continuous $C_n^+/C_n^-$ patterns (where n is an integer) in both polarities extending beyond m/z 150. Amine particles are organic carbon particles with m/z 86 and 118 being the most intense positive peaks (39). $NH_4NO_3$–rich OC-containing particles are characterized by intense ammonium and nitrate cluster peaks in the positive spectra at m/z 18, 30, 35 ($(NH_3)_2H^+$), 52 ($(NH_3)_3H^+$), 98 ($(NH_3)_3NO_2H^+$), and 115 ($(NH_3)_4NO_2H^+$); their negative spectra are dominated by nitrate peaks. This type is quite different from the ammonium nitrate particles in Pastor et al., which mainly contain m/z 18 and 30 (154). Aged OC2 is a low abundance OC cluster (<2% on average). The positive spectra of this type show distinct envelope patterns peaking around m/z 27 and 29; 39, 41 and 43; 55 and 57; 69 and 71; 81 and 83; 95 and 97. Compared to particle types in Pastor et al., the most likely reasons for observing the above four particle types in the SOAR studies are classifying submicron and supermicron particles separately and using a higher vigilance factor, although we cannot exclude a change in the ambient air quality between 1997 and 2006. All particles during the SOAR studies show some degree of aging based on the associations between the major particle types and secondary ammonium, amines, nitrate, and sulfate.

### *c. SOAR-I Diurnal Variation*

In SOAR-I, the fractions of the major particle types showed distinct diurnal trends throughout the sampling period. Submicron aerosols were dominated by carbonaceous particles; while supermicron aerosols were alternately governed by either carbonaceous particles or dust and aged sea salt particles depending upon the time of day. **Figure 30** a-d presents the hourly temporal variations of the number fractions of major particle types for the top 50 clusters, with BAM measurements superimposed on each plot in red trace. The following discussions of temporal variations refer exclusively to the ATOFMS particle type number fractions unless otherwise specified. Also included in **Figure 30** are the size distributions of total $PM_{2.5}$ in each season. **Figure 31** shows the size-resolved number fractions of each of SOAR-I top 50 ART-2a clusters at various time of day: 3:00, 9:00, 15:00 and 21:00. Clusters with similar chemical compositions are placed next to each other with the same theme color but various patterns and the data for each hour were obtained by taking the average of the same hour data over all sampling days. The size

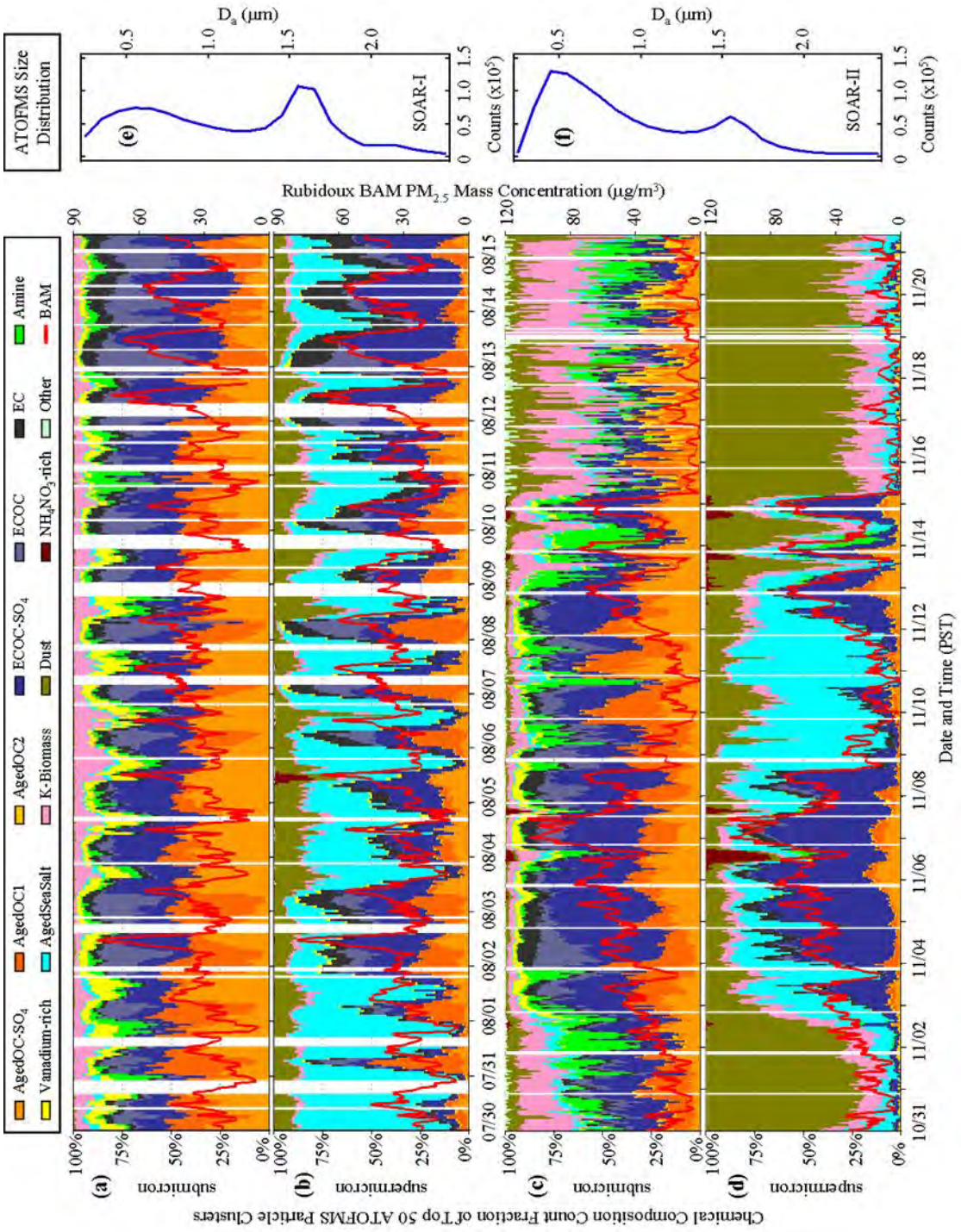


Figure 30: Temporal variations of the number fractions of major particle types for the top 50 clusters superimposed with PM2.5 mass concentrations (red line) and size distributions of total ATOFMS particle counts.

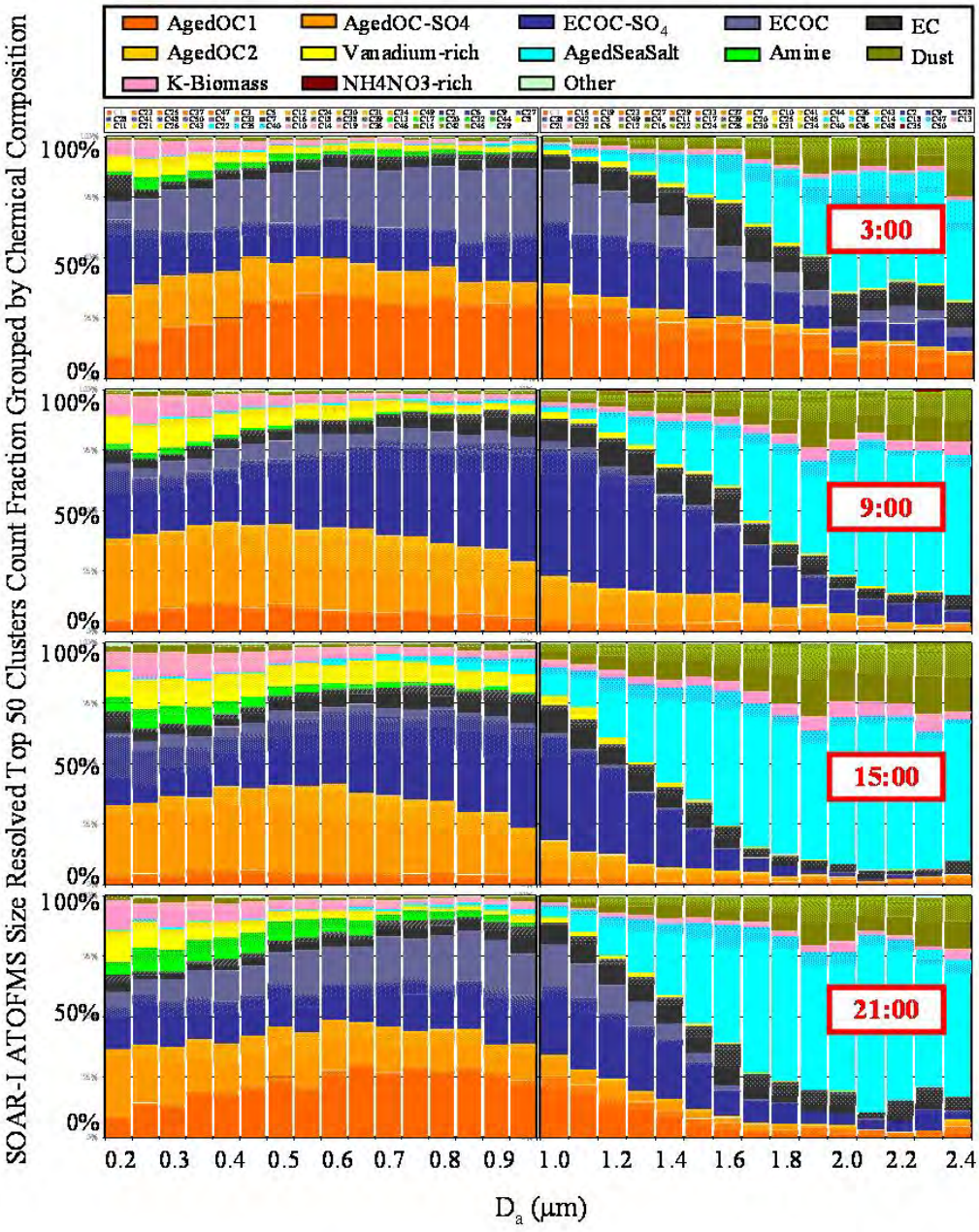


Figure 31: Hourly size-resolved number fractions of SOAR-I top 50 clusters from ART-2a results averaged for 3:00, 9:00, 15:00 and 21:00 over all sampling days. Size resolution is 0.05 μm for the submicron range and 0.10 μm for the supermicron range.

resolution is 0.05 μm for submicron and 0.1 μm for supermicron particles with the starting size indicated on the bottom axis.

SOAR-I aged OC1 and ECOC peaked in early morning around 5:00 as shown in **Figure 30 a-b**. These two types of particles only had positive spectra. They were likely the fairly aged aerosols experienced daytime photochemical reaction and nighttime aqueous phase processing, but high RH values in the early morning suppressed the

negative ions on these particles, causing them to peak at 5:00. EC showed a similar temporal trend and also peaked around 5:00. Based on the low intensity of secondary marker peaks, these particles were freshly emitted and were most likely from local vehicle sources. **Figure 31** presents complimentary information showing the highest aged OC1 and ECOC fractions appearing close to 3:00 in both submicron and supermicron ranges and lowest fractions were observed near 9:00 and 15:00, mainly distributed in the submicron range. EC, however mostly fell in the supermicron range, which is a little un-expected since freshly emitted particles are usually small in diameter (< 0.2 μm). There might be contributions from other local source that generate larger EC particles. The low wind speeds at night coupled with low inversion layers assisted the buildup of particles and led to the observed high carbonaceous fractions. Aged OC-$SO_4$ and ECOC-$SO_4$ mostly peaked subsequently later in the morning around 9:00 and showed a second peak around 14:00. The morning peaks likely correspond to transformed organic aerosols from early morning vehicle emissions and the time of the peaks was affected by local aerosol transformation rates. The afternoon peaks are due to the combination of local secondary aerosols formed through photochemical reactions and the transport of LA pollutants, which were originally emitted from LA early morning rush hour vehicles and were transported to Riverside by summer daytime westerly winds after about 8-10 hours as shown by the air mass trajectories. This afternoon peak was also observed in other studies, and the transport time have been estimated to range from a few hours to more than one day (151,165). Thus the variation in the afternoon peak hours was partly due to aerosol transport time. Aged OC-$SO_4$ were mostly submicron particles as shown in **Figure 31**. A substantial fraction of ECOC-$SO_4$ particles were in supermicron ranges, which possibly transformed from supermicron EC particles. Overall, carbonaceous particles mixed with nitrate, sulfate and ammonium dominated the submicron range throughout the day (75% - 90%), and were the major supermicron components in the morning periods.

Biomass, vanadium-rich, dust and aged sea salt particle types all peaked in the afternoon and were transported from the LA area by the daytime prevailing westerly wind. Biomass and vanadium-rich were mostly submicron particles; whereas dust and aged sea salt particles mostly fell in the supermicron range and when combined often comprised 90% of supermicron particle counts at their maxima. Dust particles also displayed a minor peak in the morning, which is likely from local sources. **Figure 31** also shows that aged sea salt and dust governed the supermicron range especially around 15:00 in the largest size bins. Vanadium has been observed in particle phase in many studies and are one of the major metal components of ship emissions (166-168). Although a minor fraction can be emitted from vehicle exhaust (36), the vanadium-rich particles during the SOAR studies were most likely emitted from ships in LA and Long Beach Harbors and were transported inland to Riverside. Vanadium measurements by Singh and co-workers in Riverside (169) show consistent results where vanadium concentrations peak from late afternoon to early evening; however, the major source of vanadium was proposed to be vehicle emissions instead of ship engine exhaust in their paper (169). As shown in **Figure 31**, SOAR-I vanadium-rich particles peaked around 15:00. The highest fractions of vanadium particles occurred in the low submicron size range, indicating that these particles were generated from combustion sources instead of crustal material, and grew to fine range during transport.

Amine particles were associated with both nitrate and sulfate. They were only observed in the submicron range and peaked between 17:00 and midnight as shown in **Figure 30** and **Figure 31**. Similar diurnal variations of ambient amine particles have been observed in previous studies in Riverside and Atlanta (39). Amine particles are small in diameter and are semivolatile because they are formed through photo-oxidation of gas-phase low molecular weight amine. (39). Therefore, most amine particles were detected at night when they participated into particle phase at low ambient temperature and high RH (39). The highest amine fractions occurred in the smallest size bins.

$NH_4NO_3$-rich particles represented highly aged aerosols containing a great amount of ammonium and nitrate as demonstrated by their weight matrix. These particles mostly fall into the supermicron range due to particle growth during aging as shown in **Figure 30 a-b**. High $NH_4NO_3$-rich particle fractions occurred around noon on August 5, as well as less distinguishable spikes from August 2 to August 9 around the same time in SOAR-I. High concentrations of nitrate particle precursors were generated from LA area morning vehicle emissions and formed nitrate as the particles were transported inland. Large amounts of $NH_4NO_3$ were produced when the high concentration nitrate particles crossed Chino dairy farm area upwind and were continuously transported east causing sharp spikes (3-5 hrs) in Riverside $NH_4NO_3$ concentrations. Similar $NH_4NO_3$ production mechanisms in Riverside have been proposed previously by Kleeman and Cass and by Singh and co-workers (169,170). Hughes and co-workers observed a higher mass fraction of $NH_4NO_3$ in particles in 1.0-1.8 μm compared to 0.56-1.0 μm during filter analysis, which is consistent with the higher $NH_4NO_3$-rich particle fractions in the supermicron range by ATOFMS (150,153). Single particle analysis by Pastor et al. showed a temporal anti-correlation between sea salt and $NH_4NO_3$ particles (154). This anti-correlation is not observed in the SOAR studies; in fact the relative fractions of aged sea salt and $NH_4NO_3$-rich particles sometimes peak around the same time.

Overall, the SOAR-I particles are fairly aged, and most particle types displayed distinct diurnal variations. Total carbonaceous fractions were high from late night to late morning, whereas amine, vanadium-rich, biomass, and aged sea salt fractions peaked in late afternoons. The daytime was greatly influenced by LA pollutants due to the prevailing westerly wind; nighttime was affected by low speed easterly wind, thus local emissions dominate aerosol composition. In most cases, BAM measurements showed maxima when carbonaceous particle fractions were the highest, indicating that carbonaceous particles which associated with nitrate, sulfate and ammonium were the major $PM_{2.5}$ components by mass.

### *d. SOAR-II Episodic Variations*

While SOAR-I and SOAR-II had similar major particle types, episodic temporal variations were observed in SOAR-II particles fractions as shown in **Figure 30 c-d**. Although no consistent diurnal trends exist with the exception of the $NH_4NO_3$-rich, SOAR-II sampling period can be characterized into unique episodes based on ambient $PM_{2.5}$ mass concentration levels. Specifically, the episodes are: SantaAna1, October 31 0:00 – November 1 19:00; Buildup1, November 1 19:00 – November 6 15:00; HighMass, November 6 15:00 – November 7 18:00; Buildup2, November 7 18:00 – November 8

22:00; Scavenging, November 8 22:00 – November 11, 13:00; Buildup3, November 11 13:00 – November 15 5:00; and SantaAna2, November 15 5:00 – November 21 10:00.

**Figure 32** presents the hourly-averaged size distributions of the top 50 clusters number fractions during each episode. Similar to **Figure 31**, clusters with the same composition are positioned next to each other and represented with the same color but different patterns. Submicron and supermicron size distributions are shown with size resolutions of 0.05 μm and 0.10 μm, respectively. The $PM_{2.5}$ mass concentrations within each respective episode are highlighted in green in **Figure 32**. Also included are seven representative HYSPLIT 48-hour back trajectories ending at Riverside with 4-hour time resolution (171). The HYSPLIT trajectories provided the origin of the air mass during each episode; the total traveling distance correlates with the speed of air mass movement. The end times of each trajectory correspond to one day in each episode at 6:00. All of the HYSPLIT plots in **Figure 32** have the same latitude-longitude scale except for SantaAna2, during which the air mass traveled very far during the past 48 hours; therefore, a much larger geographical region is needed to display the complete

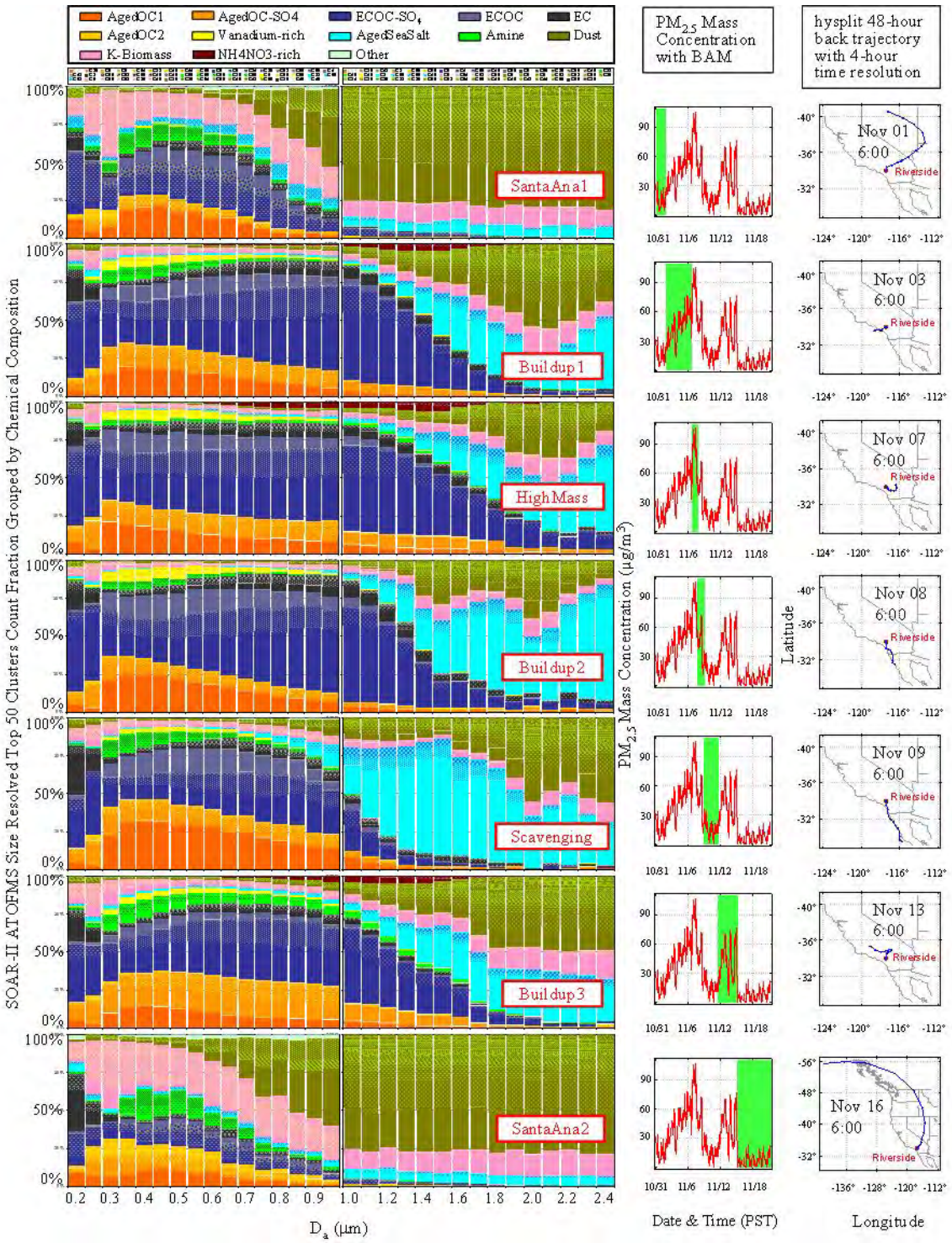


**Figure 32: Size-resolved number fractions of SOAR-II top 50 clusters from ART-2a results averaged over each episode along with corresponding PM2.5 levels and representative 48-hour HYSPLIT back trajectories.**

trajectory. All of the back trajectories illustrated the common conditions for each episode; while particular hours within the episodes could have different trajectories, they are not representative of the general conditions.

In addition to the low ambient particle mass and number concentrations, low RH and high temperature are the distinct characteristics of both Santa Ana periods. HYSPLIT back trajectories in **Figure 32** show that SantaAna1 air mass reaching Riverside at 6:00 on November 1 started from Nevada 48 hours before and consecutively traveled east through Utah, Arizona, then west to Nevada, California, and finally reached the sampling site. The air mass traveled a much greater distance compared to the non-Santa Ana periods and carried a large amount of dust particles to Riverside, while taking away many of the carbonaceous particles to the west. Even faster air mass transport was observed during the SantaAna2 period. The air mass ending at 6:00 on November 16 traveled east from the Gulf of Alaska through Canada, then south to the US during the past 48 hours. The stronger weather condition in SantaAna2 led to lower APS counts, lower $PM_{2.5}$ mass concentrations, and lower carbonaceous fractions comparing to SantaAna1. Consistent with the trajectory plots, ATOFMS measurements observed great fractions of dust particles during Santa Ana periods due to the desert influence. **Figure 30** and **Figure 32** show that carbonaceous (~50% of total counts), biomass, amine, and dust types were the major components of submicron particles; whereas supermicron particles were composed of ~75% dust, ~15% biomass and ~5% aged sea salt with very low (<5%) carbonaceous fractions in these episodes. The particle type fractions in **Figure 30c** do not appear as smooth during SantaAna2 as in other days, due to the low particle counts detected in this period. Substantial fractions of amine and biomass particles were observed; however, the increases in their relative fractions were most likely caused by much lower overall particle counts, and the actual counts for the two types were in fact lower than those during other episodes. These types are more likely emitted from local sources due to the absence of an LA influence. Vanadium-rich particle fractions were extremely low since they are mostly generated from ship emissions from the west, and the Santa Ana air masses originated from the eastern desert.

High RH and low temperature aided aerosol accumulation during Buildup1. The representative HYSPLIT trajectories show that the air mass was fairly stagnant during this episode resulting in a gradual increase of $PM_{2.5}$ mass concentrations with daily maxima occurring in the daytime. APS measurements showed consistent results with the BAM and also peaked during the day as shown in **Figure 27**. Carbonaceous particles not only dominated the submicron range, but also the supermicron range. Among the major particle types, aged OC1 spiked more at night due the effect of RH and ECOC-$SO_4$ peaked more during the day, which is consistent with SOAR-I patterns. The west-originating air mass and the accumulation aided in the formation and buildup of $NH_4NO_3$, therefore substantial fraction of $NH_4NO_3$-rich particles were observed in the supermicron range peaking around 1.5 μm.

HighMass was a 27-hour episode spanning overnight from November 6 15:00 to November 7 18:00 when the highest concentrations of the Fall study were observed. The stagnant meteorological conditions featuring 10-hours of low wind speeds led to the highest $PM_{2.5}$ particle number and mass concentrations (>500 particles/$cm^3$, 106 μg/$m^3$) on November 7 0:00 – 6:00. Once again, carbonaceous particles which were associated with nitrate, sulfate and ammonium accounted for more than 85% below 1.0 μm, and also

dominated the supermicron range. $NH_4NO_3$-rich particles were also observed in the HighMass period. Besides the large particles fraction in submicron range, $NH_4NO_3$-rich particles even spread into supermicron range due to the very stagnant condition. These particles only occurred during high ammonium nitrate episodes. Ambient mass concentrations started to decrease midday on November 7 as the wind speed rose.

The highest mass concentrations in Buildup2 occurred around noon on November 8. Air masses during this episode traveled north along the coast of Baja from Mexico to San Diego, eventually moved inland to Riverside. Thus, ATOFMS measurements show carbonaceous particles in the submicron mode, as well as an increased fraction of aged sea salt in the supermicron range due to a marine influence. No $NH_4NO_3$-rich particles were observed during this episode because the air mass did not pass over the Chino dairy area. The Scavenging episode featured very low particle number and mass concentrations due to precipitation events on November 9 and 10. Air mass back trajectories and major particle fractions are similar to those in Buildup2, however, aged sea salt dominate the supermicron range with low carbonaceous fractions. Finally, Buildup3 was a particle buildup period. Aerosol mass concentrations gradually increased on November 11 and 12 and displayed diurnal variations between November 13 and November 15 showing maxima at night. The air mass originated from the west and thus similar particle types were observed compared to Buildup1, with substantial $NH_4NO_3$-rich particles.

The only SOAR-II particle type that showed distinct diurnal variations was the $NH_4NO_3$-rich type. Four distinct $NH_4NO_3$-rich particle spikes appeared in both size ranges around November 6 12:00, November 7 15:00, November 13 18:00, and November 14 18:00, along with minor spikes shown in **Figure 30 c-d**. Most peaks occurred slightly later between 15:00-17:00 comparing to SOAR-I $NH_4NO_3$-rich type. Although SOAR-I $NH_4NO_3$-rich type peaked around 11:00 (PST), the actual local time corresponded to 12:00. The time delay between summer and fall $NH_4NO_3$-rich peaks is likely caused by the longer time required to form nitrate due to weaker solar radiation in the fall. The filter analysis by Hughes et al. showed that ammonium and nitrate fractions peak between 14:00 and 18:00 over October 31-November 1 in 1997, similar to the ATOFMS measurements in SOAR-II (150). Again, the $NH_4NO_3$ particles were formed as the nitrate particles crossed the upwind Chino area. Additionally, each $NH_4NO_3$-rich peak was followed by a high PM mass concentration spike; thus high ambient $NH_4NO_3$ levels could be one of the factors triggering high ambient mass concentrations. Similar behavior was observed by Turkiwicz et al. where $NH_4NO_3$ drove the $PM_{2.5}$ exceedances in San Joaquin Valley (172). Similar to SOAR-I, the temporal variations of the BAM measurements tracked carbonaceous particle number fractions, especially in the supermicron range, indicating that carbonaceous particles with nitrate, sulfate and ammonium are the major components in mass concentrations.

### *e. SOAR-I and SOAR-II Comparison*

Although similar ATOFMS particle types were observed in both SOAR-I and SOAR-II, temporal variations and particle fractions of major types were different in summer and fall. In general, the submicron size range was dominated by carbonaceous particles and the major particle types in supermicron range were aged sea salt, dust and carbonaceous, except during the Santa Ana periods when dust dominated. The top OC

and EC types are very similar in both summer and fall, and no new major particle type was observed in either season.

**Figure 30 e-f** shows the raw particle size distributions measured by ATOFMS during SOAR-I and SOAR-II with a resolution of 0.10 μm. Despite the size-dependant transmission efficiency (173), the SOAR-I particle size distribution peaked around 1.6 μm with more supermicron particles detected than submicron particles; whereas the size distribution in SOAR-II peaked around 0.5 μm, dominated by submicron particles. The differences in size distributions are indicative of various degrees of aerosol aging. SOAR-I particles were highly transformed through photochemical reactions and other reaction pathways. Particles grew in size during aging, leading to high supermicron particle counts. SOAR-II particles were less aged thus their original sizes were not altered as much through processing. The decrease in solar radiation during the fall is one reason for the reduction in aerosol aging. It is also evident that higher fractions of aged OC (aged OC1+aged OC-$SO_4$) were observed in SOAR-I than SOAR-II, further indicating that SOAR-I aerosols were more aged than SOAR-II aerosols.

The ternary plots of SOAR-I and SOAR-II representative submicron aged OC-$SO_4$ particles (~300 particles evenly distributed over the study period) are included in **Figure 33**. These plots showed the relative amount of nitrate, sulfate and ammonium on every single particle. A particle mostly containing nitrate (m/z -62) would appear at the lower left vertex; a particle mostly containing sulfate (m/z -97) would appear at the lower right vertex; a particle mostly containing ammonium (m/z 18) would appear at the top vertex. SOAR-I aged OC-$SO_4$ particles evenly distributed between nitrate and sulfate

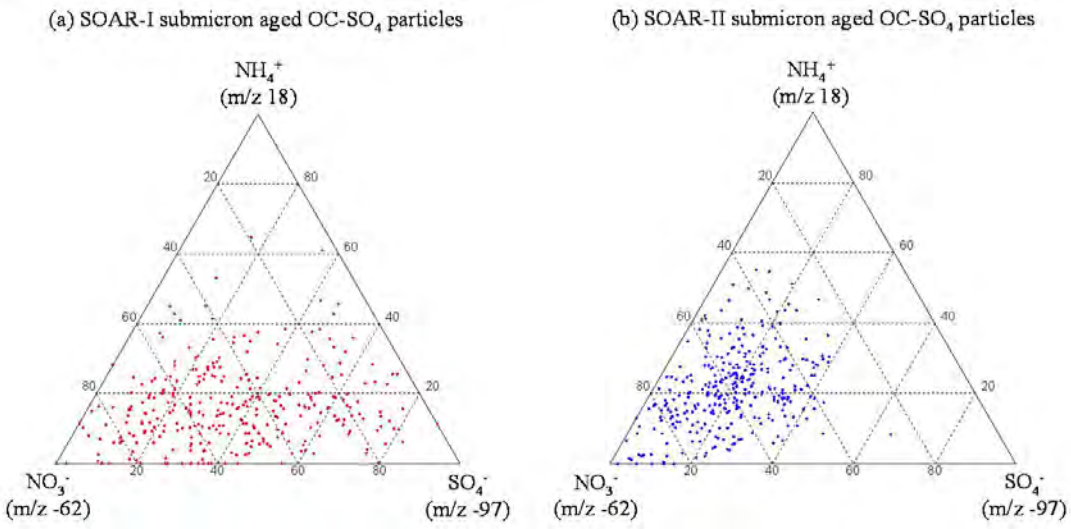


Figure 33: Ternary plots of SOAR-I and SOAR-II submicron aged OC1 particles. In each plot, a particle mostly containing nitrate would appear at the lower left vertex, a particle mostly containing sulfate would appear at the lower right vertex, a particle mostly containing ammonium would appear at the top vertex.

vertex, showing that the amount of nitrate and sulfate were comparable on these particles. In contrast, SOAR-II aged OC-$SO_4$ particles mostly distributed near lower left corner, illustrating that SOAR-II particles contained more nitrate than sulfate. Suring SOAR-I, ammonium and nitrate were baked off particle phase due to the high ambient temperature, thus there comparable amount of sulfate and nitrate in the particle phase; whereas the lower temperature in SOAR-II favors the condensation of ammonium and nitrate onto the particle phase, thus more nitrate was observed than sulfate, and ATOFMS detected the $NH_4NO_3$-rich particles during the Buildup and HighMass periods. Secondary processing of ambient aerosols will be addressed in detail in future papers.

The mass concentrations of major particle types during SOAR-I and SOAR-II are shown in **Figure 34**. The mass concentrations were obtained by scaling ATOFMS measurements with APS measurements, and the detail of scaling is discussed in Chapter 5. The sum of the major particle type mass concentrations has similar trend as the $PM_{2.5}$ mass concentrations for both SOAR-I and SOAR-II. While the major particle chemical compositions were similar in the summer and fall, these seasons were dominated by different aerosol formation mechanisms and showed different temporal trends in major particle type mass concentrations. The LA influence was observed in the current work, and carbonaceous particles associated with secondary species were found to be the major $PM_{2.5}$ component by mass in Riverside. The detailed analysis of SOAR-I and SOAR-II ATOFMS measurements in this paper provide further understanding on ambient aerosol composition, chemical associations on a single particle level, and provide important information on ambient aerosol aging process in the LA basin and similar areas with strong vehicular emission influence and intense sunlight.

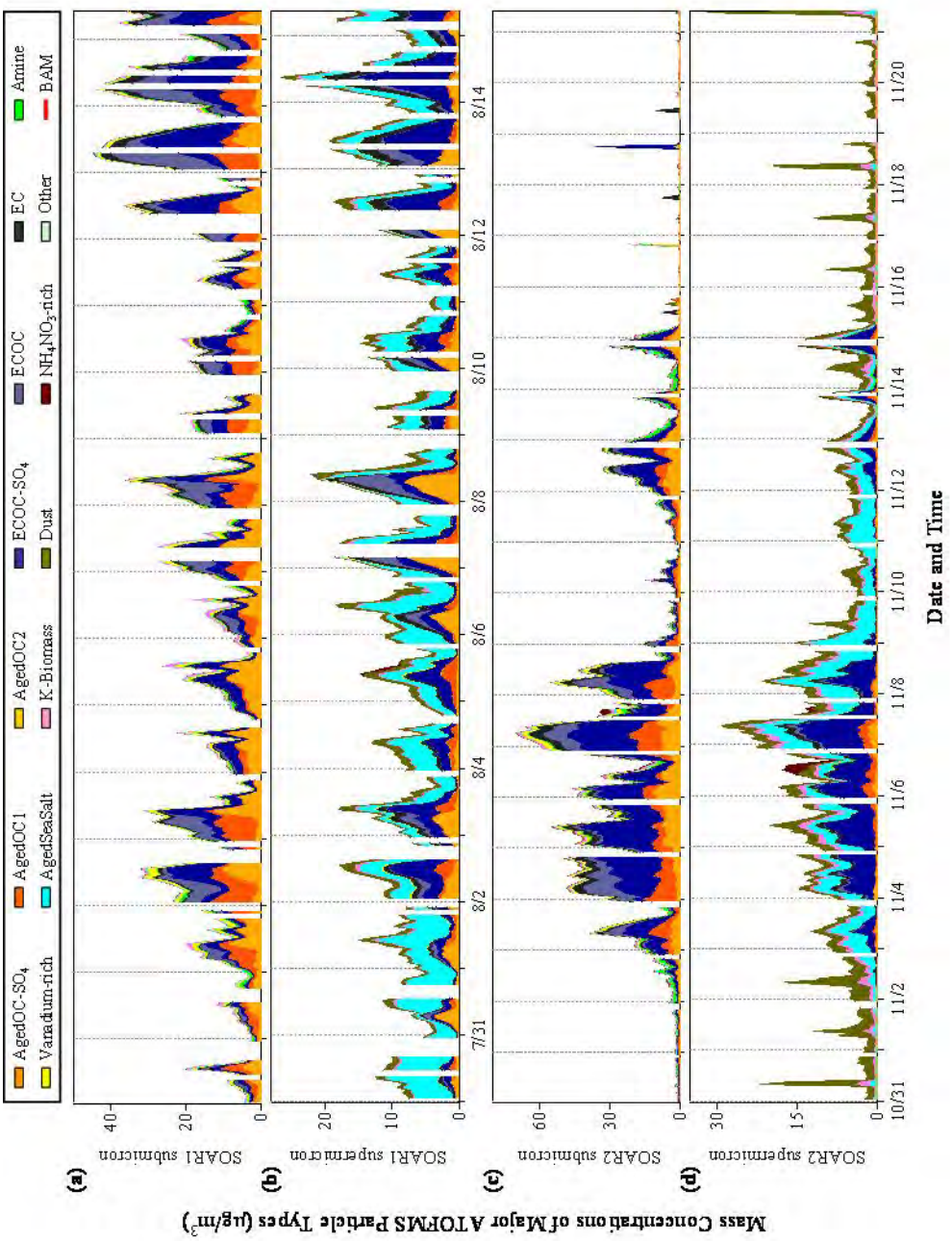


Figure 34: Temporal variation of the mass concentration of major ATOFMS particle types. Mass concentrations are obtained by scaling ATOFMS measurements with APS measurements.

## iv. Acknowledgements

This research was supported by the California Air Resources Board (CARB) through Grant #04-336. The authors gratefully acknowledge the entire Prather group for their help throughout these studies, in particular, Ryan Sullivan, Kerri Denkenberger, and Dr. Hiroshi Furutani. We thank Professor Paul Ziemann and Professor Jose-Luis Jimenez for organizing this study and providing lab space to accommodate research instruments and Dr. Kenneth Docherty for coordination. We also thank Megan McKay and the

Goldstein research group at the University of California, Berkeley for providing meteorology data and CARB for providing BAM measurements. Finally, we acknowledge the NOAA Air Resources Laboratory (ARL) for providing the HYSPLIT transport and dispersion model used in this publication.

## 5. Seasonal Volatility Dependence of Ambient Particle Phase Amines

### i. Introduction

Atmospheric aerosol particles play a major role in impacting global climate, regional air pollution, and human health (174). Organic carbon (OC) can comprise up to 50% of the total fine aerosol mass at continental midlatitudes (174), and in some areas, such as the eastern Los Angeles (LA) basin, secondary organic aerosol (SOA) can also represent a significant fraction of the total organic aerosol mass (175). During atmospheric transport, particles undergo heterogeneous reactions with trace gases as well as gas-to-particle partitioning of semivolatile species, causing changes in particle size, structure, and chemical composition (174). Understanding the partitioning of organic carbon species between the gas and particle phases remains one of the major challenges in predicting aerosol chemistry in regional and global atmospheric chemical transport models (174). In particular, semivolatile organic nitrogen species, suggested to be a significant portion of the OC aerosol mass (176), are not well understood with regard to gas-particle partitioning. The atmospheric lifetimes of organic nitrogen species are dependent on the distributions between the gas and particle phases for the different species, which in turn determine their role in the global nitrogen cycle (177). One class of semivolatile organic nitrogen species, alkylamines, is emitted from many of the same sources as ammonia, an abundant atmospheric species which has been extensively studied. In particular, a major source of nitrogen species is animal husbandry, where amine concentrations represent up to 23% of those measured for ammonia (178,179). Amines have also been identified in urban and rural atmospheres in both the gas and particle phases, including within fog and rainwater (39,180,181). Recent measurements show fine particulate amine concentrations of 0.5-6 $\mu g/m^3$ (up to ~20% of the organic matter mass) during winter inversions in Utah (182).

Amines can undergo oxidation by OH, $O_3$, and/or $NO_3$ to form amides, nitramines, and imines, which can also partition to the particle phase (176,178,182). Once in the particle phase, amines can undergo further reactions to form high-molecular-weight compounds (176,182,183). In addition, gas-phase aliphatic amines, which are stronger bases than ammonia, compete to form salts through the following reactions with nitric acid ($HNO_3$) and sulfuric acid ($H_2SO_4$), leading to secondary aerosol formation (39,176).

$$NR_{3(g)} + HNO_{3(g)} \underset{\leftarrow}{\overset{\rightarrow}{}} HNR_3NO_{3(s)} \xrightarrow{T,RH,pH} HNR_3^+{}_{(aq)} + NO_3^-{}_{(aq)} \qquad (1)$$

$$2NR_{3(g)} + H_2SO_{4(g)} \underset{\leftarrow}{\overset{\rightarrow}{}} (HNR_3)_2SO_{4(s)} \xrightarrow{T,RH,pH} 2(HNR_3)^+{}_{(aq)} + SO_4^{2-}{}_{(aq)} \qquad (2)$$

Particle phase amines associated with sulfate and nitrate have been observed in both chamber (39,176) and field measurements (184). Notably, chamber experiments by Murphy et al. (176) demonstrated the stability of nitrate salts of trimethylamine and triethylamine in the particle phase, even at very low relative humidity (RH <10%). However, one hypothesis suggests that if relative humidity is high and water is present in the particles, the aminium salts will dissolve into their ionic forms, shifting the equilibrium of the gas-phase amines toward the particle phase (39), potentially yielding

greater particle phase amine mass than predicted by Murphy et al. (176). As such, the gas/particle partitioning model described by Pankow (185) assumes that amines, as strong bases, are only volatile when present in their neutral, non-salt forms. In addition, due to low vapor pressures, organic acids may also form salts with amines, as suggested by measurements of atmospheric nanoparticles (186) and thermodynamic calculations (187).

To study the volatility behavior of alkylamine species within aged ambient particles in Riverside, CA, an automated thermodenuder (TD) was coupled to a real-time, single-particle mass spectrometer to characterize the chemical composition of the remaining individual submicrometer ambient organic carbon-containing particles following heating. Using the TD, semivolatile species were vaporized at different temperatures, leaving behind particle cores that were compared to the unheated particle chemistry (188). Herein, the partitioning of amines associated with nitrate and sulfate as a function of temperature and particle acidity are examined for individual organic carbon particles internally mixed with nitrate, sulfate, and ammonium.

## ii. Experimental

### *a. Ambient Measurements*

Measurements of individual submicrometer ambient aerosol particles by aerosol time-of-flight mass spectrometry (ATOFMS) were conducted during the Study of Organic Aerosols in Riverside (SOAR, August and November 2005, http://cires.colorado.edu/jimenez-group/Field/Riverside05/). The sampling site at the University of California, Riverside campus was located about ~60 miles east of Los Angeles, CA. Ambient temperature and atmospheric water content measurements were made using a shielded Vaisala HMP 45AC temperature and RH probe. The ATOFMS results presented here focus on TD-conditioned aerosol chemistry measurements made on August 12, 2005 (SOAR-1) and November 2-13, 2005 (SOAR-2). August 12th was the only summer day during which TD-conditioned aerosol chemistry was measured; however, it was typical of the particle chemistries and sources observed during SOAR-1 (189). From July 30 to August 15, 2005, a strong diurnal pattern was observed for ozone, particle mass concentrations, and ambient meteorological conditions, as shown in Table 6 (189). On August 12th, the wind predominantly (~80% frequency) came from the west, crossing the LA basin en route to Riverside; during SOAR-2, westerly winds were observed ~50% of the sampling time, with winds from the southwest contributing ~45% of the time (189).

An automated valve-controlled TD system (190) was utilized in series with the ATOFMS. In the fall only, a nafion dryer was used to dry the particles before the TD. In addition to water, the drying process may have removed some of the neutral amines and ammonium nitrate from the particle phase. However, the non-volatile aminium salts would not have been removed. Thus, the drying during the fall is not expected to impact the aminium salt mass present at 230°C. With continuous aerosol flow through the TD (heated) and bypass line (unheated), the particles sampled by the ATOFMS switched between heated and unheated ambient aerosol every 10 min. The heated portion of the TD stepped through 8 temperature steps: 171, 230, 201, 171, 142, 113, 83, and 54 °C;

temperatures noted here refer to actual temperatures, rather than set-points (190). Since each portion of the schedule was maintained for 10 min, one full cycle took 160 min before repeating. An activated carbon diffusion denuder

| | SOAR-1 | |
|---|---|---|
| | **July 30 - Aug. 15, 2005** | **Aug. 12, 2005** |
| **Ozone (ppb)** | 34.9 (33.3) | 26.2 (26.0) |
| **Relative humidity (%)** | 56.8 (19.2) | 68.6 (18.5) |
| **Ambient temperature (°C)** | 25.7 (5.3) | 22.9 (4.6) |
| **Wind speed (m/s)** | 0.9 (0.8) | 0.9 (0.8) |
| **Wind direction (deg.)** | 224 (66) | 223 (62) |
| **$PM_{2.5}$ mass concentrations ($\mu m/m^3$)** | 33 (13) | 37 (18) |
| **$PM_{1.0}$ agedOC-nitrate-sulfate particle type mass concentrations ($\mu m/m^3$)** | 6.1 (3.3) | 7.0 (3.4) |

Table 6: Averages and standard deviations of ozone, ambient meteorological conditions, $PM_{2.5}$ mass concentrations (measured at the California Air Resources Board Rubidoux site), and $PM_{1.0}$ agedOC-nitrate-sulfate particle type mass concentrations for July 30 – August 15, 2005 compared to August 12, 2005 (189).

prevented volatilized species from condensing back onto the particles. With a flow rate of 0.6 lpm, the residence time of the aerosol in the heating portion of the TD was approximately 9 s.

The ground-based prototype of the aircraft (A)-ATOFMS, described in detail in Chapter 2, was utilized to measure the vacuum aerodynamic diameter ($d_{va}$) and dual-polarity mass spectra of individual particles from ~70-1000 nm in real time. Particles were desorbed and ionized using 266 nm radiation from a Q-switched Nd:YAG laser; thus, one or two photon ionization would provide 4.7 or 9.4 eV, readily ionizing the alkylamines with lower ionization potentials (~7.5 eV) compared to most organic species (~8-12 eV) (NIOSH, 191). The use of lower laser powers can lead to decreased ion fragmentation (192); however, while a slightly lower average laser power was utilized in the fall (~0.6 mJ) compared to the summer (~0.95 mJ), the amine signature was not found to be impacted. Polystyrene latex spheres (PSLs) of known physical diameter from 95-1400 nm were used for the particle size calibration. Dual-polarity mass spectra were collected with the ATOFMS for 318,431 ambient particles on August 12, 2005 and 1,390,199 ambient particles from November 2-13, 2005. Data collection times were adjusted for delays in transport lines between the TD and ATOFMS, and data collected up to 20 seconds after the TD valve switch were eliminated to reduce error caused by possible aerosol mixing. Taking this delay into account, the mass spectra from 141,757 unheated and 119,888 heated particles were analyzed for August 12, and 717,705 unheated and 462,982 heated particles were analyzed for November 2-13.

For detailed analysis, single-particle mass spectra were imported into YAADA (www.yaada.org), a software toolkit for Matlab (The MathWorks, Inc.), for analysis. An adaptive resonance theory-based clustering method (ART-2a) (193) was then used to group single-particle mass spectra with a vigilance factor of 0.80, learning rate of 0.05, 20 iterations, and regrouping with a vigilance factor of 0.85. ART-2a classifies particles into separate clusters based on the presence and intensity of ion peaks in individual single-particle mass spectra. Peak identifications within this paper correspond to the most probable ions for a given *m/z* ratio. The ART-2a clusters resulting from the analysis of single SOAR unheated and heated particles (100-1000 nm) were classified into thirteen general particle types: aged organic carbon (mixed with ammonium, sulfate, and

nitrate, herein referred to as the aged OC particle type), aromatic, amine, ammonium-rich, elemental carbon-organic carbon (ECOC), inorganic-ECOC, elemental carbon (EC), vanadium, biomass, aged sea salt, dust, metals, and nitrate-sulfate particles with no positive ions (NoPos). The size-resolved chemistry of the unheated particles is shown in **Figure 35** for SOAR-1 (summer) and SOAR-2 (fall). It should be noted that the vast majority of unheated particles show evidence of organic carbon markers, nitrate, and sulfate due to aging during transport across the LA basin to Riverside (158). Detailed descriptions of mass spectral, size, and temporal patterns of the majority of the unheated SOAR ATOFMS particle types are described elsewhere (189). Herein, we focus on the aged OC (nitrate-sulfate) particle type, described below.

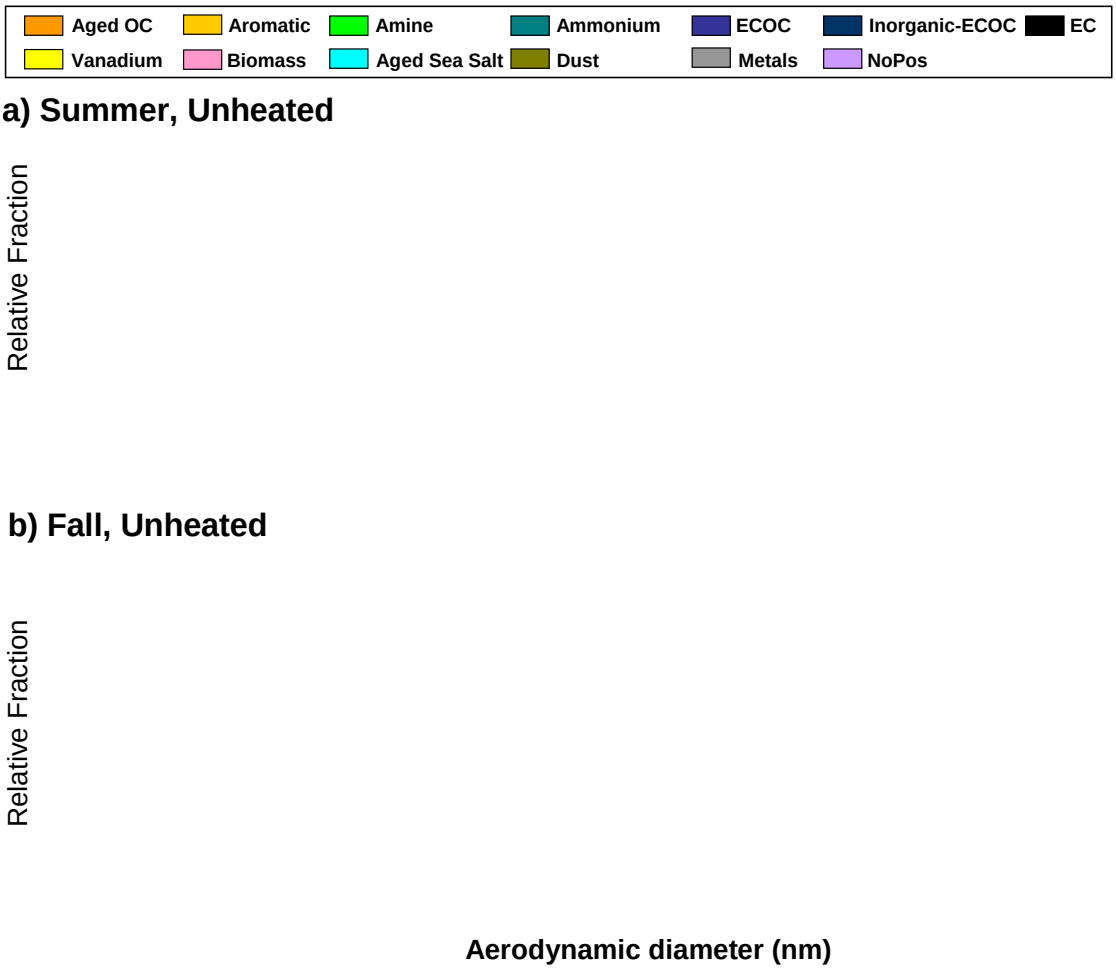


Figure 35: Size-resolved chemical composition of unheated particles during (a) SOAR-1 (summer) and (b) SOAR-2 (fall). Size resolution is 10 nm and 50 nm for the ranges of 100-350 nm and 350-1000 nm, respectively. The majority of the particles greater than ~150 nm show evidence of internally mixed organic carbon, ammonium, nitrate, and sulfate.

### *b. Amine Mass Calibration*

To determine the mass of amines present in the submicrometer aged OC (nitrate-sulfate) particle type during SOAR, triethylamine vapor was coated onto PSLs, which serve as proxies for the SOAR OC particle matrix. A schematic of the experimental

setup is shown in **Figure 36**. An aqueous (milli-Q water) solution of 270 nm PSLs (Invitrogen Corp.) was atomized using filtered ambient air at a flow rate of 3.0 $L \cdot min^{-1}$. The PSLs were dried using two silica gel diffusion dryers and the flow subsequently split between exhaust (1.0 $L \cdot min^{-1}$) and a differential mobility analyzer (DMA, TSI, Inc., Model 3081, sample flow = 2.0 $L \cdot min^{-1}$, sheath flow = 5.0 $L \cdot min^{-1}$) to narrow the particle distribution. The size-selected PSLs were passed through a dilution chamber where supplemental filtered ambient air was added (0.2 $L \cdot min^{-1}$), followed by introduction into a glass mixing chamber (~ 20 L, residence time ~10 min). To initiate coating, gas phase precursors were introduced by placing liquid reservoirs directly within the reaction chamber; the headspace over these reservoirs acted as the vapor source. In the initial experiment, aiming to condense amine salts onto the PSL seed, two flasks each containing ~2mL of either TEA (Acros Organics, 99+%) or nitric acid (Sigma-Aldrich, 99.999+%) were quickly (<1 min) placed directly into the chamber. During this trial, extensive homogeneous nucleation was observed between TEA and nitric acid, overwhelming the PSL seeds (results not shown). To eliminate new particle formation, and partition TEA exclusively to PSLs, a second experiment was performed in which TEA only was coated onto PSLs. The chamber output flowed through two inline activated carbon denuders spiked with sodium carbonate and boric acid, respectively, to remove any gaseous reactants prior to parallel analysis by a scanning mobility particle

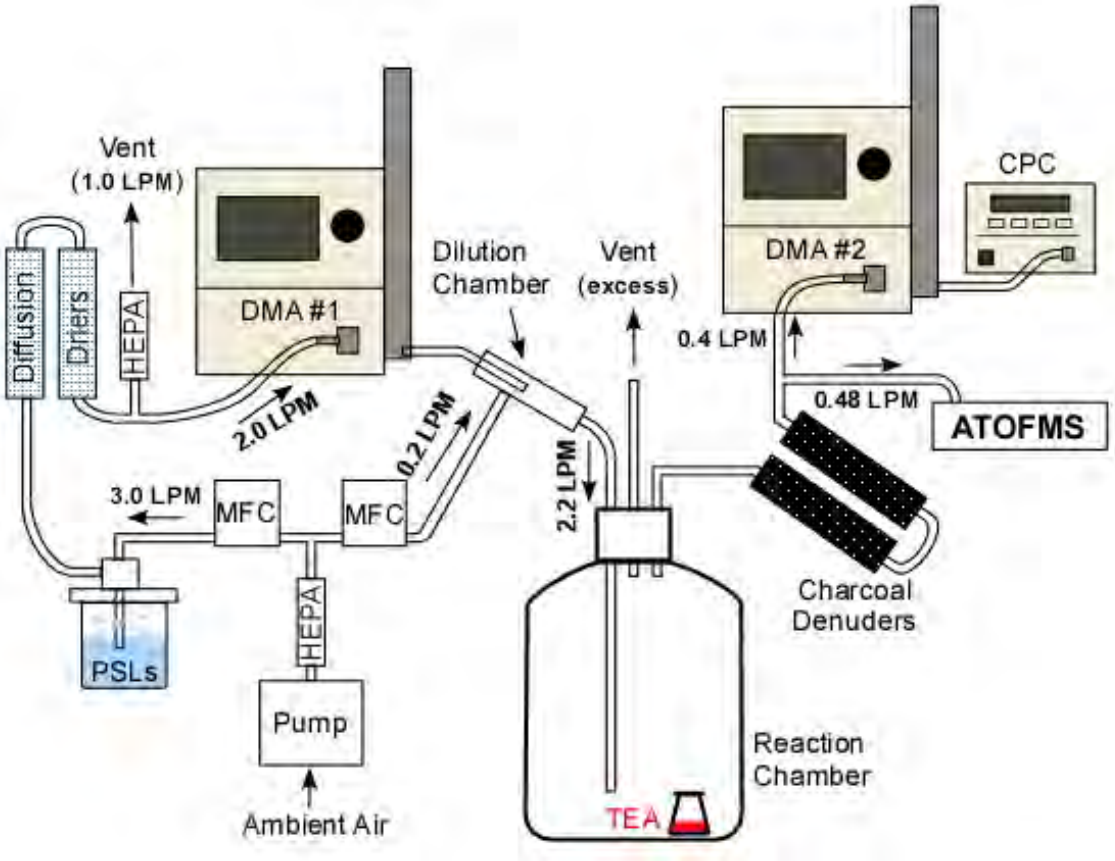


Figure 36: Amine mass calibration experimental set-up (MFC = mass flow controller; TEA = triethylamine; DMA = differential mobility analyzer; CPC = condensation particle counter; ATOFMS = aerosol time-of-flight mass spectrometer).

sizer (SMPS, TSI, Inc., DMA model 3081 – 0.4/4.0 LPM; CPC Model 3010) to monitor the particle size distribution and A-ATOFMS to obtain the single particle mass spectra and vacuum aerodynamic diameter ($D_{va}$). Background SMPS scans were obtained prior to addition of PSLs to confirm that the system was free of particle contamination; SMPS scans of uncoated PSLs were made to ensure a monodisperse seed aerosol distribution. Representative SMPS and ATOFMS size distributions of the uncoated and TEA-coated PSLs are shown in **Figure 37**.

The single particle mass spectra for uncoated and TEA-coated PSLs were imported into MatLab (The MathWorks, Inc.) for analysis following the methods described for treating the SOAR data. The dominant cluster of uncoated PSLs was identified as the PSL mass spectral signature (**Figure 38b**); only the TEA-coated aerosols exhibiting this specific PSL fingerprint (**Figure 38a**) were used in subsequent analysis to ensure a realistic comparison between coated and uncoated particles. In the TEA-coated PSLs, an ion peak representative of TEA is present at *m/z* 86($(C_2H_5)_2NCH_2^+$). It should be noted that the potential exists for differences in the UV absorption and ionization efficiency between protonated (salt bound) and neutral TEA, which would impact the calibration parameters of these two species; however these effects were not characterized in this study.

The polydisperse TEA coated particles were divided into 2 nm $D_{va}$ size bins from 274-302 nm; subsequently bins from 274-280 nm and 292-302 nm were merged due to low ATOFMS particle counts. The average $D_{va}$ and mass spectrum were calculated for each size bin as described below. A trend was observed whereby the *m/z* 86 peak area increased with decreasing $D_{va}$, as shown in **Figure 39**. However, the SMPS scans of

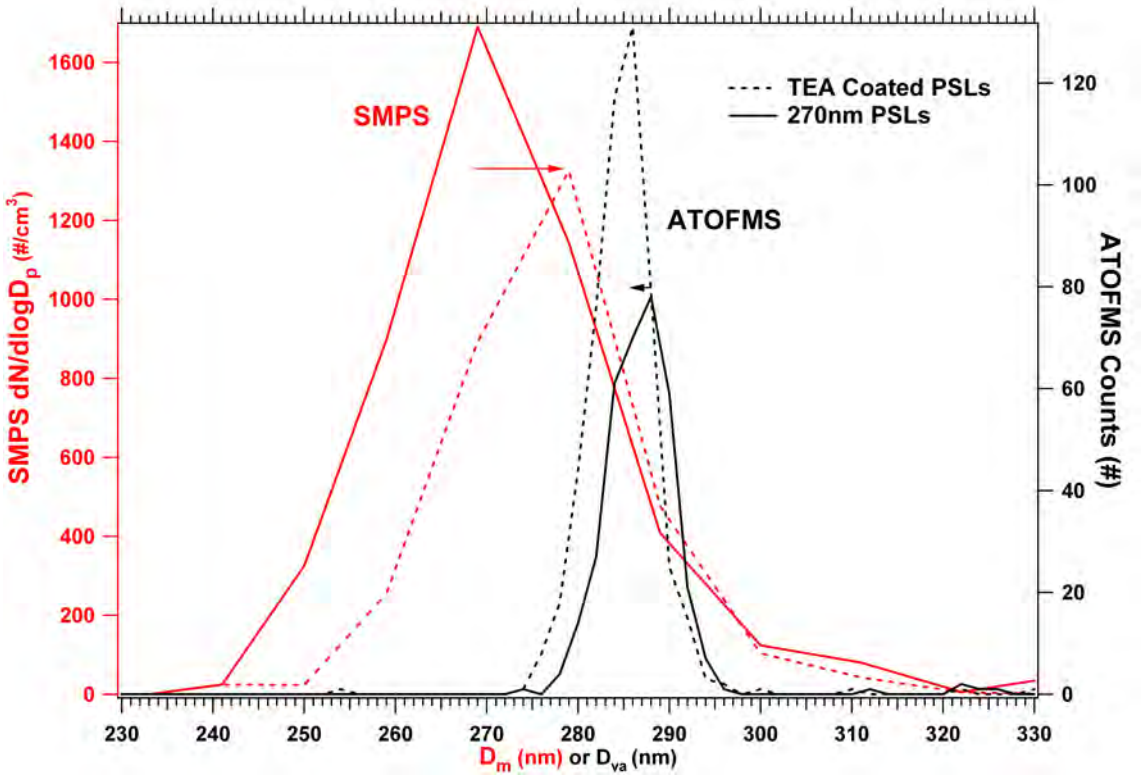


Figure 37: Size distributions of uncoated (solid) and TEA-coated (dashed) 270 nm PSLs. SMPS distributions of mobility diameter are shown in red; ATOFMS distributions of vacuum aerodynamic diameter are in black. The arrows indicate the shifts of the respective distributions.

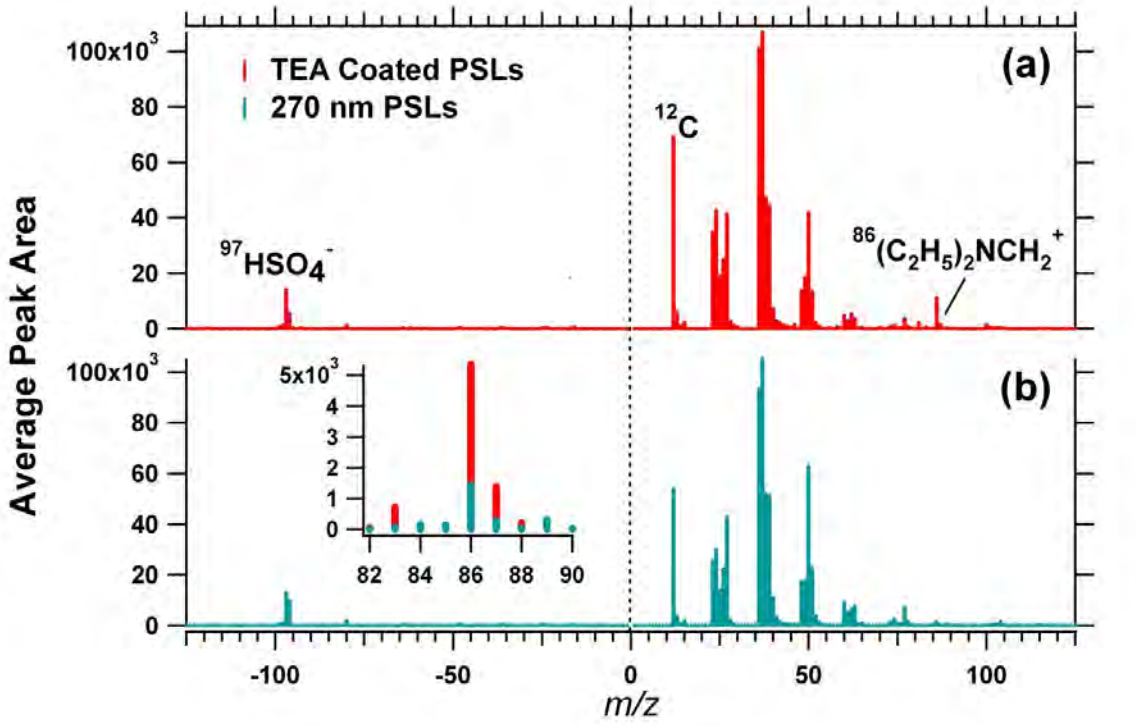


Figure 38: Average mass spectra of (a) PSLs coated with TEA and (b) uncoated 270 nm PSLs. The inset shows a comparison of the *m/z* 86 peak intensities.

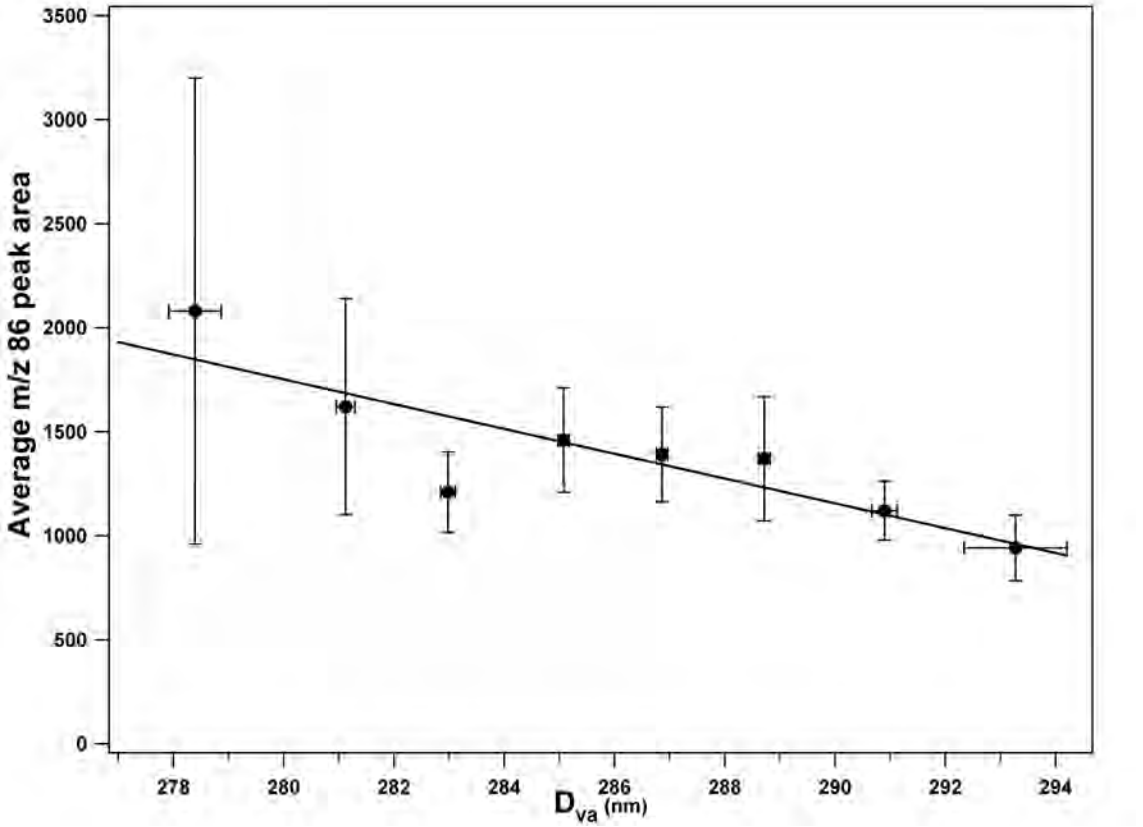


Figure 39: Absolute area of *m/z* 86 vs vacuum aerodynamic diameter for the TEA-coated PSLs.

TEA coated PSLs displayed a shift to larger mobility diameter $D_m$, consistent with an increase in particle volume upon coating. These observations and the following relationship between $D_{va}$ and $D_m$ (34):

$$\rho_p = \frac{D_{va}}{D_m}\rho_0 \qquad (3)$$

where $\rho_p$ is the particle density and $\rho_0$ is the standard density (1 g/cm$^3$), indicate a decrease in particle density upon addition of TEA, consistent with the relative material densities of PSLs (1.05 g/cm$^3$) and TEA (0.75 g/cm$^3$). The particle density of TEA coated aerosols is therefore given by:

$$\rho_p = \frac{\rho_{PSL}V_{PSL} + \rho_{TEA}V_{TEA}}{V_p} \qquad (4)$$

where $V_p$ is the coated particle volume, which can be obtained from $D_m$, as this measurement is not influenced by particle density and the partitioning of TEA is not expected to alter the particle morphology of the spherical seed PSLs. Rearranging Equation 4 and substituting for $\rho_p$ ultimately yields:

$$m_{TEA} = \rho_{TEA}V_{TEA} = \pi/6\,(D_m^2 \cdot D_{va} \cdot \rho_0 - D_{PSL}^3 \cdot \rho_{PSL}) \qquad (5)$$

where $m_{TEA}$ is the mass of TEA. The $D_m$ values corresponding to each $D_{va}$ bin were estimated by:

$$D_{m,equiv} = D_{va} - (\overline{D_{va}} - \overline{D_m}) - 2(D_{va} - \overline{D_{va}}) \qquad (6)$$

where $D_{va}$ represents the average vacuum aerodynamic diameter of a given size bin and $\overline{D_{va}}$ and $\overline{D_m}$ represent the mode diameters of the full ATOFMS and SMPS size distributions, respectively. The wide size bins (~10 nm) used in the SMPS scans precluded direct correlation to the 2nm $D_{va}$ used in the ATOFMS data. Substituting these estimated $D_m$ values into Equation 5 yields the average mass of TEA on individual particles within each size bin.

The corresponding peak area of the *m/z* 86 amine marker was then related to the calculated amine mass to generate a calibration curve (**Figure 40**). To account for detector sensitivity and voltage setting changes between 2005 and 2009, the total summed peak areas of the average mass spectra of uncoated 270 nm PSLs run on the A-ATOFMS during SOAR and this amine calibration experiment were compared, and the peak areas in this experiment were scaled to accommodate for any changes in overall mass spectral intensities. Finally, the calibration experiment data was fit using a linear regression forced through the origin and weighted by the standard deviation in *m/z* 86 peak area. The amine mass present in the aged OC particles in SOAR-1 and SOAR-2 was determined by inserting the average peak areas at each temperature into the calibration curve. All reported uncertainties represent the 95% confidence intervals. The errors associated with the derived ambient amine masses are primarily due to uncertainties in the amine calibration experiment; in general, the 95% confidence intervals associated with the average ambient *m/z* 86 peak area was less than ~6% of the value, with the exception of the low SOAR-2 areas at 201-230 ºC, where errors of 13-17% were observed.

The mass fraction of TEA was also calculated by ratioing the calculated TEA mass to the total particle mass, estimated from mean particle volume at each temperature

(calculated from the mean particle vacuum aerodynamic diameter) and the aged OC particle effective density determined during SOAR-2 (1.38 ± 0.06 g/cm$^3$)

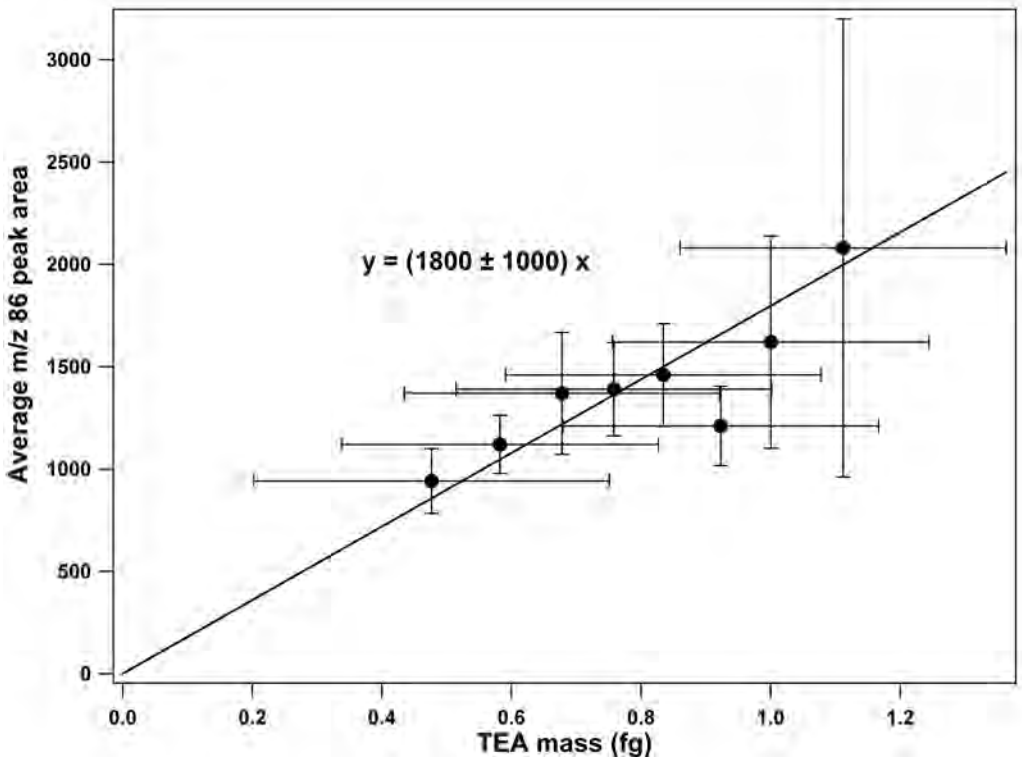


Figure 40: Absolute area of *m/z* 86 vs derived TEA mass for the TEA-coated PSLs.

(194). The mass fraction of amines present as aminium salts within the SOAR aged OC (nitrate-sulfate) particles was calculated based on the mass of TEA present at 230°C. While a combination of nitrate and sulfate salts were present in the aged OC particles, the masses of aminium salts were calculated for three extremes: 100% H-TEA-$NO_3$, 100% H-TEA-$HSO_4$, and 100% $(H\text{-}TEA)_2SO_4$. Given the number of moles of TEA calculated to be present in the 230ºC and the molecular weights of the various aminium salts, the masses of aminium salts were estimated and compared to the calculated total particle masses of the unheated and 230°C heated particles. In this way, the mass fractions were estimated for a range of possible aminium salt species. To reduce error, average fractions of amines remaining at each temperature are based on *m/z* 86 absolute peak areas, a reasonable assumption considering the observed proportionality of *m/z* 86 peak area to mass.

**iii. Results and Discussion**

Particles containing internally mixed organic carbon, ammonium, nitrate, and sulfate, herein referred to as the aged OC particle type, comprised ~60% by number of all particles across the entire size range from $d_{va}$ ~150-1000 nm during SOAR-1 (summer) and SOAR-2 (fall) (see **Figure 35**). As shown in **Figure 41**, the unheated aged OC particle type was characterized by carbonaceous marker ions at *m/z* 12($C^+$), 27($C_2H_3^+$/$CHN^+$), 36($C_3^+$), 37($C_3H^+$), and 43($CH_3CO^+$/$CHNO^+$) (195), as well as ammonium (*m/z* 18, $NH_4^+$), nitrate (*m/z* -62, $NO_3^-$, and -125, $H(NO_3)_2^-$), and sulfate (*m/z*

-97, $HSO_4^-$), all indicators of the aged nature of the Riverside aerosol (158). These particles were also characterized by marker ions for

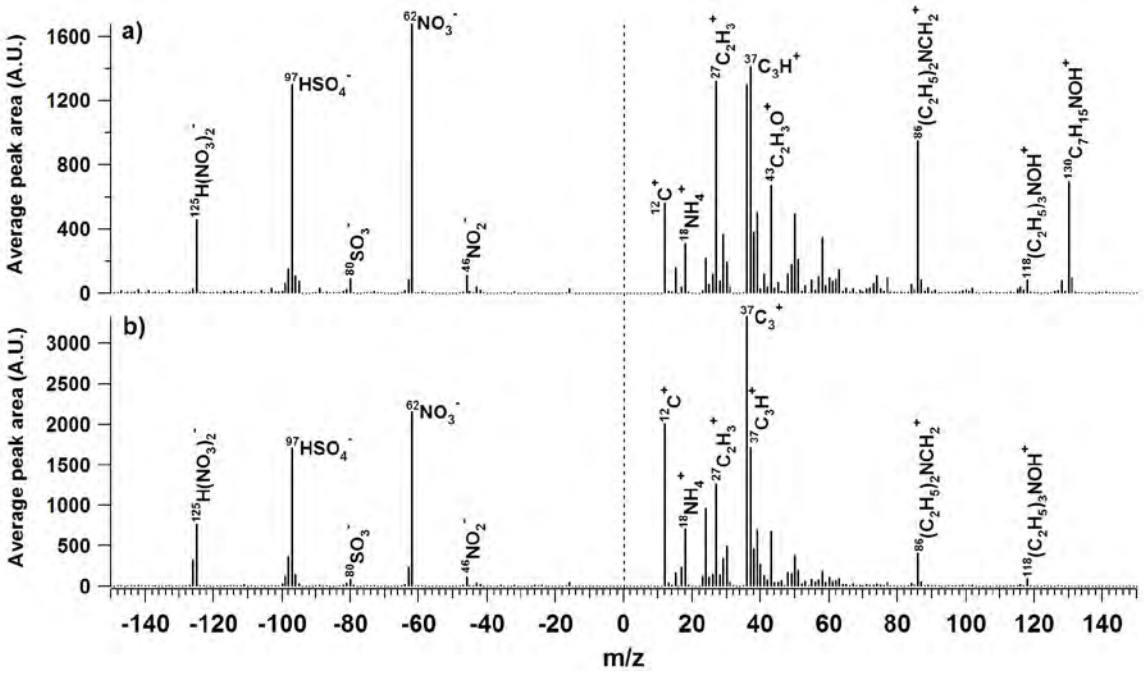


Figure 41: Average positive and negative mass spectra of the unheated aged OC (nitrate-sulfate) particles during (a) summer and (b) fall. Peak areas are reported in arbitrary units (A.U.).

alkylamines, *m/z* 86($(C_2H_5)_2NCH_2^+$) and 102($(C_2H_5)_3NH^+$), as well as oxidized amines, represented by *m/z* 118($(C_2H_5)_3NOH^+$) (39). Previously, Angelino et al. (39) found contributions of triethylamine and diethylamine to these marker ions; herein, *m/z* 86 is used as a general marker ion for the presence of amines. During SOAR-1, SOA was found to comprise ~45-90% of the total submicrometer organic mass depending on time of day (peak morning traffic vs. afternoon photochemical episodes) (196); previous studies have shown lower SOA contributions in the fall due to lower photochemical activity (54). In addition, oligomers (at *m/z* -200 to -400) were observed in approximately half of the unheated aged OC particles in both the summer and fall, although higher mass nonvolatile oligomers were detected in the summer (197).

In the summer, the presence of an intense peak at *m/z* 130, not observed in the fall, is proposed to be either an oxidized form of triethylamine or the $[MH]^+$ peak of N,N-diethylpropionamide ($C_7H_{15}NO$), which may be formed through the following dehydration reaction between propionic acid and diethylamine, observed as a small peak at *m/z* 58 $[MH]^+$ (39).

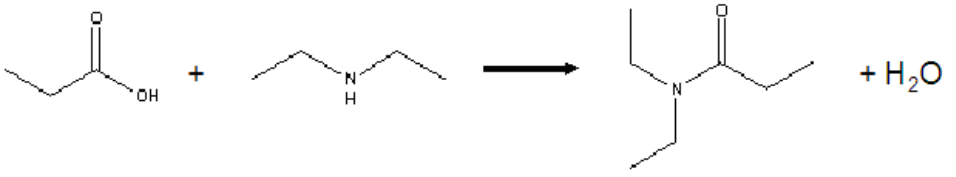


*(7)*

Propionic acid, the third most abundant gas phase organic acid in the LA basin, is formed primarily through secondary photochemical reactions and reaches its highest concentrations during summer smog episodes in the eastern LA basin (198,199).

Particle phase amide formation has been suggested to be significant in the polluted, ozone-rich troposphere (183). With a calculated vapor pressure of 0.444 Torr at 25°C, N,N-diethylpropionamide is significantly less volatile than it's parent compound diethylamine with a calculated vapor pressure of 218 Torr (25°C) (Advanced Chemistry Development, 200); likewise, *m/z* 130 does not vaporize from the particle phase with heating to 230°C. The peak at *m/z* 130 has been also been observed in chamber experiments conducted during July 2006, probing the gas-to-particle partitioning of TEA via homogeneous reaction with nitric acid (**Figure 42**), similar to the experiment completed by Angelino et al. (39). The experimental setup was similar to that described above for the amine coating experiments with the following key differences: (1) the atomizer and diffusion dryers were not used as a seed aerosol was not provided; (2) the flow rate of filtered ambient air into the chamber was 4.0 $L \cdot min^{-1}$, providing shorter residence time; (3) the chamber contained two flasks containing nitric acid and TEA. In previous chamber experiments by Angelino et al. (39), amine oxidation products were also observed due to gas-phase oxidants present in the filtered air utilized.

To probe the specific associations between amines, ammonium, nitrate, and sulfate within the SOAR aged OC particles, ternary plots of the relative distributions of the peak areas of ammonium (*m/z* 18), amines represented by *m/z* 86, nitrate (*m/z* -62), and sulfate (*m/z* -97) at different temperatures for individual aged OC particles are shown in **Figure 43**. The relative amounts and associations of either nitrate (a,c) or sulfate (b,d) with amines and ammonium are displayed for both seasons. A particle containing primarily amines relative to ammonium, nitrate, and sulfate would appear at the top vertex, primarily ammonium at the right vertex, and nitrate or sulfate would appear at the

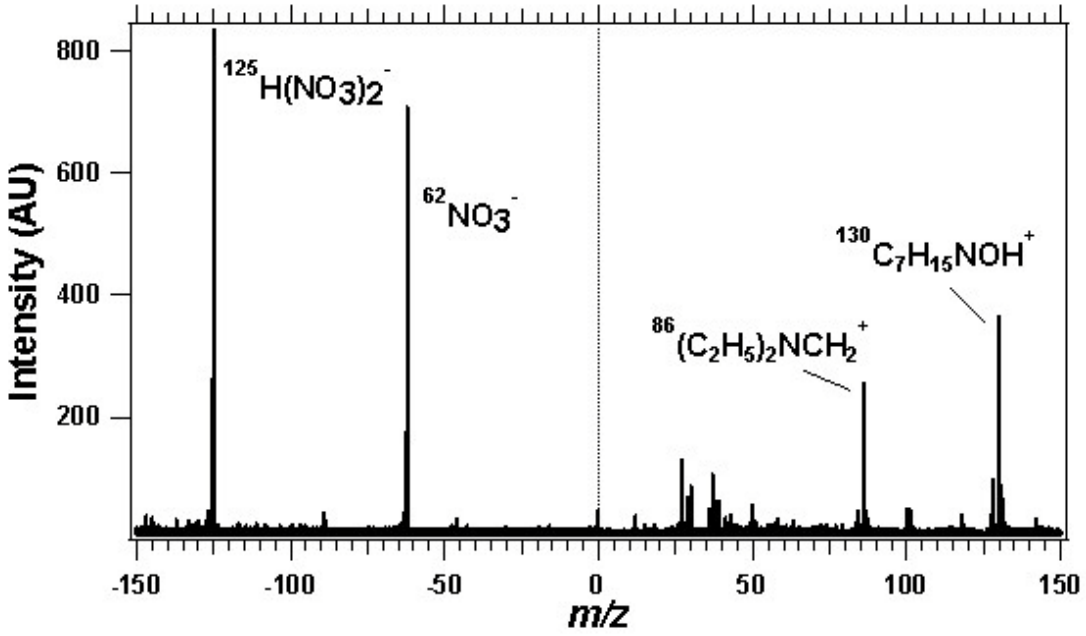


Figure 42: Positive and negative mass spectra of a single particle exhibiting *m/z* 130 measured during TEA-nitric acid chamber experiments.

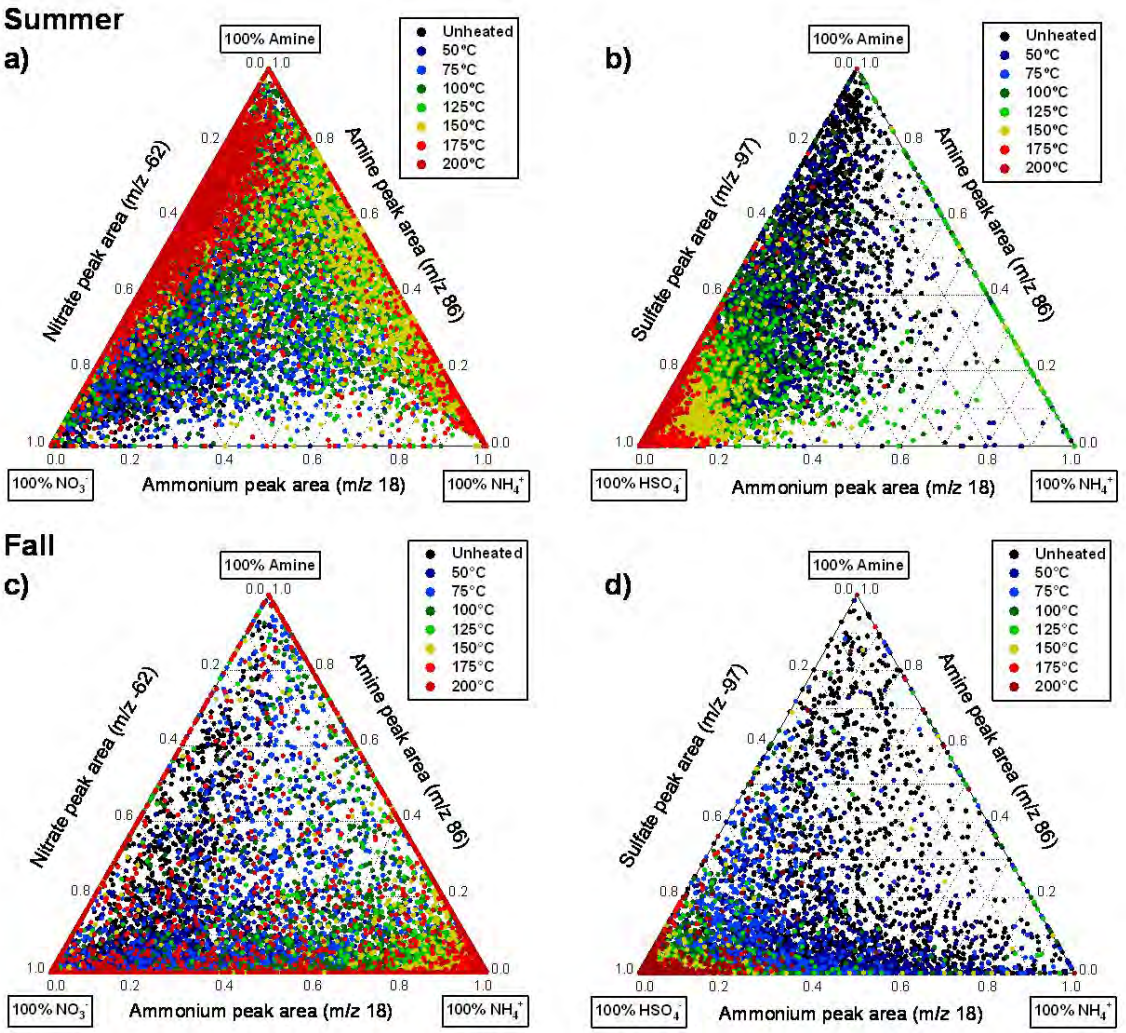


Figure 43: Summer (a,b) and fall (c,d) ternary plots show the relative distributions of peak areas of ammonium (*m/z* 18 ($NH_4^+$)), amines (*m/z* 86 ($(C_2H_5)_2NCH_2^+$)), nitrate (*m/z* -62 ($NO_3^-$)), and sulfate (*m/z* -97 ($HSO_4^-$)) for the unheated and heated (54-230°C) aged OC (nitrate-sulfate) particles. Random samples of ~2,000 single particles are plotted for each temperature.

left vertex. In the summer, the particles are distributed along the amine-nitrate and amine-sulfate axes, suggesting nitrate and sulfate are more strongly associated with amines compared to ammonium. This strong correlation between amines and nitrate and sulfate at 230 °C in the summer supports the presence of aminium nitrate and sulfate salts which are non-volatile, as predicted by Pankow (185). However, in the fall, the unheated particles are distributed primarily along the ammonium-nitrate and ammonium-sulfate axes, suggesting nitrate and sulfate are more strongly associated with ammonium compared to amines. The lack of aminium salts in the fall is because the particles were neutralized and hence the unbound amines were readily volatilized at temperatures below 113 °C, as discussed below. Ammonium and nitrate volatilized at temperatures less than 113 °C, consistent with previously reported volatilization temperature (~48-89 °C) (201). Thus, in the summer, aminium nitrate and aminium sulfate remained in the particles at 230 °C, compared to primarily ammonium sulfate in the fall.

To calculate the relative fraction of amines remaining at each TD temperature, the average absolute peak area of *m/z* 86($(C_2H_5)_2NCH_2^+$) at each temperature was divided by that observed for the unheated aged OC particles (**Figure 44a**). Next, to quantitatively assess the contribution of amines to particle mass, the average amine mass in the aged OC particle type (**Figure 44b**) was determined using a triethylamine mass/peak area calibration curve derived from the amine mass calibration experiment. Using the average vacuum aerodynamic diameter measured for the aged OC particle type at each TD temperature, the average mass fraction of amines per particle was calculated (**Figure 44**). For the SOAR unheated aged OC particles, approximately twice as much amine mass was present in the summer (0.5 ± 0.3 fg/particle; 1.7 ± 0.9%) compared to the fall

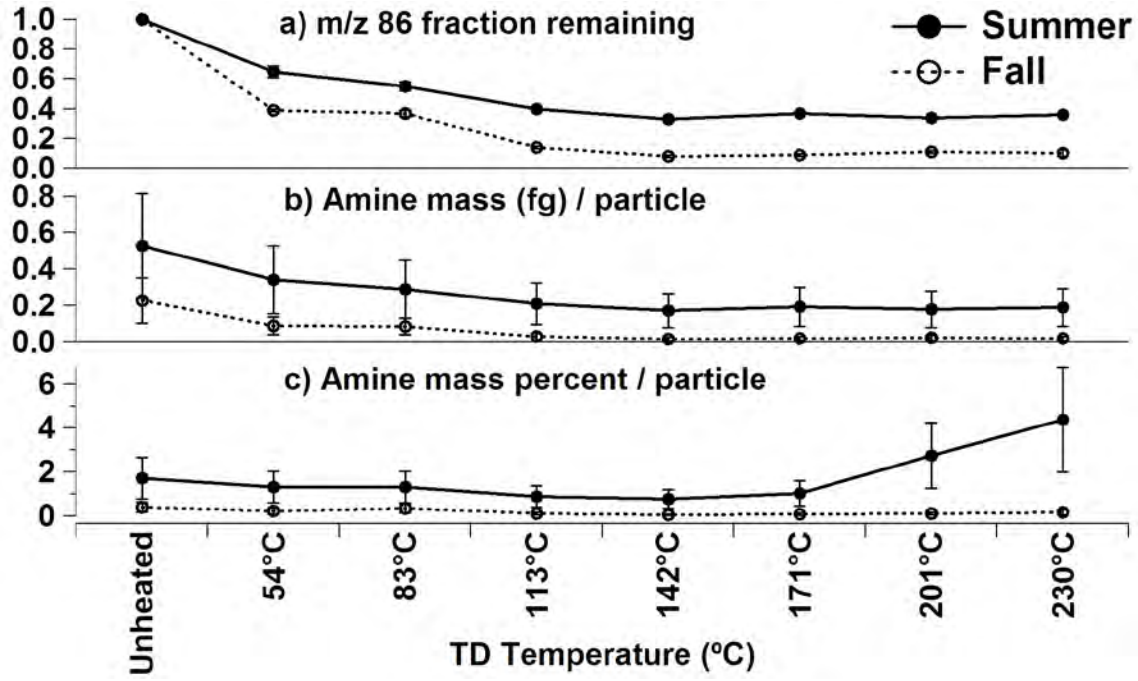


Figure 44: For aged OC (nitrate-sulfate) particles, the (a) fraction of *m/z* 86 peak area remaining over the range of thermodenuder temperatures from 54-230 °C is shown relative to the unheated particles (ambient temperature averages of 22.9 °C and 15.6 °C in the summer and fall, respectively). In addition, the (b) amine mass/particle and (c) amine mass percent/particle are shown for each temperature.

(0.2 ± 0.1 fg/particle; 0.4 ± 0.2%). During both the summer and fall, the amine mass/particle decreased with increasing temperature to 113 °C and then stabilized at ~0.2 ± 0.1 fg/particle and less than 0.1 fg/particle, respectively. These results are consistent with the vaporization of neutral diethylamine and triethylamine up to ~113 °C (boiling points of 57.3 ± 8.0 °C and 90.5 ± 8.0 °C, respectively (Advanced Chemistry Development, 202)). The amines remaining above 113 °C must be in the form of aminium salts. Consistent with the association of amines with nitrate and sulfate in the summer, 36 ± 1% of the amines present at ambient temperature remained in the aged OC particle type at 230 °C in the summer. However, in the fall, only 10 ± 2% of the amines remained at 230 °C, consistent with the decreased abundance of aminium salts due to high levels of ammonium in the particles, as discussed below. Similarly, in the summer,

a greater fraction (13 ± 1%) of nitrate remained at 230 °C compared to the fall (4 ± 1%) (**Figure 45**), consistent with more aminium nitrate salts present in the summer compared to the fall. However, as shown in **Figure 43**, a higher fraction of aminium salts was in the form of aminium sulfate, compared to aminium nitrate; this is likely due to the fact that sulfuric acid is a stronger acid than nitric acid (pKa -3.19 ± 0.15 vs. -1.4, respectively) (Advanced Chemistry Development, 202). At 230 °C, amines represented 4 ± 2% by mass/particle in the summer, compared to only 0.2 ± 0.1% by mass/particle in the fall. The increasing amine mass fraction above 171 °C in the summer was due to the volatilization of other species leaving behind primarily aminium salts and ammonium sulfate; whereas, in the fall, the amine mass fraction did not increase with temperature due to the minor contribution of aminium salts. Considering the potential nitrate, bisulfate, and sulfate salts of triethylamine, the aminium salt mass fraction at 230 °C in

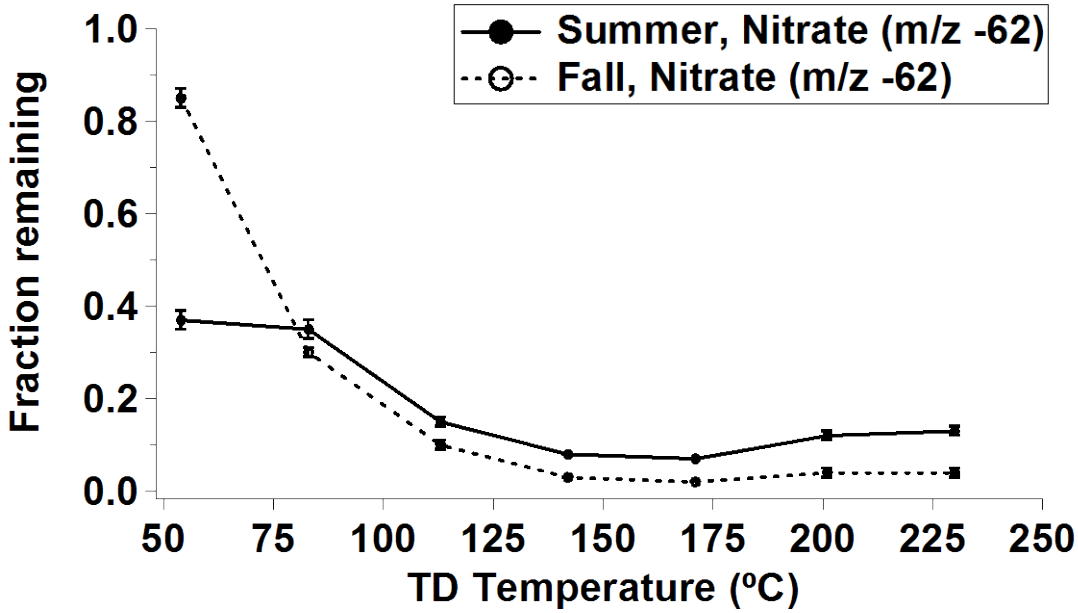


Figure 45: Relative fractions of nitrate (*m/z* -62 ($NO_3^-$)) remaining on the aged OC (nitrate-sulfate) particles at each TD temperature during SOAR-1 and SOAR-2.

the aged OC (nitrate-sulfate) particles was estimated at ~6-9% in the summer compared to less than 1% in the fall. In the unheated particles, aminium nitrate and sulfate salts were found to contribute ~1% and ~0.6% to the total particle mass in the summer.

Although not the focus of this Chapter, an amine-dominant particle type, comprised ~5-8% by number of the particles ~200-700 nm in diameter during both SOAR-1 and SOAR-2. The mass spectra were dominated by *m/z* 86($(C_2H_5)_2NCH_2^+$) with less intense amine marker ions at *m/z* 58($C_2H_5NHCH_2^+$), 102($(C_2H_5)_3NH^+$), and 118($(C_2H_5)_3NOH^+$) (39); nitrate and sulfate were observed in the negative ions. Using the calibration curve derived herein, these unheated particles were found to be 18 ± 10% and 12 ± 6% amine by mass fraction during the summer and fall, respectively. However, as discussed in Chapter 4, the amine-dominant particle type nearly disappears at ~113 °C, consistent with the volatilization of neutral amines and the reclassification of the particles within the aged OC type. This is shown by the amine mass/particle decreasing from 7 ± 4 fg/particle at ambient temperature to 4 ± 3 fg/particle at 113 °C in these amine-dominant particles in the summer; likewise, in the fall, the amine-dominant particles

contain 6 ± 3 fg amines/particle at ambient temperature and 2 ± 1 fg amines/particle at 113 °C.

Several possible explanations exist for higher amine mass concentrations in the unheated aged OC particle type in the summer compared to the fall. Ammonia has a higher vapor pressure (5990 Torr at 25 °C) than triethylamine and diethylamine (56.1 and 218 Torr at 25 °C, respectively) (Advanced Chemistry Development, 202). During the summer, higher ambient temperatures were observed (17.6-30.9 °C with a mean of 22.9 °C) compared to the fall (8.4-26.1 °C with a mean of 15.6 °C). While ammonia and amines are emitted from the same sources (178,179), primarily the Chino dairy area to the west of Riverside, their differing vapor pressures impact initial volatilization at the source during the different seasons, likely causing more ammonia and amines to be present in the vapor phase in the summer (203); however, gas-phase concentrations of these species during SOAR were not measured. The lower vapor pressure of the amines compared to ammonia allowed them to more readily partition to the particle phase in the summer at the higher ambient temperatures observed; however, the particle-phase chemistry impacted the protonation and gas/particle partitioning of the amines once in the particle phase. At the lower fall ambient temperatures, ammonia competes with amines to form ammonium nitrate and ammonium sulfate/bisulfate (187) which is supported by the greater particle phase ammonium concentrations (2.30 ± 0.04 times) observed in the aged OC particle type in the fall compared to the summer. This observation is consistent with previous studies showing higher concentrations of ammonium nitrate in the eastern LA basin in the fall (up to ~50% of the fine aerosol mass) (150,204). Thermodynamic calculations have shown that increasing ammonia/amine gas-phase ratios from 100 ppt/10 ppt to 1000 ppt/1 ppt led to lower predicted fractions of protonated amines in aqueous nanometer-sized particles (60.5% vs. 1.5%) (187). In addition to gas-phase concentrations, Henry's Law constants ($K_H$) and acid dissociation constants ($pK_a$) must be considered in the prediction of the partitioning of amines relative to ammonia (187). Triethylamine is a stronger base than ammonia ($pK_a$ 10.62 ± 0.25 vs. 9.24 ± 0.10) (Advanced Chemistry Development, 202) and has a Henry's Law constant of similar magnitude ($K_H$ 29 M atm$^{-1}$ vs 62 M atm$^{-1}$) (187), allowing the amines to compete for protons even when at lower concentrations.

In acidic particles, amines will become protonated and remain in the particle phase, forming aminium salts (185,187); thus one expects to see seasonal differences in the partitioning of amines due to changes in particle acidity. In the summer, the aged OC particles were more acidic, as shown by a more intense (1.39 ± 0.04 times) sulfuric acid cluster ion peak at *m/z* -195 ($H_2SO_4HSO_4^-$), a proxy of non-neutralized sulfate and particle acidity. In addition, higher oxalate (*m/z* -89($COOHCOO^-$)) ion peak areas (1.62 ± 0.03 times) were observed in the summer compared to the fall, suggesting that, in addition to nitric and sulfuric acid, organic acids could also form aminium salts, as suggested by Smith et al. (186) and Barsanti et al. (187). While oxalic acid, for example, has a higher $pK_a$ than nitric acid (1.38 ± 0.54 vs -1.4) (Advanced Chemistry Development, 202), it has a substantially lower vapor pressure (2.51 x 10$^{-6}$ Torr vs 49.8 Torr) (Advanced Chemistry Development, 202), allowing it to partition more readily to the particle phase to form aminium organic salts. Due to the increased particle acidity in the summer, a higher amine fraction is believed to be protonated, leading to increased concentrations of aminium salts in the summer compared to the fall, as observed.

Further, we hypothesize that the higher atmospheric water content in the summer (15.9-20.5 mMol/Mol with a mean of 18.9 mMol/Mol) compared to the fall (5.5-16.5 mMol/Mol with a mean of 12.6 mMol/Mol) caused more aminium salts to dissolve within the particle phase, causing an equilibrium shift of the amines from the gas to the particle phase (39). This equilibrium shift would further explain the higher amine mass concentrations in the unheated aged OC particles in the summer compared to the fall. In this way, aminium salts may contribute to aerosol growth, as suggested by Barsanti et al. (187).

Generally, pH is estimated using an ion balance of ammonium with nitrate and sulfate. However, previous studies have shown differences in calculated and measured pH for submicrometer aerosols (205). Based on the relatively significant contribution of amines shown during this study, it is recommended that particle acidity calculations take into account the presence of amines which act as even stronger bases than ammonia in atmospheric aerosols. Thus, for the aged OC (nitrate-sulfate) particles in this study, the particles would be predicted to be more acidic than in actuality based on only ammonium, sulfate, and nitrate concentrations. To illustrate this point, relative acidity ratios are calculated for the SOAR-1 and SOAR-2 aged OC particles; defined as the sum of the absolute average peak areas of nitrate (*m/z* -62 ($NO_3^-$)) and sulfate (*m/z* -97($HSO_4^-$)) divided by ammonium (*m/z* 18($NH_4^+$)) (i.e., the typical ion balance method used for calculating pH) or the sum of ammonium and amines (*m/z* 86($(C_2H_5)_2N{=}CH_2^+$)). These resulting ratios are shown in **Figure 46**. In the summer, the relative acidity ratio is overpredicted by a factor of 4 when amines are not taken into consideration, showing the significant role of amines as bases in the summer. In the fall, the addition of amines to the relative acidity ratio does not change the value dramatically (factor of 1.6) when ammonium is the dominant base.

These measurements represent the first quantification of the volatility behavior and mass contribution of amines to individual aged atmospheric particles. During SOAR, the partitioning of amines between the gas and particle phases depended strongly on particle acidity. The more acidic particles in the summer resulted in protonation of the

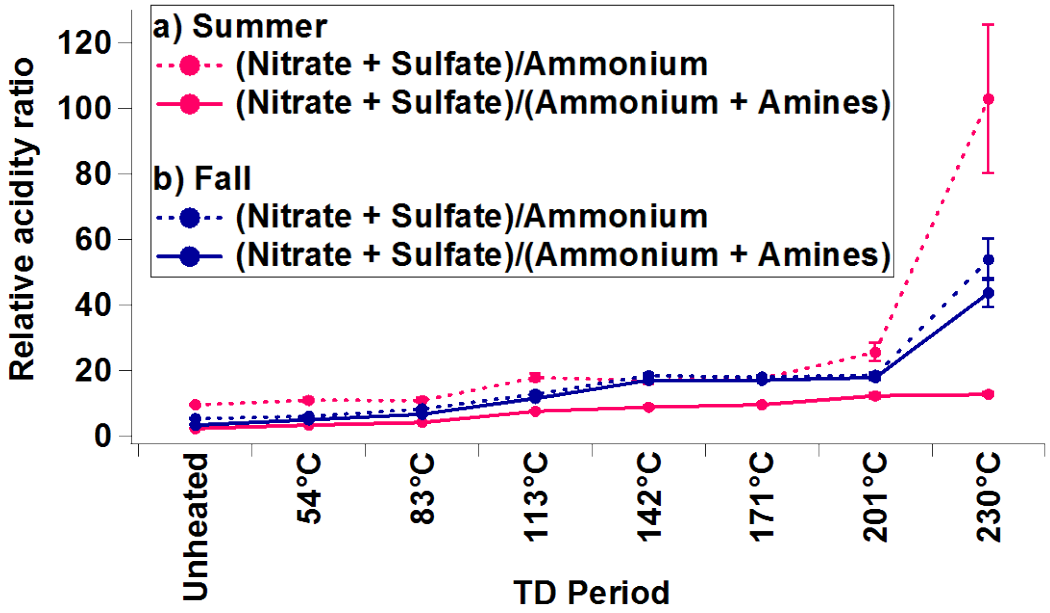


Figure 46: Relative acidity ratios for summer and fall for each thermodenuder period (unheated, 54°C, 83°C, 113°C, 142°C, 171°C, 201°C, 230°C) for the aged OC (nitrate-sulfate) particles. The ratios are defined as the sum of the absolute average peak areas of nitrate (*m/z* -62 ($NO_3^-$)) and sulfate (*m/z* -97 ($HSO_4^-$)) divided by ammonium (*m/z* 18 ($NH_4^+$)) or the sum of ammonium and amines (*m/z* 86 ($(C_2H_5)_2NCH_2^+$)).

amines, causing the formation of aminium sulfate and nitrate salts, which did not volatilize at temperatures up to 230 °C. These amine salts represent low-volatility organic carbon species that could potentially be missed by thermal analysis methods. In the fall, higher particulate ammonium concentrations and more basic particle cores produced fewer aminium salts, causing 86 ± 1% of the amines to volatilize below 113 °C. The abundance of organic carbon mixed with amine salts, as observed in this study, may form a barrier that prevents the salts from remaining at equilibrium with the gas phase (176). Previous chamber studies have found aminium nitrate salts repartition back to the gas phase under low RH conditions (<10%) (176); however, under the conditions of this study, this revolatilization process did not occur because the presence of water caused the aminium salts to dissolve, shifting the equilibrium of the gas-phase amines toward the particle phase. Further, previous chamber studies have not examined the partitioning of the amine salts with respect to pH, shown in this SOAR data to be a critical parameter affecting gas/particle partitioning. Laboratory studies of the competition between ammonia and different amine species for sulfuric, nitric, and organic acids, as a function of temperature, RH, and particle size, and the relative abundance of amines and ammonia are planned to further understand the partitioning of amines in the atmosphere. Further, it is important to note that the average bulk pH of a collection of ambient particles may in fact not be representative of the pH of any individual particle; thus, the single-particle mixing state of atmospheric aerosols must be used as a measure of pH to fully understand the partitioning of semivolatile species such as amines in gas/particle partitioning processes.

## iv. Acknowledgements

This work was supported by the National Science Foundation (NSF ATM-0321362) and the California Air Resources Board (CARB 04-336). Together Lindsay Hatch, supported by an NSF graduate research fellowship, and I completed the amine mass calibration; Lindsay wrote the amine mass calibration method portion of this Chapter and contributed to discussions of the data. Prof. Paul Ziemann (UC-Riverside), Ken Docherty (CU-Boulder), the UC Riverside Air Pollution Research Center, and the Prather Group, particularly Gary Poon, Xueying Qin, Laura Shields, and Stephen Toner, provided support during SOAR. Alex Huffman (CU Boulder) and Prof. Jose Jimenez provided and ran the TD system, developed under EPA sponsorship (STAR R831080). Megan McKay and the Goldstein group (UC-Berkeley) provided the atmospheric water content and ambient temperature data. The California Air Resources Board provided $PM_{2.5}$ mass concentrations for the Rubidoux site.

# 6. Inter-annual Comparison of Ambient, Single-Particle Chemical Mixing State in Riverside, CA

## i. Introduction

Atmospheric particles are known to cause severe adverse health effects (96). For instance, fine particulate matter ($PM_{2.5}$, particles with aerodynamic diameters $\leq$2.5 μm) has been linked to increases in cardiovascular and pulmonary diseases, leading to elevated mortality and morbidity (110). Epidemiological studies have applied generalized additive models to time series data to estimate associations between exposure to $PM_{2.5}$ and the diseases mentioned above (206). Improvement of these models based on temporal changes in $PM_{2.5}$ is important for pollution regulation, which can minimize the health effects of these particulates. Urban aerosols specifically contribute to these health effects and are of interest because 1) they represent a significant fraction of $PM_{2.5}$ mass concentrations (148) and 2) better approximations based on measurements are needed to improve the representation of urban aerosols in models and pollution regulations (207).

The Los Angeles (LA) Basin is recognized for some of the highest levels of urban particulate pollution in the United States, especially the city of Riverside, which is ~50 miles east of downtown LA (208). Westerly winds transport emissions from LA, which stagnate in Riverside due to the surrounding topography and inversion layer, increasing $PM_{2.5}$ concentrations (209,210). During transport from LA, heterogeneous reactions of particles with trace gases and gas-particle partitioning of secondary species, such as nitrate (158), sulfate (211), ammonium (212), amines (213), and oxidized organics (214) contribute greatly to changes in particle size and chemistry during transport (96,215). Particles that accumulate these secondary species may become more toxic (110). For instance, high levels of ingested nitrate can subsequently cause lethargy or coma for infants (216) and mortality rates have been related to airborne concentrations of sulfate (217). Secondary amines and oxidized organics can increase the rate of blot clots (218) and cause respiratory and cardiovascular problems (219), respectively. Overall, these secondary species can constitute a large fraction of $PM_{2.5}$ in urban areas of the Western US, with organics, nitrate, sulfate, and ammonium equaling ~70% of the total $PM_{2.5}$ mass (220). Therefore, the extent of particle aging could impact how harmful the particles are to human health. This highlights the importance of being able to detect these species in particles.

Meteorology has large impacts on particle chemistry, number, and mass concentrations, even for urban locations (215). Therefore, meteorological influences on $PM_{2.5}$ should be taken into account in models in order to better associate particulate matter with adverse health effects. In Riverside, several previous studies have linked meteorology or gas-phase concentrations with observed particle chemistry (154) or monitored seasonal variation of particulate mass concentrations (45,148,204,221,222). Pastor et al. (2003) observed increases in carbon-rich particles during elevated $O_3$ levels in the afternoons during a 40-day summer study in Riverside. Fine et al. (2004) and Geller et al. (2004) found the highest $PM_{2.5}$ in the summer months; while in contrast, Chow et al. (1994) and Kim et al. (2000) found higher $PM_{2.5}$ in the winter months. These contradictory results indicate that in order to improve model inputs, it cannot be assumed that the ambient particles are the same each year, based off of results from one study.

Hence, these results show the need for long-term monitoring and inter-annual comparison of particle chemistry that contributes to $PM_{2.5}$.

Incorporating gas-phase species and meteorology from multiple studies over time could help explain long-term changes in $PM_{2.5}$ concentrations and particle chemistry. Most previous studies have utilized off-line bulk filter measurements; however, in this study, real-time, single-particle measurements were used. This technique provides more specific information about particle mixing state with a high time-resolution, which can give more detailed insight into the influence of particulate chemistry on $PM_{2.5}$ concentration trends. Chemical composition analysis of individual particles allows the identification of particle sources and an assessment of particle aging. Here, we examined the role of meteorology (temperature, relative humidity, wind speed, and air mass back trajectories) and gas-phase $O_3$ on changes in $PM_{2.5}$ mass concentrations and measured single-particle chemistry in Riverside for three consecutive summers (2005-2007).

**ii. Experimental**

Individual ambient aerosol measurements were taken during the summers of 2005-2007 at the University of California, Riverside (UCR). Measurements were made during the Study of Organic Aerosols in Riverside (SOAR-1) campaign from July 29 – August 15, 2005, as well as subsequent studies from August 10 –21, 2006 and August 29 – September 7, 2007. All data are given in Pacific Standard Time (PST), 1 hour behind local time. Gas-phase $O_3$, $PM_{2.5}$ mass concentrations, and meteorological measurements, including wind speed, relative humidity, and temperature were acquired from the California Air Resources Board (CARB) Riverside-Rubidoux sampling site, located ~9 miles northwest of UCR in 2006-2007. In 2005, $PM_{2.5}$ mass concentrations and $O_3$ were acquired from CARB, while meteorological data were acquired from the Professor Allen Goldstein group at the UCR site.

The size-resolved chemical composition of individual particles was measured using aerosol time-of-flight mass spectrometry (ATOFMS). More specifically, a converging nozzle-inlet ATOFMS (measuring particles with vacuum aerodynamic diameter ($D_{va}$) of 0.1-1.0 μm) was operated in 2005 and 2007, and the ground-based prototype of the aircraft ATOFMS ($D_{va}$ of 0.2-2.5 μm) with an aerodynamic lens inlet was utilized in 2006; these measurements are described in detail elsewhere (127,223). The measurements of the two instruments have been shown to agree on particle chemistry when co-located (223). This comparison focuses on the overlap size region of 0.2-1.0 μm. Briefly, particles enter through differentially-pumped stages, accelerating particles to their terminal velocities. The speed is measured for individual particles via two continuous-wave diode lasers (532 nm). Aerodynamic size is determined by calibration with polystyrene latex spheres of known physical diameters. Individual particles are subsequently desorbed and ionized by a pulsed 266-nm Nd:YAG desorption-ionization laser, creating positive and negative ions, which are detected within the dual-polarity time-of-flight mass spectrometer. In 2005 the ATOFMS analyzed 1 076 812 particles, in 2006 the A-ATOFMS analyzed 1 099 868 particles, and in 2007 the ATOFMS analyzed 939 297 particles.

For detailed analysis, single-particle size and mass spectra were imported into YAADA (www.yaada.org), a software toolkit for analysis using Matlab (The Mathworks, Inc.). An adaptive resonance theory-based clustering method (ART-2a) (35) was then

used to classify and group single-particle mass spectra with a vigilance factor of 0.80, learning rate of 0.05, and 20 iterations followed by regrouping with a vigilance factor of 0.85. ART-2a classifies particles into separate clusters depending on the presence and intensity of ion peaks within the individual particles' mass spectra. For the three studies presented, the most populated 50 clusters accounted for >90% of the total ART-2a classified particles and are representative of the overall aerosol composition. Peak identifications within this paper correspond to the most probable ions for a given mass-to-charge (*m/z*) ratio. The peak area of a specific *m/z* is related to the amount of a specified species on each particle (85,224).

**iii. Results and Discussion**

### *a. Impact of meteorology on particulate mass concentrations*

**Table 7** (and **Figure 47** of the Supplementary Material) gives a synopsis of temperature (T), relative humidity (RH), wind speed (WS), $PM_{2.5}$ mass concentrations ($PM_{2.5}$), and gas-phase $O_3$ concentration measurements from the summers of 2005-2007 in Riverside, CA. It is important to note that certain parameters were correlated or anticorrelated with $PM_{2.5}$ mass concentrations and that $PM_{2.5}$ averages and temporal patterns changed each year. Of the sampling periods within the three years, 2007 was characterized by the highest Ts (average 28 ºC, maximum 45 ºC) and lowest average RH (56%) with the lowest average $PM_{2.5}$ mass concentration (22 $\mu g/m^3$). 2006 was the characterized by the lowest Ts (avg. 23 ºC, max. 34 ºC) and highest average RH (75%) year with the highest average $PM_{2.5}$ mass concentration (32 $\mu g/m^3$). In 2005, the T (avg. 26 ºC, max. 38 ºC), average RH (71%), and average $PM_{2.5}$ concentration (30 $\mu g/m^3$) were between 2006 and 2007. The strong relationship between average $PM_{2.5}$ mass concentration, temperature, and RH suggest that the majority of the species contributing to $PM_{2.5}$ could be semi-volatile by nature (225).

| Yr | Data | Avg. | σ | Range | Avg. Daily Maxima (PST) |
|---|---|---|---|---|---|
| 2007 | $PM_{2.5}$ | 22 µg/m³ | 7 µg/m³ | 5-46 µg/m³ | Various |
| 2005 | $PM_{2.5}$ | 30 µg/m³ | 13 µg/m³ | 4-79 µg/m³ | 10:00 |
| 2006 | $PM_{2.5}$ | 32 µg/m³ | 14 µg/m³ | 10-74 µg/m³ | 9:00 |
| 2007 | RH | 56% | 22% | 25-100% | 6:00 |
| 2005 | RH | 71% | 20% | 36-100% | 4:00 |
| 2006 | RH | 75% | 22% | 25-100% | 5:00 |
| 2006 | T | 23 °C | 10 °C | 16-34 °C | 13:00 |
| 2005 | T | 26 °C | 10 °C | 18-38 °C | 13:00 |
| 2007 | T | 28 °C | 14 °C | 16-45 °C | 13:00 |
| 2007 | WS | 3.93 m/s | 3.09 m/s | 0-15 m/s | 14:00 |
| 2006 | WS | 4.37 m/s | 4.28 m/s | 0-25 m/s | 15:00 |
| 2005 | WS | 4.40 m/s | 2.74 m/s | 1-14 m/s | 14:00 |
| 2006 | $[O_3]$ | 38.8 ppb | 29.8 ppb | 1-106 ppb | 13:00 |
| 2007 | $[O_3]$ | 39.5 ppb | 33.7 ppb | 1-131 ppb | 14:00 |
| 2005 | $[O_3]$ | 46.4 ppb | 39.6 ppb | 0-155 ppb | 14:00 |

Table 7: Measurements of $PM_{2.5}$ (µg/m$^3$), relative humidity (RH, %), temperature (T, °C), wind speed (WS, m/s), and gas-phase $O_3$ concentrations (ppb) for the sampling periods during 2005-2007. Standard deviations (σ) and measurement ranges are also listed. 'Avg. Daily Maxima' refers to the average time of the daily maximum of each particular factor.

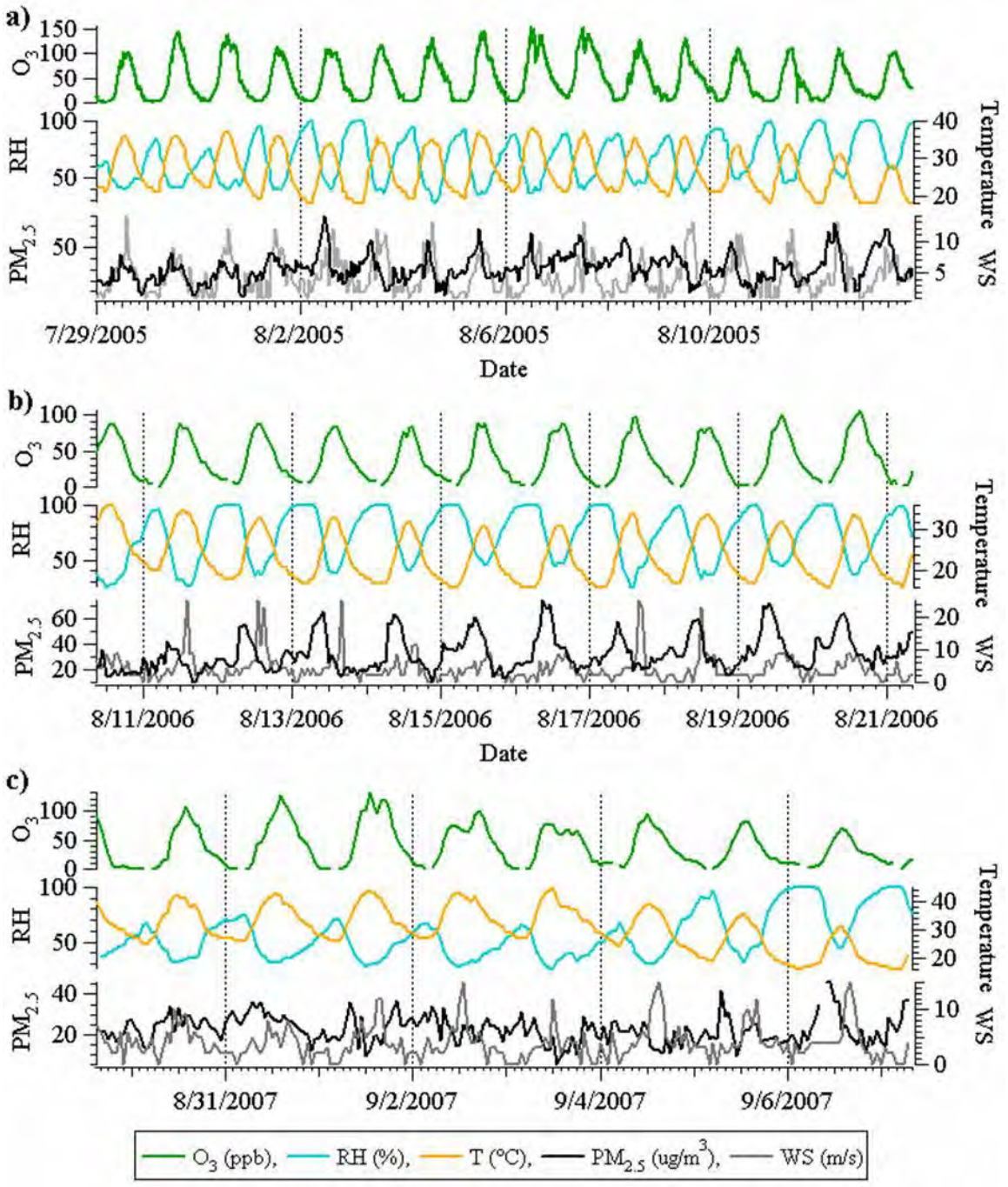


Figure 47: Illustrates the temporal profiles of gas-phase $O_3$ (ppb, green line), relative humidity (%, blue line), temperature (ºC, orange line), $PM_{2.5}$ mass concentrations (µg/m$^3$, black line), and wind speed (m/s, grey line) from the three summer studies in Riverside, CA. Plot a) has data from July 29 – August 15, 2005, b) August 10 –21, 2006, and c) August 29 – September 7, 2007. Trends of these measurements are discussed in the main manuscript.

In addition to average $PM_{2.5}$ mass concentrations, $PM_{2.5}$ temporal patterns changed from year-to-year: 2005 had distinctive diurnal variation peaking at 10:00, 2006 was usually diurnal with some days having multiple maxima, and 2007 was variable,

both in number of maxima and peak times, as shown in the Supplementary Information. These differences can be attributed to the meteorology, specifically wind speed (WS). 2005 had very diurnal WS that did not greatly deviate from the average (4.40 m/s, $\sigma$ = 2.74 m/s), similar to the $PM_{2.5}$ mass concentrations being very diurnal with single daily maxima. The studies in 2006 and especially 2007 had less diurnal $PM_{2.5}$ mass concentrations and sometimes multiple daily maxima due to less uniform temporal profiles of WS. WS influences $PM_{2.5}$ by transporting different numbers of particles with different masses, depending on how consistent and fast the wind is. In addition, air mass trajectories can identify where the particles came from and traveled, and therefore further explain differences in $PM_{2.5}$. **Figure 48** shows the representative air mass back trajectories (AMBTs) calculated using HYSPLIT (226) for the sampling periods from 2005-2007. In 2005, the representative AMBTs originated to the west 80% of the time, while three main northwesterly/southwesterly trajectories were present during 67% of the sampling time in 2006. In contrast, 2007 had highly variable AMBTs due to Santa Ana conditions, which generally have high T, low RH, and high WS originating from a high-pressure system from the northeast (227). Evidence of a Santa Ana in 2007 is confirmed by the easterly inland trajectory from the Mojave Desert area, high average T (43 ºC) and low average RH (69%), leading to low $PM_{2.5}$ concentrations. Santa Ana conditions were not observed in 2005 or 2006, which both had higher $PM_{2.5}$ concentrations than 2007.

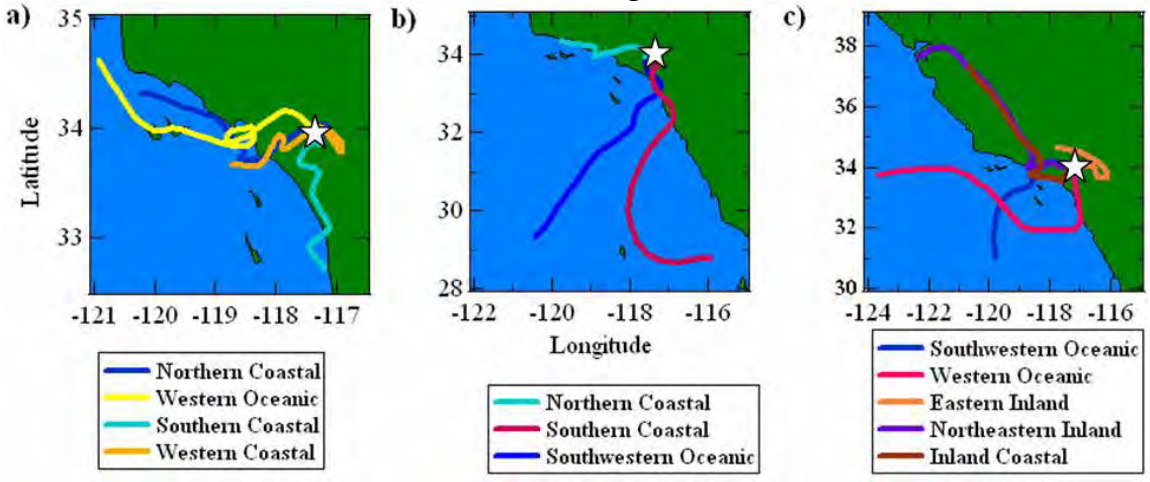


Figure 48: Representative 48-hour HYSPLIT air mass back trajectories in Riverside for a) 2005, b) 2006, and c) 2007. Trajectories are labeled by source wind direction and terrain. The sampling site is represented by the star in each map.

Particle mass is strongly dependent on meteorology and where the particles originate and travel. T and RH can affect mass concentrations by determining what semi-volatile species are in the particle-phase such that high T and low RH permit semi-volatile species to stay in the gas-phase, but low T and high RH lead these species to partition to the particle-phase, adding mass. Winds can also influence particle mass concentrations such that they can control diurnal variations in $PM_{2.5}$. WS and AMBTs affect where the particles come from and how they transform as they are exposed to different conditions in the atmosphere. The mass concentrations of particles are dependent on the source; however, meteorology has a large impact on $PM_{2.5}$ and is different on an inter-annual scale.

### *b. Overall submicron aerosol chemical composition*

Because of year-to-year differences in $PM_{2.5}$, the particles contributing to mass differ chemically and vary by concentration. More detailed analysis of individual-particle chemistry and number fractions can give insight as to what particles are contributing to the $PM_{2.5}$ each year. Further, details on particle mixing states in conjunction with meteorology can help develop more precise parameters for health models and improve pollution regulations. The mass spectral signatures of the ATOFMS particle types presented in this manuscript are similar to those described by Pastor et al. (154) and Qin et al. (208) for previous measurements in Riverside, CA and are described in **Table 8**. The major submicron particle types present during the three summer studies were aged organic carbon (AgedOC), amine-containing, elemental carbon (EC), elemental carbon/organic carbon (ECOC), biomass burning, aged sea salt (AgedSS), and dust; other minor types comprised <10% of the total over the size range of 0.2-1.0 μm.. Representative mass spectra of these particle types are found in the Supplementary Material.

| ATOFMS Particle Type | Characterization |
|---|---|
| AgedOC | Carbonaceous markers at $^{12}C^+$, $^{27}C_2H_3^+$/$CHN^+$, $^{36}C_3^+$, $^{37}C_3H^+$, $^{43}CH_3CO^+$/$CHNO^+$, and $^{86}(C_2H_5)_2NCH_2^+$ |
| Amine | Contained $^{86}(C_2H_5)_2NCH_2^+$ with less intense amine marker ions at $^{58}C_2H_5NHCH_2^+$, $^{102}(C_2H_5)_3NH^+$, and $^{118}(C_2H_5)_3NOH^+$ and other minor organic carbon peaks |
| Ammonium | Contained $^{18}NH_4^+$ with less intense organic peaks |
| EC | Characterized by intense carbon cluster positive and negative ions from $C^{+/-}$ to $C_n^{+/-}$ |
| ECOC | Similar to that of EC with less intense OC and amine ion peaks |
| Biomass | Contained potassium with less intense carbonaceous positive ions while the negative ions contained nitrate and sulfate |
| AgedSS | Intense sodium, potassium, nitrate, and sulfate ion markers with smaller ammonium and carbonaceous ion markers |
| Dust | Inorganic peaks at $^{23}Na^+$, $^{24}Mg^+$, $^{40}Ca^+$, and may contain $^{56}Fe^+$ |

Table 8: Descriptions of the major ATOFMS particle types from 2005-2007.

### *c. Assessment of single-particle mixing state and particle aging*

It is important to note that the majority of the particles from 2005-2007 were internally mixed or "aged" with secondary species, regardless of particle type: AgedOC, amines, biomass, AgedSS, dust, and ECOC showed evidence of aging based on markers of ammonium ($^{18}NH_4^+$), amines ($^{86}C_5H_{12}N^+$), oxidized OC ($^{43}C_2H_3O^+$/$CHNO^+$), sulfate ($^{97}HSO_4^-$), and nitrate ($^{46}NO_2^-$ and $^{62}NO_3^-$). **Figure 49** illustrates the mixing states of major ATOFMS particle types with secondary species during the 2005-2007 summers. Each square represents the number fraction of each particle type containing a particular *m/z* marker, i.e., the percentage of a particle type aged with a secondary species out of the total number of particles of that type. It is important to note that each particle type may be aged with more than one secondary species. These markers significantly differ each year except for the fraction of particles containing *m/z* 86 within the amine particle type, which will be disregarded as it is a reference spectral marker for this type.

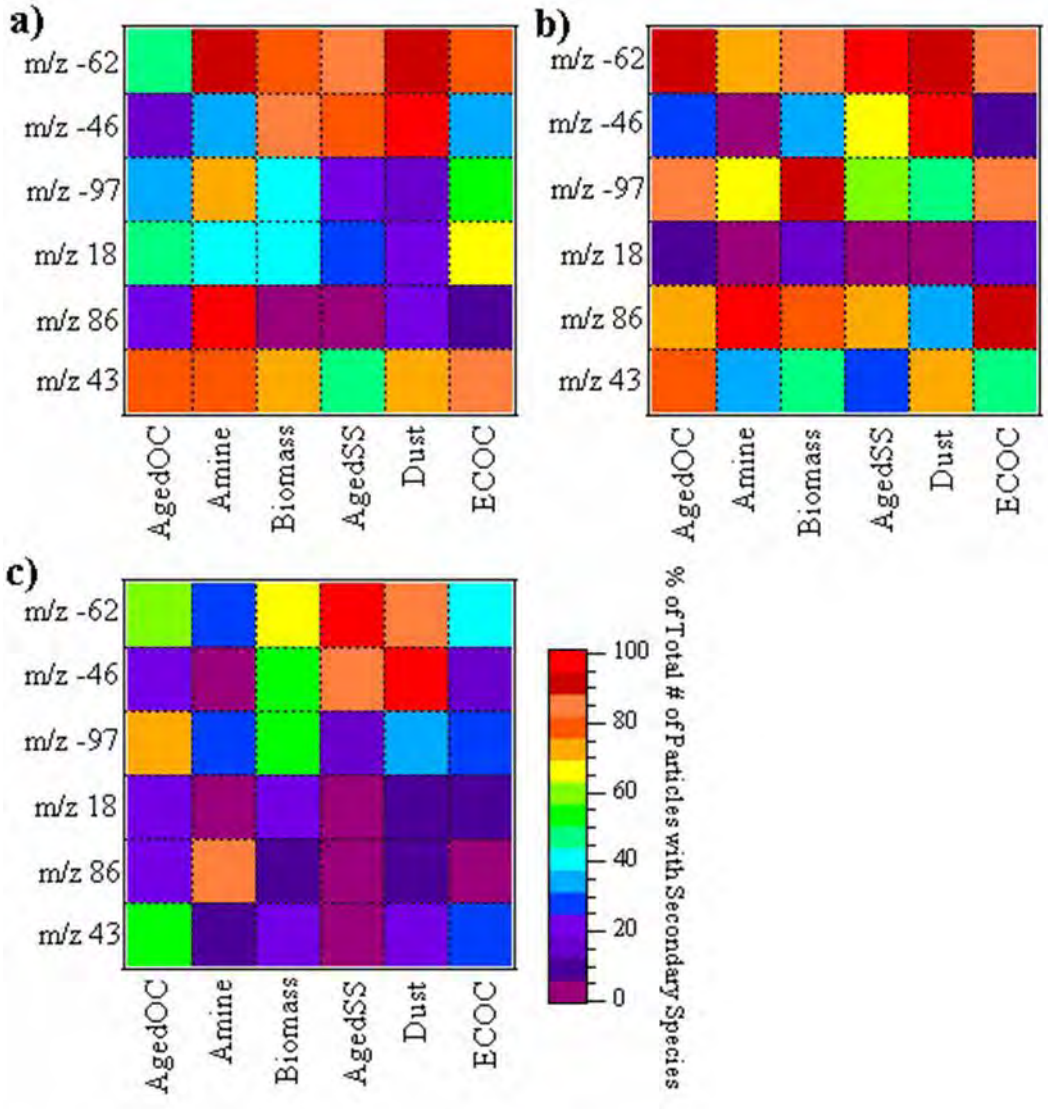


Figure 49: Mixing states of secondary species in major particle types from a) 2005, b) 2006, and c) 2007. The abscissa contains major ATOFMS particle types and the y-axis contains secondary species markers $C_2H_3O^+$ (*m/z* 43), $(C_2H_5)_2NCH_2^+$ (*m/z* 86), $NH_4^+$ (*m/z* 18), $HSO_4^-$ (*m/z* -97), $NO_2^-$

(*m/z* -46), and $NO_3^-$ (*m/z* -62). The color scale represents the number fraction of particles within a single particle type that contained each specific marker (secondary species).

Overall, all three years showed the most aging of all particle types with secondary nitrate, ranging from 53-91% of each particle type in 2005, 72-97% in 2006, and 26-95% in 2007. This suggests high nitrate levels were present, which have previously been modeled and observed in Riverside (148,158,228). In addition to nitrate in 2005, the major particle types were aged with oxidized OC (ranging from 48-88% of the total number of each particle type), consistent with the highest $O_3$ concentrations observed. Because the average $O_3$ concentration was highest in 2005, this suggests the particles were highly oxidized compared to 2006 or 2007 (particle types aged with oxidized OC = 38-79% and 6-51% of the total number of each particle type, respectively). Aging with sulfate was more apparent in 2006 (particle types aged with sulfate = 51-87% of the total number of each type) than in 2005 specifically on the amine type, which demonstrates acid-base chemistry between $H_2SO_{4(g)}$ and basic amine markers forming aminium sulfates (39,213). Although aminium nitrate salts are more significant in agricultural settings like the surroundings of Riverside, aminium sulfate may form in the presence of high sulfate concentrations (176) and have been previously shown to correlate in Riverside during the summer (213). Also apparent are higher fractions of secondary amines in all particle types (particle types aged with secondary amines = 41-87% of the total number of each type) compared to 2005 and 2007 (particles types aged with secondary amines = 7-27% and 6-24% of the total of each type, respectively). The higher average RH (and lower average T) in 2006 caused semi-volatile species, such as amines, to partition to the particle phase (39). Both 2005 and 2006 had more aging of different organic particle types (AgedOC, amines, ECOC, biomass); however, in 2007 there was more aging of inorganic types such as AgedSS and dust with nitrate (95% and 82% of the total of each type, respectively). This change in mixing state from 2005 and 2006 to 2007 can be attributed to Santa Anas transporting more dust, which readily takes up nitrate (229) and salts from AMBTs originating and traveling over the Pacific Ocean, especially from September 5-7, 2007 as discussed below.

These results show that the relative number of particle types aged with secondary species can change and that aging is not on the same type from year-to-year. The extent of particle aging can be examined by looking at a ratio of a more-oxidized marker (*m/z* 43) to a less-oxidized marker (*m/z* 37) and its relationship to $O_3$ as shown in the Supplementary Material. Also, these particles largely contribute to $PM_{2.5}$ mass and can change the chemical composition of the $PM_{2.5}$ each year. This has implications for human health because of the fact that the different secondary species can have different adverse health effects as mentioned earlier. For instance, a higher secondary amine contribution to $PM_{2.5}$ in 2006 can increase blot clotting but the presence of more oxidized organics in 2005 would be more likely to cause respiratory problems, if these particles are inhaled and penetrate through the lungs. Schlesinger (2007) stated that since relative toxicity of various constituents of $PM_{2.5}$ probably differs for different observed biological endpoints, the public health risk from each of these components is unlikely to be the same in different geographical regions where the chemical properties of ambient $PM_{2.5}$ may differ (230). Therefore, the same effect would be expected in the same geographic region if the particle chemistry of $PM_{2.5}$ mass is different from year-to-year.

Highly-aged particles accumulate more secondary species which increases toxicity level; hence, it is important to determine the extent of particle aging. The ratio of *m/z*'s 43/37 ($C_2H_3O^+$/$CHNO^+$ to $C_3H^+$) provides an indication of the extent of particle aging from year-to-year in Riverside. The OC marker *m/z* 37 has been observed as a fresh emission from light duty vehicles (231), while the oxidized OC marker *m/z* 43 signifies a more oxidized/aged species (208). Incorporating $O_3$ into this ratio can also help determine if the particles were truly aged in the atmosphere. **Figure 50** shows the temporal profile of this ratio as a function of $O_3$ concentrations. The fact that this ratio is highest during the highest $O_3$ concentration (13:00-14:00) suggests that particles during this time are more aged with oxidized organics, potentially from oxidized organic gases that condense onto particles or heterogeneous reactions, versus being primary. This trend is similar to what has been previously observed in Riverside with aerosol mass spectrometry (214) and $PM_{2.5}$ filter measurements(232), where semi-volatile organics increased during high mid-day photochemical activity and decreased at night. Even though the relationship between 43/37 and $O_3$ exists all three years, the diurnal profiles tend to become more variable from 2005-2007 similar to $PM_{2.5}$, where the temporal profiles of $PM_{2.5}$ became less diurnal from 2005-2007 because of the WS and AMBTs becoming less diurnal.

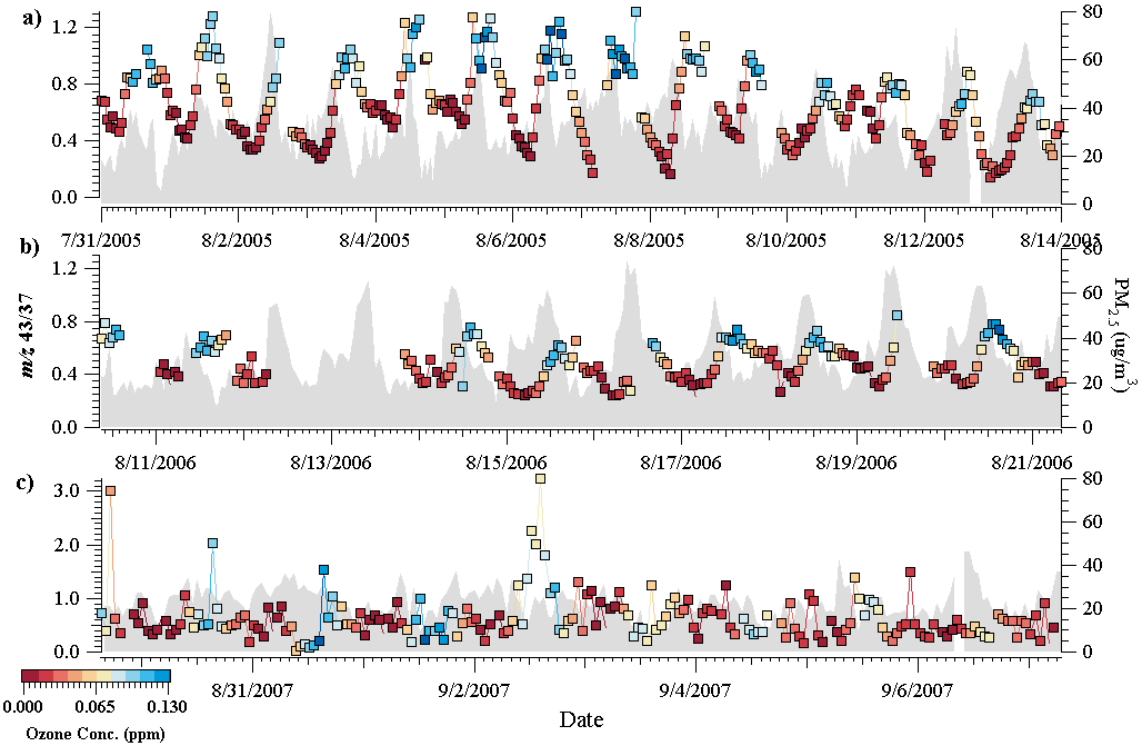


Figure 50: shows the ratio of the sum of peak areas m/z 43 to m/z 37 plotted as a function of $O_3$ concentration (ppm) from a) 2005, b) 2006, and c) 2007 with maroon being the lowest concentration and blue being the highest. Also pictured is the temporal profile of $PM_{2.5}$ mass concentrations ($\mu g/m^3$).

### *d. Relating particle chemistry to meteorology and $PM_{2.5}$ mass concentrations*

In order to assess the $PM_{2.5}$ trends and relate them to particle chemistry, an overall look at the particle chemistry is required. **Figure 50** illustrates the time-resolved

chemistry of the number fractions of each particle type relative to the total number of particles, which show large variations in particle chemistry between the three summers. Even though organic-containing particles (AgedOC, ECOC, amines, and biomass types combined) comprise the largest number fraction each year (57-86%) for particles 0.2-1.0 um, there are notable differences in the overall particle chemistry which can be tied to gas-phase concentrations and/or meteorology. 2005 had the highest number fraction of AgedOC particles (27%) compared to 2006 (8%) and 2007 (6%). This is likely because of the higher average $O_3$ concentrations (46.4 ppb) than 2006 (38.8 ppb) or 2007 (39.5 ppb), which would lead to the presence of more oxidized organics. The average RH was highest in 2006 (75%) as was the amine fraction (86% of the total number of particles), compared to 2005 and 2007 (1% and 5% of the total, respectively). Amine particle markers have been previously reported to increase at higher RH and lower T at an urban site (39), suggesting they are semi-volatile and partition to the particle phase under these conditions. In 2007 although the highest relative number fraction of particles was ECOC, there were larger fractions of AgedSS and dust (23% and 10% of the total, respectively) compared to 2005 (20% and 2%) and 2006 (1% and 0.1%), which can be attributed to Santa Anas during the study that transported more dust. The presence of more AgedSS types can be attributed to AMBTs originating over the Pacific Ocean as seen in **Figure 48**. During this time period, a large increase in the fraction of AgedSS is observed in **Figure 50**. Directly before and after this time period, AMBTs were more similar to the Coastal or Northeastern Inland trajectories.

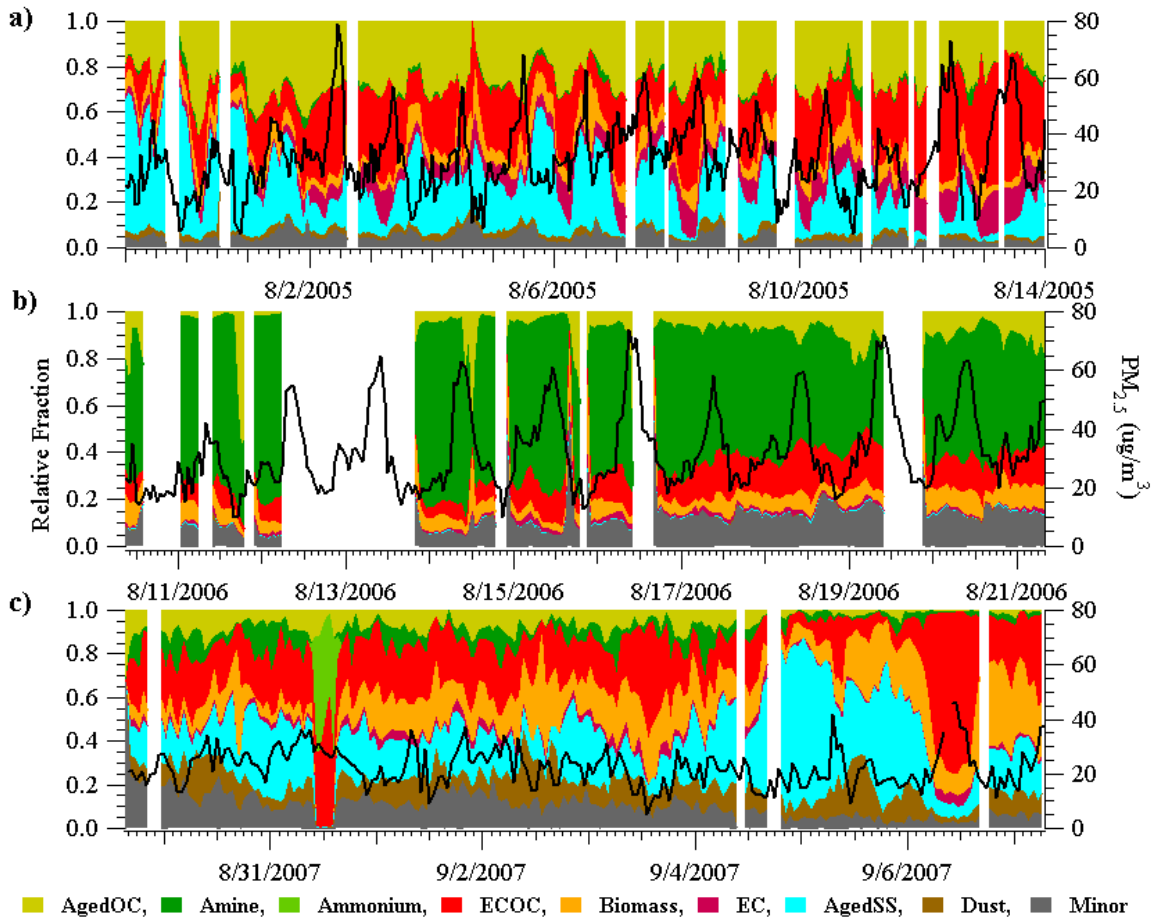


Figure 51: Temporally-resolved submicron particle chemistry from a) 2005, b) 2006, and c) 2007. Hourly $PM_{2.5}$ mass concentrations are also plotted for each year (black line).

The temporal profiles of these particle types also show distinct differences in the relative number fractions due to the diverse meteorology each year (Supplementary Material). However, almost everyday each year a pattern exists between $PM_{2.5}$ and the relative fraction of ECOC particle types, which follow very similar temporal profiles. While organics are linked to respiratory and cardiovascular problems, EC has been shown to cause respiratory problems such as chronic bronchitis, sputum, and coughing (233). The ECOC type is from the aging of EC after it has been emitted from combustion sources. ECOC is also a large number fraction of the total particle counts, equaling 29%, 13%, and 31% in 2005, 2006, and 2007, respectively. **Figure 51** shows temporally-resolved profiles of $PM_{2.5}$ mass concentrations and relative number fraction of the ECOC-type particles. In 2005 and 2007, these fractions are the highest of all particle types and in 2006 the fraction is the second highest after amines. Because ECOC largely contributes to particle number each year, this could be why it greatly influences $PM_{2.5}$ concentrations. There are days where this pattern does not exist, predominantly in 2007. This could be due to the particles from Santa Ana influences, increasing the dust fraction which contributes to the mass instead, such as on August 3, 2007 where ECOC peaks and the $PM_{2.5}$ mass concentrations fall. Also, AgedSS and dust fractions fall during this day,

suggesting that these particle types contribute to mass concentrations more than other types of particles that day.

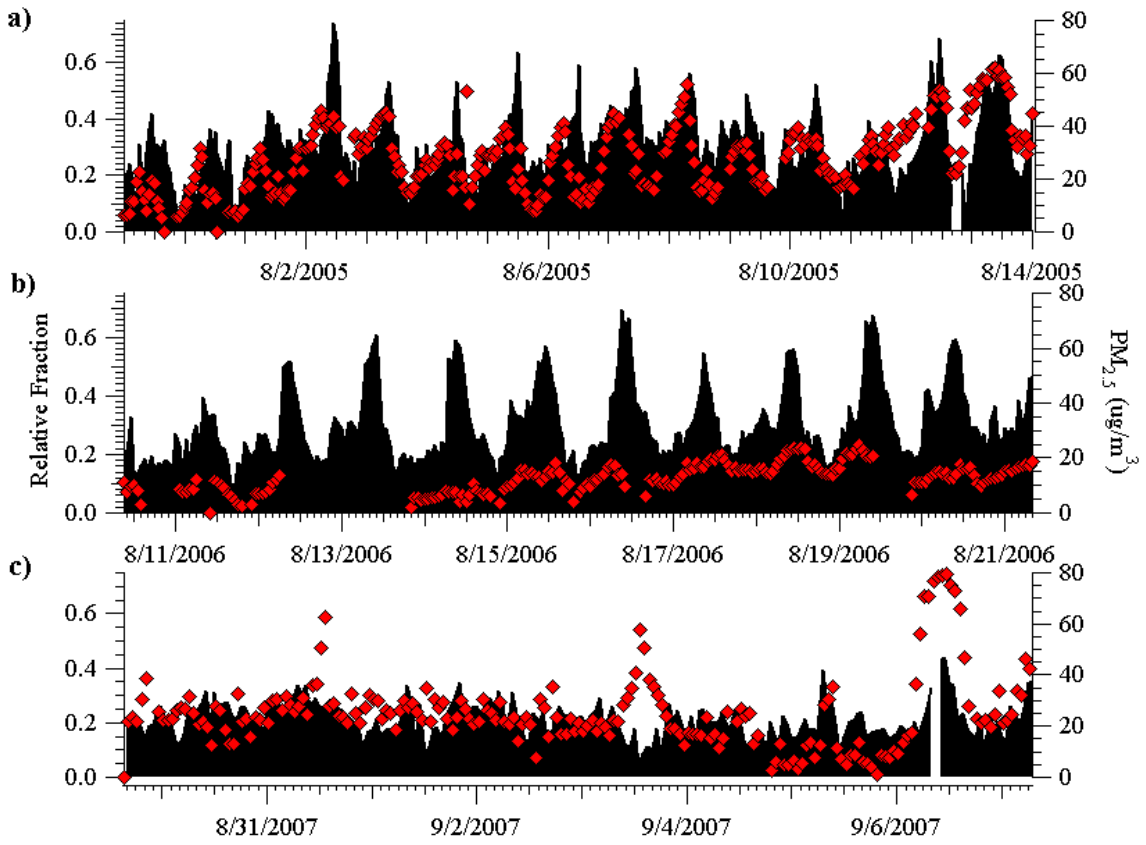


Figure 52: Temporally-resolved relative number fraction of ECOC particle types (red diamonds) from a) 2005, b) 2006, and c) 2007. The black shaded regions are the $PM_{2.5}$ mass concentrations for each year.

**Figure 53** shows the size-resolved submicron particle chemistry in Riverside, CA during the three studies of a) 2005, b) 2006, and c) 2007. Similar to the temporally resolved profiles, 2005 showed more evidence of an aged organic atmosphere over the entire submicron size range with larger fractions of the total number of particles being AgedOC and ECOC types and very little fractions of biomass, amines, and inorganics such as dust and AgedSS. In 2006, the high relative humidity and low temperature atmosphere correlated to the presence of a large fraction of amine-containing particle types over the entire submicron size range, with smaller fractions of AgedOC, ECOC, biomass, and inorganic types. The Santa Ana conditions in 2007 led to an increase in the dust fraction, while AgedSS was also present in a high fraction. Organic types (AgedOC, ECOC, biomass, and amines) were smaller fractions than the previous years. Dust was present over the entire size range, while AgedSS was predominant at larger sizes (> 600 nm).

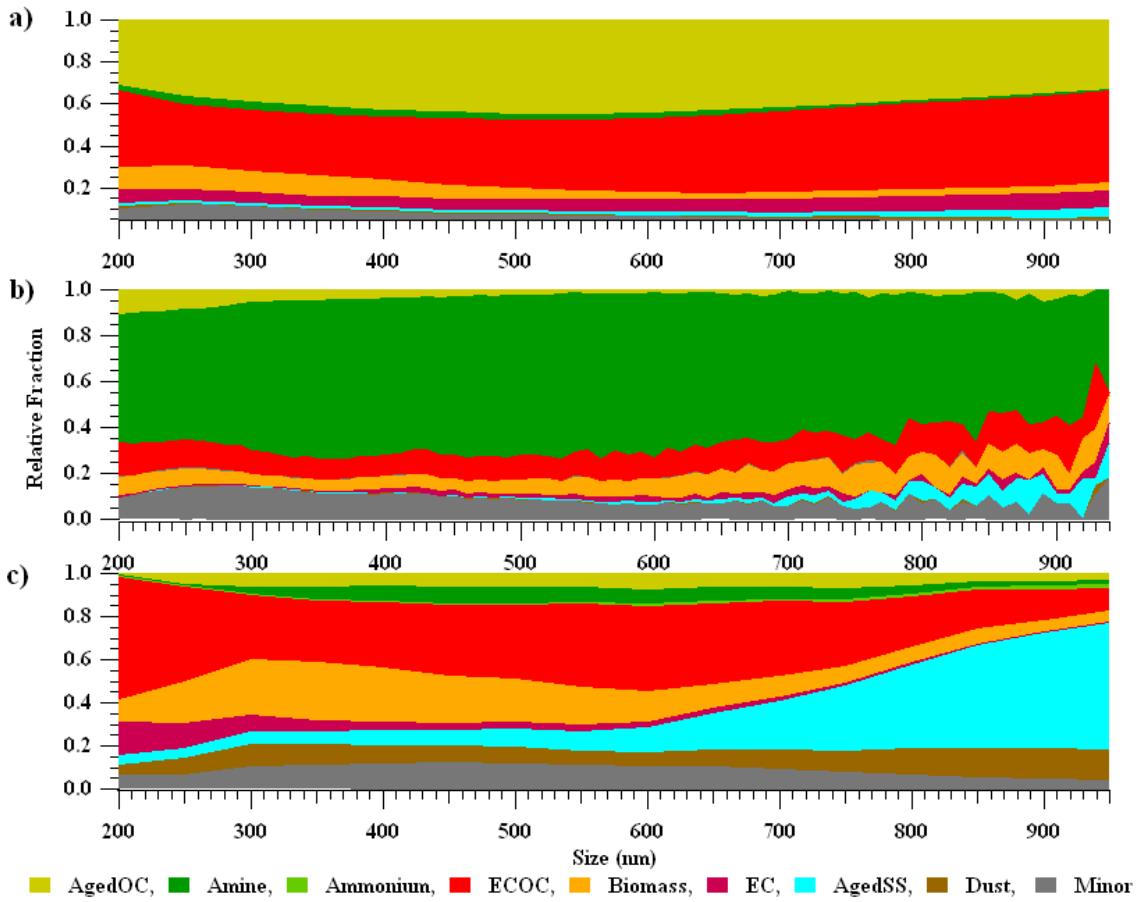


Figure 53: Size resolved submicron particle chemistry in Riverside, CA.

Although inter-annual similarities exist with the relationship between ECOC and $PM_{2.5}$ mass concentrations, the aging of the ECOC types differ each year as seen in **Figure 49**, meaning these particles could have different physical properties, levels of toxicity, and health effects. As mentioned throughout this manuscript, 2005 was a highly-aged atmosphere because of high $O_3$ levels, while 2006 contained an amine-rich environment because of high RH, and 2007 was highly variable with high T because of Santa Anas. This points out that diverse agconditions affect differences in ECOC each year: 2005 ECOC types were mostly aged with oxidized OC (88% of the total ECOC-type particles), 2006 ECOC were mostly aged with secondary amines (87% of the total ECOC-type particles), while in 2007 ECOC types were mainly aged with nitrate (39% of the total ECOC-type particles). Also, along with $PM_{2.5}$ as discussed earlier, the temporal profiles of ECOC become less diurnal because the WS became less diurnal.

**iv. Conclusions**

Using ATOFMS, ambient submicron single-particle chemical composition was examined in Riverside, CA over the course of three summers from 2005-2007. Meteorological factors such as T, RH, WS, and $O_3$ concentrations affected overall particle chemistry and thus $PM_{2.5}$ mass concentrations. In 2005, diurnal profiles of the WS and AMBTs from similar sources led to a very consistent, diurnal profile in $PM_{2.5}$.

$O_3$ levels were highest in 2005, leading to more aged organic species. 2006 was the moistest year with the lowest average T, leading to more amines versus 2005 and 2007. Santa Anas in 2007 led to high average T and inconsistent WS and AMBTs, which also caused variation in the particle chemistry and $PM_{2.5}$ mass concentrations due to transport from different sources. Besides aging with nitrate each year, particle mixing states were extremely different, with 2005 and 2006 having a higher fraction of organic-containing particles (AgedOC and amines, respectively) aged with secondary species and 2007 having larger fractions of AgedSS and dust aged with secondary species, although organic-containing particles were still highly aged. It is important to consider number and relative amount of secondary species in single-particle mixing states because it can lead to more specific insight on source, on how a particle is altered after emission into the atmosphere, and what sort of adverse health effects are associated with it.

The major particle types varied all three years as shown by the time-resolved chemistry, but evident each year was a similar temporal pattern between the fraction of ECOC-type particles and $PM_{2.5}$ mass concentrations. This suggests that ECOC types are a large contributor to particulate mass concentrations and inhaling these particles can cause acute and chronic respiratory problems. However, this pattern does not exist everyday, meaning other species still contribute to mass and are important to consider.

In general, it cannot be assumed that particle chemistry only seasonally fluctuates with similar particle mixing states and concentrations every year. Variation in particle quantity ($PM_{2.5}$ mass concentrations) and quality (chemical mixing state) exists due to differences in meteorology on top of emissions from different sources year-to-year. Looking at single-particle mixing state can provide more detailed information on what types of particles are contributing to $PM_{2.5}$. However, understanding how a single particle can chemically change with meteorology cannot be based on one major study to represent all years, particularly in a model that relates $PM_{2.5}$ concentrations with adverse health effects such as generalized additive models. Evident from these three studies, each year has very different meteorology which could be used to optimize parameters in health models and therefore improve pollution regulations. Since continuous intensive particle measurements are difficult long-term, the optimized parameters can be used in models to predict how $PM_{2.5}$ changes and what implications it would have on health during a specific type of meteorological condition. In the future, these results could be used as a first approximation as to what the detailed chemical composition of $PM_{2.5}$ may be and therefore generate stricter pollution regulations based on better-defined health effects models.

## v. Acknowledgements

We acknowledge Prof. Paul Ziemann (UCR), the UCR Air Pollution Research Center, and the Prather group, particularly Laura Shields and Hiroshi Furutani for support during SOAR. We thank Megan McKay and the Goldstein group (UC-Berkeley) for the meteorological measurements in 2005. Air mass back trajectories were produced with the Hybrid Single-Particle Lagrangian Integrated Trajectory model (NOAA). This work was supported by the California Air Resources Board (CARB 04-336) and the National Science Foundation (NSF ATM-0321362). K. Pratt has been supported by a NSF Graduate Research Fellowship and in part by an EPA STAR Graduate Fellowship (2006-

2009); the EPA has not officially endorsed this publication, and the views expressed herein may not reflect the views of the EPA.

# Mass Comparisons and Investigations into the Volatile and Semivolatile Fraction of Particles

## 7. Comparison of Two Methods for Obtaining Quantitative Mass Concentrations from Aerosol Time-of-Flight Mass Spectrometry Measurements

### i. Introduction

Over the past two decades, the number of studies on airborne particulate matter has increased substantially due to increased awareness of the role of aerosols in reducing visibility, affecting climate change, and endangering human health (141,143,234-238). Health risks have been shown for particles with aerodynamic diameters less than 2.5 μm ($PM_{2.5}$), based on mortality rates which show a positive correlation with particles in this size range (239). Therefore, it is very important to perform regional-scale long term monitoring in order to better understand the major sources impacting the annual $PM_{2.5}$ mass concentrations.

Although traditional off-line filter based measurements are able to provide robust information on aerosol mass concentration and chemical composition, they still have limitations such as low time resolution, sampling artifacts (240), and very limited information on aerosol mixing state which is essential for understanding the impacts of aerosols on climate and visibility (241). Real-time single particle mass spectrometry (SPMS) measurements provide continuous on-line information on single particle size and chemical composition (242-244). These measurements can be used to provide further insight into the associations between chemical species within individual particles, allowing one to link composition with specific sources and atmospheric processing. Particles are rapidly analyzed (<1 ms), minimizing the changes in particle morphology and the repartitioning of chemical species during the analysis. Despite these advantages, it has been a challenge for real-time SPMS instruments to provide quantitative information on aerosol mass concentrations. Several factors present obstacles in quantifying SPMS measurements. First, particle transmission efficiency is size-dependent and needs to be corrected using number concentrations from other co-located instruments (173). Second, in most real-time SPMS methods, the ion signals in the mass spectra for identical particles can vary considerably from shot-to-shot due to inhomogeneities in the laser beam (245). Third, instrument sensitivities to different aerosol chemical species vary (161,246), and can change as a function of matrix composition (247) and particle size (85). Fourth, when instrument operation and data acquisition are controlled by the same computer, the ability to detect incoming particles decreases with increasing ambient particle concentration due to instrument busy time (248).

Due to the aforementioned issues, the quantitative potential of SPMS measurements has not been fully realized. A number of efforts have been dedicated to acquiring high temporal resolution quantitative information from SPMS data by scaling with co-located reference measurements (30,36,85,248-251). Among the various SPMS instruments developed to date, most of the quantification efforts have been applied to

aerosol time-of-flight mass spectrometry (ATOFMS), which acquires real-time information on single particle aerodynamic diameter ($D_a$) and chemical composition. Although ATOFMS measures $D_a$, only Allen et al. (248,249), Bhave et al. (85), and Moffet et al. (251) used $D_a$-based reference measurements to reconstruct quantitative results from ATOFMS data. Allen et al. (248,249) and Bhave et al. (85) used a micro-orifice uniform deposit impactor (MOUDI) as the reference method for quantification. Typical MOUDI measurements have a time resolution of 5 ~ 8 hours and a size resolution of 4 bins per decade. Moffet et al. (251) compared ATOFMS measurements against aerodynamic particle sizer (APS) measurements, which provide higher time and size resolution than the MOUDI, to obtain quantitative number concentrations.

In this paper, we compare both MOUDI scaling and APS scaling methods to quantify ATOFMS single particle measurements taken during a field campaign conducted in central California. We adapt the busy-time estimation methodology of Allen et al. (248) to account for recent changes in the ATOFMS data acquisition procedure. We advance the APS scaling methodology of Moffet et al. (251) by utilizing composition dependent density values to obtain quantitative mass concentrations. We present the first evaluation of scaled ATOFMS mass concentrations against multiple, independent co-located $PM_{2.5}$ measurement devices. These scaling approaches will be used for future ambient studies to obtain quantitative ATOFMS mass concentrations and can be easily applied to other SPMS measurements.

**ii. Experimental**

As part of the California Regional Particulate Air Quality Study (CRPAQS), two ATOFMS instruments were operated continuously, sampling ambient aerosols from November 30, 2000 to February 4, 2001. The two sampling sites were an urban site in Fresno and a rural site in Angiola, both of which are located in central California (252). Single particle size and chemical composition information on more than 2 million particles was acquired at each site. ATOFMS data are scaled with MOUDI (MSP Corp.) measurements at Fresno and with APS (TSI 3320) measurements at Angiola to obtain quantitative information. Other $PM_{2.5}$ measurements are also used for comparison and evaluation, including a beta attenuation monitor (BAM, Met One BAM 1020), tapered element oscillating microbalance (TEOM, Rupprecht & Patashnick TEOM 1400A), dust aerosol monitor (TSI DustTrak 8520), nephelometer (Radiance Research M903), and aethalometer (Magee Scientific RTAA1000). Only the measurements taken from January 9, 2001 to February 4, 2001 are presented in this work, representing 711,289 particles in Fresno and 614,915 particles in Angiola.

***a. ATOFMS Data Acquisition***

ATOFMS acquires single particle diameter utilizing particle time-of-flight and obtains particle chemical composition based on the mass spectra. The design and operating principles of ATOFMS have been described in section 1.5.1 and are also discussed in detail elsewhere (127). Not all particles that are sized produce a corresponding mass spectrum, due to differences in the particle trajectories between the light scattering and ion source regions. Particles that produce both aerodynamic diameters and mass spectra are called hit particles, whereas particles that only yield aerodynamic diameters are called missed particles. A special ATOFMS operating

condition is the fast scatter mode. When operating under this condition, ATOFMS only records missed particle size information without attempting to acquire mass spectra. Fast scatter measurements were often used for obtaining overall particle size distribution.

After the field study, an in-house software program was used to calibrate the mass spectra and make a list of the individual ion peaks for each particle. These peak lists were then imported into a single particle mass spectrometry data analysis tool YAADA, for further analysis (160).

### *b. MOUDI Measurements*

The MOUDI is based on particle impaction and has been extensively used for obtaining size resolved particle mass and composition measurements (253). During the CRPAQS study, MOUDI data were collected at Fresno during six intensive operating periods (IOPs) within the time of interest for this study: 31 January 1000-1600; 1 February 0500-1000; 2 February 0000-0500; 2 February 1000-1600; 3 February 0500-1000; and 3 February 1600-2400. Angiola MOUDI measurements were not used in this study since we were unable to accurately estimate ATOFMS busy time at that site due to a change in the data acquisition hardware in the middle of the study period.

### *c. APS Measurements*

The APS provides information on both single particle number concentrations and aerodynamic diameter via light scattering and time-of-flight measurements (254). It detects particles in the size range of 0.3 μm to 20 μm, with accurate size-resolved counting of particles with aerodynamic diameters between 0.5 and 20 μm. APS measurements were not collected at Fresno during the CRPAQS. At Angiola, measurements were obtained with a commercial APS (TSI 3320, Minnesota) from December 1, 2000 to February 4, 2001 with a temporal resolution of 5 minutes. The APS data were averaged over 1-hour time periods. These hourly data are used in the scaling procedure described below

## iii. Results and Discussion

### *a. Scaling with MOUDI*

Previous investigations have shown that by comparing co-located ATOFMS and MOUDI data, quantitative information on particle mass concentrations can be acquired from ATOFMS measurements (248,249). The advantage of scaling with MOUDI measurements is that they not only provide information on size segregated total particle mass concentrations, but also the size segregated concentrations of individual chemical species which allow the derivation of ATOFMS relative sensitivity factors to different chemical species (85). The disadvantage is that MOUDI samples are analyzed offline and provide coarse temporal- and size-resolution data. In this work, we adapt and modify the busy time estimation method developed by Allen et al. (248) and use it to scale the Fresno ATOFMS dataset with MOUDI measurements.

#### 1. ATOFMS Busy Time

Busy time ($t_b$) is defined as the amount of time that an ATOFMS instrument cannot detect incoming particles because it is busy processing data from a particle that just arrived. Previous studies revealed that three parameters are needed to compute ATOFMS instrument busy time: the time required to record a missed particle (*A*), the time required to record the first hit particle in a folder (*B*), and the incremental increase in time required to save each subsequent hit particle in a folder (*C*). Laboratory experiments have been conducted to estimate these parameters, but when lab-based parameters are applied to field data, the results are at times not physically meaningful (e.g., busy time occasionally exceeds total sampling time). Thus, empirical methods have been developed to estimate busy time directly from field data. During the 1999 Bakersfield Instrument Intercomparison Study (BIIS), the ATOFMS instrument was operated alternately in normal data collection mode and fast scatter mode. Allen et al. (248) used data collected in fast scatter mode to estimate particle arrival rates ($\lambda$). They demonstrated that Poisson with Busy Time (PBT) distributions in conjunction with $\lambda$ values can be used to compute *A*, and that this information in combination with the particle data collected in normal operating mode can be used to compute *B* and *C*.

During CRPAQS and subsequent field campaigns, ATOFMS instruments were not routinely operated in fast scatter mode so the methodology of Allen et al. (248) cannot be applied directly. In the present study, we adapt the previous methodology to estimate busy time parameters for the ATOFMS instrument that was stationed at Fresno. An analysis of the Fresno data set reveals five discrete time periods when the rate of missed particle detection ($r_m$) doubled while the hit particle detection rate ($r_h$) dropped substantially: 16 January 2150 – 17 January 0200; 28 January 0335 – 1115; 31 January 0430 – 0845; 1 February 0750 – 1040; and 2 February 0610 – 1000. As an example, **Figure 54** illustrates the time series of $r_m$ and $r_h$ in 6-minute intervals throughout 28 January. Several possible reasons for these "high-miss periods" were explored, but a definitive conclusion was not obtained. Nevertheless, even without a full understanding, it was determined that the data from these high-miss periods may be exploited to calculate *A*. The strong anti-correlations between $r_m$ and $r_h$ suggest that the busy time associated with missed particles caused the hit rate to drop during each high-miss period. Assuming that the degree to which $r_h$ drops during the high-miss periods is determined by the time remaining to record hit particles after all missed particles are recorded,

$$\frac{N_{Hit}}{N_{EstHit}} = \frac{t - (A \cdot N_{Missed})}{t - (A \cdot N_{EstMissed})} \tag{5.1}$$

where *t* is the length of each sampling interval; $N_{Hit}$ and $N_{Missed}$ are the number of hit and missed particles recorded during a sampling interval; and $N_{EstHit}$ and $N_{EstMissed}$ are the estimated number of hit and missed particles if the high-miss event had not occurred. As illustrated in **Figure 54a**, $N_{EstHit}$ and $N_{EstMissed}$ are calculated in 6-minute intervals by linear interpolation of $r_h$ and $r_m$, respectively, over each high-miss period. By solving

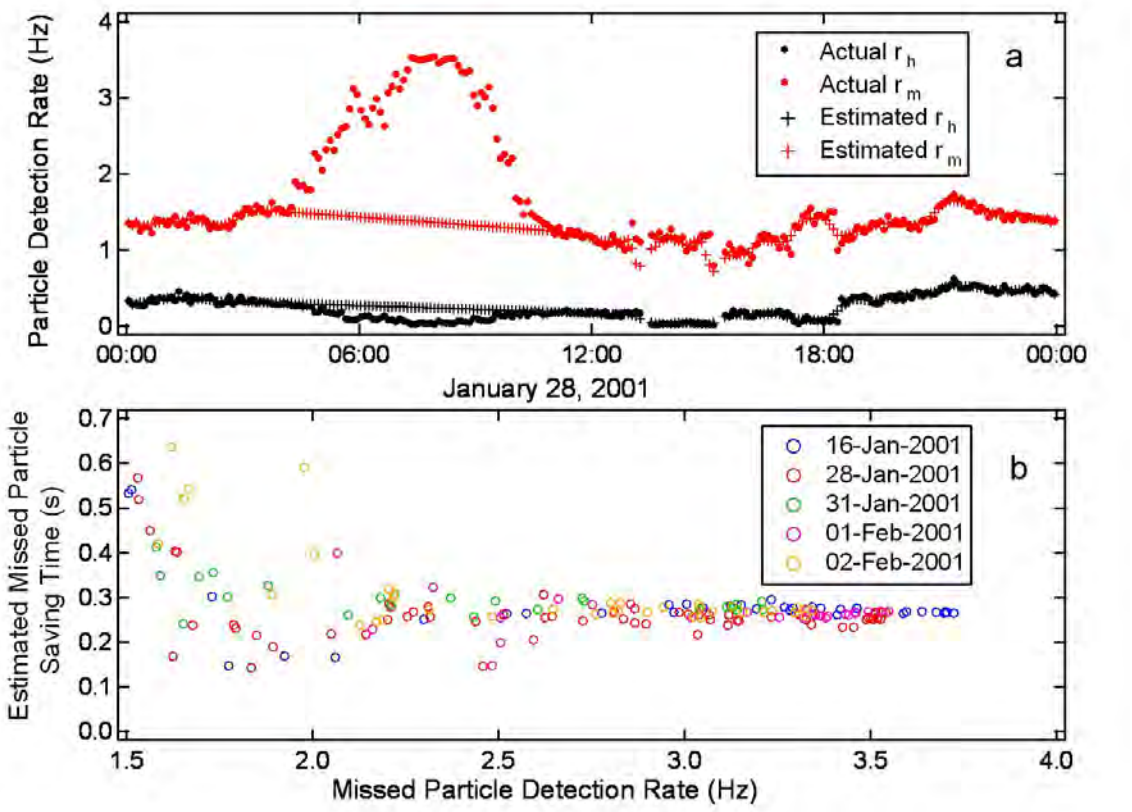


Figure 54: (a) Linear interpolation over the Fresno high-miss period to obtain estimated hit counts and estimated missed counts for the period of January 28th, 3:35 – 11:15; (b) estimated missed particle recording time vs. missed particle detection rate for all five high-miss periods with a time resolution of 6 minutes for Fresno dataset.

Equation (5.1) for A, we obtain:

$$A = \frac{t \cdot \left(N_{Hit} - N_{EstHit}\right)}{\left(N_{Hit} \cdot N_{EstMissed}\right) - \left(N_{EstHit} \cdot N_{Missed}\right)} \tag{5.2}$$

The values of $A$ calculated during 6-minute time intervals within each high-miss period are plotted against $r_m$ in **Figure 54b**. The five different colors in **Figure 54b** represent results from different high-miss periods. As can be seen, there is remarkable consistency in the values of $A$ across all five high-miss periods when $r_m$ exceeds 2.5 Hz. These time intervals occurred at the peak of each high-miss period, when the instrument was devoting the vast majority of the sampling time to detecting missed particles. Thus, the $A$ values calculated during these times are most robust. Whether setting the minimum $r_m$ thresholds at 2.0, 2.5, 3.0, or 3.5 Hz, the mean value of $A$ remains fairly constant at 0.26 seconds with the standard deviation being less than 0.05 seconds. Based on the above inspection, we use 3.0 Hz as the minimum $r_m$ threshold since at this frequency, $A$ values are quite robust and some data from all five high-miss periods are included. We therefore conclude that $A = 0.264 \pm 0.013$ s. Note that the standard deviation is less than 5% of the mean $A$ value.

PBT distributions using $A$ = 0.264 are used to estimate λ throughout the study period by following the procedure of Allen et al. in reverse order (248). Excluding the "high-miss periods" when the application of PBT distributions is not justified, hourly λ values range between 0.11 Hz and 15.1 Hz, with an average of 3.5 Hz. The best-fit $B$ and $C$ values are also calculated according to Allen et al. (248), but the C value is not statistically significant due to smaller folder limits used during CRPAQS (500 spectra per folder) relative to the BIIS (1000). We use our best-fit $B$ value of 0.264 s, and a $C$ value of 0.00024 s taken from laboratory experiments conducted under similar conditions (H. Furutani, Personal Communication). The difference between the $A$ values from this study and previous studies is attributed to a change in the ATOFMS data acquisition mode. ATOFMS can be operated in either non-wide dynamic range (non-WDR) or wide dynamic range (WDR) data acquisition mode (255). When connecting two identical digitizers via a signal splitter to the signal source and attenuating one digitizer (30 db), WDR mass spectra (signal level ranging from 0 to 8000 instead of 0 to 255) can be obtained by combining the two signals (256). Although operating ATOFMS in WDR mode produces mass spectra with a much greater dynamic range, it requires significant computer time and significantly increases both the $A$ and $B$ values. During the current study, WDR spectra were acquired for positive ions, leading to a value of $A$ that is higher than that in previous work when only non-WDR spectra were acquired (248). The lab experiments also support our conclusion that $A$ and $B$ are comparable when operating in WDR mode, since the most time-consuming process in obtaining single particle data is the data transfer from the acquisition board to the computer; the actual data saving time represents only a minor fraction of the data transfer process.

**2. Scaling of ATOFMS Measurements with MOUDI Measurements**

Scaled mass concentrations are calculated based on the effective sampling duration which excludes instrument busy time and offline periods. After obtaining ATOFMS busy time parameters, ATOFMS hit and missed particle information was processed for comparison with the MOUDI measurements. Hit particles were binned into size and time bins matching the MOUDI data. The MOUDI size bins are: 0.18 – 0.32, 0.32 – 0.56, 0.56 – 1.00, and 1.00 – 2.50 μm. The time frame is limited to the six MOUDI IOPs listed above. A total of 24 time-size bins are considered in the comparison, but data from two bins are excluded from the scaling procedure for the following reasons: (a) the MOUDI mass concentration was less than twice the mass uncertainty in the 1.00-2.50 μm bin on 31 January 1000 – 1600, indicating high uncertainty in the MOUDI measurement; and (b) the total number of hit particles by ATOFMS in the 0.18-0.32 μm bin on 1 February 0500 – 1000 was less than 100, which is deemed too few for a statistically representative measurement. Ultimately, mass concentrations in 22 bins were compared for quantitative analysis. Single particle sizes and counts were collected for each bin within the specified size range and time range. Using the measured flow rate through the instrument, an ATOFMS total particle mass concentration was calculated for each bin assuming all the particles were spherical. Morawska and coworkers obtained an overall average ambient submicron particle density of 1.7 $g \cdot cm^{-3}$ (257). The average density of supermicron particles would be even higher due to the increased fraction of sea salt and dust particles which have densities of 1.9 $g \cdot cm^{-3}$ and 2.7 $g \cdot cm^{-3}$, as reported by Hänel and Thudlum (258). Thus we use a density of

1.9 g·cm$^{-3}$ for all $PM_{2.5}$ particles in mass concentration calculation instead of the 1.3 g·cm$^{-3}$ value used in previous work (85,154,248,249). The scaling factor, $\phi_{MOUDI}$, was constructed as the parameter to compensate for the difference between ATOFMS and MOUDI measurements. $\phi_{MOUDI}$ represents the inverse of the ATOFMS

particle detection efficiency and is defined with the following expression:

$$\phi_{MOUDI} = \frac{m_{MOUDI}}{m_{ATOFMS}} \tag{5.3}$$

where $m_{MOUDI}$ is MOUDI mass concentration, and $m_{ATOFMS}$ is ATOFMS mass concentration before scaling. $\phi_{MOUDI}$ is a function of particle size and can be expressed with a power law relationship with $D_a$:

$$\phi_{MOUDI} = \alpha \cdot D_a^{\beta} \tag{5.4}$$

where α and β are the best-fit parameters determined by non-linear regression of $m_{MOUDI}$ on $m_{ATOFMS}$ over all 22 bins. Physically, 1/α is the particle detection efficiency for a 1.0 μm particle and β represents the degree to which particles with sub-optimal sizes are deflected from the centerline in the ATOFMS inlet. Based on Equation (5.4), it is clear that varying the density value will not affect the scaled results; only the scaling parameters will change. The best-fit values of α and β are 1747.52 ± 363.96 and−4.41 ± 0.28 for this study, so $\phi_{MOUDI}$ varies from $3.4\times10^6$ for a 0.18 μm particle to 31 for a 2.5 μm particle.

Upon obtaining α and β, the value of $\phi_{MOUDI}$ was calculated for every single particle using Equation (5.4) based on the measured particle diameters by ATOFMS. The following equation was used to calculate scaled ATOFMS mass concentrations:

$$m_{ATOFMS-MOUDI} = \sum_i \phi_{Da,i} \cdot m_i \tag{5.5}$$

where $m_{ATOFMS\text{-}MOUDI}$ is the ATOFMS mass concentration after scaling with MOUDI, ϕ and $m_i$ are the scaling factors and mass concentrations for each single particle respectively. Comparison of the scaled ATOFMS and the MOUDI mass concentrations for all 22 bins results in an $R^2$ value of 0.85 as shown in **Figure 55**, indicating that two parameters (α and β) are sufficient to explain 85% of the variability in ATOFMS transmission efficiencies over the 0.18 – 2.5 μm $D_a$ range during 6 different IOPs. It is important to note that the high $R^2$ value would not have been obtained if busy-time corrections had not been applied. Note the mass concentrations for the non-IOP periods can be calculated with the same scaling function at higher temporal resolution (1 hour) if one assumes that the ATOFMS scaling factors do not change over time. There is some uncertainty associated with this assumption, so scaling with real-time particle concentration measurements may be favorable for obtaining total mass concentrations as described in the next section.

**3. Comparison between MOUDI Scaled ATOFMS Measurements and BAM Measurements**

Both hourly BAM and hourly TEOM $PM_{2.5}$ mass measurements were made at the Fresno site. Because the TEOM inlet was heated to 50 ºC during sampling in order to remove interferences from water, other semivolatile compounds were also removed (259), yielding values that were systematically lower than the co-located BAM measurements by an average of 42%. Therefore, since ATOFMS does not remove water or semivolatile compounds to a significant extent due to short analysis times, hourly BAM mass concentration measurements ($m_{BAM}$) were chosen as the reference mass concentration to evaluate $m_{ATOFMS\text{-}MOUDI}$ for the entire study period as shown in

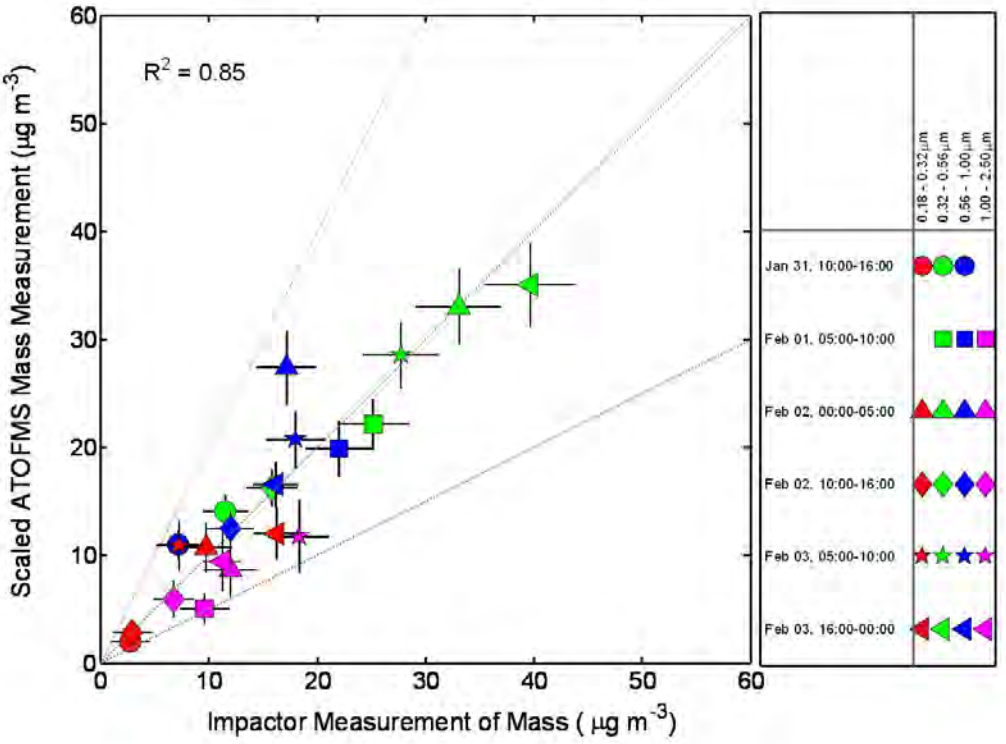


Figure 55: Comparison of scaled ATOFMS mass concentrations and MOUDI measurements in Fresno.

**Figure 56**. Both mass concentration measurements show distinct diurnal temporal variations, reaching maxima and minima at nearly the same time each day. Particulate matter concentrations remained relatively low during the day and increased substantially at night in Fresno during this study. The correlation between $m_{BAM}$ and $m_{ATOFMS\text{-}MOUDI}$ is notably high with a $R^2$ value of 0.79. However, **Figure 56** also shows that $m_{ATOFMS\text{-}MOUDI}$ is systematically lower (about 30% less) than $m_{BAM}$. The ratio of mean values between these two measurements is 0.69 over the 26-day sampling period of interest. Several factors account for this difference. First, particles below 0.20 μm are not included in the $m_{ATOFMS\text{-}MOUDI}$ value as this represents the lowest size detectable by the ATOFMS instrument used in this study. An analysis of the MOUDI data during the six IOPs of interest indicates that particles larger than 0.18 μm make up 86% of the total $PM_{2.5}$ mass summed over all impaction stages from 0 - 2.5 μm ($\Sigma m_{MOUDI}$). Second, the mean value

of $m_{MOUDI}$ during the six IOPs is only 88% of the mean value of $m_{BAM}$. These two factors alone make it so the value of $m_{ATOFMS\text{-}MOUDI}$ cannot exceed 76% of the $m_{BAM}$ value (0.86 × 0.88 = 0.76). Furthermore, the scaling function derived from the six IOPs most likely varied during the 26-day period. Thus, these factors result in the absolute values of $m_{ATOFMS\text{-}MOUDI}$ being 30% lower than the $m_{BAM}$ values.

### *b. Scaling with the APS*

#### 1. Scaling ATOFMS Measurements with APS Measurements

Another quantification approach involves comparison of the ATOFMS particle counts at Angiola with particle number concentrations acquired with a co-located APS. Although APS measurements are not able to provide mass concentrations of individual chemical species like the MOUDI, they can provide particle number concentrations with

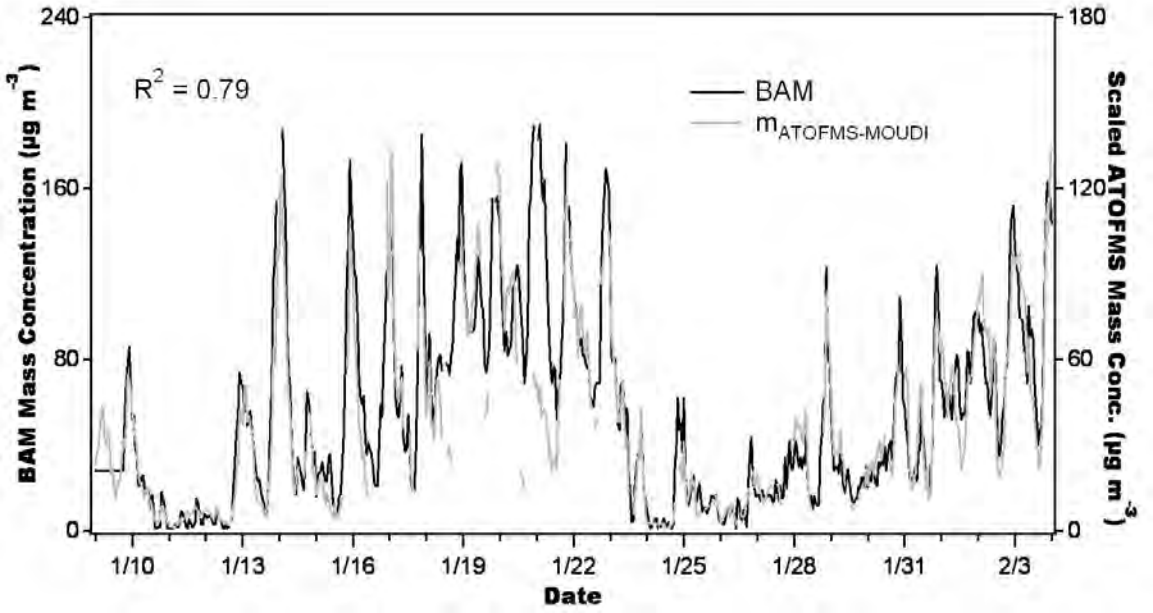


Figure 56: Temporal variation of hourly BAM and scaled ATOFMS PM2.5 mass concentrations in Fresno. The scaling function for the ATOFMS was obtained by comparison with MOUDI measurements.

very high temporal and size resolutions. This high resolution reference data can potentially provide more accurately scaled ATOFMS mass concentrations.

To scale the ATOFMS data with APS measurements, we follow an approach similar to the MOUDI scaling method by deriving scaling functions to correct for ATOFMS particle undercounting. To take advantage of the high time resolution properties of both measurements, one scaling function was constructed for each hour of the entire study period. Within each hour, single particle number counts collected by both ATOFMS and APS were segregated into 12 size ranges: 0.300-0.523, 0.523-0.605 μm, 0.605-0.699, 0.699-0.807, 0.807-0.933, 0.933-1.077, 1.077-1.243, 1.243-1.435, 1.435-1.655, 1.655-1.911, 1.911-2.207, and 2.207-2.547 μm. These size bins were adapted directly from the APS size bins by combining pairs of adjacent bins between 0.523 μm and 2.547 μm so that higher ATOFMS hit particle counts could be obtained for each bin. The smallest APS bin (0.300 - 0.523 μm) is also included in this calculation.

When the smallest APS bin is not used, the results do not change substantially from the 12 bin scaling discussed below. Since scaling is performed hourly, the factors that affect ATOFMS sampling, such as busy time and instrument offline time, are accounted for implicitly. The scaling factor, $\phi_{APS}$, is defined as the following:

$$\phi_{APS} = \frac{Count_{APS}}{Count_{ATOFMS}} \tag{5.6}$$

One scaling factor was acquired for each size bin with Equation (5.6) for each hour. Like the scaling factors used in MOUDI scaling, $\phi_{APS}$ is also size dependant. By plotting the scaling factors against $D_a$, a scaling curve can be constructed for particles with aerodynamic diameters below 2.5 μm. **Figure 57a** shows the hourly scaling curves for the ATOFMS instrument stationed at Angiola on February 3. The error bars are generally not significant except for those at 5:00 and 6:00 during which APS measurements showed variations. The instrument was offline between 13:00 and 14:00, and therefore no scaling curve for this time period is presented. In **Figure 57a**, we see that $\phi_{APS}$ varies substantially from hour to hour. In the largest size bin, this variation spans nearly one order of magnitude. Most of this variability results from differences in ambient particle concentrations leading to differences in instrument busy times (36). This result further emphasizes the importance of high time resolution (hourly) scaling. The scaling factors obtained with MOUDI measurements will not be as accurate as $\phi_{APS}$ due to the time and size resolution limit and will not be able to reflect short term ambient particle concentration changes. In general, the APS scaling curve reaches a minimum at 1.655 μm – 1.911 μm size bin (bin midpoint is 1.783 μm) due to the higher ATOFMS transmission efficiency of particles in this size range than others. Two scaling functions were obtained for each hour by fitting the scaling curve separately on each side of the minimum point. Examples of the fitting of the scaling curve are included in **Figure 57b** and **Figure 57c** for 22:00 on February 03, 2001. The scaling function for the size range of 1.783 μm and below was obtained by exponential regression and was extrapolated down to 0.2 μm to obtain the scaling factors for smaller particles in the mass concentration calculation. The scaling function for the size range above 1.783 μm was obtained by a 2$^{nd}$ order polynomial regression. Thus, each scaling function can be fully described with five parameters which are used to calculate $\phi_{APS}$ as shown in Equation (5.7):

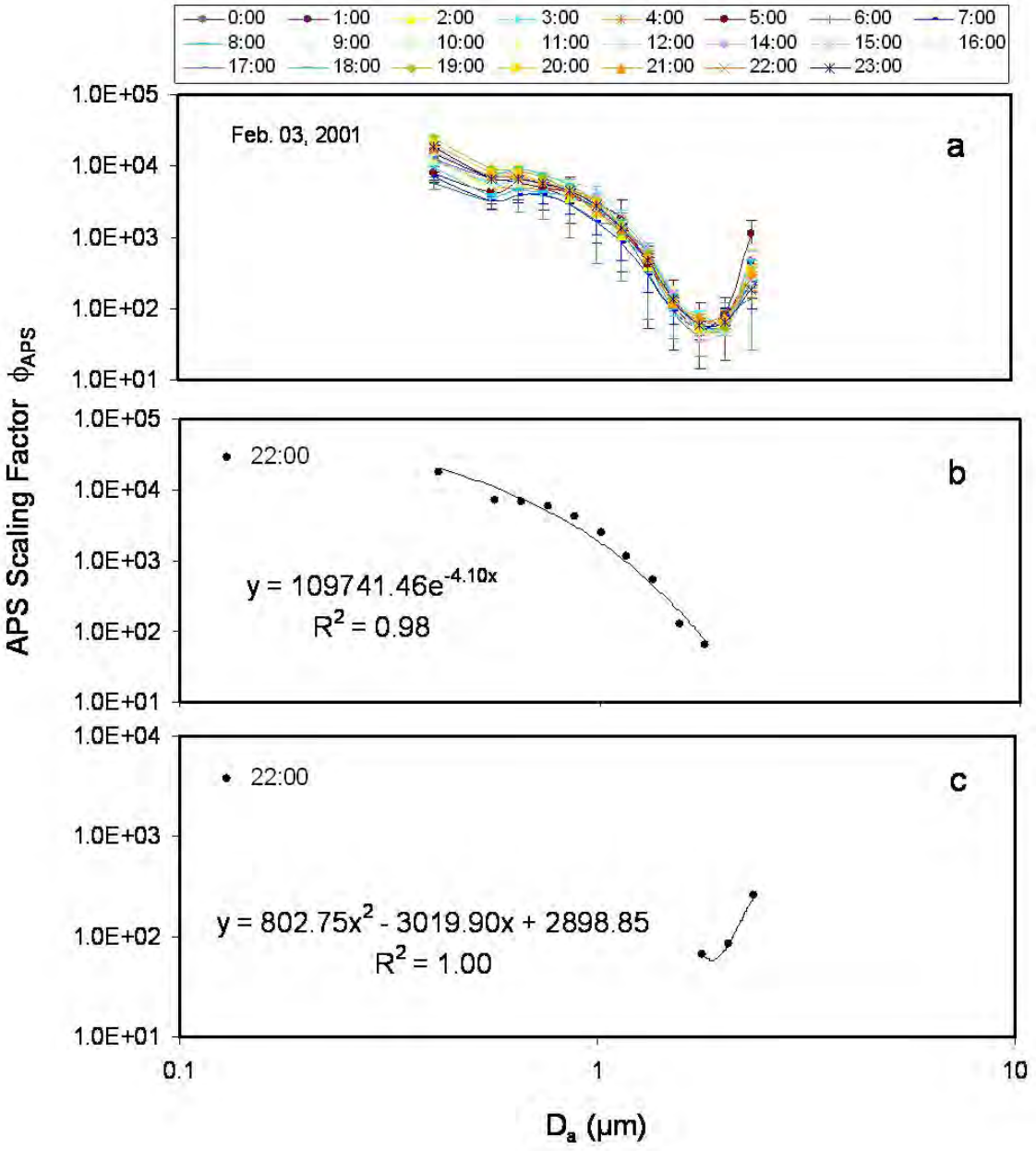


Figure 57: APS scaling curve for Angiola measurements. (a) hourly scaling curve for February 03, except for 13:00; (b) exponential regression of left half of scaling curve at 22:00; (c) polynomial regression of right half of scaling curve at 22:00

$$\phi_{APS} = \begin{cases} C_1 \cdot e^{C_2 \cdot D_a} & (when\ D_a < 1.783\ um) \\ C_3 \cdot {D_a}^2 + C_4 \cdot D_a + C_5 & (when\ D_a \geq 1.783\ um) \end{cases} \quad (5.7)$$

Five parameters were obtained for each hour of data collected at Angiola to correct ATOFMS measurements with APS measurements, generating number concentrations with 1 hour temporal resolution. The form of Equation (5.7) will allow a similar relationship to be applied other studies to obtain APS scaling factors.

With the scaling functions acquired, quantitative ATOFMS mass concentrations ($m_{ATOFMS\text{-}APS}$) were calculated. The $\phi_{APS}$ value for each particle can be obtained using the

$D_a$ measured and the time when the datum was acquired. $m_{ATOFMS\text{-}APS}$ is calculated with the following equation knowing the instrument nozzle flow rate and assuming particles are spherical:

$$m_{ATOFMS-APS} = \sum_i \frac{M(D_{a,i}) \cdot \phi_{APS}(D_{a,i})}{V_{ATOFMS}} \tag{5.8}$$

where $M(D_{a,i})$ is the mass of each particle and $V_{ATOFMS}$ is the volume of flow within each time period. Equation (5.8) makes it possible to construct quantitative particle mass concentration information for individual particle classes with any size and temporal resolution from ATOFMS measurements assuming no preferential transmission of certain particle classes. Unlike MOUDI scaling, $m_{ATOFMS\text{-}APS}$ is sensitive to assumed particle density values. Rather than assuming all particles have the same density, we may assign different density values to particles with different sizes or chemical compositions for improved estimates of the total mass concentration.

**2. Comparison between BAM Measurements and APS Scaled ATOFMS Mass Concentrations Obtained with Different Density Values**

The most straightforward approach to obtaining mass concentrations from ATOFMS data is to assign a single density value to all particles. **Figure 58a** shows the correlation between $m_{BAM}$ and $m_{ATOFMS\text{-}APS}$ when utilizing fixed density values of 1.8 $g \cdot cm^{-3}$, 1.9 $g \cdot cm^{-3}$, and 2.0 $g \cdot cm^{-3}$, respectively, for APS scaling. The slope of each regression represents the ratio of mean values between $m_{BAM}$ and $m_{ATOFMS\text{-}APS}$. The value for $m_{ATOFMS\text{-}APS}$ shows the best agreement with $m_{BAM}$ is obtained when utilizing a density of 1.9 $g \cdot cm^{-3}$ (shown in red in **Figure 58a**). The temporal variations of the above two mass concentrations are presented in **Figure 59**. They track each other extremely well with an $R^2$ value of 0.91. The Angiola aerosols were aged and dominated by carbonaceous aerosols with significant quantities of nitrate and ammonium associated with them. Based on ATOFMS chemical analysis, more than 80% of Angiola particles were aged carbonaceous particles. As particles age, they become more internally mixed aerosols composed of organic carbon, ammonium, nitrate, sulfate, and water, and in general, the particle-to-particle chemical variability decreases over time. Thus the good agreement between ATOFMS mass concentrations scaled with a single density and BAM measurements is most likely due to the chemical homogeneity of aged ambient aerosols. When applying the above method to scale ATOFMS measurements in a region where fresh emissions occur and many distinct particle types dominate, it is likely that applying one density value for all particles will not be sufficient.

Since ATOFMS measures the aerodynamic diameter of individual particle, it is possible to apply specific density values based on particle size. The unscaled ATOFMS

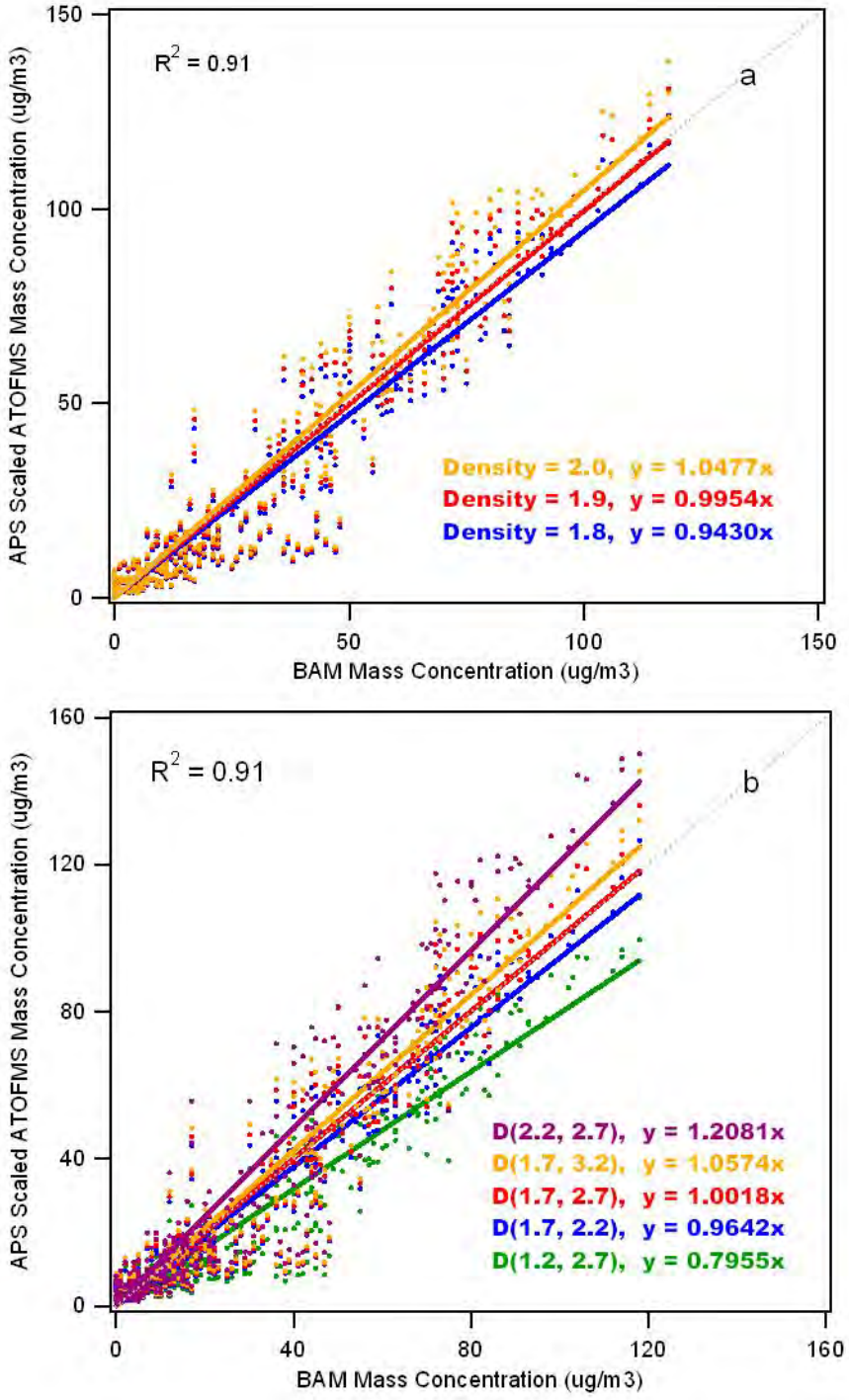


Figure 58: Correlations between BAM and APS scaled ATOFMS mass concentrations. (a) ATOFMS mass concentrations are obtained with single density (ρ) values for all particles (ρ = 1.8 g·cm$^{-3}$, ρ = 1.9 g·cm$^{-3}$, or ρ = 2.0 g·cm$^{-3}$); (b) ATOFMS mass concentrations are obtained with different density pairs for submicron and supermicron particles: 1.2 and 2.7 g·cm$^{-3}$, 1.7 and 2.2 g·cm$^{-3}$, 1.7 and 2.7 g·cm$^{-3}$, 1.7 and 3.2 g·cm$^{-3}$, and 2.2 and 2.7 g·cm$^{-3}$.

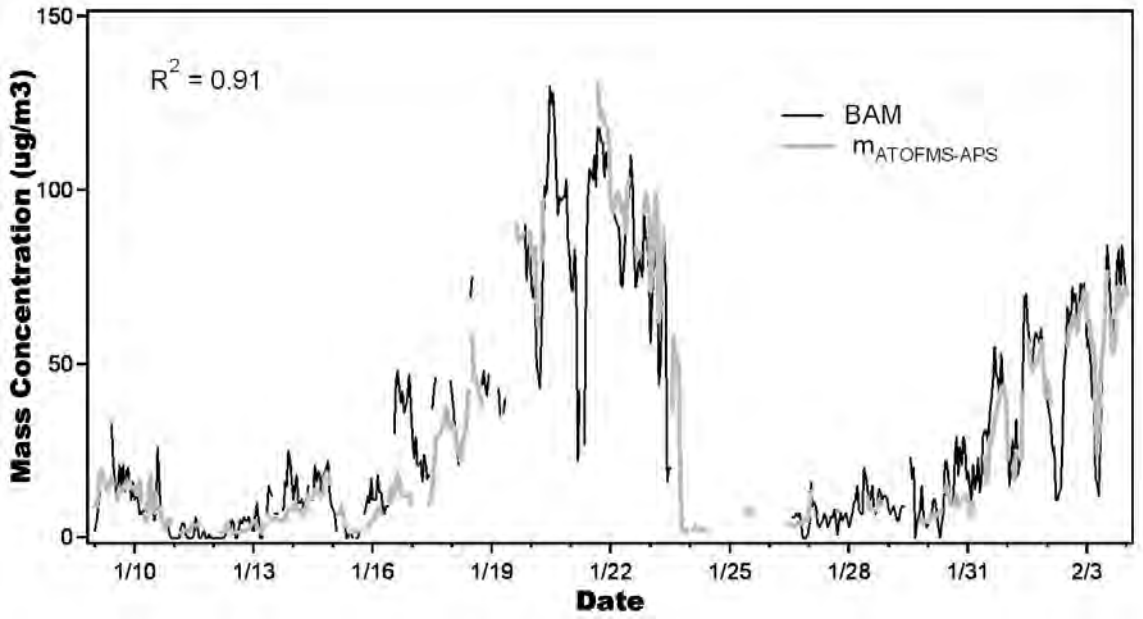


Figure 59: Temporal variation of Angiola particulate mass concentrations obtained with BAM and APS scaled ATOFMS ($\rho$ = 1.9 g·cm$^{-3}$).

ambient particle size distribution shows that particles smaller than 1.0 μm in aerodynamic diameter account for a large portion of total particle numbers in Angiola. ATOFMS chemical composition measurements have shown that particles smaller than 1.0 μm are mainly carbonaceous particles with associated secondary inorganic components, while the relative fraction of inorganic particles increases substantially above 1.0 μm (156). Thus we segregate particles into two size ranges: submicron (0.2 < Da < 1.0 μm) and supermicron (1.0 ≤ Da < 2.5 μm). We use literature value of 1.7 g·cm$^{-3}$ as the density for submicron particles (257), and 2.7 g·cm$^{-3}$ for supermicron particles, an intermediate value for the various chemical components reported in this size range (258). The scatter plot between $m_{ATOFMS\text{-}APS}$ acquired with this pair of density values and $m_{BAM}$ is included in **Figure 58b** (in red). Scaled ATOFMS and BAM mass concentrations track each other very well with a high correlation coefficient of 0.91. The absolute values are quite close to one another and nearly on top of the 1:1 line. We also varied the densities by 0.5 g·cm$^{-3}$ in both directions for the sub- and super-micron particles separately. The correlations between each of these density pairs with the BAM measurements are also included in **Figure 58b**. The correlation values remain high ($R^2$ ~ 0.91) in all cases and only the ratios between $m_{ATOFMS\text{-}APS}$ and $m_{BAM}$ are different. From the change in slope it is apparent that the total scaled ATOFMS mass concentrations are more sensitive to the submicron particle density than the supermicron particle density. This is due to the fact that the majority of the Angiola particle mass is in the submicron size mode.

We can go beyond just using size information and utilize chemically specific density values applied to each different particle type to obtain scaled ATOFMS mass concentrations. To convert from number to mass concentrations, we used the density value of 1.9 g·cm$^{-3}$ for carbonaceous particles, 2.7 g·cm$^{-3}$ for dust particles, 1.9 g·cm$^{-3}$ for Na rich salt particles, 2.0 g·cm$^{-3}$ for biomass emission particles and EC rich particles, and 1.9 g·cm$^{-3}$ for the rest of the particle types (258,260,261). The multi-density scaled

ATOFMS mass concentrations also show a strong and very similar correlation with BAM measurements with a high $R^2$ of 0.91. As discussed earlier in this section, the advantages of utilizing various density values for each chemical composition are not fully realized in this particular study due to the fact that Angiola ambient particles are aged and thus very chemically homogeneous. In regions or seasons with more fresh emissions, it will most likely become necessary to assign chemically specific density values for individual particle types. Additional lab and field investigations are underway to develop universal scaling factors that use specific density and shape factors for each particle type.

### *c. $PM_{2.5}$ Measurement Intercomparison*

A number of different continuous particle measurements were available in both Fresno and Angiola during the CRPAQS. Thus it is possible to compare the correlations among different measurements. Such comparisons are helpful for evaluating the different methods used for scaling the ATOFMS mass concentrations. At the Fresno site, the available continuous $PM_{2.5}$ measurements are BAM, TEOM, Dust Aerosol Monitor (DAM), Nephelometer, Aethelometer, and $m_{ATOFMS\text{-}MOUDI}$. Several hours of nephelometer data points were removed in the morning periods of January 30, January 31 and February 1 due to the extraordinarily high uncertainties in nephelometer measurements. The continuous $PM_{2.5}$ measurements for the Angiola site include BAM, nephelometer, aethelometer, and $m_{ATOFMS\text{-}APS}$ with density values of 1.9 $g \cdot cm^{-3}$ for all particles. Although the measurements of all these instruments represent the total $PM_{2.5}$ particle mass concentrations, each instrument is based on a different theory and has its own strengths and weaknesses. Therefore, it is quite reasonable to expect the correlation between any two measurements to be less than 1 (262).

The correlation coefficients between every pair of measurements are tabulated in **Table 9** for both Fresno and Angiola. For Fresno site comparisons, using an $R^2$ value of 0.7 and above to represent a good correlation, only the BAM measurement shows a fairly good correlation with all the other measurements with correlation coefficients ranging from 0.73 – 0.93. The TEOM measurement only correlates well with BAM and aethelometer measurements. This suggests that in this environment, the heated TEOM does not provide measurements of mass concentrations that are as accurate as those of the BAM. The $m_{ATOFMS\text{-}MOUDI}$ correlates well with the BAM, DAM, and nephelometer measurements. The overall correlation for MOUDI scaled ATOFMS $PM_{2.5}$ mass concentrations is as good as most other $PM_{2.5}$ measurements in Fresno. Similarly, Angiola correlation comparisons are shown in **Table 9b**. The BAM, nephelometer, and $m_{ATOFMS\text{-}APS}$ measurements show high correlation coefficients of greater than 0.90. The aethelometer measurements differ substantially and show lower correlation coefficients with the other three measurements. The strong correlation of ATOFMS mass concentrations with other $PM_{2.5}$ measurements provides support that the ATOFMS data can be scaled using peripheral instruments, such as the APS, to provide a measure of real ambient particle mass concentrations. The ultimate goal in developing this scaling procedure is not to just provide total $PM_{2.5}$ mass concentrations since these can be

(a)

| Fresno $R^2$ | BAM | TEOM | DAM | NEPH | AETH | ATOF-M |
|---|---|---|---|---|---|---|
| BAM | 1.00 | 0.86 | 0.93 | 0.75 | 0.79 | 0.79 |
| TEOM | 0.86 | 1.00 | 0.59 | 0.60 | 0.94 | 0.64 |
| DAM | 0.93 | 0.59 | 1.00 | 0.70 | 0.53 | 0.78 |
| NEPH | 0.75 | 0.60 | 0.70 | 1.00 | 0.58 | 0.81 |
| AETH | 0.79 | 0.94 | 0.53 | 0.58 | 1.00 | 0.62 |
| ATOF-M | 0.79 | 0.64 | 0.78 | 0.81 | 0.62 | 1.00 |

(b)

| Angiola $R^2$ | BAM | NEPH | AETH | ATOF-N |
|---|---|---|---|---|
| BAM | 1.00 | 0.92 | 0.60 | 0.91 |
| NEPH | 0.92 | 1.00 | 0.77 | 0.93 |
| AETH | 0.60 | 0.77 | 1.00 | 0.63 |
| ATOF-N | 0.91 | 0.93 | 0.63 | 1.00 |

BAM: beta attenuation monitor
DAM: dust aerosol monitor
NEPH: nephelometer
AETH: aethelometer
TEOM: tapered element oscillating microbalance
ATOF-N: APS scaled ATOFMS mass concentrations
ATOF-M: MOUDI scaled ATOFMS mass concentrations

Table 9: Correlation coefficients of $PM_{2.5}$ measurements. (a) Fresno site. (b) Angiola site.

measured using a variety of other dedicated techniques, but instead to use ATOFMS to provide mass concentrations of particles from specific sources. Thus, this study represents a critical step in the development of the most appropriate scaling procedures that will allow us to use ATOFMS to obtain quantitative source apportionment results in future studies.

**iv. Conclusions**

In this paper, we compare two methods for scaling ATOFMS measurements using reference measurements to obtain quantitative particle mass concentrations. By comparing ATOFMS single particle measurements with MOUDI mass measurements, we obtain scaled ATOFMS mass concentrations that correlate well ($R^2 = 0.79$) with a BAM, which serves as an independent mass concentration reference method. However, the absolute values of scaled ATOFMS mass concentration is only close to MOUDI measurements during the IOPs within the specified size range. Reduced ratios between the scaled ATOFMS and BAM mass concentrations are obtained when applying the scaling function to other periods during the study. Increasing the time resolution of the scaled ATOFMS mass concentrations to 1 hour (i.e. shorter than that of the MOUDI which is 5-8 hours) also introduces uncertainties. Both of these factors result in the absolute values of scaled ATOFMS mass concentration being only 70% of those measured by the BAM over the full study. Some of this difference can be explained by the underestimation of particles smaller than 0.18 μm by ATOFMS. The main advantage of scaling with the MOUDI measurements is to obtain size segregated mass concentrations of individual chemical species, making it possible to derive relative sensitivity factors (85).

APS measurements provide high temporal resolution particle number concentrations. By scaling ATOFMS particle counts with the APS and applying composition specific density values to the ATOFMS particle types, we are able to obtain ambient particle mass concentrations that correlate extremely well with BAM measurements ($R^2 = 0.91$). Future papers will address using chemically specific scaling factors which correct for density and shape factors.

In conclusion, continuous and quantitative ambient particle mass concentrations can be obtained from ATOFMS measurements by scaling with measurements from a co-located MOUDI or APS. The MOUDI method should be used if one is interested in deriving chemical sensitivity factors for different species. If one is more interested in real-time variations in particle mass concentrations (i.e. from different sources), the APS method is a more appropriate choice. The use of these methods for scaling extends ATOFMS to a more quantitative tool for studying ambient aerosol composition, transformations, and reaction mechanisms. When applying these scaling methods to individual particle types measured by the ATOFMS and correcting for chemical differences, quantitative mass concentrations of individual particle (or source) types with high time and size resolution can be obtained. The ultimate goal is use these scaling procedures to obtain quantitative mass fractions of particles from different sources in future ambient source apportionment studies.

**v. Acknowledgements**

We thank the California Air Resources Board for financial support (Contract No. 04-336) and the SJV funding agency for supporting CRPAQS. We also thank Dr. Hiroshi Furutani for sharing his busy time results and Dr. William Vance of ARB for a careful critique of this manuscript.

## 8. The Effect of APS Scaling Functions on the Quantification of Aerosol Time-of-Flight Mass Spectrometry Measurements

### i. Introduction

Traditionally, particulate matter is characterized with off-line filter/impactor based techniques, which normally require long sampling durations and labor-intensive analysis. Newly developed real-time particulate mass measurements, like the beta attenuation monitor, the tapered element oscillating microbalance, the Dusttrak sampler, and the continuous aerosol mass monitor, are able to provide high temporal resolution of particulate matter mass concentrations by utilizing the absorbing or scattering properties of the particles; however, no information on individual chemical species can be obtained from these methods (263-266).

Real-time single particle mass spectrometry (RTSPMS) measurements are able to overcome many disadvantages of the above techniques and provide continuous on-line particulate matter measurements (243,244,267). Despite the fact that extensive information on individual particle size and chemical composition can be acquired with RTSPMS measurements, it has been a challenge for these methods to provide quantitative aerosol mass concentrations. Most of the RTSPMS measurements introduce particles into a vacuum from atmospheric pressue via a supersonic expansion through an orifice. During transmission into the reduced pressures of a mass spectrometer, only a certain fraction of the particles are able to reach the center of the ionization region and become ionized (173). In order to compensate for these transmission losses, efforts are made to scale the data to obtain quantitative number or mass concentrations of ambient particles (30,36,85,249,250,268,269).

In a recent study, Qin et. al demonstrated the ability to obtain high temporal and size resolved quantitative particulate matter mass concentrations from ATOFMS measurements by scaling with reference methods (157). ATOFMS measurements provide the aerodynamic diameter and mass spectra of individual particles in real-time, enabling the study of particle transformation, mixing state, and source apportionment. One of the reference methods used for this study was an aerodynamic particle sizer (APS) which measures number concentrations for sizes between 0.2 and 2.5 μm. APS acquires real-time particulate aerodynamic size distribution by accelerating particles to different size-dependant terminal velocities which can be calculated with particle time-of-flight through the scattering lasers (254). By comparing ATOFMS and APS measurements for individual size ranges, a size dependant scaling function can be constructed, which is further used to acquire a scaling factor for each particle. The scaling factor represents the degree that ATOFMS undercounts particles for different sized particles. By multiplying ATOFMS measurements by scaling factors to correct for undercounting, a true representation of the ambient aerosols without biases due to transmission losses can be obtained . Qin and co-workers demonstrated that the APS scaled ATOFMS mass concentrations strongly correlate with independent beta attenuation monitor mass measurements, effectively providing quantitative particulate matter mass concentrations (157). The above scaling method also enables one to obtain the mass concentrations of

individual ATOFMS particle classes, assuming no preferential transmission of particles in each type and similar detection efficiencies.

The procedure used by Qin et al (2006) works well when APS data are available. A question arises as to how to scale ATOFMS data when no APS is available in a study. One also might ask whether this approach for scaling is universal and can be applied to all field studies with an ATOFMS. In this paper, the ATOFMS measurements from two field studies were scaled with APS scaling functions from five different field studies to study the effect of using different scaling functions on the scaling results. The ATOFMS data from the two test studies were acquired during the California Regional Particulate Air Quality Study (CRPAQS) in Fresno and Angiola (270). The five reference studies that provided APS scaling functions from a broad range of ambient conditions and aerosol types are the: Texas Air Quality Study in 2000 (TexAQS) (271), North Carolina Ambient Coarse Particle Concentrator Characterization Study (NC-CCS) (268), Cloud Indirect Effects Experiment (CIFEX) (272), UCSD Freeway Study (Freeway) (273), and Atmospheric Brown Clouds Post-Monsoon Experiment (APMEX) (274). Co-located APS data were also available during the Angiola study, which will be used to compare the results between using scaling functions from both the same study and the reference studies.

**ii. Experimental**

All studies including Angiola, TexAQS, NC-CCS, CIFEX, Freeway, and APMEX had side-by-side ATOFMS and APS measurements, except for the Fresno study where no APS measurements were made. A TSI APS Model 3320 was used during the TexAQS and Angiola studies, and Model 3321 was used for all other studies (TSI, Minnesota). The details of the transportable ATOFMS have been described by Gard and co-workers (127).

***a. CRPAQS ATOFMS Measurements and Data Analysis***

California's San Joaquin Valley is one of the most polluted areas of the country, experiencing extremely high particulate matter mass concentrations throughout the winter season due to the stagnant meteorological conditions (275). In order to better understand particulate matter pollution and identify major emission sources, a multi-year, multi-agency field campaign, the California Regional Particulate Air Quality Study (CRPAQS), was deployed at selected locations in the valley (172,276-279). Two ATOFMS were operated continuously in Fresno and Angiola from November 30, 2000 to February 4, 2001 as part of the CRPAQS to study wintertime aerosol composition, transformations, mixing state, and source apportionment. The size and chemical composition of more than 2 million particles was acquired with ATOFMS at each site. The data collected between January 9$^{th}$, 2001 and February 4$^{th}$, 2001 will be scaled with reference APS scaling functions to study the effect of different scaling curves on ATOFMS scaling results. Particles with diameters 0.2 – 2.5 μm were the focus of this study.

Custom software was used to calibrate the mass spectra and extract ion peaks into peak lists. These peak lists were imported into a single particle mass spectrometry data analysis tool kit, YAADA, for extensive analysis (160). The spectra were then classified with an adaptive resonance theory based clustering method (ART-2a) (35), which groups particles into clusters based on the existence and intensity of ion peaks in individual

particle mass spectra. Single particle mass spectral information is converted into a weight matrix for classification. Two particles are considered to belong to the same cluster if the dot product of their weight matrices is higher than a pre-determined threshold value, which was set to 0.8 for the current work. Upon applying ART-2a on the CRPAQS datasets, major particle types that accounted for 90% of total particles were isolated for further analysis. The majority of the single particle mass spectra contain information on both positive and negative ions, however, about 5.9% of the particles in Fresno study and 1.5% of the particles in Angiola study did not produce positive mass spectra. These particles were excluded from the classification step.

### *b. Reference Studies with APS Scaling Functions*

APS scaling functions from five reference studies, including TexAQS, NC-CCS, CIFEX, UCSD Freeway, and APMEX were applied to the Fresno and Angiola ATOFMS measurements to study the impact of using multiple scaling functions.

TexAQS is a comprehensive research project to address the air pollution problems in the state of Texas, as a result of the high number of days in exceedance of the national 1-hour standard of ozone and fine particulate matter concentrations (271). The goal of this study is to investigate ground level ozone and fine particulate matter in the Houston region and the east half of Texas to determine whether the pollutants are from local sources or long-range transport. ATOFMS was operating continuously for 4 weeks from August 20 to September 15, 2000 at the La Porte airport, which is located 40 km east of downtown Houston. TexAQS measurements represent a polluted urban environment. The NC-CCS collected lab based ambient measurements at the EPA Human Studies Facility in Chapel Hill, NC in the summer of 2003. The main purpose of this study was to characterize the effect of the coarse particle concentrator on ambient particulate matter chemical composition and size distributions (268). During the first concentrator characterization study (NC-CCS-I), the ATOFMS was operated for 10 hours of switching between non-concentrated and concentrated ambient particles. ATOFMS was operated for 8 hours during the second concentrator characterization study (NC-CCS-II), a period when substantially higher (nearly 100%) ambient relative humidity (RH) was encounted which led to severe degradation in visibility. CIFEX was conducted in April 2004 at Trinidad Head, California to observe long range transport of Asian dust traveling across the Pacific Ocean (272). The sampling site is located on the coast of California about 60 miles south of the California-Oregon border. This study captured particles in a remote marine environment with occasional influence from local anthropogenic activities and long-range transport of Asian dust. The UCSD Freeway Study took place in the summer of 2004 where continuous ambient measurements were conducted with an ATOFMS for nearly 5 weeks inside a trailer at the University of California, San Diego (273). The sampling site was only 10 meters away from a major freeway with heavy traffic. The purpose of this measurement was to study the instantaneous chemistry of vehicular emission particles under ambient conditions, to aid in source apportionment of particles from vehicle emissions. Finally, during the APMEX, ambient ATOFMS sampling was conducted in October, 2004 at Hanimaadhoo, a very remote location near the north edge of the Maldives islands (274). The main

purpose of this study was to understand the atmospheric impact of anthropogenic activities.

### *c. The Calculation of the Scaling Functions in Reference Studies*

The detailed APS scaling procedure is described in the recent paper by Qin and co-workers (157). The same method is adapted here with minor modifications. Briefly, particle number counts were first tabulated from both APS and ATOFMS measurements for the following 12 size ranges: 0.300-0.523, 0.523-0.605, 0.605-0.699, 0.699-0.807, 0.807-0.933, 0.933-1.077, 1.077-1.243, 1.243-1.435, 1.435-1.655, 1.655-1.911, 1.911-2.207, and 2.207-2.547 μm. A scaling factor is calculated for each size bin by calculating the ratio of APS to ATOFMS particle counts for the corresponding size range. By plotting the scaling factors against the mid point of each size bin, a scaling curve can be obtained which is used to fit the scaling functions. Since the purpose of the current work is to test the applicability of scaling functions from reference studies to test studies, generating hourly scaling functions from reference studies for the object studies is not applicable. Thus, only one average scaling function is obtained from each reference study in the current work. For each reference study, time periods were removed if either APS or ATOFMS were offline. Since scaling curves can change substantially at different times of the day due to the variation in ambient particle concentrations and compositions, an average scaling curve for the same hour of the day throughout the whole study period was first calculated. The final scaling curve was obtained by averaging the mean scaling curves for each hour of the day. Similar to the previous work by Qin et al., each scaling function is fitted separately for the size range below and above 1.783 μm which can be characterized with 5 parameters:

$$\phi_{APS} = \begin{cases} C_1 \cdot e^{C_2 \cdot D_a} & \left(when\ D_a < 1.783\ um\right) \\ C_3 \cdot {D_a}^2 + C_4 \cdot D_a + C_5 & \left(when\ D_a \geq 1.783\ um\right) \end{cases} \quad (1)$$

where C1 and C2 are the best-fit parameters determined by exponential regression of scaling factors over the size bins. The first function was extrapolated down to 0.2 μm to obtain the scaling factors for the smallest particles detected by ATOFMS. C3, C4, C5 were obtained by second-order polynomial regression.

## iii. Results and Discussion

### *a. Scaling Curves and Scaling Functions*

The scaling curves for the reference studies: TexAQS, NC-CCS-I, NC-CCS-II, CIFEX, Freeway, APMEX, and Angiola are presented in **Figure 60**. Since APS measurements are available during the Angiola study, the Angiola APS scaling curve is also included along with the reference scaling curves. All scaling curves resemble a reverse check mark in the $PM_{2.5}$ ($Da \leq 2.5$ μm) size range with the lowest point at 1.783 μm for most curves. The exceptions are the NC-CCS curves which dip at 1.545 μm and the APMEX curve which dips at 2.059 μm. The scaling curves from all six studies are similar in shape but the absolute scaling factors can vary by several orders of magnitude. The APS scaling parameters for each study are listed in **Table 10**.

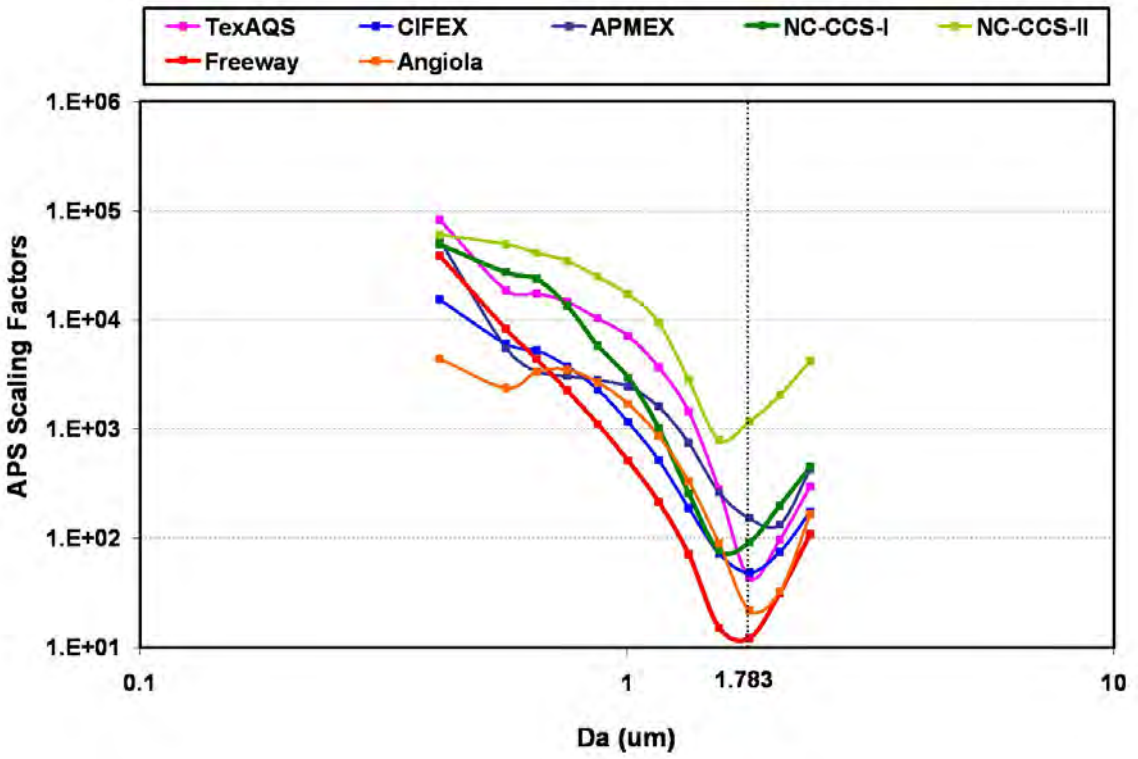


Figure 60: APS scaling curves for all studies, including TexAQS, NC-CCS-I, NC-CCS-II, CIFEX, Freeway, APMEX, and Angiola studies.

Table 10: APS scaling parameters for all studies.

| Study | C1 | C2 | C3 | C4 | C5 |
|---|---|---|---|---|---|
| CIFEX | 90538.75 | -4.42 | 372.61 | -1336.04 | 1245.93 |
| Freeway | 241360.23 | -5.96 | 289.94 | -1043.43 | 950.88 |
| TexAQS | 598326.07 | -4.91 | 742.50 | -2658.89 | 2423.82 |
| Angiola | 41576.86 | -3.81 | 635.66 | -2403.85 | 2287.07 |
| NC-CCS-I | 558422.02 | -5.33 | 682.05 | -2233.29 | 1905.64 |
| NC-CCS-II | 381091.24 | -3.46 | 6250.30 | -20892.62 | 18551.49 |
| APMEX | 66592.45 | -3.48 | 1674.69 | -6501.40 | 6420.04 |

### *b. Major Particle Types in CRPAQS*

Detailed discussions of the major particle types are provided in another paper by Qin and co-workers (270), and only a brief description is provided here. The majority of particles analyzed during the CRPAQS study were transformed, as indicated by the presence of secondary ammonium (m/z 18) and nitrate (m/z -46, -62 and -125) ion marker peaks in their mass spectra. OC represent particles mainly containing organic carbon with secondary ammonium and nitrate; biomass are organic carbon particles with

very intense potassium peak; HMOC represent organic carbon particles that contain characteristic peaks between m/z 100 and 200 in both positive and negative spectra (162); ECOC are particles containing both elemental carbon and organic carbon; EC represent elemental carbon particles with intense $C_n^+/C_n^-$ peaks (n is integer); sea salt are freshly emitted sea salt particles with intense sodium and chloride peaks; aged sea salt are sea salt particles containing significant amount of nitrate and some organics; dust are inorganic mineral species mixed with nitrate and organic carbon; and $NH_4NO_3$-OC represent organic carbon particles but with huge amount of ammonium nitrate. All the aforementioned particle types are present in both the Fresno and Angiola studies. There are also particle types that are specific to each location.

Knowing the ATOFMS sample flow rate, the un-scaled particle type mass concentrations can be obtained from raw ATOFMS counts by assuming all particles are spherical with a density of 1.9 g/cm$^3$ (157). **Figure 61** shows the un-scaled daily average particle type mass concentrations and mass fractions in the size range of 0.2- 2.5 μm. The size resolution is 0.1 μm with the label representing the bin midpoint. The low mass concentration values within each bin (< 0.2 μg/m$^3$) illustrate the significant

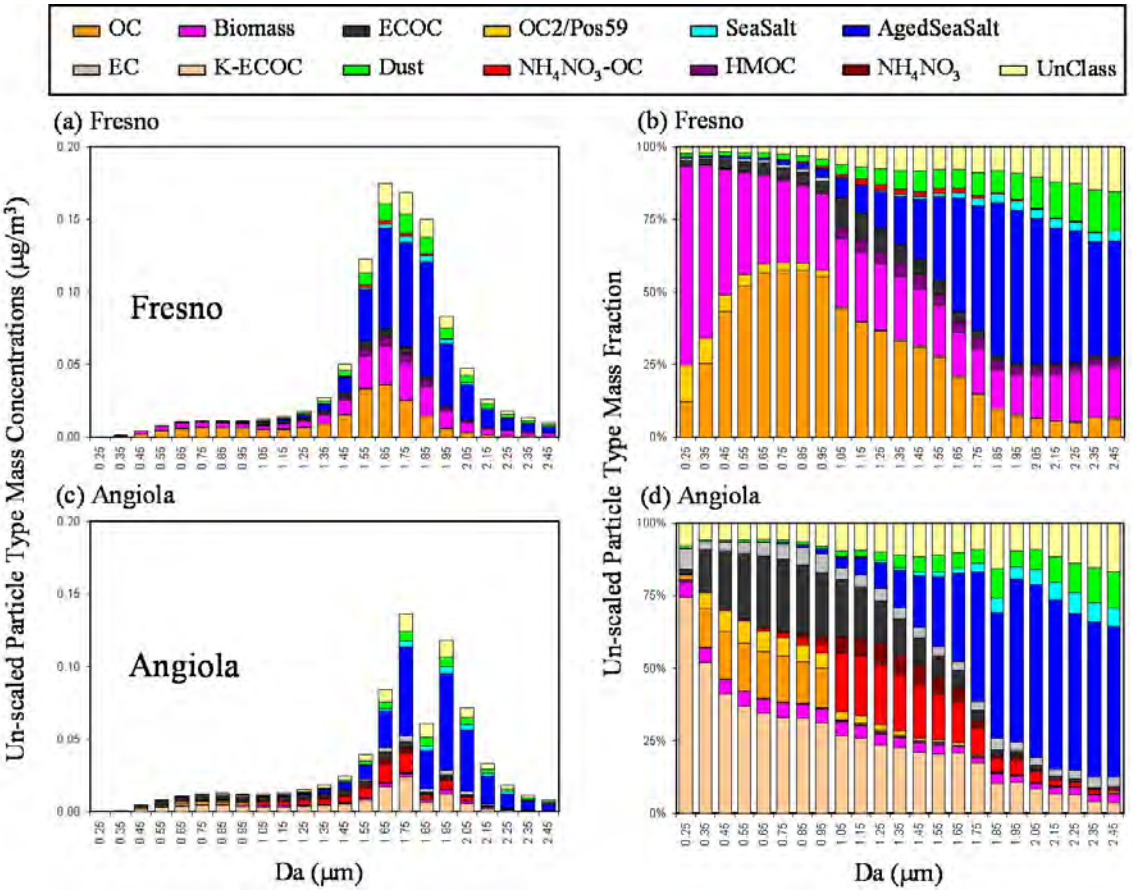


Figure 61: Size-resolved un-scaled particle type mass concentrations and mass fractions for Fresno and Angiola. (a) un-scaled particle type mass concentrations in Fresno (b) un-scaled particle type mass fractions in Fresno (c) un-scaled particle type mass concentrations in Angiola (d) un-scaled particle type mass fractions in Angiola.

undercounting of particles by the ATOFMS as shown in **Figure 61a** and **Figure 61c**. Without scaling, the ambient particle mass concentrations are centered near 1.5 – 1.9 μm. These size-resolved mass concentration distributions are not indicative of the atmospheric concentrations, but reflect the preferential transmission of particles around 1.7 μm by the ATOFMS nozzle. This preferential transmission is one aspect that can be corrected using APS scaling functions. Since particle transmission efficiency mainly depends on size (173), particles within the same size range are undercounted to the same extent. Therefore, the particle type mass fractions as a function of size shown in **Figure 61b** and **Figure 61d** represent the true ambient particle fractions without scaling..

The major particle type mass fractions illustrate that carbonaceous particles dominate the submicron size range ($0.2 \leq D_a < 1.0$ μm), however their fractions decrease substantially in the supermicron range ($1.0 \leq D_a \leq 2.5$ μm) as aged sea salt and dust particles becoming the dominant components. **Figure 61** also show that despite the fact that carbonaceous particles (mainly organic carbon, elemental carbon, and biomass) account for more than 90% of the total mass in the submicron size range at both sites, the percentages of biomass and OC particles are much lower in Angiola. The combined mass fractions of carbonaceous particles are similar in Fresno and Angiola, however, a lower fraction of biomass and a higher fraction of K-ECOC are observed in Angiola due to particle aging (270).

***c. Scaled ATOFMS Mass Concentrations***

Scaling causes a dramatic shift in the size distributions of major particle type mass concentrations compared to those shown in **Figure 61a** and **Figure 61c**.

Representative distributions after scaling are included in **Figure 62**. The y-axis represents the 24-hour

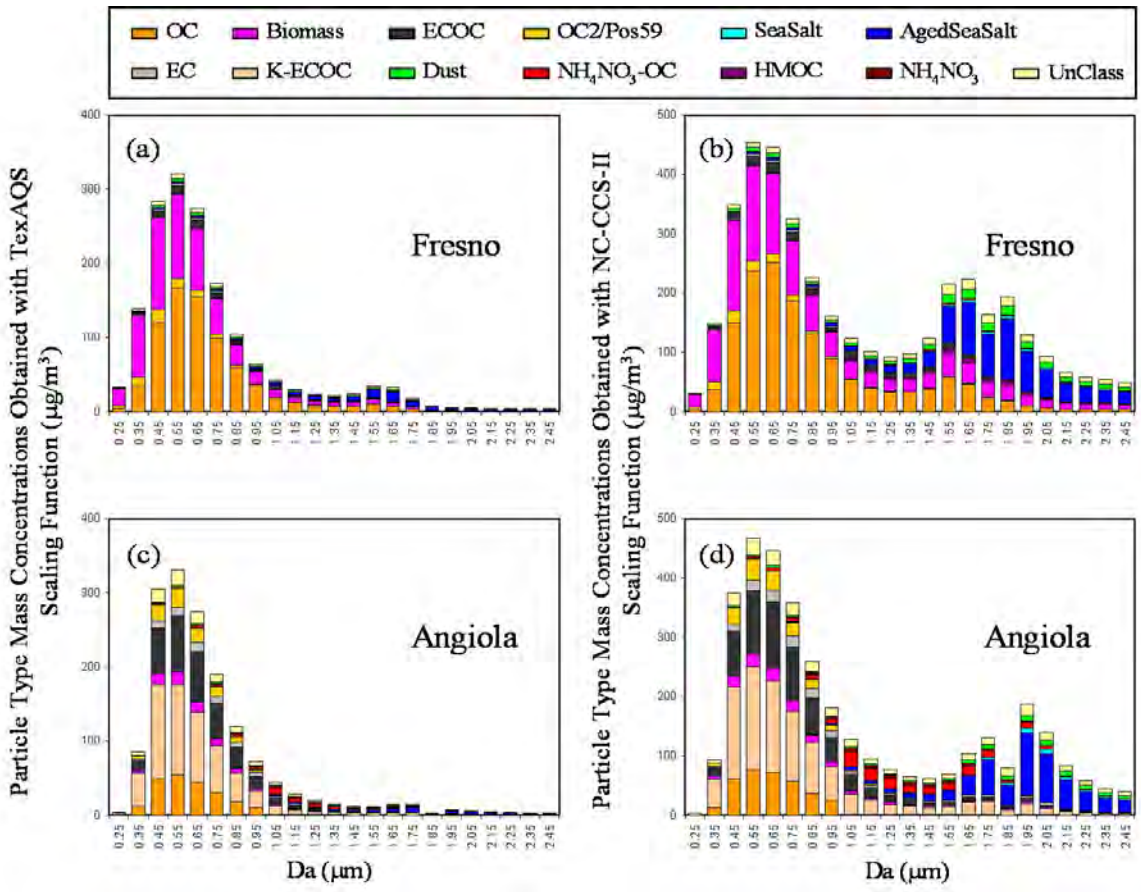


Figure 62: Fresno and Angiola size-resolved particle type mass concentrations scaled with TexAQS and APMEX scaling functions. (a) Fresno particle type mass concentrations with TexAQS APS scaling function (b) Fresno particle type mass concentrations with APMEX APS scaling function (c) Angiola particle type mass concentrations with TexAQS APS scaling function (d) Angiola particle type mass concentrations with APMEX APS scaling function.

average mass concentrations over the whole sampling duration; the x-axis shows the midpoint of each size bin with a resolution of 0.1 μm. **Figure 62a** and **Figure 62c** correspond to the scaled mass concentrations in Fresno and Angiola using the TexAQS APS scaling function. The total particulate mass concentration peaks between 0.5 - 0.6 μm with carbonaceous species dominating the submicron size range. The mass concentrations of aged sea salt particles increase in the supermicron range. Applying scaling functions from Freeway, CIFEX, and NC-CCS-I studies results in similar size distributions to those in **Figure 62a** and **Figure 62c**. **Figure 62b** and **Figure 62d** represent the scaled mass concentration of major particle types using APMEX scaling function. Compared to the results in **Figure 62a** and **Figure 62c**, the size distribution of APMEX scaled mass concentrations has an additional peak around 1.7 μm as well as the peak between 0.5 - 0.6 μm. The scaled mass concentrations calculated with the NC-CCS-II scaling function show similar distribution to that obtained with APMEX, except that the peak at 1.7 μm is a little more intense.

One major factor that affects the supermicron scaling results is the shape of the scaling curve. As shown in **Figure 60**, neither APMEX nor NC-CCS-II scaling curves

reach the minima within 1.655-1.911 μm, which sets these scaling curves apart from most other curves. The minimum point on APMEX scaling curve is within 1.911-2.207 μm, while that on NC-CCS-II is within 1.435-1.655 μm. For these two curves, particles within 1.655-1.911 μm no longer have the lowest scaling factors, thus the relative fractions of these particles increase significantly. **Figure 61a** and **Figure 61c** show that majority of aged sea salt and dust particles fall within the size range of 1.6 – 2.0 μm, thus these particles are impacted the most by a shift of scaling curve minimum. As a result, higher mass concentrations of aged sea salt and dust particles are obtained for the supermicron size range with the APMEX and NC-CCS-II scaling functions. One exception to this trend is that the scaling curve of NC-CCS-I does not reach the minimum between 1.655-1.911 μm, although its scaling results are similar to those with TexAQS, CIFEX, and Freeway scaling functions. The reason for this exception is not known; however, it shows that the change in scaling curve shape does not necessarily correspond to a change in the scaling results. One thing worth to point out is that all the reference APS scaling curves are only similar in shape, the actual scaling factor values vary substantially for the same particle diameter. Thus, it is expected that the absolute scaled mass concentrations would also vary considerably depending on the APS scaling function used. This difference in mass concentrations is also illustrated in **Figure 62** (a vs. b and c vs. d) where a different Y-axis scale is needed for the same study when using different scaling curves. Thus, comparing the absolute values of scaled particle type mass concentrations will not provide much insight on the true ambient concentrations.

### *d. APS Scaled Particle Mass Fraction*

Although the mass concentrations obtained by scaling the test studies with APS scaling functions from reference studies do not reflect the real ambient concentrations, a remarkable consistency is observed in the mass fractions of individual particle types. The scaled major particle type mass fractions for the Fresno and Angiola studies are shown in **Figure 63**. Particles were segregated into submicron, supermicron and $PM_{2.5}$ size ranges for finer comparisons. Each pie chart corresponds to the mass fractions obtained with the scaling function from a specific reference study as listed on top. Besides the reference

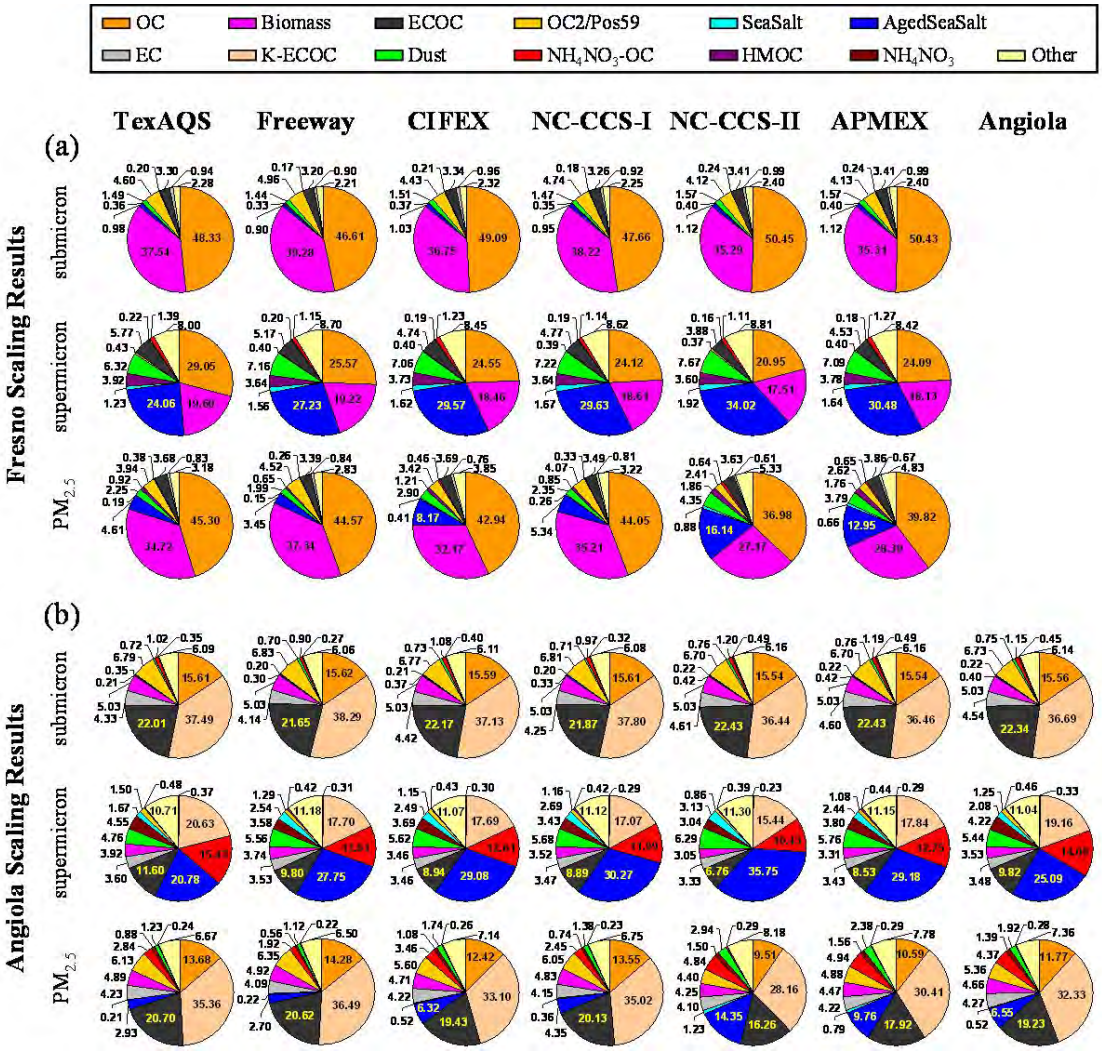


Figure 63: Fresno and Angiola individual particle type mass fractions for submicron, supermicron and PM2.5 range obtained with APS scaling functions from TexAQS, Freeway, CIFEX, NC-CCS, APMEX, and Angiola studies.

scaling functions, Angiola measurements are also scaled with co-located APS measurements for comparison purposes.

Surprising consistency can be observed in Figure 63 for the mass fractions of submicron particle types regardless of the scaling function used. In general, Fresno submicron particles consist 49% OC, 37% biomass, 4.5% Pos27, 3.3% ECOC, 1.5% dust, and 1.0% aged sea salt. The rest of the particle types account for less than 1% each in the mass fractions, and the unclassified particles account for 2.3% of total submicron mass. The standard deviations of each particle type mass fraction obtained with all 6 reference scaling functions are less than 9% of the average values, except for $NH_4NO_3$-OC which is 13%. Angiola scaled mass fractions are shown in **Figure 63b**. Scaled submicron particle type mass fractions also showed very good consistencies, with 16% OC, 37% K-ECOC, 22% ECOC, 6.8% Pos59, 5.0% biomass, 4.4% EC, and 1.1% $NH_4NO_3$-OC particle. Sea salt, aged sea salt, HMOC, $NH_4NO_3$, and dust account for less than 1% each, and the unclassified particles explain 6.1% of Angiola submicron mass. The mass fraction

standard deviations are less than 4% of the corresponding average values, with the exception of 12% for aged sea salt, 11% for $NH_4NO_3$-OC, and 22% for $NH_4NO_3$ particles. In addition to the consistency in submicron particle type mass fractions acquired with various APS scaling functions, **Figure 63b** also illustrates that similar results are obtained when scaling Angiola submicron particles with co-located APS scaling function and with reference study scaling functions. Therefore, a resonably accurate estimation of the mass fractions of submicron particle types can be acquired by scaling ATOFMS measurements with scaling functions from other studies.

Compared to the submicron scaling results, supermicron particles contain lower fractions of carbonaceous particles and higher fractions of aged sea salt, dust and $NH_4NO_3$ rich particles. More variation is obtained for the supermicron mass fractions obtained by using various scaling functions. One major factor causing this variation is the shift in scaling curve minima as discussed in section 6.4.4. The change in the minimum of the scaling curve at larger sizes can significantly increase the relative amount of the particles between 1.655-1.911 μm, into which most aged sea salt particles fall. This increase on aged sea salt mass fraction will then affect the mass fractions of other particle types. For Fresno particles in the supermicron size range, compared to utilizing other scaling functions, scaling with APMEX and NC-CCS-II leads to lower mass fractions of OC (22.5% instead of 25.8%), biomass (17.8% instead of 19.0%) and ECOC (4.2% instead of 5.1%) particles, and a higher fraction of aged sea salt particles (32.3% instead of 27.6%). Angiola scaled supermicron particle type mass fractions show similar patterns to those in Fresno. Moreover, the supermicron mass fractions obtained with co-located APS scaling function fall within the mass fraction range calculated with other scaling functions, showing that particle type mass fractions obtained with reference scaling functions are good estimates of the ambient aerosol concentrations.

The particle type mass concentrations for $PM_{2.5}$ is calculated by adding the mass concentrations of the corresponding types in the submicron and supermicron ranges. Although there appears to be more variations in the mass fractions, especially for the aged sea salt particles (varied from 3.4% to 16.1% in Fresno), it is mainly caused by the changes in the scaling curve minima, as mentioned earlier. **Figure 62** clearly illustrates the difference caused by scaling curves. Scaling Fresno and Angiola data with APMEX scaling function generates a second peak near 1.5 – 1.9 μm, in which most of the aged sea salt particles fall. This second peak is not present when scaling with the TexAQS scaling function. APMEX scaled mass concentrations contain a much higher fraction of the aged sea salt particles in the $PM_{2.5}$ range (13.0% for Fresno and 9.8% for Angiola) compared to those scaled with TexAQS (4.6% for Fresno and 2.9% for Angiola), causing the variations observed in the $PM_{2.5}$ mass fractions as shown in **Figure 63**.

**iv. Conclusions**

ATOFMS measurements at two ambient sampling locations, Fresno and Angiola in California's San Joaquin Valley, are scaled with APS scaling functions to obtain quantitative information on individual particle type mass fractions. The effect of APS scaling functions on the results was investigated by taking the scaling functions from five different studies acquired under a wide range of ambient conditions. The Angiola measurements were also scaled using co-located APS measurements to evaluate the results obtained from reference scaling functions.

Although the mass concentrations of individual particle types can vary more than one order of magnitude depending on the scaling functions used, nearly identical particle type mass fractions are observed in the submicron size range regardless of the APS scaling functions used. More variations in the mass fractions is observed for the supermicron and $PM_{2.5}$ size ranges, mainly caused by the shift on the scaling curve minimum point. Lower mass fractions of carbonaceous particles (44.5% instead of 49.9%) and higher fractions of aged sea salt (32.3% instead of 27.6%) and dust (7.4% instead of 6.9%) particles are obtained in Fresno when scaling with APMEX and NC-CCS-II scaling functions compared to using other scaling functions. Even though the mass fractions in the supermicron and $PM_{2.5}$ range are not as consistent as those in the submicron region when scaling with different APS scaling functions, we can still obtain the particle type mass fractions in these size ranges with errors less than 19%. Similar trends are observed in Angiola particle type mass fractions as those in Fresno. When Angiola measurements are scaled with a co-located APS scaling function, the submicron particle type mass fractions are almost identical to those obtained with reference scaling functions, the supermicron and $PM_{2.5}$ mass fractions also fall within the ranges obtained with reference scaling functions. Therefore, to obtain quantitative information from ATOFMS measurements from a study that does not have co-located APS measurements, the APS scaling functions from other studies can be used to provide a very good estimate of submicron particle type mass fractions and a close estimate of supermicron and $PM_{2.5}$ mass fractions.

**v. Acknowledgements**

This research was supported by the California Air Resources Board (Contract No. 04-336). The author would also like to thank John Holecek, Ryan Moffet, Laura Shields, Dr. David Sodeman, Matt Spencer and Steve Toner for providing the APS scaling functions for the reference studies.

# Changes in Size-Resolved Particle Composition Linked with Meteorology Measurements and Air Mass Back Trajectories to Increase Understanding of Sources and Secondary Contributions to Particulate Matter

## 9. Characterization of trace metals in single urban particles during the SOAR 2005 campaign

### i. Introduction

Now that epidemiologic studies have substantiated an association between increased exposure to particulate matter (PM) and risk for cardiopulmonary disease and mortality (280), the next step for research studies is to improve the overall understanding of the mechanisms and specific physical and chemical PM characteristics are causing these human health effects. Recent studies have linked exposure to trace metal-rich ambient PM with acute airway inflammation, which likely induces chronic diseases (281) and potentially causes mortality and morbidity (282). Greater knowledge of the sources, transformations, and fates of these metal-containing particles also will clarify their impact on the environment. Trace metals are distributed in the urban environment by natural processes (including wind erosion, volcanism, and biomass burning) as well as anthropogenic activities (such as fossil fuel combustion, municipal waste disposal, industrial metallurgical processes, and wear of vehicular and construction materials) (283). In the atmosphere, even a small presence of transition metal ions in particles can influence cloud chemistry (284). Dry and wet deposition of PM also constitute a major load of trace metal contamination to soils, agroecosystems, and aquatic systems (283,285). Deposition processes can contribute as much as 57-100% of the trace metals in stormwater in semi-arid regions such as southern California (286). These health and environmental ramifications warrant detailed analysis of ambient metal-containing particles.

Most data on trace metals in PM have been obtained from bulk filter analysis; the results are informative, although the approach has some caveats. Depending upon the sensitivity of the analytical technique, the low metal mass concentrations require collection times of varying lengths, often as long as 24 hours, for sufficient detection. Before measurement, the PM-loaded substrates must undergo precise multi-step extraction procedures to reduce the loss of sample (287,288). Online aerosol instrumentation offer an alternative approach which avoids many of these sampling artifacts and limitations and yields high temporally resolved data, which once correlated with wind speed and direction can locate potential sources (289). Moreover, techniques like single particle mass spectrometry (SPMS) provide detailed chemical analysis on the individual particle level with better statistical representation than other single particle methods, such as scanning electron microscopy (SEM) (290,291). SPMS data help decipher the chemical complexity of aerosols, granting insight into how trace metals in PM are damaging human health and the environment. Though SPMS techniques are not as quantitative as bulk filter methods, they do provide “fingerprints” and the chemical

species with which the metals are associated – key information for determining the sources of metal-containing particles.

This study employs an SPMS technique, known as aerosol time-of-flight mass spectrometry (ATOFMS), to determine the chemical speciation of size-segregated trace metal-containing urban ambient particles in southern California. ATOFMS simultaneously acquires positive and negative ion spectra, as well as size information, for single particles in real-time. Along with chemical speciation, the number concentrations, size, temporal trends, and wind directionality of trace metal-containing particles will be used to identify the most probable sources as well as gain insights into the short term variability of metal particles in urban air.

## ii. Experimental

### *a. Sampling Location*

Located approximately 80 km east of downtown Los Angeles, the city of Riverside, California commonly experiences air masses that have crossed the Los Angeles basin. Sampling occurred via a mobile laboratory on the campus of the University of California, Riverside (33°58′18″N, 117°19′22″W) in conjunction with the Study of Organic Aerosols at Riverside (SOAR) 2005 campaign. This work focuses on continuous data collected in the summer (July 30 - August 15) and fall (October 31 - November 21) seasons.

### *b. Instrumentation*

Single particle size and chemical composition were measured by ATOFMS. Ultrafine ATOFMS (UF-ATOFMS) detected particles with aerodynamic diameters between 100 nm and 350 nm, while standard inlet ATOFMS measured particles with aerodynamic diameters between 300 nm and 2.5 µm. The trace metal-containing ultrafine particles (50-100 nm) detected by UF-ATOFMS were statistically too low to be included here. Details of the transportable instrumentation have been described previously (1,2). In this work, $PM_{2.5}$ refers to all particular matter in the aerodynamic size range of 100 to 2500 nm. To account for the ATOFMS size-dependent transmission efficiency, the number concentrations of ATOFMS chemical composition data could be scaled to concurrently-measured particle size distribution data, such as a scanning mobility particle sizer (SMPS) (36). As described in previous chapters, it has been shown that there can be sufficient size differences between the ATOFMS aerodynamic diameter and the SMPS mobility diameter for certain chemical particle types (48,292). Due to the limited knowledge of shape factor and density values for the specific trace metal-containing particle types in Riverside during this campaign, the ATOFMS data were not scaled and are presented in raw counts in this study. Suitable scaling conversions between aerodynamic and mobility diameters are still under development.

### *c. Data analysis*

This study uses a similar data analysis approach to that of Tolocka and coworkers (291), which involves pre-selection of potential spectra before running a clustering algorithm. Because trace metal-containing particles represent only a small fraction of the millions of particle spectra collected during the SOAR campaigns, it was necessary to

isolate probable metal spectra based upon a relatively low threshold level for ion areas (peak area of 100) at the mass-to-charge ratio(s) (*m/z*) of the common isotope(s) (≥20% natural abundance) of the specified metal. For example, three of the four main lead isotopes have a natural abundance greater than 20% ($^{206}$Pb, $^{207}$Pb, and $^{208}$Pb), so only these three *m/z* values were used to extract the possible lead-containing particles. Once the potential spectra were pulled out, the adaptive resonance theory neural network algorithm, ART-2a, sorted and classified particles with similar spectral characteristics (35). The ART-2a learning rate, number of iterations, and vigilance factor (VF) were set to 0.05, 20, and 0.70, respectively, for this publication. This work focuses on the main metal types, and therefore it was not necessary to use a higher VF value to produce highly specific clusters, which are more commonly used in source characterization datasets for source apportionment studies. The VF value of 0.70 was sufficient to obtain distinct major classes. The resulting ART-2a clusters then were examined manually for the presence of trace metals, confirmed by the appropriate isotopic patterns and/or metal oxides. The trace metals examined in this study were V, Fe, Ni, Cu, Zn, Sr, Mo, Sn, Sb, Ba, W, and Pb.

**iii. Results and Discussion**

Though trace metal-containing particles generally represent small percentages of the overall PM, correlations between trace metals and other pollutants have made trace metal concentrations a potential air quality index (293,294). Day-of-week patterns in trace metal concentrations can provide insight into the ambient sources, particularly those based on dependent on human activities (295). For instance, high concentrations on working days (weekdays) and low concentrations on non-working days (weekends) indicate an anthropogenic source, particularly standard business hour facilities rather than continuously operating industries. Motor vehicle traffic is lightest on Sundays, and therefore, particle types with the lowest concentrations on Sundays compared to the rest of the week most likely originate from vehicle emissions. Nevertheless, it is important to consider that not only do vehicle emissions decrease with reduced traffic but so does re-suspended road dust (296). Alternatively, natural sources would be expected to have no day-of-week trends. However, when these considerations are applied to the bulk (24-hour) data, it can be difficult to identify strong day-of-week patterns for trace metals. This day-of-week bulk-analysis approach may not perform well for locations like Riverside, where multiple sources of trace metals can convolute the daily patterns. Such environments need more detailed analysis on smaller time scales.

One of the advantages of ATOFMS is high time resolution, so the dataset is not limited to 24-hour periods, as normally shown for metals. ATOFMS also yields highly resolved sizing data. Details on the size distribution of trace metal-containing ambient aerosols are informative from a health perspective as well as for understanding the atmospheric fate of these particles; the particle size determines the extent of its penetration into the airways or lungs and thereby the extent of its toxicity, and it also dictates the range of transport and deposition rate (297). In order to gain further insight into the temporal variability of metal-containing aerosols as well as their size, the following figures present high temporal (half-hour) resolution and size resolved number concentrations.

Because different particle classes can all contain the same trace metal, the metal-specific figures provide the detailed features for three main particle types, based on the ART-2a clusters, for each of the most abundant trace metals: vanadium, iron, zinc, barium, and lead. Nickel was excluded due to its correlation with vanadium, as explained below. Plots (a)-(c) of each figure show representative mass spectra for the main particle types. For each mass spectrum, the main ion m/z peaks are labeled, and the corresponding color is maintained throughout the remaining plots. The half-hourly ATOFMS counts for the types are displayed in plots (d) and (e) for the summer and fall seasons, respectively. These temporal plots utilize the same scale within each figure for easy seasonal comparison. The gray line tracks all particles containing the specified element to help illustrate how well the three types represent all particles with that metal. Breaks in the continuous traces indicate intervals in which the instruments were offline due to daily quality control checks or maintenance. The fractions each particle type represents relative to all chemically analyzed particles per size range are supplied in plots (f) and (g) for summer and fall, respectively. Again, the gray trace represents all particles containing that metal, and the scale ranges are the same within each figure. Finally, plots (h)-(j) show the wind directionality for each particle type, which can be used to help in identifying sources. The distance each symbol is from the origin signifies the magnitude of the specific metal-containing particle counts per half-hour bin, and the angle represents the direction from which the wind was coming during that half-hour. The open circle symbols indicate summer data, whereas the open triangles indicate fall data.

Vanadium and vanadium compounds are hazardous; in fact, the oxidized form of vanadium, vanadium pentoxide, is even more toxic than the elemental form (298). A study on urban particles around Seville, Spain determined that vanadium, compared to the other metals, had the highest percentage (50.4%) in the soluble and exchangeable fraction, meaning that vanadium is the most available metal to the human body via respiration (299). The properties of vanadium allow it to be employed in a variety of products: its strength and hardness are ideal for alloy formation, such as nickel/vanadium, ferrovanadium, and chrome/vanadium; industries like printing, textiles, and ceramics use it as a drying or reducing agent in paints, inks, dyes, and pigments; and finally, vanadium compounds also manifest in crude oils in the form of organic complexes (298). Thereby, human activities that rely on heavy oil combustion such as industrial boilers, ships, and power plants emit vanadium via residual fly ash (300-303). The dominant m/z peaks in the representative mass spectrum of Type V1 are vanadium [$^{+51}$V] and vanadium oxide [$^{+67}$VO] (**Figure 64**). Other positive ion peaks indicate the presence of iron [$^{+56}$Fe], nickel [$^{+58/60}$Ni], and carbonaceous species, mainly organic carbon (OC). The main negative ion species are nitrates ([$^{-46}NO_2$], [$^{-62}NO_3$], [$^{-}$

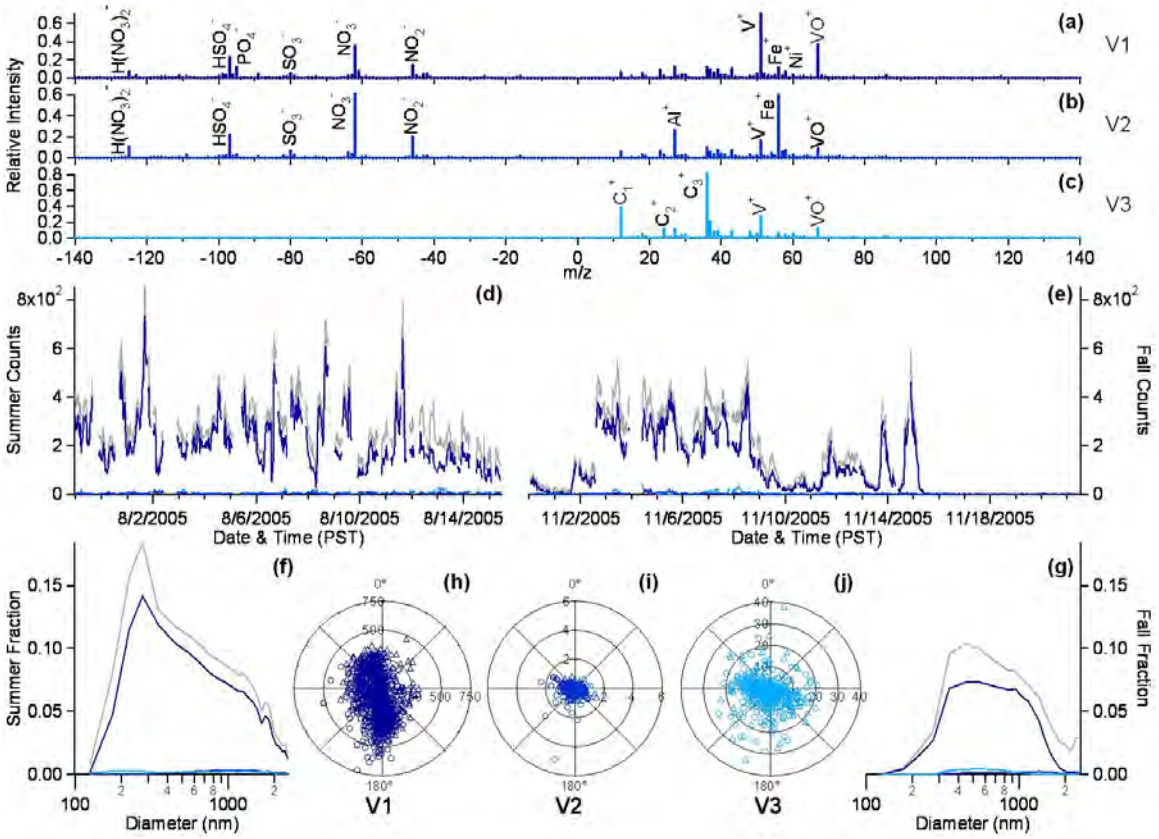


Figure 64: Trends of the three main vanadium particle types: representative mass spectra (a-c); half-hourly temporal variations in summer (d) and fall (e); size-resolved total particle fractions in summer (f) and fall (g); and half-hourly wind direction profiles based on particle counts (h-j).

$^{125}H(NO_3)_2$]) and sulfates ([$^{-80}SO_3$], [$^{-97}HSO_4$]). Type V1 is clearly the dominant vanadium particle class temporally for both seasons and across all sizes. Type V2 is similar to type V1, except that the inorganic species of iron and aluminum [$^{+27}Al$] are the dominant positive peaks for V2. However, type V2 tended to be observed in larger sized particles and was rarely observed by UF-ATOFMS which measures particles up to 350 nm. Type V2 could be agglomerates of type V1 with dust. Type V3 is an elemental carbon (EC) vanadium-containing particle class, as indicated by the intense carbon peaks of [$^{12}C^+$], [$^{24}C_2^+$], and [$^{36}C_3^+$] without strong OC ion peaks that are present in type V1. No negative ions were detected for this particle type which indicates these particles were heavily aged and had taken up water (304).

The two time series plots for vanadium demonstrate clear seasonal differences. In the overview of the general particle classes observed by ATOFMS during the SOAR campaigns, Qin and coworkers characterized ambient particle trends as diurnal for the summer season and episodic for the fall season (31). The vanadium particle classes appear to also follow the overall pattern of the ambient concentrations in both seasons, especially with the dramatic decline in number concentration during the Santa Ana periods (10/31-11/1 and 11/15-11/21). Occurring in the fall and early winter months, Santa Ana wind episodes bring warm and dry easterly winds to Southern California, which normally experiences westerly winds from over the Pacific Ocean. In the summer, the vanadium-containing $PM_{2.5}$ number concentrations tended to peak during the

afternoon and early evening hours. **Figure 65** and **Figure 66** include detailed plots on the local winds throughout both seasons. Westerly winds produced the highest wind speeds and were the dominant wind direction during daylight hours in the

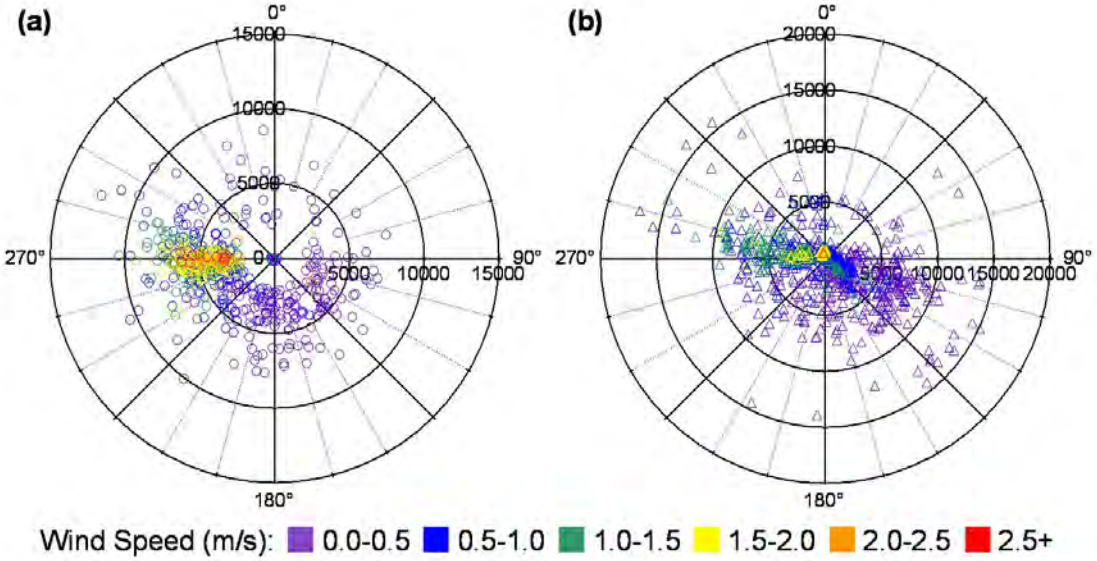


Figure 65: Half-hourly wind direction and wind speed (color scale) distribution for all $PM_{2.5}$ particle types in summer (a) and fall (b).

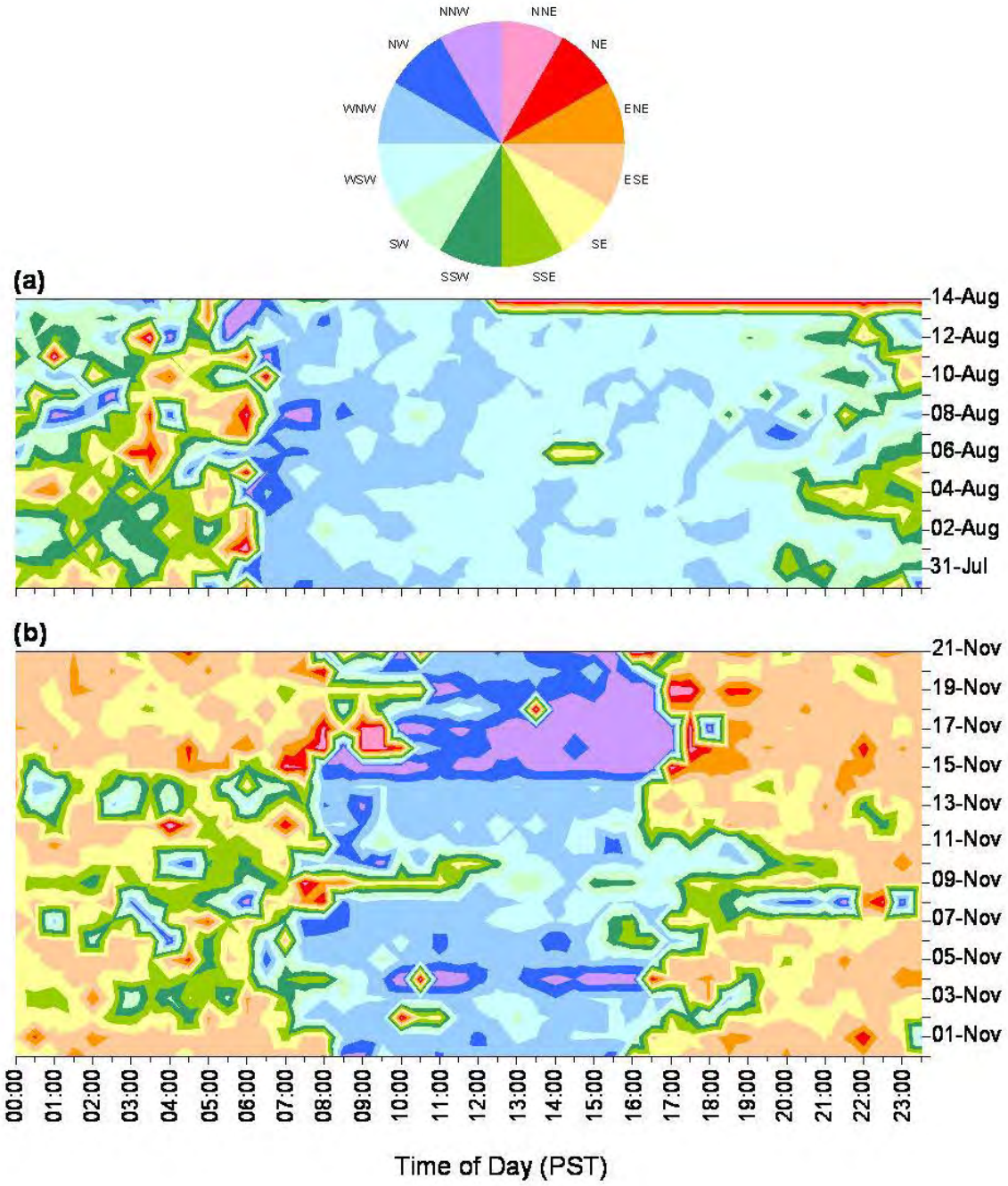


Figure 66: Half-hourly wind direction based on time of day for summer (a) and fall (b). Note that for the summer season, the meteorological data ended at 12:00 on August 14th.

summer. As shown in **Figure 64 h-j**, the wind direction plots specific to the particle types indicate foremost that vanadium-containing PM appear from all directions, since all the points are distributed around the center and there is no strong direction dependency based on the local winds. However, the plots do show more of a southwesterly/westerly direction dependency for the summer data (circles), which agrees with the vanadium-containing particles dominating during the afternoons when the westerly winds were the

strongest. The emissions from the millions of vehicles that drive daily in the south coast region as well as from the ships at the major shipping ports (Port of Los Angeles and Port of Long Beach) could travel east to the sampling site in Riverside (see the map in **Figure 67**). In fact, back trajectories from HYSPLIT (HYbrid Single-Particle Lagrangian Integrated Trajectory) model analysis (305) confirm that the air masses resulting in summertime V peaks passed over the major port and freeway areas of LA county before reaching Riverside. Currently, the source signatures for ship emissions are being investigated with a particular focus on the V particles (306).

Iron-containing urban particles have important influences on the surrounding environment; determining the solubility of iron-containing PM is a key piece of information for understanding the extent of which iron particles play a role in ocean productivity, which in turn impacts global climate (307). As expected, types Fe1 and Fe2 resemble types V1 and V2, because these particle types all contain vanadium and iron species (**Figure 68**). Additionally, the temporal trends, size profiles, and wind directionality also are similar to the corresponding V types. However, the mass spectrum for type Fe3 looks different; it contains more inorganic species, such

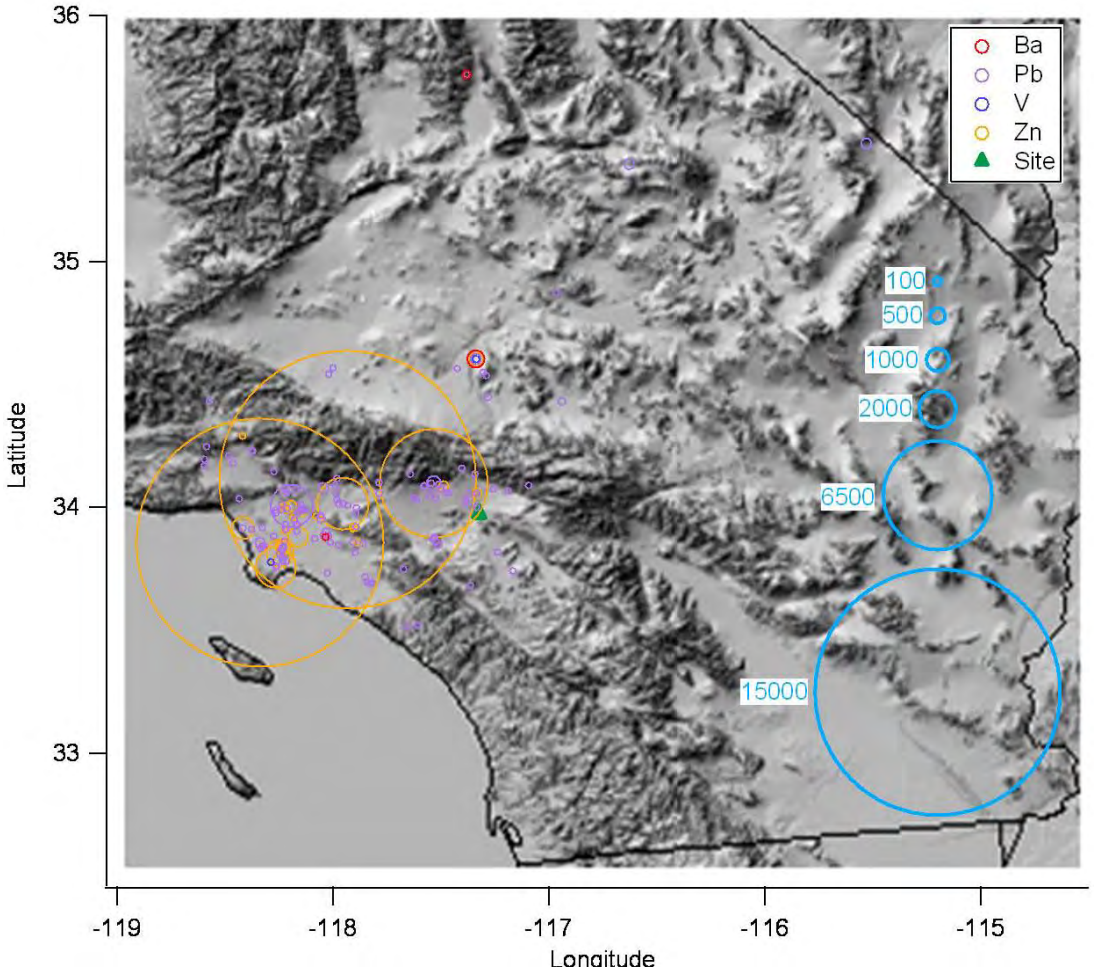


Figure 67: Reported annual atmospheric emissions of the specified metal and metal compounds in Riverside, Los Angeles, Orange, and San Bernardino counties in 2005 based on the data from the Environmental Protection Agency (EPA) Toxics Release Inventory (TRI).

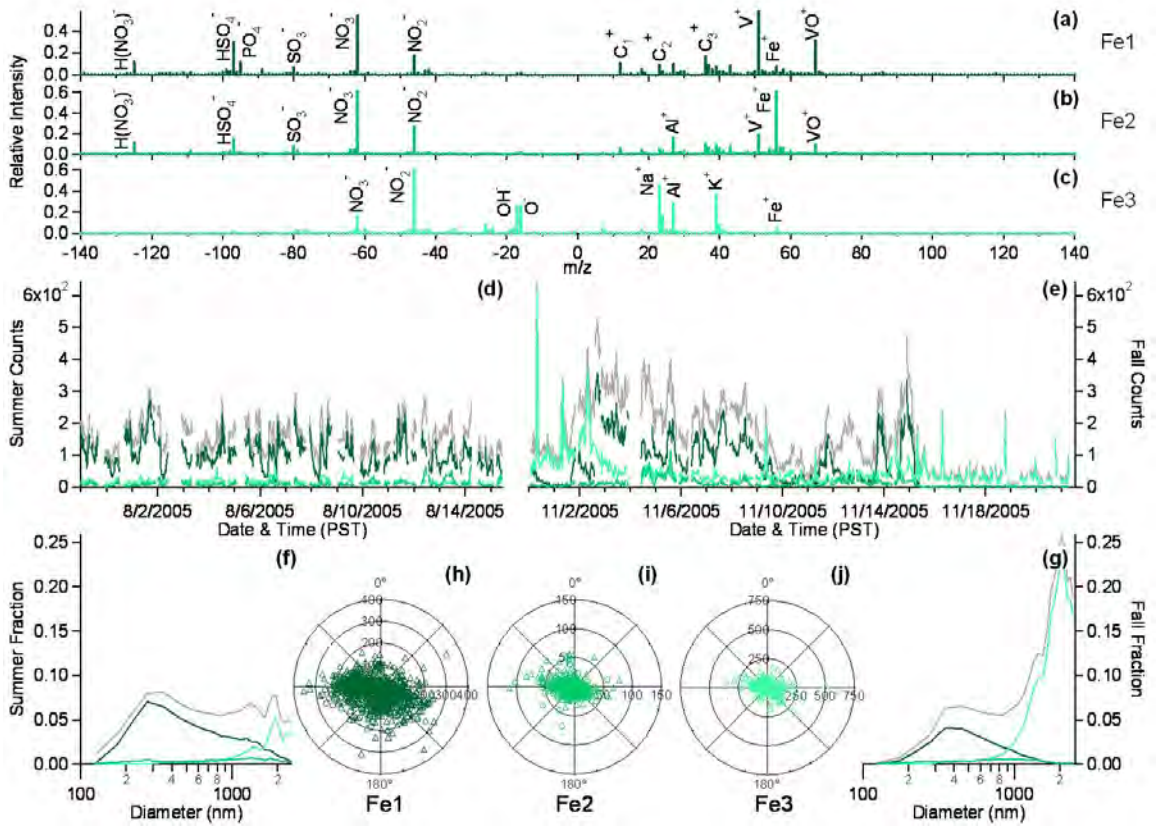


Figure 68: Trends of the three main iron particle types: representative mass spectra (a-c); half-hourly temporal variations in summer (d) and fall (e); size-resolved total particle fractions in summer (f) and fall (g); and half-hourly wind direction profiles based on particle counts (h-j).

as sodium [$^{+23}$Na], aluminum, and potassium [$^{+39}$K]. In addition to nitrates, the negative ions have oxygen [$^{-16}$O] and hydroxide [$^{-17}$OH] peaks. Type Fe3 is a dust particle class, and its size distribution is quite distinct when compared to the other metal types. The other profiles decrease sharply in the supermicron range, whereas the profile for type Fe3 remains increases with size; this size difference likely indicates the difference between metals of crustal origin, found in larger sized particles, and anthropogenic metals, found in smaller particles (308). Riverside particles that originate from urban Los Angeles anthropogenic sources are expected to be in the accumulation size mode due to the agglomeration of ultrafine and deposition of coarse particles via long-range transport (169). Because dust is generally resuspended PM, one might expect type Fe3 to be correlated with wind speed and direction; actually, most of the higher number concentrations of type Fe3 occurred when the local winds came from the east, particularly during the Santa Ana wind episodes in the fall season. According to the HYSPLIT results, the air masses with high Fe3 concentrations crossed desert areas east of the sampling site (Mojave Desert to the northeast and Sonoran Desert to the southeast). Zinc represents another major metal detected in particles during the fall and summer seasons. Hunt and coworkers examined archival lung tissues from humans known to have passed away from exposure during the 1952 London Smog in order to characterize the PM of this high mortality event captured within the lung compartments; they found evidence that Pb and Zn particle types in particular could be related to mortality (282).

Zinc is one of those biologically essential metals that has the potential for toxicity at high concentrations (283). Zinc-containing PM has several potential anthropogenic sources, such as tire wear, additives in lubricant oils, emissions from industries with galvanizing activities, and municipal and medical waste combustion emissions from incinerators (309,310). The type Zn1 mass spectrum shows the presence of sodium, potassium, zinc [$^{+64/66/68}$Zn], zinc chloride [$^{+99/101/103/105}$ZnCl], lead [$^{+206/207/208}$Pb], chloride [$^{-35/37}$Cl], nitrates, and phosphate [$^{-79}PO_3$] (**Figure 69**). Choel et al. studied the lead and zinc particle types downwind of a lead smelter and concluded that the association of sodium and chloride to these trace metals particles was due to internal mixing of aged marine particles (311). However, they also determined a mean particle diameter larger than the size profile obtained for type Zn1. Compared to the PbZn particle type observed in Mexico City, type Zn1 (which also has Pb) appears less aged and more freshly-emitted, based on its higher intensity of phosphate and zinc chloride peaks and the lower intensity of aging markers such as nitrate (304). Type Zn3 is similar to type Zn1, though it lacks those dominant sodium and potassium peaks. In contrast, type Zn2 has ammonium [$^{+18}$NH4], zinc, zinc chloride, and nitrate, and has much larger diameters than the other two classes. The time series for all zinc types are composed mainly of sharp spikes (lasting 1 to 3 hours long) at seemingly random time periods, though the highest summer peaks generally occurred in the early afternoon. On a 24 hour basis which is typical for mass measurements, the zinc particles would appear extremely insignificant; whereas the high temporal resolution used here shows that there are short periods during which one is exposed to elevated concentrations of zinc particles. The chloride in these particles most likely originated from the same zinc sources. The presence of chlorine in waste combustion incinerators is known to influence the speciation of the metals, and chlorine compounds such as hydrochloric acid and zinc ammonium chloride, are used in hot-dip

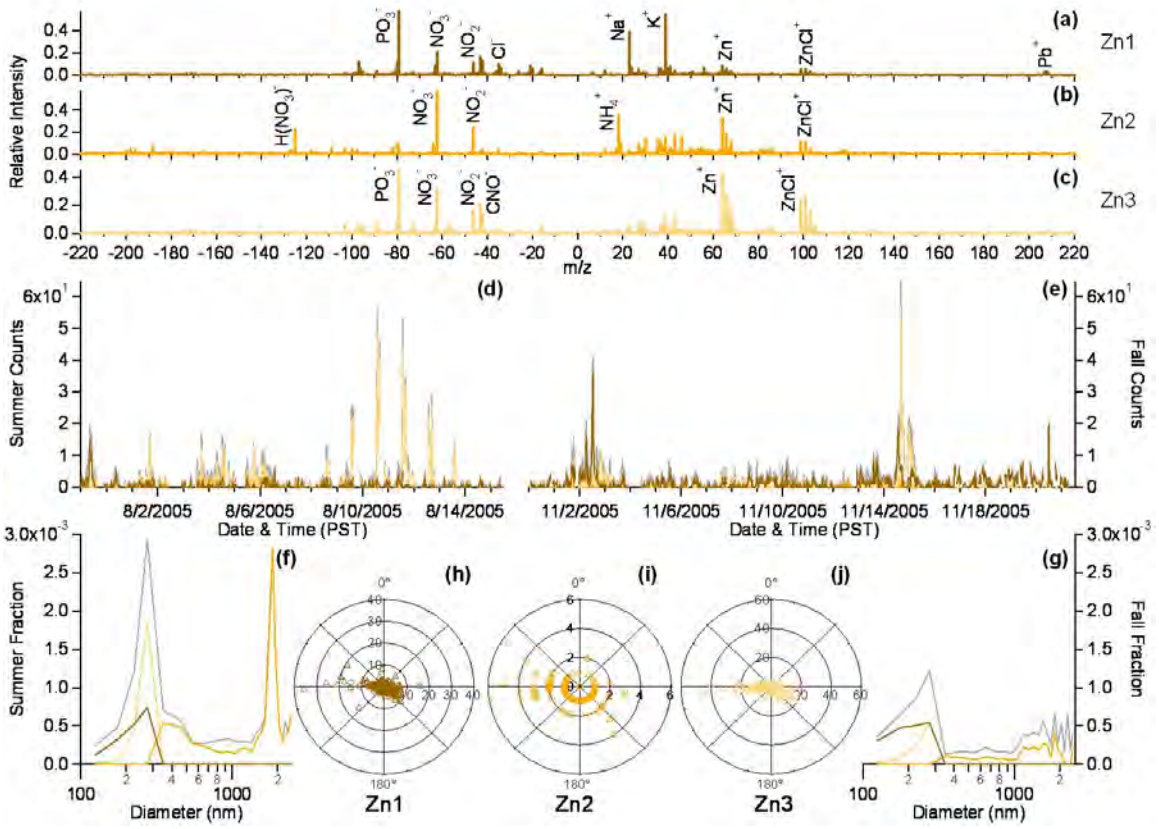


Figure 69: Trends of the three main zinc particle types: representative mass spectra (a-c); half-hourly temporal variations in summer (d) and fall (e); size-resolved total particle fractions in summer (f) and fall (g); and half-hourly wind direction profiles based on particle counts (h-j).

batch galvanizing methods (312,313). All three types generally have western wind direction preference. Interestingly, two facilities that galvanize steel materials and are among the top three facilities with reported 2005 zinc and zinc compounds emissions are located northwest of the sampling site (see **Figure 67**). These industries are the most likely source of this particle type. The fact that there is no strong seasonal dependence supports the link between these zinc particles and the galvanizing industries, because such facilities operate year round.

Barium and barium compounds are used in drilling, automotive brake pads and lubricant oils, bricks, tiles, and pesticides (314). The dominant barium class Ba1 is an organic barium particle type, containing OC, barium [$^{+138}$Ba], barium oxide [$^{+154}$BaO], barium hydroxide [$^{+155}$BaOH], chloride, nitrates, and intense peaks at m/z +59 and -101 (**Figure 70**). This unique type was also noted in Spencer et al. (48). The other barium classes contain other inorganic species, like sodium, aluminum, potassium, iron, and nitrates, and are brake dust, which is a mechanically abraded source based on their larger size distributions (315,316). The time series plots show clear seasonal differences, particularly for the organic Ba1 type; there were several consecutive summer days in which very low concentrations were detected, whereas significant concentrations were detected every day during the fall, including during the Santa Ana periods. Additionally, the high number concentrations generally were observed during the late night to early morning hours, when the wind speeds were at the lowest. Low wind speeds and the small

size of this particle type could imply a local source. The exact origin of the Ba1 type remains inconclusive.

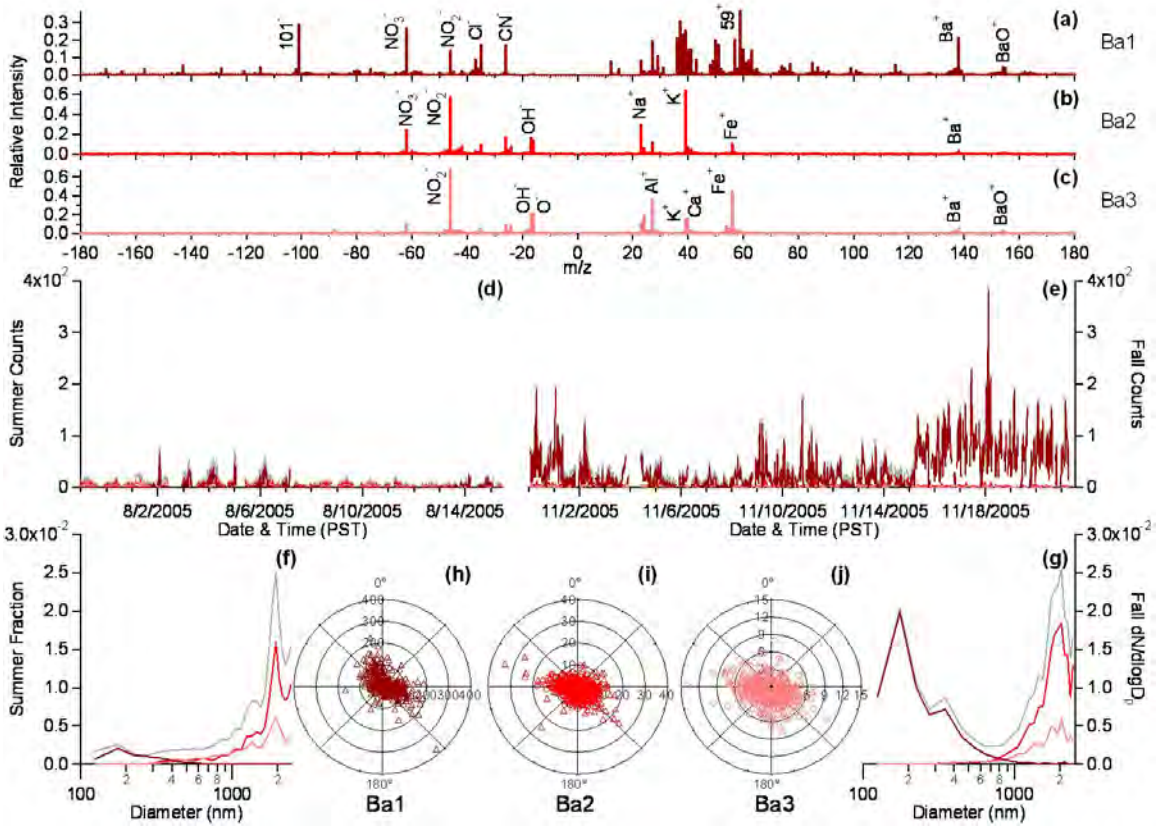


Figure 70: Trends of the three main barium particle types: representative mass spectra (a-c); half-hourly temporal variations in summer (d) and fall (e); size-resolved total particle fractions in summer (f) and fall (g); and half-hourly wind direction profiles based on particle counts (h-j).

Lead is one of the oldest known environmental toxins (records date back to 4000 years ago), and because it was used in a broad variety of products, humans are still exposed to lead on a daily basis (317). The Pb1 mass spectrum indicates an ECOC lead particle type, containing both elemental and organic carbon markers, lead, nitrates, and sulfates (**Figure 71**). The ECOC signature suggest that the Pb1 type is a combustion particle type. Types Pb2 and Pb3 are inorganic lead types, containing additional species such as sodium, potassium, iron, and nitrates. Although leaded gasoline has been phased out, the deposition of over 20,000 metric tons of lead in LA and its suburbs during the decades of its use has made the resuspension of soil a potential source of atmospheric lead in the presence and the future (318). Resuspended soil particles resemble mainly inorganic types like Pb2 and Pb3 and will generally be larger than 1 µm. Both Pb1 and Pb2 types had higher particle counts during the fall compared to the summer. These two classes both display southeast directionality, and local winds from this direction were more frequent during the fall season. **Figure 67** illustrates that over 100 facilities reported lead emissions for 2005, indicating a multitude of potential point sources for lead and the difficulty in discerning a single source. However, as both the local wind and HYSPLIT results agree that the high lead concentrations came from the east of Riverside (where there are few facilities that report lead emissions), it is clear that there is a larger source

or sources of lead than the reported anthropogenic emissions. One of the largest sources of airborne Pb in the United States is aviation gasoline [*Murphy et al.*, 2007], which is not accounted for in the point source based EPA TRI. Aircraft emissions are the likely source for the

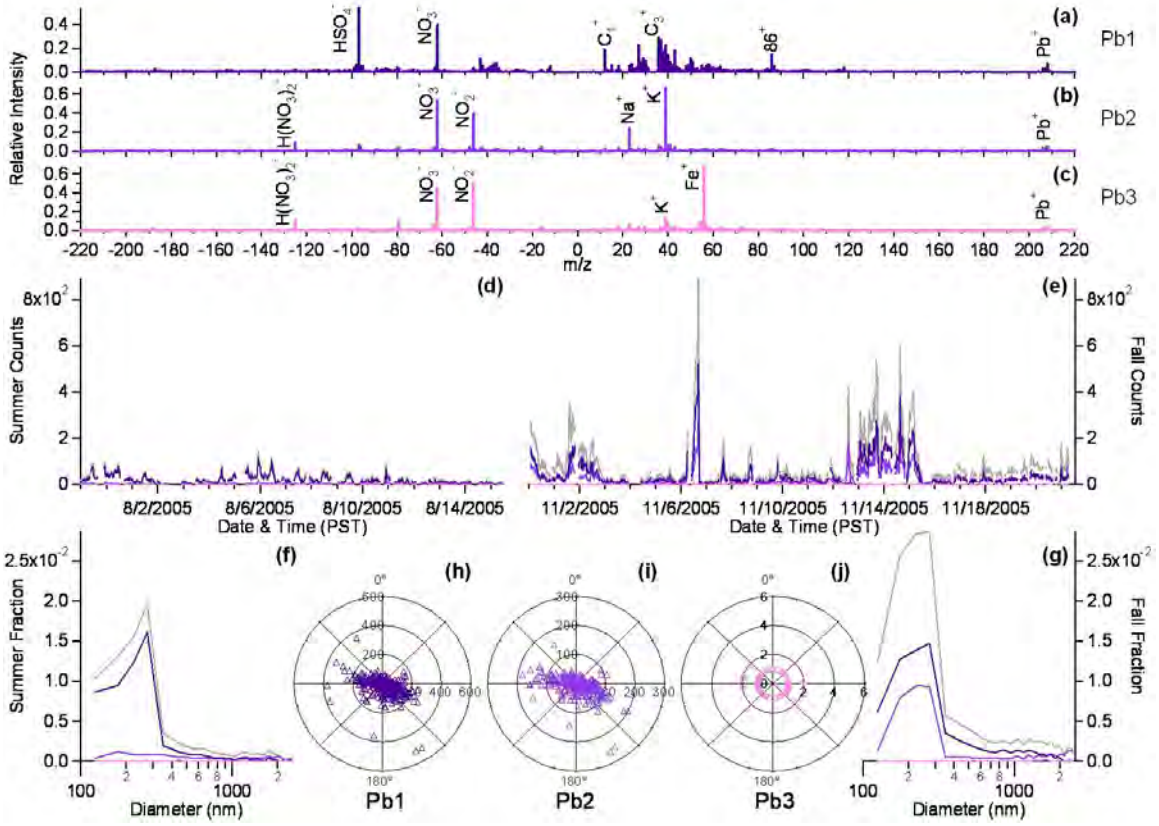


Figure 71: Trends of the three main lead particle types: representative mass spectra (a-c); half-hourly temporal variations in summer (d) and fall (e); size-resolved total particle fractions in summer (f) and fall (g); and half-hourly wind direction profiles based on particle counts (h-j).

combustion-related Pb1 type, especially considering the proximity of the local airports harboring small aircraft.

Although the analysis approach in this work focuses on the separate trace metals, it is clear that the individual particles often contain more than one trace metal. The unique combination of species provides further insights into the identification of potential sources. **Table 11** presents the percentages of metal-containing particles associated with other trace metals. For example, the V row provides the percentages of summer (S) and fall (F) vanadium-containing $PM_{2.5}$ that also have Fe, Ni, Cu, Zn, etc. All percentages greater than 5% are in bold for increased visibility. It is important to understand which metals are in the same individual particles, because the combined toxicity of metals can be greater than the toxicity of a single metal (301). Lead, as expected based on its history of broad uses, was detected in significant percentages (~20%) of several other trace metal particle types. These associations have been noted before in both Switzerland and the United States [*Murhpy et al.*, 2007]. The high correlations among vanadium, iron, and nickel also were expected based on the mass spectra described earlier. In fact, nickel was

rarely detected in a particle that did not also have vanadium, although not every vanadium particle contained nickel, particularly during the summer. Therefore, vanadium must have multiple sources, including one that also emits nickel. Interestingly, barium has very little correlation with other trace metals studied here. Because the highest percentage of another metal also associated with barium particles was only 1.7% (Fe in summer), this finding further exhibits how dominant the unique organic barium particle type was in comparison to the brake dust barium types, which both indicate the presence of iron in their spectra. Additionally, the table demonstrates some strong seasonal differences, such as the percentage of iron on copper-containing particles (1.5% versus 56.7%) and zinc-containing particles (4.6% versus 38.3%) during the summer and fall, respectively. The differences are likely a result of different sources due to the seasonal wind direction and atmospheric conditions described earlier.

| | V | | Fe | | Ni | | Cu | | Zn | | Sr | | Mo | | Sn | | Sb | | Ba | | W | | Pb | |
|---|---|---|---|---|---|---|---|---|---|---|---|---|---|---|---|---|---|---|---|---|---|---|---|---|
| | S | F | S | F | S | F | S | F | S | F | S | F | S | F | S | F | S | F | S | F | S | F | S | F |
| V | | | **32.0** | **70.9** | **20.4** | **72.2** | 0.0 | 0.0 | 0.2 | 0.0 | 0.0 | 0.0 | 0.1 | 0.2 | 0.0 | 0.0 | 0.0 | 0.0 | 0.0 | 0.0 | 0.0 | 0.1 | 0.2 | 0.6 |
| Fe | **62.8** | **75.0** | | | **27.5** | **66.6** | 0.0 | 0.8 | 0.1 | 1.4 | 0.0 | 0.0 | 0.0 | 0.0 | 0.0 | 0.0 | 0.0 | 0.0 | 0.1 | 0.4 | 0.0 | 0.1 | 0.3 | 2.2 |
| Ni | **100.0** | **99.1** | **70.1** | **86.4** | | | 0.0 | 0.0 | 0.0 | 0.0 | 0.0 | 0.0 | 0.0 | 0.0 | 0.0 | 0.0 | 0.0 | 0.0 | 0.0 | 0.0 | 0.0 | 0.0 | 0.2 | 0.6 |
| Cu | 0.9 | 0.1 | 1.5 | **56.7** | 0.0 | 0.0 | | | **6.2** | 0.0 | 0.0 | 0.0 | 0.0 | 0.0 | 0.0 | 0.0 | 0.2 | 0.4 | 0.0 | 0.2 | 0.0 | 0.0 | **7.4** | **16.1** |
| Zn | **19.1** | 0.1 | 4.6 | **38.3** | 0.1 | 0.0 | 0.7 | 0.0 | | | 0.0 | 0.0 | 0.0 | 0.0 | 0.0 | 1.2 | 0.1 | 2.0 | 0.1 | 4.1 | 0.9 | 0.0 | **17.6** | **23.5** |
| Sr | 0.0 | 0.0 | 1.0 | 0.0 | 0.0 | 0.0 | 0.0 | 0.0 | 0.0 | 0.0 | | | 0.0 | 0.0 | 0.0 | 0.0 | 0.0 | 0.0 | 3.5 | 1.4 | 0.0 | 0.0 | 0.0 | **23.1** |
| Mo | **33.0** | **18.0** | 0.9 | 3.6 | 0.0 | 0.1 | 0.0 | 0.0 | 0.0 | 0.0 | 0.0 | 0.0 | | | 0.4 | 0.0 | 0.0 | 0.0 | 0.0 | 0.0 | **5.1** | **14.3** | 1.2 | 3.8 |
| Sn | **11.7** | 0.5 | 0.4 | 3.4 | 0.0 | 0.0 | 0.0 | 0.0 | 0.0 | **6.6** | 0.0 | 0.0 | 0.0 | 0.0 | | | 0.0 | 1.6 | 0.4 | 2.1 | 0.0 | 0.0 | 1.0 | **14.3** |
| Sb | 0.0 | 0.5 | 0.0 | 1.5 | 0.0 | 0.0 | 0.6 | 1.1 | 1.2 | **13.2** | 0.0 | 0.0 | 0.0 | 0.0 | 0.0 | 1.9 | | | 1.2 | **6.5** | 0.0 | 0.0 | **7.1** | **21.9** |
| Ba | 0.4 | 0.1 | 1.7 | 0.9 | 0.2 | 0.0 | 0.0 | 0.0 | 0.0 | 0.3 | 0.1 | 0.0 | 0.0 | 0.0 | 0.0 | 0.0 | 0.1 | | | | 0.0 | 0.0 | 0.1 | 0.7 |
| W | **7.8** | 4.0 | 3.5 | **5.5** | 0.0 | 1.6 | 0.0 | 0.0 | 1.9 | 0.0 | 0.0 | 0.0 | 2.2 | 10.0 | 0.0 | 0.0 | 0.0 | 0.0 | 0.0 | 0.0 | | | **42.7** | **22.7** |
| Pb | 2.6 | 0.4 | 0.8 | 1.6 | 0.2 | 0.3 | 0.0 | 0.2 | 1.0 | 0.6 | 0.0 | 0.0 | 0.0 | 0.0 | 0.0 | 0.1 | 0.0 | 0.1 | 0.0 | 0.2 | 1.1 | 0.2 | | |

S - Summer; F - Fall

Table 11: Metal association percentages (%)

In summary, the locations of potential sources and the wind direction dictate which metal-containing particles dominate during which season. In general, anthropogenic sources, mainly in the industrial and transportation sectors, in the LA Basin produced the different metal-containing particles. These observations made herein show the importance of conducting long term studies through multiple seasons to gain further understanding on how seasonal fluctuations and urban air dynamics influence

ambient particles, especially for particle types that show strong seasonal variations, such as trace metal-containing particles.

**iv. Acknowledgements**

The authors express their gratitude to the entire Prather group for their help in the preparation and overall support of these studies. We thank Megan McKay and the Goldstein research group at the University of California, Berkeley for the meteorology data. We also acknowledge Professor Paul Ziemann (University of California, Riverside) for hosting the SOAR field campaigns, as well as Professor Jose Jimenez (Colorado University, Boulder) and Dr. Ken Docherty (Colorado University, Boulder) for setting up the logistics. We express gratitude to the NOAA Air Resources Laboratory (ARL) for the provision of the HYSPLIT transport and dispersion model. Funding for this project was supplied by the California Air Resources Board (Contract 04-336).

# 10. Impact of Emissions from the Los Angeles Port Region on San Diego Air Quality During Regional Transport Events

## i. Introduction

Atmospheric aerosols regionally and globally impact climate and health. Regionally transported particles contribute significantly to $PM_{2.5}$ as observed in multiple studies (319,320). Oceangoing ships emit an estimated 1.2–1.6 million metric tons (Tg) of $PM_{10}$ per year(321) and the 2006 California Air Resources Board emissions inventory estimates that ships emit more $PM_{2.5}$ (4.94 tons/day) than refineries and power plants combined (3.45 tons/day), representing the second highest PM mobile source in Los Angeles County behind diesel trucks (5.87 tons/day) (322). In coastal regions, models show a significant impact from the emissions of ships and residual fuel combustion on air pollution levels. Strong implications exist for human health (64,323,324), but major uncertainties exist regarding the spatial and seasonal variability of particulate pollution that need further investigation (325). Field observations have confirmed that ships produce significant amounts of soot, vanadium, nickel, and sulfate (168,326). Ships typically burn residual fuel oil, which produces higher concentrations of heavy metals and soot than distillate fuels such as gasoline and diesel (77,327,328). Additional residual fuel oil sources, such as refineries, are often located near large ports and emit metal-containing particles that are particularly harmful to human health (303,329,330). These deleterious effects can be explained by the chemistry of the emissions as well as proposed synergistic relationships between coemitted chemical species such as soot and iron or vanadium and nickel (65,105,331). Recent studies in the Los Angeles and Long Beach (LA-LB) port region have shown vanadium as having the strongest correlation to reactive oxygen species using a macrophage assay (332). These negative health effects combined with the transport of particles from residual fuel combustion make it imperative to determine their contributions to the air pollution in coastal locations along the California coast.

Regionally transported air pollution has been shown to influence the San Diego region in previous studies. Aircraft measurements have shown $O_3$ transport from the Los Angeles (LA) basin and $SO_2$ transport from offshore to San Diego (333). Particles transported from LA have also been observed in San Diego at an urban freeway location by ATOFMS (334). This paper discusses distinct episodes quantifying the impact of regional transport when the air masses originated near the vicinity of the Port of LA observed by real-time single particle mass spectrometry at the Scripps Institution of Oceanography (SIO) Pier in La Jolla, California. During these transport periods, the highest concentrations of submicron carbonaceous and transition metal particles (V, Ni, and Fe) were measured. This study examines the impact of these transported aerosols on PM concentrations in the San Diego region.

## ii. Experimental

### *a. Scripps Institution of Oceanography of Pier 2006 Study*

From August 17 to October 3, 2006, sampling was conducted at the end of the SIO Pier, three hundred meters from shore. Ambient particles were sampled through a

four meter mast, seven meters above the pier, and fifteen meters above the ocean. Different instruments sampled in parallel through insulated sampling lines into multiple instruments. A five hour period of sampling on September 28, 2006 was dominated by submicron particles from a local wildfire, as determined by the ATOFMS mass spectral signatures, and because the focus of this paper is on regional transport impacts, this period is not discussed. Particle size distributions were optically measured using an aerodynamic particle sizer spectrometer (APS 3321, TSI Inc.), which measures size distributions between 0.5-3 μm. Air mass back trajectory calculations were made using HYSPLIT 4.8 (130).

***b. Real-Time Single Particle Mass Spectrometry***

The aerodynamic size and chemical composition of individual particles between 0.2 and 3.0 μm were measured in real-time using an aerosol time-of-flight mass spectrometer (ATOFMS); the design and details have been described in detail elsewhere (127). Briefly, particles are introduced into the ATOFMS through a converging nozzle into a differentially pumped vacuum chamber where they are accelerated to a terminal velocity. The particles then pass through two continuous wave lasers (diode pumped Nd:YAG lasers operating at 532 nm) located 6 cm apart. The velocity of each particle is used to determine the aerodynamic size using speeds from calibration with polystyrene latex spheres of known aerodynamic size, shape, and density. The sized particles are then desorbed and ionized by irradiation from a Q-switched Nd:YAG laser (266nm, 1.2-1.4 mJ/pulse) that is triggered when the particle enters the center of the mass spectrometer ion source. Positive and negative ions from each particle are detected using a dual-polarity, reflectron time-of-flight mass spectrometer. During this study, ambient particles were dried using a silica gel diffusion drier prior to analysis with the ATOFMS to decrease particle water content and, therefore, increase negative ion signal intensities (82). The ATOFMS sized and chemically analyzed 3,502,907 particles during the study.

***c. Data Analysis***

Single particle size and mass spectral information were analyzed with YAADA 1.2 (www.yaada.org) a data analysis toolkit for MATLAB 6.5.1 (The MathWorks, Inc.). Particles were analyzed via two approaches: (1) searching mass spectral, aerodynamic size, and temporal features and (2) clustering mass spectra using an adaptive resonance theory based neural network algorithm (ART-2a) at a vigilance factor of 0.8 (35). ART-2a combines particles into clusters based on the intensity of ion peaks in individual mass spectra. General particle types are defined by the characteristic chemical species or possible source to simplify the naming scheme; these labels do not reflect all of the species present within a specific particle type, but reflect the most intense ion peaks. Peak identifications within this paper correspond to the most probable ions for a given *m/z* ratio.

***d. Scaling ATOFMS to Mass Concentrations***

ATOFMS counts were scaled to number and mass concentrations using APS size-resolved number concentrations, a method shown previously to yield quantitative mass concentrations (128). Briefly, ATOFMS counts are binned into sizes that correspond to the APS size bins (0.5-2.5 μm) and scaling factors for each hour and size bin are

determined to account for ATOFMS transmission biases and busy time. After scaling the number concentrations, density is used to convert from number to mass concentrations. The bins were summed to give the mass of particulate matter less than 1 μm ($PM_1$) or less than 2.5 μm ($PM_{2.5}$). Scaled ATOFMS $PM_{2.5}$ mass concentrations have been shown previously to be well correlated with standard mass measurements, including the beta attenuation monitor (BAM) and micro-orifice uniform deposit impactor (MOUDI) (128). ATOFMS scaled $PM_1$ concentrations have been shown to track mass concentrations (335,336). Previous work has shown that with high relative humidity (129) or liquid water content conditions (48) particle density is low; thus, a density of 1.2 $\mu g/m^3$ has been used for the scaling herein due to an average relative humidity of 93% during sampling.

**iii. Results and Discussion**

**Figure 72** shows the PM concentrations measured over the full study, highlighting the three high concentration regional transport periods. During many of the regional events, daily PM concentration maxima were observed over several days due to diurnal changes in wind speed and direction. Details on the impacts of the regional events on PM concentrations are described below. **Table 12** lists each identified regional event with accompanying properties, discussed in detail in the following sections. The fraction of $PM_1$ contributing to $PM_{2.5}$ is shown per hour in **Figure 73**. During submicron events, $PM_1$ mass accounted for 60% of the $PM_{2.5}$ mass compared to 36% on average during non-event periods.

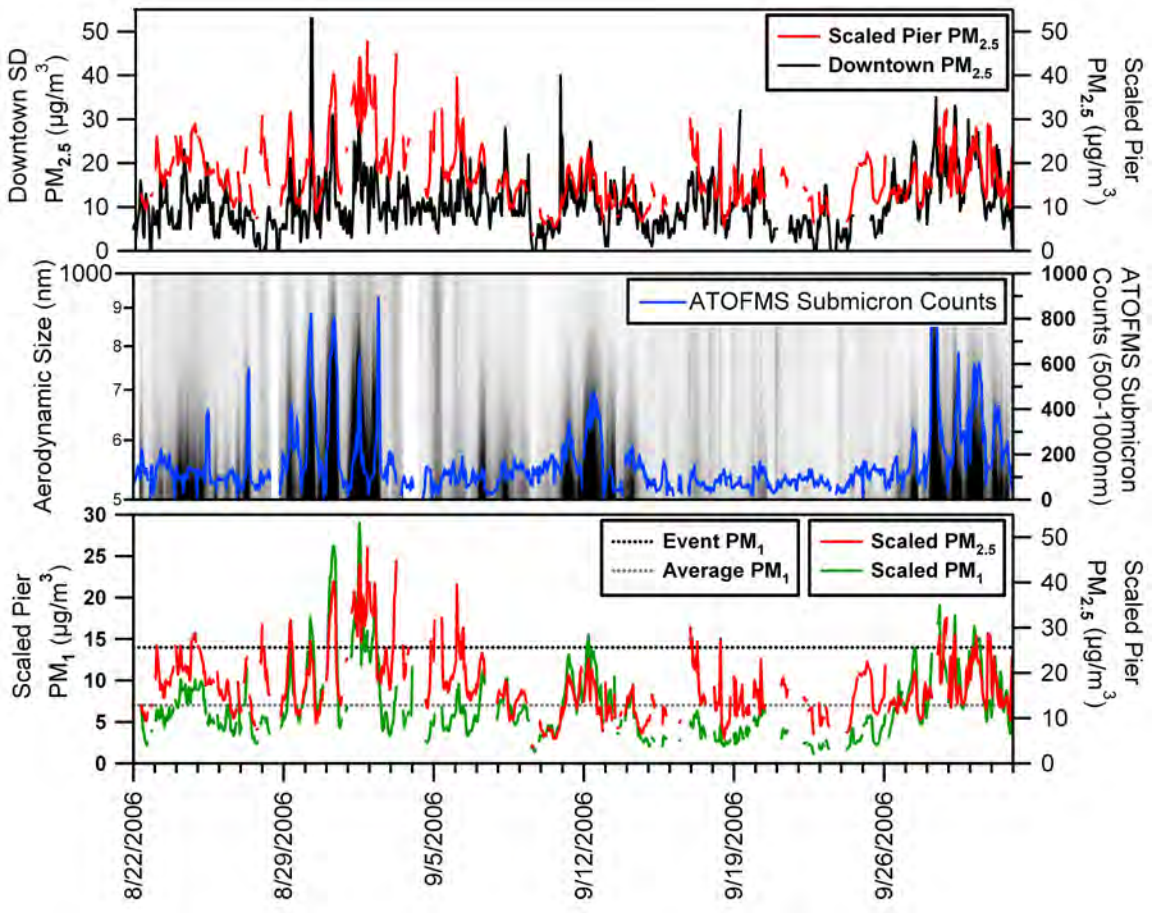


Figure 72: A) The lower portion of the graph shows time series of scaled $PM_{2.5}$ mass concentrations at the SIO Pier (red line) and $PM_{2.5}$ data from downtown San Diego (black line). B) Hourly size distributions measured by an aerodynamic particle sizer (APS) from 0.5-1 µm from August 17, 2006 – October 2, 2006. The overlaid blue line is the sum of ATOFMS counts in the 0.5-1 µm size range per hour. C) Scaled $PM_1$ (green line) and $PM_{2.5}$ (red line) mass concentrations are shown over the sampling period. The gray dashed line represents the average $PM_1$ mass concentration during the study, and the black dashed line represents the $PM_1$ threshold set for regional events.

Table 12: Properties of different regional events are listed including: peak $PM_1$ and $PM_{2.5}$ mass concentrations, fraction of $PM_1$ contributing to $PM_{2.5}$ mass, and the mass percentage of V-Ni-Fe and ECOC particles contributing to the $PM_1$ mass.

| Event Number | Peak Time | Peak $PM_1$ ($\mu g/m^3$) | Peak $PM_{2.5}$ ($\mu g/m^3$) | $PM_1/PM_{2.5}$ Fraction | V+EC % of $PM_1$ |
|---|---|---|---|---|---|
| 1 | 8/29/2006 9:00 | 14 | 32 | 0.43 | 0.68 |
| | 8/30/2006 7:00 | 18 | 27 | 0.65 | 0.63 |
| | 8/31/2006 9:00 | 26 | 40 | 0.65 | 0.86 |
| | 9/1/2006 13:00 | 29 | 44 | 0.66 | 0.85 |
| | 9/2/2006 10:00 | 21 | 40 | 0.54 | 0.72 |
| 2 | 9/12/2006 12:00 | 16 | 23 | 0.67 | 0.72 |
| 3 | 9/27/2006 8:00 | 14 | 18 | 0.78 | 0.67 |
| | 9/28/2006 8:00* | 21 | 28 | 0.75 | 0.07 |
| | 9/29/2006 11:00 | 18 | 25 | 0.72 | 0.24 |
| | 9/30/2006 5:00 | 17 | 25 | 0.66 | 0.45 |

* period impacted by significantly by a local fire

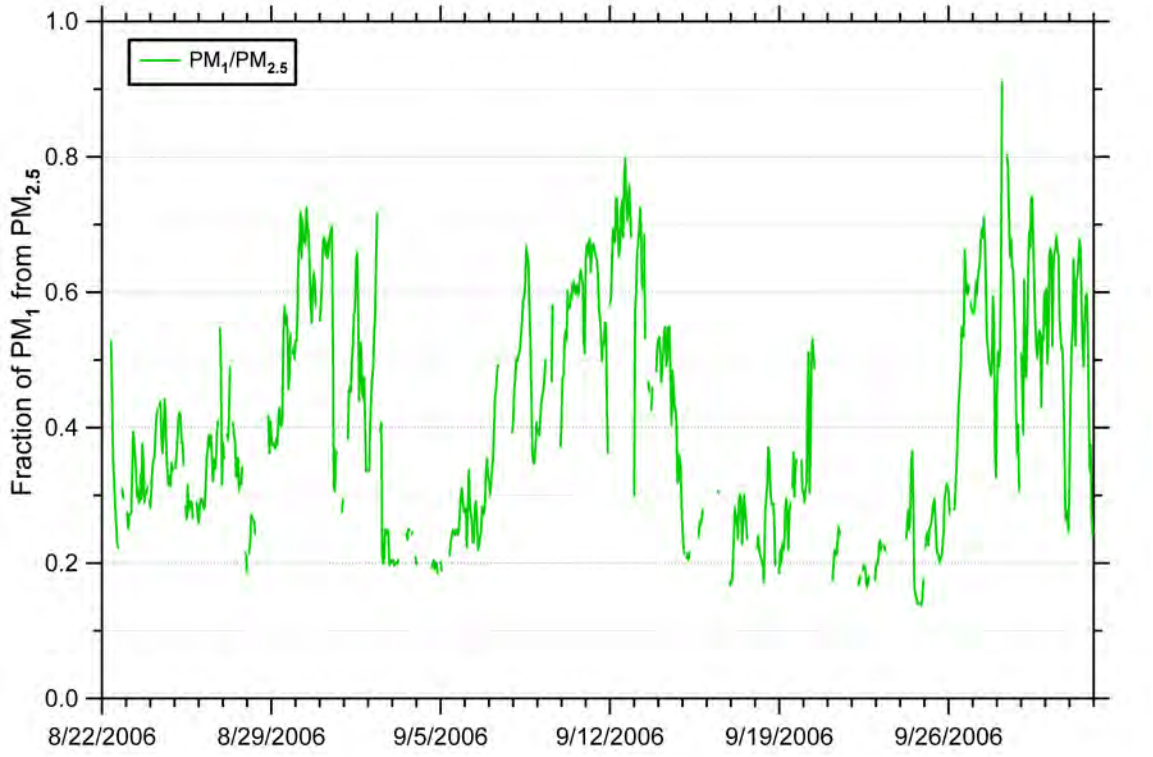


Figure 73: Fraction of scaled $PM_{2.5}$ corresponding to $PM_1$ hourly.

### *a. Mass Concentrations Across San Diego County*

To verify that the scaled PM values at the SIO Pier were reasonable, the $PM_{2.5}$ measurements were compared to 3 other sites in San Diego County operated by the San

Diego Air Pollution Control District (SDAPCD). The average $PM_{2.5}$ measured at the SIO pier during the study (16 $\mu g/m^3$) was similar to the other sites (downtown 10 $\mu g/m^3$, Escondido 18 $\mu g/m^3$, and Alpine 16 $\mu g/m^3$). The downtown San Diego site is the most comparable site to the SIO Pier due to its close proximity and air mass back trajectory patterns. Despite 12 miles separating the SIO Pier and downtown sites, similar trends in $PM_{2.5}$ mass were observed at both sites during the study (**Figure 72a**). This suggests that these transport events described herein likely influence even larger portions of San Diego County.

***b. Identification of Regional Events***

During sampling at the SIO pier, time periods with high submicron particle concentrations were observed using average hourly submicron (0.5-1 μm) size-resolved particle concentrations from an APS. Trends in submicron ATOFMS particle counts are correlated with submicron APS particle concentrations as shown in **Figure 72b**. The relationship between the APS and ATOFMS submicron counts shows that, despite transmission biases from the ATOFMS inlet, temporal variations in submicron ATOFMS counts directly correspond to changes in atmospheric concentrations (128,337). Multiple time periods showed elevated $PM_1$ mass concentrations. **Figure 72c** shows $PM_1$ (blue line) versus $PM_{2.5}$ (red line) mass concentrations calculated using the APS, as described above. The average $PM_1$ concentration during the study was 7 $\mu g/m^3$ (dashed gray line); this represents an upper limit because certain time periods with low particle concentrations were excluded from the analysis as they did not have the requisite statistics for scaling the ATOFMS counts to mass. Regional events are defined as any period when the peak $PM_1$ mass was at least twice the average $PM_1$ concentration (14 $\mu g/m^3$). During regional events, $PM_1$ accounted for 52% of $PM_{2.5}$ mass and 70% of $PM_{2.5}$ number concentrations.

***c. Air Mass History during Regional Events***

To determine the source(s) of the submicron particles at the SIO pier, HYSPLIT air mass back trajectories (48 hours) were calculated at 500 meters and patterns were verified by comparing to back trajectories at 200, 400, 600, 800, and 1000 meters (130). Back trajectories calculated for the peak hour of each submicron concentration spike are shown in **Figure 74a**. Many events had back trajectories coming from the vicinity of the LA-LB Port region, while a small number of additional events were more local and passed near the SD Port. These more local events most likely still had contributions from LA-LB transport that stagnated over the region for several days. **Figure 74b** shows air mass back trajectories during nonevent periods. These air masses either came from the west over the ocean or from inland locations but did not pass near the SD or LA-LB Ports.

**Figure 74c** groups the main air mass back trajectories by type (Port of LA-LB, San Diego, inland, and oceanic) and includes how frequently each type was observed. Back trajectories came from the vicinity of the Ports of LA-LB (32% of the sampling period), the Port of SD (17%), inland (5%), and the ocean (46%). During periods when the air masses came from the LA-LB Port region, regional events were observed 40% of the time. Not all air mass back trajectories coming from the LA-LB port region produced high concentration regional events. In order to create these conditions, high levels of

emissions at the port, consistent boundary layer height, relatively short air mass transport times, and meteorological conditions all have to occur simultaneously. It is important to note that the amount of ship traffic in the LA-LB Port region remained relatively constant (25-40 major ships per day) and thus the major factor contributing to the regional events appears to be proper meteorological conditions (338). Based on the HYSPLIT trajectories, emissions from the Port of SD most likely contributed to two of the events. When oceanic back trajectories occurred, no regional events were observed; this indicates that ship traffic in the open ocean west of San Diego, which is much lower than traffic near the ports, did not contribute significantly to San Diego air quality. During regional transport periods when trajectories came from the LA-LB Port region, it is likely additional sources and processes contributed along the way. Also, the very limited recreational boating in close proximity to the pier and lower ship traffic at the Port of San Diego (1% of LA-LB) leads to lower emissions compared to the Ports of LA-LB and helps explain the lack of events during inland or oceanic time periods (339).

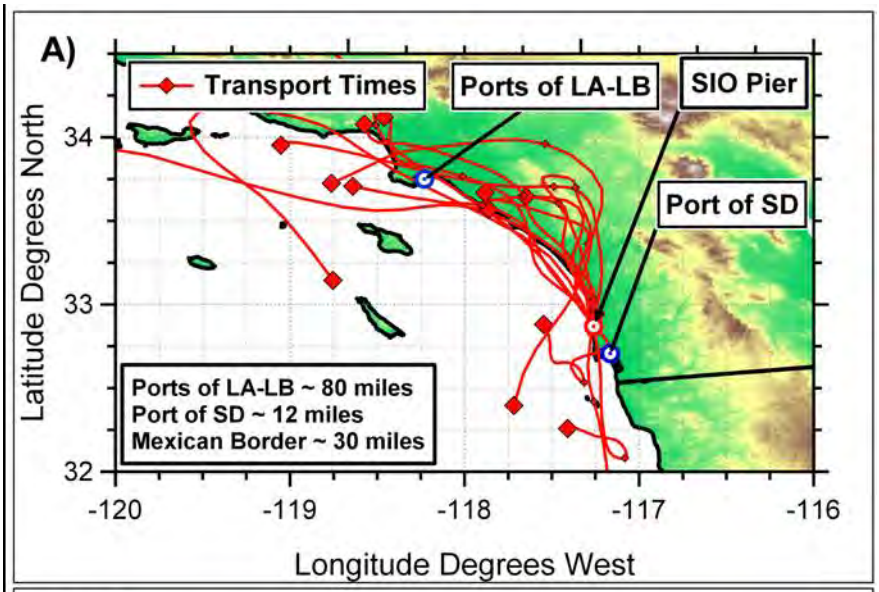


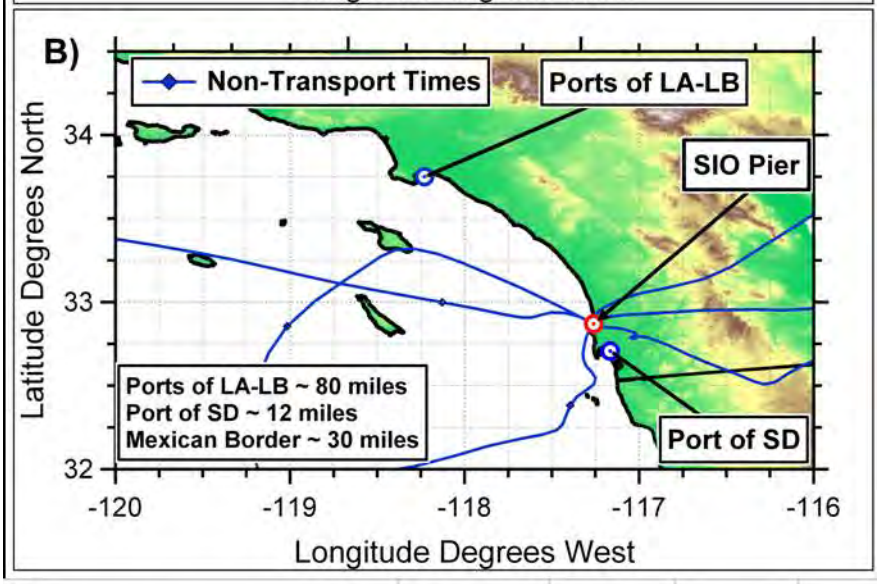


C)

| Primary Air Mass Source Region | Port-Coastal | San Diego | Inland CA | Ocean |
|---|---|---|---|---|
| Transport Type | Regional | Local | Long Range | Mixed |
| Sample to Source Distance (miles) | 77 | 12 | >200 | 0-500 |
| Fraction of Sampling Time | 0.32 | 0.17 | 0.05 | 0.46 |
| Percent Time Submicron Events | 0.4 | 0.29 | 0 | 0 |

Figure 74: HYSPLIT (24 hour) back trajectory analysis at 500 meters for the peak hour of each regional event. Large diamonds represent 24 hours back from the source and small diamonds present 12 hours. A) Trajectories in red pass near the LA Port while trajectories in blue pass over the SD Port. B) Trajectories in purple are representative of non-transport time periods. C) The table included displays the frequency of different air mass types and source regions, as well as the number of regional events observed during each back trajectory type.

### *d. Particle Chemistry during Regional Transport Events*

The most prevalent submicron particle types observed during these regional events were external mixtures of soot, organic carbon, biomass burning, metals, and sea

salt. **Figure 75** shows the average mass spectra of the two most common particle types observed during the regional events. These included an elemental carbon (or soot) particle type mixed with organic carbon, sulfate, nitrate and water, labeled as ECOC(sulfate-nitrate). The second type included vanadium-nickel-iron particles mixed with sulfate, nitrate, carbonaceous species, and water, labeled as V-Ni-Fe(sulfate-nitrate). The particle labeling scheme used herein first indicates the most dominant peaks in the positive ion particle spectra, followed by secondary species detected in the negative ion spectra in parentheses. The positive ion peaks indicate the primary source of the particles, whereas the negative ions provide insight into the atmospheric aging the particles have undergone during transport. Notably, the primary source makes up a high number fraction of particles, but the secondary species make up the bulk of the mass of the particles. The mass spectra of the ECOC(sulfate-nitrate) or soot particles were characterized by elemental carbon cluster ions ($^{12}C_1^+$, $^{24}C_2^+$,…, $C_n^+$) with less intense organic carbon markers ($^{27}C_2H_3^+$, $^{29}C_2H_5^+$, $^{37}C_3H^+$, and $^{43}C_2H_3O^+$) (81). The V-Ni-Fe(sulfate-nitrate) particle type is characterized by intense peaks at $^{51}V^+$ and $^{67}VO^+$ with less intense iron ($^{56}Fe^+$) and nickel ($^{58,60}Ni^+$) ion peaks. It should be noted that a small percentage of spectra in the other submicron particle types showed minor vanadium and vanadium oxide peaks during these events. These mixtures were most likely formed by coagulation processes, but only represented 2-5% of the total particle spectra.

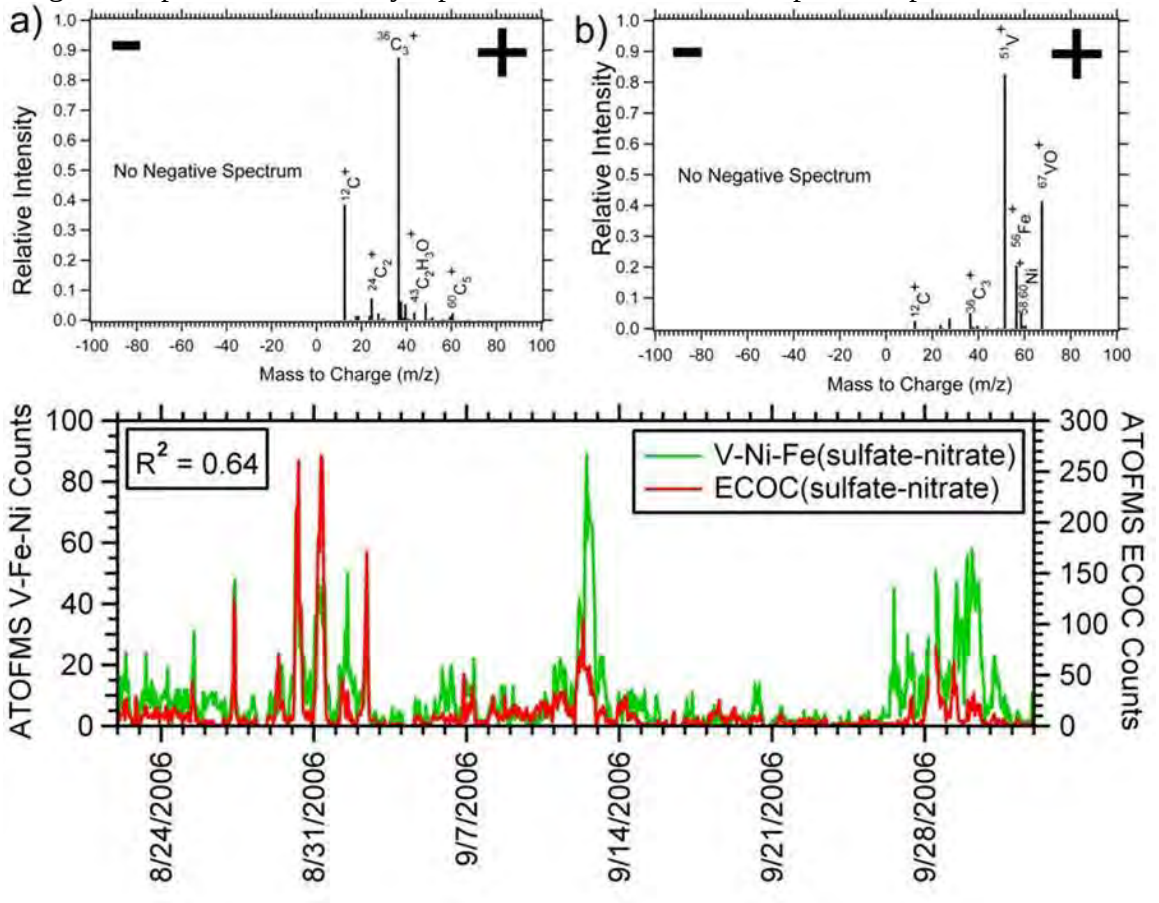


Figure 75: Average negative and positive ion mass spectra for a) ECOC(sulfate-nitrate) and b) V-Ni-Fe(sulfate-nitrate) particles. c) Time series of hourly ECOC(sulfate-nitrate) and V-Ni-Fe(sulfate-nitrate) particle type counts.

***e. General submicron particle types***

Average mass spectra of each particle type (beyond ECOC(sulfate-nitrate) and V-Ni-Fe(sulfate-nitrate)) are shown in **Figure 76** and described below. Elemental carbon particles were identified by carbon cluster ions ($^{12}C_1$, $^{24}C_2$,…, $C_n$) as the dominant peaks in the positive and negative ion mass spectra, as well as sulfate and nitrate ions ($^{97}HSO_4^-$, $^{62}NO_3^-$, and $^{46}NO_2^-$), markers that are associated with aging (81). Organic carbon particles have intense ion markers at $^{27}C_2H_3^+$, $^{29}C_2H_5^+$, $^{37}C_3H^+$, and $^{43}C_2H_3O^+$ (81). Biomass burning particles have a dominant potassium peak ($^{39}K^+$), as well as elemental and organic carbon marker ions. This particle type also has a significant sulfate ion peak ($^{97}HSO_4^-$) and a minor $^{213}K_3SO_4^+$ peak (not shown) which has been linked previously with biomass burning (87,162). Sea salt particles were identified by $^{23}Na^+$, $^{62}Na_2O^+$, $^{63}Na_2OH^+$, and $^{81,83}Na_2Cl^+$ (337). Sea salt with soot particles were characterized by an intense $^{23}Na^+$ peak, elemental carbon cluster ions, organic markers, and other sea salt ion peaks (m/z 62, 63, 81, and 83). This particle type is formed from coagulation of SS and ECOC particles during transport (337,340).

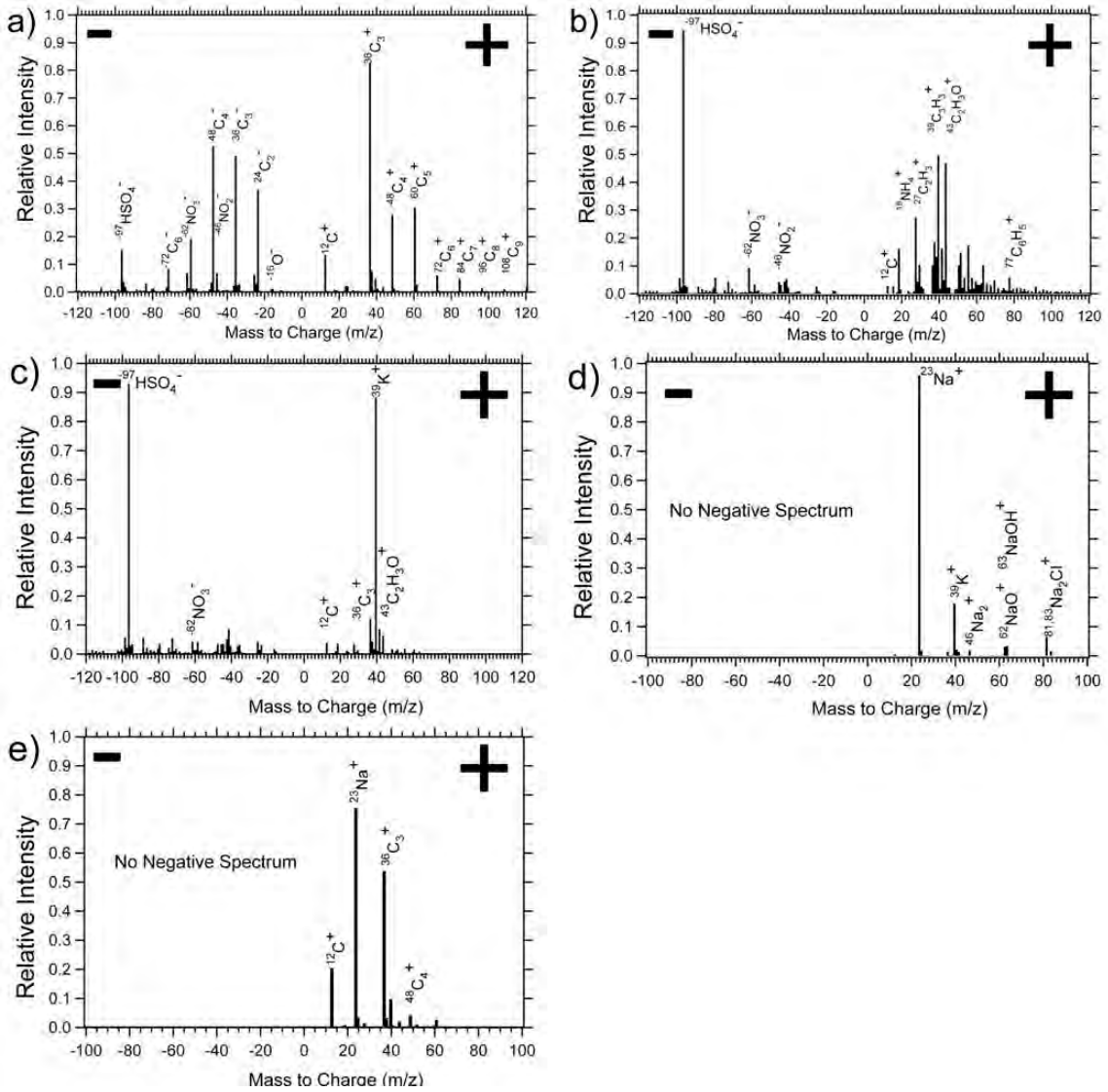


Figure 76: Average negative and positive ion mass spectra for the top six particle types (excluding ECOC and V-Ni-Fe which are discussed in the main paper): a) Elemental carbon, b) Organic carbon, c) Biomass Burning, d) Sea salt, e) Sea salt with soot.

### *f. Sulfate Formation and Aging Processes During Transport*

It is important to note that a high percentage (30-80%) of particles did not produce negative ion mass spectra. Based on optical measurements of single particles with similar chemical signatures (129), water has been shown to remain on the particles which can suppress negative ion formation (82,341). The larger (0.5-1 μm) size of these particles also suggests they have undergone a significant amount of chemical aging during transport. The aging processes include condensation of secondary species, aqueous phase processing of $SO_2$, as well as coagulation with pre-existing sulfate marine background particles (158).

Due to high $SO_2$ concentrations in the port region coupled with high average ambient relative humidity (~93%), it is likely that the particles acquired sulfate due to $SO_2$ oxidative processing when initially formed. In addition, the particles most likely picked

up additional secondary species (sulfate and nitrate), water soluble organic carbon, and water during transport. This is supported by the fact that for both particle types, the limited particles with negative ion mass spectra showed a major bisulfate ion peak ($^{97}HSO_4$), as well as nitrate ion peaks ($^{46}NO_2$ and $^{62}NO_3$). The observations from this study, along with a previous study in the southern California coastal region showing marine background particles with high levels of sulfate, suggest that the ECOC and V-Ni-Fe particles are likely composed of relatively small primary particle cores mixed with sulfate, nitrate, and water (158). Similar observations in previous studies of single soot particles, where core sizes of less than 0.2 μm were observed (84), show that sulfate and nitrate species contribute the majority of the mass to these aged particles. Previous work has also shown that sulfate is associated with ship emissions at the source (61,79). Concurrent filter-based triple oxygen isotope measurements of sulfate at the SIO Pier estimate that ships represent 10-44% of non-sea salt sulfate mass concentrations below 1.5 μm (342). These co-located isotope measurements also suggest the ECOC(sulfate-nitrate) and V-Ni-Fe(sulfate-nitrate) particles acquired significant quantities of sulfate and water at the point of emission as well as through secondary aging processing during transport.

***g. Temporal Variations by Particle Type***

**Figure 77** shows the scaled a) relative fractions and b) contributions to $PM_1$ mass of the different submicron particle types by hour throughout the study. The black line shows the hourly $PM_1$ mass concentrations ($\mu g/m^3$). The particle type representing the majority of submicron mass varies strongly with the concentration of submicron mass. When $PM_1$ levels were high (>14 $\mu g/m^3$), soot and V-Ni-Fe particles account for 24-86% (52% average) of submicron mass. Sea salt, the primary background submicron particle type, represented a significant fraction of submicron particles (75-80%) during periods when the lowest $PM_1$ mass concentrations were observed and $PM_1$ was the smallest fraction of $PM_{2.5}$. These represent marine background periods with high wind speeds. Biomass burning and organic carbon showed low correlations with $PM_1$ ($R^2 = 0.09$ and $R^2 = 0.11$), suggesting these particle types did not come from the same sources as most of the submicron particles detected at the pier.

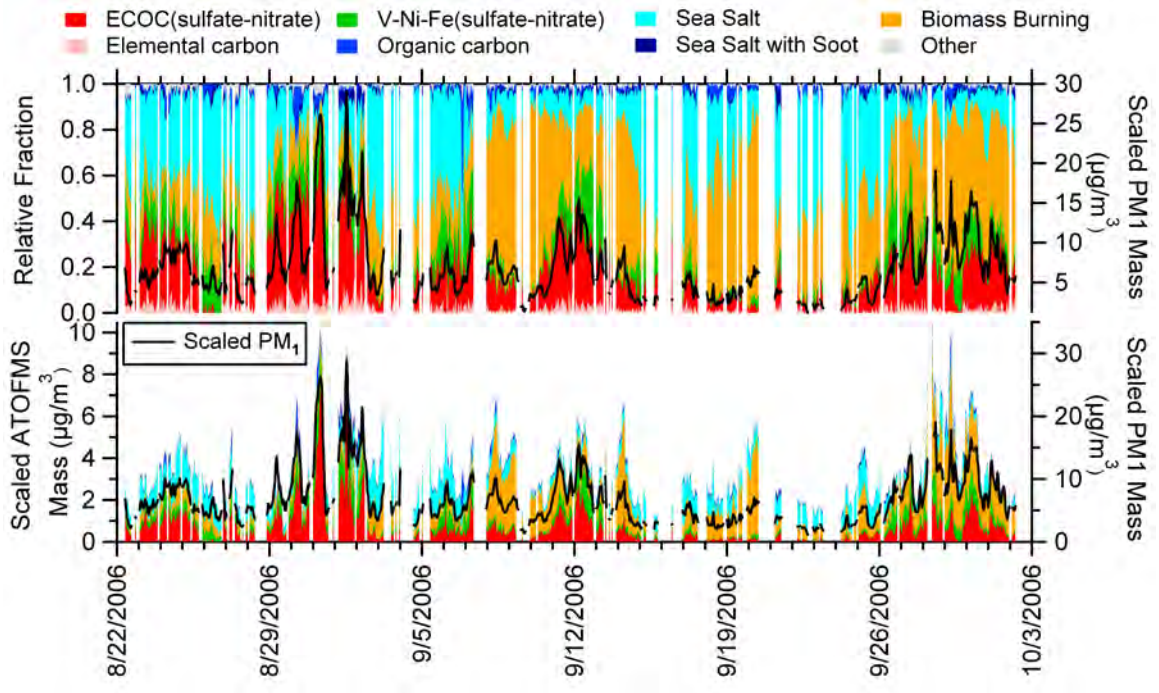


Figure 77: a) Time series of the relative fractions of submicrometer particles types b) Time series of counts of submicron particle types. The black line on both plots is the scaled $PM_1$ mass concentration ($\mu g/m^3$).

### *h. Correlation between Major Particle Types*

Metal-containing particles composed of trace amounts of V, Fe, and Ni mixed with carbonaceous species are primarily emitted from residual fuel combustion processes and as such have limited sources, including ships and refineries (73,343). Since no refineries exist in San Diego or Orange County and residual fuel is burned only on large ocean going vessels, this limits likely sources to ships from the Ports of LA-LB and Port of SD, as well as refineries near the Ports of LA-LB. ECOC particles represent a general type produced by most combustion sources, including diesel truck and automobile emissions (36,344); however the larger sizes observed (> 0.5 μm) and low percentage of particles with negative ion mass spectra, indicate that the particles were highly aged and not from local vehicle sources. **Figure 75c** shows the high correlation ($R^2$ = 0.64) observed between the number concentrations of V-Ni-Fe(sulfate-nitrate) particles and ECOC(sulfate-nitrate) particles with one hour resolution. Ships burn a variety of fuels (i.e. distillate and residual) that produce the soot and V-Ni-Fe(sulfate-nitrate) particle types in different proportions (79,345), that depend on the type of engine, fuel, and operating conditions. The temporal correlation of the V-Ni-Fe(sulfate-nitrate) and ECOC(sulfate-nitrate) particle types (**Figure 75c**) and the significant contributions to $PM_1$ mass (**Figure 78**) during regional events suggests that these two particle types originate from the same source and/or source region. The Supporting Information shows one specific event where a strong correlation between the mass concentrations of ECOC(sulfate-nitrate) and V-Ni-Fe(sulfate-nitrate) for a regional event and the number of ship radio contacts for that period. This occurred during the period with the most rapid (6 hours) transport from the LA-LB Port to the pier. In general, the number of ship

counts in the LA-LB Port region was relatively constant. As described, meteorology, rather than a change in source emissions, appeared to control the high concentrations and regional events observed at the SIO Pier during this study.

### *i. Size-Resolved Chemistry of Regional Events*

The size-resolved chemical mass distributions, calculated using the APS method discussed above, are shown for the average of regional events (**Figure 78a**) as well as the average of non-event time periods for comparison (**Figure 78b**). Regional events showed higher mass concentrations across all submicron sizes (4.7-6.5 μg/m$^3$) when compared to non-event time periods (2.9-3.8 μg/m$^3$). During regional events, the ECOC(sulfate-nitrate) particles represent the most significant fraction of submicron mass in each bin (35-44%), while V-Ni-Fe(sulfate-nitrate) particles contribute 10-19% of particle submicron mass. Note that this is a unique single particle perspective of the mass fractions, and it focuses on the mass fraction of the entire particle type. As previously noted, the majority of the mass of these particles was most likely sulfate, nitrate, and water, as well as a smaller amount of carbonaceous species from residual oil and secondary organic carbon. Soot mixed with sea salt, which has been observed in previous studies during long range transport episodes, showed higher mass concentrations during the event periods (340). These particles were most likely formed by coagulation processes occurring during the longer transport periods. Non-event time periods had much lower ECOC(sulfate-nitrate) (4-22%) and V-Ni-Fe(sulfate-nitrate) (2-10%) mass fractions, showing significantly higher fractions of background particle types. These background types included more sea salt (16-81%) and biomass burning (9-43%) than sea salt (4-28%) and biomass burning during (11-28%) regional events. During these periods, $PM_1$ mass represents only 36% of $PM_{2.5}$ compared with 60% during regional events. The increase in the overall PM mass and contributions from ECOC(sulfate-nitrate) and V-Ni-Fe during regional events shows the major influence of transported emissions on San Diego air quality. Notably, these transported aerosols (ships, refineries, and port vehicle traffic) make much higher contributions to PM concentrations than local San Diego sources during these events.

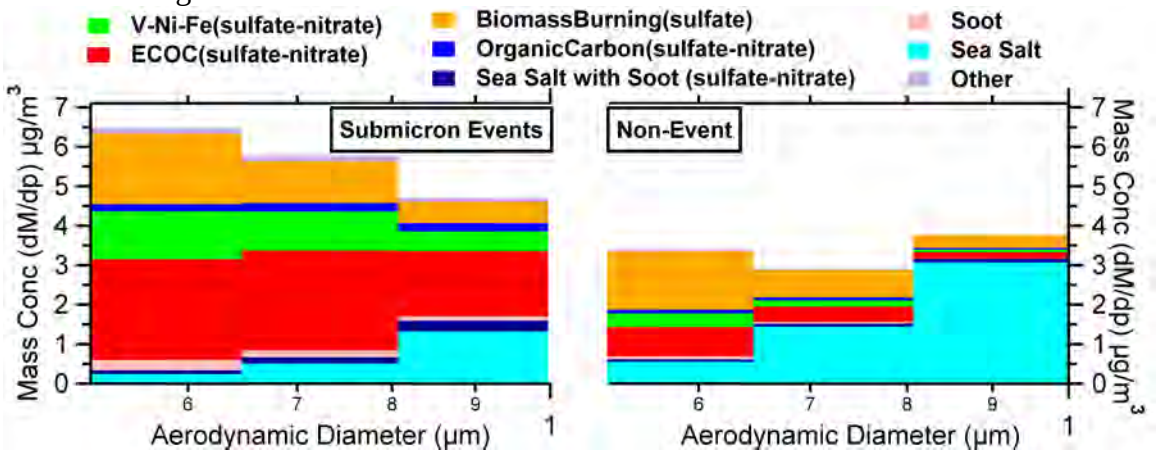


Figure 78: Comparison of the average size-resolved mass distributions of major particle types during regional events and non-events.

### *i. Correlation between Ships at Sea and Selected Particle Types*

Radio transmissions of the location, speed, and heading were recorded in real time for ships in Southern California waters with an automated identification system (AIS) antenna in La Jolla, CA and binned as the number of transmissions per hour (75). These transmissions are required for ships at sea over 299 gross tons every minute by the International Maritime Organization (IMO). **Figure 79** shows one major regional transport event, based on HYSPLIT back trajectories, from September 12-13 with the black line representing the number of recorded ship positions per hour. The transport time from the LA-LB port region during this particular event was ~6 hours and the peak in radioed positions occurred roughly 5-7 hours before the peaks in V-Fe-Ni and ECOC particles, suggesting ships were a contributor to the increase in particle concentrations. To observe this strong correlation required many conditions including favorable meteorology, air mass direction and speed, meteorology favorable to radio transmissions, and a sharp spike in the number of ships at sea. This correlation occurred only one time during sampling, but provides further evidence that the LA-LB port region is a significant source of PM in San Diego.

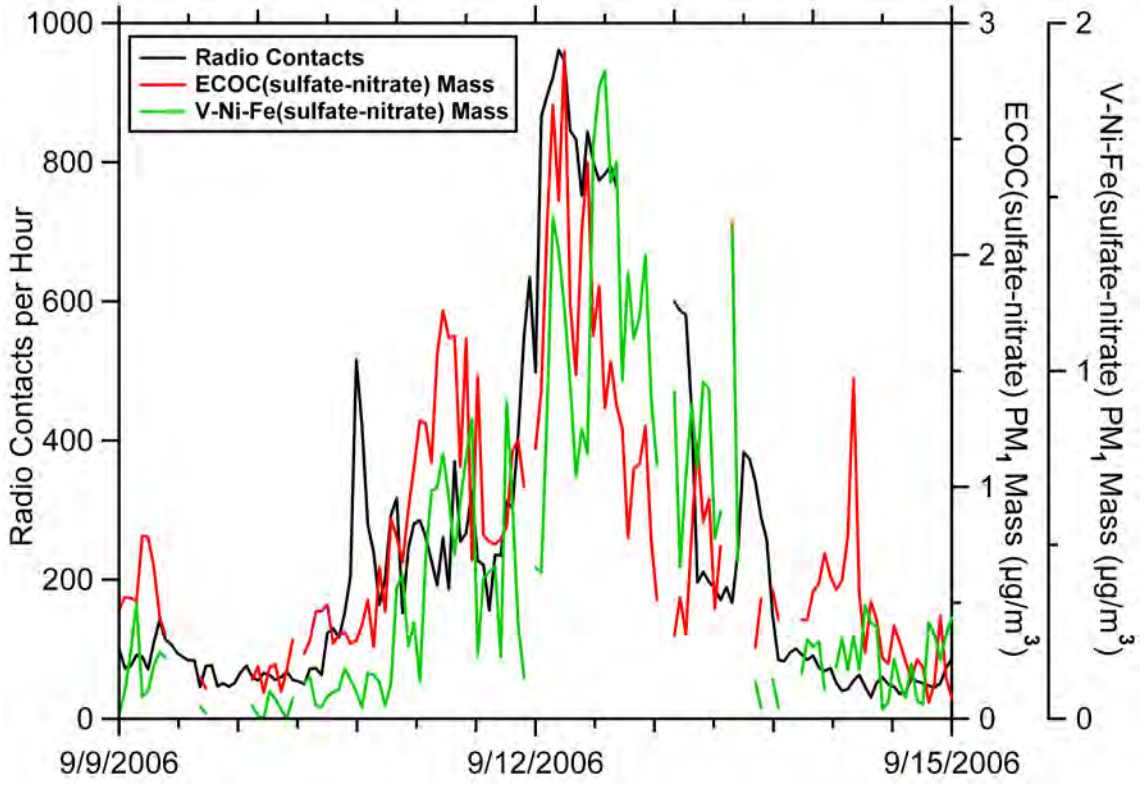


Figure 79: Time series of hourly counts of the ECOC and V-Fe-Ni particle types during 6 day period with ship positions recorded per hour.

### *j. Impact of Regional Events*

Regional transport periods resulted in $PM_1$ mass concentrations that were increased by a factor of 2-4, showing how strongly ships, refineries, vehicles, and other port combustion sources from the Ports of Los Angeles and Long Beach impact air quality in the San Diego area. Emissions transported 12 miles north from the Port of San Diego, while less frequent, most likely mixed with regionally transported emissions and

play a role in lowering the overall air quality of the San Diego region. Particles between 0.5-1 μm contribute the most mass to $PM_1$ and $PM_{2.5}$ for the regional events. The majority of the mass for these particles is likely a mixture of sulfate, nitrate, and water, but identifying the core (ECOC or V-Ni-Fe) is critical to identifying the original particle source and allowing the proper regulations to be established. The adverse health effects of residual fuel combustion particles, which contain a complex mixture of carbonaceous and metals, on residents of San Diego county as well as other coastal cities could be quite significant (64).

Long-term sampling at a coastal site with speciated aerosol number and mass concentration measurements will shed further light on the frequency and intensity of these transport periods and how they vary seasonally. The impact of regionally transported pollution on receptor site locations beyond San Diego needs to be considered when evaluating the health impacts of particles in urban and rural areas. These emissions will become even more important as vehicle emissions become further regulated and residual oil sources such as shipping continue to grow. The strong influence of regional transport on San Diego air quality in comparison to the impact of local emissions demonstrates the importance of monitoring and further regulating these sources in the future.

**iv. Acknowledgements**

The authors gratefully acknowledge Dr. Gerardo Dominguez and Prof. Mark Thiemens for providing the ship tracking data. The authors acknowledge and thank Dr. Ryan Sullivan, Lindsay Hatch, Margaret Yandell, Elizabeth Fitzgerald, and John Holecek for their support and assistance with measurements at the SIO Pier. William Brick at the San Diego Air Pollution Control District is thanked for sharing San Diego County $PM_{2.5}$ mass concentrations. Funding was provided by the California Air Resources Board under contracts 04-336 and 05-346. The authors gratefully acknowledge the NOAA Air Resources Laboratory for the provision of the HYSPLIT transport model and READY website (http://www.arl.noaa.gov/ready.html) used in this publication.

## 11. Single Particle Composition, Hygroscopicity, and CCN Activity during the 2007 San Diego Wildfires

### i. Introduction

Biomass burning can be a significant source of aerosols in many regions of the world (346). Biomass burning aerosol particles (BBA) are a common component of tropospheric aerosol and have been observed to varying degrees in several locations with various techniques including Proton-Induced X-ray Emission (PIXE), Scanning Electron Microscopy (SEM) and single particle mass spectrometry (SPMS) (346-352). Since most of BBA are smaller than 400nm(351,353,354), their removal from the atmosphere is not dominated by dry deposition, but preferably by cloud droplet activation and wet deposition (355). BBA can also become transported to high altitudes and undergo long range transport, affecting global climate (348,356,357). Risk of wildfires is an increasing concern because of increased dryness in certain regions due to climate change (358). Smoke and pollution aerosol can either increase or decrease cloud cover through indirect effects by modifying cloud microphysics, and can directly alter radiative transfer by absorbing and reflecting radiation. These aerosol-climate feedbacks are some of the largest uncertainties in climate research (359-364). Biomass burning can cause intense convection, where the aerosol is transported to high levels in the atmosphere (365). The resulting large updraft velocities can produce high water supersaturations and thus cause the BBA to nucleate cloud droplets.

Due to the abundance, cloud interactions, and wet removal of BBA, it is especially important to understand its interaction with water. Uptake of water by aerosols is determined by their chemical content and thus hygroscopicity, and interactions with water can in turn alter their physical and chemical properties (366). Water content can alter the partitioning of semi-volatile species between the gas and particle phases, which further effects aerosol composition (367) and aqueous chemistry (368). Hygroscopicity strongly influences the light scattering, cloud condensation nuclei (CCN) activity, refractive index and size of aerosols. These properties are essential for understanding the aerosol direct and indirect effect on the global radiation budget (358,362).

An important factor determining the composition of BBA is fire type, fuel type, and age of the smoke (369,370). Flaming fires (pyrolysis) tend to produce particles with higher inorganic content and more elemental carbon, while smoldering fires (charring) tend to produce more organic carbon rich aerosol (351,354,371-374), which include water-soluble sugars such as levoglucosan. If the particles contain relatively little inorganic salts that can absorb water, they may exist as tarballs (353). In fact, it has been shown that fire type is more important than fuel type for chemical signatures of the resulting particles (375), while others have shown large differences in chemical signatures with both fire type and fuel type (374). In general, the carbon content of the fuel is a limited range (~37-54%), therefore emission factors are a function of combustion conditions for carbon, oxygen and hydrogen containing compounds (376). Other minor elements like nitrogen, sulfur and the halogens emission factors depend on the concentrations in the fuel and combustion conditions(376). The large fractions of soluble inorganic and organic compounds can make BBA hygroscopic and thus efficient CCN (368,377), and some of these organic compound are hygroscopic enough to cause cloud

droplet activation without the association of inorganic compounds (377). Previous studies have shown that knowledge of the contribution of water soluble organic carbon (WSOC) is essential to predicting the hygroscopicity of ambient aerosol (365,378-380). Using filter extractions of biomass burning aerosol, (381) have shown that hygroscopicity depended on the type of biofuel. A wide range of hygroscopicities ($\kappa$ = 0.06-0.7) was measured from a variety of biomass materials that were strongly dependent on fuel type (370).

Fresh biomass burning particles, consisting of mostly potassium, chloride, and organic carbon(382,383), can be readily converted to potassium nitrate ($KNO_3$) and potassium sulfate ($K_2SO_4$) via heterogeneous reactions with secondary acids such as $HNO_3$ and $H_2SO_4$ during atmospheric transport (371,384-386). These heterogeneous reactions have important implications for BBA hygroscopic properties, as the deliquescence relative humidity (DRH) of $K_2SO_4$ and $KNO_3$ are 97.4 and 92.5%, respectively, while KCl is 84.3% (371); as well as releasing chlorine gases to the atmosphere.

During the fall 2007 wildfires in San Diego, over 2,000 homes and 300,000 acres were burned in San Diego County for a total of 3069 homes and 516,465 acres in all of Southern California (387). Particle number concentrations were 10 times higher than normal background (36,748 ± 21,646 particles $cm^{-3}$), especially for particles with diameters < 300nm. In this study we compare CCN concentrations and aerosol hygroscopicity with submicron single-particle size and chemical composition in various air masses during October and November 2007 to investigate the different factors that influenced aerosol chemical composition and their resulting hygroscopicity during a period heavily influenced by biomass burning.

## ii. Experimental

### *a. Sampling locations and instrumentation*

Ambient particles were sampled from outside the laboratory on the second floor of Urey Hall (32°52'31.66"N, 117°14'28.64"W) on the campus of the University of California, San Diego (UCSD) from Sunday, October 21 to Thursday, November 1, 2007. The aerosol was sampled through a 3/8" stainless steel tube that extended outside through the exterior wall, and delivered to the various instruments. The lab is located approximately 1 km from the Pacific Ocean coastline at an elevation of ~130 m above sea level. Single particle aerodynamic size and chemical composition were measured in real-time with an ultrafine aerosol time-of-flight mass spectrometer (UF-ATOFMS) instrument equipped with an aerodynamic lens that transmitted an aerodynamic diameter ($D_a$) size range of 50 to 300nm. Single particles are sized based on their time-of-flight between two 532 nm CW lasers and then ablated and ionized by a Q-switched 266 nm Nd:YAG laser. The resulting positive and negative ions are analyzed by a dual-polarity reflectron time-of-flight mass spectrometer. Further details on the UF-ATOFMS instrument design and operation are described elsewhere (388). The particle size distributions and number concentrations were measured concurrently by a scanning mobility particle sizer (SMPS, TSI Model 3936) with sheath and aerosol flows of 4.0 and 0.4 lpm, respectively. CCN concentrations were measured with a streamwise thermal-gradient CCN counter at a supersaturation of 0.29% (389). The instrument was calibrated

before use with ammonium sulfate aerosol (99.999%, Sigma Aldrich). Total particle condensation nuclei (CN) concentrations were measured with a condensation particle counter (CPC, TSI model 3007). The fraction of CCN active particles, or fCCN, was obtained from the CCN/CN ratio. A second CCN counter and CPC (TSI model 3010) was located at the Scripps Institution of Oceanography (SIO) Pier (32° 51'47.232"N, 117° 15'21.6"W) and operated at a supersaturation of 0.13%. The sampling setup on the SIO Pier was approximately 50 feet above sea level and a quarter of a mile from the coast. We will refer to the Urey Hall CCN as CCN_0.3 and the SIO Pier CCN as CCN_0.1. Meteorological data was also obtained from the SIO pier.

### *b. ATOFMS data analysis*

The UF-ATOFMS single particle data were automatically sorted and grouped into clusters of particles with similar mass spectral characteristics using the adaptive resonance theory neural network algorithm, ART-2a. The main user-defined parameters for ART-2a are the learning rate, number of iterations, and vigilance factor, which were set to 0.05, 20, and 0.85, respectively (390). The resulting clusters were then analyzed manually and classified into distinct particle types based on their mass spectral features(348,350,391-393). The dual polarity (having both positive and negative ion spectra) biomass clusters were combined to yield the subset of particles presented herein. We have observed no significant change in average chemical marker peak areas as a function of vacuum aerodynamic diameter 50-300nm on the BBA.

### *c. Single hygroscopicity parameter*

To summarize the hygroscopicity measurements made with the CCNcs, a single parameter for particle hygroscopicity ($\kappa$) is used (394). The following equation defines the relationship between a growing particle's equilibrium water saturation ratio, $S$, diameter, $D$, dry diameter, $D_{dry}$, and hygroscopicity, $\kappa$:

$$S(D) = \frac{D^3 - D_{dry}^3}{D^3 - D_{dry}^3(1-\kappa)} \exp\left(\frac{A}{D}\right) \qquad (1)$$

where $A$ = 2.1x10$^{-9}$ m is a constant evaluated for a surface tension of 0.072 J m$^{-2}$ (pure water) and temperature of 298.15 K (394). $\kappa$ describes a particle's water activity and typical values range from 1.4 (hygroscopic soluble salt) to about 0 (insoluble but wettable) for atmospherically relevant systems. Plotting the critical supersaturation of identical particles of varying size in log $s_c$ – log $D_{\mathrm{dry}}$ space yields kappa isolines where particles lying along one isoline will all have the same hygroscopicity ($\kappa$). The CCN activation diameter ($D_{act}$) of atmospheric aerosols at s = 0.29% (CCN_0.3) and s = 0.13% (CCN_0.1) was estimated using the measured size distributions, CN, and CCN concentrations. $D_{act}$ was derived by

$$1 - \frac{CCN}{CN} = \frac{\int_{D_0}^{D_{act}} n(D)dD}{N_{total}} \qquad (2)$$

where $N_{\mathrm{total}}$ is the cumulative concentration obtained by integrating the observed size distribution of $n(D)$, $D$ is the electric mobility diameter selected by the SMPS and $D_o$ the smallest size measured by the SMPS (~11 nm). The CCN/CN ratio represents the fraction

of the CCN-active aerosols (fCCN). Therefore, the quantity 1-CCN/CN represents the fraction of non-CCN active aerosols. Eqn. (2) assumes that all chemical compositions are internally mixed (i.e. one particle composition). This approach was taken to simplify the data analysis and still reflects how much the relative degree of variation in the chemical composition affects CCN activity, as the size resolved chemistry was measured (391). We have estimated an approximate relationship between $D_{act}$ and $\kappa$ to be $D_{act} \sim \kappa^{-1/3}$(395). In the estimation of $D_{act}$, contributions from particles larger than the range of the SMPS (upper range = 600 nm for our settings) were not considered, but were most likely relatively quite low and made minor contributions to the total aerosol concentration as biomass particles are primarily less than 400 nm (354).

### iii. Results and Discussion

This study can be described by five different time periods based on the Urey Hall laboratory-based CCN and fCCN (from now on referred to as CCN_0.3, fCCN_0.3), size distributions, particle chemistry and air mass back trajectories. HYSPLIT air mass back trajectories during different time periods are displayed in **Figure 80**. A summary of time periods and their CCN, fCCN, CN, size distributions, particle chemistry and HYSPLIT is provided in **Table 13** and **Table 14**.

| Period Name/time | fCCN_0.3 | NCCN1_0.3 | CN_0.3 | Kappa_0.3 | SMPS | Biomass Particle Chemistry | HYSPLIT |
|---|---|---|---|---|---|---|---|
| 1. Santa Ana Fire 10/22-10/23 | 0.36 +/- 0.09 | 7448 +/- 4453 | 21984 +/-17906 | 0.05 +/-0.05 | 125 nm (11.8/209.1) | Larger inorganic signatures | Strong Santa Ana |
| 2. 10/24-10/25 12:00 Local stagnation | 0.34 +/- 0.11 | 4114 +/- 1531 | 12495 +/-3485 | 0.04 +/- 0.008 | 150 nm (25.9/209.1) | Small increase in ammonium | Stagnated; from ocean and inland |
| 3. 10/25 12:00-10/26 12:00 1st Ammonium Period | 0.36 +/- 0.10 | 4013 +/- 1208 | 11047 +/-2578 | 0.05 +/- 0.02 | 190 nm (27.9/299.6) | Large increase in ammonium | From ocean |
| 4. 10/26 12:00-10/28 00:00 2nd Ammonium period | 0.17 +/- 0.06 | 1195 +/- 243 | 7570 +/- 2627 | 0.03 +/- 0.008 | 60 nm (15.1/278.8) | Ammonium signal still high | From coast, ocean, inland |
| 5. 10/31 12:00- 11/1 12:00 Local background | 0.20 +/- 0.09 | 1035 +/- 275 | 10038 +/-13227 | 0.06 +/-0.03 | 20nm (14.6/117.6) | Many particle types; none specifically tracking CCN | From North along coast |

Table 13: Overview of different Urey Hall CCN periods based on CCN activity, size distributions, particle chemistry and hysplit back trajectories (see dividing lines in **Figure 81**). SMPS data is the average mode for that period with the min/max mode of $dN/dlogD_p$ in parenthesis.

| Period Name/time | fCCN_0.1 | NCCN2_0.1 | CN_0.1 | Kappa_0.1* |
|---|---|---|---|---|
| 1. Santa Ana Fire 10/22-10/23 a; b | 0.60 +/- 0.15 | 9600 +/- 5974 | 15477 +/- 6896 | 0.5 +/- 0.4 |
| 2. 10/24-10/25 12:00 Local stagnation | 0.47 +/- 0.13 | 4567 +/- 1437 | 9941 +/- 1948 | 0.3 +/- 0.08 |
| 3. 10/25 12:00- 10/26 12:00 1st Ammonium Period | 0.53 +/- 0.08 | 4267 +/- 990 | 8160 +/- 1843 | 0.4 +/- 0.4 |
| 4. 10/26 12:00- 10/28 00:00 2nd Ammonium period | 0.33 +/- 0.15 | 1610 +/- 446 | 5641 +/- 2136 | 0.3 +/- 0.1 |
| 5. 10/31 12:00- 11/1 12:00 Local background | 0.39 +/- 0.11 | 1177 +/- 352 | 3106 +/- 722 | 0.5 +/- 0.3 |

Table 14: Overview of SIO Pier CCN, fCCN, CN and Dact during Urey Hall CCN periods (from table 1a).

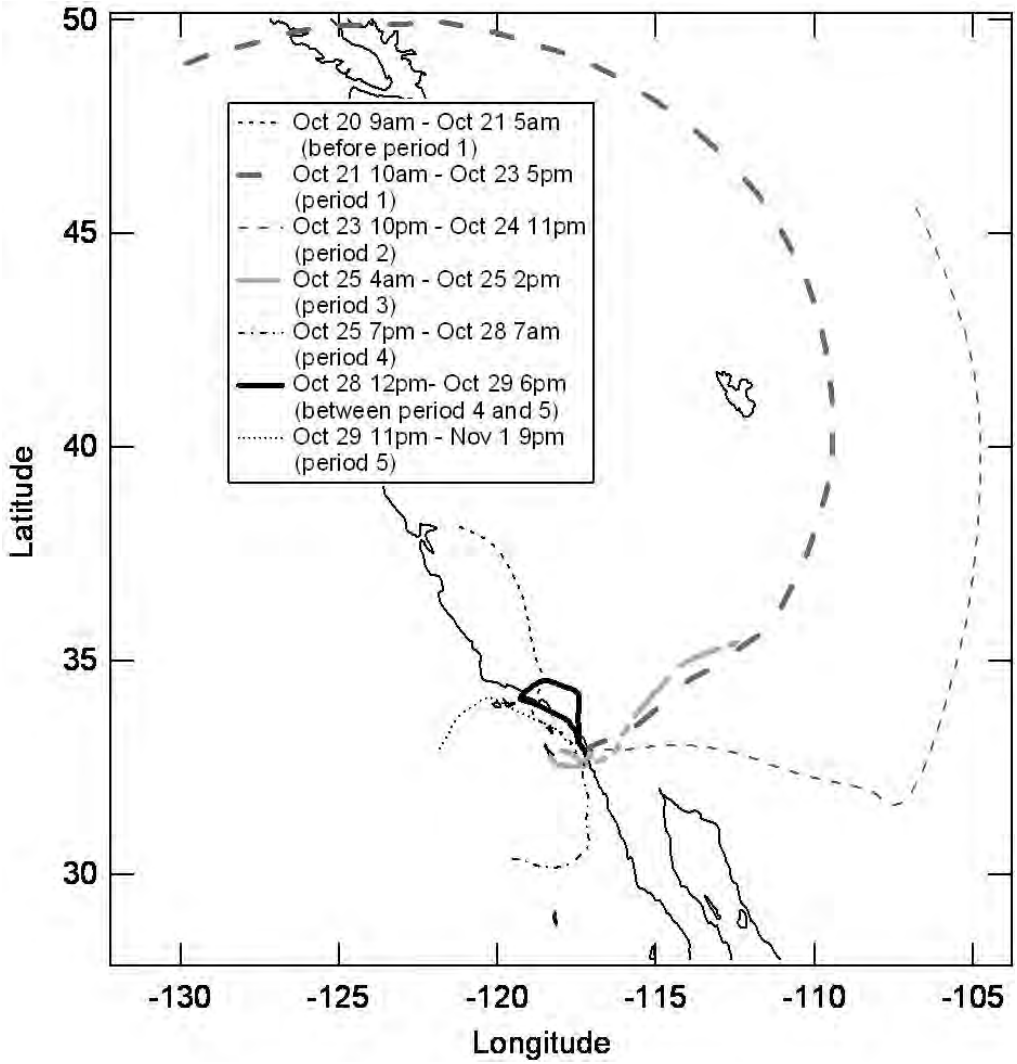

Figure 80: HYSPLIT back trajectories during wildfire sampling period. Each line is a representative 48 hour backtrajectory during that period at 500m. Corresponding periods for comparison to sampling data are in parenthesis.

### *a. Temporal trends of UCSD CCN_0.3, UCSD CN*

Period 1, Santa Ana fire, was dominated by Santa Ana winds and had UCSD CCN_0.3 concentrations up to 14,000/cm$^3$ and UCSD CN concentrations up to 58,000/cm$^3$. Period 2, local stagnation, was dominated by air stagnated over the inland region; period 3 by high ammonium content in the particles and air masses from the ocean; period 4 also by high ammonium content and air from the coast and ocean; and period 5 by local coast/ocean air masses. Typical background CN concentrations are 5,000-10,000/cm$^3$, as were observed during Period 5. As shown in **Figure 81**, CCN_0.3 and CN counts were very high (>10,000) during the Santa Ana fire period. The fraction of CCN_0.3, or fCCN_0.3 (UCSD CCN_0.3/UCSD CN) was also high (0.23-0.47) during the Santa Ana fire period (period 1). Overtime, going from period 1 to period 4 there is a gradual decrease in both CCN_0.3 concentrations, and fCCN_0.3 with notable spikes in fCCN_0.3 along the way. During the first ammonium period (period 3), there is a large increase in UCSD fCCN_0.3 from 0.2 to 0.5. There is also a large increase in relative humidity (RH) during this period.

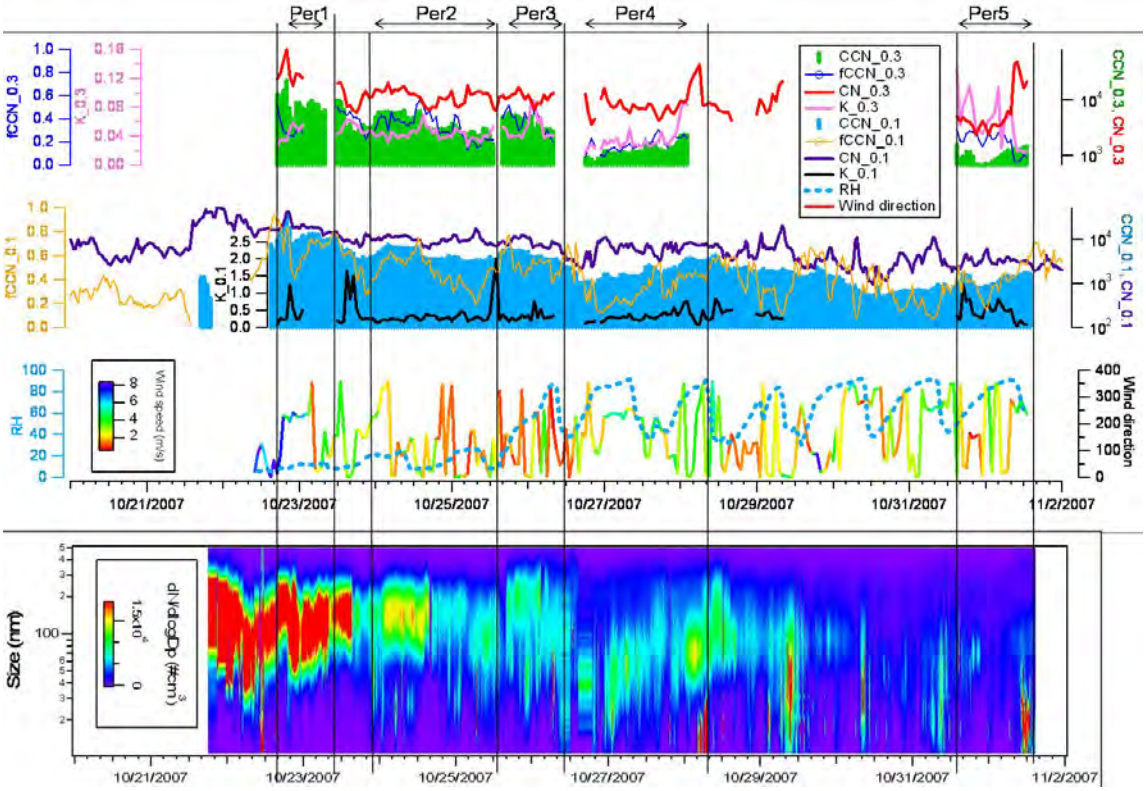


Figure 81: Overview of Urey Hall CCN (UCSD CCN_0.3) and SIO CCN (SIO CCN_0.1) concentrations (s=0.29, 0.13 respectively), fCCN_0.3, fCCN_0.1, Dact_0.3, meteorological data and Urey Hall SMPS

### *b. Composition, size and CCN*

Single particle size and chemical composition was measured concurrently with fCCN_0.3. As the majority of BBA are < 400 nm (353,354), by comparing the composition of particles at these sizes will help determine the relationship between particle size, chemistry and hygroscopicity that control $D_{act}$. As shown in **Figure 82**, the majority (70-95%) of the particles during periods 1 through 3 were BBA. After period 3, other particles types including elemental carbon and amines had an increased contribution (30-60%) to the total particles < 300nm. Period 5 occurred well after the fires ended began and represents more typical background conditions in the San Diego area (**Figure 81** and **Figure 82**). The SMPS size distribution (**Figure 81**) shows that during the Santa Ana fire period, the BBA dominated (**Figure 82**) and had a mean diameter around 125 nm (**Table 13**).

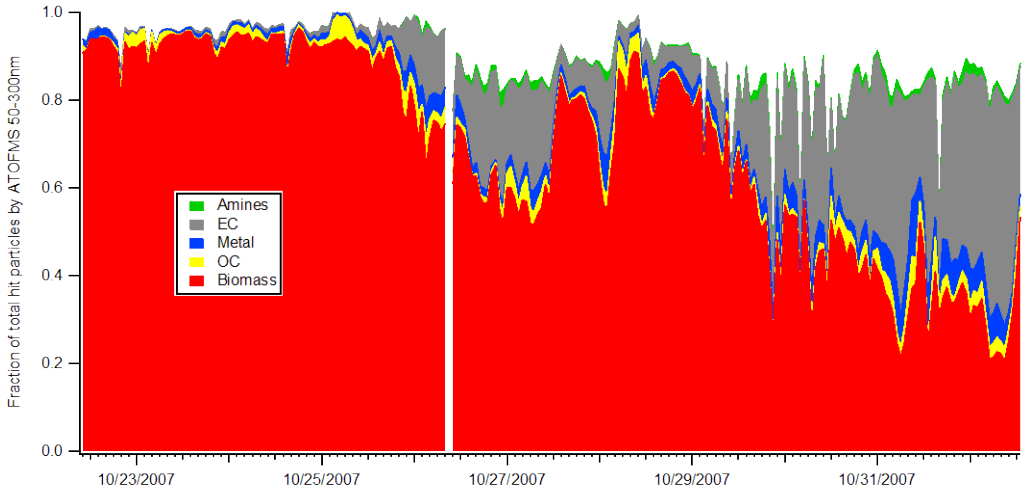


Figure 82: Particle classification temporal. Shown is the classification of particles detected between 50 and 300 nm by the ATOFMS during the study. Biomass is shown in red and is the dominant type during most of the period. Gray is elemental carbon (EC) and grows in as biomass decreases.

Using single-particle mass spectrometry in real time with an ATOFMS allows us to track single-particle mixing state with high time resolution. Each particle that is ionized via laser desorption gives both a positive- and negative-ion mass spectrum. During this study the dominant submicron particle type between 50-300 nm was biomass. The ATOFMS has previously been used to determine biomass burning markers from Southern California biota (393). Fine particle potassium with carbonaceous signatures are known to be markers for biomass combustion (347,354,371,393,396). The concentration of potassium can range depending on the type of fuel. It has been shown that both sulfate and nitrate can be internally mixed with potassium in biomass burning single particles produced from flaming fires (393). Levoglucosan has also been used as a marker for biomass burning (397). Due to the variability in the laser desorption process, we cannot be strictly quantitative, but due to the relatively constant ionization matrix of the BBA particles, we can look at relative abundances of various chemical species by tracking their peak areas on a specific particle type. Main ion peaks used in this manuscript are: $NH_4$ (m/z +18); K (m/z +39); $(C_2H_5)_2NCH_2$ (m/z +86); $(C_2H_5)_3N$(m/z +101); Cl (m/z -35); $CHO_2$ (m/z -45); $NO_2$ (m/z -46); $CH_3CO_2$ (m/z -59); NO3 (m/z -62); $C_3H_3O_2$ (m/z -71); $CH_3CH_2CHO_2$ (m/z -73); $SO_3$ (m/z -80); $CH_3COCO_2$ (m/z -87); $COOHCO_2$ (m/z -89) and $HSO_4$ (m/z -97).

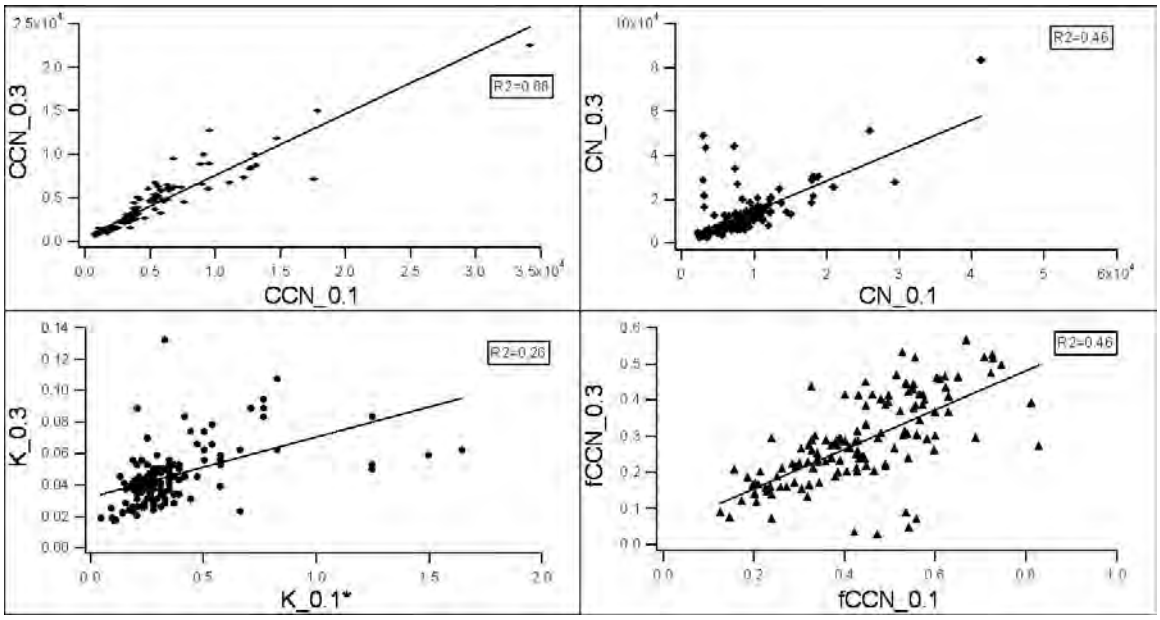

Figure 83: Comparison of CCN_0.3 and CCN_0.1 for entire study.

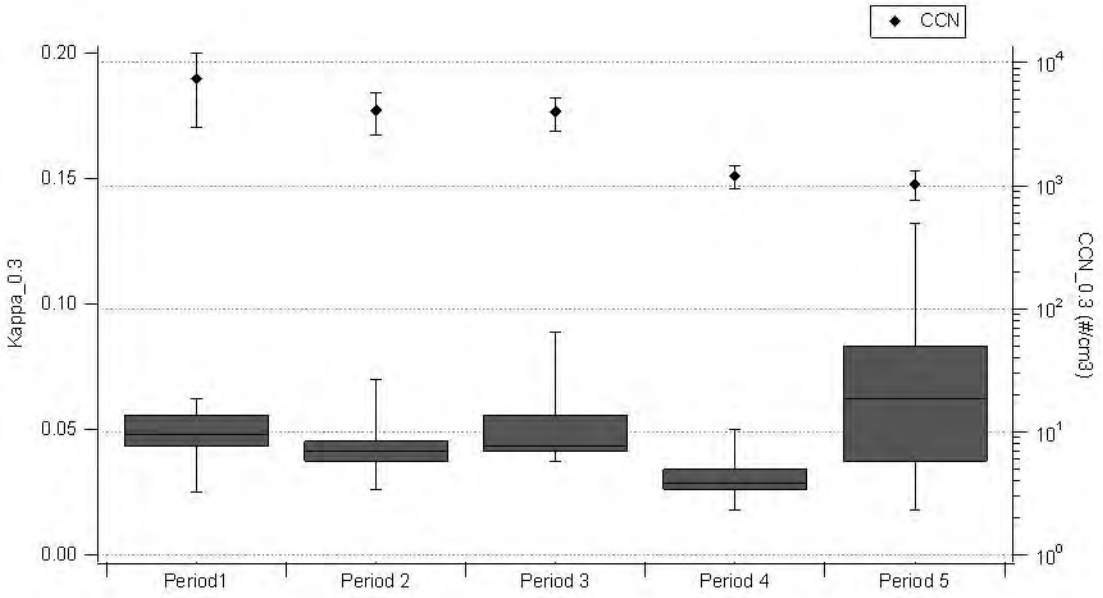


Figure 84: Single parameter hygroscopicity (Kappa) values of the particles during different air mass periods for CCN_0.3. The top of the boxes are the 3rd quartile of kappa values for that period, the bottoms are the 1st quartile values for that period. Whiskers show the minimum and maximum values for each period. Median values are the middle lines dividing the top and bottom of the boxes. Black diamonds are average CCN concentrations for those periods with standard deviation as error bars.

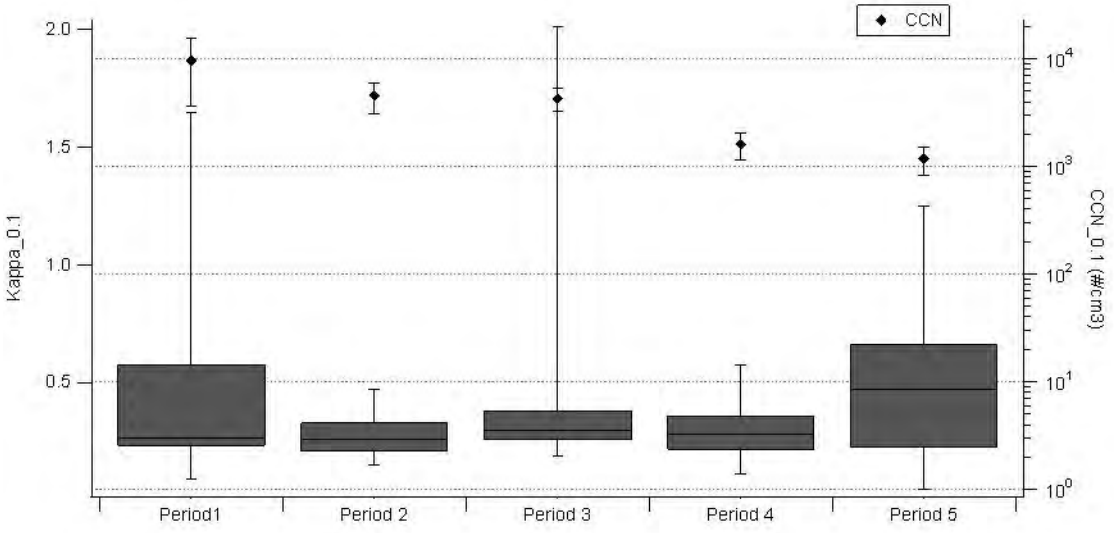


Figure 85: Single parameter hygroscopicity (Kappa) values of the particles during different air mass periods for CCN_0.1. The top of the boxes are the 3rd quartile of kappa values for that period, the bottoms are the 1st quartile values for that period. Whiskers show the minimum and maximum values for each period. Median values are the middle lines dividing the top and bottom of the boxes. Black diamonds are average CCN concentrations for those periods with standard deviation as error bars.

### *c. Air Mass and hygroscopicity*

Shown in **Figure 82** and **Figure 83** are the $\kappa$ values for the various air masses sampled during the fires, derived from CCN_0.3 with corresponding average CCN concentrations for each time period. The Santa Ana fire period's CCN activity was fairly constant with a $\kappa$ range 0.015 - 0.07, with a median value of 0.045, close to $\kappa$ of fresh anthropogenic emissions (0.05) when compared to previous studies (391). (391) measured the effect of atmospheric aging on the CCN activity of atmospheric aerosols by comparing different air masses with different degrees of aging during a research cruise in November 2004 along the southern coast of California over the Pacific Ocean. The local stagnation period (period 2) had $\kappa$ values from 0.019 - 0.16, with a median value of 0.045, close to fresh anthropogenic emissions (0.05). The 1st ammonium period (period 3) had $\kappa$ ranging from 0.019 - 0.15, with a median of 0.047, close to fresh anthropogenic emissions (0.05. Period 4 (2nd Ammonium period) $\kappa$ ranged from 0.016 to 0.18, with a median of 0.041, close to fresh anthropogenic emissions (0.05). During period 5 (local ocean) the $\kappa$ values had the widest range, from 0.004 to 0.3, with a median value of 0.052, where the air was stagnant and had mixing from various sources. Periods 1 -3 were the most dominated by BBA. The range of $\kappa$ values during these periods was 0.015 – 0.16 with a median around 0.045. During a biomass influenced period in China (398) a $\kappa$ value of 0.2 was measured, that of levoglucosan. Previous measurements of BBA hygroscopicity show a range of $\kappa$ starting from 0.01 for fresh soot-rich biomass (358), 0.06 for ponderosa pine (370) up to a of $\kappa$ of 0.55 for grass burning (358) and 0.7 for swamp sawgrass (370). (358) have noted aged biomass $\kappa$ ranging from 0.1 to 0.3. (381) have observed a $\kappa$ of 0.064 for filter of burned duff core extracted in methanol and 0.252

of burned sagebrush extracted in water. Therefore, it appears that the BBA in San Diego during October 2007 were somewhat below the range of previously determined biomass hygroscopicities, and likely had a large fraction of weakly hygroscopic and/or insoluble compounds present, producing the lower $\kappa$ range observed. The large variability during the local ocean period (period 5) is most likely due to local meteorological events that were not captured during the HYSPLIT back trajectories, such as local sources. It is also important to note that $\kappa$ values during the Santa Ana fire and local stagnation periods are just as CCN active as the $\kappa$ values measured during the local ocean period, which is well after the fires that represents more typical background conditions in the San Diego area (**Figure 80** and **Figure 81**). While there could be influence from very local sources, these show that the BBA are moderately CCN active and as hygroscopic as ocean influenced periods, as shown in period 5. In addition, during period 5 CCN concentrations were 600-1200 $cm^{-3}$ and particle counts were 3,000-23,000 $cm^{-3}$, those of a more typical San Diego background. However, as the wind started to shift from inland to from the coast/ocean, there was also a decrease in the fraction of biomass particles < 300nm, and an increase in elemental carbon particles (**Figure 81**).

## iv. Conclusions

During the San Diego Wildfires 2007, aerosol size, composition and hygroscopicity were measured in real-time. With the decreased contribution of flaming fires, both Urey Hall CCN_0.3 concentrations and fCCN_0.3 decreased overtime, indicating the dominant contribution of inorganic compounds to the CCN activity and particle hygroscopicity. As CCN concentrations and fCCN decreased overtime, total particle concentrations and the average particle size were both decreasing. The decrease in particle concentrations was caused by a decrease in the contribution of biomass particle counts. In addition, the decrease in contribution of inorganic compounds to the BBA could explain the decrease in CCN concentrations as the wildfires died out and the BBA became less dominant and more aged. Elemental carbon (EC) particles then became more dominant as the relative contribution of BBA decreased, but had no notable temporal variations, and did not correspond to changes in fraction of active particles or the CCN concentration. Therefore the changes in CCN activity and hygroscopicity can be contributed to BBA chemistry changes (aging, change from flaming to smoldering phase); and not to overall aerosol chemistry changes with the influx of EC particles' increasing contribution to total aerosol fraction < 300nm during the duration of this study.

The lower $\kappa$ range observed in this study for Urey Hall CCN (0.004 – 0.3) indicates that there were non-hygroscopic or insoluble compounds also present in the biomass burning aerosol. Previous studies have indicated that soot rich biomass has a $\kappa$ value of 0.01 (358); therefore biomass emissions in San Diego during the October 2007 Wildfires were generally lower than previously determined biomass burning hygroscopicities (0.06 - 0.7)(370).

BBA are important contributions to global CCN concentrations because they are significantly large in initial size for combustion particles, and hygroscopic enough to activate into cloud droplets under typical supersaturations. Changes in the BBA chemistry and a dominating contribution of BBA to total particles, as we have shown here, can have a large effect on CCN concentration and particle hygroscopicity.

## v. Acknowledgements

The authors are grateful to Andy Ault, Cassandra Gaston, and Melanie Zauscher for their help with data collection. They are also grateful to Dr. Satoshi Takahama (UCSD) for his helpful discussions and assistance with data analysis. Funding was provided by the California Air Resources Board grant # 04-336.

# Development of Source Apportionment Algorithms

## 12. Using mass spectral source signatures to apportion exhaust particles from gasoline and diesel powered vehicles in a freeway study using UF-ATOFMS

### i. Introduction

Many studies have shown that vehicle emissions represent a major source of pollution in urban areas (399-403). With growing concern over the health effects pertaining to pollution from vehicles (280,404,405), a goal of major federal and state agencies is to set regulations which will lead to a reduction of pollutants from these sources. The first step in this process involves distinguishing between the emissions from gasoline powered light duty vehicle (LDV), heavy duty diesel vehicle (HDDV), and other combustion sources in ambient aerosols which will allow state and federal air control agencies to quantify the relative contributions from the major pollution sources and develop effective control strategies.

Several methods have been used for aerosol source apportionment using a variety of techniques. Filter and impactor sampling methods, such as Micro Orifice Uniform Deposit Impactors (MOUDI), are useful in collecting particles that can be chemically analyzed using a variety of off-line techniques. These techniques have proved useful in determining organic markers for various aerosol sources in the atmosphere (170,406,407). On-line measurements are being used more and more for source apportionment. Some of these instruments include Scanning Mobility Particle Sizers (SMPS), where particle source contributions are estimated based on the measured size modes of the particles (408-410). Other on-line instruments, such as Thermal Desorption Particle Mass Spectrometers (TDPMS) and Aerosol Mass Spectrometers (AMS) have been used for particle source apportionment as well (411-413). However, these thermal desorption techniques are unable to detect refractory components (such as inorganic compounds and elemental carbon), and they do not sample single particles. Single particle techniques such as aerosol time-of-flight mass spectrometry (ATOFMS) provide an alternative method for source apportionment (87,414-416). The ATOFMS uses a laser to desorb and ionize species from individual particles and thus can detect all chemical species (refractory and non-refractory) of each particle simultaneously with a dual polarity time-of-flight mass spectrometer (127,417). An ultrafine aerosol time-of-flight mass spectrometer (UF-ATOFMS) was used in this study, because the majority of particles emitted in both LDV and HDDV exhaust are in the ultrafine size range (aerodynamic diameter ($D_a$) < 100nm).

The purpose of this study involves determining whether mass spectral signatures obtained from previous vehicle dynamometer characterization studies are representative of those detected in an area with fresh roadside emissions (37,418,419). Logistically, a freeway-side location was chosen in a coastal “clean” environment so there would be little influence from sources other than vehicles. Also, in such a location, the particles would be less aged which would “skew” the mass spectral signatures. A major objective of this study is to test whether the ART-2a neural network clustering algorithm matching

method can be used to distinguish mass spectral signatures from very similar vehicle sources. Finally, upon method validation, the goal is to apportion aerosols near the roadway and determine their overall contribution to the total ambient aerosol at the freeway location.

**ii. Experimental**

This study was conducted in San Diego, California from Jul. 21-Aug. 25, 2004. The sampling site was stationed in a low-use parking lot during the summer on the UCSD campus directly adjacent to the I-5 freeway (GPS position 32°52'49.74"N 117°13'40.95"W) with the sampling line within 10 meters of the freeway. The site housed a suite of instruments including an UF-ATOFMS. This same UF-ATOFMS instrument was used in two previous studies for the characterization of aerosols from LDVs and HDDVs (37,418). A summary of the instrumentation operated at the site (that will be discussed in this paper) is provided in **Table 15**. Meteorological stations were operated on each side of the freeway for complete wind trajectory information. A digital Webcam was used for freeway traffic monitoring and recorded digital video continuously throughout the study.

Traffic counts were determined by counting individual LDVs and HDDVs on both sides of the freeway for the first five minutes of each hour. The number of vehicles counted in the first five minutes was multiplied by twelve in order to approximate the total LDV and HDDV counts for the entire hour. The LDV fleet consisted primarily of newer vehicles (model year 2000 or newer), which was determined by routine traffic observations and from the video. The HDDV fleet along this portion of the freeway was predominantly tractor trailers, with a much smaller contribution from buses and medium sized diesel delivery trucks.

| Instrument | Make & Model | Measurement | Units | Sample Resolution | Sampling Period |
|---|---|---|---|---|---|
| Ultrafine Aerosol Time-of-Flight Mass Spectrometer (UF-ATOFMS) | | size range: 50-300nm | | real-time | Jul 21 to Aug 25, 2004 |
| Scanning Mobility Particle Sizer (SMPS) | TSI Model 3936L10 | particle number conc. (10-500nm) | #/cm$^3$ | 5 min | Jul 21 to Aug 25, 2004 |
| Aethalometer | Magee Scientific 'Spectrum' AE-3 Series | optical absorption cross-section per unit mass | μg/m$^3$ | 5 min | Jul 21 to Aug 25, 2004 |
| Chemiluminescence NO-NO2-NOx Analyzer | Thermo Environmental Instruments (TEI) Model 42C | NO & NOx concentration levels | ppb | 1 min | Aug 5 to Aug 25, 2004 |
| CO Analyzer | Advanced Pollution Instrumentation (API) Model M300 | CO concentration levels | ppm | 5 min | Jul 30 to Aug 10 & Aug 13 to Aug 25, 2004 |
| Webcam | Creative Model PD1001 | traffic video surveillance | | 1 sec | Jul 21 to Aug 25, 2004 |

Table 15: List of instrumentation.

The particle mass spectra from the vehicles studies were previously analyzed and clustered with the ART-2a clustering algorithm as described in Sodeman *et al* and Toner *et al* (37,418). The ART-2a algorithm and its use for single particle characterization are described in detail elsewhere (10,420). ART-2a has been compared to other approaches (8) where it is shown that ART-2a yielded very comparable results to other clustering techniques including several variants of hierarchical clustering as well as K-means clustering. For the PM emissions in vehicle studies, the ART-2a parameters used were a vigilance factor (VF) of 0.85, learning rate of 0.05, and 20 iterations. The resulting mass spectral signatures (clusters) were used to apportion particles detected near the freeway using the same ART-2a algorithm, but using a matching approach. The match-ART-2a function (YAADA v1.20 – http://www.yaada.org) uses existing ART-2a clusters as source "seeds" for the purpose of determining whether other particles match those seeds. In this case, ART-2a runs normal with prescribed particle clusters unable to be changed by the addition of new particles to each cluster. Since the clusters do not change as particles are matched to them, this function allows the clusters to stay "true" to the original source signature. Particles being considered in the matching are either matched exclusively to a particular cluster (above the VF) or not at all. If a particle matches above the threshold for two or more clusters, it will be added to the one with which yields the highest dot product. The VF used for match-ART-2a for this study is 0.85 which represents a very high VF. If the dynamometer signatures are truly representative of the signatures from vehicles, this VF should be effective because the vehicle emissions are expected to be fresh near the freeway. In a more aged environment, it is likely a lower VF will be necessary to match a reasonable number of particles. The effect of varying VF for source matching is discussed in Appendix 2.

The results obtained from match-ART-2a were compared to various peripheral data, to validate the results of the matching technique. Such peripheral instruments are described in **Table 15**. The outcome of these comparisons will be discussed below.

**iii. Results and Discussion**

### *a. Creation and Comparison of Particle Seeds From Source Studies*

As described in the Experimental section, the particles detected with the UF-ATOFMS during the freeway-side study were analyzed via a matching version of the ART-2a algorithm. The particle clusters used for matching (as the reference library) were obtained in previous LDV and HDDV dynamometer studies (37,418,419). While the papers written on these studies refer to distinct particle classes, these classes are descriptive of the many (~100) ART-2a clusters resulting from the studies. Since ART-2a does not converge, these classes were grouped by running ART-2a and then regrouped using a function that combines resulting ART-2a clusters that match above a set vigilance factor (regrouped VF = 0.90). These regrouped clusters can then be even further grouped based on visual inspection of the ion patterns. Similar clusters that appear to belong within the same "class" as each other based on the presence or absence of key species (i.e. elemental carbon (EC), organic carbon (OC), sulfate, nitrate) are regrouped by hand. Such classes have minor differences in the relative ion peak patterns among their collective clusters, however; the overall chemical species making up each major type of cluster are the same.

For matching purposes, instead of using the combined weight matrices from the regrouped representative particle classes, the top ART-2a clusters that account for ~90% of the particles from each vehicle study were used. Additionally, it was hypothesized that the top particle types detected in the vehicle studies should also be the top types detected in the fresh emissions near the highway. In order to create source seeds more representative of the freeway environment, only particles generated during warm/hot engine conditions for both HDDV and LDV studies were used to make the source seed clusters. These clusters still correspond to their representative classes described in previous papers (as stated earlier), however, there are minor differences in some clusters that make it more advantageous to use the separate ART-2a clusters for matching purposes. In addition, clusters generated by running ART-2a on the UF-ATOFMS freeway detected particles were also incorporated into the source seed library. The majority of these clusters were attributed to HDDVs, as their weight matrices correlated much better to the HDDV library source seeds than to the LDV seeds. The seeds are also separated by size, where ultrafine (50–100nm) and accumulation mode (100–140nm & 140-1000nm) mass spectral libraries have been created for each source. This is done because there are distinct chemical differences for each source based on size, and these size ranges show the largest chemical distinctions. For example, as found in the dynamometer studies using UF-ATOFMS, LDVs produce more organic carbon than elemental carbon particles for sizes above 100 nm. Two separate libraries were made for the accumulation mode to compensate for a regional background elemental carbon particle type that was detected above 140nm during the freeway study. This particle type will be discussed in a future publication (421). For this manuscript, the matching results obtained from both accumulation mode libraries are combined to represent the UF-ATOFMS accumulation mode results (100-300nm). This was done because the trends in HDDV/LDV apportionment were found to be very similar between the two accumulation mode libraries once the regional background EC particles above 140 nm were identified as non-freeway particles. Further details on the number of seeds in the vehicle source library and the frequency at which they match particles for this study are provided in Appendix 1.

Since HDDVs and LDVs combust chemically similar fuels, it is important to first investigate the similarity between the HDDV and LDV exhaust particle types from the dynamometer source studies. The first method used to compare these particle types involved taking the representative area matrix for each class described for each study and calculating the dot product between them. The area matrices used to represent the particle classes are similar to the weight matrices that ART-2a yields except that the area matrices are not weighted. The area matrices represent an average of all particles within a particular class. Since ART-2a distinguishes particle types bases on their dot products, this type of comparison between the two studies allows one to determine if the area matrices of the general particle types would be distinguishable using ART-2a. **Figure 86** displays a color mapped table of this comparison, with cooler colors (i.e. blue) indicating less similarity (lower dot product) and warmer colors (i.e. red) indicating more similarity (higher dot product). The labels for the classes are based on the most abundant ion peaks in the mass spectra and are described in detail in previous source characterization manuscripts by Sodeman et al. and Toner et al. (37,418). **Figure 86** shows that some of the dot product comparisons between the two

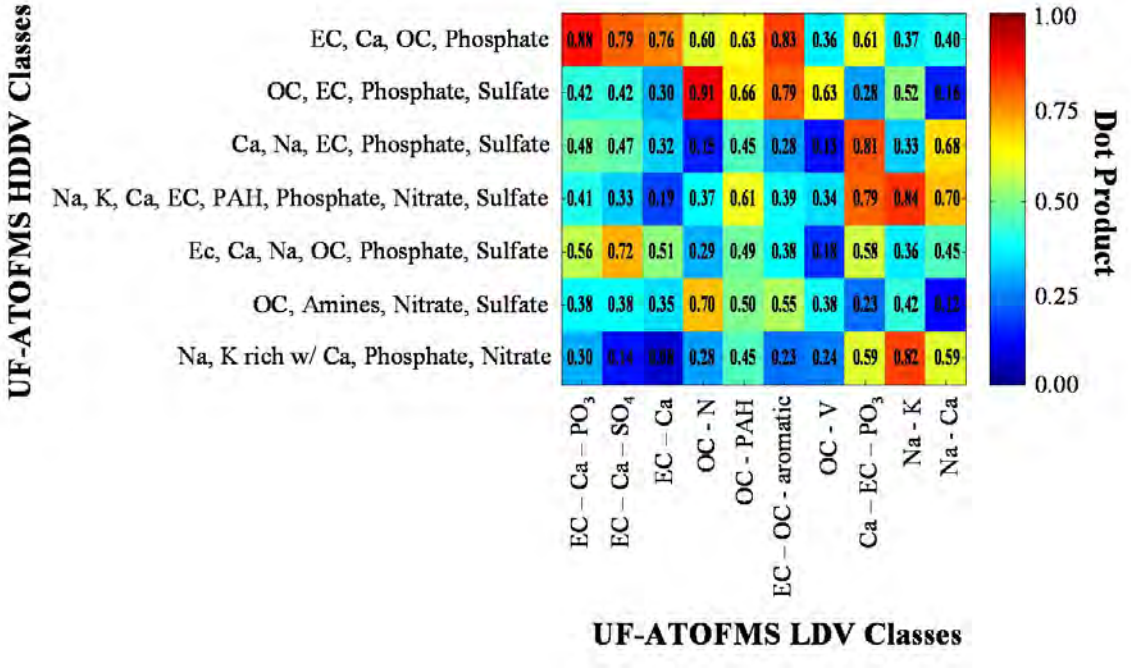


Figure 86: Dot product comparisons of the representative area matrices between the general classes from the HDDV and LDV dynamometer experiments using UF-ATOFMS. Classes are labeled in the same manner as in the manuscripts from Sodeman *et al.* 2005 and Toner *et al.* 2006.

source studies result in strong matches (i.e. orange and red colors). As expected, those classes that match the best are chemically similar types; i.e. the EC, Ca, OC, Phosphate classes from HDDV matching to the EC-Ca-$PO_3$ class from LDV (note this was produced by a smoking LDV). Also, the OC, EC, Phosphate, and Sulfate classes from HDDV match to the OC-N class from LDV. While these classes have dot products above the vigilance factor used for ART-2a analysis (VF = 0.85), they are visually distinct (as described in the two manuscripts) and still readily distinguishable using the matching procedure. One of the major problems with this comparison is the fact that the area matrices represent an average of the particles within the class and are not weighted to the majority. As stated previously though, the representative spectra of the general classes are not used for apportionment matching purposes. Instead, the size segregated mass spectral libraries for HDDV and LDV particles, as described above, are used. Using size information in the apportionment turns out to be quite important because those particles that are chemically similar between sources fall into quite different size ranges.

Another method for comparing the two studies involves taking the particles from the dynamometer studies detected with the UF-ATOFMS and matching them to the HDDV/LDV reference library clusters using a non-exclusive matching process with ART-2a. This process adds a matched particle to HDDV, LDV, or combination of both cluster types if the particle matches above a vigilance factor of 0.85. This method of matching allows for determining the amount of similarity of the particle types between the two studies. Between 19 – 33% of the HDDV dynamometer particles and 30 – 49% of the LDV dynamometer particles matched both the HDDV and LDV reference clusters. These results are shown in **Figure 87**. With such a large degree of overlap between the

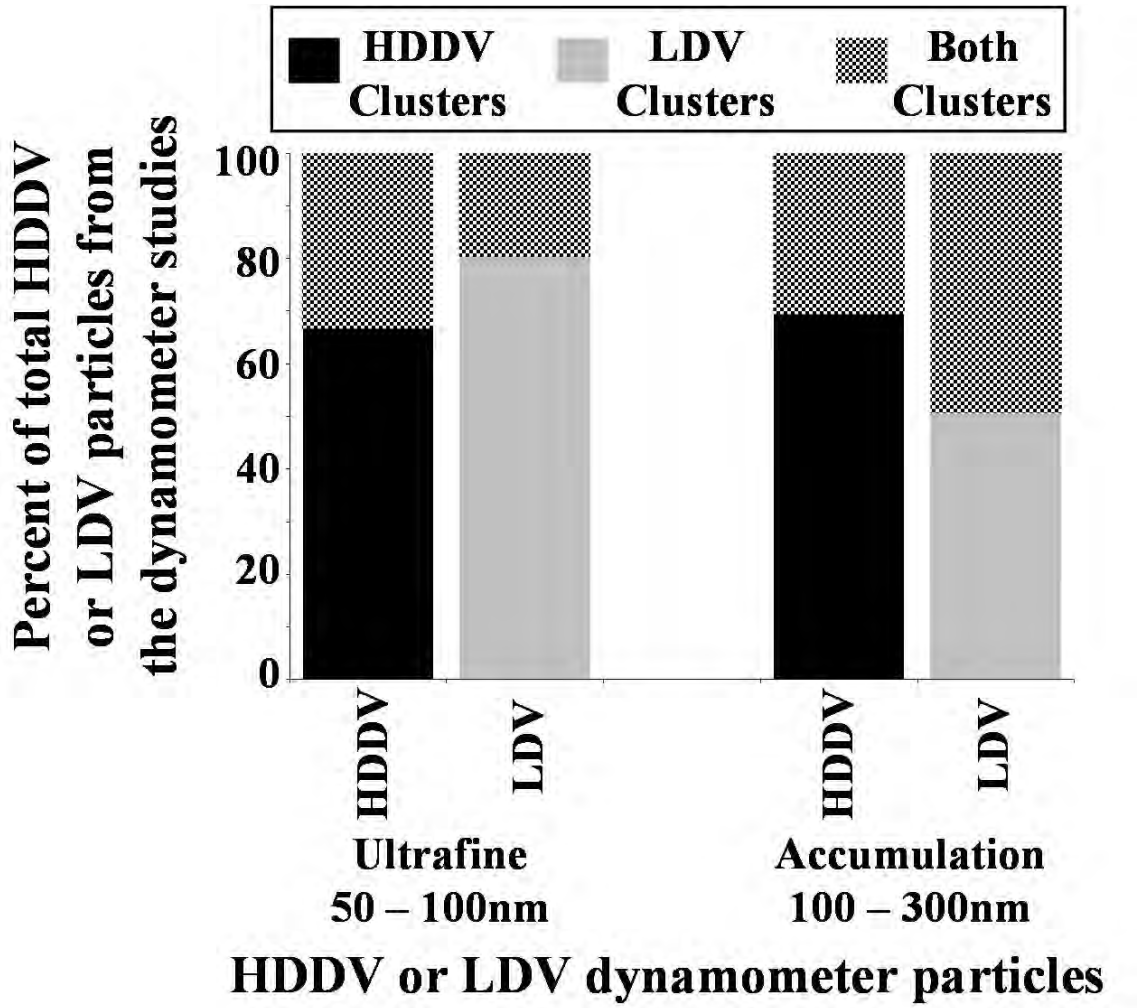


Figure 87: ART-2a matching error analysis using non-exclusive matching of HDDV and LDV dynamometer particles. For each, the fraction of HDDV and LDV particles that matched to the HDDV, LDV, or both HDDV and LDV clusters from the HDDV/LDV reference library are shown for ultrafine (50–100nm) and accumulation (100–300nm) mode particles.

particle types from both clusters, it would appear to be a challenging task to distinguish between HDDV and LDV particles using the ART-2a matching method. This is not the case though as particles within the overlapping region turn out to be quite distinguishable for reasons described below.

The main goal of this paper involves using ART-2a to distinguish between HDDV and LDV particles in an environment dominated by relatively fresh vehicle emissions. To accomplish this, an exclusive matching procedure was used where particles were matched to the HDDV/LDV reference clusters and they either matched exclusively or not at all. If a particle matched to more than one cluster above the vigilance factor, it was placed in the cluster to which it matched the most closely (i.e. the highest dot-product value). If a particle did not match to either HDDV or LDV, it was placed into the "other" category. Particles falling into the "other" category included sea salt, dust, biomass burning, and other sources not related to LDV or HDDV exhaust emissions. Quality assurance of this matching technique was carried out by using the same HDDV/LDV

cluster library to match to particles from the previous source studies. The amount of error in matching was calculated based on the number of particles from the known source that matched to the incorrect source. **Figure 88** shows the matching fraction of particles from each study to the same HDDV/LDV reference library. The most error (mismatching) is about 4%, which occurs for the larger accumulation mode particles from the LDV source particles matching to HDDV clusters within the reference library. Given this low error, this provides confidence in the ART-2a apportionment approach used in this study. The errors associated with matching to the source seeds at varying VF's, as well as results from using source seeds created at a lower VF, are discussed in Appendix 2.

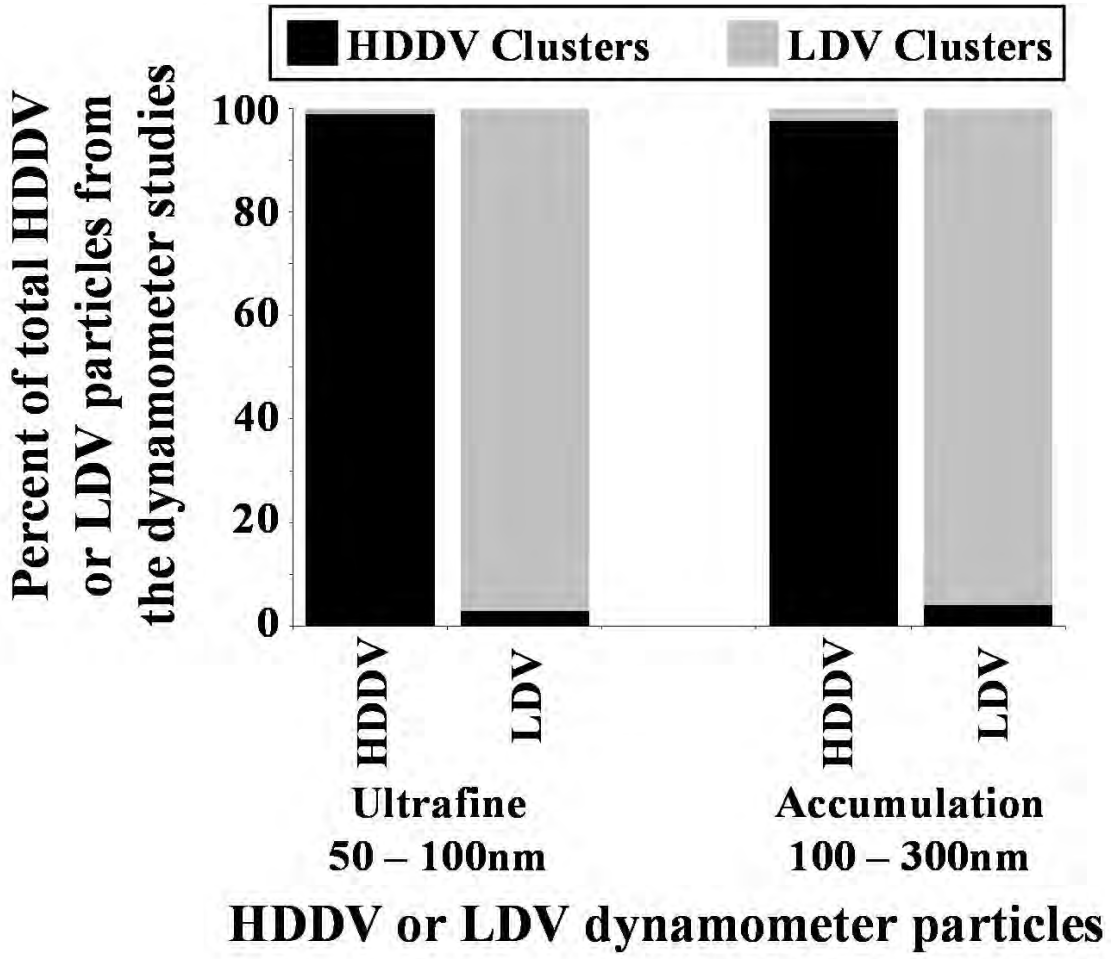


Figure 88: ART-2a matching error analysis using exclusive matching of HDDV and LDV dynamometer particles. For each, the fraction of HDDV and LDV particles that matched to the HDDV or LDV clusters from the HDDV/LDV reference library are shown for ultrafine (50–100nm) and accumulation (100–300nm) mode particles.

***b. Particles Detected that Match to HDDV/LDV Source Seeds***

The ART-2a algorithm was used to cluster the particles detected with the UF-ATOFMS during the freeway-side study using a VF of 0.85. This approach creates the top particle types separately from the match-ART-2a technique to determine how closely the

resulting clusters compare with those from the vehicle studies. **Figure 89** (A-D) shows the representative ART-2a weight matrices (WM) /spectra from this analysis that match to the top particle types from the dynamometer studies. The top particle classes from the HDDV and LDV vehicle source characterization studies were used for this comparison because they should theoretically be the top particle types seen in a vehicle dominated environment. Indeed, this is the case, where the majority of the top ten freeway ART-2a results match to the top HDDV dynamometer classes. The top HDDV particle type detected from the dynamometer studies is the top type detected during this freeway-side study (as shown in **Figure 89A**) and matches with an $R^2$ of 0.97 when the m/z peak pattern and intensities are plotted against each other. **Figure 89B** shows the second most abundant type from the HDDV dynamometer studies compared to the second most abundant type detected during the freeway study which matches with an $R^2$ of 0.98. This particle class is also the most abundant type detected in 100 – 400 nm particles detected with a standard inlet ATOFMS (419). The spectra shown in **Figure 89C** represent the third cluster from the freeway ART-2a results which match the top LDV type from the dynamometer study with an $R^2$ of 0.99. The last

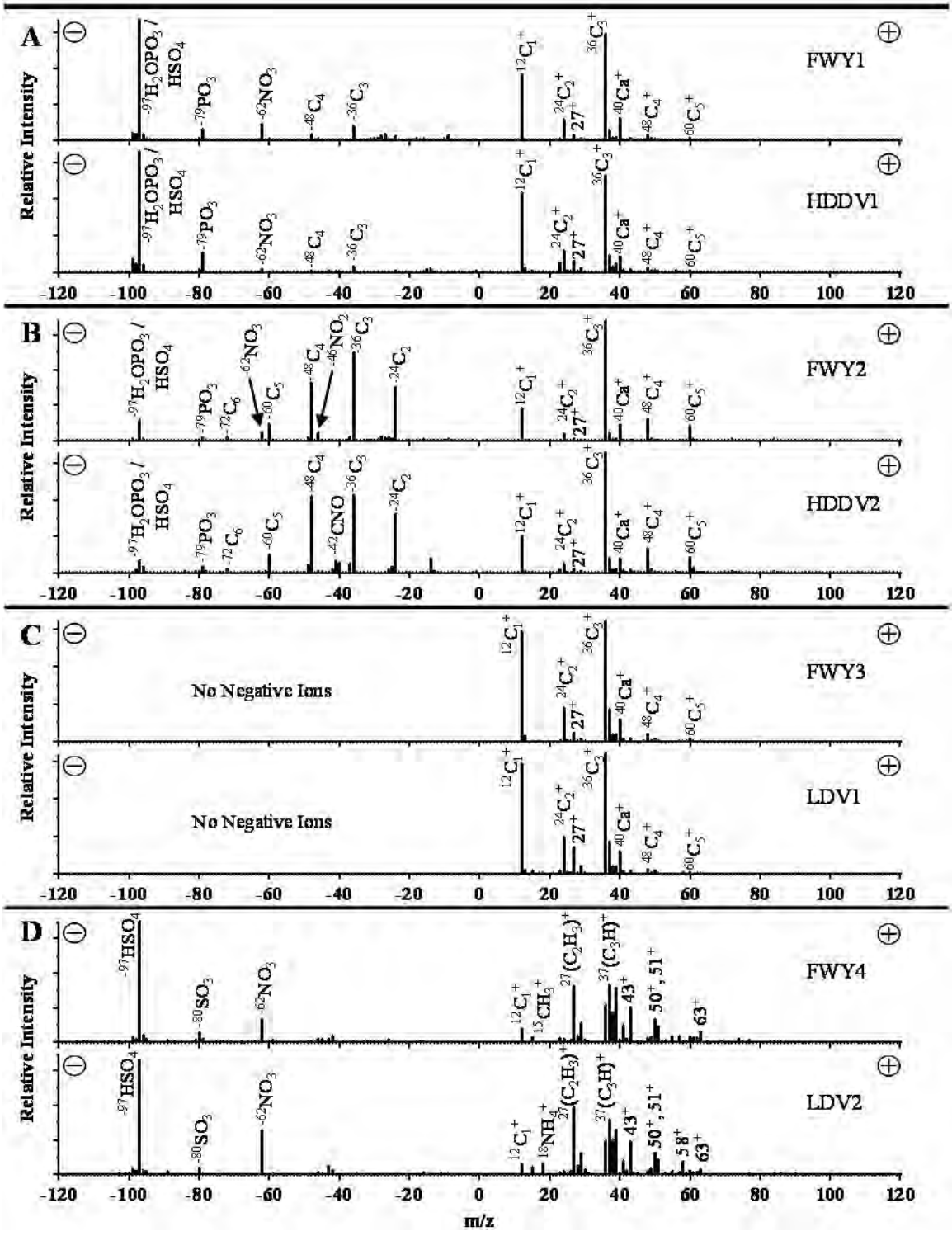


Figure 89: Weight matrices of the top particle types detected during freeway study that match to vehicle study signatures.

spectra (**Figure 89D**) show the sixth freeway particle cluster that matches the third most abundant type from the LDV dynamometer study ($R^2 = 0.98$).

There has been speculation as to whether mass spectral signatures from different sources obtained from laboratory and dynamometer experiments can be detected during ambient studies and used for source apportionment purposes. Such questions result from the concern that the dilution and residence systems used during source characterization studies do not properly mimic real-world dilution and aging conditions that occur in on-road driving exhaust (422,423). The freeway-side study was chosen to lessen the effects of aging on the particle signatures. It was expected that the "fresh" emissions would be more comparable to the particle signatures obtained from the dynamometer experiments. The high $R^2$ values for the comparison of particle classes confirms the chemistry of the particle types detected in dynamometer studies are consistent with those produced in ambient environments.

The high $R^2$ values serves as further validation that the ART-2a clustering technique is a reliable method for ATOFMS particle mass spectral clustering. A discussion of whether mathematical clustering algorithms can properly separate and cluster similar particle types has been addressed in the literature (6,414,424). Some concerns about ART-2a have included that too low of a vigilance factor will yield a manageable number of end clusters, but will not distinguish between different types of particles. Also, too high of a vigilance factor will yield too many clusters to properly classify all particles. Through laboratory work conducted with ATOFMS data of known particle types, the proper vigilance factor for source apportionment using ART-2a has been found to be 0.85 (245). While this tends to create many clusters for ambient data sets, the number is quite manageable because similar clusters can still be mathematically regrouped (which greatly reduces the number of clusters). For example, in this freeway study 2,763 clusters were generated after running ART-2a (VF = 0.85) on fine mode particles, but mathematically regrouping these clusters using a VF of 0.90 reduces the number to 370 clusters (of which, the top 72 represent 90% of the total freeway-side particles detected with the UF-ATOFMS). The $R^2$ values obtained for these comparisons show that these techniques work very well and should lessen concerns about their legitimacy.

***c. Temporal Trends and Correlations with UF-ATOFMS Data***

A number of peripheral instruments accompanied the UF-ATOFMS instrument for this study to test the apportionment process being used. Previous vehicle apportionment studies show that $NO_x$ emissions can be used as a tracer gas for HDDV emissions (425-427). Also, an aethalometer measures absorptivity by particles and can be used as an indicator of elemental carbon (or soot) containing particles (particularly at $\lambda$ = 880nm). Indeed, previous HDDV and LDV source studies show more EC associated with HDDVs (37,418,419). CO gas emissions have been shown to act as a tracer for LDV emissions (426); however, the CO monitor used in this study was not running during all the time periods. **Figure 90** (A,B) shows a plot of $NO_x$ vs. aethalometer data as well as HDDV counts (from video footage) vs. aethalometer. The time periods for the two plots are different as the NOx monitor began later in the study. However, the plot between the $NO_x$ and aethalometer (**Figure 90A**) show a good

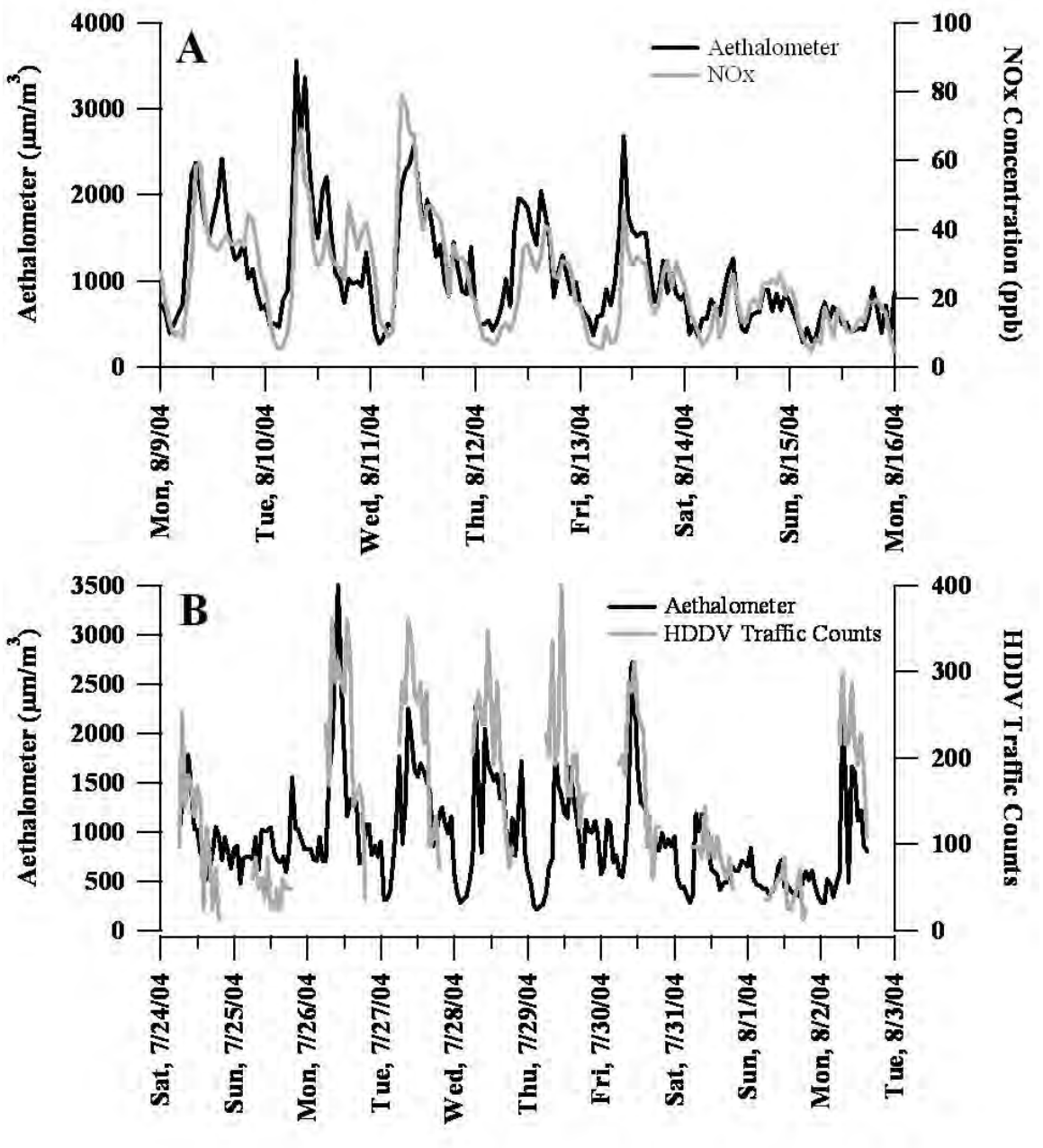


Figure 90: Temporal plots of A) NOx gas data vs. aethalometer data; and B) HDDV video counts vs. aethalometer data. Both NOx and aethalometer data show a good correlation with each other ($R^2 = 0.7$). The HDDV video counts also track the aethalometer data.

correlation ($R^2 = 0.7$), tracking for the remainder of the study, which suggests it is safe to assume that they most likely tracked during the time period before the $NO_x$ instruments arrival. This correlation can allow the use of the aethalometer data trends as a surrogate for the $NO_x$ concentrations during periods when the $NO_x$ data were not available. **Figure 90B** shows the comparison of HDDV video counts versus the aethalometer trends. The breaks in the counts come at night when there is insufficient light to properly distinguish

between vehicles. The trends in HDDV counts versus aethalometer data also show a very strong correlation. Since HDDV's are shown to emit a larger mass of black carbon compared to LDV's (428,429), it is expected that the HDDV counts should be closely correlated with the aethalometer data. HDDVs make up about 2% of the fleet for this particular region of the freeway, and when HDDV traffic counts peak, there is generally a very large amount of LDV traffic as well. Even though HDDVs make such a low contribution to the traffic on this stretch of freeway, their particle emissions are quite prevalent and readily discernable.

**Figure 91** and **Figure 92** shows the time series of the ART-2a matching results for the fine and ultrafine mode particles, respectively. Using the fractions from both the ultrafine and fine mode temporal plots, on average 83% of the aerosols detected near this roadside with the UF-ATOFMS are attributed to vehicle exhaust emissions, with 32% apportioned to LDV and 51% to HDDV emissions. For the fine mode particles ($D_a$ = 100–300nm), 66% of the aerosols are attributed to vehicle exhaust emissions, with 25% from LDV and 41% from HDDV. And, for ultrafine particles ($D_a$ = 50–100nm), 95% of the aerosols are apportioned to vehicles, with 37% from LDV and 58% from HDDV. The fact that such a large number of particles in the roadside environment matched to the vehicle seeds using a relatively high vigilance factor (0.85) produces confidence that the seeds used in the source library are representative of a broad range of vehicles. If a particular particle type had been missed in the seeds, it would be apparent in a large number of "other" particles.

**Figure 91** shows the ART-2a matching results for fine mode particles ($D_a$ = 100–300nm) along with wind data and video traffic counts for July 24 to Aug 03, 2004. This time period is of particular interest because MOUDI samplers ran at the same time and the source apportionment results from both approaches will be compared in a future study. The plot of the unscaled matching counts shows that both wind and traffic counts play a major role in the particle concentrations for this site. The matching counts peak around 9:00 each morning, which is when HDDV traffic counts peak. This also occurs just prior to, and during the beginning of daily peak wind speeds. The sampling site was located on the east side of the freeway because the prevailing daily wind blows from the west ($270^o$). This allowed for the ideal positioning to detect freeway traffic exhaust particles. The matched fraction and unscaled count plots show that there is a larger number of diesel particles detected (relative to LDV matched particles), which follow the trend in diesel traffic observed from the video footage. It is interesting to note that the detection of LDV particles is always lower than that of HDDV particles for the fine particle mode. This was expected, as roadside and ambient studies have shown that HDDV's contribute a much higher concentration of particles even in LDV dominated areas (410,430-432). Vehicle studies have also shown that HDDV's emit a significantly higher fraction

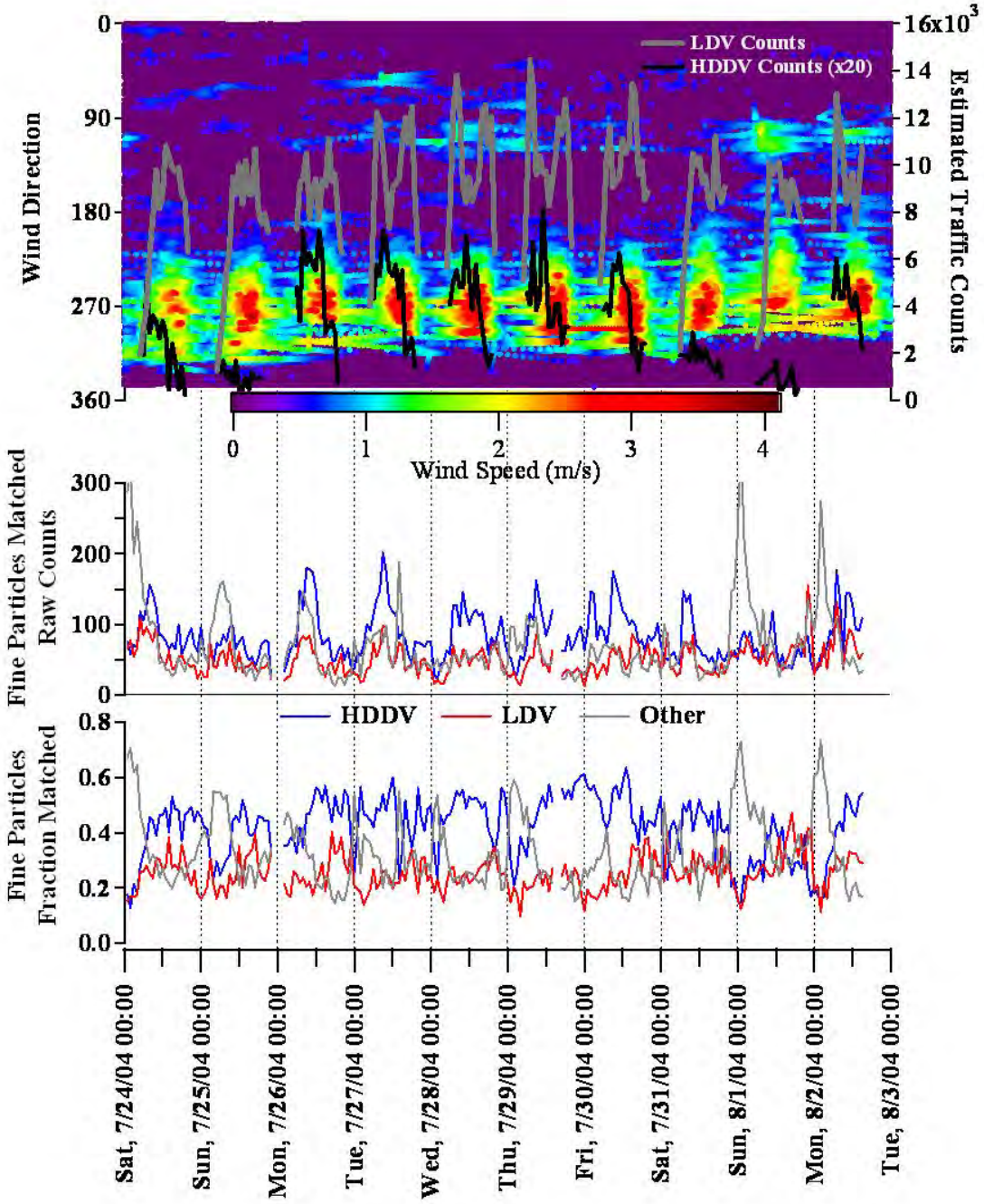


Figure 91: Top: Wind data (blowing from: N = $0^o$/$360^o$, E = $90^o$, S = $180^o$, W = $270^o$) along with LDV & HDDV traffic counts (from video). HDDV counts are multiplied by 20 to keep them on the same scale as LDV traffic counts. Middle: HDDV/LDV/Other ART-2a matching result unscaled counts from UF-ATOFMS data. Bottom: HDDV/LDV/Other ART-2a matching fraction results from UF-ATOFMS data. Data shown are accumulation mode particles ($D_a$ = 100–300nm) for July 24 to Aug 03, 2004.

of fine particles compared to LDV's (37,418,419). Another note to make about **Figure 91** is that the temporal trend for the fraction of particles attributed to other sources has no

correlation with the fractions matched to HDDV or LDV. This randomness of the accumulation mode "Other" type indicates that the particles within this class are not associated with either fresh HDDV or LDV emissions.

**Figure 92** shows the times series of the ART-2a matching results for ultrafine particles ($D_a$ = 50–100nm) along with SMPS data and video traffic counts for July 24 to Aug 03, 2004. Traffic counts are shown on both **Figure 91** and **Figure 92** to allow for comparison. This figure depicts how strong of a role the traffic counts play on the particle concentrations detected at this site. Comparing the ultrafine unscaled matched counts to the SMPS data illustrates how well the UF-ATOFMS particle detection tracks the changes in particle concentrations at this site. Since ultrafine particles provide an indication of freshly emitted particles, it was expected that the UF-ATOFMS ultrafine counts would track the SMPS data and the vehicle counts. This figure also shows how strong an influence the LDV emissions, though still less than HDDV emissions, have on the ultrafine particle concentrations in this area versus the fine mode particles. The fraction plot shows that there is a fairly consistent trend between the LDV and HDDV contribution to the ultrafine mode. As was discussed for **Figure 91** in reference to the fine particles, HDDV's are known to emit a greater number of ultrafine particles in comparison to LDV's (37,418,419). Once again, this can account for the larger number of HDDV particles detected by the UF-ATOFMS than for LDV's, despite the dominating LDV traffic counts. Another note

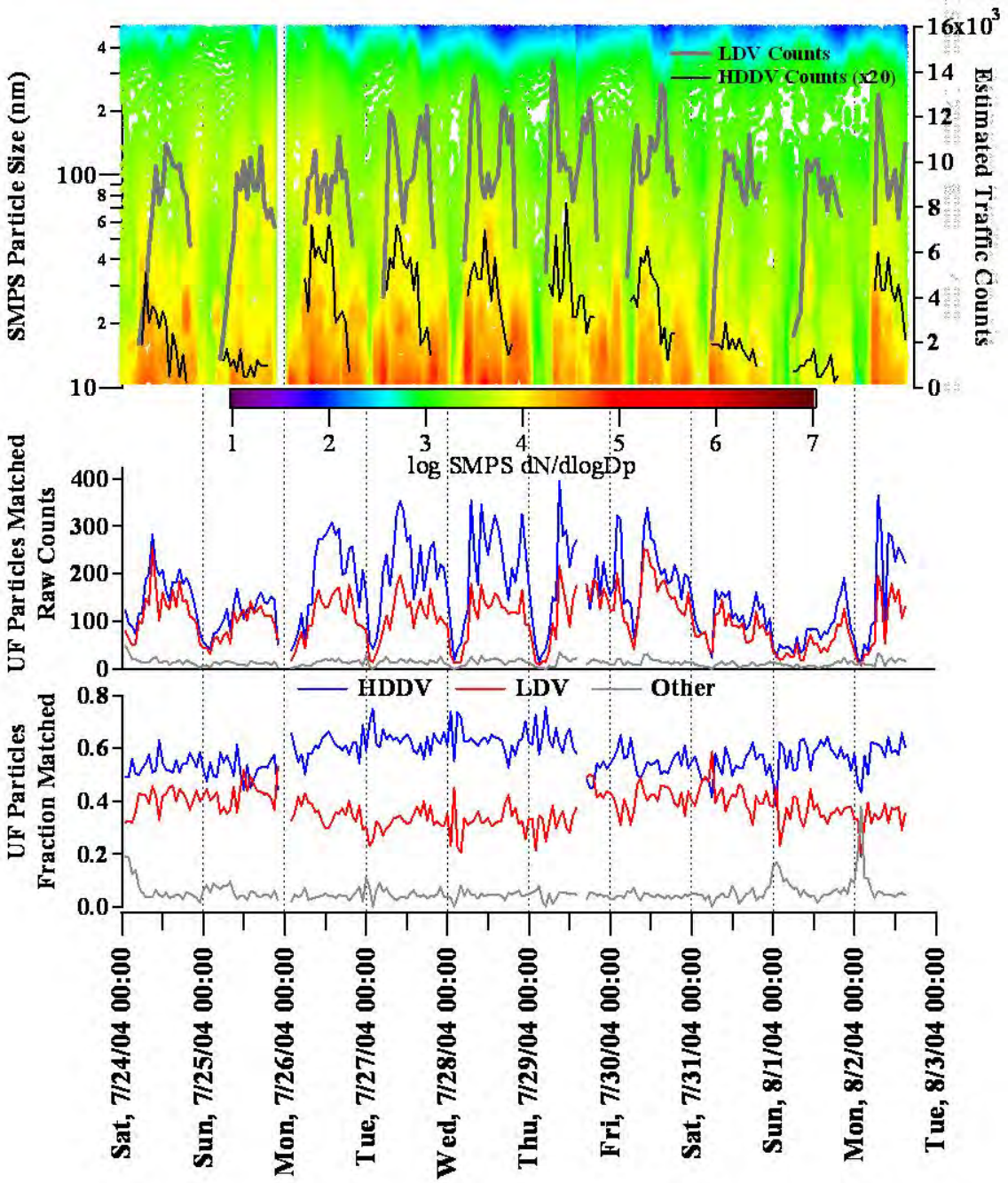


Figure 92: Top: SMPS data along with LDV & HDDV traffic counts (from video). HDDV counts are multiplied by 20 to keep them on the same scale as LDV traffic counts. Middle: HDDV/LDV/Other ART-2a matching result unscaled counts from UF-ATOFMS data. Bottom: HDDV/LDV/Other ART-2a matching fraction results from UF-ATOFMS data. Data shown are ultrafine mode particles ($D_a$ = 50–100nm) for July 24 to Aug 03, 2004.

to make about **Figure 92** is that it clearly shows a difference in weekday versus weekend traffic and particle detection. The first Saturday (7/24/04) had a high amount of traffic,

including HDDV traffic, and shows almost the same amount of matching contributions as the weekdays. The first Sunday (7/25/04), as well as the following weekend show a reduced amount of HDDV traffic and, hence, a lower number of particles matching to HDDVs. When HDDV traffic increased on the weekdays, the number of HDDV apportioned particles were much greater than those apportioned to LDV's. It wasn't until Friday (7/30/04) that the LDV detected UF particle counts began to resemble those for HDDV's, and they remained about even through the weekend. Then, on Monday (8/02/04), the HDDV emissions began to dominate again. Also, an interesting feature to note about **Figure 91** & **Figure 92** is that while the weekend LDV video counts remained relatively high (especially compared to the HDDV counts), the fraction of LDV and HDDV particles did not seem to change by the same magnitude. The weekend HDDV fraction goes down by about 10% for the UF particles and 9% for the accumulation mode particles, while the LDV fraction goes up by 7% for the UF particles and 2% for the accumulation mode. Also, the LDV apportioned counts go down despite the video traffic counts staying relatively high due to the fact that the winds were not as strong towards the site on the weekend as they were throughout the week. On 8/1, in addition to the winds not being as strong, they had more of an influence from the southwest and the east.

**Figure 93** shows correlation plots along with a temporal plot of particles matched to HDDV and LDV along with aethalometer data ($\lambda$ = 880nm). There is a stronger correlation between the aethalometer and the HDDV matched particles ($R^2$ = 0.77) than

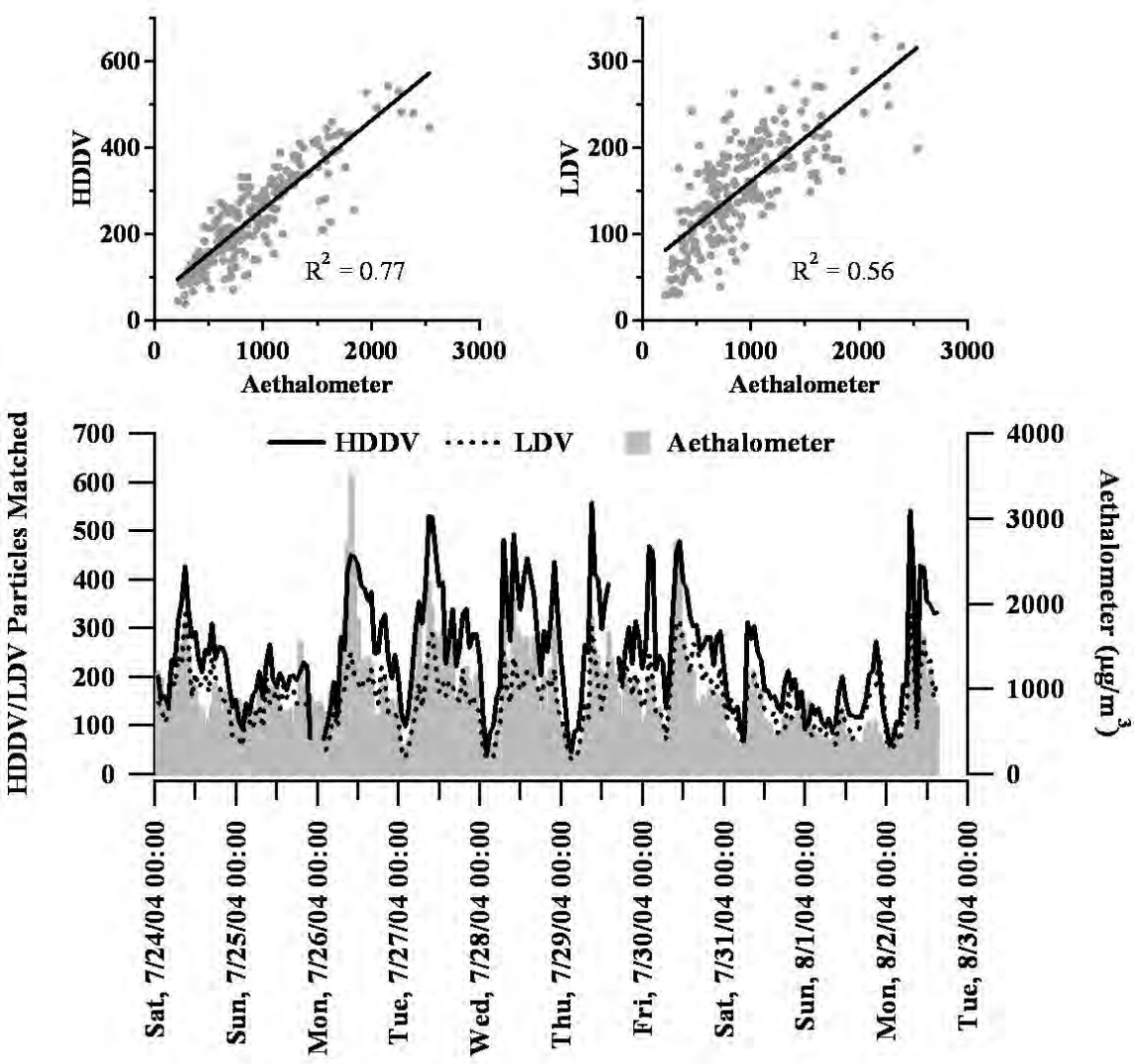


Figure 93: Time series of aethalometer data with HDDV/LDV apportioned particles. The $R^2$ values for aethalometer to HDDV is 0.77, and 0.56 for the aethalometer to LDV.

with the LDV matched particles ($R^2$ = 0.56). Aethalometers measure the absorptivity of particles in the UV to IR regions, and since HDDVs emit a larger number of elemental carbon than do LDVs, the trends of aethalometer data should reflect trends in HDDV exhaust particles. Based on the trends of the $NO_x$ and aethalometer data with the ATOFMS data, the observed correlations provide support to the ART-2a apportionment approach used in this study. The results presented in this paper represent the first step in using mass spectral source signatures acquired in LDV and HDDV dynamometer source characterization studies for ambient source apportionment. As expected, a high percentage (83%) of the ultrafine and accumulation mode aerosols sampled near the freeway are attributed to vehicle exhaust emissions, with 32% and 51% being attributed to LDV and HDDV, respectively. Future studies using different algorithms, including Hierarchical clustering and Positive Matrix Factorization, will be performed and the

results will be compared to those obtained in this study. Also, comparisons will be made between single particle source apportionment results and standard organic tracer methods (433). Such comparisons will be necessary for determining the most appropriate method for performing source apportionment using single particle mass spectral data.

**iv. Acknowledgements**

The authors thank Dan Cayan and Alex Revchuk of the Scripps Institution of Oceanography (SIO) at UCSD for setting up the micro-meteorological stations and providing data for this study. We also thank UCSD and their facilities management for all their cooperation and help with setting up power to the sampling site, as well as the members from the Prather group who helped in transporting equipment to the site. This work was supported by the California Air Resources Board (CARB) (Contract 04-336).

## 13. Source apportionment of freeway-side PM2.5 using ATOFMS

### i. Introduction

Recent studies have shown that vehicle emissions are a major source of pollution in urban areas (399-403,434,435). With an ever growing concern over the health effects associated with vehicle emissions, a goal of major federal and state agencies is to set regulations which lead to a reduction in these pollutants (280,404,405). The ability to apportion gasoline powered light duty vehicles (LDV), heavy duty diesel vehicles (HDDV), and other combustion emissions in ambient aerosols will allow city and state agencies to channel their efforts and resources into targeting the major polluters (LDV, HDDV, and other combustion sources) in their area. Distinguishing between LDV and HDDV exhaust aerosols may represent the greatest challenge (compared to other combustion sources) due to the similar chemical characteristics of the PM in their emissions, which result from their similar fuel and oil composition (403,436-440).

The purpose of this work is to test whether aerosol mass spectral source signatures acquired from ATOFMS source characterization studies, including vehicle dynamometer studies, can be used to apportion ambient aerosols in a freeway-side study. A freeway-side location was chosen in a coastal area because this location should be dominated by particles from fresh vehicle exhaust emissions and should display a relatively low concentration of aged or transformed particles. The background particles are expected to be mostly sea salt since this is a coastal region. The steps involved in data quality assurance will be discussed as well as how particle size measurements and gas phase instrumentation can be incorporated for aerosol source apportionment.

### ii. Experimental

The experimental setup used for this study has been described in Chapter 4 (441). The study was conducted from July 21 to August 25, 2004 at two sites. First, a "clean" upwind site was stationed at the Prather Laboratory in Urey Hall at the University of California, San Diego (UCSD) with the goal of determining the signatures of background ambient aerosols (GPS position 32°52'31.66"N 117°14'28.64"W). This site is relatively close to the ocean (within 950 meters) so the prevailing winds (from the west) should introduce little-to-no fresh source emissions. This site housed a standard inlet ATOFMS instrument (127) along with an aerodynamic particle sizer (APS) (TSI Model 3321 – Minnesota) and a scanning mobility particle sizer (SMPS) (TSI Model 3936L10 – Minnesota). The second site was located at a trailer stationed in a

Table 16: List of Instrumentation used at the freeway and upwind sampling sites.

| Instrument | Make & Model | Measurement | Units | Sample Resolution | Site | Sampling Period |
|---|---|---|---|---|---|---|
| Ultrafine Aerosol Time-of-Flight Mass Spectrometer (UF-ATOFMS) | | size range: 50–300 nm | | real-time | Freeway | Jul 21 to Aug 25, 2004 |
| Standard Aerosol Time-of-Flight Mass Spectrometer (ATOFMS) 1 | | size range: 200–3000 nm | | real-time | Freeway | Jul 21 to Aug 25, 2004 |
| Standard Aerosol Time-of-Flight Mass Spectrometer (ATOFMS) 2 | | size range: 200–3000nm | | real-time | Upwind | Jul 21 to Aug 2, 2004 |
| | | | | | Freeway | Aug 10 to Aug 25, 2004 |
| Aerodynamic Particle Sizer (APS) 1 | TSI Model 3321 | particle number conc. (0.5–20µm) | #/cm$^3$ | 5 min | Freeway | Jul 21 to Aug 25, 2004 |
| Aerodynamic Particle Sizer (APS) 2 | TSI Model 3321 | particle number conc. (0.5–20µm) | #/cm$^3$ | 5 min | Upwind | Jul 21 to Aug 2, 2004 |
| Scanning Mobility Particle Sizer (SMPS) 1 | TSI Model 3936L10 | particle number conc. (10–500nm) | #/cm$^3$ | 5 min | Freeway | Jul 21 to Aug 25, 2004 |
| Scanning Mobility Particle Sizer (SMPS) 2 | TSI Model 3936L10 | particle number conc. (10–500nm) | #/cm$^3$ | 5 min | Upwind | Jul 21 to Aug 2, 2004 |
| Aethalometer | Magee Scientific 'Spectrum' AE-3 Series | optical absorption cross-section per unit mass | µm/m$^3$ | 5 min | Freeway | Jul 21 to Aug 25, 2004 |
| Nephelometer | Radiance Model M903 | light scattering coefficient (bscat) | km$^{-1}$ | 5 min | Freeway | Jul 21 to Jul 22 & Jul 25 to Aug 25, 2004 |
| Photoelectric Aerosol Sensor (PAS) | EcoChem Model 2000 | concentration of total particle-bound PAH | ng/m$^3$ | 5 min | Freeway | Jul 30 to Aug 25, 2004 |
| Tapered Element Oscillating Microbalance (TEOM) | Rupprecht & Patashnick (R & P) Series 1400a | mass concentration ($PM_{2.5}$) | µg/m$^3$ | 30 min | Freeway | Jul 21 to Aug 25, 2004 |
| Chemiluminescence NO-NO2-NOx Analyzer | Thermo Environmental Instruments (TEI) Model 42C | NO & NOx concentration levels | ppb | 1 min | Freeway | Aug 5 to Aug 25, 2004 |
| CO Analyzer | Advanced Pollution Instrumentation (API) Model M300 | CO concentration levels | ppm | 5 min | Freeway | Jul 30 to Aug 10 & Aug 13 to Aug 25, 2004 |
| Webcam | Creative Model PD1001 | traffic video surveillance | | 1 sec | Freeway | Jul 21 to Aug 25, 2004 |

low-use parking lot (particularly during the summer) on the UCSD campus directly adjacent to the I-5 freeway (GPS position 32°52'49.74"N 117°13'40.95"W) with the sampling line within 10 meters of the freeway. The trailer housed a suite of instruments including an ATOFMS and UF-ATOFMS (417). A detailed summary of the instrumentation operated at both sites is provided in **Table 16**. Dr. Michael Kleeman's research group (UC Davis) also sampled PM at both sites with micro orifice uniform deposit impactors (MOUDI's), Anderson Impactors, an APS, and an SMPS. The Kleeman group sampled from July 21 - August 1. Their measurements focused on obtaining size-resolved concentrations of organic and metal tracers to be used for conventional source apportionment. Ultimately, when their results become available, a comparison will be made between the ATOFMS apportionment results and the impactor-

based predictions. Meteorological stations were operated on each side of the freeway for complete wind trajectory information.

### iii. Results and Discussion

#### *a. Quality Assurance of ATOFMS Data*

Data from the three ATOFMS instruments as well as all peripheral instruments were loaded into a database that allows for direct comparison of the temporal trends of gas phase, particle phase, and meteorological data. Before beginning data analysis of the ATOFMS particle types, quality assurance (QA) graphs were prepared for all three instruments over the relevant size ranges of the study. The purpose of these graphs is to examine whether any anomalies occurred during sampling that would result in improper interpretation of the acquired data.

A question that often arises with ATOFMS data concerns whether any chemical biases are leading to particles being "missed" in the LDI analysis step. In order to check for the presence of chemical biases, temporal plots are compared of the number of particles which scatter light to the number of particles which scatter light and produce a mass spectrum. If there is a chemical bias, where a particular type is being "missed", it will show up as lots of "scatters" with very few "scatters + mass spectra" (442). These plots were made for all three ATOFMS instruments over multiple size ranges for the full duration of the study. An example of this type of plot is shown in **Figure 94A** for the UF-ATOFMS. As can be seen, there are no major deviations between the scatters and scatters + mass spectra over the time of the study, indicating that there are major period with missed particle types. It is important to note that the smallest sized particles have the highest probability of showing a chemical bias since smaller particles are more "pure" (i.e. less chemically complex). In the freeway study, there was no major evidence of any particle types being missed by the ATOFMS in any of the size ranges examined (50 – 3000 nm). This is not surprising since the particle emissions from vehicles strongly absorb the ultraviolet light at 266 nm used for the laser desorption/ionization process with the ATOFMS. It should also be noted that all temporal plots for ATOFMS data shown in this manuscript show unscaled ATOFMS number concentrations. As will be shown, the unscaled temporal trends of the ATOFMS track the peripheral instruments without scaling; the main reason for scaling is to obtain atmospherically representative concentrations that can be directly compared to results from other studies.

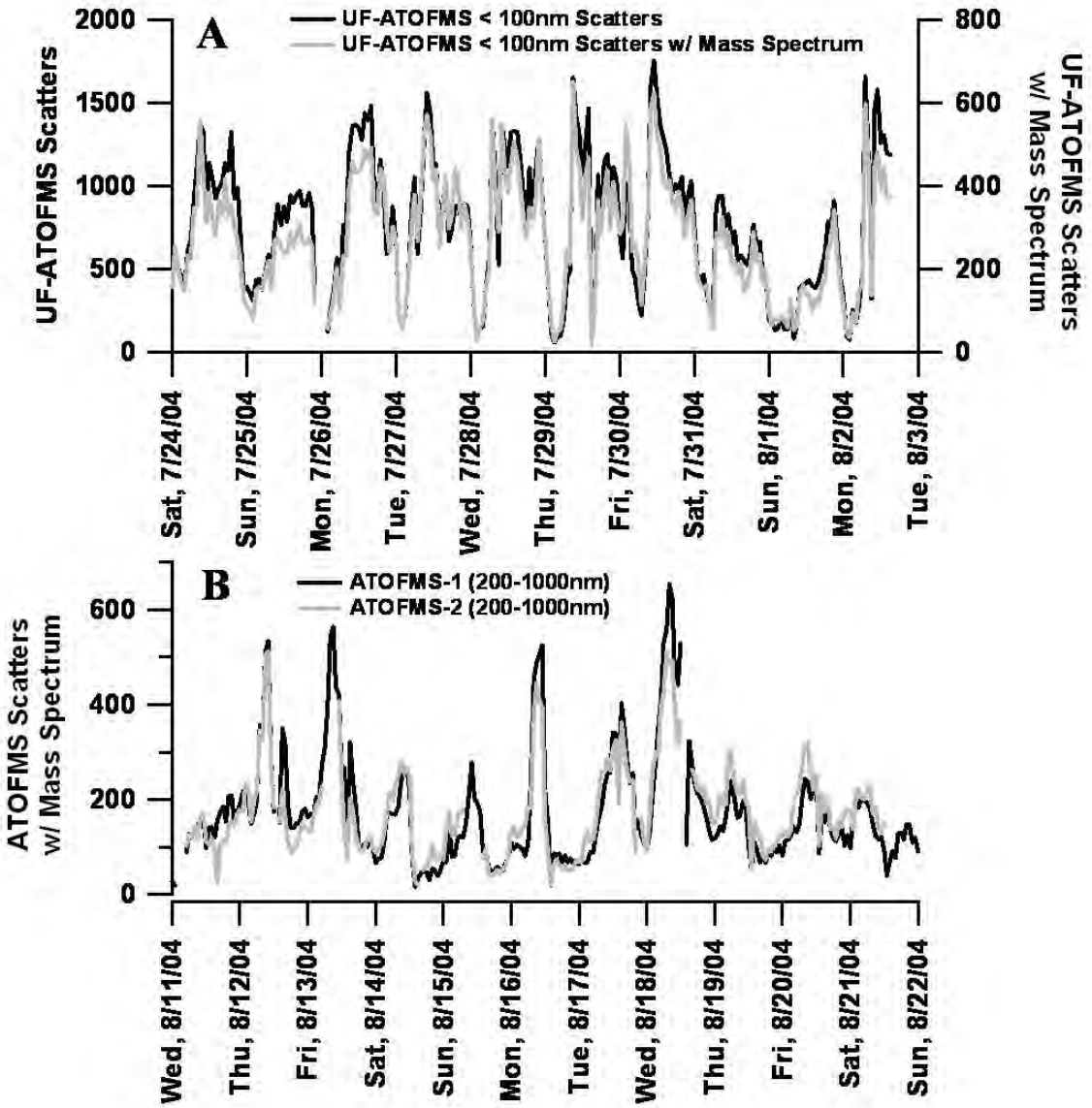


Figure 94: A) QA plot of UF-ATOFMS particle scatters vs. particles scattered that produced a mass spectrum to determine if there are any chemical biases or particle types being missed. B) Comparison of the two standard inlet ATOFMS instruments particle detections when running side-by-side at the freeway site. Plots are in one hour resolution.

As part of the QA process, it is also important to compare the temporal trends for the two standard inlet ATOFMS instruments when they were sampling side-by-side for the last part of the study near the freeway. **Figure 94B** shows this comparison, demonstrating how when the instruments were located at the same site almost identical trends in particle counts are obtained, demonstrating the reproducibility of the ATOFMS systems.

***b. Comparison with standard particle counts***

Comparing the ATOFMS size distribution measurements with those from other particle size measuring instruments is an additional method for determining whether the trends observed with the ATOFMS reflect ambient particle concentrations. **Figure 95A** shows a comparison of the SMPS against the UF-ATOFMS for sub-100 nm particle counts. Despite being on different absolute scales, it is evident that the basic temporal trends measured by these two instruments track one another quite well ($R^2$ = 0.60), providing additional validation of the ATOFMS temporal trends. In general, the ultrafine counts increased during periods when the winds were blowing from the west directly from the freeway to the sampling site. At night, the wind speeds typically became quite low (< 1.0 m/s), the traffic was reduced, and the ultrafine particle counts were at their lowest. This pattern was repeated each day over the entire study.

The two standard inlet ATOFMS systems measured particles in the larger size modes (200 – 3000 nm). **Figure 95B** shows a comparison of the ATOFMS by the freeway with the APS for submicron counts. The APS only samples particles down to 500 nm so a slightly different size range is covered. The standard ATOFMS detected

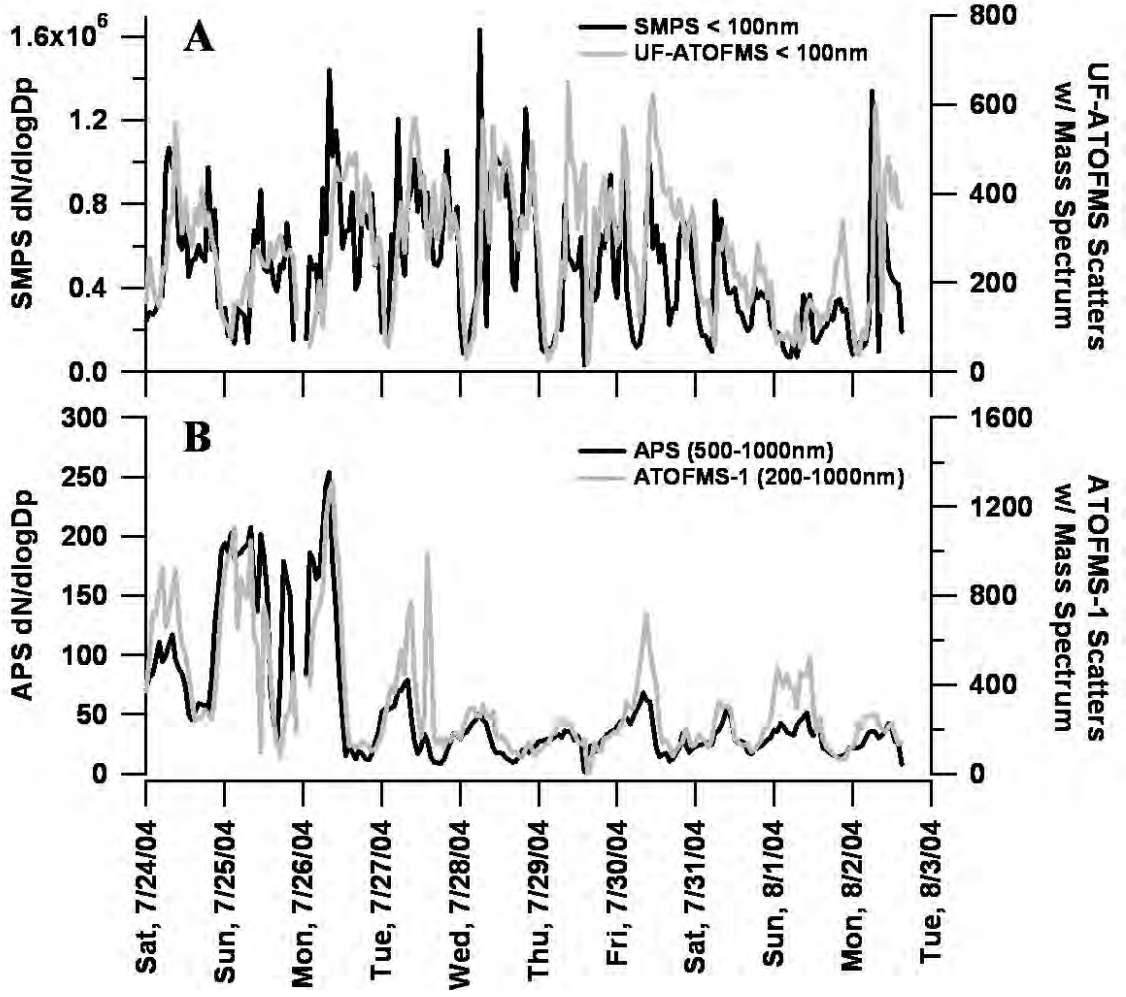


Figure 95: A) Comparison of sub-100 nm particle counts with the SMPS to sub-100 nm particles detected (that produced mass spectra) with the UF-ATOFMS at the freeway site. B) Comparison of fine mode particles (500 – 1000 nm) with the APS to fine mode particles (200 – 1000 nm)

detected (that produced mass spectra) with the standard inlet ATOFMS at the freeway site. Plots are in one hour resolution.

very few particles below 300 nm due to limitations in the transmission efficiency of the inlet. The important thing to note about this comparison is how strongly correlated the trends are ($R^2 = 0.70$), offering further credence to the temporal variations measured with the ATOFMS. **Figure 95A-B** shows the ATOFMS instruments tracking particle number concentrations measured using traditional particle sizing instruments over a broad range of sizes. This validation step is extremely important to future studies probing the temporal variability of different source contributions to the various ambient particles sampled by ATOFMS.

***c. Comparison of particle phase and gas phase data***

It is interesting to compare the UF-ATOFMS measurements with gas phase measurements. **Figure 96A** and **Figure 96B** show a comparison of gas phase CO and $NO_x$ concentration measurements versus UF-ATOFMS counts, indicating time periods when fresh emissions were impacting the sampling site. **Figure 96C** shows an expanded view of each gas phase species plotted over a larger time span. Typically it is expected that time periods where UF particles and CO peak may be related to LDV exhaust periods (426), whereas increases in $NO_x$ concentrations could be more indicative of HDDV emissions (425-427). When comparing the trends between CO and $NO_x$ emissions though, their trends tracked each other very closely ($R^2 = 0.71$). Since the trends are so similar, one cannot generalize that the CO is for LDVs and the $NO_x$ represents HDDVs in this case. More likely, these trends follow so closely because they are tracking both the trends in traffic as well as wind patterns. The CO and $NO_x$ values presented here (where the CO emissions are

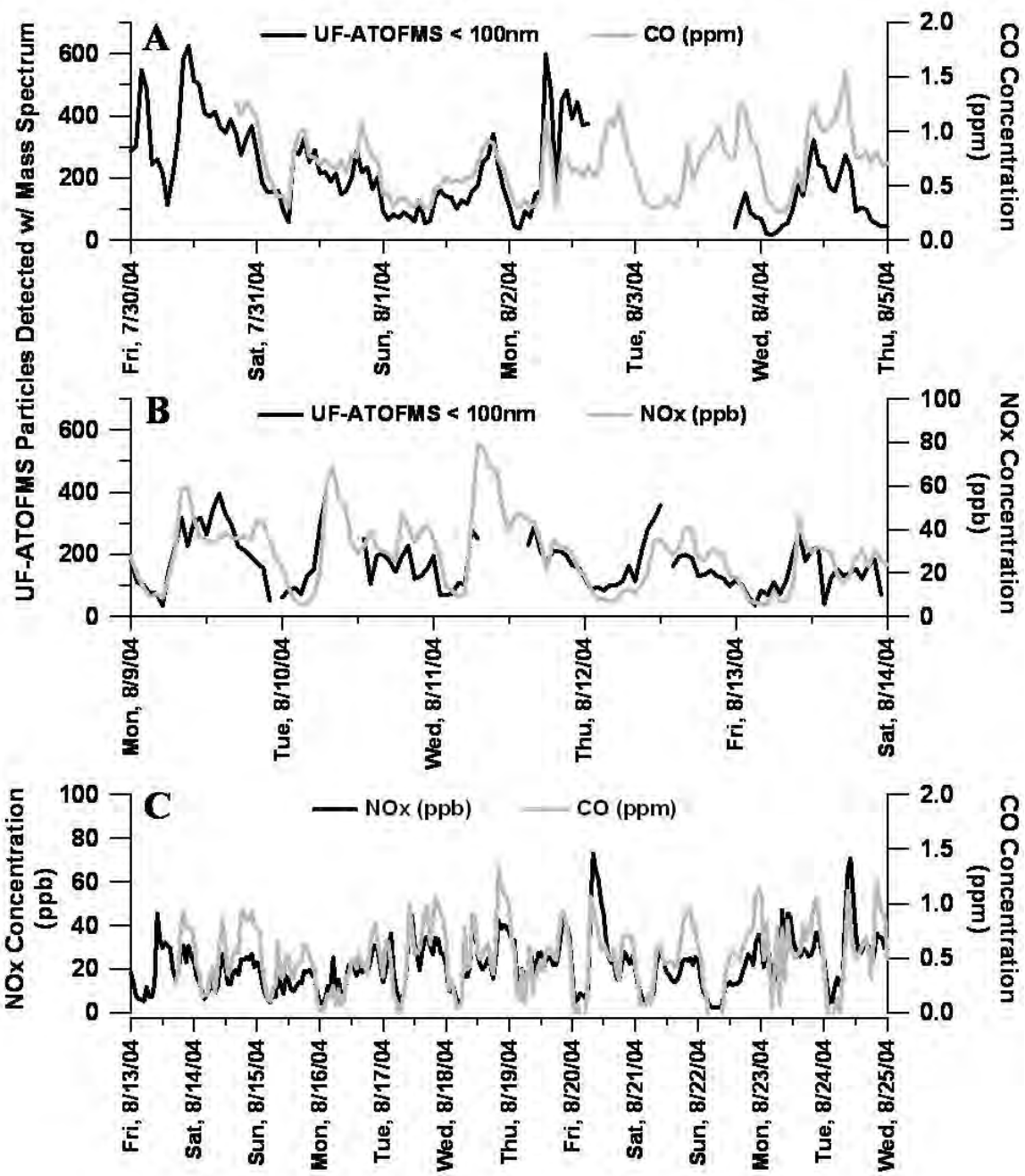


Figure 96: A) Comparison of sub-100 nm UF-ATOFMS particles detected that produced mass spectra with CO measurements. B) Comparison of sub-100 nm UF-ATOFMS particles detected that produced mass spectra with $NO_x$ measurements. C) Comparison of CO and $NO_x$ measurements at the freeway site. Plots are in one hour resolution.

continuously higher than the $NO_x$ emissions) are consistent with previous findings for areas with similar traffic conditions (426,443).

***d. Comparison of temporal trends from peripheral instruments***

Analysis of gas phase species such as $NO_x$ and CO coupled with aethalometer data can provide insight into the time periods when vehicle exhaust plumes were impacting the sampling site. There is some speculation as to whether this combination of instruments coupled with ultrafine size distribution measurements made with an SMPS can be used to identify HDDV impacted events (408,409,444-446). **Figure 97A** shows a comparison of the aethalometer and $NO_x$ measurements made over a time period when all instruments were operational. In general, the trends observed between the ultrafine particle concentrations (<100 nm), CO, aethalometer, and $NO_x$ measurements tracked each other, following peak wind speeds, which occurred mostly during daytime hours. Likewise, in **Figure 97B**, the data from the nephelometer (which detects light scattering particles) has similar trends as the aethalometer. This correlation is a strong indication that the local winds control when the particles reach the sampling site.

By comparing the aethalometer and $NO_x$ concentrations, one can see the trends track extremely well. In addition, one can see increases during weekdays versus weekends as has been reported in previous studies (444,445,447). This has been attributed to a relative increase in HDDV traffic during the week in Chapter 4. However, based on traffic count data, in addition to fewer HDDVs being on the road on weekends, there are also fewer LDVs

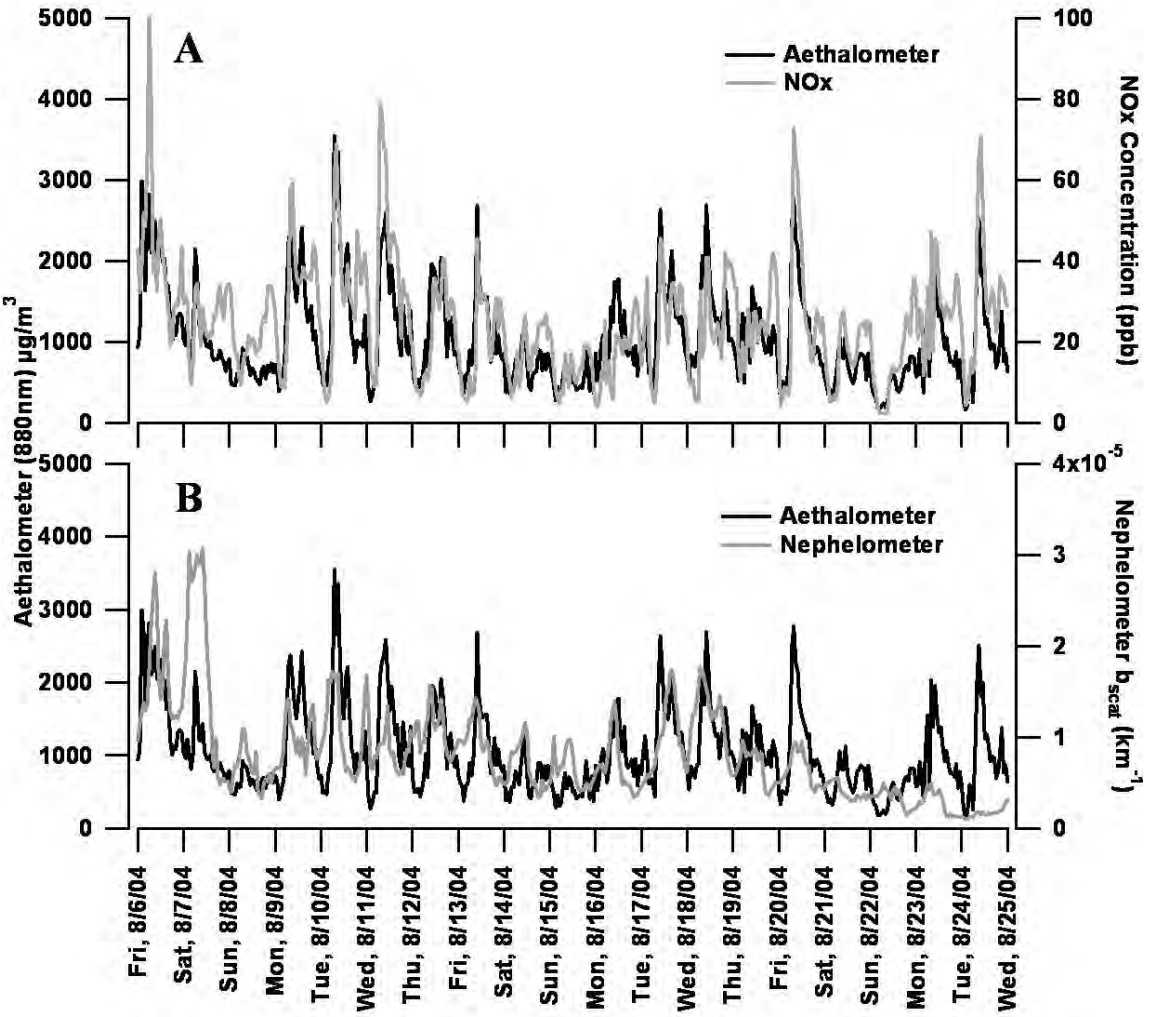


Figure 97: A) Comparison of aethalometer and $NO_x$ measurements at the freeway site. B) Comparison of aethalometer and nephelometer measurements at the freeway site. Plots are in one hour resolution.

overall (441). Therefore, the traffic flow is lower on this stretch of freeway during the weekends compared to the weekdays.

***e. Upwind/Downwind Sampling***

A major goal of the freeway study involved determining the contributions of vehicle emissions to ambient air near a major freeway. As previously described, an upwind sampling site was established so a comparison could be made between source contributions at a freeway-impacted site and a background (upwind) site. In addition to composition measurements being made with the ATOFMS and filters (Kleeman, UC-Davis), size distribution measurements were made using an APS and SMPS at both locations.

**Figure 98A** shows the APS and SMPS concentrations for the period between Jul. 24 and Aug. 3, 2004 at the freeway sampling site. **Figure 98B** shows the same data for the upwind sampling site. As can be seen, there is a constant band of particles with sizes

from 250 – 800 nm at the two locations, suggesting a strong regional contribution to the ambient PM levels at both sites. It is important to note that the wind was blowing from the upwind site (onshore) towards the freeway site during daytime hours when the concentrations show maxima at both locations. This figure shows that the concentrations of accumulation mode particles above 200 nm at the upwind/background site were not always lower than those at the freeway site as one would expect if the freeway was the major source of PM in this area.

The ultrafine mode and low size end of the accumulation mode (50 – 300 nm) show higher concentrations at the freeway location (**Figure 98A**), suggesting fresh

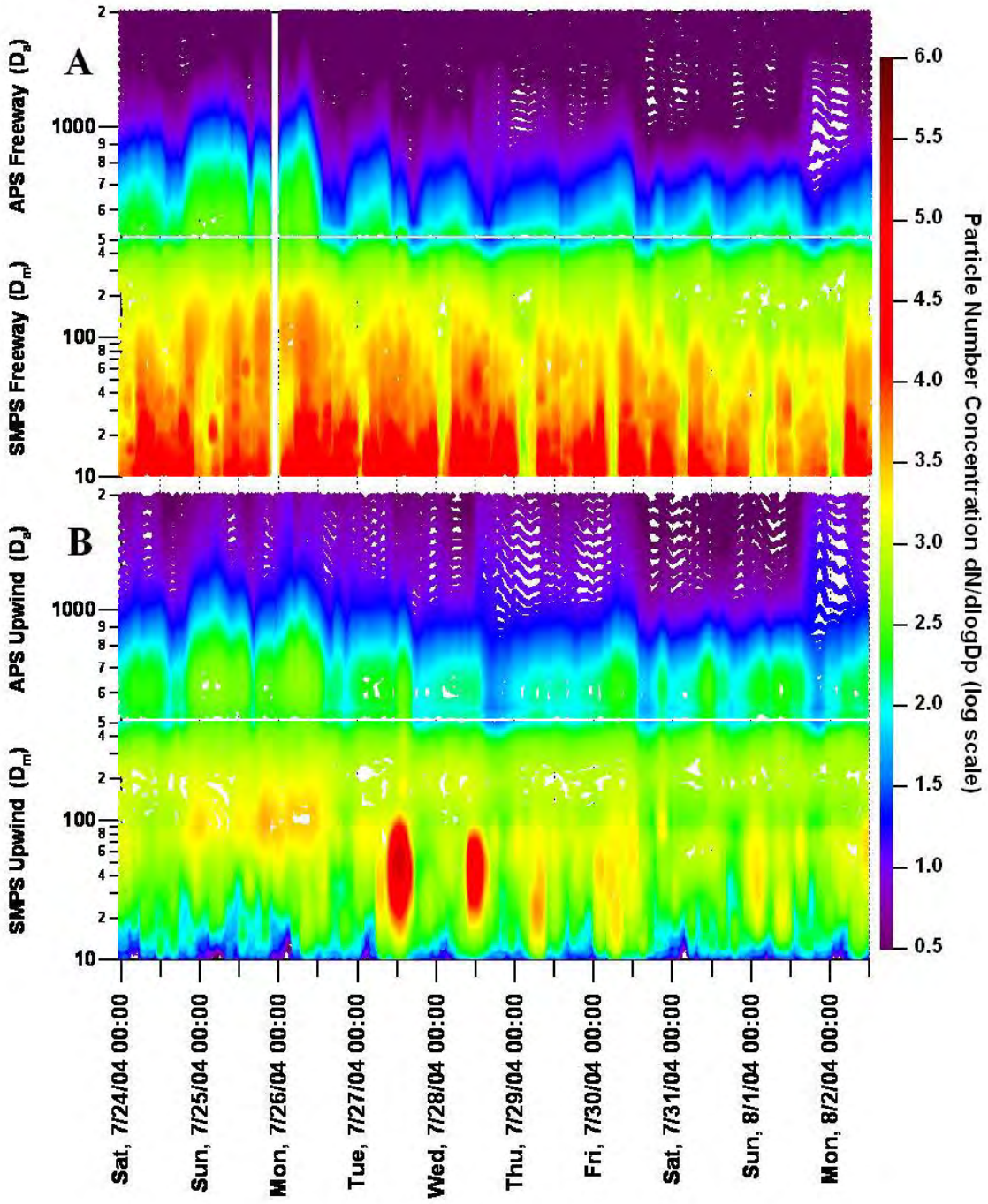


Figure 98: A) SMPS and APS particle number concentrations at the freeway site from. B) SMPS and APS particle number concentrations at the upwind sampling site. Both plots are shown from Jul. 24 to Aug. 3, 2004 in order to directly compare the two sites. The data is shown in log scale.

vehicle emissions from the freeway are contributing to particles in the 50 – 300 nm size range. However, it is interesting to note that on July 27 and 28, at around noon, significantly higher ultrafine and accumulation mode concentrations are observed at the upwind lab site indicating contributions from a local source. The standard instrument (ATOFMS-2) was sampling at the upwind location during this period. An examination

of the single particle composition revealed a unique single particle signature that has been detected as a major particle type in meat cooking emissions in previous meat cooking studies conducted in our laboratory (448). A large potential source of PM on the UCSD campus near the sampling site is a cafeteria where food is grilled. The peak in emissions corresponds to the period of the day when the most people eat at this establishment. Notably, a meat cooking aroma is often detected at the upwind site.

On July 29 and 30, ultrafine concentrations at the upwind site peaked at approximately 6:00 am (**Figure 98B**) and most likely came from traffic on a local road that borders the UCSD campus located close to the upwind site (about 300 m away) which is highly traveled at this hour of the day. In general, ultrafine particle concentrations show the highest spatial variability and represent ideal markers for local source inputs, as they spike only near the emission source. The ultrafine particles are also the most straightforward to identify and apportion since they have undergone very little aging and thus their signatures closely resemble the source (in this case dynamometer testing) signatures.

As shown in **Figure 98**, regional background PM concentrations made significant contributions to the accumulation mode. **Figure 99** compares the size distributions of the ATOFMS instruments [upwind (5.6A) and freeway (5.6B,C)] for the same time period as

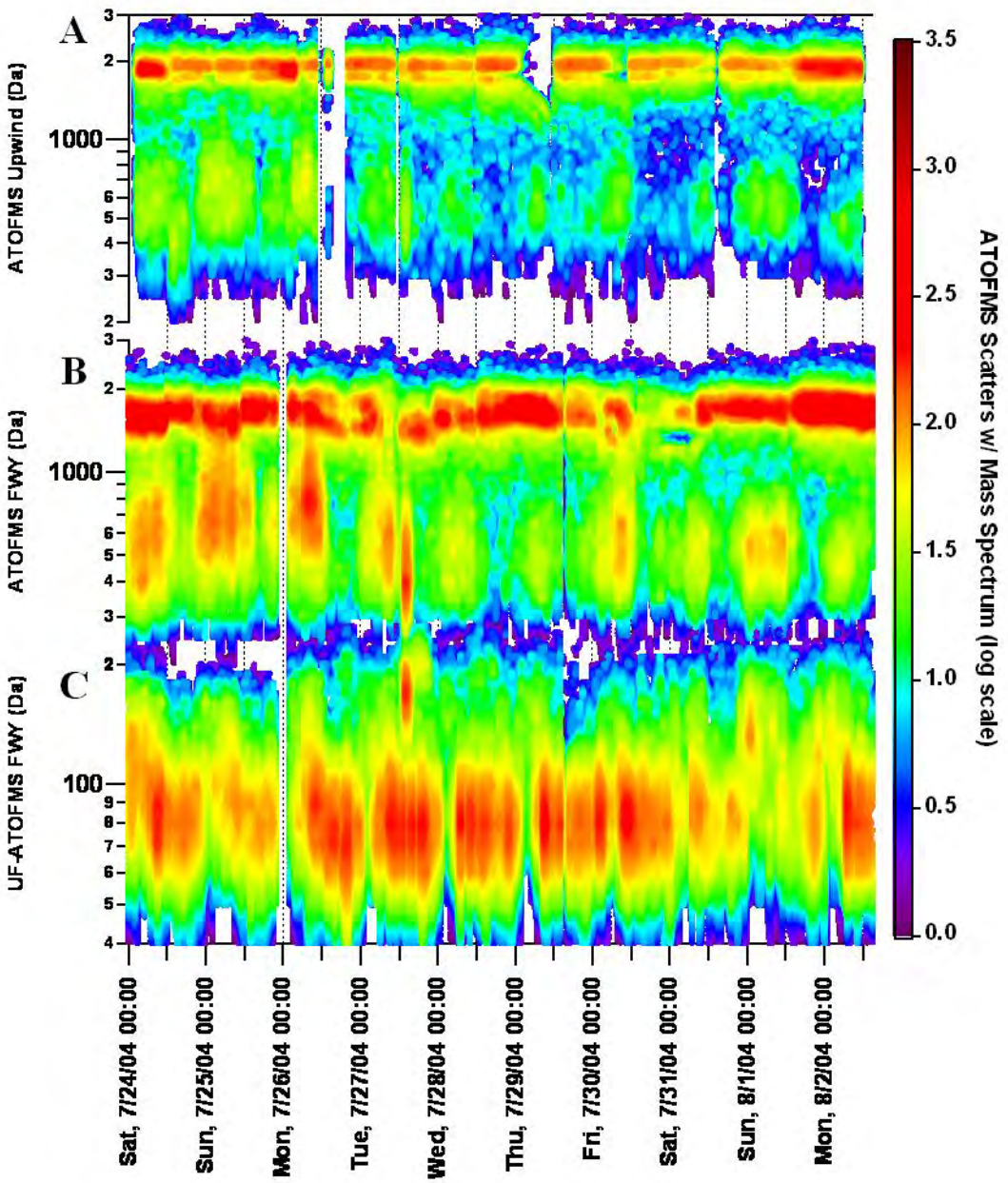


Figure 99: Particle size distribution data of: A) Standard inlet ATOFMS at the upwind sampling site. B) Standard inlet ATOFMS at the freeway sampling site. C) UF-ATOFMS at the freeway site. The particle size data shown is only for particles that were detected that produced a mass spectrum with the particular ATOFMS instrument. The data shown is from Jul. 24 to Aug. 3, 2004 in order to compare the two sites and to the APS and SMPS data shown in Figure 98.

the comparison of APS and SMPS data compared in **Figure 98**. One can see that the accumulation mode size distributions show very similar trends between the upwind and freeway sites. While the freeway site shows higher concentrations in the accumulation mode, the upwind site shows peaks at the same times. The difference in concentrations may be due to the topography of the area. Since the freeway site is located in a lower,

valley-like area, the background aerosols may be more prevalent at this site than at the upwind site which is closer to the coast and at a higher elevation. Evident in this figure is a relatively high PM concentration in the accumulation mode from July 24-27. It can also be seen that the accumulation mode peaks at nighttime and early morning hours, which corresponds to when the local wind speeds are at their lowest levels. This suggests that the accumulation mode particles are either due to smaller particles growing via condensation and/or agglomeration or from background particles at higher altitude settling to ground level. The latter of these scenarios is the most likely because of specific particle types detected that are unique to these time periods.

Due to these accumulation mode background contributions, other particle types were detected during this study that did not match to the vehicle dynamometer signatures. **Figure 100 (A,B)** shows the mass spectra for two such particle types: vanadium and elemental carbon (EC). These particle types peaked during the first few days of the study (July 24-27) in the accumulation mode at both sites usually when the local winds were low, likely indicating a regional contribution. The temporal trends for the vanadium and EC particle types are shown in **Figure 100 (C,D)**. HYSPLIT model (449) 24-hour back trajectories during these peak times show the winds at 500 m coming (southward) down along the California coastline, passing directly over the major shipping

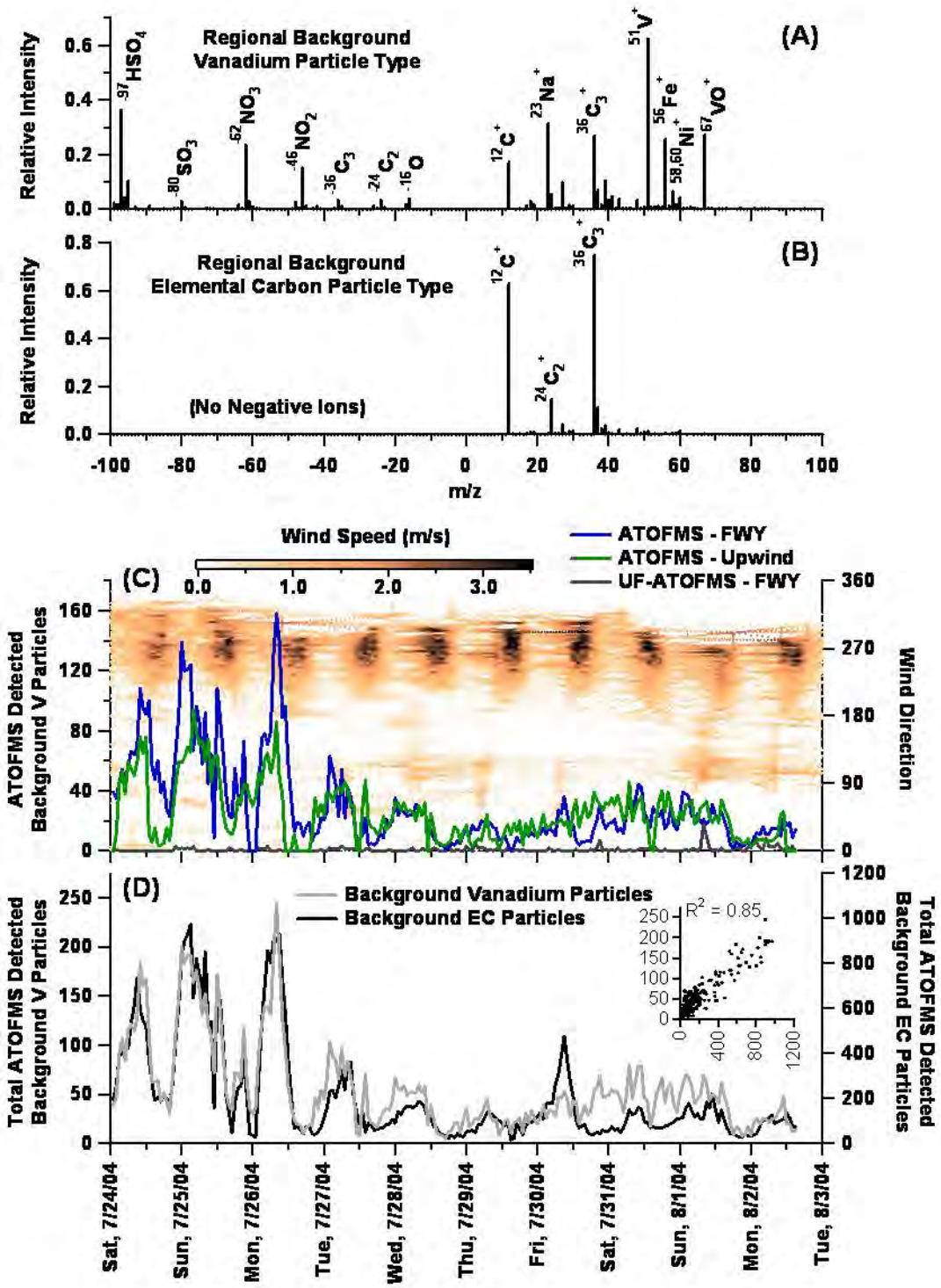


Figure 100: Positive and negative ion mass spectra for the regional background (A) vanadium and (B) EC particle types. (C) The temporal trends of the vanadium particle type detected with all three ATOFMS instruments compared to wind data. (D) Temporal trends (and correlation) of total background vanadium particles versus the total background EC particles for the three ATOFMS instruments.

ports in Long Beach and San Pedro. The HYSPLIT model back-trajectories are shown in **Figure 101**. When comparing the temporal trends of the vanadium & EC particles to the HYSPLIT back trajectories, it can be seen that largest peaks (7/24-7/26) occur when the nighttime wind trajectories are strong and coming straight down the southern California coast from the Los Angeles area. The days with smaller peaks occur when the nighttime trajectories are either not as strong, or are coming into the sampling site from out over the ocean.

Oil combustion has been shown to be the primary source for atmospheric vanadium aerosols (168,291,450,451). Vanadium particles have also been shown to come from vehicles, dust, and industrial sources (418,452,453). The correlation between V, Fe, and Ni associated with this type (as shown in **Figure 100A**) agree with findings by Xie et al. 2006 for ship oil combustion emissions (168). It is interesting to compare the temporal trend for these V-particles in the accumulation mode versus the ultrafine mode. On August 1, the number concentration of these particles shows a spike with the UF-ATOFMS that is not apparent in the accumulation mode, mostly likely indicating a local source. The temporal trends for the background vanadium and EC type, as well as the correlation between EC and V particle types, are shown in **Figure 100D**. As can be seen, the EC and vanadium trends track each other very strongly ($R^2$ = 0.85), especially from 7/24 to 7/30, with only minor variations occurring between 7/30 and 8/1. This correlation is an indication that the EC and V particle types are transported together and are likely from the same source. The relationship between these types of vanadium and elemental carbon particles and the use

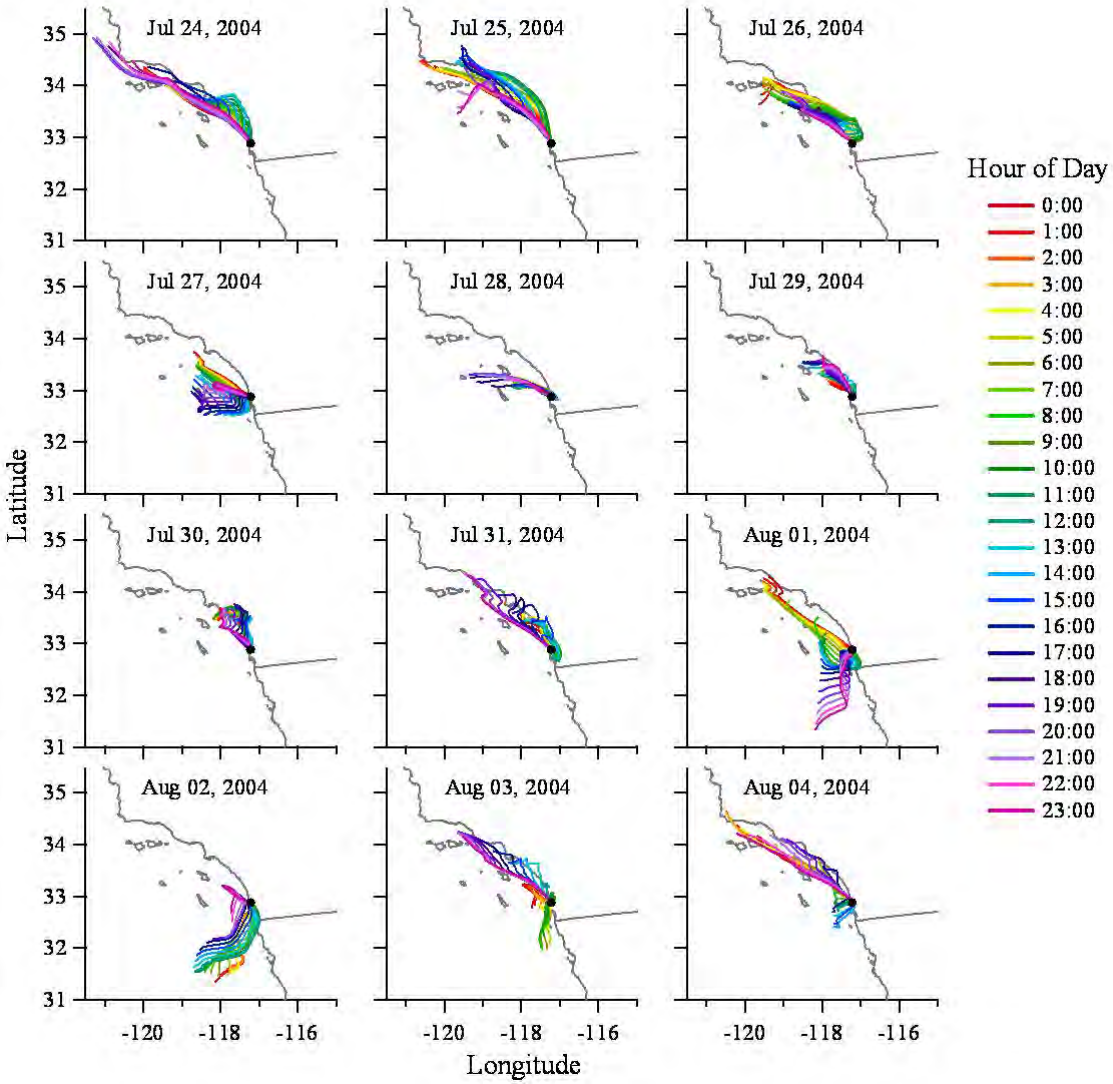


Figure 101: Hourly HYSPLIT model 24-hour back trajectories at 500 m for each day at the freeway study site.

of these signatures for apportioning ship emissions will be discussed in a future publication (454).

In general, all of the major particle types observed at the freeway site were also detected at the laboratory site. The similarities between the major particle types sampled by the standard ATOFMS instrument that was initially located at the upwind site (ATOFMS-2) and then moved to the freeway site were compared by taking the dot product of the top clusters detected at each site. All of the particle types detected at both sites had matching clusters with vigilance (similarity) factors of 0.85 and greater, meaning their mass spectral signatures were very similar to one another (a dot product of 1 indicates they are identical to one another). It is important to keep in mind that slight modifications due to uptake of organic carbon, ammonium, nitrate, and other secondary species will not have much of an effect on the comparison as the ART-2a weight vectors are sensitive to the most intense peaks in the spectra. The particle types deemed as

"unique" at both sites were mainly sea salt particles. This is because they had undergone less processing in general at the upwind site since it is closer to the ocean. The spectral modifications due to heterogeneous processing involve the loss of one peak from a relatively complex particle spectrum and the addition of another. For example, the uptake of $NO_x$ or $SO_x$ species on a sea salt particle will displace the chlorine on the particle which will result in the ATOFMS spectrum of the "aged" particle having different negative ion peaks than a fresh sea salt spectrum (455). Reducing the vigilance factor to 0.7 instead of 0.85 resulted in all particle types at the freeway site, including sea salt, matching the clusters at the upwind site. As would be expected, the rank order (based on the number of particles in each cluster) of the various types and their relative contributions to ambient PM was different at the two sites (i.e. there was more sea salt detected at the upwind site than at the freeway site, and more vehicle emissions detected at the freeway site than at the upwind site).

### *f. Data Analysis Used for Apportionment*

The same method described in Chapter 4 for source apportionment using mass spectral source signatures was also used here (441). In short, several ATOFMS source characterization studies have been conducted for the purpose of obtaining unique mass spectral signatures for each source. The particle source library includes signatures for HDDV and LDV exhaust emissions, coal burning, biomass burning, meat cooking, sea salt, dust, and industrial emissions; as well as non-source specific signatures for aged elemental carbon (aged EC), aged organic carbon (aged OC), amines, $NH_4$-containing, vanadium-containing, EC particles, and PAH-containing particles. These source signatures are used as a "seed" database, where the mass spectra of particles from other studies can be compared to the seeds using a matching version of the ART-2a algorithm (456,457) (YAADA v1.20 – http://www.yaada.org). Each particle mass spectrum is compared to all the mass spectra (ART-2a weight matrices) in the source database one at a time taking the dot product between each. If the particle matches to a particular source seed above a designated dot product vigilance factor (VF) threshold, then the particle is assigned to that type. If the particle matches to two or more different source seeds above the VF, then it will be assigned to the one that provided the highest dot product. The dot product values range from 0 to 1 with a value of 1 indicating the particle types are identical. For this analysis, a relatively high VF of 0.85 was used.

The ART-2a matching method has shown that a significant fraction of the HDDV and LDV particle types acquired during dynamometer sampling are indeed representative of those produced near a roadway (37,441). The results in Chapter 4 also show that the particles detected near the freeway are readily matched to particles from the vehicle dynamometer studies (441). These previous results focused on particles sampled with the UF-ATOFMS sampling near the freeway in the 50 – 300 nm size range, because particles in this size regime denote freshly emitted particles that would have a greater probability of originating from vehicular traffic on the freeway. The previous results also focused mainly on matching LDV and HDDV particles, since those would be the most similar types and thus, the potentially hardest to distinguish from one another. For this paper, the particles from the UF-ATOFMS and the two standard ATOFMS instruments were subjected to the same mass spectral matching procedures. However, since there is such a large size range sampled by these instruments, particles are only matched to source

library particles of the same size range. Therefore, ultrafine particles (50 – 100 nm) are only matched to source particles in the same size range, and likewise for small accumulation mode particles (SAM) (100 – 140 nm), larger accumulation mode particles (LAM) (140 – 1000 nm), and supermicron particles (1000 – 3000 nm). Size segregated matching ensures that particle types from one source that may be similar to those of another source, but having very different particle size ranges, don't conflict with each other. The reason the accumulation mode was split into two libraries (for this study) was because of the regional background EC and vanadium types discussed earlier which were found to influence the apportionment of the accumulation mode particles with sizes above 140 nm (441). As previously mentioned, the source library currently contains signatures for HDDVs, LDVs, dust, sea salt, biomass, and meat cooking, along with non-source specific signatures for aged organic carbon, aged elemental carbon, amine containing particles, PAH's, ammonia rich particles, vanadium particles, and elemental carbon particles. The signatures for HDDVs and LDVs were primarily obtained from dynamometer studies. Additionally, some of the HDDV and LDV signatures were obtained directly from ambient sampling after such particles were found to match with the dynamometer seeds. Other sources, such as biomass, dust, sea salt, and meat cooking were obtained from both lab studies and previous ambient measurements. The seeds for aged organic carbon, aged elemental carbon, amine containing particles, PAH's, ammonia rich particles, vanadium particles, and elemental carbon particles were obtained directly from classified ambient data from several different studies. As mentioned earlier though, the vanadium and elemental carbon seeds (many of which were derived from this study) may actually be signatures for ship emissions (454).

***g. Source Apportionment Using ART-2a***

As described, ART-2a analysis was used to "match" ambient data to source seeds for the duration of the study. **Figure 102** shows the size resolved apportionment for the first part of the study (Jul. 24 to Aug. 3, 2004) and averaged over those days. In Chapter 4, the one hour temporal apportionment of LDV and HDDV particles is shown for this same time period (441). From those results, it was shown that for ultrafine

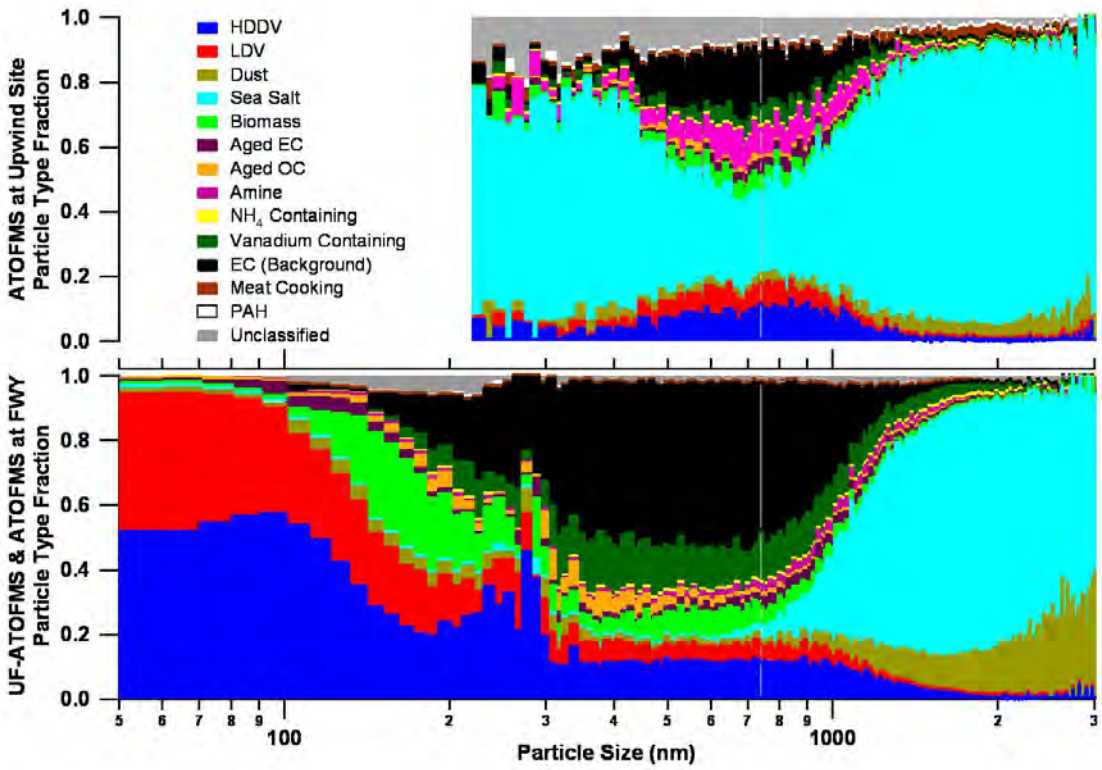


Figure 102: Size resolved source apportionment of the particles detected at the upwind (top) and freeway (bottom) sampling sites. Both plots are averages for ATOFMS data acquired from July 24 to Aug 3, 2004. In the bottom plot for the freeway site, the sizing region of overlap between the UF-ATOFMS and standard inlet ATOFMS is 200 – 300 nm.

particles, 37% of the particles were apportioned to LDVs and 58% to HDDVs. For accumulation mode particles (Da = 100 – 300 nm), 25% were LDV and 41% were HDDV. It was also shown that the trends of the apportioned particles tracked very well with LDV and HDDV vehicle counts. It is important to note that those results were only for particles detected with the UF-ATOFMS. Thus, when examining **Figure 102**, the ultrafine apportionment at the freeway site shows the same apportionment percentages as in Chapter 4. With the data from the standard ATOFMS being incorporated into the apportionment, size fraction trends through the region between 200 – 300 nm (where the two instruments overlap in particle size detection) for the HDDV apportionment is not as smooth due to the low number counts between 200 – 300 nm for both ATOFMS instruments. The trends of the other particle types in the 200 – 300 nm region are also not as smooth for the same reason as for the HDDV and LDV trends. The UF-ATOFMS was tuned to transmit ultrafine particles most effectively for this study by sampling ambient air drawn through a MOUDI with a 50% size cut at 100 nm to remove most of the particles larger than 200 nm, and thus making the transmission of particles above 200 nm relatively low (417). Likewise, the detection of particles below 300 nm by the standard inlet ATOFMS was low for this study. These size detection barriers for each instrument can be seen quite clearly in **Figure 99 (B,C)**. The relatively low detection efficiency of particles for each instrument between 200 and 300 nm during this study

accounts for the lack of a smooth transition for the particle types in the 200 – 300 nm size range.

As shown in **Figure 102**, ATOFMS allows for the determination of aerosol apportionment with very fine (10 nm) size resolution. This is important, because it can be seen that the fraction of particle types changes with size, especially above 100 nm. Above 100 nm, particles associated with biomass burning start to contribute to the ambient particles at the site, as well as particles apportioned to aged EC and aged OC. Most noticeable is the contribution from the EC (background) and vanadium-containing particle types starting around 140 nm (particularly for the EC background period). As discussed earlier, the regional background types were detected primarily at night, when local wind speeds were very low and when HYSPLIT back trajectories (**Figure 101**) come down the California coastline over Long Beach. These regional background types make up a major fraction of the particles from 200 – 1000 nm. The overall apportionment fractions stay relatively constant between 300 – 800 nm. Above 800 nm, sea salt particles start to contribute and become the dominant type above 1000 nm.

While seeds for non-aged and aged sources are included in the source signature library for non-vehicle sources, it should be noted that the sources are not currently being distinguished between aged and non-aged species to keep the apportionment simple. However, the majority of the particles from non-vehicle sources above 100 nm are coated with sulfate, nitrate, ammonium, as well as secondary organic aerosols (SOA) and that the amount of sec species increases with size based on ion intensities as one would expect.

When comparing the upwind site to the freeway site in **Figure 102**, one can see that sea salt particles dominated the detected particles at the upwind site. Interestingly, the particles apportioned to LDVs and HDDVs at the upwind site were primarily detected from 300 – 1000 nm. This observation could be an indication of growth of the vehicle particles as they were transported from the nearby roadway that is 200 meters upwind from this site. Unfortunately, there was not another UF-ATOFMS at the upwind site to see if there was an influence of vehicle emission on the UF mode. As shown in **Figure 98B**, there was very little contribution to the UF mode at the upwind site except when cooking emissions from a nearby cafeteria impacted the site. Over the 400 – 1000 nm size range, there is a greater fraction of amine-containing particles that do not match to any source library particles, a possible indication of aging occurring on the vehicle particles as they were transported to this site. A commonality between the freeway site and the upwind site is the detection of the regional background vanadium and EC particles over the same size range. As explained earlier, while the freeway site shows a higher contribution than the upwind site (40% of the total particles at the freeway versus 10% at the upwind site over the 140 – 1000 nm size range), the difference may be due to the topography of the area. The fact that the EC and vanadium particles are detected over the same size range is further evidence that these particles are part of a regional background as shown in **Figure 100**.

### *h. Size Resolved Source Apportionment Temporal Series*

As previously mentioned, the initial time series of the ATOFMS source apportioned freeway particles using the mass spectral source library was presented in Chapter 4. In that chapter, the focus was on the apportionment of HDDV and LDV

emissions in the ultrafine size range. The particles that were not apportioned to HDDV and LDV were designated as "other" particles (441). For this current study, a mass spectral source signature library with additional clusters besides HDDV and LDV signatures was used. Therefore, many of the particles originally designated as "other" are now apportioned, as can be seen in size resolved apportionment results presented in **Figure 102**. **Figure 103 (A-D)** shows the time series of the ultrafine and accumulation mode apportionment results at the freeway site, similar to those shown in Chapter 4, but with less particles in the "other" category. **Figure 103** is ordered from the smallest size range at the top down to the largest size range at the bottom. Evident in this figure is the influence of non-vehicle particle types with the increase in particle size, just as **Figure 102** shows. Also, the time series shows that certain particle types, such as biomass, are more prevalent on the weekends than the weekdays. Another interesting feature is the Aged OC class spikes on July 27, 2004 in the UF-ATOFMS 140 – 300 nm size range and the ATOFMS 200 – 1000 nm size range. This spike can also be seen in the ATOFMS number concentration plot in **Figure 99**, occurring at the same time across the same size ranges. The particles that matched to the Aged OC signatures during this time are fairly unique, as they only spiked with the two instruments on this one day during the study. One of the main points of **Figure 103** is to show that even near a freeway, one is not just being exposed to freeway aerosols. During times with a high regional background influence, the freeway related PM above 100 nm represented a relatively small fraction of the overall concentrations.

The time series of the ATOFMS (300 – 1000 nm) particle fractions in **Figure 103** compliment **Figure 100** & **Figure 102**. As shown in **Figure 103**, the EC background type dominates the particles between 300 and 1000 nm, with a strong contribution from the vanadium particles as well. The time series in **Figure 100** shows that the EC & vanadium made a large contribution to the particle concentrations from 7/24 – 7/27. This is also quite evident in **Figure 103** for the ATOFMS 300 – 1000 nm time series.

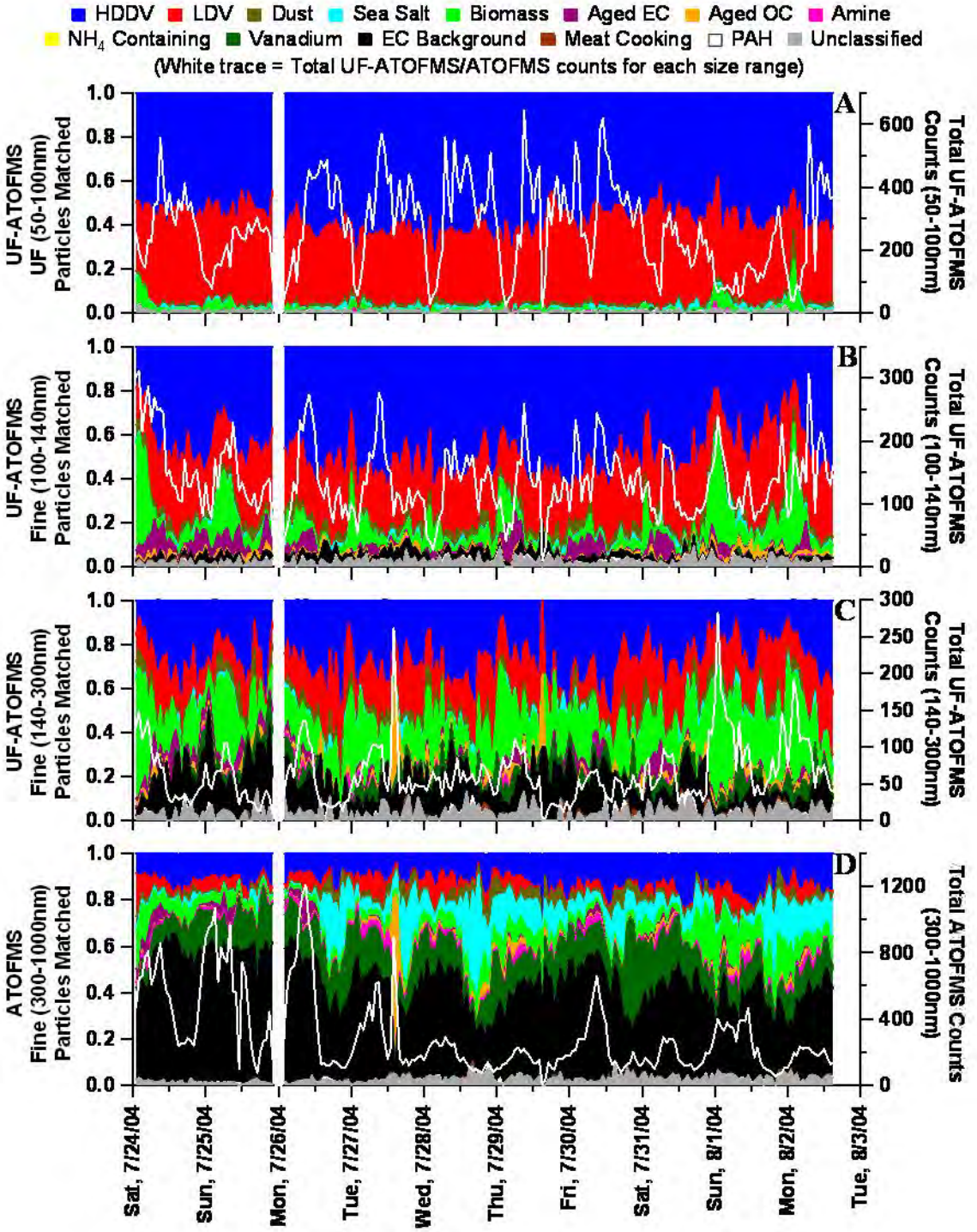


Figure 103: Time series of the size segregated source apportionment fractions for the freeway site ultrafine and accumulation mode particles detected with the UF-ATOFMS and ATOFMS.

One should note that all results presented here are based on a relatively simplistic univariate data analysis approach using ART-2a. However, even with this simplistic approach, the results demonstrate how single particle data can be used to apportion source contributions to ambient data. Particle aging, coating, agglomeration, and water uptake will play important roles in affecting particle source apportionment in other studies using this source library technique. These changes will, undoubtedly, make matching to source signatures more challenging, particularly at locations further from the source. Many of the sources, such as biomass, sea salt, and dust are readily distinguishable whether or not the particles are aged. The biggest challenge with aging will be with differentiating LDV and HDDV exhaust particles from one another. However, there are unique features to the HDDV and LDV sources that should make matching consistent, whether the particles have aged or not. One of the most important factors is that HDDV particles tend to have more calcium and phosphate associated with them in an elemental carbon/calcium type particle (EC-Ca) (37,419). LDV particles have much less calcium and/or phosphate associated with them, but do produce elemental carbon particles in the UF size mode (418). These kinds of distinctions could be used to identify HDDV and LDV particles in highly aged environments that do not match to the source seeds.

One of the ultimate goals of this study is to eventually compare single particle source apportionment with impactor filter samples acquired during this study. Single particle measurements hopefully can distinguish between unique vehicle source signatures superimposed on a high ambient background concentrations that may not be apparent in MOUDI mass concentrations where only slight changes are due to vehicle emissions (at least for the accumulation mode). Also, once the data are available, the source percentage predictions made with ART-2a on the ATOFMS data will be compared with organic tracer MOUDI and impactor based method results from this study obtained by the Kleeman research group from UC-Davis. Additionally, future analysis using different clustering algorithms, such as Hierarchical clustering and Positive Matrix Factorization, will be used in comparison to the results found in this chapter and Chapter 4 (441).

**iv. Acknowledgements**

The authors thank Dan Cayan and Alex Revchuk of the Scripps Institution of Oceanography (SIO) at UCSD for setting up the micro-meteorological stations and providing their data for this study. We also thank UCSD and their facilities management for all their cooperation and help with setting up power to the freeway site. Lastly, we thank Michael Kleeman and Michael Robert from UC-Davis for their collaboration with this study. The HYSPLIT transport and dispersion model used in this publication was provided by the NOAA Air Resources Laboratory (ARL). Funding for this study was provided by the California Air Resources Board (CARB) (Contract 04-336).

## 14. Aging effects on source apportionment from the single particle perspective

### i. Introduction

Landmark cohort studies published over a decade ago recognized an association between mortality and long term exposure to air pollution (specifically to particulate matter with diameters less than 2.5 μm or $PM_{2.5}$) (458,459), but improvements in recent epidemiological studies have allowed for better linkage between specific sources and their adverse health effects (460). Through understanding the health impacts and the ambient contributions to a particular region by specific sources (a process which is called source apportionment), government agencies can establish necessary regulations to effectively reduce the pollutants from targeted anthropogenic sources and, therefore, the negative health effects. The alternative for these agencies are blanket reductions, which are far more expensive and less effective than source-specific ones.

The majority of source apportionment methods rely on data from bulk aerosol sampling techniques coupled with off-line chemical analysis; these traditional receptor-orientated techniques include chemical mass balance (CMB) modeling, which utilizes unique nonreactive or stable tracer species, and factor analysis modeling by principal component analysis (PCA) or positive matrix factorization (PMF) (461-463). Recently, a new approach to source apportionment has been developed that compares all of the chemical information of individual ambient particles to the mass spectral signatures in a library of known sources (41,344). Designed for the single particle technique aerosol time-of-flight mass spectrometry (1), this new method has the advantage of producing size-segregated and high temporal resolution results. One of the potential challenges of using the source signature library approach involves its ability to accurately apportion aerosols that have "aged" or undergone atmospheric processing since being freshly emitted. Aerosol aging by physical and chemical processes such as reactive uptake, mass transfer, and condensed-phase processes can change the chemical composition and properties of individual particles (464,465). In fact, recent laboratory and field studies have demonstrated that the aging of aerosols increases their cloud condensation nuclei (CCN) activity or ability to form cloud droplets, which is part of one of the largest uncertainties in the radiation balance of the earth (466-470). The issue for source apportionment with the source signature library is whether or not the aging of a particle alters its chemical signature enough from that of the original source fingerprint that the particle is mislabeled or unassigned.

It has been established that the source signature library approach works successfully (matching 97% of the particles) for relatively "fresh" environments, such as directly alongside a major freeway (41,344). The goal of this study is to apply the library matching technique in order to evaluate and improve its performance on ambient measurements made during two different seasons (summer and fall) in the highly aged environment of Riverside, California. Located east and downwind of the Los Angeles (LA) Basin, Riverside is a receptor site for the LA air pollutants which have time to age during transport, as already described in Chapters 3 and 4. The source apportionment of Riverside represents an extreme challenge, as this environment is both highly polluted and aged. Two different approaches (lowering the "matching" factor and introducing

new aged source signatures to the library) to handling the aging effects of particles are examined. An area of particular interest in this study includes the aging effects on similar particle types, such as the combustion exhaust emissions of heavy duty diesel vehicles (HDDV) and light duty gasoline vehicles (LDV) which can be distinguished and separated under fresh conditions (38,41,344). Also in this study, which secondary chemical species on particles apportioned to such primary sources are dominate will be investigated.

## ii. Experimental

### *a. Sampling location and instrumentation*

Ambient sampling on the campus of the University of California, Riverside (33°58′18″N, 117°19′22″W) during the summer (July-August) and fall (October-November) of 2005 occurred in conjunction with the Study of Organic Aerosols at Riverside (SOAR) field campaign. Details on the sampling location and inlets of the mobile laboratory can be found elsewhere (31) and in previous chapters (3 and 4). Single particle size and chemical composition were measured by two collocated aerosol time-of-flight mass spectrometers (ATOFMS). An ultrafine ATOFMS (UF-ATOFMS), equipped with an aerodynamic lens system, detected particles with aerodynamic diameters between 50 and 400 nm, while a standard nozzle inlet ATOFMS measured particles with aerodynamic diameters between 140 and 3000 nm. Details of the transportable instrumentation have been described previously (1,2). During the summer, the UF-ATOFMS operated continuously from July 23$^{rd}$ to August 15$^{th}$, whereas the standard ATOFMS ran from July 29$^{th}$ to August 15$^{th}$. Both instruments operated from October 31$^{st}$ to November 21$^{st}$ during the fall season. All results are presented in Pacific Standard Time (PST), which is one hour behind local time during the summer.

### *b. Data analysis*

During the SOAR campaigns, the combined ATOFMS instruments acquired millions of individual particle mass spectra. Using a matching function of the ART-2a clustering algorithm (35), these spectra were apportioned and classified based on their similarity to a set of predefined seeds (or signatures) based on the dot product of their vectors. ART-2a has a user-defined threshold parameter called the vigilance factor (VF), which represents the minimum degree of similarity necessary for a particle spectrum to match a seed; with a range of 0 to 1.0, the main VF used in this study (0.85) represents a relatively high VF value. The ambient particles are matched to predefined seeds in a source signature library, as developed and described in detail by Toner et al. (41,344). Briefly, this size-segregated source signature library contains mass spectral signatures from a series of source and ambient characterization studies (including vehicle dynamometer studies) for sources including HDDV and LDV exhaust emissions, dust, sea salt, biomass, and meat cooking. The representative seeds were made from the top (most populated) ART-2a clusters that accounted for ~90% of the particles in the datasets of the source characterization studies. For example, roughly 30 ART-2a clusters account for 90% of the particles in the HDDV (36-38,471) and LDV (36-38,471) studies. The library also contains non-source specific signatures such as aged elemental carbon (EC), aged organic carbon (OC), amine-containing particles, ammonium-rich particles,

vanadium-rich particles, EC, and polycyclic aromatic hydrocarbon (PAH)-containing particles. Certain specific sources, such as sea salt, dust, biomass burning, and meat cooking, have proven to be readily distinguishable in previous ATOFMS ambient characterization measurements; therefore, representative seeds for these particle types were made from several lab and ambient studies and incorporated into the library. The studies used to obtain the source signatures included: freeway 2004 (FWY) study (41,344), SOAR 1 & 2 (31), the Cloud Indirect Effects Experiment in Trinidad Head, CA (CIFEX) study (472,473), the ABC Post Monsoonal Experiment in Hanimaadhoo, Republic of Maldives (APMEX) study (474), and the Megacity Initiative: Local and Global Research Observations in Mexico City, Mexico (MILAGRO) study (475). The library is separated into three different size ranges, because there are distinct chemical differences for each source based on size. It was determined that these size ranges (50-100 nm, 100-140 nm, and 140+ nm) reflect the largest chemical, and hence source specific, differences. Currently, there are 322, 369, and 423 total seeds in the 50-100 nm, 100-140 nm, and 140+ nm libraries, respectively. **Table 17** provides the number of seeds used for each source in the original source signature library based on size.

After matching the ambient particles to the source signature library, a significant fraction of particles were not assigned to any category. Some of these unclassified particles had noisy spectra due to poor signal-to-noise ratios or erroneous peaks and need to be removed from the dataset. With cluster analysis, these particles form many clusters occupied by a single particle, because the peaks are noise and randomly occur at various mass/charge values. In order to isolate these noisy spectra in each size range, ~20,000 (due to computer memory limitations) unclassified particles spread temporally across the study were analyzed by ART-2a with a VF of 0.85. Of the resulting clusters, all singly-occupied clusters were removed, so that the remaining clusters could be used as seeds. Next, all of the unclassified particles in that size range were compared to these seeds at a VF of 0.85. All particles that did not match one of these seeds were removed from the dataset. This removal process was verified by selecting a different set of ~20,000 particles to create the seeds. The resulting unmatched particles agreed with the unmatched particles obtained from the first set of ~20,000 particles, indicating that the first set was indeed representative of all the unclassified particles in that size range. In the end, approximately 8.2% of the ~2.1 million particles obtained by the standard inlet ATOFMS and approximately 9.6% of the ~5.3 million particles obtained by the UF-ATOFMS were removed from all future analysis.

### iii. Results and Discussion

#### *a. Source signature library matching*

The hourly temporal results from matching the ambient particles detected during

Table 17: Number of library seeds for each source per size range

| Category | Source Study | UF (50-100 nm) | | SAM (100-140 nm) | | LAM, SUB, & SUPER (140-3000 nm) | |
|---|---|---|---|---|---|---|---|
| | | # of Seeds | Seed Order in Library | # of Seeds | Seed Order in Library | # of Seeds | Seed Order in Library |
| HDDV | HDDV 2001 and 2003 dynamometer, FWY 2004 | 36 | 1-30, 35, 41-42, 45, 47, 58 | 71 | 1-60, 68, 337-339, 344-350 | 83 | 1-60, 68, 369-373, 375-378, 384-386, 391-394, 397-399, 402-404 |
| LDV | LDV 2002 dynamometer, FWY 2004 | 24 | 31-34, 36-40, 43-44, 46, 48-57, 59-60 | 29 | 61-67, 69-90 | 29 | 61-65, 67, 69-81, 83-90, 395-396 |
| Dust | APMEX, CIFEX, FWY 2004, SOAR2, Lab samples | 129 | 84, 89-192, 197-209, 214-217, 287-293 | 129 | 114, 119-222, 227-239, 244-247, 317-323 | 129 | 114, 119-222, 227-239, 244-247, 317-323 |
| Sea Salt | CIFEX, APMEX, FWY 2004, SOAR2 | 44 | 62, 67-69, 78-83, 85-88, 195-196, 210-213, 263-286 | 48 | 92, 97-99, 108-113, 115-118, 225-226, 240-243, 293-316, 340-343 | 48 | 92, 97-99, 108-113, 115-118, 225-226, 240-243, 293-316, 387-390 |
| Biomass | CIFEX, FWY 2004, SOAR1 | 20 | 61, 63-66, 70-77, 193-194, 234-238 | 20 | 91, 93-96, 100-107, 223-224, 264-268 | 20 | 91, 93-96, 100-107, 223-224, 264-268 |
| Aged EC | FWY 2004, SOAR1 | 2 | 227-228 | 2 | 257-258 | 3 | 257-258, 406 |
| Aged OC | FWY 2004, SOAR1 | 5 | 229-233 | 8 | 259-263, 351-353 | 8 | 259-263, 383, 400-401 |
| Amine | FWY 2004, SOAR1 | 17 | 218-221, 294-306 | 17 | 248-251, 324-336 | 18 | 248-251, 324-336, 407 |
| $NH_4$ rich | SOAR1 | 2 | 222-223 | 2 | 252-253 | 2 | 252-253 |
| Vanadium rich | FWY 2004, SOAR1, SOAR2 | 27 | 224-226, 239-262 | 27 | 254-256, 269-292 | 57 | 254-256, 269-292, 337-364, 379-380 |
| EC (pos only) | FWY 2004 | 0 | | 0 | | 10 | 66, 82, 365-368, 374, 381-382, 405 |
| Meat Cooking | FWY 2004, MILAGRO 2006 | 16 | 1-16* (separate order) | 16 | 1-16* (separate order) | 16 | 1-16* (separate order) |

the summer and fall SOAR field campaigns to the original source signature library are shown in **Figure 104** and **Figure 105**, respectively. The results are size-segregated to better illustrate the size dependence of the different particle types. Size-segregated source apportionment also is useful for linking sources with specific health effects. The top three plots represent the relative chemical class fractions for ultrafine (UF: 50-100 nm), small accumulation mode (SAM: 100-140 nm), and large accumulation mode (LAM: 140-400 nm) particles as detected by the UF-ATOFMS. The last two plots provide the combined relative fractions for submicron (SUB: 140-1000 nm) and supermicron (SUPER: 1000-3000 nm) particles as detected by the standard ATOFMS. The missing periods (white effective density measurements (48), or low particle statistics in that hour (<10 particles). As additional information, **Figure 106** and **Figure 107** illustrate the matching process with the summer and fall data, respectively, by providing the number of particles that matched to each source seed in the library.

Of all the different size ranges, the plot for the ultrafine particles show the smallest percentage (~3%) of particles that did not match the source signature library at a VF of 0.85 or above, which are labeled as the unclassified particles. Actually, the initial percentage of unclassified ultrafine particles was ~64% mainly due to detector "crosstalk" issues. Detector "crosstalk" is produced in the UF-ATOFMS negative ion mass spectra due to the interference of extremely intense peaks in the positive polarity. These crosstalk issues are not accounted for in the source signature library; therefore, after the initial matching, the ~64% of unclassified particles were matched again to the bars) are due to instrument downtime for quality control procedures and maintenance, source signature library at a VF of 0.85 using only the positive mass spectral information

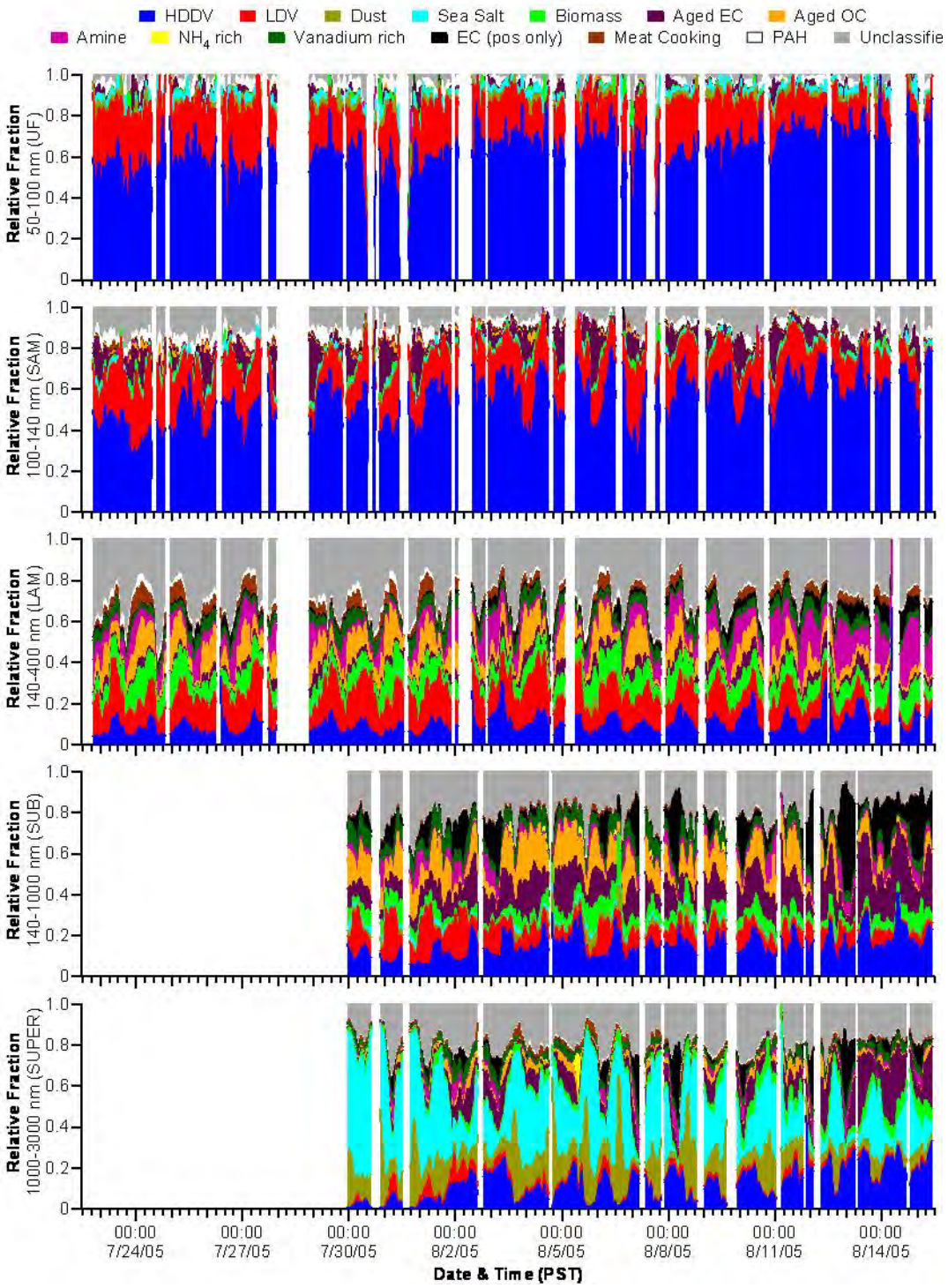


Figure 104: Hourly temporal series of the size segregated source apportionment fractions (VF = 0.85) for the summer SOAR ultrafine (UF), small accumulative mode (SAM), large accumulation mode (LAM), submicron (SUB), and supermicron (SUPER) particles detected with the UF-ATOFMS and ATOFMS.

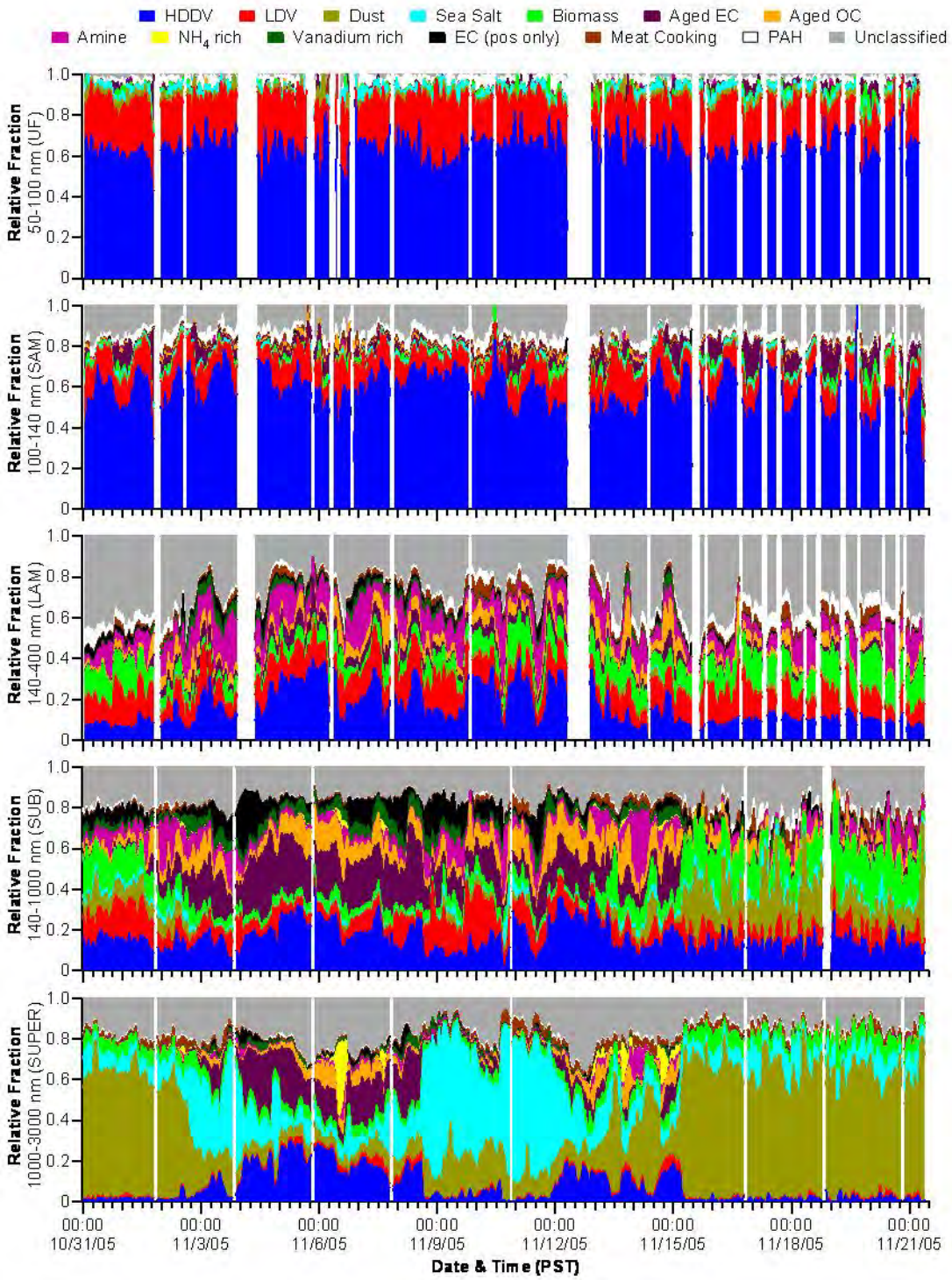


Figure 105: Hourly temporal series of the size segregated source apportionment fractions (VF = 0.85) for the fall SOAR ultrafine (UF), small accumulative mode (SAM), large accumulation mode (LAM), submicron (SUB), and supermicron (SUPER) particles detected with the UF-ATOFMS and ATOFMS.

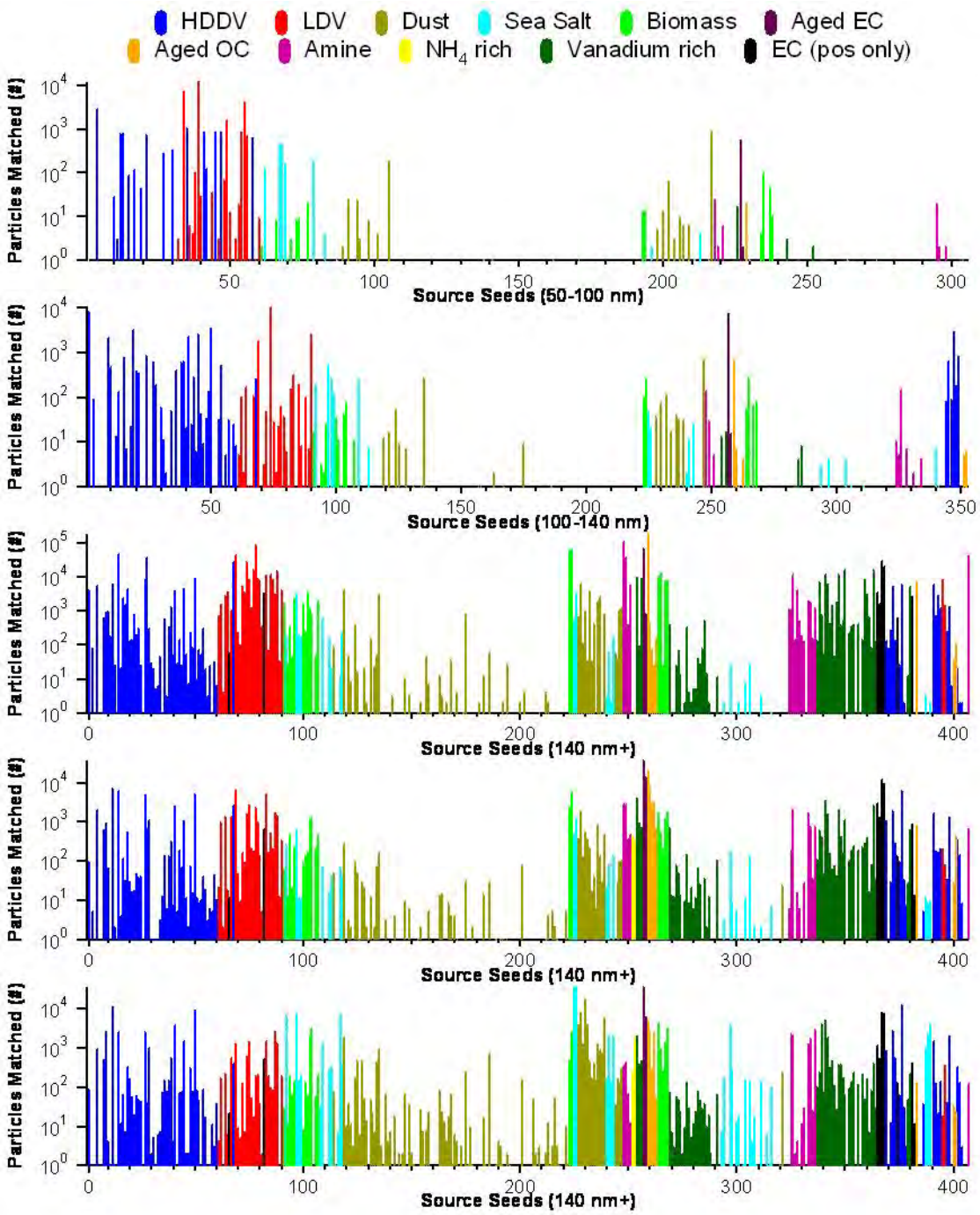


Figure 106: Number of summer particles matched to each source seed for a) UF (50-100 nm), b) SAM (100-140 nm), c) LAM (140-400 nm), d) SUB (140-1000 nm), and e) SUPER (1000-3000 nm) particles.

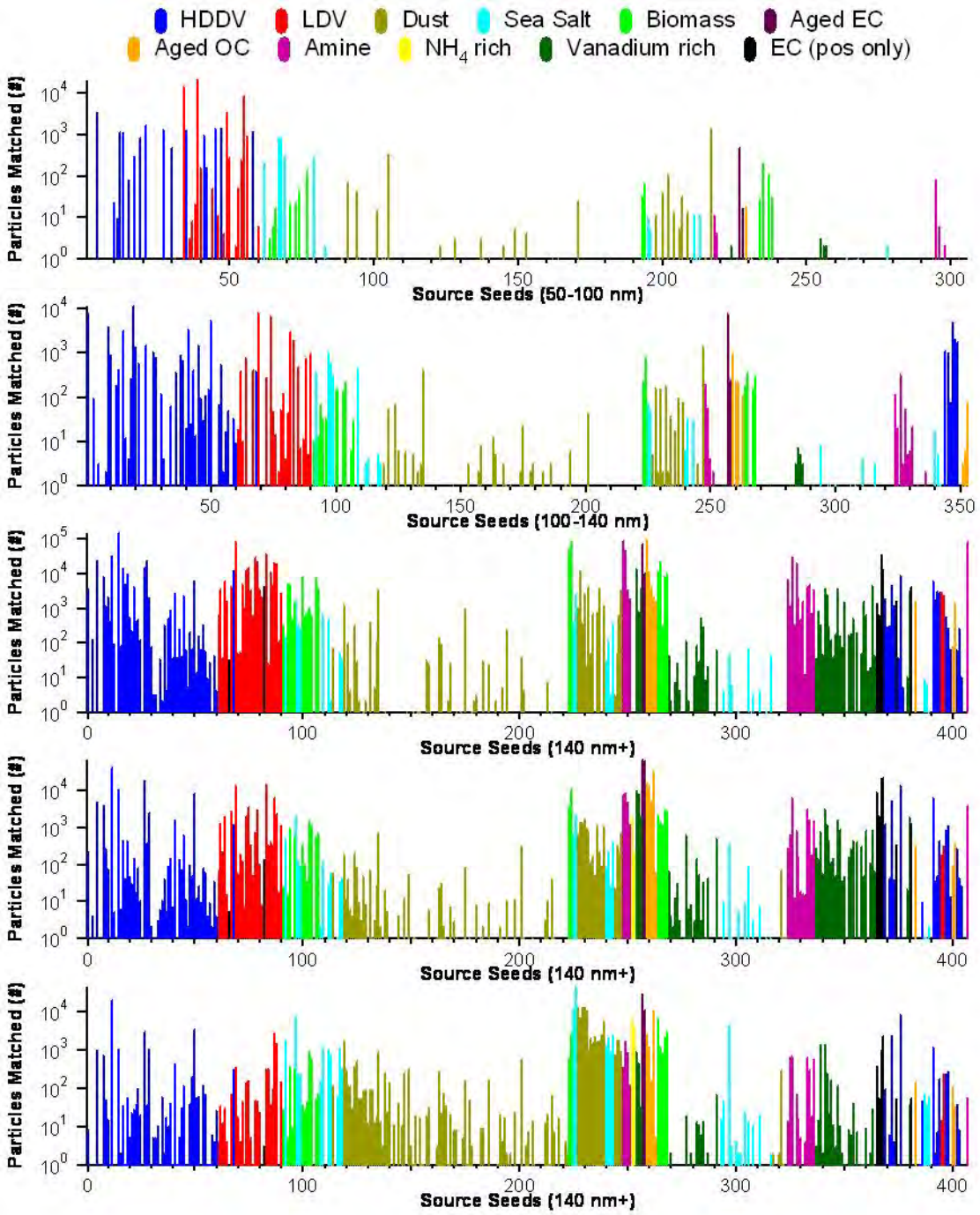


Figure 107: Number of fall particles matched to each source seed for a) UF (50-100 nm), b) SAM (100-140 nm), c) LAM (140-400 nm), d) SUB (140-1000 nm), and e) SUPER (1000-3000 nm) particles.

(344,476). As the ultrafine particles are the ones most strongly impacted by crosstalk issues, the second matching iteration using only positive ion information was performed only on this size range. The resulting relative fractions show that over 80% of the ultrafine particles are apportioned to vehicle exhaust emissions with the HDDV emissions being nearly three times that of the LDV emissions. Previous studies have

already shown that fresh local vehicle exhaust emissions are the dominant source of primary ultrafine particles in Riverside, though they did not distinguish between HDDV and LDV emissions (44,45). The ultrafine plots in **Figure 104** and **Figure 105** show that the relative contributions by HDDV and LDV exhaust emissions stay fairly constant with time. A focused study (Chapter 3) on the ultrafine particles observed during the SOAR campaigns determined that the raw number counts, rather than the relative percentages, of ultrafine particles detected by the UF-ATOFMS represent a good proxy for traffic activity (477). Although some of the particles in the 100 to 140 nm size range are also impacted by crosstalk issues, a second matching iteration with positive only information was not run on this size range. The spectra of ultrafine particles (seeds and ambient) are relatively simple and chemically pure, which allows the positive only matching to work well. When the spectra become more complex (as with particles of a larger size), the results from positive only matching become less reliable. When manually inspecting the unclassified category left after matching the 100 to 140 nm particles to the source signature library, it was determined that the top unclassified type was impacted by crosstalk issues and that this type belonged in the HDDV category. The positive ion spectra of this top type contained an elemental carbon with calcium signature that closely resembled one of the dominant chemical classes from HDDV exhaust emissions during dynamometer studies (36-38,471). Therefore, the SAM results shown in **Figure 104** and **Figure 105** include the matching results from the source signature library and the top crosstalk particle type that was manually added to the HDDV category.

As particle size increases, the relative fraction of particle apportioned to HDDV and LDV become less dominant and the contributions of the other particle types emerge. For example, **Figure 104** and **Figure 105** illustrate that for the two size ranges covering 140-1000 nm, there is no obvious prevailing particle source, as none of them (excluding the unclassified category) contribute more than 16% of the ambient particles, indicating that submicron ambient Riverside particles originate from a mixture of sources. On the other hand, the supermicron size ranges for both summer and fall are clearly dominated by the mechanically-generated sources of sea salt (26.3% and 19.8%) and dust (13.0% and 33.0%). As described in Chapter 1, it is expected that the mechanically-generated sources, such as sea salt and dust, dominate the supermicron size range, whereas particles from combustion and chemical processes dominate the submicron size range. It is worth noting that the percentage of Riverside particles apportioned to the aged non-source specific particle types (aged EC, aged OC, amine, and $NH_4$ rich: ~27% of the 140-1000 nm size range) is far greater than at sampling sites in Athens, Greece (August 2003) and Mexico City, Mexico (March 2006), due to the aged nature of the particles that have advected across the LA Basin (476). This observation shows how highly aged the ambient environment is in Riverside, compared to these other large urban cities. A more detailed view of how highly aged the Riverside aerosol is will be examined in the next section.

As mentioned earlier, Riverside is typically downwind of the LA Basin due to an onshore flow. However, seasonal differences are expected based on two distinct meteorological conditions involving a high pressure system over the desert areas that occur primarily in the fall and winter months: a weak system counterbalances the onshore flow, creating stagnant conditions; and under a strong system, there are warm and dry easterly (offshore) winds, known as Santa Ana winds (204). Both of these conditions

were observed during the fall SOAR field campaign. In fact, the summer measurements followed a diurnal pattern, whereas the measurements made during the fall season were episodic (31). These seasonal differences are clearly illustrated in **Figure 104** and **Figure 105**, especially with the larger sized particles. During the Santa Ana wind periods at the beginning (October 31 0:00 – November 1 19:00) and end (November 15 5:00 – November 21 10:00) of the fall study, resuspended dust was the dominant supermicron source as the easterly winds crossed the deserts before reaching Riverside. Qin et al. reported stagnant conditions from November 1 19:00 – November 7 18:00 during a buildup and high mass periods, when the hourly $PM_{2.5}$ mass concentrations reached 106 $\mu g\ m^{-3}$ which clearly exceeded the 24-hour national ambient air quality standard of 35 $\mu g\ m^{-3}$ (31). During this time frame, the aged EC particle type made its strongest contribution to both the submicron and supermicron size ranges. Additionally, there was an extremely strong spike in $NH_4$ rich particles; the nearby Chino dairy area is the largest single source of ammonia emissions in the LA area (150). The particles during this spike have intense ammonium and nitrate cluster peaks. The smallest size ranges shown in **Figure 105** show little episodic variation. These fresh emissions are mainly dependent on very local sources, and, as described in Chapter 3, their *number* concentrations do vary but this trend is not reflected in the relative percentage plots.

***b. Aging effects***

Particles in the unclassified category were examined closely to determine why these particles were not apportioned to either a primary source or a non-source specific class using the original source signature library. There are a few reasons why a particle may have not been classified: crosstalk issues (as discussed above), miscalibrations in the spectra, or no appropriate seed exists in the source library. Miscalibrations occur when the peak area is listed under the incorrect *m/z*; often the mass spectral information is shifted by a single unit as in the common example of observing the $^{62}NO_3^-$ peak at *m/z* -61. Even though the peaks may be shifted by only one unit, the dot product of a miscalibrated spectrum with a source seed will yield a very different (lower) value than that of a properly calibrated spectrum. How often miscalibrations affect the spectral information varies from dataset to dataset. The lack of the proper seeds in the source library could be due either by missing sources that have yet to be characterized and added to the library or by heavy aging of the particles. The source library does contain some pseudo-aged signatures of the primary sources (41,344). These aged signatures did a fair job of matching the aged particles from primary sources, because the majority of the properly calibrated unclassified particles are heavily aged and would best fit in the aged non-source specific categories (mainly aged OC and amine). Because the purpose of this study is to understand how aging impacts the source apportionment results, aged particles that ended up in the unclassified category are the primary focus.

One approach to decreasing the percentage of aged particles that are placed into the unclassified category is to the lower the matching factor used with the source library. To examine how lowering the matching factor impacts the apportionment results, **Figure 108** provides the average source contribution pie charts when the ambient particles are matched with a VF of 0.85 or a VF of 0.75. Lowering the matching factor does reduce the percentage of unclassified particles, but previous error analysis has shown that the percent of error in properly apportioning 100 nm+ particles increases nearly fourfold

when using a VF of 0.75 instead of 0.85 (41,344). The percent error continues to increase with lower and lower VF values. An example of how the lower matching factor increases the error in apportionment is illustrated in **Figure 109**. This figure shows the average mass spectral information of summer particles in the 140 to 400 nm size range that were apportioned to the LDV category. The top plot (red) shows an average mass spectrum for all particles in that size range that were apportioned to LDV at a matching factor of 0.85. The middle plot (blue) shows an average mass spectrum for all of the additional particles that matched to LDV when the matching factor was lowered to 0.80 from 0.85. Likewise, the bottom plot (green) shows an average mass spectrum for all of the additional particles that matched to LDV when the matching factor was lowered to 0.75 from 0.80. **Figure 109** illustrates that the particles that were added to the LDV category when using a lower matching factor than 0.85 have mass spectral signatures that are more indicative of an aged OC particle type than that of LDV exhaust emissions. It is

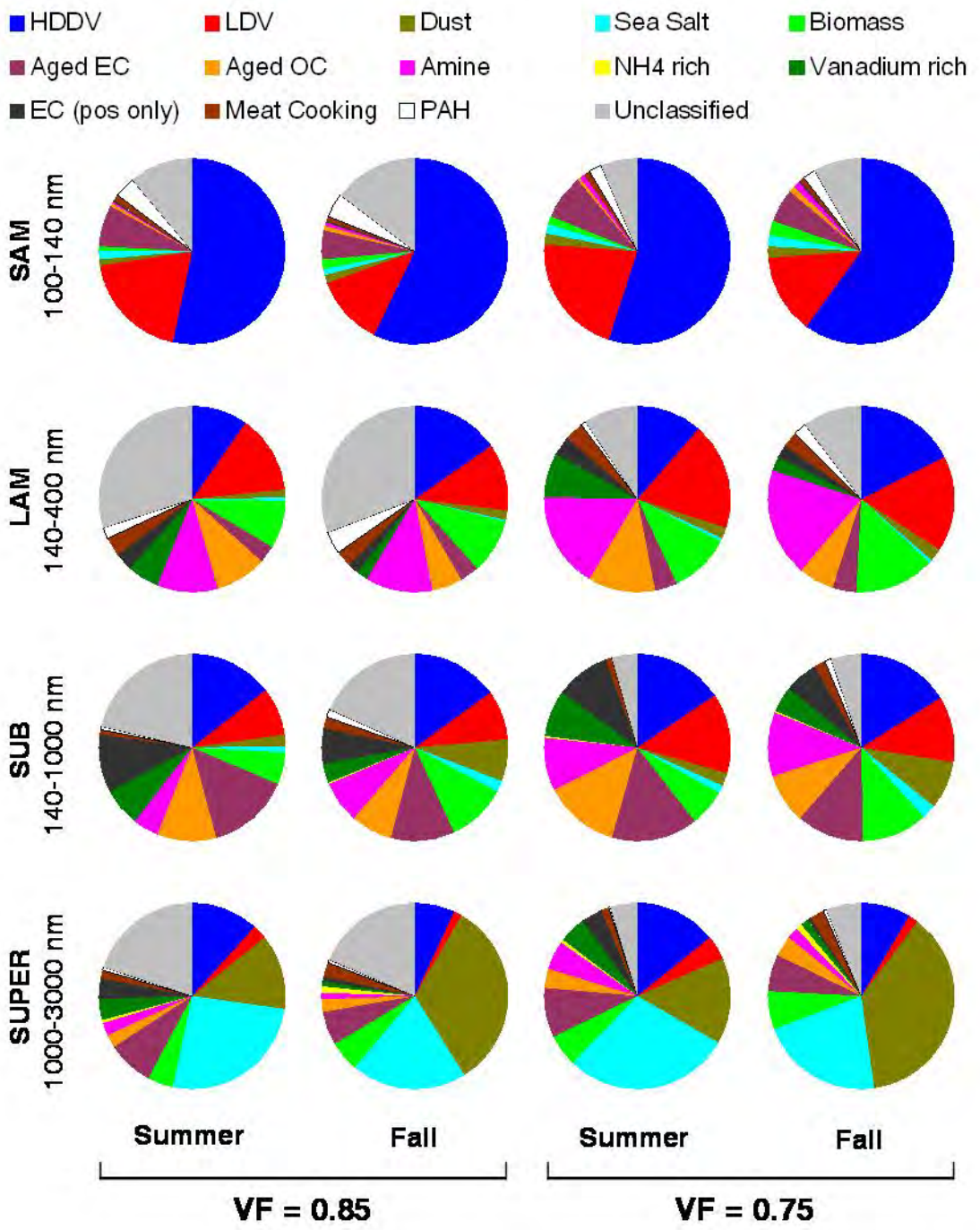


Figure 108: Average source contribution particles matched to the source library at different VF per size bin.

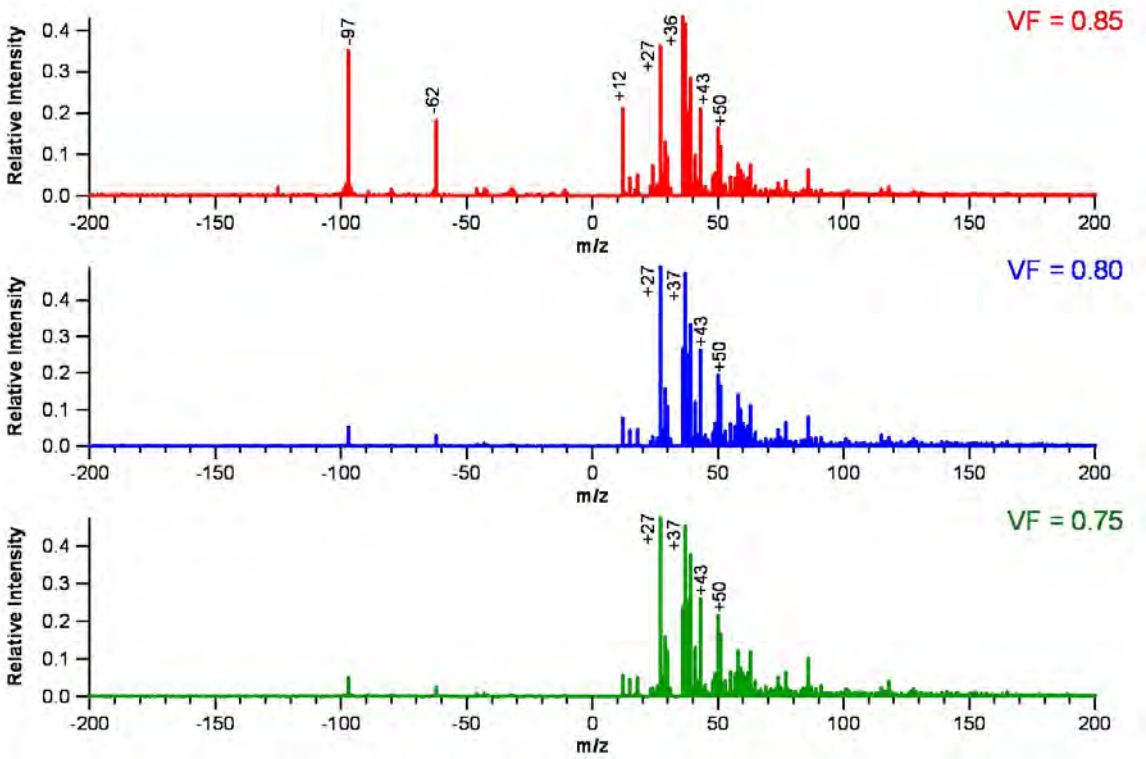


Figure 109: Average mass spectra obtained by lowering the matching factor for summer SOAR LAM (140-400 nm) particles apportioned to LDV.

possible that some of these additional particles are indeed aged LDV particles, but until controlled laboratory experiments can verify that this is the signature of aged LDV particles, they are being falsely labeled as LDV and should be in the aged OC category. Additional figures like **Figure 109** for LDV and HDDV particles in the other size ranges are provided in the Appendix.

The better method to reduce the unclassified category is to add appropriate seeds to the library and to use a matching factor of 0.85. By adding more aged seeds to the source library, the apportionment results of ambient particles in aged environments will have smaller fractions of unclassified particles and better estimations of the aged categories. The new aged seeds were created from the ART-2a results (VF = 0.85) of the unclassified category. ART-2a was run separately on the SAM, LAM, SUB, and SUPER unclassified particles for both summer and fall datasets. The top 30 clusters resulting from each of these ART-2a runs were manually examined to find all aged particle types that were not miscalibrated. A total of 47 properly calibrated aged seeds (22 for aged OC, 16 for amine, 7 for aged EC, and 2 for $NH_4$ rich) were found and all were added to both the 100-140 nm and 140+ nm size ranges of the source library. These seeds were not added to the ultrafine size range of the library, because particles of this small size are still relatively fresh and show little sign of aging. In fact, when the aged seeds were added to the ultrafine source library for testing purposes, it was determined that these additional seeds impacted the apportionment of less than 0.2% of all the ultrafine particles, thus justifying that the aged seeds need not to be added to the ultrafine size

range of the library. All particles (except for ultrafine particles) were matched to the updated source library, and the temporal results are shown in **Figure 110** and **Figure 111**.

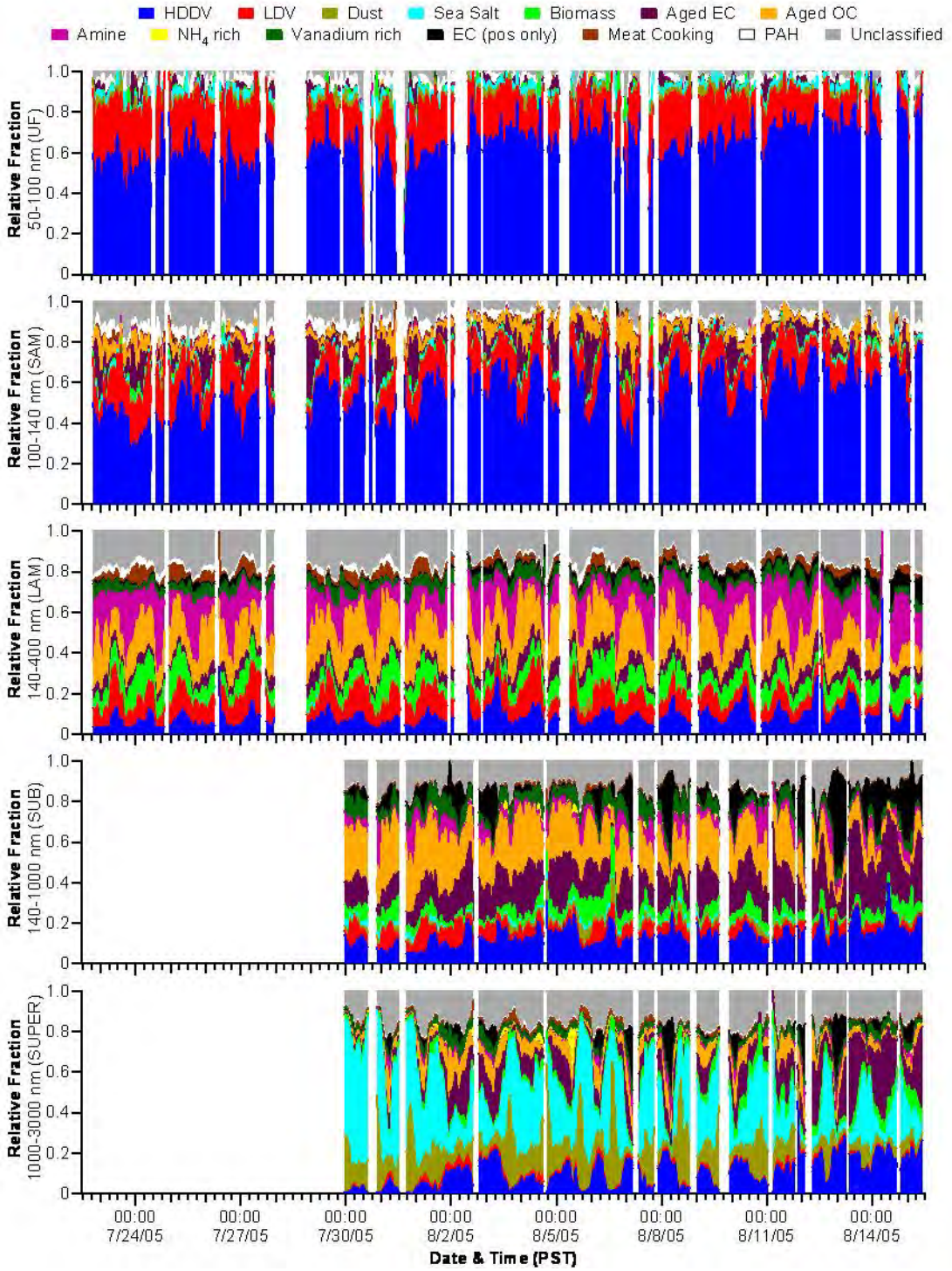


Figure 110: Hourly temporal series of the size segregated source apportionment fractions (VF = 0.85) for the summer SOAR ultrafine (UF), small accumulative mode (SAM), large accumulation mode (LAM), submicron (SUB), and supermicron (SUPER) particles using the updated source signature library.

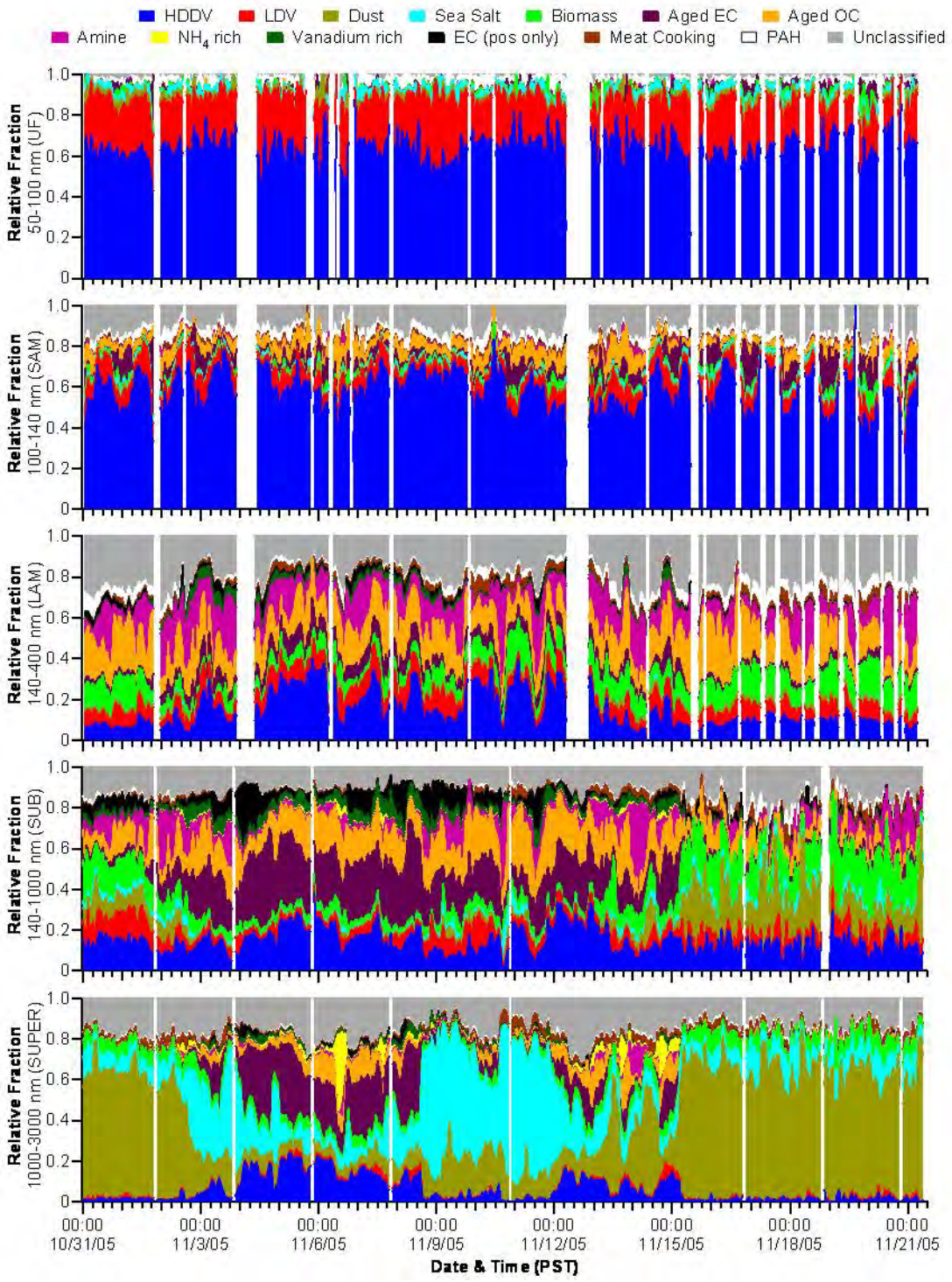


Figure 111: Hourly temporal series of the size segregated source apportionment fractions (VF = 0.85) for the fall SOAR ultrafine (UF), small accumulative mode (SAM), large accumulation mode (LAM), submicron (SUB), and supermicron (SUPER) particles using the updated source signature library.

| | SAM (100-140 nm) | | LAM (140-400 nm) | | SUB (140-1000 nm) | | SUPER (1000-3000 nm) | |
|---|---|---|---|---|---|---|---|---|
| | Summer | Fall | Summer | Fall | Summer | Fall | Summer | Fall |
| HDDV | -0.2 | -0.2 | -1.4 | -1.0 | -1.4 | -1.2 | -1.8 | -1.4 |
| LDV | -4.3 | -5.2 | -4.4 | -4.9 | -3.2 | -2.9 | -0.9 | -0.3 |
| Dust | | | -0.1 | | | | | |
| Sea Salt | | | | | -0.1 | | | |
| Biomass | | | -0.2 | -0.1 | | -0.1 | | |
| Aged EC | +0.6 | +0.7 | +2.6 | +1.6 | +3.5 | +3.4 | +3.3 | +2.3 |
| Aged OC | +5.5 | +5.7 | +9.6 | +10.8 | +8.4 | +6.0 | +4.0 | +1.3 |
| Amine | +0.2 | +0.2 | +7.9 | +3.1 | +1.8 | +0.6 | -0.6 | -0.2 |
| $NH_4$ rich | | | | | +0.1 | +0.2 | +0.2 | +0.4 |
| Vanadium rich | | | -0.1 | | -0.1 | | | -0.1 |
| EC (pos only) | -0.2 | -0.1 | -0.3 | -0.2 | -0.7 | -0.7 | -0.3 | -0.1 |
| Meat Cooking | | | | | | | | |
| PAH | -0.1 | -0.1 | -0.1 | -0.1 | -0.1 | | | |
| Unclassified | -1.5 | -1.2 | -13.7 | -9.4 | -6.2 | -5.2 | -3.9 | -1.9 |

Table 18: Percent difference between particles matched to the original source library and particles matches to the updated source library.

**Table 18** provides the percent differences of matched particles to each category between using the old and the updated source libraries. Negative values indicate how much the percent of particles matched to that category dropped with using the updated library, whereas positive values indicate how much the percent of particles matched increased. The figures and table illustrate that not only were the percentage of particles matched to the aged categories increased and the percentage of unclassified particles decreased, but they also show that the percentage of particles apportioned to other categories (mainly LDV and HDDV) was also impacted by the addition of the aged seeds to the library. This result was expected, because the LDV seeds are largely OC and the HDDV seeds are largely EC. Some of aged ambient particle (aged OC and aged EC) could have matched these "fresh" OC and EC signatures, because they did not have a better alternative. However, with the addition of the new aged seeds, they matched the new signatures better (with a higher dot product value) and were properly placed into the aged categories. For example, it would be expected that the fraction of fresh OC (LDV) particles in the accumulation mode would be less at this location than another sampling site located closer to the major freeway; in fact, the average LAM LDV percentage at a roadside study during the summer (18.4%) is double the equivalent percentage (9.2%) in Riverside during the summer (41,344). The shift of LDV particles to the aged OC category was most highly anticipated for particles in the supermicron size mode, because on-road and laboratory (dynamometer) studies of LDV exhaust indicate that the number of particles emitted by gasoline or spark ignition engine fall off significantly well before 1000 nm (478,479). Therefore, it was expected that the LDV contribution to supermicron particles would be very small, which is the case (~1%). Kittelson and coworkers show that the number of particles emitted by diesel engines does not drop off as rapidly as those from gasoline engines [*Kittelson et al.*, 2006], which explains why the HDDV contribution to supermicron particles is much larger than the LDV contribution.

The improved source library successfully reduced the large spikes of unclassified particles during the afternoon/evening periods that were especially predominant in **Figure 104** (summer season). **Figure 110** shows that the contribution of aged types

(mainly aged OC and amine) are strongest during this time of day, as expected in the summer. Now the source apportionment results more closely match the hand-classified ART-2a results presented in Qin et al. (31). For example, Qin and coworkers determined that the average contribution of the aged OC and amine classes in the submicron size range during the summer was 40-45% by manually classifying the top 50 populated clusters from running ART-2a analysis at a VF of 0.80, and the combined contribution as determined by the updated source library for submicron particles during the summer was ~37%. Similarly, the average contribution of the aged OC and amine classes in the submicron size range during the fall was ~25% by manual classification and ~21% by the source library. The ART-2a method is slightly higher, because some of the fresh OC particles were placed into the aged OC clusters at the lower VF value and also the miscalibrated spectra were added to the appropriate category. The source signature library contains no miscalibrated seeds, so these ambient particles are currently placed in (and make up the majority of) the unclassified category. Improvements are presently being made on the peak writing program to reduce the number of particles with miscalibrated spectra. The remaining properly calibrated particles in the unclassified category (~35%) from using the updated source library are unique types for which there is no appropriate seed, such as the unique OC type with Ba that was described in Chapter 9. As more sources are characterized in future studies, new seeds (and source categories) can be added to the library, which will further reduced the unclassified category.

This episodic behavior of the fall season can be further examined by comparing the source contributions based on the different air masses. Using HYSPLIT (HYbrid Single-Particle Lagrangian Integrated Trajectory) model analysis, it is possible to determine the back trajectories of air masses arriving at the sampling site at specified heights (305). The 48 hour back trajectories at a starting height of 100 m (also verified at 500 m) were calculated for each hour of the study so that the air masses could be separated into 6 regions of origin. Representative back trajectories for each region are shown in **Figure 112**. Most air masses during the summer had LA and marine influences, though some traveled north along the Baja, San Diego (SD), and LA coastline or through Baja (inland) and over the Salton Sea (SS). On the other hand, the air masses sampled during the fall derived from all directions around Riverside, including from the San Joaquin Valley (SJV) in central California. Starting in Canada, the long trajectory representing the Santa Ana air masses illustrates how quickly these air masses transported to Riverside. The short trajectory representing the Northeastern (NE) Desert air masses indicates how stagnant they were. Under these stagnant conditions, higher concentrations of $NH_4$ rich particles are expected, as shown in **Figure 113**. This figure provides the relative source fraction based on HYSPLIT region and size range. Also as expected, the dust and sea salt apportionments are at their highest and lowest under the

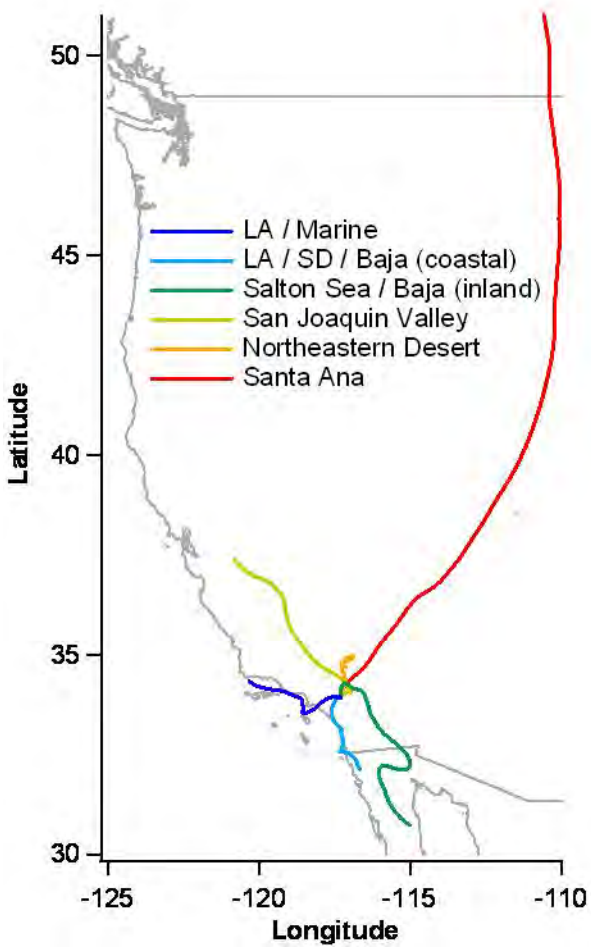


Figure 112: Representative 48 hour HYSPLIT back trajectories at a height of 100 m for six defined regions. (LA = Los Angeles, SD = San Diego)

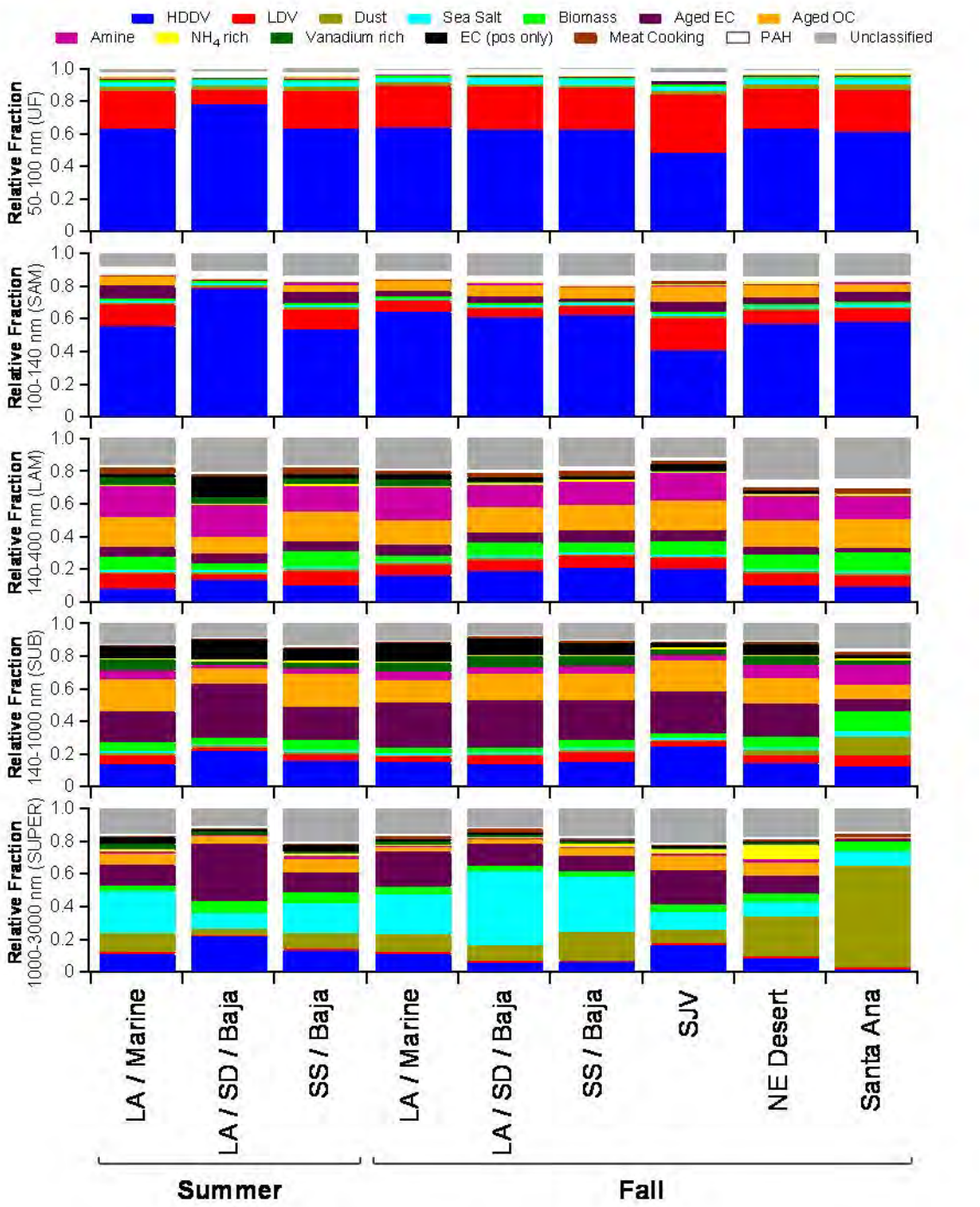


Figure 113: Relative class abundance based on air mass origin and size range. (LA = Los Angeles, SD = San Diego, SS = Salton Sea, SJV = San Joaquin Valley, NE = Northeastern)

### *c. Secondary species as aging markers*

Since many of the Riverside aerosol particles are aged due to being freshly emitted in a highly aging environment, it is interesting to examine the extent of aging for particles apportioned to a source. There are a number of markers that can indicate the presence of specific secondary species. For example, the peak at *m/z* $^{18}NH_4^+$ indicates the presence of

ammonium, the peak at *m/z* $^{43}C_2H_3O^+$ indicates oxidized organic compounds, and the peak at *m/z* +86 commonly indicates the presence of amines in ATOFMS data. For the negative ion peaks, nitrate species are denoted by peaks at *m/z* $^{46}NO_2^-$, $^{62}NO_3^-$, or $^{125}H(NO_3)_2^-$ and sulfate by $^{97}HSO_4^-$. By comparing how the average amount of these secondary species adjusts with increasing size for each source, it should be possible to infer how the chemistry of particles of a particular source influences the aging processes. Based on the source characterization studies, it is already known that the original particle chemistry from HDDV (more EC) and LDV (more OC) is different, so the particles from these two types of vehicle exhaust can be expected to age differently (36-38,471). **Figure 114** shows the average area of these secondary markers (for both the UF-ATOFMS and ATOFMS data combined) on particles matched to the top primary sources (HDDV, LDV, dust, sea salt, and biomass) using the updated aged library. Particles detected by UF-ATOFMS cover the 50 to 400 nm range in 50 nm bins, and particles detected by the

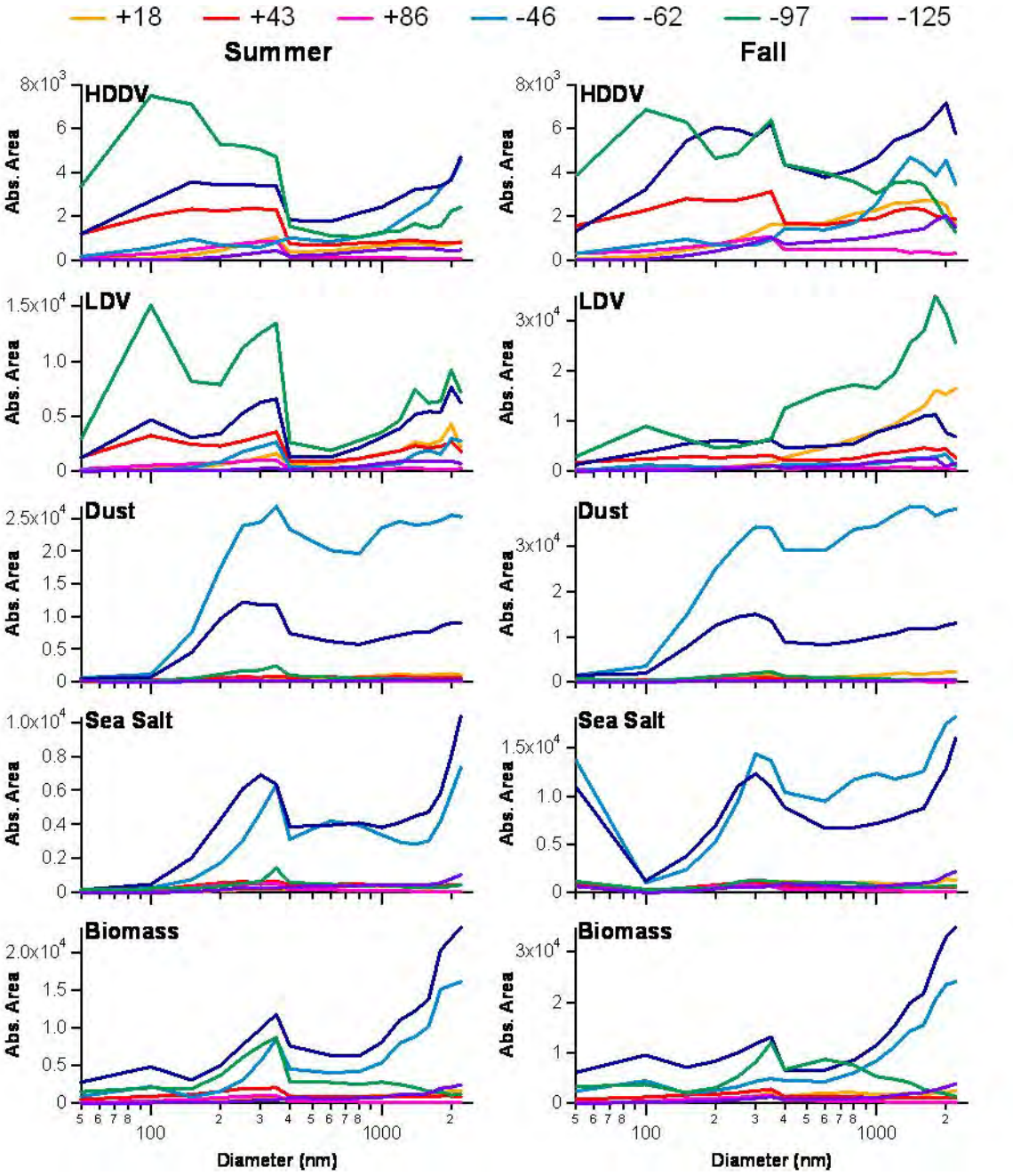


Figure 114: Size-resolved average area of secondary markers for particles matched to specific sources during the summer (left column) and fall (right column).

standard inlet ATOFMS cover the 400 to 2400 nm range in 200 nm bins. Some of the plots display a jump around 400 nm due to the transition between instruments measuring different size range. Each source has its own plot for both summer (left column) and fall (right column) measurements.

The average areas for several of the secondary species remain rather constant across all size bins above 100 nm. They include the relative areas for +43, +86, -125 and

sometimes +18. Therefore, there must be little addition of oxidized organics and amines as the particles emitted by these sources grow compared to nitrate and sulfate. Recall that particles whose spectra had significant amounts of +86 (heavily aged) were separately apportioned to the amine class. On the other hand, the average area markers for the secondary species of nitrate (-46 and -62) and sulfate (-97) do show changes with particle size and account for significant amounts of negative ion intensities. The general trend for all sources is an increase in the area of nitrate with increasing diameter. For most of the sources, the nitrate marker at *m/z* -62 is the dominant secondary species. This finding is not surprising, because in a previous study in nearby Mira Loma, it was determined that nitrate contributed to 26% of the total $PM_{2.5}$ mass (480). Large quantities of the reactive gas $NO_2$ are transported across the LA Basin. The plots in **Figure 114** suggest that there are different seasonal sources or mechanisms of nitrate on Riverside particles. During the fall season, the area of ammonium increases with the increasing diameter of HDDV and LDV particles, whereas the ammonium area stayed relatively flat for the same particles during the summer. This observation implies that while ammonium nitrate is important during the fall season, there is a different photochemical source of nitrate during the summer or that $HNO_3$ partitions with some other species during the summer, besides ammonium and amines (also flat). It is also interesting to note that -46 is the dominant nitrate peak on dust. In the ATOFMS reference mass spectra of unprocessed mineral dusts (obtained by analyzing Asian dust samples collected from various source regions), the peak at *m/z* -46 $[NO_2]^-$ is the only nitrate ion detected and there is no significant peak at *m/z* -62 (134). As with dust, nitrate represents the main secondary species on sea salt particles. Neither dust nor sea salt indicate a significant presence of sulfate. In previous ATOFMS studies of sea salt particles, sulfate has been observed at *m/z* 165 $[Na_3SO_4]^+$; however, this peak is not significant for other particle types and, thus, was not chosen as a marker of focus. The lack of sulfate (at *m/z* -97) on the dust particles contrasts the observation of large sulfate ion signals on ambient aged dust particles analyzed aboard a ship in the Pacific Ocean during the ACE-Asia campaign (134). One of the key findings of that study was that dust particles could contain large amounts of either nitrate or sulfate but rarely would they contain both ions (134,481). On the other hand, sulfate is shown on particles of HDDV and LDV emissions during the SOAR campaign, but not for dust and sea salt particles. Understanding which particle types are internally mixed with sulfate is important, because sulfate associated particles have been shown to have the potential to modify the radiation budget of the atmosphere (482). Relatively fresh emissions of HDDV, LDV, and biomass burning already show the presence of sulfate ions (36-38,471), so *m/z* -97 can also represent primary sulfate. However, sulfate on dust could be secondary in nature. In Riverside, there is no sulfate present on dust, because the LA Basin has less $SO_2$ than locations in and nearby Asia (due to coal-fired power plants). A modeling study determined that the available surface area is a critical factor in the preferential deposition of secondary sulfate by $SO_2/H_2SO_4$ (12). In locations such as Riverside, the particle types with the most available surface area dominate the submicron size mode, and so if there were any significant secondary sulfate, it would prefer the carbonaceous types (HDDV, LDV, and biomass). In fact, this preference may explain the seasonal differences with the sulfate marker for LDV particles. The peak in average area for sulfate occurs in smaller sized LDV particles during the summer than in the fall.

In summary, a source signature library was used to determine the relative contributions of primary sources and non-source specific types to ambient particles collected in Riverside during the summer and fall of 2005. It was determined that local vehicle exhaust emissions (specifically HDDV) account for the majority of the small (50-140 nm) particles detected. Varying meteorological conditions caused seasonal differences in the apportionment of the larger (140+ nm) particles during the summer (diurnal trends) and fall (episodic behavior). These results were supported by the air mass back trajectories calculated with HYSPLIT. The main impacts of aging effects on the original source apportionment results were an increase in the unclassified fraction and thereby an underestimation of the contributions by aged non-source specific types. Therefore, it was determined that the aging of a particle can alter its chemical signature enough so that the particle is unassigned. Adding aged seeds obtained from this dataset to the source signature library did reduce the impact of aging effects and improved the ability of the source signature library to perform successfully for future source apportionment studies in highly aged environments. Depending upon the size range, these additional seeds reduced the percentage of unclassified particles by ~1 to 14% and increased the percentage of particles categorized to aged categories by ~4 to 20%. Finally, a close examination of markers of secondary species revealed that nitrate, despite having different seasonal sources, is the dominant secondary species for aged particles from all of the primary sources in Riverside.

**iv. Acknowledgements**

The authors express their gratitude to the entire Prather group for their help in the preparation and overall support of these studies. We thank Megan McKay and the Goldstein research group at the University of California, Berkeley for the meteorology data. We also acknowledge Professor Paul Ziemann (University of California, Riverside) for hosting the SOAR field campaigns, as well as Professor Jose Jimenez (Colorado University, Boulder) and Dr. Ken Docherty (Colorado University, Boulder) for setting up the logistics. We express gratitude to the NOAA Air Resources Laboratory (ARL) for the provision of the HYSPLIT transport and dispersion model. Funding for this project was supplied by the California Air Resources Board (Contract 04-336).

# III. Summary and Conclusions

Through a combination of ground based measurements in different locations during different seasons new details regarding single particle mixing state were discovered. A key element leading to these findings was the development of the mobile laboratory that was used 6 of the 8 principle studies conducted during the course of this grant. The mobile laboratory allowed for rapid and flexible deployment while lowering the barriers to sampling in locations with varying availability of power.

The list of objectives accomplished during this study included: investigations into time and size resolved chemical composition detailing short term changes in composition, monitoring spatial variability of particulate matter and sources, seasonal and interannual variability in particulate matter size and composition, mass comparisons and investigations into the volatile and semivolatile fraction of particles, analyzing changes in particle composition linked with meteorology and air mass back trajectories, and development of source apportionment algorithms. With respect to short term changes in composition two chapters (Chapters 1 and 2) demonstrate the ability of the ATOFMS to measure ultrafine particles and ship plumes on the time scale of a few minutes. This increase in time resolution allowed us to detect and characterize processes that would not have been possible previously. In the future higher time resolution will allow for greater investigations into the transformative processes that convert fresh aerosols to aged background particles.

Investigations into spatial variability were made possible by the ability to move site to site multiple times within a day, as made possible by the mobile laboratory. Chapter 3 describes mobile laboratory results showing the difference between a clean background day and a moderately polluted day. In the two cases for San Diego both spatial and temporal (diurnal) patters were observed, with temporal patterns playing a larger role in the accumulation mode with spatial and temporal being roughly equal within the ultrafine mode. Future investigations focusing on ultrafine particles will link well with the high time resolution capabilities described above to monitor source to background transitions.

One of the primary objectives of this report was to investigate seasonal and interannual differences in aerosol size and chemical composition within California. Chapter 4 focused on SOAR I and II in 2005 provides a detailed analysis of the change from diurnal patterns in the summer to buildup periods in the fall over several days. A more detailed analysis comparing seasonal differences in the chemistry of alkylamines is described in Chapter 5. By analyzing particle volatility ATOFMS was able to show that acidic particle cores in summer led to the formation of aminium nitrate and sulfate salts, while less acidic cores during the fall led to more volatile amine species. Linking the chemistry to volatility demonstrates the utility of exploring further systems using the thermodenuder-ATOFMS system discussed. Chapter 6 details the changes in particle size and chemistry interannually and finds that the summers of 2005, 2006, and 2007 had considerable differences between them. The chapter then discusses how best to characterize the chemistry observed and simplify it for incorporation into future modeling efforts.

A key advance with respect to quantifying ATOFMS measurements has been the ability to convert to mass concentrations from the raw counts measured by the ATOFMS.

A method to quantitatively scale the data using an aerodynamic particle sizer (APS) is described in Chapter 7 and compared with standard mass measurements including the micro-orifice uniform deposit impactor (MOUDI) and beta attenuation monitor (BAM). Variation within the calculations used for this conversion are discussed in detail in Chapter 8 and when taken together demonstrate the ability to present ATOFMS data on both a number and mass basis. This method is used in both Chapter 3 and Chapter 10 to present meaningful comparisons to standard mass measurements in the field and in trailer and will be used frequently in future analysis.

The intercomparison of ATOFMS data with meteorology and air mass back trajectories for the purpose of understanding sources and secondary contributors to particulate matter (PM) concentrations was a key focus of this report. The impact of trace metals in the particle phase on human health has received considerable attention in recent years and in Chapter 9 meteorology and air mass history are used to predict source regions for a plethora of metals in the urban atmosphere of Riverside, CA. Transported aerosols (including those containing metals such as vanadium) have also been studied in detail. The impact of transported emissions from the Los Angeles Port region on San Diego are discussed in detail in Chapter 10, where it is shown that port sources can make a significant contribution to local PM in San Diego. The impact of transported emissions during unique episodes such as the 2007 San Diego wildfires were also studied as a part of this report and Chapter 11 describes both the types of particles observed as well as their ability to act as cloud condensation nuclei (CCN), which has important implications for clouds and precipitation.

Significant advances have been made in our ability to apportion the sources of different particles in the atmosphere. Chapter 12 ties our initial dynamometer studies that were conducted as part of a previous CARB grant with field measurements to determine the fraction of cars and trucks in an urban environment. The methods that originated with car/truck differentiation are then expanded to incorporate major sources of $PM_{2.5}$ in Chapter 13. These two chapters provide detailed information both on the location studied, but also led to development that will allow for future analysis of sources from a more mathematical perspective. Lastly, the issue of aging and its impact on source apportionment are discussed in Chapter 14. The ability to determine the sources of aged particles in critical in a polluted urban environment and considerable advances in our ability to apportion this quantitatively are shown.

Together the research described in this report depicts a number of advances in field capabilities, analysis capabilities, as well as the answers to many of the complex scientific questions posed in the initial proposal. In the future single particle analysis has considerable potential to provide information on mixing state with impacts ranging from source apportionment to climate and precipitation patterns.

# IV. References


(1) Gard, E.; Mayer, J. E.; Morrical, B. D.; Dienes, T.; Fergenson, D. P.; Prather, K. A., Real-time analysis of individual atmospheric aerosol particles - design and performance of a portable ATOFMS. *Analytical Chemistry* **1997**, *69*, (20) 4083-4091.

(2) Su, Y. X.; Sipin, M. F.; Furutani, H.; Prather, K. A., Development and characterization of an aerosol time-of-flight mass spectrometer with increased detection efficiency. *Anal. Chem.* **2004**, *76*, (3) 712-719.

(3) Liu, P.; Ziemann, P. J.; Kittelson, D. B.; Mcmurry, P. H., Generating Particle Beams of Controlled Dimensions and Divergence.1. Theory of Particle Motion in Aerodynamic Lenses and Nozzle Expansions. *Aerosol Science and Technology* **1995**, *22*, (3) 293-313.

(4) Liu, P.; Ziemann, P. J.; Kittelson, D. B.; Mcmurry, P. H., Generating Particle Beams of Controlled Dimensions and Divergence.2. Experimental Evaluation of Particle Motion in Aerodynamic Lenses and Nozzle Expansions. *Aerosol Science and Technology* **1995**, *22*, (3) 314-324.

(5) Hinz, K. P.; Greweling, M.; Drews, F.; Spengler, B., Data processing in on-line laser mass spectrometry of inorganic, organic, or biological airborne particles. *Journal of the American Society for Mass Spectrometry* **1999**, *10*, (7) 648-660.

(6) Phares, D. J.; Rhoads, K. P.; Wexler, A. S.; Kane, D. B.; Johnston, M. V., Application of the ART-2a algorithm to laser ablation aerosol mass spectrometry of particle standards. *Analytical Chemistry* **2001**, *73*, (10) 2338-2344.

(7) Murphy, D. M.; Middlebrook, A. M.; Warshawsky, M., Cluster analysis of data from the Particle Analysis by Laser Mass Spectrometry (PALMS) instrument. *Aerosol Science and Technology* **2003**, *37*, (4) 382-391.

(8) Rebotier, T. P.; Prather, K. A., Aerosol time-of-flight mass spectrometry data analysis: A benchmark of clustering algorithms. *Analytica Chimica Acta* **2007**, *585*, (1) 38-54.

(9) Hinz, K. P.; Spengler, B., Instrumentation, data evaluation and quantification in on-line aerosol mass spectrometry. *Journal of Mass Spectrometry* **2007**, *42*, (7) 843-860.

(10) Xie, Y.; Hopke, P. K.; Wienke, D., Airborne particle classification with a combination of chemical composition and shape index utilizing an adaptive resonance artificial neural network. *Environmental Science & Technology* **1994**, *28*, (11) 1921-1928.

(11) Hopke, P. K.; Song, X. H., Classification of single particles by neural networks based on the computer-controlled scanning electron microscopy data. *Analytica Chimica Acta* **1997**, *348*, (1-3) 375-388.

(12) Song, C. H.; Carmichael, G. R., The aging process of naturally emitted aerosol (sea-salt and mineral aerosol) during long range transport. *Atmospheric Environment* **1999**, *33*, (14) 2203-2218.

(13) Toner, S. M.; Shields, L. G.; Sodeman, D. A.; Prather, K. A., Using mass spectral source signatures to apportion exhaust particles from gasoline and diesel

powered vehicles in a freeway study using UF-ATOFMS, in press. *Atmospheric Environment* **2007**.

(14) Kulmala, M.; Vehkamaki, H.; Petajda, T.; Dal Maso, M.; Lauri, A.; Kerminen, V. M.; Birmili, W.; McMurry, P. H., Formation and growth rates of ultrafine atmospheric particles: a review of observations. *Journal of Aerosol Science* **2004**, *35*, (2) 143-176.

(15) Cohen, B. S. In *Aerosols Handbook: Measurement, Dosimetry, and Health Effects*; Ruzer, L. S., Harley, N. H., Eds.; CRC Press: Boca Raton, 2005.

(16) Harrison, R. M.; Shi, J. P.; Xi, S.-h.; Khan, A.; Mark, D.; Kinnersky, R.; Yin, J. In *Ultrafine Particles in the Atmosphere*; Brown, L. M., Collings, N., Harrison, R. M., Maynard, A. D., Maynard, R. L., Eds.; Imperial College Press: London, 2003; pp 1-18.

(17) Zhang, K. M.; Wexler, A. S., A hypothesis for growth of fresh atmospheric nuclei. *Journal of Geophysical Research-Atmospheres* **2002**, *107*, (D21) -.

(18) Zhang, R. Y.; Suh, I.; Zhao, J.; Zhang, D.; Fortner, E. C.; Tie, X. X.; Molina, L. T.; Molina, M. J., Atmospheric new particle formation enhanced by organic acids. *Science* **2004**, *304*, (5676) 1487-1490.

(19) Woo, K. S.; Chen, D. R.; Pui, D. Y. H.; McMurry, P. H., Measurement of Atlanta aerosol size distributions: Observations of ultrafine particle events. *Aerosol Science and Technology* **2001**, *34*, (1) 75-87.

(20) Rodriguez, S.; Van Dingenen, R.; Putaud, J. P.; Dell'Acqua, A.; Pey, J.; Querol, X.; Alastuey, A.; Chenery, S.; Ho, K. F.; Harrison, R.; Tardivo, R.; Scarnato, B.; Gemelli, V., A study on the relationship between mass concentrations, chemistry and number size distribution of urban fine aerosols in Milan, Barcelona and London. *Atmospheric Chemistry and Physics* **2007**, *7*, (9) 2217-2232.

(21) Watson, J. G.; Chow, J. C.; Park, K.; Lowenthal, D. H.; Park, K., Nanoparticle and ultrafine particle events at the Fresno Supersite. *Journal of the Air & Waste Management Association* **2006**, *56*, (4) 417-430.

(22) Chow, J. C.; Watson, J. G., Review of measurement methods and compositions for ultrafine particles. *Aerosol and Air Quality Research* **2007**, *7*, (2) 121-173.

(23) Sardar, S. B.; Fine, P. M.; Mayo, P. R.; Sioutas, C., Size-fractionated measurements of ambient ultrafine particle chemical composition in Los Angeles using the NanoMOUDI. *Environmental Science & Technology* **2005**, *39*, (4) 932-944.

(24) Stanier, C. O.; Khlystov, A. Y.; Pandis, S. N., Nucleation events during the Pittsburgh air quality study: Description and relation to key meteorological, gas phase, and aerosol parameters. *Aerosol Science and Technology* **2004**, *38(S1)*, 253-264.

(25) Mark, D. In *Atmospheric Aerosols*; Harrison, R. M., van Grieken, R. E., Eds.; John Wiley & Sons: Chichester, 1998; pp 29-94.

(26) Hinds, W. C. *Aerosol Technology: Properties, Behavior, and Measurement of Airborne Particles*; John Wiley & Sons: New York, **1999**.

(27) Sem, G. J., Design and performance characteristics of three continuous-flow condensation particle counters: a summary. *Atmospheric Research* **2002**, *62*, (3-4) 267-294.

(28) Rhoads, K. P.; Phares, D. J.; Wexler, A. S.; Johnston, M. V., Size-resolved ultrafine particle composition analysis, 1. Atlanta. *Journal of Geophysical Research-Atmospheres* **2003**, *108(D7)*, 8418.

(29) Phares, D. J.; Rhoads, K. P.; Johnston, M. V.; Wexler, A. S., Size-resolved ultrafine particle composition analysis - 2. Houston. *Journal of Geophysical Research-Atmospheres* **2003**, *108(D7)*, 8420.

(30) Lake, D. A.; Tolocka, M. P.; Johnston, M. V.; Wexler, A. S., Mass spectrometry of individual particles between 50 and 750 nm in diameter at the Baltimore supersite. *Environmental Science & Technology* **2003**, *37*, (15) 3268-3274.

(31) Qin, X.; Shields, L. G.; Toner, S. M.; Prather, K. A., Single particle characterization in Riverside, CA during the SOAR 2005 campaign - Part 1: Seasonal comparisons. in preparation.

(32) Kane, D. B.; Johnston, M. V., Size and composition biases on the detection of individual ultrafine particles by aerosol mass spectrometry. *Environmental Science & Technology* **2000**, *34*, (23) 4887-4893.

(33) Flagan, R. C. In *Aerosol Measurement: Principles, Techniques, and Applications*; Baron, P. A., Willeke, K., Eds.; John Wiley & Sons: New York, 2001; pp 537-568.

(34) DeCarlo, P. F.; Slowik, J. G.; Worsnop, D. R.; Davidovits, P.; Jimenez, J. L., Particle morphology and density characterization by combined mobility and aerodynamic diameter measurements. Part 1: Theory. *Aerosol Science and Technology* **2004**, *38*, (12) 1185-1205.

(35) Song, X. H.; Hopke, P. K.; Fergenson, D. P.; Prather, K. A., Classification of single particles analyzed by ATOFMS using an artificial neural network, ART-2A. *Analytical Chemistry* **1999**, *71*, (4) 860-865.

(36) Sodeman, D. A.; Toner, S. M.; Prather, K. A., Determination of single particle mass spectral signatures from light-duty vehicle emissions. *Environ. Sci. Technol.* **2005**, *39*, (12) 4569-4580.

(37) Toner, S. M.; Sodeman, D. A.; Prather, K. A., Single particle characterization of ultrafine and accumulation mode particles from heavy duty diesel vehicles using aerosol time-of-flight mass spectrometry. *Environmental Science & Technology* **2006**, *40*, (12) 3912-3921.

(38) Shields, L. G.; Suess, D. T.; Prather, K. A., Determination of single particle mass spectral signatures from heavy-duty diesel vehicle emissions for PM2.5 source apportionment. *Atmospheric Environment* **2007**, *41*, (18) 3841-3852.

(39) Angelino, S.; Suess, D. T.; Prather, K. A., Formation of aerosol particles from reactions of secondary and tertiary alkylamines: Characterization by aerosol time-of-flight mass spectrometry. *Environ. Sci. Technol.* **2001**, *35*, (15) 3130-3138.

(40) Shields, L. G.; Qin, X.; Toner, S. M.; Prather, K. A., Aging effects on source apportionment from the single particle perspective, manuscript in preparation.

(41) Toner, S. M.; Shields, L. G.; Prather, K. A., Source apportionment of freeway-side PM2.5 using ATOFMS, submitted. *Atmospheric Environment*.

(42) Noble, C. A.; Mukerjee, S.; Gonzales, M.; Rodes, C. E.; Lawless, P. A.; Natarajan, S.; Myers, E. A.; Norris, G. A.; Smith, L.; Ozkaynak, H.; Neas, L. M., Continuous measurement of fine and ultrafine particulate matter, criteria pollutants and

meteorological conditions in urban El Paso, Texas. *Atmospheric Environment* **2003**, *37*, (6) 827-840.

(43) Marconi, A.; Cattani, G.; Cusano, M.; Ferdinandi, M.; Inglessis, M.; Viviano, G.; Settimo, G.; Forastiere, F., Two-years of fine and ultrafine particles measurements in Rome, Italy. *Journal of Toxicology and Environmental Health-Part a-Current Issues* **2007**, *70*, (3-4) 213-221.

(44) Kim, S.; Shen, S.; Sioutas, C.; Zhu, Y. F.; Hinds, W. C., Size distribution and diurnal and seasonal trends of ultrafine particles in source and receptor sites of the Los Angeles basin. *Journal of the Air & Waste Management Association* **2002**, *52*, (3) 297-307.

(45) Fine, P. M.; Chakrabarti, B.; Krudysz, M.; Schauer, J. J.; Sioutas, C., Diurnal variations of individual organic compound constituents of ultrafine and accumulation mode particulate matter in the Los Angeles basin. *Environmental Science & Technology* **2004**, *38*, (5) 1296-1304.

(46) Snyder, D. C.; Schauer, J. J., An inter-comparison of two black carbon aerosol instruments and a semi-continuous elemental carbon instrument in the urban environment. *Aerosol Science and Technology* **2007**, *41*, (5) 463-474.

(47) Cubison, M. J.; Ervens, B.; Feingold, G.; Docherty, K.; Ulbrich, I.; Denkenberger, K.; Shields, L.; Prather, K.; Snyder, D.; Schauer, J. J.; Jimenez, J. L., The influence of chemical composition and mixing state of Los Angeles urban aerosol on CCN number and cloud properties, manuscript in preparation.

(48) Spencer, M. T.; Shields, L. G.; Prather, K. A., Simultaneous measurement of the effective density and chemical composition of ambient aerosol particles. *Environmental Science & Technology* **2007**, *41*, (4) 1303-1309.

(49) Ravishankara, A. R., Heterogeneous and multiphase chemistry in the troposphere. *Science* **1997**, *276*, (5315) 1058-1065.

(50) Blando, J. D.; Turpin, B. J., Secondary organic aerosol formation in cloud and fog droplets: a literature evaluation of plausibility. *Atmospheric Environment* **2000**, *34*, (10) 1623-1632.

(51) Reid, J. P.; Sayer, R. M., Heterogeneous atmospheric aerosol chemistry: laboratory studies of chemistry on water droplets. *Chemical Society Reviews* **2003**, *32*, (2) 70-79.

(52) Su, Y. X.; Sipin, M. F.; Spencer, M. T.; Qin, X. Y.; Moffet, R. C.; Shields, L. G.; Prather, K. A.; Venkatachari, P.; Jeong, C. H.; Kim, E.; Hopke, P. K.; Gelein, R. M.; Utell, M. J.; Oberdorster, G.; Berntsen, J.; Devlin, R. B.; Chen, L. C., Real-time characterization of the composition of individual particles emitted from ultrafine particle concentrators. *Aerosol Science and Technology* **2006**, *40*, (6) 437-455.

(53) Moore, K. F.; Ning, Z.; Ntziachristos, L.; Schauer, J. J.; Sioutas, C., Daily variation in the properties of urban ultrafine aerosol - Part I: Physical characterization and volatility, in press. *Atmospheric Environment* **2007**.

(54) Na, K. S.; Sawant, A. A.; Song, C.; Cocker, D. R., Primary and secondary carbonaceous species in the atmosphere of Western Riverside County, California. *Atmospheric Environment* **2004**, *38*, (9) 1345-1355.

(55) Liu, P. S. K.; Deshler, T., Causes of concentration differences between a scanning mobility particle sizer and a condensation particle counter. *Aerosol Science and Technology* **2003**, *37*, (11) 916-923.

(56) Biswas, S.; Fine, P. M.; Geller, M. D.; Hering, S. V.; Sioutas, C., Performance evaluation of a recently developed water-based condensation particle counter. *Aerosol Science and Technology* **2005**, *39*, (5) 419-427.

(57) Hering, S. V., manuscript in preparation.

(58) Hering, S. V.; Stolzenburg, M. R.; Quant, F. R.; Oberreit, D. R.; Keady, P. B., A laminar-flow, water-based condensation particle counter (WCPC). *Aerosol Science and Technology* **2005**, *39*, (7) 659-672.

(59) De Bock, L. A.; Joos, P. E.; Noone, K. J.; Pockalny, R. A.; Van Grieken, R. E., Single particle analysis of aerosols, observed in the marine boundary layer during the Monterey Area Ship Tracks Experiment (MAST), with respect to cloud droplet formation. *Journal Of Atmospheric Chemistry* **2000**, *37*, (3) 299-329.

(60) Kim, D.; Wang, C.; Ekman, A. M. L.; Barth, M. C.; Rasch, P. J., Distribution and direct radiative forcing of carbonaceous and sulfate aerosols in an interactive size-resolving aerosol-climate model. *J. Geophys. Res.-Atmos.* **2008**, *113*, (D16).

(61) Agrawal, H.; Malloy, Q. G. J.; Welch, W. A.; Wayne Miller, J.; Cocker Iii, D. R., In-use gaseous and particulate matter emissions from a modern ocean going container vessel. *Atmos. Environ.* **2008**, *42*, (21) 5504.

(62) Isakson, J.; Persson, T. A.; Lindgren, E. S., Identification and assessment of ship emissions and their effects in the harbour of Goeteborg, Sweden. *Atmos. Environ.* **2001**, *35*, (21) 3659-3666.

(63) Eyring, V.; Kohler, H. W.; Lauer, A.; Lemper, B., Emissions from international shipping: 2. Impact of future technologies on scenarios until 2050. *J. Geophys. Res.-Atmos.* **2005**, *110*, (D17).

(64) Corbett, J. J.; Winebrake, J. J.; Green, E. H.; Kasibhatla, P.; Eyring, V.; Lauer, A., Mortality from ship emissions: A global assessment. *Environ. Sci. Technol.* **2007**, *41*, (24) 8512-8518.

(65) Campen, M. J.; Nolan, J. P.; Schladweiler, M. C. J.; Kodavanti, U. P.; Evansky, P. A.; Costa, D. L.; Watkinson, W. P., Cardiovascular and thermoregulatory effects of inhaled PM-associated transition metals: A potential interaction between nickel and vanadium sulfate. *Toxicological Sciences* **2001**, *64*, (2) 243-252.

(66) South Coast Air Quality Management District, S. "Multiple Air Toxics Exposure Study III," South Coast Air Quality Management District, 2008.

(67) Eyring, V.; Isaksen, I. S. A.; Berntsen, T.; Collins, W. J.; Corbett, J. J.; Endresen, O.; Grainger, R. G.; Moldanova, J.; Schlager, H.; Stevenson, D. S., Transport Impacts on Atmosphere and Climate: Shipping. *Atmos. Environ.* **2009**, *In Press, Accepted Manuscript*.

(68) Wang, C. F.; Corbett, J. J.; Winebrake, J. J., Cost-effectiveness of reducing sulfur emissions from ships. *Environ. Sci. Technol.* **2007**, *41*, (24) 8233-8239.

(69) Silverman, B., Pacific Merchant Shipping Association v. James Goldstene. *United States Court of Appeals for the Ninth Circuit* **2008**, *No. 07-16695*.

(70) Murphy, S. M.; Agrawal, H.; Sorooshian, A.; Padro, L. T.; Gates, H.; Hersey, S.; Welch, W. A.; Jung, H.; Miller, J. W.; Cocker, D. R.; Nenes, A.; Jonsson, H. H.; Flagan, R. C.; Seinfeld, J. H., Comprehensive Simultaneous Shipboard and Airborne Characterization of Exhaust from a Modern Container Ship at Sea. *Environ. Sci. Technol.* **2009**, *43*, (13) 4626-4640.

(71) Lack, D. A.; Corbett, J. J.; Onasch, T.; Lerner, B.; Massoli, P.; Quinn, P. K.; Bates, T. S.; Covert, D. S.; Coffman, D.; Sierau, B.; Herndon, S.; Allan, J.; Baynard, T.; Lovejoy, E.; Ravishankara, A. R.; Williams, E., Particulate emissions from commercial shipping: Chemical, physical, and optical properties. *Journal of Geophysical Research* **2009**, *114*.

(72) Sinha, P.; Hobbs, P. V.; Yokelson, R. J.; Christian, T. J.; Kirchstetter, T. W.; Bruintjes, R., Emissions of trace gases and particles from two ships in the southern Atlantic Ocean. *Atmos. Environ.* **2003**, *37*, (15) 2139-2148.

(73) Reinard, M. S.; Adoua, K.; Martini, J. M.; Johnston, M. V., Source characterization and identification by real-time single particle mass spectrometry. *Atmos. Environ.* **2007**, *41*, (40) 9397-9409.

(74) Ault, A. P.; Moore, M. J.; Furutani, H.; Prather, K. A., Impact of emissions from the Los Angeles port region on San Diego air quality. *Environ. Sci. Technol.* **2009**, *43*, (10) 3500-3506.

(75) Organization, I. M., International Convention on Safety of Life at Sea (SOLAS) Chapter V. **2000**.

(76) The Marine Exchange, Ship Traffic Logs for the Ports of Los Angeles/Long Beach, **2007**, San Pedro, CA

(77) International Standards Organization *Petroleum products -- Fuels (class F) -- Specifications of marine fuels*; 3rd ed., **2005**.

(78) Lake, D. A.; Tolocka, M. P.; Johnston, M. V.; Wexler, A. S., The character of single particle sulfate in Baltimore. **2004**, *38*, (31) 5311-5320.

(79) Agrawal, H.; Welch, W. A.; Miller, J. W.; Cocker, D. R., Emission Measurements from a Crude Oil Tanker at Sea. *Environ. Sci. Technol.* **2008**.

(80) Pratt, K. A.; Mayer, J. E.; Holecek, J. C.; Moffet, R. C.; Sanchez, R. O.; Rebotier, T. P.; Furutani, H.; Gonin, M.; Fuhrer, K.; Su, Y. X.; Guazzotti, S.; Prather, K. A., Development and Characterization of an Aircraft Aerosol Time-of-Flight Mass Spectrometer. *Anal. Chem.* **2009**, *81*, (5) 1792-1800.

(81) Spencer, M. T.; Prather, K. A., Using ATOFMS to determine OC/EC mass fractions in particles. *Aerosol Sci. Technol.* **2006**, *40*, (8) 585-594.

(82) Neubauer, K. R.; Johnston, M. V.; Wexler, A. S., On-line analysis of aqueous aerosols by laser desorption ionization. *Int. J. Mass Spectrom. Ion Process.* **1997**, *163*, (1-2) 29-37.

(83) Lack, D.; Lerner, B.; Granier, C.; Baynard, T.; Lovejoy, E.; Massoli, P.; Ravishankara, A. R.; Williams, E., Light absorbing carbon emissions from commercial shipping. *Geophys. Res. Lett.* **2008**, *35*, (13).

(84) Moffet, R. C.; Prather, K., Aging of soot captured with in situ measurements: Implications for aerosol climate forcing. *Proceedings Of The National Academy Of Sciences Of The United States Of America* **2008**, *Submitted*.

(85) Bhave, P. V.; Allen, J. O.; Morrical, B. D.; Fergenson, D. P.; Cass, G. R.; Prather, K. A., A field-based approach for determining ATOFMS instrument sensitivities to ammonium and nitrate. *Environ Sci Technol* **2002**, *36*, (22) 4868-4879.

(86) Pratt, K. A.; Hatch, L. E.; Prather, K. A., Seasonal volatility dependence of ambient particle phase amines. *Environ. Sci. Technol.* **2009**, *43*, (14) 5276-5281.

(87) Silva, P. J.; Liu, D. Y.; Noble, C. A.; Prather, K. A., Size and chemical characterization of individual particles resulting from biomass burning of local Southern California species. *Environ. Sci. Technol.* **1999**, *33*, (18) 3068-3076.

(88) Finlayson-Pitts, B. J.; Pitts, J. N. *Chemistry of the Upper and Lower Atmosphere*; Academic Press: San Diego, CA, **2000**.

(89) McMurry, P. H.; Wilson, J. C., Droplet Phase (Heterogeneous) And Gas-Phase (Homogeneous) Contributions To Secondary Ambient Aerosol Formation As Functions Of Relative-Humidity. *Journal Of Geophysical Research-Oceans And Atmospheres* **1983**, *88*, (NC9) 5101-5108.

(90) Barbaray, B.; Contour, J. P.; Mouvier, G., Effects Of Nitrogen-Dioxide And Water-Vapor On Oxidation Of Sulfur-Dioxide Over V2o5 Particles. **1978**, *12*, (12) 1294-1297.

(91) Barbaray, B.; Contour, J. P.; Mouvier, G., Sulfur-Dioxide Oxidation Over Atmospheric Aerosol - X-Ray Photoelectron-Spectra Of Sulfur-Dioxide Adsorbed On V2o5 And Carbon. **1977**, *11*, (4) 351-356.

(92) Chosson, F.; Paoli, R.; Cuenot, B., Ship plume dispersion rates in convective boundary layers for chemistry models. *Atmos. Chem. Phys.* **2008**, *8*, (16) 4841.

(93) Sahle-Demessie, E.; Devulapelli, V. G., Vapor phase oxidation of dimethyl sulfide with ozone over V2O5/TiO2 catalyst. **2008**, *84*, (3-4) 408-419.

(94) Gaston, C. J.; Pratt, K. A.; Qin, X. Y.; Prather, K. A., Real-time detection and mixing-state of methanesulfonate in single aerosol particles in Riverside, CA during a phytoplankton bloom. *Environ. Sci. Technol.* **2009**, *Submitted*.

(95) California Air Resources Board Personal Communication, **2009.**

(96) Poschl, U., Atmospheric aerosols: Composition, transformation, climate and health effects. *Angewandte Chemie-International Edition* **2005**, *44*, (46) 7520-7540.

(97) Valavanidis, A.; Fiotakis, K.; Vlachogianni, T., Airborne Particulate Matter and Human Health: Toxicological Assessment and Importance of Size and Composition of Particles for Oxidative Damage and Carcinogenic Mechanisms. **2008**, *26*, (4) 339-362.

(98) Pope, C. A., Mortality effects of longer term exposures to fine particulate air pollution: Review of recent epidemiological evidence. *Inhalation Toxicology* **2007**, *19*, 33-38.

(99) Pope, C. A.; Muhlestein, J. B.; May, H. T.; Renlund, D. G.; Anderson, J. L.; Horne, B. D., Ischemic heart disease events triggered by short-term exposure to fine particulate air pollution. *Circulation* **2006**, *114*, (23) 2443-2448.

(100) Orru, H.; Teinemaa, E.; Lai, T.; Tamm, T.; Kaasik, M.; Kimmel, V.; Kangur, K.; Merisalu, E.; Forsberg, B., Health impact assessment of particulate pollution in Tallinn using fine spatial resolution and modeling techniques. **2009**, *8*.

(101) Nel, A., Air pollution-related illness: Effects of particles. **2005**, *308*, (5723) 804-806.

(102) Asgharian, B., A model of deposition of hygroscopic particles in the human lung. **2004**, *38*, (9) 938-947.

(103) Yeh, H. C.; Cuddihy, R. G.; Phalen, R. F.; Chang, I. Y., Comparisons of calculated respiratory tract deposition of particles based on the proposed NCRP model and the new ICRP66 model. **1996**, *25*, (2) 134-140.

(104) Park, S. S.; Wex, A. S., Size-dependent deposition of particles in the human lung at steady-state breathing. **2008**, *39*, (3) 266-276.

(105) Zhou, Y. M.; Zhong, C. Y.; Kennedy, I. M.; Leppert, V. J.; Pinkerton, K. E., Oxidative stress and NF kappa B activation in the lungs of rats: a synergistic interaction between soot and iron particles. *Toxicol. Appl. Pharmacol.* **2003**, *190*, (2) 157-169.

(106) Zhu, Y. F.; Hinds, W. C.; Kim, S.; Sioutas, C., Concentration and size distribution of ultrafine particles near a major highway. *Journal Of The Air & Waste Management Association* **2002**, *52*, (9) 1032-1042.

(107) Delfino, R. J.; Sioutas, C.; Malik, S., Potential role of ultrafine particles in associations between airborne particle mass and cardiovascular health. *Environmental Health Perspectives* **2005**, *113*, (8) 934-946.

(108) Sioutas, C.; Delfino, R. J.; Singh, M., Exposure assessment for atmospheric ultrafine particles (UFPs) and implications in epidemiologic research. *Environmental Health Perspectives* **2005**, *113*, (8) 947-955.

(109) Ntziachristos, L.; Polidori, A.; Phuleria, H.; Geller, M. D.; Sioutas, C., Application of a diffusion charger for the measurement of particle surface concentration in different environments. *Aerosol Sci. Technol.* **2007**, *41*, (6) 571-580.

(110) Pope, C. A.; Dockery, D. W., Health effects of fine particulate air pollution: Lines that connect. *J Air Waste Manage* **2006**, *56*, (6) 709-742.

(111) Krudysz, M.; Moore, K.; Geller, M.; Sioutas, C.; Froines, J., Intra-community spatial variability of particulate matter size distributions in Southern California/Los Angeles. **2009**, *9*, (3) 1061-1075.

(112) Fine, P. M.; Sioutas, C.; Solomon, P. A., Secondary particulate matter in the United States: Insights from the particulate matter supersites program and related studies. *Journal Of The Air & Waste Management Association* **2008**, *58*, (2) 234-253.

(113) Solomon, P. A.; Sioutas, C., Continuous and semicontinuous monitoring techniques for particulate matter mass and chemical components: A synthesis of findings from EPA's particulate matter supersites program and related studies. **2008**, *58*, (2) 164-195.

(114) Moore, K. F.; Ning, Z.; Ntziachristos, L.; Schauer, J. J.; Sioutas, C., Daily variation in the properties of urban ultrafine aerosol - Part I: Physical characterization and volatility. *Atmos. Environ.* **2007**, *41*, (38) 8633-8646.

(115) Ntziachristos, L.; Ning, Z.; Geller, M. D.; Sioutas, C., Particle concentration and characteristics near a major freeway with heavy-duty diesel traffic. **2007**, *41*, (7) 2223-2230.

(116) Kuhn, T.; Biswas, S.; Sioutas, C., Diurnal and seasonal characteristics of particle volatility and chemical composition in the vicinity of a light-duty vehicle freeway. **2005**, *39*, (37) 7154-7166.

(117) Mejia, J. F.; Morawska, L.; Mengersen, K., Spatial variation in particle number size distributions in a large metropolitan area. **2008**, *8*, (5) 1127-1138.

(118) Kim, E.; Hopke, P. K., Source characterization of ambient fine particles in the Los Angeles basin. *J. Environ. Eng. Sci.* **2007**, *6*, (4) 343-353.

(119) Moffet, R. C.; de Foy, B.; Molina, L. T.; Molina, M. J.; Prather, K. A., Measurement of ambient aerosols in northern Mexico City by single particle mass spectrometry. **2008**, *8*, (16) 4499-4516.

(120) Kolb, C. E.; Herndon, S. C.; McManus, B.; Shorter, J. H.; Zahniser, M. S.; Nelson, D. D.; Jayne, J. T.; Canagaratna, M. R.; Worsnop, D. R., Mobile laboratory with rapid response instruments for real-time measurements of urban and regional trace gas and particulate distributions and emission source characteristics. *Environ. Sci. Technol.* **2004**, *38*, (21) 5694-5703.

(121) Bukowiecki, N.; Dommen, J.; Prevot, A. S. H.; Richter, R.; Weingartner, E.; Baltensperger, U., A mobile pollutant measurement laboratory-measuring gas phase and aerosol ambient concentrations with high spatial and temporal resolution. *Atmos. Environ.* **2002**, *36*, (36-37) 5569-5579.

(122) Zavala, M.; Herndon, S. C.; Wood, E. C.; Jayne, J. T.; Nelson, D. D.; Trimborn, A. M.; Dunlea, E.; Knighton, W. B.; Mendoza, A.; Allen, D. T.; Kolb, C. E.; Molina, M. J.; Molina, L. T., Comparison of emissions from on-road sources using a mobile laboratory under various driving and operational sampling modes. **2009**, *9*, (1) 1-14.

(123) Zavala, M.; Herndon, S. C.; Slott, R. S.; Dunlea, E. J.; Marr, L. C.; Shorter, J. H.; Zahniser, M.; Knighton, W. B.; Rogers, T. M.; Kolb, C. E.; Molina, L. T.; Molina, M. J., Characterization of on-road vehicle emissions in the Mexico City Metropolitan Area using a mobile laboratory in chase and fleet average measurement modes during the MCMA-2003 field campaign. **2006**, *6*, 5129-5142.

(124) Canagaratna, M. R.; Jayne, J. T.; Ghertner, D. A.; Herndon, S.; Shi, Q.; Jimenez, J. L.; Silva, P. J.; Williams, P.; Lanni, T.; Drewnick, F.; Demerjian, K. L.; Kolb, C. E.; Worsnop, D. R., Chase studies of particulate emissions from in-use New York City vehicles. **2004**, *38*, (6) 555-573.

(125) Bukowiecki, N.; Dommen, J.; Prevot, A. S. H.; Weingartner, E.; Baltensperger, U., Fine and ultrafine particles in the Zurich (Switzerland) area measured with a mobile laboratory: an assessment of the seasonal and regional variation throughout a year. *Atmos. Chem. Phys.* **2003**, *3*, 1477-1494.

(126) Isakov, V.; Touma, J. S.; Khlystov, A., A method of assessing air toxics concentrations in urban areas using mobile platform measurements. *Journal Of The Air & Waste Management Association* **2007**, *57*, (11) 1286-1295.

(127) Gard, E.; Mayer, J. E.; Morrical, B. D.; Dienes, T.; Fergenson, D. P.; Prather, K. A., Real-time analysis of individual atmospheric aerosol particles: Design and performance of a portable ATOFMS. *Analytical Chemistry* **1997**, *69*, (20) 4083-4091.

(128) Qin, X. Y.; Bhave, P. V.; Prather, K. A., Comparison of two methods for obtaining quantitative mass concentrations from aerosol time-of-flight mass spectrometry measurements. *Anal. Chem.* **2006**, *78*, (17) 6169-6178.

(129) Moffet, R. C.; Qin, X. Y.; Rebotier, T.; Furutani, H.; Prather, K. A., Chemically segregated optical and microphysical properties of ambient aerosols measured in a single-particle mass spectrometer. *J. Geophys. Res.-Atmos.* **2008**, *113*, (D12).

(130) Draxler, R. R.; Rolph, G. D., **2003**, *HYSPLIT (HYbrid Single Particle Lagrangian Integrated Trajectory) v. 4.8 Model access via NOAA ARL READY Website (http://www.arl.noaa.gov/ready/hysplit4.html). NOAA Air Resources Laboratory,*Silver Spring, MD.

(131) *San Diego International Airport Weather Underground*.

(132) DeCarlo, P. F.; Slowik, J. G.; Worsnop, D. R.; Davidovits, P.; Jimenez, J. L., Particle morphology and density characterization by combined mobility and aerodynamic diameter measurements. Part 1: Theory. **2004**, *38*, (12) 1185-1205.

(133) Guazzotti, S. A.; Whiteaker, J. R.; Suess, D.; Coffee, K. R.; Prather, K. A., Real-time measurements of the chemical composition of size-resolved particles during a Santa Ana wind episode, California USA. *Atmos. Environ.* **2001**, *35*, (19) 3229-3240.

(134) Sullivan, R. C.; Guazzotti, S. A.; Sodeman, D. A.; Prather, K. A., Direct observations of the atmospheric processing of Asian mineral dust. *Atmospheric Chemistry and Physics* **2007**, *7*, 1213-1236.

(135) Noble, C. A.; Prather, K. A., Real-time single particle monitoring of a relative increase in marine aerosol concentration during winter rainstorms. *Geophys. Res. Lett.* **1997**, *24*, (22) 2753-2756.

(136) Whiteaker, J. R.; Prather, K. A., Hydroxymethanesulfonate as a tracer for fog processing of individual aerosol particles. *Atmos. Environ.* **2003**, *37*, (8) 1033-1043.

(137) Pratt, K. A.; Prather, K. A., Real-time, single-particle volatility, size, and chemical composition measurements of aged urban aerosols. *Environ. Sci. Technol.* **2009**, *In Preparation*.

(138) Rostami, A. A., Computational Modeling of Aerosol Deposition in Respiratory Tract: A Review. **2009**, *21*, (4) 262-290.

(139) EPA., National Air Quality and Emissions Trends Report, 2003 Special Studies Edition. **2003**.

(140) Horvath, H., Atmospheric Light-Absorption - a Review. *Atmospheric Environment, Part A - General Topics* **1993**, *27*, (3) 293-317.

(141) Robock, A., Volcanic eruptions and climate. *Reviews of Geophysics* **2000**, *38*, (2) 191-219.

(142) Dubovik, O.; Holben, B.; Eck, T. F.; Smirnov, A.; Kaufman, Y. J.; King, M. D.; Tanre, D.; Slutsker, I., Variability of absorption and optical properties of key aerosol types observed in worldwide locations. *Journal of the Atmospheric Sciences* **2002**, *59*, (3) 590-608.

(143) Brunekreef, B.; Holgate, S. T., Air pollution and health. *Lancet* **2002**, *360*, (9341) 1233-1242.

(144) Gauderman, W. J.; Gilliland, G. F.; Vora, H.; Avol, E.; Stram, D.; McConnell, R.; Thomas, D.; Lurmann, F.; Margolis, H. G.; Rappaport, E. B.; Berhane, K.; Peters, J. M., Association between air pollution and lung function growth in Southern California children - Results from a second cohort. *American Journal of Respiratory and Critical Care Medicine* **2002**, *166*, (1) 76-84.

(145) Hatch, T. F., Distribution and Deposition of Inhaled Particles in Respiratory Tract. *Bacteriological Reviews* **1961**, *25*, (3) 237-&.

(146) Stuart, B. O., Deposition of Inhaled Aerosols. *Archives of Internal Medicine* **1973**, *131*, (1) 60-73.

(147) Geiser, M.; Rothen-Rutishauser, B.; Kapp, N.; Schurch, S.; Kreyling, W.; Schulz, H.; Semmler, M.; Hof, V. I.; Heyder, J.; Gehr, P., Ultrafine particles cross cellular membranes by nonphagocytic mechanisms in lungs and in cultured cells. *Environmental Health Perspectives* **2005**, *113*, (11) 1555-1560.

(148) Chow, J. C.; Watson, J. G.; Fujita, E. M.; Lu, Z. Q.; Lawson, D. R.; Ashbaugh, L. L., Temporal and Spatial Variations of Pm(2.5) and Pm(10) Aerosol in the Southern California Air-Quality Study. *Atmos Environ* **1994**, *28*, (12) 2061-2080.

(149) Chow, J. C.; Liu, C. S.; Cassmassi, J.; Watson, J. G.; Lu, Z. Q.; Pritchett, L. C., A Neighborhood-Scale Study of PM-10 Source Contributions in Rubidoux, California. *Atmospheric Environment* **1992**, *26A*, (4) 693-706.

(150) Hughes, L. S.; Allen, J. O.; Salmon, L. G.; Mayo, P. R.; Johnson, R. J.; Cass, G. R., Evolution of nitrogen species air pollutants along trajectories crossing the Los Angeles area. *Environmental Science & Technology* **2002**, *36*, (18) 3928-3935.

(151) Sardar, S. B.; Fine, P. M.; Sioutas, C., Seasonal and spatial variability of the size-resolved chemical composition of particulate matter (PM10) in the Los Angeles Basin. *Journal of Geophysical Research-Atmospheres* **2005**, *110*, (D7).

(152) Lawson, D. R., The Southern California Air-Quality Study. *Journal of the Air & Waste Management Association* **1990**, *40*, (2) 156-165.

(153) Hughes, L. S.; Allen, J. O.; Kleeman, M. J.; Johnson, R. J.; Cass, G. R.; Gross, D. S.; Gard, E. E.; Galli, M. E.; Morrical, B. D.; Fergenson, D. P.; Dienes, T.; Noble, C. A.; Silva, P. J.; Prather, K. A., Size and composition distribution of atmospheric particles in southern California. *Environmental Science & Technology* **1999**, *33*, (20) 3506-3515.

(154) Pastor, S. H.; Allen, J. O.; Hughes, L. S.; Bhave, P.; Cass, G. R.; Prather, K. A., Ambient single particle analysis in Riverside, California by aerosol time-of-flight mass spectrometry during the SCOS97-NARSTO. *Atmospheric Environment* **2003**, *37*, S239-S258.

(155) Singh, M.; Bowers, K.; Sioutas, C., Seasonal and spatial trends in particle number concentrations and size distributions at the children's health study sites in Southern California. *Journal of Exposure Science and Environmental Epidemiology* **2006**, *16*, (1) 3-18.

(156) Noble, C. A.; Prather, K. A., Real-time measurement of correlated size and composition profiles of individual atmospheric aerosol particles. *Environmental Science & Technology* **1996**, *30*, (9) 2667-2680.

(157) Qin, X.; Bhave, P. V.; Prather, K. A., Comparison of Two Methods for Obtaining Quantitative Mass Concentrations from Aerosol Time-of-Flight Mass Spectrometry Measurements. *Analytical Chemistry* **2006**, *78*, (17) 6169-6178.

(158) Hughes, L. S.; Allen, J. O.; Bhave, P.; Kleeman, M. J.; Cass, G. R.; Liu, D. Y.; Fergenson, D. F.; Morrical, B. D.; Prather, K. A., Evolution of atmospheric particles along trajectories crossing the Los Angeles basin. *Environ Sci Technol* **2000**, *34*, (15) 3058-3068.

(159) Docherty, K. S.; Jimenez, J. L., Study of Organic Aerosols at Riverside (SOAR) HomePage. *http://cires.colorado.edu/jimenez-group/Field/Riverside05/* **2005**.

(160) Allen, J. O., YAADA Software Toolkit to Analyze Single-Particle Mass Spectral Data: Reference Manual Version 1.1. *Arizona State University* **2002**, http://www.yaada.org.

(161) Gross, D. S.; Galli, M. E.; Silva, P. J.; Prather, K. A., Relative sensitivity factors for alkali metal and ammonium cations in single particle aerosol time-of-flight mass spectra. *Analytical Chemistry* **2000**, *72*, (2) 416-422.

(162) Qin, X. Y.; Prather, K. A., Impact of biomass emissions on particle chemistry during the California Regional Particulate Air Quality Study. *International Journal of Mass Spectrometry* **2006**, *258*, (1-3) 142-150.

(163) Schauer, J. J.; Kleeman, M. J.; Cass, G. R.; Simoneit, B. R. T., Measurement of emissions from air pollution sources. 3. C-1-C-29 organic compounds from fireplace combustion of wood. *Environmental Science & Technology* **2001**, *35*, (9) 1716-1728.

(164) Sexton, K.; Liu, K. S.; Hayward, S. B.; Spengler, J. D., Characterization and Source Apportionment of Wintertime Aerosol in a Wood-Burning Community. *Atmospheric Environment* **1985**, *19*, (8) 1225-1236.

(165) Pandis, S. N.; Harley, R. A.; Cass, G. R.; Seinfeld, J. H., Secondary Organic Aerosol Formation and Transport. *Atmospheric Environment Part a-General Topics* **1992**, *26*, (13) 2269-2282.

(166) Vouk, V. B.; Piver, W. T., Metallic Elements in Fossil-Fuel Combustion Products - Amounts and Form of Emissions and Evaluation of Carcinogenicity and Mutagenicity. *Environmental Health Perspectives* **1983**, *47*, (JAN) 201-225.

(167) Isakson, J.; Persson, T. A.; Lindgren, E. S., Identification and assessment of ship emissions and their effects in the harbour of G(o)over-circleteborg, Sweden. *Atmospheric Environment* **2001**, *35*, (21) 3659-3666.

(168) Xie, Z. Q.; Sun, L. G.; Blum, J. D.; Huang, Y. Y.; He, W., Summertime aerosol chemical components in the marine boundary layer of the Arctic Ocean. *Journal of Geophysical Research-Atmospheres* **2006**, *111*, (D10).

(169) Singh, M.; Jaques, P. A.; Sioutas, C., Size distribution and diurnal characteristics of particle-bound metals in source and receptor sites of the Los Angeles Basin. *Atmospheric Environment* **2002**, *36*, (10) 1675-1689.

(170) Kleeman, M. J.; Cass, G. R., Source contributions to the size and composition distribution of urban particulate air pollution. *Atmospheric Environment* **1998**, *32*, (16) 2803-2816.

(171) Draxler, R. R.; Rolph, G. D., HYSPLIT (HYbrid Single-Particle Lagrangian Integrated Trajectory) Model access via NOAA ARL READY Website (http://www.arl.noaa.gov/ready/hysplit4.html). *NOAA Air Resources Laboratory* **2003**, Silver Spring, MD.

(172) Turkiewicz, K.; Magliano, K.; Najita, T., Comparison of two winter air quality episodes during the California Regional Particulate Air Quality Study. *Journal of the Air & Waste Management Association* **2006**, *56*, (4) 467-473.

(173) Dahneke, B. E.; Cheng, Y. S., Properties of Continuum Source Particle Beams.1. Calculation Methods and Results. *Journal of Aerosol Science* **1979**, *10*, (3) 257-274.

(174) Kanakidou, M.; Seinfeld, J. H.; Pandis, S. N.; Barnes, I.; Dentener, F. J.; Facchini, M. C.; Van Dingenen, R.; Ervens, B.; Nenes, A.; Nielsen, C. J.; Swietlicki, E.; Putaud, J. P.; Balkanski, Y.; Fuzzi, S.; Horth, J.; Moortgat, G. K.; Winterhalter, R.; Myhre, C. E. L.; Tsigaridis, K.; Vignati, E.; Stephanou, E. G.; Wilson, J., Organic aerosol and global climate modelling: a review. *Atmos. Chem. Phys.* **2005**, *5*, 1053-1123.

(175) Turpin, B. J.; Huntzicker, J. J., Identification of secondary organic aerosol episodes and quantitation of primary and secondary organic aerosol concentrations during SCAQS. *Atmos. Environ.* **1995**, *29*, (23) 3527-3544.

(176) Murphy, S. M.; Sorooshian, A.; Kroll, J. H.; Ng, N. L.; Chhabra, P.; Tong, C.; Surratt, J. D.; Knipping, E.; Flagan, R. C.; Seinfeld, J. H., Secondary aerosol formation from atmospheric reactions of aliphatic amines. *Atmos. Chem. Phys.* **2007**, *7*, (9) 2313-2337.

(177) Neff, J. C.; Holland, E. A.; Dentener, F. J.; McDowell, W. H.; Russell, K. M., The origin, composition and rates of organic nitrogen deposition: A missing piece of the nitrogen cycle? *Biogeochemistry* **2002**, *57*, (1) 99-136.

(178) Schade, G. W.; Crutzen, P. J., Emission of aliphatic-amines from animal husbandry and their reactions - potential source of N2O and HCN. *J. Atmos. Chem.* **1995**, *22*, (3) 319-346.

(179) Sorooshian, A.; Murphy, S. M.; Hersey, S.; Gates, H.; Padro, L. T.; Nenes, A.; Brechtel, F. J.; Jonsson, H.; Flagan, R. C.; Seinfeld, J. H., Comprehensive airborne characterization of aerosol from a major bovine source. *Atmos. Chem. Phys.* **2008**, *8*, 5489-5520.

(180) Gronberg, L.; Lovkvist, P.; Jonsson, J. A., Measurement of aliphatic-amines in ambient air and rainwater. *Chemosphere* **1992**, *24*, (10) 1533-1540.

(181) McGregor, K. G.; Anastasio, C., Chemistry of fog waters in California's Central Valley: 2. Photochemical transformations of amino acids and alkyl amines. *Atmos. Environ.* **2001**, *35*, (6) 1091-1104.

(182) Silva, P. J.; Erupe, M. E.; Price, D.; Elias, J.; Malloy, Q. G. J.; Li, Q.; Warren, B.; Cocker, D. R., Trimethylamine as precursor to secondary organic aerosol formation via nitrate radical reaction in the atmosphere. *Environ. Sci. Technol.* **2008**, *42*, (13) 4689-4696.

(183) Zahardis, J.; Geddes, S.; Petrucci, G. A., The ozonolysis of primary aliphatic amines in fine particles. *Atmos. Chem. Phys.* **2008**, *8*, 1181-1194.

(184) Tan, P. V.; Evans, G. J.; Tsai, J.; Owega, S.; Fila, M. S.; Malpica, O., On-line analysis of urban particulate matter focusing on elevated wintertime aerosol concentrations. *Environ. Sci. Technol.* **2002**, *36*, (16) 3512-3518.

(185) Pankow, J. F., Gas/particle partitioning of neutral and ionizing compounds to single and multi-phase aerosol particles. 1. Unified modeling framework. *Atmos. Environ.* **2003**, *37*, (24) 3323-3333.

(186) Smith, J. N.; Dunn, M. J.; VanReken, T. M.; Iida, K.; Stolzenburg, M. R.; McMurry, P. H.; Huey, L. G., Chemical composition of atmospheric nanoparticles formed from nucleation in Tecamac, Mexico: Evidence for an important role for organic species in nanoparticle growth. *Geophys. Res. Lett.* **2008**, *35*, (L04808) doi:10.1029/2007GL032523.

(187) Barsanti, K. C.; McMurry, P. H.; Smith, J. N., The potential contribution of organic salts to new particle growth. *Atmos. Chem. Phys.* **2009**, *9*, 2949-2957.

(188) Burtscher, H.; Baltensperger, U.; Bukowiecki, N.; Cohn, P.; Hüglin, C.; Mohr, M.; Matter, U.; Nyeki, S.; Schmatloch, V.; Streit, N.; Weingartner, E., Separation of volatile and non-volatile aerosol fractions by thermodesorption: instrumental development and applications. *J. Aerosol Sci.* **2001**, *32*, 427-442.

(189) Qin, X.; Shields, L. G.; Toner, S. M.; Pratt, K. A.; Prather, K. A., Seasonal comparisons of the single particle mixing state in Riverside, CA during the SOAR 2005 campaign. *Aerosol Sci. Technol.* **2009**, *In preparation.*

(190) Huffman, J. A.; Ziemann, P. J.; Jayne, J. T.; Worsnop, D. R.; Jimenez, J. L., Development and characterization of a fast-stepping/scanning thermodenuder for chemically-resolved aerosol volatility measurements. *Aerosol Sci. Technol.* **2008**, *42*, (5) 395-407.

(191) Kim, E.; Hopke, P. K., Source identifications of airborne fine particles using positive matrix factorization and US environmental protection agency positive matrix factorization. *Journal Of The Air & Waste Management Association* **2007**, *57*, (7) 811-819.

(192) Steele, P. T.; Tobias, H. J.; Fergenson, D. P.; Pitesky, M. E.; Horn, J. M.; Czerwieniec, G. A.; Russell, S. C.; Lebrilla, C. B.; Gard, E. E.; Frank, M., Laser power dependence of mass spectral signatures from individual bacterial spres in bioaerosol mass spectrometry. *Anal. Chem.* **2003**, *75*, 5480-5487.

(193) Song, X. H.; Hopke, P. K.; Fergenson, D. P.; Prather, K. A., Classification of single particles analyzed by ATOFMS using an artificial neural network, ART-2A. *Anal. Chem.* **1999**, *71*, (4) 860-865.

(194) Moffet, R. C.; Qin, X.; Rebotier, T.; Furutani, H.; Prather, K. A., Chemically segregated optical and microphysical properties of ambient aerosols measured in a single-particle mass spectrometer. *J. Geophys. Res.* **2008**, *113*, doi:10.1029/2007JD009393.

(195) Silva, P. J.; Prather, K. A., Interpretation of mass spectra from organic compounds in aerosol time-of-flight mass spectrometry. *Anal. Chem.* **2000**, *72*, (15) 3553-3562.

(196) Docherty, K. S.; Stone, E. A.; Ulbrich, I. M.; DeCarlo, P. F.; Snyder, D. C.; Schauer, J. J.; Peltier, R. E.; Weber, R. J.; Murphy, S. M.; Seinfeld, J. H.; Grover, B. D.; Eatough, D. J.; Jimenez, J. L., Apportionment of primary and secondary organic aerosols in southern California during the 2005 Study of Organic Aerosols in Riverside (SOAR-1). *Environ. Sci. Technol.* **2008**, *42*, 7655-7662.

(197) Denkenberger, K. A.; Moffet, R. C.; Holecek, J. C.; Rebotier, T. P.; Prather, K. A., Real-time, single-particle measurements of oligomers in aged ambient aerosol particles. *Environ. Sci. Technol.* **2007**, *41*, 5439-5446.

(198) Kawamura, K.; Steinberg, S.; Kaplan, I. R., Homologous series of C-1-C-10 monocarboxylic acids and C-1-C-6 carbonyls in Los Angeles air and motor vehicle exhausts. *Atmos. Environ.* **2000**, *34*, (24) 4175-4191.

(199) Nolte, C. G.; Fraser, M. P.; Cass, G. R., Gas phase C-2-C-10 organic acids concentrations in the Los Angeles atmosphere. *Environ. Sci. Technol.* **1999**, *33*, (4) 540-545.

(200) **2006**, *Calculated using Advanced Chemistry Development (ACD/Labs) Software V8.14 for Solaris*,

(201) Johnson, G.; Ristovski, Z.; Morawska, L., Application of the VH-TDMA technique to coastal ambient aerosols. *Geophys. Res. Lett.* **2004**, *31*, (16).

(202) **2009**, *Calculated using Advanced Chemistry Development (ACD/Labs) Software V8.14 for Solaris*,

(203) Stelson, A. W.; Seinfeld, J. H., Relative humidity and temperature dependence of the ammonium nitrate dissociation constant. *Atmos. Environ.* **1982**, *16*, (5) 983-992.

(204) Kim, B. M.; Teffera, S.; Zeldin, M. D., Characterization of PM2.5 and PM10 in the South Coast Air Basin of southern California: Part 2 - Temporal variations. *Journal of the Air & Waste Management Association* **2000**, *50*, (12) 2045-2059.

(205) Yao, X.; Ling, T. Y.; Fang, M.; Chan, C. K., Size dependence of in situ pH in submicron atmospheric particles in Hong Kong. *Atmos. Environ.* **2007**, *41*, 382-393.

(206) Ramsay, T. O.; Burnett, R. T.; Krewski, D., The effect of concurvity in generalized additive models linking mortality to ambient particulate matter. *Epidemiology* **2003**, *14*, (1) 18-23.

(207) Vedal, S., Ambient particles and health: Lines that divide. *J Air Waste Manage* **1997**, *47*, (5) 551-581.

(208) Qin, X. Y., Shields, L. G., Toner, S. M., Prather, K. A., A Seasonal Comparison of the Single Particle Mixing State in RIverside, CA During the SOAR 2005 Campaign. ***In preparation.***

(209) Edinger, J. G., Modification of the Marine Layer over Coastal Southern California. *Journal of Applied Meteorology* **1963**, *2*, (6) 706-712.

(210) Stephens, E. R., Marine Layer and Its Relation to a Smog Episode in Riverside California. *Atmos Environ* **1968**, *2*, (4) 393-&.

(211) Ying, Q.; Kleeman, M. J., Source contributions to the regional distribution of secondary particulate matter in California. *Atmos Environ* **2006**, *40*, (4) 736-752.

(212) Russell, A. G.; Cass, G. R.; Seinfeld, J. H., On Some Aspects of Nighttime Atmospheric Chemistry. *Environ Sci Technol* **1986**, *20*, (11) 1167-1172.

(213) Pratt, K. A.; Hatch, L. E.; Prather, K. A., Seasonal Volatility Dependence of Ambient Particle Phase Amines. *Environ Sci Technol* **2009**, *43*, 5276–5281.

(214) Docherty, K. S.; Stone, E. A.; Ulbrich, I. M.; DeCarlo, P. F.; Snyder, D. C.; Schauer, J. J.; Peltier, R. E.; Weber, R. J.; Murphy, S. M.; Seinfeld, J. H.; Grover, B. D.; Eatough, D. J.; Jiimenez, J. L., Apportionment of Primary and Secondary Organic Aerosols in Southern California during the 2005 Study of Organic Aerosols in Riverside (SOAR-1). *Environ Sci Technol* **2008**, *42*, (20) 7655-7662.

(215) Finlayson-Pitts, B. J., Pitts, J. N. *Chemistry of the Upper and Lower Atmosphere*; Academic Press: San Diego, **2000**.

(216) Kross, B. C.; Ayebo, A. D.; Fuortes, L. J., Methemoglobinemia - Nitrate Toxicity in Rural America. *Am Fam Physician* **1992**, *46*, (1) 183-188.

(217) Pope, C. A.; Thun, M. J.; Namboodiri, M. M.; Dockery, D. W.; Evans, J. S.; Speizer, F. E.; Heath, C. W., Particulate Air-Pollution as a Predictor of Mortality in a Prospective-Study of Us Adults. *Am J Resp Crit Care* **1995**, *151*, (3) 669-674.

(218) Nemmar, A.; Hoylaerts, M. F.; Hoet, P. H. M.; Dinsdale, D.; Smith, T.; Xu, H. Y.; Vermylen, J.; Nemery, B.; Nemery, B., Ultrafine particles affect experimental thrombosis in an in vivo hamster model. *Am J Resp Crit Care* **2002**, *166*, (7) 998-1004.

(219) Mauderly, J. L.; Chow, J. C., Health effects of organic aerosols. *Inhal Toxicol* **2008**, *20*, (3) 257-288.

(220) Harrison, R. M.; Yin, J. X., Particulate matter in the atmosphere: which particle properties are important for its effects on health? *Sci Total Environ* **2000**, *249*, (1-3) 85-101.

(221) Geller, M. D.; Fine, P. M.; Sioutas, C., The relationship between real-time and time-integrated coarse (2.5-10 mu m), intermodal (1-2.5 mu m), and fine (< 2.5 mu

m) particulate matter in the Los Angeles Basin. *J Air Waste Manage* **2004**, *54*, (9) 1029-1039.

(222) Kim, B. M.; Teffera, S.; Zeldin, M. D., Characterization of PM2.5 and PM10 in the South Coast Air Basin of southern California: Part 1 - Spatial variations. *J Air Waste Manage* **2000**, *50*, (12) 2034-2044.

(223) Pratt, K. A. New Insights into Single-Particle Mixing State using Aircraft Aerosol Time-of-Flight Mass Spectrometry. University of California, San Diego, La Jolla, 2009.

(224) Gross, D. S.; Galli, M. E.; Silva, P. J.; Wood, S. H.; Liu, D. Y.; Prather, K. A., Single particle characterization of automobile and diesel truck emissions in the Caldecott Tunnel. *Aerosol Sci Tech* **2000**, *32*, (2) 152-163.

(225) Pang, Y. B.; Ren, Y.; Obeidi, F.; Hastings, R.; Eatough, D. J.; Wilson, W. E., Semi-volatile species in PM2.5: Comparison of integrated and continuous samplers for PM2.5 research or monitoring. *J Air Waste Manage* **2001**, *51*, (1) 25-36.

(226) Draxler, R. R.; Rolph, G. D., HYSPLIT (HYbrid Single Particle Lagrangian Integrated Trajectory) v. 4.8 Model access via NOAA ARL READY Website (http://www.arl.noaa.gov/ready/hysplit4.html). *NOAA Air Resources Laboratory* **2003**, Silver Spring, MD.

(227) Raphael, M. N., The Santa Ana Winds of California. *Earth Interact* **2003**, *7*, -.

(228) Kleeman, M. J.; Hughes, L. S.; Allen, J. O.; Cass, G. R., Source contributions to the size and composition distribution of atmospheric particles: Southern California in September 1996. *Environ Sci Technol* **1999**, *33*, (23) 4331-4341.

(229) Jordan, C. E.; Dibb, J. E.; Anderson, B. E.; Fuelberg, H. E., Uptake of nitrate and sulfate on dust aerosols during TRACE-P. *J Geophys Res-Atmos* **2003**, *108*, (D21) 1-10.

(230) Schlesinger, R. B., The health impact of common inorganic components of fine particulate matter (PM2.5) in ambient air: A critical review. *Inhal Toxicol* **2007**, *19*, (10) 811-832.

(231) Toner, S. M.; Shields, L. G.; Sodeman, D. A.; Prather, K. A., Using mass spectral source signatures to apportion exhaust particles from gasoline and diesel powered vehicles in a freeway study. *Abstr Pap Am Chem S* **2005**, *229*, U127-U127.

(232) Grover, B. D.; Eatough, N. L.; Woolwine, W. R.; Cannon, J. P.; Eatough, D. J.; Long, R. W., Semi-continuous mass closure of the major components of fine particulate matter in Riverside, CA. *Atmos Environ* **2008**, *42*, (2) 250-260.

(233) Gardiner, K.; Trethowan, N. W.; Harrington, J. M.; Rossiter, C. E.; Calvert, I. A., Respiratory Health-Effects of Carbon-Black - a Survey of European Carbon-Black Workers. *Brit J Ind Med* **1993**, *50*, (12) 1082-1096.

(234) Horvath, H., Atmospheric Light-Absorption - a Review. *Atmospheric Environment Part a-General Topics* **1993**, *27*, (3) 293-317.

(235) Jacobson, M. C.; Hansson, H. C.; Noone, K. J.; Charlson, R. J., Organic atmospheric aerosols: Review and state of the science. *Reviews of Geophysics* **2000**, *38*, (2) 267-294.

(236) McClellan, R. O., Health-Effects of Exposure to Diesel Exhaust Particles. *Annual Review of Pharmacology and Toxicology* **1987**, *27*, 279-300.

(237) Oberdorster, G., Pulmonary effects of inhaled ultrafine particles. *International Archives of Occupational and Environmental Health* **2001**, *74*, (1) 1-8.

(238) Sydbom, A.; Blomberg, A.; Parnia, S.; Stenfors, N.; Sandstrom, T.; Dahlen, S. E., Health effects of diesel exhaust emissions. *European Respiratory Journal* **2001**, *17*, (4) 733-746.

(239) Pope, C. A., Epidemiology of fine particulate air pollution and human health: Biologic mechanisms and who's at risk? *Environmental Health Perspectives* **2000**, *108*, 713-723.

(240) Zhang, X. Q.; McMurry, P. H., Theoretical-Analysis of Evaporative Losses from Impactor and Filter Deposits. *Atmospheric Environment* **1987**, *21*, (8) 1779-1789.

(241) Heintzenberg, J., Fine particles in the global troposphere: A review. *Tellus* **1989**, *41(B)*, 142-160.

(242) Suess, D. T.; Prather, K. A., Mass spectrometry of aerosols. *Chemical Reviews* **1999**, *99*, (10) 3007-3035.

(243) Noble, C. A.; Prather, K. A., Real-time single particle mass spectrometry: A historical review of a quarter century of the chemical analysis of aerosols. *Mass Spectrometry Reviews* **2000**, *19*, (4) 248-274.

(244) Johnston, M. V., Sampling and analysis of individual particles by aerosol mass spectrometry. *Journal of Mass Spectrometry* **2000**, *35*, (5) 585-595.

(245) Wenzel, R. J.; Prather, K. A., Improvements in ion signal reproducibility obtained using a homogeneous laser beam for on-line laser desorption/ionization of single particles. *Rapid Communications in Mass Spectrometry* **2004**, *18*, (13) 1525-1533.

(246) Mansoori, B. A.; Johnston, M. V.; Wexler, A. S., Quantitation of Ionic Species in Single Microdroplets by Online Laser Desorption/Ionization. *Analytical Chemistry* **1994**, *66*, (21) 3681-3687.

(247) Reilly, P. T. A.; Lazar, A. C.; Gieray, R. A.; Whitten, W. B.; Ramsey, J. M., The elucidation of charge-transfer-induced matrix effects in environmental aerosols via real-time aerosol mass spectral analysis of individual airborne particles. *Aerosol Science and Technology* **2000**, *33*, (1-2) 135-152.

(248) Allen, J. O.; Bhave, P. V.; Whiteaker, J. R.; Prather, K. A., Instrument Busy Time and Mass Measurement using Aerosol Time-of-Flight Mass Spectrometry. *Aerosol Science & Technology (in press)* **2006**.

(249) Allen, J. O.; Fergenson, D. P.; Gard, E. E.; Hughes, L. S.; Morrical, B. D.; Kleeman, M. J.; Gross, D. S.; Galli, M. E.; Prather, K. A.; Cass, G. R., Particle detection efficiencies of aerosol time of flight mass spectrometers under ambient sampling conditions. *Environmental Science & Technology* **2000**, *34*, (1) 211-217.

(250) Wenzel, R. J.; Liu, D. Y.; Edgerton, E. S.; Prather, K. A., Aerosol time-of-flight mass spectrometry during the Atlanta Supersite Experiment: 2. Scaling procedures. *Journal of Geophysical Research-Atmospheres* **2003**, *108*, (D7).

(251) Moffet, R. C.; Shields, L. G.; Bernstsen, J.; Devlin, R. B.; Prather, K. A., Characterization of an Ambient Coarse Particle Concentrator Used for Human Exposure Studies: Aerosol Size Distributions, Chemical Composition, and Concentration Enrichment. *Aerosol Science & Technology* **2004**, *38*, 1123-1137.

(252) Watson, J. G.; Chow, J. C.; Bowen, J. L.; Lowenthal, D. H.; Hering, S.; Ouchida, P.; Oslund, W., Air quality measurements from the Fresno Supersite. *Journal of the Air & Waste Management Association* **2000**, *50*, (8) 1321-1334.

(253) Marple, V.; Rubow, K.; Ananth, G.; Fissan, H. J., Micro-Orifice Uniform Deposit Impactor. *Journal of Aerosol Science* **1986**, *17*, (3) 489-494.

(254) Wilson, J. C.; Liu, B. Y. H., Aerodynamic Particle-Size Measurement by Laser-Doppler Velocimetry. *Journal of Aerosol Science* **1980**, *11*, (2) 139-150.

(255) Dienes, T., Development, Characterization and Refinement of a Transportable Aerosol Time-of-Flight Mass Spectrometer. *Ph. D Thesis* **2003**.

(256) Beavis, R. C., Increasing the dynamic range of a transient recorder by using two analog-to-digital converters. *Journal of the American Society for Mass Spectrometry* **1996**, *7*, (1) 107-113.

(257) Morawska, L.; Johnson, G.; Ristovski, Z. D.; Agranovski, V., Relation between particle mass and number for submicrometer airborne particles. *Atmospheric Environment* **1999**, *33*, (13) 1983-1990.

(258) Hänel, G.; Thudium, J., Mean Bulk Densities of Samples of Dry Atmospheric Aerosol-Particles - Summary of Measured Data. *Pure and Applied Geophysics* **1977**, *115*, (4) 799-803.

(259) Charron, A.; Harrison, R. M.; Moorcroft, S.; Booker, J., Quantitative interpretation of divergence between PM10 and PM2.5 mass measurement by TEOM and gravimetric (Partisol) instruments. *Atmospheric Environment* **2004**, *38*, (3) 415-423.

(260) McMurry, P. H.; Wang, X.; Park, K.; Ehara, K., The relationship between mass and mobility for atmospheric particles: A new technique for measuring particle density. *Aerosol Science and Technology* **2002**, *36*, (2) 227-238.

(261) Pitz, M.; Cyrys, J.; Karg, E.; Wiedensohler, A.; Wichmann, H. E.; Heinrich, J., Variability of apparent particle density of an urban aerosol. *Environmental Science & Technology* **2003**, *37*, (19) 4336-4342.

(262) Lee, J. H.; Hopke, P. K.; Holsen, T. M.; Polissar, A. V.; Lee, D. W.; Edgerton, E. S.; Ondov, J. M.; Allen, G., Measurements of fine particle mass concentrations using continuous and integrated monitors in eastern US cities. *Aerosol Science and Technology* **2005**, *39*, (3) 261-275.

(263) Babich, P.; Wang, P. Y.; Allen, G.; Sioutas, C.; Koutrakis, P., Development and evaluation of a continuous ambient PM2.5 mass monitor. *Aerosol Science and Technology* **2000**, *32*, (4) 309-324.

(264) Chung, A.; Chang, D. P. Y.; Kleeman, M. J.; Perry, K. D.; Cahill, T. A.; Dutcher, D.; McDougall, E. M.; Stroud, K., Comparison of real-time instruments used to monitor airborne particulate matter. *Journal of the Air & Waste Management Association* **2001**, *51*, (1) 109-120.

(265) Jaklevic, J. M.; Gatti, R. C.; Goulding, F. S.; Loo, B. W., A Beta-Gauge Method Applied to Aerosol Samples. *Environmental Science & Technology* **1981**, *15*, (6) 680-686.

(266) Patashnick, H.; Rupprecht, E. G., Continuous PM-10 Measurements Using the Tapered Element Oscillating Microbalance. *Journal of the Air & Waste Management Association* **1991**, *41*, (8) 1079-1083.

(267) Suess, D. T.; Prather, K. A., Mass spectrometry of aerosols. *Chemical Reviews* **1999**, *99*, (10) 3007-3036.

(268) Moffet, R. C.; Shields, L. G.; Berntsen, J.; Devlin, R. B.; Prather, K. A., Characterization of an Ambient Coarse Particle Concentrator Used for Human Exposure Studies: Aerosol Size Distributions, Chemical Composition, and Concentration Experiment. *Aerosol Science and Technology* **2004**, *38*, (11) 1123-1137.

(269) Allen, J. O.; Bhave, P. V.; Whiteaker, J. R.; Prather, K. A., Instrument Busy Time and Mass Measurement using Aerosol Time-of-Flight Mass Spectrometry. *Aerosol Science & Technology* **2006**, *40*, (8) 615-626.

(270) Qin, X.; Whiteaker, J. R.; Coffee, K. R.; Khairallah, G.; Suess, D. T.; Prather, K. A., Comparison of ATOFMS Single Particle Measurements at Fresno and Angiola in the San Joaquin Valley during the California Regional Particulate Air Quality Study. *Manuscript in preparation* **2007**.

(271) Bates, T. S.; Quinn, P. K.; Coffman, D. J.; Covert, D. S.; Miller, T. L.; Johnson, J. E.; Carmichael, G. R.; Uno, I.; Guazzotti, S. A.; Sodeman, D. A.; Prather, K. A.; Rivera, M.; Russell, L. M.; Merrill, J. T., Marine boundary layer dust and pollutant transport associated with the passage of a frontal system over eastern Asia. *J. Geophys. Res.-Atmos.* **2004**, *109*, (D19).

(272) Holecek, J. C.; Spencer, M. T.; Prather, K. A., Enhanced concentrations of humic-like substances (HULIS) and dust in rainwater samples from the Northern Pacific and Indian Ocean. *Manuscript in preparation* **2007**.

(273) Toner, S. M.; Shields, L. G.; Sodeman, D. A.; Prather, K. A., Using Mass Spectral Source Signatures to Apportion Exhaust Particles from Gasoline and Diesel Powered Vehicles in a Freeway Study using UF-ATOFMS. *Submitted to Atmospheric Environment* **2007**.

(274) Spencer, M. T.; Holecek, J. C.; Corrigan, C. E.; Ramanathan, V.; Prather, K. A., Size-resolved Chemical Composition of Aerosol Particles During a Monsoonal Transition Period over the Indian Ocean. *Submitted to Journal of Geophysical Research-Atmospheres* **2007**.

(275) Watson, J. G.; Chow, J. C., A wintertime PM2.5 episode at the Fresno, CA, Supersite. *Atmospheric Environment* **2002**, *36*, (3) 465-475.

(276) Solomon, P. A.; Magliano, K. L., The 1995-Integrated Monitoring Study (IMS95) of the California Regional PM10/PM2.5 air quality study (CRPAQS): Study overview. *Atmospheric Environment* **1999**, *33*, (29) 4747-4756.

(277) Chow, J. C.; Chen, L. W. A.; Watson, J. G.; Lowenthal, D. H.; Magliano, K. A.; Turkiewicz, K.; Lehrman, D. E., PM2.5 chemical composition and spatiotemporal variability during the California Regional PM10/PM2.5 Air Quality Study (CRPAQS). *Journal of Geophysical Research-Atmospheres* **2006a**, *111*, (D10).

(278) Rinehart, L. R.; Fujita, E. M.; Chow, J. C.; Magliano, K.; Zielinska, B., Spatial distribution of PM2.5 associated organic compounds in central California. *Atmospheric Environment* **2006**, *40*, (2) 290-303.

(279) Brown, S. G.; Roberts, P. T.; McCarthy, M. C.; Lurmann, F. W.; Hyslop, N. P., Wintertime vertical variations in particulate matter (PM) and precursor concentrations in the San Joaquin Valley during the California Regional coarse PM/fine PM Air Quality Study. *Journal of the Air & Waste Management Association* **2006**, *56*, (9) 1267-1277.

(280) Pope, C. A., Review: Epidemiological basis for particulate air pollution health standards. *Aerosol Science & Technology* **2000**, *32*, (1) 4-14.

(281) Schaumann, F.; Borm, P. J. A.; Herbrich, A.; Knoch, J.; Pitz, M.; Schins, R. P. F.; Luettig, B.; Hohlfeld, J. M.; Heinrich, J.; Krug, N., Metal-rich ambient particles (Particulate Matter(2.5)) cause airway inflammation in healthy subjects. *American Journal of Respiratory and Critical Care Medicine* **2004**, *170*, (8) 898-903.

(282) Hunt, A.; Abraham, J. L.; Judson, B.; Berry, C. L., Toxicologic and epidemiologic clues from the characterization of the 1952 London smog fine particulate matter in archival autopsy lung tissues. *Environmental Health Perspectives* **2003**, *111*, (9) 1209-1214.

(283) Wong, C. S. C.; Li, X. D.; Thornton, I., Urban environmental geochemistry of trace metals. *Environmental Pollution* **2006**, *142*, (1) 1-16.

(284) Deguillaume, L.; Leriche, M.; Desboeufs, K.; Mailhot, G.; George, C.; Chaumerliac, N., Transition metals in atmospheric liquid phases: Sources, reactivity, and sensitive parameters. *Chemical Reviews* **2005**, *105*, (9) 3388-3431.

(285) He, Z. L. L.; Yang, X. E.; Stoffella, P. J., Trace elements in agroecosystems and impacts on the environment. *Journal of Trace Elements in Medicine and Biology* **2005**, *19*, (2-3) 125-140.

(286) Sabin, L. D.; Lim, J. H.; Stolzenbach, K. D.; Schiff, K. C., Contribution of trace metals from atmospheric deposition to stormwater runoff in a small impervious urban catchment. *Water Research* **2005**, *39*, (16) 3929-3937.

(287) Astolfi, M. L.; Canepari, S.; Catrambone, M.; Perrino, C.; Pietrodangelo, A., Improved characterisation of inorganic components in airborne particulate matter. *Environmental Chemistry Letters* **2006**, *3*, (4) 186-191.

(288) Fernandez, A. J.; Ternero, M.; Fernandez, F.; Gutierrez, A.; Trigo, D., Chemical speciation of trace metals in fine airborne particles: advances in operational performance of a new sequential extraction scheme. *International Journal of Environmental Analytical Chemistry* **2006**, *86*, (9) 641-651.

(289) Sullivan, R. C.; Prather, K. A., Recent advances in our understanding of atmospheric chemistry and climate made possible by on-line aerosol analysis instrumentation. *Analytical Chemistry* **2005**, *77*, (12) 3861-3885.

(290) Svane, M.; Janhall, S.; Hagstrom, M.; Hallquist, M.; Pettersson, J. B. C., On-line alkali analysis of individual aerosol particles in urban air. *Atmospheric Environment* **2005**, *39*, (36) 6919-6930.

(291) Tolocka, M. P.; Lake, D. A.; Johnston, M. V.; Wexler, A. S., Number concentrations of fine and ultrafine particles containing metals. *Atmospheric Environment* **2004**, *38*, (20) 3263-3273.

(292) Spencer, M. T.; Shields, L. G.; Prather, K. A., Simultaneous measurement of the effective density and chemical composition of ambient aerosol particles. *Environmental Science & Technology*, accepted.

(293) Shaheen, N.; Shah, M. H.; Jaffar, M., A study of airborne selected metals and particle size distribution in relation to climatic variables and their source identification. *Water Air and Soil Pollution* **2005**, *164*, (1-4) 275-294.

(294) Zheng, M.; Fang, M., Correlations between organic and inorganic species in atmospheric aerosols. *Environmental Science & Technology* **2000**, *34*, (13) 2721-2726.

(295) Lough, G. C.; Schauer, J. J.; Lawson, D. R., Day-of-week trends in carbonaceous aerosol composition in the urban atmosphere. *Atmospheric Environment* **2006**, *40*, (22) 4137-4149.

(296) Almeida, S. M.; Pio, C. A.; Freitas, M. C.; Reis, M. A.; Trancoso, M. A., Source apportionment of atmospheric urban aerosol based on weekdays/weekend variability: evaluation of road re-suspended dust contribution. *Atmospheric Environment* **2006**, *40*, (11) 2058-2067.

(297) Allen, A. G.; Nemitz, E.; Shi, J. P.; Harrison, J. P.; Greenwood, J. C., Size distributions of trace metals in atmospheric aerosols in the United Kingdom. *Atmospheric Environment* **2001**, *35*, (27) 4581-4591.

(298) Moskalyk, R. R.; Alfantazi, A. M., Processing of vanadium: a review. *Minerals Engineering* **2003**, *16*, (9) 793-805.

(299) Espinosa, A. J. F.; Rodriguez, M. T.; de la Rosa, F. J. B.; Sanchez, J. C. J., A chemical speciation of trace metals for fine urban particles. *Atmospheric Environment* **2002**, *36*, (5) 773-780.

(300) Jang, H.-N.; Seo, Y.-C.; Lee, J.-H.; Hwang, K.-W.; Yoo, J.-I.; Sok, C.-H.; Kim, S.-H., Formation of fine particles enriched by V and Ni from heavy oil combustion: Anthropogenic sources and drop-tube furnace experiments. *Atmospheric Environment*, in press.

(301) Figueroa, D. A.; Rodriguez-Sierra, C. J.; Jimenez-Velez, B. D., Concentrations of Ni and V, other heavy metals, arsenic, elemental and organic carbon in atmospheric fine particles (PM2.5) from Puerto Rico. *Toxicology and Industrial Health* **2006**, *22*, (2) 87-99.

(302) Xie, Z. Q.; Sun, L. G.; Blum, J. D.; Huang, Y. Y.; He, W., Summertime aerosol chemical components in the marine boundary layer of the Arctic Ocean. *Journal of Geophysical Research-Atmospheres* **2006**, *111*, (D10) -.

(303) Jang, H. N.; Seo, Y. C.; Lee, J. H.; Hwang, K. W.; Yoo, J. I.; Sok, C. H.; Kim, S. H., Formation of fine particles enriched by V and Ni from heavy oil combustion: Anthropogenic sources and drop-tube furnace experiments. *Atmos. Environ.* **2007**, *41*, (5) 1053-1063.

(304) Moffet, R. C.; de Foy, B.; Molina, L. T.; Molina, M. J.; Prather, K. A., Measurement of ambient aerosols in northern Mexico City by single particle mass spectrometry. *Atmospheric Chemistry and Physics Discussions* **2007**, *7*, 6413-6457.

(305) Draxler, R. R.; Rolph, G. D., HYSPLIT (HYbrid Single-Particle Lagrangian Integrated Trajectory) Model access via NOAA ARL READY website (http://www.arl.noaa.gov/ready/hysplit4.html). *NOAA Air Resources Laboratory, Silver Springs, MD* **2003**.

(306) Ault, A. P.; Furutani, H.; Dominguez, G.; Thiemens, M. H.; Prather, K. A., A mass spectral fingerprint of ship emission particles by aerosol time-of-flight mass spectrometry and applications for source apportionment, manuscript in preparation.

(307) Baker, A. R.; Jickells, T. D., Mineral particle size as a control on aerosol iron solubility. *Geophysical Research Letters* **2006**, *33*, (17) -.

(308) Yi, S. M.; Totten, L. A.; Thota, S.; Yan, S.; Offenberg, J. H.; Eisenreich, S. J.; Graney, J.; Holsen, T. M., Atmospheric dry deposition of trace elements measured around the urban and industrially impacted NY-NJ harbor. *Atmospheric Environment* **2006**, *40*, (34) 6626-6637.

(309) Wang, X.; Sato, T.; Xing, B., Size distribution and anthropogenic sources apportionment of airborne trace metals in Kanazawa, Japan. *Chemosphere* **2006**, *65*, 2440-2448.

(310) Harrison, R. M.; Tilling, R.; Romero, M. S. C.; Harrad, S.; Jarvis, K., A study of trace metals and polycyclic aromatic hydrocarbons in the roadside environment. *Atmospheric Environment* **2003**, *37*, (17) 2391-2402.

(311) Choel, M.; Deboudt, K.; Flament, P.; Lecornet, G.; Perdrix, E.; Sobanska, S., Fast evolution of tropospheric Pb- and Zn-rich particles in the vicinity of a lead smelter. *Atmospheric Environment* **2006**, *40*, (24) 4439-4449.

(312) Linak, W. P.; Wendt, J. O. L., Toxic metal emissions from incineration - Mechanisms and control. *Progress in Energy and Combustion Science* **1993**, *19*, (2) 145-185.

(313) Marder, A. R., The metallurgy of zinc-coated steel. *Progress in Materials Science* **2000**, *45*, (3) 191-271.

(314) Malina, G., Ecotoxicological and environmental problems associated with the former chemical plant in Tarnowskie Gory, Poland. *Toxicology* **2004**, *205*, (3) 157-172.

(315) Silva, P. J. Source profiling and apportionment of airborne particles: A new approach using aerosol time-of-flight mass spectrometry. University of California, Riverside, Riverside, CA, 2000.

(316) Birmili, W.; Allen, A. G.; Bary, F.; Harrison, R. M., Trace metal concentrations and water solubility in size-fractionated atmospheric particles and influence of road traffic. *Environmental Science & Technology* **2006**, *40*, (4) 1144-1153.

(317) Florea, A. M.; Busselberg, D., Occurrence, use and potential toxic effects of metals and metal compounds. *Biometals* **2006**, *19*, (4) 419-427.

(318) Harris, A. R.; Davidson, C. I., The role of resuspended soil in lead flows in the California South Coast Air Basin. *Environmental Science & Technology* **2005**, *39*, (19) 7410-7415.

(319) Allen, D. T.; Turner, J. R., Transport of atmospheric fine particulate matter: Part 1 - Findings from recent field programs on the extent of regional transport within North America. *Journal Of The Air & Waste Management Association* **2008**, *58*, (2) 254-264.

(320) Lall, R.; Thurston, G. D., Identifying and quantifying transported vs. local sources of New York City PM2.5 fine particulate matter air pollution. *Atmos. Environ.* **2006**, *40*, S333-S346.

(321) Corbett, J. J.; Koehler, H. W., Updated emissions from ocean shipping. *J. Geophys. Res.-Atmos.* **2003**, *108*, (D20).

(322) California Air Resources Board *Estimated Annual Average Emissions* Sacramento, 2006.

(323) Capaldo, K.; Corbett, J. J.; Kasibhatla, P.; Fischbeck, P.; Pandis, S. N., Effects of ship emissions on sulphur cycling and radiative climate forcing over the ocean. *Nature* **1999**, *400*, (6746) 743-746.

(324) Vutukuru, S.; Dabdub, D., Modeling the effects of ship emissions on coastal air quality: A case study of southern California. *Atmos. Environ.* **2008**, *42*, (16) 3751-3764.

(325) Martien, P. T.; Harley, R. A.; Milford, J. B.; Russell, A. G., Evaluation of incremental reactivity and its uncertainty in Southern California. *Environ. Sci. Technol.* **2003**, *37*, (8) 1598-1608.

(326) Lu, G.; Brook, J. R.; Alfarra, M. R.; Anlauf, K.; Leaitch, W. R.; Sharma, S.; Wang, D.; Worsnop, D. R.; Phinney, L., Identification and characterization of inland ship plumes over Vancouver, BC. *Atmos. Environ.* **2006**, *40*, (15) 2767-2782.

(327) Vallius, M.; Lanki, T.; Tiittanen, P.; Koistinen, K.; Ruuskanen, J.; Pekkanen, J., Source apportionment of urban ambient PM2.5 in two successive measurement campaigns in Helsinki, Finland. *Atmos. Environ.* **2003**, *37*, (5) 615-623.

(328) Pattanaik, S.; Huggins, F. E.; Huffman, G. P.; Linak, W. P.; Miller, C. A., XAFS studies of nickel and sulfur speciation in residual oil fly-ash particulate matters (ROFA PM). *Environ. Sci. Technol.* **2007**, *41*, (4) 1104-1110.

(329) Eatough, D. J.; Eatough, N. L.; Hill, M. W.; Mangelson, N. F.; Hansen, L. D., Identification Of Vo2+ In Particles From The Flue Lines Of Oil-Fired Power-Plants. *Environ. Sci. Technol.* **1984**, *18*, (2) 124-126.

(330) Fang, S. C.; Eisen, E. A.; Cavallari, J. M.; Mittleman, M. A.; Christiani, D. C., Acute changes in vascular function among welders exposed to metal-rich particulate matter. *Epidemiology* **2008**, *19*, (2) 217-225.

(331) Pinkerton, K. E.; Zhou, Y. M.; Teague, S. V.; Peake, J. L.; Walther, R. C.; Kennedy, I. M.; Leppert, V. J.; Aust, A. E., Reduced lung cell proliferation following short-term exposure to ultrafine soot and iron particles in neonatal rats: Key to impaired lung growth? *Inhalation Toxicology* **2004**, *16*, 73-81.

(332) Hu, S.; Polidori, A.; Arhami, M.; Shafer, M. M.; Schauer, J. J.; Cho, A.; Sioutas, C., Redox activity and chemical speciation of size fractioned PM in the communities of the Los Angeles-Long Beach harbor. *Atmos. Chem. Phys.* **2008**, *8*, (21) 6439.

(333) Kauper, E. K.; Niemann, P. L., Los Angeles to San Diego three dimensional ozone study. *ARB Contract Number A-6-090-30* **1977**.

(334) Toner, S. M. Anthropogenic Particulate Source Characterization and Source Apportionment Using Aerosol Time-of-Flight Mass Spectrometry. Doctoral Thesis, University of California San Diego, La Jolla, 2007.

(335) Qin, X. Y. Characterization of Ambient Aerosol Composition and Formation Mechanisms and Development of Quantification Methodologies Utilizing ATOFMS. Doctoral Thesis, University of California San Diego, La Jolla, 2007.

(336) Liu, D. Y.; Prather, K. A.; Hering, S. V., Variations in the size and chemical composition of nitrate-containing particles in Riverside, CA. *Aerosol Sci. Technol.* **2000**, *33*, (1-2) 71-86.

(337) Spencer, M. T.; Holecek, J. C.; Corrigan, C. E.; Ramanathan, V.; Prather, K. A., Size-Resolved Chemical Composition of Aerosol Particles During a Monsoonal Transition Period over the Indian Ocean. *J. Geophys. Res.-Atmos.* **2008**.

(338) Ship Arrivals-Departures-Transfers Ports of Los Angeles/Long Beach, **2006**, San Pedro, CA

(339) American Association of Port Authorities *2006 U.S. Port Cargo Tonnage Rankings*, 2006; Vol. 2008.

(340) Holecek, J. C.; Spencer, M. T.; Prather, K. A., Analysis of rainwater samples: Comparison of single particle residues with ambient particle chemistry from the northeast Pacific and Indian oceans. *J. Geophys. Res.-Atmos.* **2007**, *112*, (D22).

(341) Neubauer, K. R.; Johnston, M. V.; Wexler, A. S., Humidity effects on the mass spectra of single aerosol particles. *Atmos. Environ.* **1998**, *32*, (14-15) 2521-2529.

(342) Dominguez, G.; Jackson, T.; Brothers, L.; Barnett, B.; Nguyen, B.; Thiemens, M. H., Discovery and measurement of an isotopically distinct source of sulfate in Earth's atmosphere. *Proceedings Of The National Academy Of Sciences Of The United States Of America* **2008**, *105*, (35) 12769-12773.

(343) Agrawal, H.; Malloy, Q. G. J.; Welch, W. A.; Miller, J. W.; Cocker, D. R., In-use gaseous and particulate matter emissions from a modern ocean going container vessel. *Atmos. Environ.* **2008**.

(344) Toner, S. M.; Shields, L. G.; Sodeman, D. A.; Prather, K. A., Using mass spectral source signatures to apportion exhaust particles from gasoline and diesel powered vehicles in a freeway study using UF-ATOFMS. *Atmos. Environ.* **2008**, *42*, (3) 568-581.

(345) Ault, A.; Gaston, C.; Wang, Y.; Dominguez, G.; Thiemens, M. H.; Prather, K., Single Particle Mixing State of Individual Ship Plumes at the Port of Los Angeles. *Environ. Sci. Technol.* **2008**, *in prep*.

(346) Kaufman, Y. J.; Koren, I.; Remer, L. A.; Rosenfeld, D.; Rudich, Y., The effect of smoke, dust, and pollution aerosol on shallow cloud development over the Atlantic Ocean. *PNAS* **2005**, *102*, (32) 11207-11212.

(347) Andreae, M. O., Soot Carbon and Excess Fine Potassium: Long-Range Transport of Combustion-Derived Aerosols. *Science* **1983**, *220*, (4602) 1148-1151.

(348) Guazzotti, S. A.; Suess, D. T.; Coffee, K. R.; Quinn, P. K.; Bates, T. S.; Wisthaler, A.; Hansel, A.; Ball, W. P.; Dickerson, R. R.; Neususess, C.; Crutzen, P. J.; Prather, K. A., Characterization of carbonaceous aerosols outflow from India and Arabia: Biomass/biofuel burning and fossil fuel combustion. *Journal of Geophysical Research* **2003**, *108*, (D15) 4485, doi:4410.1029/2002JD003277.

(349) Hudson, P. K.; Murphy, D. M.; Cziczo, D. J.; Thomson, D. S.; de Gouw, J. A.; Warneke, C.; Holloway, J.; Jost, H.; Huebler, G., Biomass-burning particle measurements: Characteristic composition and chemical processing. *Journal of Geophysical Research* **2004**, *109*, (D23S27) doi:10.1029/2003JD004398.

(350) Moffet, R. C.; de Foy, B.; Molina, L. T.; Molina, M. J.; Prather, K. A., Measurement of ambient aerosols in northern Mexico City by single particle mass spectrometry. *Atmospheric Chemistry and Physics* **2008**, *8*, 4499-4516.

(351) Posfai, M.; Simonics, R.; Li, J.; Hobbs, P. V.; Buseck, P. R., Individual aerosol particles from biomass burning in southern Africa: 1. Compositions and size distributions of carbonaceous particles. *Journal of Geophysical Research* **2003**, *108*, (D13) 8483, doi:8410.1029/2002JD002291.

(352) Yokelson, R.; Crounse, J. D.; DeCarlo, P.; Karl, T.; Urbanski, S.; Atlas, E.; Campos, T.; Shinozuka, Y.; Kapustin, V. N.; Clarke, A. D.; Weinheimer, A.; Knapp, D. J.; Montzka, D. D.; Holloway, J.; Weibring, P.; Flocke, F.; Zheng, W.; Toohey, D.; Wennberg, P. O.; Wiedinmyer, C.; Mauldin, L.; Freid, A.; Richter, D.; Walega, J.; Jimenez, J. L.; Adachi, K.; Buseck, P. R.; Hall, S. R.; Shetter, R., Emissions from biomass burning in the Yucatan. *Atmospheric Chemistry and Physics Discussions* **2009**, *9*, 767-835.

(353) Posfai, M.; Gelencser, A.; Simonics, R.; K. Arato, K.; Li, J.; Hobbs, P. V.; Buseck, P. V., Atmospheric tar balls: Particles from biomass and biofuel burning. *Journal of Geophysical Research* **2004**, *109*, (D06213) doi:10.1029/2003JD004169.

(354) Reid, J. S.; Koppmann, R.; Eck, T. F.; Eleuterio, D. P., A review of biomass burning emissions part II: intensive physical properties of biomass burning particles. *Atmospheric Chemistry and Physics* **2005**, *5*, 799-825.

(355) Lee, Y. S.; Collins, D. R.; Li, R.; Bowman, K. P.; Feingold, G., Expected impact of an aged biomass burning aerosol on cloud condensation nuclei and cloud droplet concentrations. *Journal of Geophysical Research* **2006**, *111*, (D22204) doi:10.1029/2005JD006464.

(356) Ramanathan, V.; Crutzen, P. J.; Lelieveld, J.; Mitra, A. P.; Althausen, D.; Anderson, J.; Andreae, M. O.; Cantrell, W.; Cass, G. R.; Chung, C. E.; Clarke, A. D.; Coakley, J. A.; Collins, W. D.; Conant, W. C.; Dulac, F.; Heintzenberg, J.; Heymsfield, A. J.; Holben, B.; Howell, S.; Hudson, J.; Jayaraman, A.; Kiehl, J. T.; Krishnamurti, T. N.; Lubin, D.; McFarquhar, G.; Novakov, T.; Ogren, J. A.; Podgorny, I. A.; Prather, K. A.; Priestley, K.; Prospero, J. M.; Quinn, P. K.; Rajeev, E.; Rasch, P.; Rupert, S.; Sadourny, R.; Satheesh, S. K.; Shaw, G. E.; Sheridan, P.; Valero, F. P. J., Indian Ocean Experiment: An integrated analysis of the climate forcing and effects of the great Indo-Asian haze. *Journal of Geophysical Research* **2001**, *106*, (D22) 28,371-328,398.

(357) Tivanski, A. V.; Hopkins, R. J.; Tyliszczak, T.; Gilles, M. K., Oxygenated Interface on Biomass Burn Tar Balls Determined by Single Particle Scanning Transmission X-ray Microscopy. *Journal of Physical Chemistry A* **2007**, *111*, 5448-5458.

(358) Andreae, M. O.; Rosenfeld, D., Aerosol-cloud-precipitation interactions. Part 1. The nature and sources of cloud-active aerosols. *Earth Science Reviews* **2008**, *89*, 13-41.

(359) Kaufman, Y. J.; Fraser, R. S., The Effect of Smoke Particles on Clouds and Climate Forcing. *Science* **1997**, *277*, (5332) 1636-1639.

(360) Kaufman, Y. J.; Koren, I., Smoke and Pollution Aerosol Effect on Cloud Cover. *Science* **2006**, *313*, 655-658.

(361) Rosenfeld, D., TRMM Observed First Direct Evidence of Smoke from Forest Fires Inhibiting Rainfall. *Geophysical Research Letters* **1999**, *26*, (20) 3105-3108.

(362) Solomon, S.; Qin, D.; Manning, M.; Chen, Z.; Marquis, M.; Averyt, K. B.; Tignor, M.; Miller, H. L. e., Climate Change 2007: The Physical Science Basis. Contribution of Working Group I to the Fourth Assessment Report of the Intergovernmental Panel on Climate Change. *Cambridge University Press* **2007**.

(363) Petters, M. D.; Parsons, M. T.; Prenni, A. J.; DeMott, P. J.; Kreidenweis, S. M.; Carrico, C. M.; Sullivan, A. P.; McMeeking, G. R.; Levin, E.; Wold, C. E.; Collett, J. L.; Moosmueller, H., Ice nuclei emissions from biomass burning. *Journal of Geophysical Research* **2009**, *114*, (D07209) doi:10.1029/2008JD011532.

(364) Crutzen, P. J.; Andreae, M. O., Biomass Burning in the Tropics: Impact on Atmospheric Chemistry and Biogeochemical Cycles. *Science* **1990**, *250*, (4988) 1669-1678.

(365) Mircea, M.; Facchini, M. C.; Decesari, S.; Cavalli, F.; Emblico, L.; Fuzzi, S.; Vestin, A.; Rissler, J.; Swietlicki, E.; Frank, G.; Andreae, M. O.; Maenhaut, W.; Rudich, Y.; Artaxo, P., Importance of the organic aerosol fraction for modeling aerosol hygroscopic growth and activation: a case study in the Amazon Basin. *Atmospheric Chemistry and Physics* **2005**, *5*, 3111-3126.

(366) Khlystov, A.; Stanier, C. O.; Takahama, S.; Pandis, S. N., Water content of ambient aerosol during the Pittsburg Air Quality Study. *Journal of Geophysical Research* **2005**, *110*, (D07S10) doi:10.1029/2004JD004651.

(367) Ansari, A. S.; Pandis, S. N., Water absorption by secondar organic aerosol and its effect on inorganic aerosol behavior. *Environmental Science and Technology* **2000**, *34*, (1) 71-77.

(368) Jacobson, M. C.; Hansson, H. C.; Noone, K. J.; Charlson, R. J., Organic atmospheric aerosols: Review and state of the science. *Reviews of Geophysics* **2000**, *38*, 267-294.

(369) Hungershoefer, K.; Zeromskiene, K.; Iinuma, Y.; Helas, G.; Trentmann, J.; Trautmann, T.; Parmar, R. S.; Wiedensohler, A.; Andreae, M. O.; Schmid, O., Modelling the optical properties of fresh biomass burning aerosol produced in a smoke chamber: results from EFEU campaign. *Atmospheric Chemistry and Physics* **2008**, *8*, 3427-3439.

(370) Petters, M. D.; Carrico, C. M.; Kreidenweis, S. M.; Prenni, A. J.; DeMott, P. J.; Collett, J. L.; Moosmueller, H., Cloud Condensation Nuclei Activity of Biomass Burning Aerosol. *submitted to Journal of Geophysical Research* **2009**.

(371) Li, J.; Posfai, M.; Hobbs, P. V.; Buseck, P. R., Individual aerosol particles from biomass burning in southern Africa: 2. Compositions and aging of inorganic particles. *Journal of Geophysical Research* **2003**, *108(D13)*, (8484) doi:10.1029/2002JD002310.

(372) Semeniuk, T. A.; Wise, M. E.; Martin, S. T.; Russell, L. M.; Buseck, P. R., Hygroscopic behavior of aerosol particles from biomass fires using environmental transmission electron microscopy. *Journal of Atmospheric Chemistry* **2006**, *56*, 259-273.

(373) Hopkins, R. J.; Lewis, K.; Desyaterik, Y.; Wang, Z.; Tivanski, A. V.; Arnott, W. P.; Laskin, A.; Giles, M. K., Correlations between optical, chemical and physical properties of biomass burn aerosols. *Geophysical Research Letters* **2007**, *34*, (L18806) doi:10.1029/2007GL030502.

(374) Yamasoe, M. A.; Artaxo, P.; Miguel, A. H.; Allen, A. G., Chemical composition of aerosol particles from direct emissions of vegetation fires in the Amazon Basin: water-soluble species and trace elements. *Atmospheric Environment* **2000**, *34*, 1641-1653.

(375) Weimer, S.; Alfarra, M. R.; D. Schreiber, D.; M. Mohr, M.; Prevot, A. S. H.; Baltensperger, U., Organic aerosol mass spectral signatures from wood-burning emissions: Influence of burning conditions and wood type. *Journal of Geophysical Research* **2008**, *113*, (D10304) doi:10.1029/2007JD009309.

(376) Andreae, M. O.; Merlet, P., Emission of trace gases and aerosols from biomass burning. *Global Biogeochemical Cycles* **2001**, *15*, (4) 955-966.

(377) Novakov, T.; Corrigan, C. E., Cloud condensation nucleus activity of the organic component of biomass smoke particles. *Geophysical Research Letters* **1996**, *23*, (16) 2141-2144.

(378) Rissler, J.; Swietlicki, E.; Zhou, J.; Roberts, G.; Andreae, M. O.; Gatti, L. V.; Artaxo, P., Physical properties of the sub-micrometer aerosol over the Amazon rain forest during the wet-to-dry season transition- comparison of modeled and measured CCN concentrations. *Atmospheric Chemistry and Physics* **2004**, *4*, 2119-2143.

(379) Roberts, G. C.; Artaxo, P.; Zhou, J.; Swietlicki, E.; Andreae, M. O., Sensitivity of CCN spectra on chemical and physical properties of aerosol: A case study from the Amazon Basin. *Journal of Geophysical Research* **2002**, *107*, (D20) 8070, doi:8010.1029/2001JD000583.

(380) Chang, R. Y.-W.; Liu, P. S. K.; Leaitch, W. R.; Abbatt, J. P. D., Comparison between measured and predicted CCN concentrations at Egbert, Ontario: Focus on the organic aerosol fraction at a semi-rural site. *Atmospheric Environment* **2007**, *41*, 8172-8182.

(381) Carrico, C. M.; Petters, M. D.; Kreidenweis, S. M.; Collett, J. L.; Engling, G.; Malm, W. C., Aerosol hygroscopicity and cloud droplet activation of extracts of filters from biomass burning experiments. *Journal of Geophysical Research* **2008**, *113*, (D08206) doi:10.1029/2007JD009274.

(382) Formenti, P.; Elbert, W.; Maenhaut, W.; Haywood, J. M.; Osborne, S.; Andreae, M. O., Inorganic and carbonaceous aerosols during Southern African Regional Science Initiative (SAFARI 2000) experiment: Chemical characteristics, physical properties, and emission data for smoke from African biomass burning. *Journal of Geophysical Research* **2003**, *108(D13)*, (8488) doi:10.1029/2002JD002408.

(383) Allen, A. G.; Miguel, A. H., Biomass Burning in the Amazon: Characterization of the Ionic Component of Aerosols Generated from Flaming and Smoldering Rainforest and Savannah. *Environmental Science and Technology* **1995**, *29*, (2) 486-493.

(384) Liu, X. D.; Van Espen, P.; Adams, F.; Cafmeyer, J.; Maenhaut, W., Biomass burning in southern Africa: Individual particle characterization of atmospheric aerosols and savanna fire samples. *Journal of Atmospheric Chemistry* **2000**, *36*, (2) 135-155.

(385) Trebs, I.; Metzger, S.; Meixner, F. X.; Helas, G.; Hoffer, A.; Rudich, Y.; Falkovich, A. H.; Moura, M. A. L.; da Silva, R. S.; Artaxo, P.; Slanina, J.; Andreae, M. O., The NH4+ -NO3- -Cl- -SO42- -H2O aerosol system and its gas phase precursors at a pasture site in the Amazon Basin: How relevant are mineral cations and soluble organic acids? *Journal of Geophysical Research* **2005**, *110*, D07303.

(386) Gaudichet, A.; Echalar, F.; Chatenet, B.; Quisefit, J. P.; Malingre, G.; Cachier, H.; Buatmenard, P.; Artaxo, P.; Maenhaut, W., Trace-Elements in Tropical African Savanna Biomass Burning Aerosols. *Journal of Atmospheric Chemistry* **1995**, *22*, (1-2) 19-39.

(387) Grijalva, R.; Moore, R.; Renteria, H., California Fire Siege 2007, An Overview. *California Department of Forestry and Fire Protection* **2008**.

(388) Su, Y. X.; Sipin, M. F.; Furutani, H. F.; Prather, K. A., Development and characterization of an aerosol time-of-flight mass spectrometer with increased detection efficiency. *Analytical Chemistry* **2004**, *76*, 712-719.

(389) Roberts, G. C.; Nenes, A., A Continuous-Flow Streamwise Thermal-Gradient CCN Chamber for Atmospheric Measurements. *Aerosol Science and Technology* **2005**, *39*, 206-221.

(390) Rebotier, T. P.; Prather, K. A., Aerosol time-of-flight mass spectrometry data analysis: A benchmark of clustering algorithms. *Analytica Chimica Acta* **2007**, *585*, (1) 38-54.

(391) Furutani, H. F.; Dall'osto, M.; Roberts, G. C.; Prather, K. A., Assessment of the relative importance of atmospheric aging on CCN activity derived from field observations. *Atmospheric Environment* **2008**, *42*, 3130-3142.

(392) Sullivan, R. C.; Guazzotti, S. A.; Sodeman, D. A.; Prather, K. A., Direct observations of the atmospheric processing of Asian mineral dust. *Atmospheric Chemistry and Physics* **2007**, *7*, (5) 1213-1236.

(393) Silva, P. J.; Liu, D.; Noble, C. A.; Prather, K. A., Size and Chemical Characterization of Individual Particles Resulting from Biomass Burning of Local Southern California Species. *Environmental Science and Technology* **1999**, *33*, (18) 3068-3076.

(394) Petters, M. D.; Kreidenweis, S. M., A single parameter representation of hygroscopic growth and cloud condensation nucleus activity. *Atmospheric Chemistry and Physics* **2007**, *7*, (8) 1961-1971.

(395) Shinozuka, Y.; Clarke, A. D.; DeCarlo, P. F.; Jimenez, J. L.; Dunlea, E. J.; Roberts, G. C.; Tomlinson, J. M.; Collins, D. R.; Howell, S. G.; Kapustin, V. N.; McNaughton, C. S.; Zhou, J., Aerosol optical properties relevant to regional remote sensing of CCN activity and links to their organic mass fraction: airborne observations over Central Mexico and the US West Coast during MILAGRO/INTEX-B. *Atmospheric Chemistry and Physics Discussions* **2009**, *9*, 12519-12558.

(396) Fine, P. M.; Cass, G. R.; Simoneit, B. R. T., Chemical Characterization of Fine Particle Emissions from the Fireplace Combustion of Wood Types Grown in the Midwestern and Western United States. *Environmental Engineering Science* **2004**, *21*, (3) 387-409.

(397) Fabbri, D.; Marynowski, L.; Fabianska, M. I.; Zaton, M.; Simoneit, B. R. T., Levoglucosan and Other Cellulose Markers in Pyrolysates of Miocene Lignites: Geochemical and Environmental Implications. *Environmental Science and Technology* **2008**, *42*, 2957-2963.

(398) Rose, D.; Nowak, A.; Achtert, P.; Wiedensohler, A.; Hu, M.; Shao, M.; Zhang, Y.; Andreae, M. O.; Poeschl, U., Cloud condensation nuclei in polluted air and biomass burning smoke near the mega-city Guangzhou, China - Part 1: Size-resolved measurements and implications for the modeling of aerosol particle hygroscopicity and CCN activity. *Atmospheric Chemistry and Physics Discussions* **2008**, *8*, 17343-17392.

(399) Vanvorst, W. D.; George, S., Impact of the California Clean Air Act. *International Journal of Hydrogen Energy* **1997**, *22*, (1) 31-38.

(400) Marshall, J. D.; Riley, W. J.; McKone, T. E.; Nazaroff, W. W., Intake fraction of primary pollutants: motor vehicle emissions in the South Coast Air Basin. *Atmospheric Environment* **2003**, *37*, (24) 3455-3468.

(401) Mysliwiec, M. J.; Kleeman, M. J., Source apportionment of secondary airborne particulate matter in a polluted atmospbere. *Environmental Science & Technology* **2002**, *36*, (24) 5376-5384.

(402) Fruin, S. A.; St Denis, M. J.; Winer, A. M.; Colome, S. D.; Lurmann, F. W., Reductions in human benzene exposure in the California South Coast Air Basin. *Atmospheric Environment* **2001**, *35*, (6) 1069-1077.

(403) Rogge, W. F.; Hildemann, L. M.; Mazurek, M. A.; Cass, G. R.; Simoneit, B. R. T., Sources of fine organic aerosol 2: Noncatalyst and catalyst-equipped

automobiles and heavy-duty diesel trucks. *Environmental Science & Technology* **1993**, *27*, (4) 636-651.

(404) Seagrave, J.; McDonald, J. D.; Gigliotti, A. P.; Nikula, K. J.; Seilkop, S. K.; Gurevich, M.; Mauderly, J. L., Mutagenicity and in vivo toxicity of combined particulate and semivolatile organic fractions of gasoline and diesel engine emissions. *Toxicological Sciences* **2002**, *70*, (2) 212-226.

(405) Riediker, M.; Cascio, W. E.; Griggs, T. R.; Herbst, M. C.; Bromberg, P. A.; Neas, L.; Williams, R. W.; Devlin, R. B., Particulate matter exposure in cars is associated with cardiovascular effects in healthy young men. *American Journal of Respiratory & Critical Care Medicine* **2004**, *169*, (8) 934-940.

(406) Cass, G. R.; Hughes, L. A.; Bhave, P.; Kleeman, M. J.; Allen, J. O.; Salmon, L. G., The chemical composition of atmospheric ultrafine particles. *Philosophical Transactions of the Royal Society of London, Series A: Mathematical, Physical and Engineering Sciences* **2000**, *358*, (1775) 2581-2592.

(407) Kleeman, M. J.; Schauer, J. J.; Cass, G. R., Size and composition distribution of fine particulate matter emitted from motor vehicles. *Environmental Science and Technology* **2000**, *34*, (7) 1132-1142.

(408) Reilly, P. T. A.; Gieray, R. A.; Whitten, W. B.; Ramsey, J. M., Real-time characterization of the organic composition and size of individual diesel engine smoke particles. *Environmental Science and Technology* **1998**, *32*, (18) 2672-2679.

(409) Lehmann, U.; Mohr, M.; Schweizer, T.; Rutter, J., Number size distribution of particulate emissions of heavy-duty engines in real world test cycles. *Atmospheric Environment* **2003**, *37*, (37) 5247-5259.

(410) Zhang, K. M.; Wexler, A. S.; Niemeier, D. A.; Zhu, Y. F.; Hinds, W. C.; Sioutas, C., Evolution of particle number distribution near roadways. Part III: Traffic analysis and on-road size resolved particulate emission factors. **2005**, *39*, (22) 4155-4166.

(411) Tobias, H. J.; Beving, D. E.; Ziemann, P. J.; Sakurai, H.; Zuk, M.; McMurry, P. H.; Zarling, D.; Waytulonis, R.; Kittelson, D. B., Chemical analysis of diesel engine nanoparticles using a nano-DMA/thermal desorption particle beam mass spectrometer. *Environmental Science and Technology* **2001**, *35*, (11) 2233-2243.

(412) Tobias, H. J.; Kooiman, P. M.; Docherty, K. S.; Ziemann, P. J., Real-time chemical analysis of organic aerosols using a thermal desorption particle beam mass spectrometer. *Aerosol Science and Technology* **2000**, *33*, (1-2) 170-190.

(413) Canagaratna, M. R.; Jayne, J. T.; Ghertner, D. A.; Herndon, S.; Shi, Q.; Jimenez, J. L.; Silva, P. J.; Williams, P.; Lanni, T.; Drewnick, F.; Demerjian, K. L.; Kolb, C. E.; Worsnop, D. R., Chase studies of particulate emissions from in-use New York City vehicles. *Aerosol Science & Technology* **2004**, *38*, (6) 555-573.

(414) Bhave, P. V.; Fergenson, D. P.; Prather, K. A.; Cass, G. R., Source apportionment of fine particulate matter by clustering single-particle data: tests of receptor model accuracy. *Environmental Science and Technology* **2001**, *35*, (10) 2060-2072.

(415) Bein, K. J.; Zhao, Y.; Pekney, N. J.; Davidson, C. I.; Johnston, M. V.; Wexler, A. S., Identification of sources of atmospheric PM at the Pittsburgh Supersite-Part II: Quantitative comparisons of single particle, particle number, and particle mass measurements. *Atmospheric Environment* **2006**, *40*, (Suppl. 2) S424-S444.

(416) Owega, S.; Evans, G. J.; Jervis, R. E.; Fila, M.; D'Souza, R.; Khan, B.-U.-Z., Long-range sources of Toronto particulate matter (PM2.5) identified by Aerosol Laser Ablation Mass Spectrometry (LAMS). *Atmospheric Environment* **2004**, *38*, (33) 5545-5553.

(417) Su, Y.; Sipin, M. F.; Furutani, H.; Prather, K. A., Development and characterization of an aerosol time-of-flight mass spectrometer with increased detection efficiency. *Analytical Chemistry* **2004**, *76*, (3) 712-719.

(418) Sodeman, D. A.; Toner, S. M.; Prather, K. A., Determination of single particle mass spectral signatures from light duty vehicle emissions. *Environmental Science & Technology* **2005**, *39*, (12) 4569-4580.

(419) Shields, L. G.; Suess, D. T.; Prather, K. A., Determination of single particle mass spectral signatures from heavy duty diesel vehicle emissions for $PM_{2.5}$ source apportionment. *Atmospheric Environment* **2007**, *41*, (18) 3841-3852.

(420) Song, X.-H.; Hopke, P. K.; Fergenson, D. P.; Prather, K. A., Classification of single particles analyzed by ATOFMS using an artificial neural network, ART-2A. *Analytical Chemistry* **1999**, *71*, (4) 860-865.

(421) Toner, S. M.; Shields, L. G.; Prather, K. A., Source apportionment of freeway-side $PM_{2.5}$ using ATOFMS. **2007**, *manuscript in preparation*.

(422) Kawai, T.; Goto, Y.; Odaka, M., Influence of dilution process on engine exhaust nano-particles. *Society of Automotive Engineers, [Special Publication] SP* **2004**, *SP-1862*, (Emissions Measurement & Testing) 113-119.

(423) Graskow, B. R.; Ahmadi, M. R.; Morris, J. E.; Kittelson, D. B., Influence of fuel additives and dilution conditions on the formation and emission of exhaust particulate matter from a direct injection spark ignition engine. *Society of Automotive Engineers, [Special Publication] SP* **2000**, *SP-1551*, (Diesel and Gasoline Performance and Additives) 261-271.

(424) Song, X. H.; Faber, N. M.; Hopke, P. K.; Suess, D. T.; Prather, K. A.; Schauer, J. J.; Cass, G. R., Source apportionment of gasoline and diesel by multivariate calibration based on single particle mass spectral data. *Analytica Chimica Acta* **2001**, *446*, (1-2) 329-343.

(425) Johnson, T. V., Diesel emission control technology - 2003 in review. *Society of Automotive Engineers, [Special Publication] SP* **2004**, *SP-1835*, (Diesel Emissions) 1-14.

(426) Gorse, R. A., Jr., On-road emission rates of carbon monoxide, nitrogen oxides, and gaseous hydrocarbon. *Environmental Science and Technology* **1984**, *18*, (7) 500-507.

(427) Funasaka, K.; Miyazaki, T.; Kawaraya, T.; Tsuruho, K.; Mizuno, T., Characteristics of particulates and gaseous pollutants in a highway tunnel. *Environmental Pollution* **1998**, *102*, (2-3) 171-176.

(428) Robert, M. A.; Jakober, C. A.; VanBergen, S.; Kleeman, M. J., Size and composition distributions of particulate matter emissions 1. Light duty gasoline vehicles. **2007**, *submitted for publication*.

(429) Robert, M. A.; Jakober, C. A.; Kleeman, M. J., Size and composition distributions of particulate matter emissions 2. Heavy duty diesel vehicles. **2007**, *submitted for publication.*

(430) Kittelson, D. B.; Watts, W. F.; Johnson, J. P.; Schauer, J. J.; Lawson, D. R., On-road and laboratory evaluation of combustion aerosols-Part 2: Summary of spark ignition engine results. *Journal of Aerosol Science* **2006**, *37*, (8) 931-949.

(431) Zhao, W.; Hopke, P. K., Source apportionment for ambient particles in the San Gorgonio wilderness. *Atmospheric Environment* **2004**, *38*, (35) 5901-5910.

(432) Imhof, D.; Weingartner, E.; Ordonez, C.; Gehrig, R.; Hill, M.; Buchmann, B.; Baltensperger, U., Real-world emission factors of fine and ultrafine aerosol particles for different traffic situations in Switzerland. *Environmental Science and Technology* **2005**, *39*, (21) 8341-8350.

(433) Schauer, J. J.; Rogge, W. F.; Hildemann, L. M.; Mazurek, M. A.; Cass, G. R.; Simoneit, B. R. T., Source apportionment of airborne particulate matter using organic compounds as tracers. *Atmospheric Environment* **1996**, *30*, (22) 3837-3855.

(434) Kleeman, M. J.; Ying, Q.; Lu, J.; Mysliwiec, M. J.; Griffin, R. J.; Chen, J.; Clegg, S., Source apportionment of secondary organic aerosol during a severe photochemical smog episode. *Atmospheric Environment* **2007**, *41*, (3) 576-591.

(435) Buzcu-Guven, B.; Brown Steven, G.; Frankel, A.; Hafner Hilary, R.; Roberts Paul, T., Analysis and apportionment of organic carbon and fine particulate matter sources at multiple sites in the midwestern United States. *Journal of the Air & Waste Management Association* **2007**, *57*, (5) 606-619.

(436) Allen, J. O.; Mayo, P. R.; Hughes, L. S.; Salmon, L. G.; Cass, G. R., Emissions of size-segregated aerosols from on-road vehicles in the Caldecott Tunnel. *Environmental Science & Technology* **2001**, *35*, (21) 4189-4197.

(437) Fraser, M. P.; Buzcu, B.; Yue, Z. W.; McGaughey, G. R.; Desai, N. R.; Allen, D. T.; Seila, R. L.; Lonneman, W. A.; Harley, R. A., Separation of fine particulate matter emitted from gasoline and diesel vehicles using chemical mass balancing techniques. *Environmental Science & Technology* **2003**, *37*, (17) 3904-3909.

(438) Kleeman, M. J.; Schauer, J. J.; Cass, G. R., Size and composition distribution of fine particulate matter emitted from motor vehicles. *Environmental Science & Technology* **2000**, *34*, (7) 1132-1142.

(439) Miguel, A. H.; Kirchstetter, T. W.; Harley, R. A.; Hering, S. V., On-road emissions of particulate polycyclic aromatic hydrocarbons and black carbon from gasoline and diesel vehicles. *Environmental Science & Technology* **1998**, *32*, (4) 450-455.

(440) Watson, J. G.; Chow, J. C.; Lowenthal, D. H.; Pritchett, L. C.; Frazier, C. A.; Neuroth, G. R.; Robbins, R., Differences in the carbon composition of source profiles for diesel-powered and gasoline-powered vehicles. *Atmospheric Environment* **1994**, *28*, (15) 2493-2505.

(441) Toner, S. M.; Shields, L. G.; Sodeman, D. A.; Prather, K. A., Using mass spectral source signatures to apportion exhaust particles from gasoline and diesel powered vehicles in a freeway study using UF-ATOFMS. *Atmospheric Environment* **2007**, *doi:10.1016/j.atmosenv.2007.08.005*.

(442) Wenzel, R. J.; Liu, D. Y.; Edgerton, E.; Prather, K. A., Aerosol time-of-flight mass spectrometry during the Atlanta Supersite Experiment: 2. Scaling procedures. *Journal of Geophysical Research-Atmospheres* **2003**, *108*, (D7) 8427.

(443) Pelkmans, L.; Debal, P., Comparison of on-road emissions with emissions measured on chassis dynamometer test cycles. *Transportation Research Part D-Transport and Environment* **2006**, *11*, (4) 233-241.

(444) Johnson, J. P.; Kittelson, D. B.; Watts, W. F., Source apportionment of diesel and spark ignition exhaust aerosol using on-road data from the Minneapolis metropolitan area. *Atmospheric Environment* **2005**, *39*, (11) 2111-2121.

(445) Wahlin, P.; Palmgren, F.; Van Dingenen, R., Experimental studies of ultrafine particles in streets and the relationship to traffic. *Atmospheric Environment* **2001**, *35*, S63-S69.

(446) Zhang, K. M.; Wexler, A. S.; Niemeier, D. A.; Zhu, Y. F.; Hinds, W. C.; Sioutas, C., Evolution of particle number distribution near roadways. Part III: Traffic analysis and on-road size resolved particulate emission factors. *Atmospheric Environment* **2005**, *39*, (22) 4155-4166.

(447) Charron, A.; Harrison, R. M., Fine (PM2.5) and Coarse (PM2.5-10) Particulate Matter on A Heavily Trafficked London Highway: Sources and Processes. *Environmental Science and Technology* **2005**, *39*, (20) 7768-7776.

(448) Silva, P. J., Source profiling and apportionment of airborne particles: A new approach using aerosol time-of-flight mass spectrometry. Ph.D. Dissertation, University of California, Riverside. **2000**, p 428.

(449) Draxler, R. R.; Rolph, G. D., **2003**, *HYSPLIT (HYbrid Single-Particle Lagrangian Integrated Trajectory) Model access via NOAA ARL READY Website (http://www.arl.noaa.gov/ready/hysplit4.html).*Silver Spring, MD.

(450) Divita, F., Jr.; Ondov, J. M.; Suarez, A. E., Size spectra and atmospheric growth of V-containing aerosol in Washington, DC. *Aerosol Science and Technology* **1996**, *25*, (3) 256-273.

(451) Phares, D. J.; Rhoads, K. P.; Johnston, M. V.; Wexler, A. S., Size-resolved ultrafine particle composition analysis 2. Houston. *Journal of Geophysical Research, [Atmospheres]* **2003**, *108*, (D7) SOS 8/1-SOS 8/14.

(452) Ondov, J. M.; Choquette, C. E.; Zoller, W. H.; Gordon, G. E.; Biermann, A. H.; Heft, R. E., Atmospheric behavior of trace elements on particles emitted from a coal-fired power plant. *Atmospheric Environment (1967-1989)* **1989**, *23*, (10) 2193-2204.

(453) Rossini Oliva, S.; Fernandez Espinosa, A. J., Monitoring of heavy metals in topsoils, atmospheric particles and plant leaves to identify possible contamination sources. *Microchemical Journal* **2007**, *86*, (1) 131-139.

(454) Ault, A. P.; Furutani, H.; Dominguez, G.; Thiemens, M. H.; Prather, K. A., A mass spectral fingerprint of ship emission particles by aerosol time-of-flight mass spectrometry and applications for source apportionment. *In Preparation* **2007**.

(455) Gard, E. E.; Kleeman, M. J.; Gross, D. S.; Hughes, L. S.; Allen, J. O.; Morrical, B. D.; Fergenson, D. P.; Dienes, T.; Galli, M. E.; Johnson, R. J.; Cass, G. R.; Prather, K. A., Direct observation of heterogeneous chemistry in the atmosphere. *Science* **1998**, *279*, (5354) 1184 -1187.

(456) Song, X. H.; Hopke, P. K.; Fergenson, D. P.; Prather, K. A., Classification of single particles analyzed by ATOFMS using an artificial neural network, ART-2A. *Analytical Chemistry* **1999**, *71(4)*, 860-865.

(457) *Software toolkit to analyze single-particle mass spectral data - http://www.yaada.org*, 2006.

(458) Dockery, D. W.; Pope, C. A.; Xu, X. P.; Spengler, J. D.; Ware, J. H.; Fay, M. E.; Ferris, B. G.; Speizer, F. E., An Association between Air-Pollution and Mortality in 6 United-States Cities. *New England Journal of Medicine* **1993**, *329*, (24) 1753-1759.

(459) Pope, C. A.; Thun, M. J.; Namboodiri, M. M.; Dockery, D. W.; Evans, J. S.; Speizer, F. E.; Heath, C. W., Particulate air pollution as a predictor of mortality in a prospective study of US adults. *American Journal of Respiratory & Critical Care Medicine* **1995**, *151*, (3) 669-674.

(460) Grahame, T. J.; Schlesinger, R. B., Health effects of airborne particulate matter: Do we know enough to consider regulating specific particle types or sources? *Inhalation Toxicology* **2007**, *19*, (6-7) 457-481.

(461) Hopke, P. K. *Receptor modeling for air quality management*; Elsevier; Distributors in the United States and Canada, Elsevier Science Pub. Co.: Amsterdam; New York
New York, NY, USA, **1991**.

(462) Finlayson-Pitts, B. J.; Pitts, J. N. *Chemistry of the upper and lower atmosphere: theory, experiments, and applications*; Academic Press: San Diego, **2000**.

(463) Yakovleva, E.; Hopke, P. K.; Wallace, L., Receptor modeling assessment of particle total exposure assessment methodology data. *Environmental Science & Technology* **1999**, *33*, (20) 3645-3652.

(464) Rudich, Y., Laboratory perspectives on the chemical transformations of organic matter in atmospheric particles. *Chemical Reviews* **2003**, *103*, (12) 5097-5124.

(465) Kanakidou, M.; Seinfeld, J. H.; Pandis, S. N.; Barnes, I.; Dentener, F. J.; Facchini, M. C.; Van Dingenen, R.; Ervens, B.; Nenes, A.; Nielsen, C. J.; Swietlicki, E.; Putaud, J. P.; Balkanski, Y.; Fuzzi, S.; Horth, J.; Moortgat, G. K.; Winterhalter, R.; Myhre, C. E. L.; Tsigaridis, K.; Vignati, E.; Stephanou, E. G.; Wilson, J., Organic aerosol and global climate modelling: a review. *Atmospheric Chemistry and Physics* **2005**, *5*, 1053-1123.

(466) Broekhuizen, K.; Kumar, P. P.; Abbatt, J. P. D., Partially soluble organics as cloud condensation nuclei: Role of trace soluble and surface active species. *Geophysical Research Letters* **2004**, *31*, (1) -.

(467) Petters, M. D.; Prenni, A. J.; Kreidenweis, S. M.; DeMott, P. J.; Matsunaga, A.; Lim, Y. B.; Ziemann, P. J., Chemical aging and the hydrophobic-to-hydrophilic conversion of carbonaceous aerosol. *Geophysical Research Letters* **2006**, *33*, (24) -.

(468) Rojas, S.; Gomes, L.; Villani, P., Behavior of CCN to CN fraction during aging and mixing processes of atmospheric particles. *Atmospheric Chemistry and Physics Discussions* **2006**, *6*, 9545-9562.

(469) Shilling, J. E.; King, S. M.; Mochida, M.; Martin, S. T., Mass spectral evidence that small changes in composition caused by oxidative aging processes alter aerosol CCN properties. *Journal of Physical Chemistry A* **2007**, *111*, (17) 3358-3368.

(470) Furutani, H.; Dall'Osto, M.; Roberts, G. C.; Prather, K. A., Assessment of the relative importance of atmospheric aging on CCN activity derived from field observations, in press. *Atmospheric Environment*.

(471) Shields, L. G.; Su, Y.; Prather, K. A., Impact of the October 2003 San Diego wildfires on particle chemistry and aging processes, manuscript in preparation.

(472) Holecek, J. C.; Spencer, M. T.; Prather, K. A., Single particle analysis of rainwater samples: insoluble particles and direct comparisons with ambient concentrations from the Northeast Pacific and Indian Ocean. *Journal of Geophysical Research - Atmospheres* **2007**, *Accepted*.

(473) Wilcox, E. M.; Roberts, G.; Ramanathan, V., Influence of aerosols on the shortwave cloud radiative forcing from North Pacific oceanic clouds: Results from the Cloud Indirect Forcing Experiment (CIFEX). *Geophysical Research Letters* **2006**, *33*, (21).

(474) Spencer, M. T.; Holecek, J. C.; Corrigan, C. E.; Ramanathan, V.; Prather, K. A., Size-resolved chemical composition of individual particles during a monsoonal transition period in the north Indian Ocean. *Journal of Geophysical Research - Atmospheres* **2007**, *Submitted*.

(475) Moffet, R. C.; de Foy, B.; Molina, L. T.; Molina, M. J.; Prather, K. A., Characterization of ambient aerosols in northern Mexico City by single particle mass spectrometry. **2007**, *manuscript in preparation*.

(476) Toner, S. M.; Moffet, R. C.; Dall'Osto, M.; Harrison, R. M.; Prather, K. A., Source apportionment of PM2.5 in Athens (Greece) and Mexico City using an ATOFMS derived mass spectral source library, manuscript in preparation.

(477) Shields, L. G.; QIn, X.; Toner, S. M.; Prather, K. A., Detection of ambient ultrafine aerosols by single particle techniques during the SOAR 2005 campaign, submitted. *Aerosol Science and Technology*.

(478) Kittelson, D. B.; Watts, W. F.; Johnson, J. P.; Schauer, J. J.; Lawson, D. R., On-road and laboratory evaluation of combustion aerosols - Part 2: Summary of spark ignition engine results. *Journal of Aerosol Science* **2006**, *37*, (8) 931-949.

(479) Giechaskiel, B.; Ntziachristos, L.; Samaras, Z.; Scheer, V.; Casati, R.; Vogt, R., Formation potential of vehicle exhaust nucleation mode particles on-road and in the laboratory. *Atmospheric Environment* **2005**, *39*, (18) 3191-3198.

(480) Sawant, A. A.; Na, K.; Zhu, X. N.; Cocker, D. R., Chemical characterization of outdoor PM2.5 and gas-phase compounds in Mira Loma, California. *Atmospheric Environment* **2004**, *38*, (33) 5517-5528.

(481) Arimoto, R.; Kim, Y. J.; Kim, Y. P.; Quinn, P. K.; Bates, T. S.; Anderson, T. L.; Gong, S.; Uno, I.; Chin, M.; Huebert, B. J.; Clarke, A. D.; Shinozuka, Y.; Weber, R. J.; Anderson, J. R.; Guazzotti, S. A.; Sullivan, R. C.; Sodeman, D. A.; Prather, K. A.; Sokolik, I. N., Characterization of Asian Dust during ACE-Asia. *Global and Planetary Change* **2006**, *52*, (1-4) 23-56.

(482) Langmann, B.; Herzog, M.; Graf, H. F., Radiative forcing of climate by sulfate aerosols as determined by a regional circulation chemistry transport model. *Atmospheric Environment* **1998**, *32*, (16) 2757-2768.

# V. Appendices

## *Publications and Presentations*

### 1. Publications


1) Qin, X. Y.; Bhave, P. V.; Prather, K. A., Comparison of two methods for obtaining quantitative mass concentrations from aerosol time-of-flight mass spectrometry measurements. Anal. Chem. 2006, 78, (17) 6169-6178.
2) Shields, L. G.; Qin, X.; Toner, S. M.; Prather, K. A., Detection of ambient ultrafine aerosols by single particle techniques during the SOAR 2005 campaign. Aerosol Sci. Technol. 2008.
3) Toner, S. M.; Shields, L. G.; Sodeman, D. A.; Prather, K. A., Using mass spectral source signatures to apportion exhaust particles from gasoline and diesel powered vehicles in a freeway study using UF-ATOFMS. Atmos. Environ. 2008, 42, (3) 568-581.
4) Pratt, K. A.; Prather, K. A., Real-time, single-particle volatility, size, and chemical composition measurements of aged urban aerosols. Environ. Sci. Technol. 2009, In Preparation.
5) Ault, A. P.; Moore, M. J.; Furutani, H.; Prather, K. A., Impact of emissions from the Los Angeles port region on San Diego air quality. Environ. Sci. Technol. 2009, 43, (10) 3500-3506.
6) Pratt, K. A.; Hatch, L. E.; Prather, K. A., Seasonal volatility dependence of ambient particle phase amines. Environ. Sci. Technol. 2009, 43, (14) 5276-5281.
7) Ault, A.; Gaston, C.; Wang, Y.; Dominguez, G.; Thiemens, M. H.; Prather, K., Characterization of the Single Particle Mixing State of Individual Ship Plume Events measured at the Port of Los Angeles. Environ. Sci. Technol. 2009, submitted.
8) Toner, S. M.; Moffet, R. C.; Dall'Osto, M.; Harrison, R. M.; Prather, K. A., Source apportionment of PM2.5 in Athens (Greece) and Mexico City using an ATOFMS derived mass spectral source library. Atmos. Environ. in prep.
9) Toner, S. M.; Shields, L. G.; Prather, K. A., Source Apportionment of freeway-side PM2.5 using ATOFMS. Atmos. Environ. in prep.
10) Shields, L. G.; Qin, X.; Toner, S. M.; Prather, K. A., Aging effects on source apportionment from the single particle perspective. Atmos. Environ. in prep.
11) Shields, L. G.; Qin, X.; Toner, S. M.; Prather, K. A., Characterization of tracemetals in single urban particles during the SOAR 2005 campaign. Science of the Total Environment in prep.
12) Qin, X.; Shields, L. G.; Toner, S. M.; Prather, K. A., Single Particle Characterization in Riverside, CA during the SOAR 2005 Campaign – Part 1: Seasonal Comparisons. Environ. Sci. Technol. in prep.
13) Qin, X.; Prather, K. A., The Effect of APS Scaling functions on the Quantification of Aerosol Time-of-Flight Mass Spectrometry. Atmos. Environ. in prep.
14) Yandell, M. A.; Ault, A. P.; Pratt, K. A.; Wang, Y.; Zauscher, M.; Gaston, C. J.; Prather, K. A., Air pollution transport from the Ports of Long Beach and Los

Angeles and its impacts on the local community. Aerosol Sci. Technol. 2009, In Prep.

15) Creamean, J. M.; Pratt, K. A.; Ault, A. P.; Qin, X.; Gaston, C. J.; Shields, L. G.; Prather, K. A., Inter-annual Comparison of Real-Time, Single-Particle Ambient Aerosol Measurements Using ATOFMS in Riverside, CA. 2009, in prep.
16) Ault, A. P.; Creamean, J. M.; Prather, K. A., Mobile Laboratory Observations of Temporal and Spatial Variability within the Coastal Urban Aerosol. Aerosol Sci. Technol. in prep.

## 2. Presentations

1) **Qin, X.Y.**; Bhave, P.V.; Prather, K.A.; ATOFMS single particle measurements and quantification. ACS Spring 2005 National Meeting San Diego, CA March, **2005**
2) **Shields L.G.**, Suess D.T., Prather K.A. Determination of single particle mass spectral signatures from heavy duty vehicle emissions in the 0.1 to 3 micrometer size range. ACS Spring 2005 National Meeting San Diego, CA March, **2005**
3) **Toner, S.M.,** Shields, L.G., Sodeman, D.A., Prather, K.A.; Using mass spectral source signatures to apportion exhaust particles from gasoline and diesel powered vehicles in a freeway study. ACS Spring 2005 National Meeting San Diego, CA March, **2005**.
4) **Prather, K.A.**; Sullivan, R.C; Guazzotti, S.; Denkenberger, K.A.; Holecek, J.; Moffet, R.C.; Spencer, M.T.; Qin, X.Y.; Using the temporal variability of single particle mixing state to understand aging, heterogeneous chemistry, and the sources of atmospheric particles. ACS Spring **2006** National Meeting
5) **X. Qin** and K. A. Prather. "Direct Measurements of Ambient Aerosols Mixing State and Source Apportionment Using Single Particle Mass Spectrometry", Invited Talk, United States Department of Agriculture, Manhattan, KS, March, 2007.
6) **X. Qin** and K. A. Prather. "Direct Measurements of Ambient Aerosols Mixing State Using Single Particle Mass Spectrometry", Invited Talk, NanoScale Corporation, Manhattan, KS, March, 2007.
7) **Ault, Andrew P.**; Dominguez, G.; Furutani, H.; Thiemens, M.; Prather, K A Mass Spectral Fingerprint of Ship Emission Particles by Aerosol Time-of-Flight Mass Spectrometry. *AAAR 26th Annual conference*, Reno, NV, United States, September 24-28, **2007**.
8) **Ault, Andrew**; Gaston, Cassandra, Wang, Ying, Kimberly Prather Observation and Characterization of Individual Ship Plumes by Aerosol Time-of-Flight Mass Spectrometry. *25th Informal Symposium on Kinetics and Photochemical Processes in the Atmosphere*, UCLA, Los Angeles California, February 19, **2008**.
9) **Ault, A.**; Gaston, C; Wang, Y.; Zauscher, M.; Moison, R; Prather, K; Single Particle Observations of Variability within the Urban Aerosol. *AAAR 27th Annual Conference*, Orlando, FL, United States, October 20-24, **2008**.
10) **Yandell, Margaret A.**; Ault, Andrew P.; Pratt, Kerri A.; Wang, Ying; Zauscher, Melanie; Gaston, Cassandra J.; Prather, Kimberly A. Air pollution transport from the Ports of Long Beach and Los Angeles and its impacts on the local community. 26th Informal Symposium on Kinetics and Photochemical Processes in the

Atmosphere. Informal Conference on Atmospheric Kinetics University of California, Riverside, **2009**.

11) **Ault, A.P.**; Creamean, J.M.; Prather, K.A.; Measurements of Spatial Variability in the Urban Atmosphere With Aerosol Time-of-Flight Mass Spectrometry. *AAAR 28th Annual Conference*, Minneapolis, MN, United States, October 26-30, **2009**